Development of Single-Source CVD Precursors for Group IV, V and VI Metal Disulfides

Thompson, Joseph

Award date:
2017

Awarding institution:
University of Bath

Development of Single-Source CVD Precursors for Group IV, V and VI Metal Disulfides

Joseph Robert Thompson

A thesis submitted for the degree of Doctor of Philosophy

University of Bath

Department of Chemistry

October 2016

Contents

Acknowledgements

First and foremost I would like to thank Andy Johnson for giving me such an interesting and exciting project to work on. I have thoroughly enjoyed my time working in the Johnson Group and I am grateful for Andy's patience, support, friendship and guidance throughout my postgraduate years. I would also like to thank Daniel Wolverson for his advice throughout my PhD.

Words cannot describe the Johnson Group office, from perfectly flat to Jurassic Park I have enjoyed every minute. Thank you to Dave, Jeff, Andrew, Jamie, Prem, Hannah, Anna, Ibbi and Sam for getting me through this. Thanks also to Tilly and Emily for being such great project students. A big thank you to DTC cohort 2012 for an amazing four years, it has been awesome. I would also like to thank Alex, Anneke, Matt, Amanda, Niall and all the other chemists who have made my time in Bath such a happy one.

For all the technical help I have received, I would like to thank Dr John Mitchels, Mrs Ursula Potter and Dr Philip Fletcher in MAS, as well as Dr Gabriele Kociok-Köhn, Dr John Lowe and Dr Rémi Castaing in CCAF. I would also like to thank all those in the Material Properties & Surface Analysis department at NSG Group.

I am also grateful to the Centre for Sustainable Chemical Technologies, University of Bath, and EPSRC for providing the facilities and funding to perform the work presented. I would also like to thank all of those at NSG Group in Lathom for giving me the opportunity to work with them on my placement.

A big thank you to my family for their continuous support and encouragement. I would especially like to thank Mum and Emily for all of their proof reading. And to Tash for being the light at the end of the PhD tunnel.

Declaration

The work described in this thesis was conducted by the author at the University of Bath between October 2013 and October 2016. It represents the author's original and independent work, except where specific reference is made to the contrary. This thesis does not exceed the prescribed limit, including tables, references and appendices.

Abstract

Transition metal dichalcogenides (TMDs) exhibit a wide range of interesting properties and potential applications. The major barrier to the use of these materials in devices is the formation of high quality thin films. Chemical vapour deposition (CVD) is a scalable technique which can provide high quality thin films over large areas. The principal objective of this work is to synthesise and characterise a range of single-source precursors for the deposition of metal disulfides.

Chapter 1 provides an introduction to the applications, properties and synthesis of TMDs. An overview of CVD highlights the major variants used while the major classes of metal chalcogenide single-source precursors are reviewed.

Chapter 2 describes the synthesis, characterisation and structures of group IV metal thioureide complexes formed by the insertion of isothiocyanates into group IV metal amides. Heteroleptic and homoleptic group IV metal dithiocarbamates are also investigated with selected complexes used as precursors in aerosol-assisted CVD (AACVD) and low pressure CVD (LPCVD) experiments.

Chapter 3 describes the synthesis, characterisation and structures of tantalum thioureide complexes formed by the insertion of isothiocyanates into PDMAT or [(^{t}BuN)Ta(NMe_2)$_3$]. Thermal decomposition studies of these complexes are discussed. *tert*-butylimide based tantalum dithiocarbamates are also investigated as both AACVD and LPCVD precursors for the deposition of TaS_2.

Chapter 4 describes the synthesis, characterisation and structures of group VI metal thioureide complexes formed by the reactions of bis(*tert*-butylimido)bis(amido) group VI metal complexes and either isothiocyanates or disubstituted thioureas. The suitability of these complexes as AACVD precursors is explored. Homoleptic group VI metal dithiocarbamates and xanthates are also investigated as AACVD precursors. Deposition of WS_2 onto graphene substrates is studied using the precursor [$W(S_2CNEt_2)_4$].

Chapter 5 contains experimental procedures and characterisation data for the complexes and thin films described.

Appendix lists the crystal structure refinement tables and EDX analysis spectra.

List of complexes

(**1**) $[(Me_2N)_2Ti(SC\{NMe_2\}N^iPr)_2]$

(**2**) $[(Me_2N)_2Ti(SC\{NMe_2\}N^tBu)\ (SC\{N^tBu\}NMe_2)]$

(**3**) $[(Me_2N)_2Ti(SC\{NMe_2\}NPh)_2]$

(**4**) $[\{Ti(SC\{NMe_2\}NPh)_2(\mu\text{-}S)\}_2]$

(**5**) $[(Me_2N)Zr(Me_2NC\{S\}N^iPr)(SC\{NMe_2\}N^iPr)_2]$

(**6**) $[(Me_2N)Zr(SC\{NMe_2\}N^tBu)(SC\{N^tBu\}NMe_2)_2]$

(**7**) $[Zr(SC\{NMe_2\}NPh)_4]$

(**8**) $[(Me_2N)Hf(Me_2NC\{S\}N^iPr)(SC\{NMe_2\}N^iPr)_2]$

(**9**) $[(Me_2N)Hf(SC\{NMe_2\}N^tBu)(SC\{N^tBu\}NMe_2)_2]$

(**10**) $[(Me_2N)Hf(SC\{NMe_2\}NPh)_3]$

(**11**) $[Ti(S_2CNEt_2)_4]$

(**11a**) $[\{\mu\text{-}O\}\{Ti(S_2CNEt_2)_3\}_2]$

(**12**) $[Zr(S_2CNEt_2)_4]$

(**13**) $[Hf(S_2CNEt_2)_4]$

(**14**) $[Zr(S_2CNEtMe)_4]$

(**15**) $[Hf(S_2CNEtMe)_4]$

(**16**) $[CpTi(S_2CNEt_2)_3]$

(**17**) $[CpZr(S_2CNEt_2)_3]$

(**18**) $[(Me_2N)_4Ta(Me_2NC\{N^iPr\ \}S)]$

(**19**) $[(Me_2N)_4Ta(Me_2NC\{S\}N^tBu)]$

(**20**) $[(^tBuN)Ta(NMe_2)_3]$

(**21**) $[(^tBuN)Ta(NMe_2)(SC\{NMe_2\}N^iPr)_2]$

(**22**) $[(^tBuN)Ta(SC\{NMe_2\}NPh)_3]$

(**23**) $[(^tBuN)Ta(S_2CNMe_2)_3]$

(**24**) $[(^{t}BuN)Ta(S_2CNEt_2)_3]$

(**25**) $[(^{t}BuN)Ta(SC_3H_4NS)_3]$

(**26**) $[(^{t}BuN)_2Mo(NMe_2)_2]$

(**26a**) $[(^{t}BuN)_2MoCl_2(dme)]$

(**26b**) $[(^{t}BuN)_2MoCl_2py_2]$

(**27**) $[(^{t}BuN)_2W(NH^{t}Bu)_2]$

(**28**) $[(^{t}BuN)_2Mo(SC\{NHMe\}NMe)_2]$

(**29**) $[(^{t}BuN)_2Mo(SC\{NHEt\}NEt)_2]$

(**30**) $[(^{t}BuN)_2Mo(SC\{NH^{n}Bu\}N^{n}Bu)_2]$

(**31**) $[(^{t}BuN)W(MeNC\{S\}NMe)(NH^{t}Bu)(SC\{NHMe\}NMe)]$

(**32**) $[(^{t}BuN)W(EtNC\{S\}NEt)(NH^{t}Bu)(SC\{NHEt\}NEt)]$

(**33**) $[(^{t}BuN)W(^{n}BuNC\{S\}N^{n}Bu)(NH^{t}Bu)(SC\{NH^{n}Bu\}N^{n}Bu)]$

(**34**) $[\{(^{t}BuN)W(SC\{NH^{t}Bu\}N^{t}Bu)(\mu\text{-}S)\}_2]$

(**35**) $[^{t}Bu(Me_3Si)NH]$

(**36**) $[(^{t}BuN)_2W(NMe_2)_2]$

(**36a**) $[(^{t}BuN)_2WCl_2(NH_2{}^{t}Bu)]_2$

(**36b**) $[(^{t}BuN)_2WCl_2py_2]$

(**37**) $[(^{t}BuN)_2Mo(SC\{NMe_2\}N^{i}Pr)_2]$

(**38**) $[(^{t}BuN)_2Mo(SC\{NMe_2\}NPh)_2]$

(**39**) $[(^{t}BuN)_2W(SC\{NMe_2\}N^{i}Pr)_2]$

(**40**) $[(^{t}BuN)_2W(SC\{NMe_2\}NPh)_2]$

(**41**) $[Mo(S_2CNEt_2)_4]$

(**42**) $[W(S_2CNEt_2)_4]$

(**43**) $[Mo(S_2COEt)_4]$

(**44**) $KS_2CO^{i}Pr$

(**45**) $[Mo(S_2CO^{i}Pr)_4]$

Abbreviations

AACVD	Aerosol-Assisted Chemical Vapour Deposition
AFM	Atomic Force Microscopy
ALD	Atomic Layer Deposition
CDW	Charge Density Wave
CVD	Chemical Vapour Deposition
DCM	Dichloromethane
dme	1,2-dimethoxyethane
E	Chalcogen (S, Se and Te)
e.s.d.s	Estimated Standard Deviations
EDX	Energy-Dispersive X-ray Spectroscopy
FET	Field Effect Transistor
H	Hexagonal
h-BN	Hexagonal Boron Nitride
HER	Hydrogen Evolution Reaction
IPA	Iso-propanol
JCPDS	Joint Committee on Powder Diffraction Standards
LPCVD	Low Pressure Chemical Vapour Deposition
M	Metal
MBE	Molecular Beam Epitaxy
NMR	Nuclear Magnetic Resonance
PDMAT	Pentakis(dimethylamido)tantalum(V) [$Ta(NMe_2)_5$]
PMMA	Poly(methylmethacrylate)
PXRD	Powder X-ray Diffraction
py	Pyridine

R	Rhombohedral
RMS	Root Mean Square
SEM	Scanning Electron Microscope
T	Trigonal
TGA	Thermogravimetric Analysis
TGA-MS	Thermogravimetric Analysis - Mass Spectrometry
THF	Tetrahydrofuran
TMD	Transition Metal Dichalcogenide
VSEPR	Valence Shell Electron Pair Repulsion
XPS	X-ray Photoelectron Spectroscopy

Chapter 1

Introduction

1.1 Two dimensional materials

Two dimensional (2D) materials consist of single crystalline layers of atomic thickness.[1] In most 2D materials these layers are one atom thick (e.g. graphene) although some materials like transition metal dichalcogenides (TMDs) have layers which are three atoms thick.[2] The major interest in these 2D materials is due to their electronic properties, which differ quite dramatically to those found in the bulk.[3]

The isolation of graphene by Andre Geim and Konstantin Novoselov in 2004 generated huge interest in this area of research, which has expanded rapidly in recent years.[4] The majority of early work focussed on graphene but this has now expanded to encompass a variety of other layered compounds. Materials of interest include: silicene, germanene, phosphorene, TMDs, layered metal oxides, metal halides and hexagonal boron nitride (h-BN), although this list is continually expanding. These 2D materials can be insulators, semiconductors, conductors and even superconductors, providing a wide range of electronic properties. Figure 1.1 shows the structures of a variety of 2D materials, side-on views show the atomically thin nature of the layers which can be one to four atoms thick and can be planar or puckered.[1, 2, 5]

While graphene has extremely impressive properties such as high electron mobility, strength and flexibility, materials with alternative electronic properties are also required for the fabrication of electronic devices.[6] The combination of graphene with other 2D materials allows the development of Van der Waals heterostructures which greatly expands the scope of 2D materials. These heterostructures resemble stacks of bricks with each brick representing a different 2D material. Altering the stacking sequence or the identity of the various 2D materials provides a variety of different electronic devices. Examples of Van der Waals heterostructure devices include: photovoltaic cells, thermoelectric cells and field effect transistors (FETs).[7] Amongst the 2D materials, TMDs probably possess the greatest range of electronic properties and are extremely popular due to the semiconducting nature of MoS_2 and WS_2.[2]

The focus of this thesis is the development of CVD precursors for the deposition of TMDs. The following section will discuss selected aspects of the chemistry and physics of 2D TMDs.

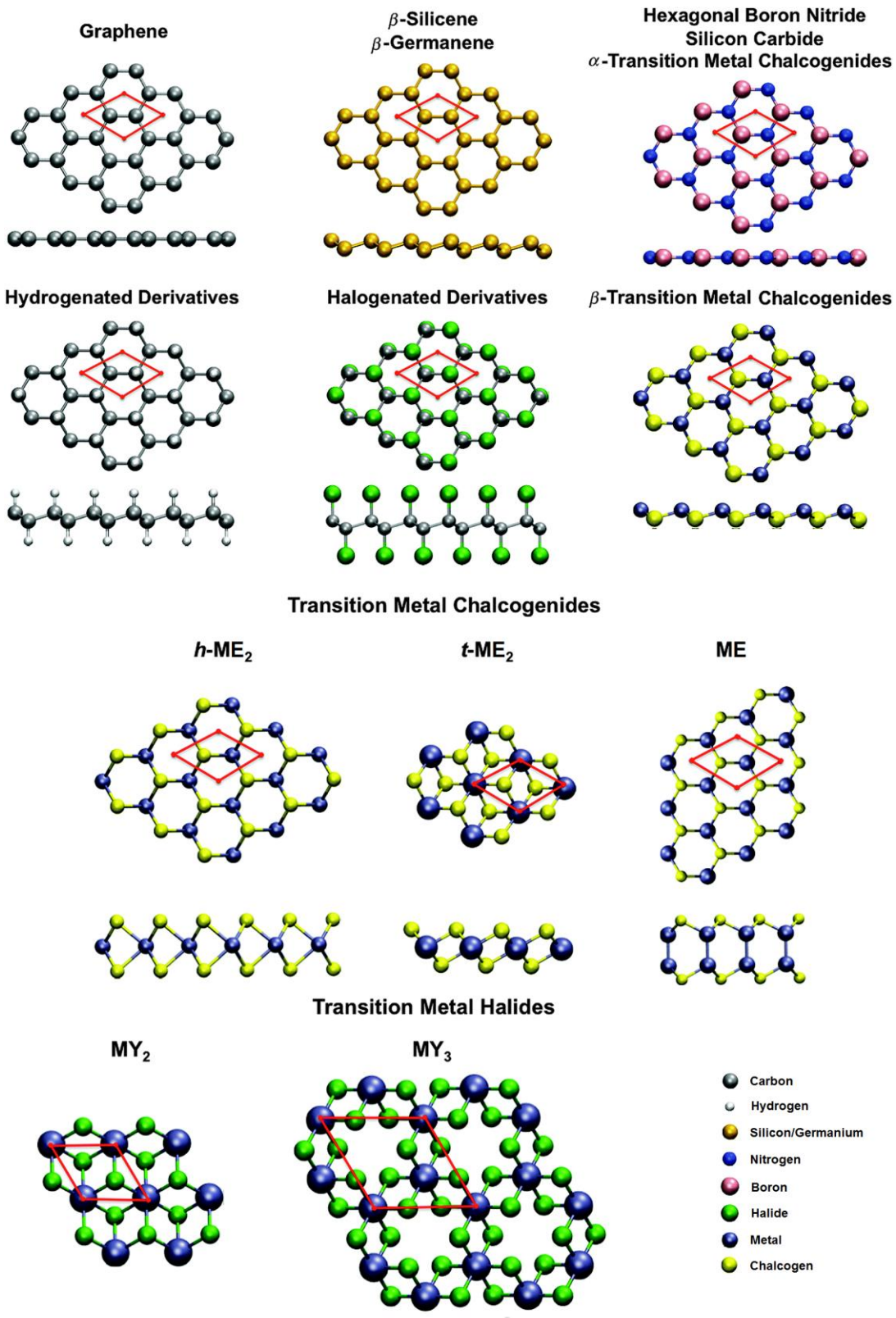

Figure 1.1 Structures of various 2D materials (unit cell in red, *h* – hexagonal, *t* - trigonal), adapted from reference.[5]

1.2 Transition metal dichalcogenides

TMDs are a group of compounds that possess the formula ME_2, where M is a transition metal and E is a chalcogen (sulfur, selenium or tellurium). The majority of TMDs (Figure 1.2) adopt a layered structure composed of individual monolayers stacked on top of each other. Similar to graphene, these monolayers can be isolated and their properties differ to that of the bulk.[2] While graphene is a zero band gap semimetal, TMDs possess a wide variety of electronic properties from semiconducting to superconducting.[4, 8] These materials are extremely anisotropic with mechanical and electronic properties differing when measured in plane and perpendicular to the plane.[9] This wide range of properties makes TMDs extremely useful in two dimensional device fabrication. Only TMDs that adopt a layered structure will be covered in this thesis.

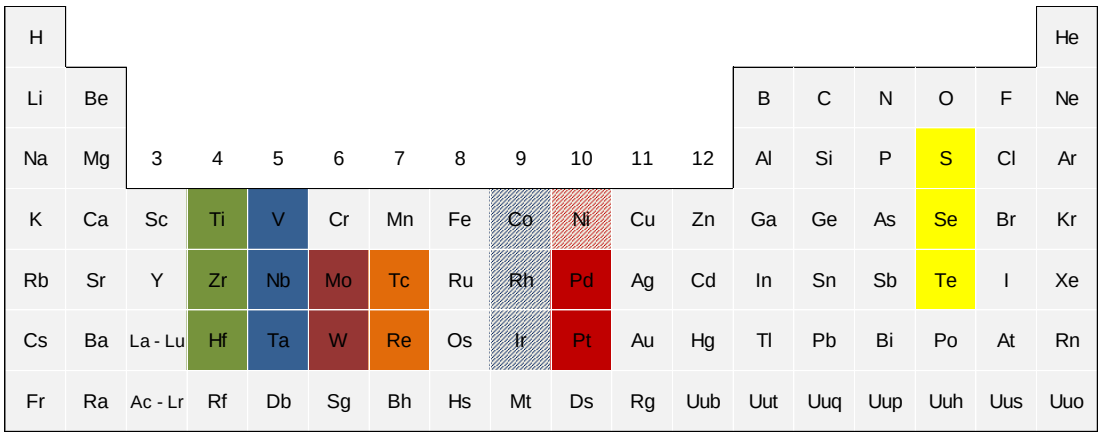

Figure 1.2 The highlighted elements adopt layered TMD structures; the partially highlighted elements only adopt a layered structure with some of the chalcogens.[2]

1.2.1 Structure

The layered structure of TMDs, as shown in Figure 1.3, is composed of individual E-M-E layers which stack to form the bulk material. Within each E-M-E layer is a three atom thick stack where a hexagonally packed layer of transition metal atoms is sandwiched between two layers of chalcogen atoms. Bonding within the E-M-E layer is mainly covalent whereas the separate layers are held together by Van der Waals forces.[10] It is these weak interactions between the E-M-E layers that allow single sheets (monolayers) of TMDs to be isolated. The monolayers are typically 6 – 7 Å thick and their properties can differ quite drastically to those of the bulk.[2, 9]

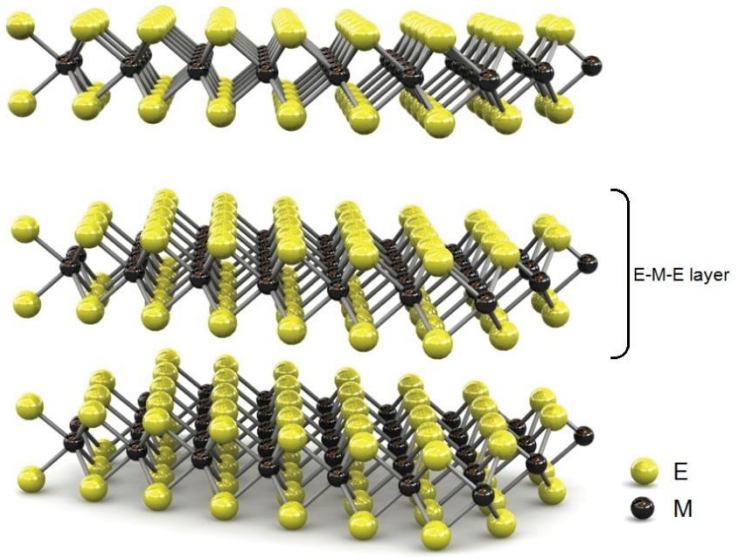

Figure 1.3 Layered structure of TMDs, adapted from reference.[11]

TMDs can adopt a wide variety of polymorphs and polytypes due to differing metal atom coordination environments and a variety of stacking sequences. The chalcogen atoms can coordinate to the metal centre in either an octahedral (O_h or D_{3d} point group) or more commonly a trigonal prismatic (D_{3h} point group) geometry with the environment dependant on the metal and chalcogen combination. Monolayers of TMDs only exhibit octahedral or trigonal prismatic geometries, as shown in Figure 1.4.[2, 9]

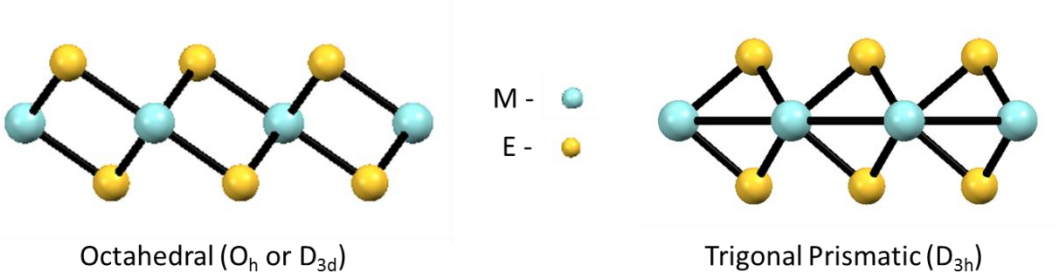

Figure 1.4 Metal atom coordination geometries in monolayer TMDs, view down b axis.[12, 13]

Figure 1.5 shows the three main stacking sequences exhibited in bulk TMDs: 1T, 2H and 3R, where the digit represents the number of layers within the unit cell and the letter corresponds to trigonal, hexagonal and rhombohedral respectively. The 1T phase is typically adopted by group 4 chalcogenides with the metal centre exhibiting an octahedral geometry. The metal atoms within the layers sit directly above those in the layers above and below.[12] The 2H phase is most commonly found in natural

group 6 chalcogenides with the metal centre adopting a trigonal prismatic geometry. Here, the unit cell contains two layers with metal atoms in one layer sitting above the chalcogenide atoms in the layer below or above.[13] The 3R phase is frequently found in synthetic group 6 chalcogenides; again the metal centre adopts a trigonal prismatic geometry. Within the three layer unit cell, a metal atom sits above the chalcogen atom in the layer below and below a void in the layer above.[2, 9, 14]

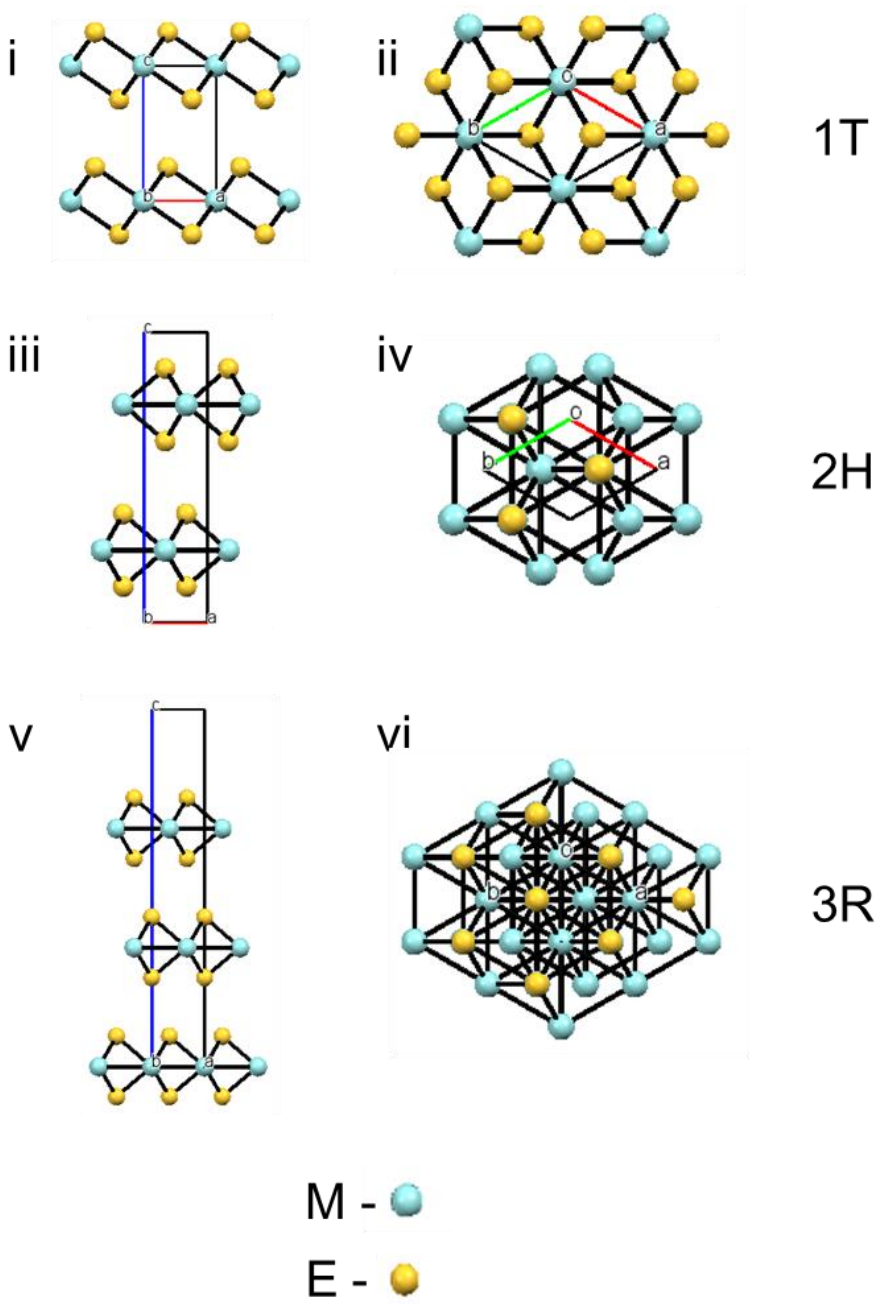

Figure 1.5 1T, 2H and 3R stacking sequences of TMDs – i, iii, v: viewed down b axis – ii, iv, vi: viewed down c axis. a, b and c denote the crystallographic axes and o the origin.[12-14]

1.2.2 Electronic properties

Depending on the metal and chalcogen combination (Table 1.1), TMDs can be: semiconductors (MoS_2 and WS_2), semimetals (WTe_2 and $TiSe_2$), true metals (NbS_2 and VSe_2) or even superconductors at low temperatures ($NbSe_2$ and TaS_2). The metal atoms within the TMD are in the +4 oxidation state while the two chalcogen atoms are in the -2 oxidation state. Each metal atom provides four electrons to the bonding states whilst the chalcogen atoms both provide two.[2, 15] TMDs are highly anisotropic with conductivities in the plane of the layers a factor of 10^2 greater than those measured perpendicular to the layers.[9] Some of these materials are also highly efficient at absorbing light with absorption coefficients in the region of 10^7 cm^{-1}.[16]

Table 1.1 Electronic properties of TMDs, adapted from reference.[2]

Group	Metals	Properties
4	Ti, Zr, Hf	Semimetallic or semiconducting, diamagnetic.
5	V, Nb, Ta	Metallic or semimetallic, superconducting, charge density wave (CDW). Paramagnetic, antiferromagnetic or diamagnetic.
6	Mo, W	Sulfides and selenides are semiconducting, tellurides are semimetallic, diamagnetic.
7	Tc, Re	Small band gap semiconductors, diamagnetic
10	Pd, Pt	Sulfides and selenides are semiconducting and diamagnetic. Tellurides are metallic and paramagnetic. $PdTe_2$ is superconducting.

The electronic properties of TMDs are dependent on the occupancy, number and energy of the compound's *d* bands which are influenced by both the identity of the metal/chalcogen and the TMD's structure. Metals within certain groups tend to adopt either an octahedral or trigonal prismatic geometry providing the band structures displayed in Figure 1.6. The compound's *d* bands are non-bonding bands that sit between the bonding (σ) and antibonding (σ*) bands of the M-E bonds. TMDs with semiconducting properties possess filled bands, while TMDs with semimetallic character have half-filled bands. As the atomic number of the chalcogen increases, band broadening is observed which results in the reduction of the band gap.[17]

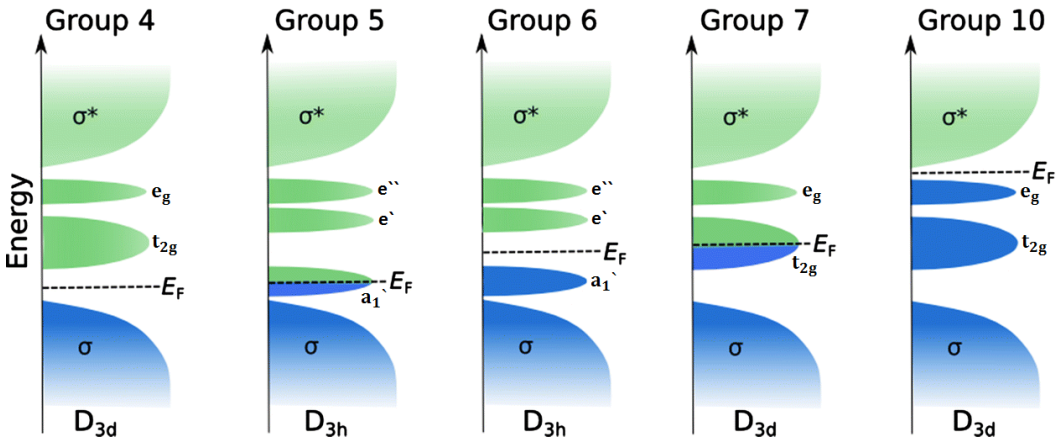

Figure 1.6 Schematic representation of the density of states in selected TMDs showing the different *d* bands present in octahedral (D_{3d}) and trigonal prismatic (D_{3h}) geometries (E_F – Fermi energy). Adapted from reference.[17]

When the metal centre adopts an octahedral geometry the compound has two bands: the t_{2g} band comprising of the d_{xy}, d_{xz} and d_{yz} orbitals, and the e_g band consisting of the d_{z^2} and $d_{x^2-y^2}$ orbitals. Whereas when the metal centre assumes a trigonal prismatic geometry the compound has three bands: the a_1` ($d_{z^2}$), e` ($d_{x^2-y^2}$, d_{xy}) and e`` (d_{xz}, d_{yz}). Figure 1.7 shows the orbital alignments of the *d* orbitals in octahedral and trigonal prismatic geometries.[2]

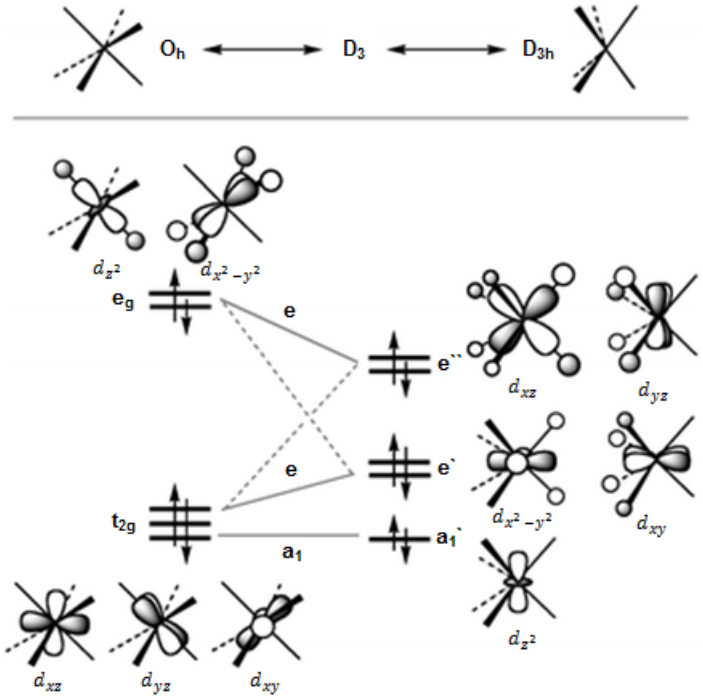

Figure 1.7 Molecular orbital diagram and orbital alignment of *d* orbitals in octahedral and trigonal prismatic geometries, adapted from reference.[18]

While the metal atoms tend to adopt the most common geometry for their group, it is possible to alter the geometry to attain different electronic properties. For example, the 2H phase of MoS_2 (metal in trigonal prismatic geometry) can be chemically altered to the 1T phase (metal in octahedral geometry) using lithium intercalation. This change in geometry alters the band structure (changes from D_{3h} to D_{3d} in Figure 1.6) which makes the material metallic (half filled t_{2g} band) rather than semiconducting (filled a_1` band).[19]

Altering the thickness of the TMD also changes the electronic properties due to changes in interlayer coupling and quantum confinement effects. Bulk MoS_2 is an indirect semiconductor with a band gap of 1.29 eV,[20] while monolayer MoS_2 is a direct semiconductor with a band gap of 1.9 eV.[15] Figure 1.8 shows the band structure changing as the number of MoS_2 layers reduces, the black arrow in the monolayer graph shows the direct transition which is only observed when MoS_2 is one layer thick.

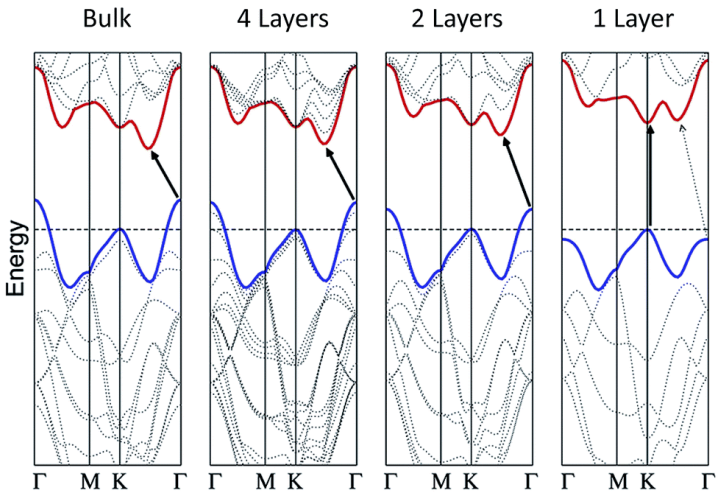

Figure 1.8 Calculated electronic band structure of bulk, four-layer, two-layer and monolayer MoS_2. The black arrow represents the major transition.[21, 22]

1.2.3 Mechanical properties

Bulk TMDs are typically soft and have a consistency similar to that of graphite. The laminar structure of TMDs and the weak interactions between layers allow the sheets to slide over each other and provide a lubricating effect. Friction coefficients as low as 0.01 have been attained for MoS_2 under vacuum conditions showing high

performance lubricating properties.[23] MoS_2 is already marketed as a dry lubricant for use in high temperature and pressure applications such as engines and bearings.[24]

The mechanical strength of monolayer TMDs is highly important for their incorporation into devices, especially when flexible devices are desired. Materials are required to be both flexible and strong for viable device fabrication. Single layers of MoS_2 have been shown to have comparable Young's modulus values to that of stainless steel (270 GPa vs. 205 GPa) while having a considerably greater breaking strength (16-30 GPa vs. 0.9 GPa). While these values are smaller than those attained for graphene (Young's modulus – 1000 GPa, breaking strength – 130 GPa), they are still large enough for realistic device incorporation. The monolayers also exhibit a similar flexibility to that of polyimide and polydimethylsiloxane which are popular substrates for flexible devices.[25]

1.2.4 Applications of bulk TMDs

In terms of industrial applications, only bulk MoS_2 is used on a large scale due to the prevalence of its natural form, molybdenite. As previously described, MoS_2 is already widely used as a high temperature dry lubricant.[23] It is also extensively used industrially in combination with WS_2 as hydrodesulfurisation, hydrodenitrogenation, and hydrogenation catalysts for the removal of sulfur, nitrogen, and other impurities from petrochemicals.[26]

Bulk TMDs have long been investigated as cathode materials in lithium ion batteries due to the facile intercalation of lithium ions in between the TMD layers (Figure 1.9). TiS_2 is by far the most reported TMD cathode material with Exxon commercially producing a TiS_2 containing battery from 1977 to 1979.[27] Devices developed with TiS_2 have high energy densities, conductivities, and lithium diffusion rates with long cycle lives although safety issues with the liquid electrolytes prevented their continued commercialisation.[28] Subsequently, devices containing MoS_2 cathodes have also been developed with the natural 2H phase chemically altered to the 1T phase to improve rechargeability.[29]

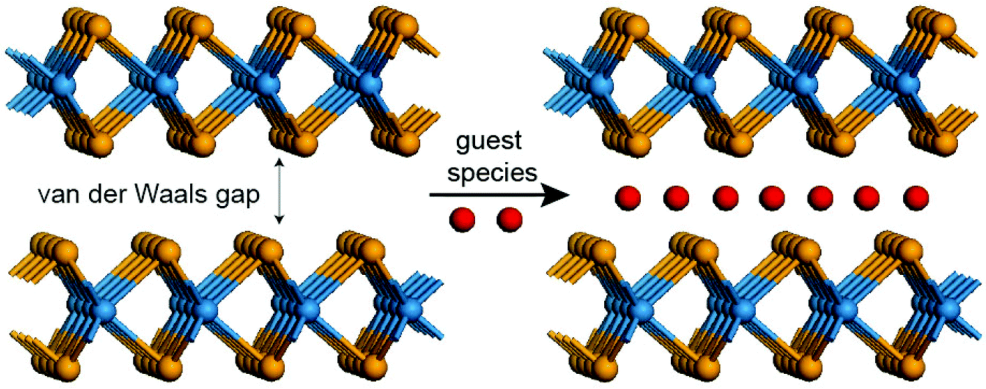

Figure 1.9 Intercalation of lithium ions into TMDs, Li ion in red.[30]

1.2.5 Applications of monolayers

The potential applications of monolayer TMDs have increased dramatically since the isolation of the first monolayers. Probably the most prevalent application is the use of monolayer TMDs in the hydrogen evolution reaction (HER) where the TMD is used as an electrocatalyst to evolve hydrogen gas from an aqueous solution ($2H^+ + e^- \rightarrow H_2$).[2] Again, by far the most popular TMD used for this application is MoS_2, although WS_2 and ZrS_2 have also been used.[31-33] Historically, the noble metals have been used as HER electrocatalysts but these are extremely expensive and cheaper alternatives are required for the viable large scale production of hydrogen. Jaramillo *et al.* reported that MoS_2 has a similar HER activity to that of the noble metals (Figure 1.10), with the edge sites of the MoS_2 determined to be the active sites.[34] It is the availability of these edge sites in monolayer TMDs that means monolayer TMDs are preferred over bulk TMDs.

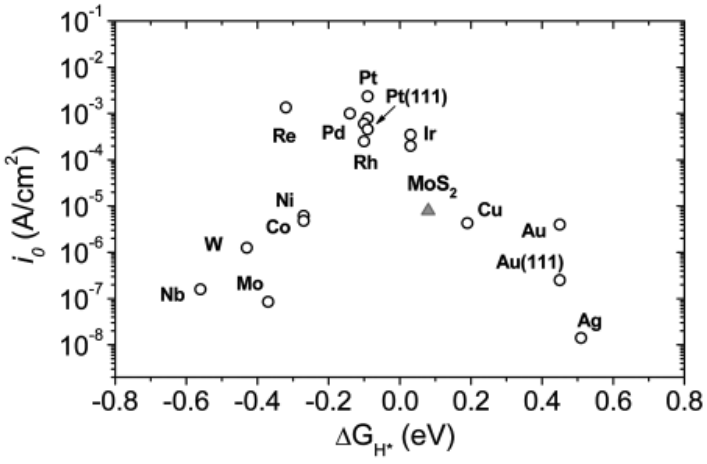

Figure 1.10 Volcano plot of the exchange current density as a function of the DFT-calculated Gibbs free energy of adsorbed atomic hydrogen for nanoparticulate MoS_2 and the pure metals.[34]

FETs are another potential application of monolayer TMDs. A large proportion of TMDs are semiconductors with high on/off ratios which means they can be used as the gate material within devices (Figure 1.11). The flexibility of monolayers and the ability to alter the band gap by changing the number of layers are also favourable properties for device incorporation. FETs made from monolayer TMDs can be used in flexible devices unlike silicon based FETs, which greatly expands their scope of use. The potential to produce extremely small components is also highly advantageous as electronic chip sizes reduce and component densities increase. Monolayer TMD based FETs have mainly been produced from MoS_2, WS_2 and HfS_2.[35-37]

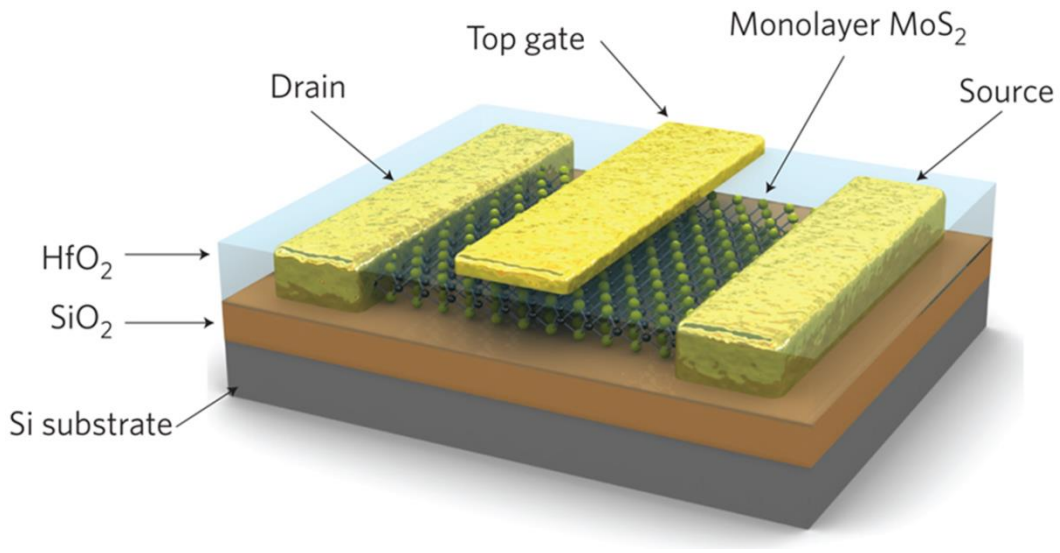

Figure 1.11 Three dimensional schematic of a monolayer MoS_2 based FET.[11]

Other potential applications reported for monolayer TMDs include: thermoelectric devices,[38] photovoltaic devices,[16] light emitting diodes,[39, 40] and molecular sensors.[41] Many of these devices utilise the transparent and flexible properties of the single layered TMDs. Some of these devices are also good examples of Van der Waals heterostructures where a number of different 2D materials are stacked on top of each other to form a device.[7] Britnell *et al.* for example have used a stack of h-BN/graphene/WS_2/graphene (Figure 1.12) to fabricate a photovoltaic cell.[16]

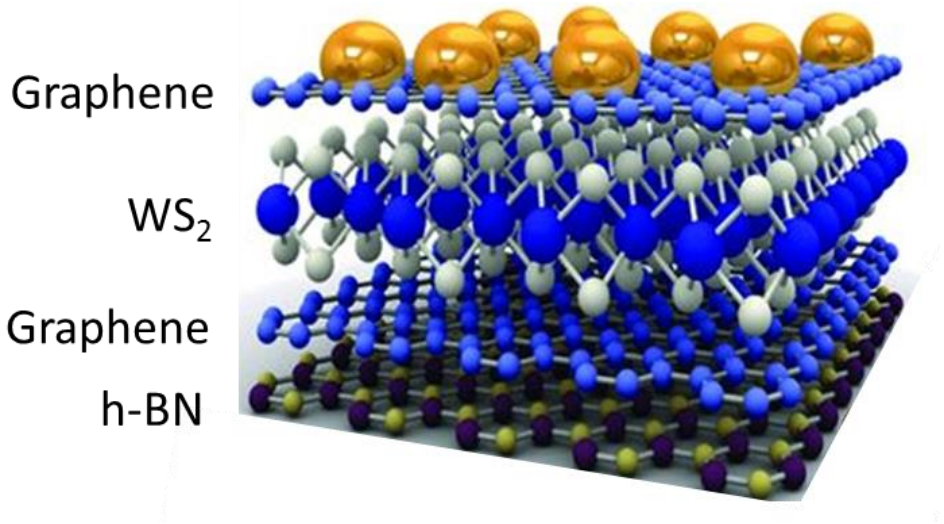

Figure 1.12 Photovoltaic Van der Waals heterostructure based on WS_2, adapted from reference.[16]

1.2.6 Synthesis of TMD thin films

Thin films of TMDs can be produced using two different methodologies: the top-down approach, where a bulk crystal is mechanically or chemically exfoliated to isolate thin films, or the bottom-up approach, where a thin film is grown directly on a substrate. The top-down method tends to produce very small quantities of high quality TMD thin films applicable for fundamental research, while the bottom-up method produces larger areas of TMD films more applicable for industrial applications.[42-44]

For the use of top-down methods, bulk crystals of the TMD are required. The crude TMD is typically synthesised by the reaction between the metal and the elemental chalcogen at elevated temperatures. Bulk crystals are then obtained using the chemical vapour transport technique where iodine vapours transport the TMD along a temperature gradient to deposit crystalline samples of the TMD.[9, 45]

One of the most popular methods for producing high quality single to multi layered TMD films is mechanical exfoliation. This is the same method used to isolate the first samples of graphene and encompasses either the rubbing of a bulk crystal against a surface (‘drawing by chalk on a blackboard’ method) or repeatedly peeling flakes off a bulk crystal using adhesive tape (‘Scotch tape method’).[4, 46] Mechanical exfoliation methods yield high quality samples of TMDs but this technique is not scalable and there is no control of sample thickness or size.[2, 40]

As previously described, lithium ions readily intercalate into TMDs, this mechanism has been utilised to break apart the TMD layers and produce thin films. Lithium intercalation is typically achieved by either electrochemical or chemical methods. In the quicker electrochemical lithiation process (Figure 1.13), an electrochemical cell with a lithium foil anode and TMD cathode is assembled and a potential difference drives the lithium intercalation process.[47] In the chemical process, a sample of TMD powder is added to a solution of *n*-butyllithium where the lithium ions are allowed to intercalate over several days. Once lithium intercalation is achieved using either method, water is then added to react with the lithium and form H_2 gas which separates the layers.[48, 49] These methods can form alternative polymorphs of the various TMDs, for example 1T-MoS_2 (metallic) can be formed rather than the expected 2H-MoS_2 (semiconducting). However, this can be overcome by post annealing the TMD samples which restores the expected polymorph.[50] These methods afford high yields of monolayer or few-layer TMDs however film thickness can be difficult to control and the size of each sheet can vary quite considerably.[2, 40]

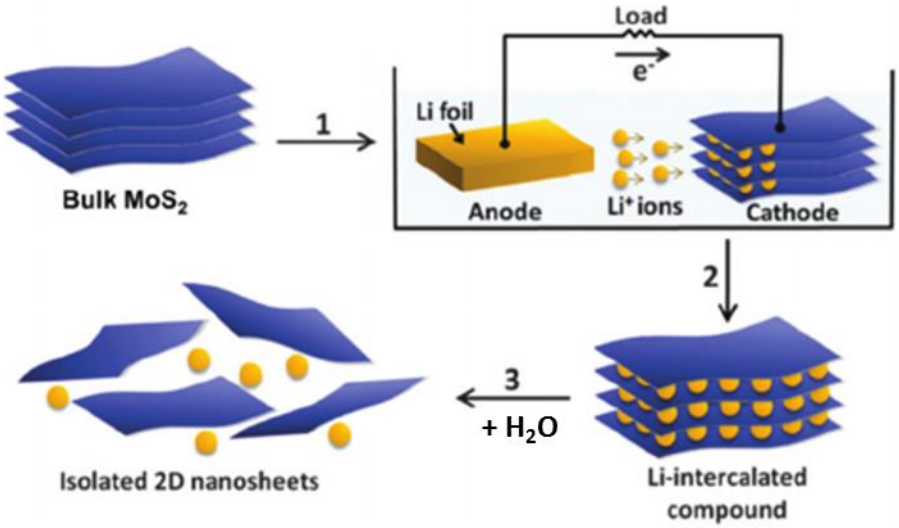

Figure 1.13 Electrochemical lithiation process for the production of single layer TMDs.[47]

A number of liquid exfoliation techniques have also been developed which involve the sonication of a TMD powder in solvents such as methyl-pyrrolidone and isopropanol. Only solvents which have a similar surface energy to the material will work effectively.[51] This method uses the combined action of sonication and solvent to overcome the Van der Waals forces holding the layers together. Liquid exfoliation has also been shown to occur in an aqueous environment when a surfactant is used in

conjunction with sonication.[52] This method provides high yields of multi-layered TMDs ideal for bulk applications such as composites but provides low yields of high quality single layers.[2, 40]

Bottom-up methods centre on three main techniques: molecular beam epitaxy (MBE), chemical vapour deposition (CVD) and atomic layer deposition (ALD).[53] MBE takes place under ultra-high vacuum conditions where pure element sources are sublimed and epitaxial growth of the compound takes place on a substrate.[54] Films produced by MBE are very high quality and have very high purity although expensive and specialised equipment is required to achieve this. TMDs can be grown on a variety of Van der Waals terminated surfaces (so called Van der Waals Epitaxy) with the TMDs retaining their own lattice parameters rather than those of the surface.[55, 56]

CVD is by far the most prevalent bottom-up method utilised in the literature.[2] This technique uses volatile precursors which decompose at a heated substrate surface to deposit the desired film.[57] The CVD methods reported in the literature for monolayer deposition can be categorised into four major methods shown in Figure 1.14. In the first method (Figure 1.14a), the chalcogen and metal powder sources are placed upstream of the substrate. The precursors are held at the most appropriate temperature for volatilisation and the carrier gas transports the vapours to the substrate where a film is formed.[58-60] The second method (Figure 1.14b) uses a chalcogen powder source upstream of a substrate coated in a very thin layer of either a metal or metal oxide. Chalcogen vapours are transported to the substrate by a carrier gas where the thin film is grown.[61] Again in the third method (Figure 1.14c), a substrate coated in metal or metal oxide is used but the chalcogen is supplied in the gaseous form. Finally in the fourth method (Figure 1.14d), both metal and chalcogen precursors are supplied as a gas.[44, 62, 63]

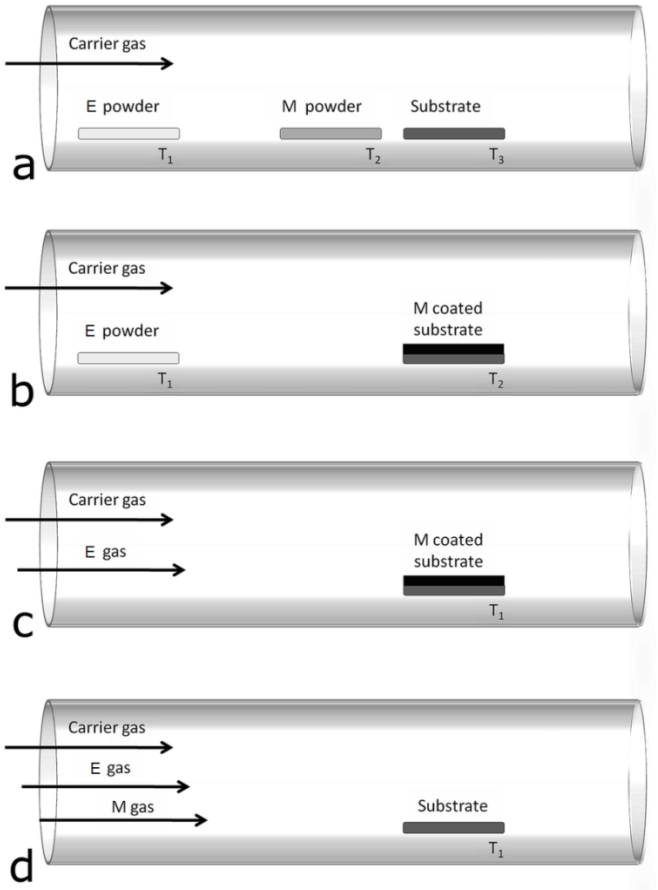

Figure 1.14 Schematic of the four most common CVD methods for depositing TMDs. a – Metal and chalcogen powders, b – metal coated substrate and chalcogen powder, c – metal coated substrate and chalcogen gas, d – metal and chalcogen gases. Adapted from reference.[44]

Typical metal precursors include: substrates coated in elemental metal, metal oxide powders, metal carbonyls and metal halides, while common chalcogen precursors include: elemental chalcogen powders, hydrogen chalcogenides and chalcogenols.[44] The CVD methods above utilise multi-source precursors but there are also a number of examples of single-source precursor use. For example, molybdenum thiols and molybdenum dithiocarbamates have been used for the deposition of MoS_2 thin films.[64, 65] While single-source precursors have not yet been used to deposit monolayers, they do provide potential for lower growth temperatures and simpler equipment construction.[66] Metal chalcogenide single-source precursors are the focus of this thesis and will be discussed in greater detail in Section 1.5.

The final bottom-up method, ALD, is a variant of CVD which allows greater control of film thickness. In this method, metal and chalcogen precursors are alternately pulsed over a substrate and the film grows layer by layer, after each precursor pulse

the reactor chamber is purged to prevent non-ALD growth.[67] This technique allows good control of film thickness but is little utilised due to the more complex nature of the equipment and the number of viable precursors.[68] Most examples reported involve the atomic layer deposition of a metal or metal oxide film with a subsequent annealing step under an atmosphere of the chalcogen to produce the TMD thin film.[44, 69] There are now examples of the direct growth of monolayer MoS_2 by ALD which involve the precursors $MoCl_5$ and H_2S at 500 to 900 °C.[70]

1.3 Chemical Vapour Deposition

1.3.1 Overview

CVD is the formation of a solid film on a surface by a chemical reaction in the vapour phase close to, or on, that surface. In a typical CVD process (Figure 1.15), one or more precursors are introduced via an inert carrier gas into the reaction chamber, here they adsorb onto the (typically) heated substrate surface where they react to form the desired material and by-products. Any volatile by-products desorb from the surface and are removed from the reaction chamber while the remaining material combines to form a film on the substrate surface.[57, 71, 72]

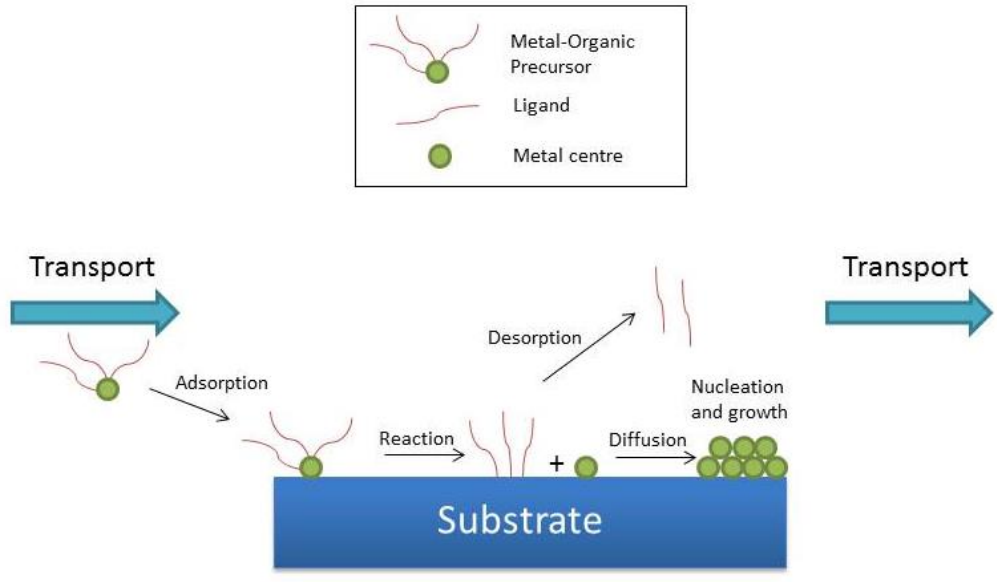

Figure 1.15 Diagram showing the steps involved in a CVD process.[57]

The mechanisms involved in the adsorption of chemical precursors to a substrate and their subsequent reactions to form thin films are relatively complex. While complicated, these mechanisms can be categorised into three main growth modes

shown in Figure 1.16: (1) Volmer-Weber (three dimensional island growth), (2) Frank-van der Merwe (two dimensional layer by layer growth), and (3) Stranski-Krastanov (layer plus island growth).[73, 74]

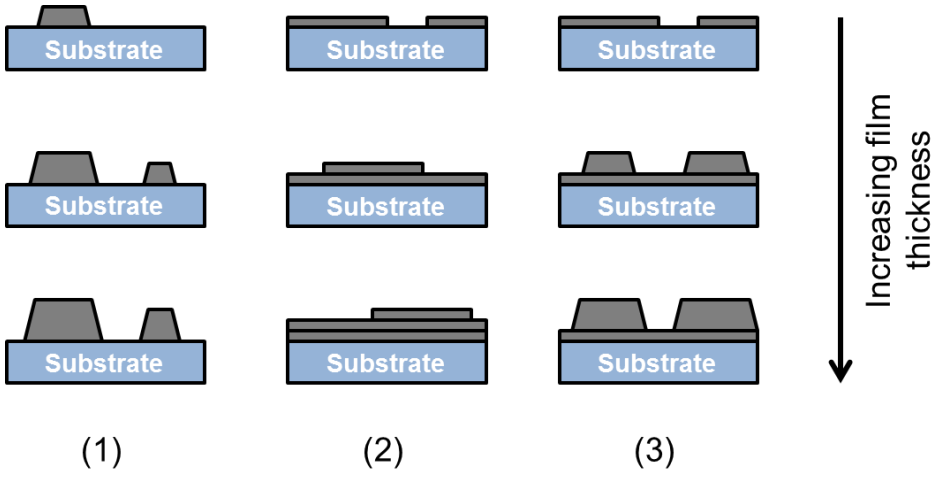

Figure 1.16 Thin film growth modes: (1) Volmer-Weber, (2) Frank-van der Merwe, and (3) Stranski-Krastanov. Adapted from reference.[74]

Volmer-Weber growth occurs when the film atoms have stronger interactions with other film atoms rather than the substrate surface. Small three dimensional clusters of the film atoms nucleate on the surface and grow into islands, expansion continues until the islands coalesce to form a film. Alternatively, Frank-van der Merwe growth occurs when the film atoms have stronger interactions with the substrate surface rather than other film atoms. This growth mode forms a film layer by layer with expansion of the layer preferred over formation of another. Stranski-Krastinov growth is a combination of the previous two modes with layer by layer growth occurring until island growth becomes more favourable. Changes in the surface energy or lattice parameters are the most common factors that convert layer by layer growth to island growth.[73, 74]

Substrates, precursors, impurities, temperature, pressure and gas flow all impact the identity, morphology and microstructure of the final thin film, therefore it is vital to control and understand all of these factors when performing CVD. The appropriate choice of substrate is important when trying to obtain a preferred thin film polymorph or orientation as the surface of the substrate can template the film. The cleanliness of the substrate is also important for good adhesion of the film to the growth surface. Use of the most appropriate precursor or precursors is essential for

the elemental content of the film and can also impact the final stoichiometry. Impurities can be present in the precursor, reactor or substrate and can also be formed from unwanted gas phase reactions of the precursor. Inclusion of impurities in the film creates defects which alter the morphology and composition.[71]

Temperature, pressure and gas flow can all control the growth rate of films by altering the diffusion rate of species in the vapour phase. The temperature also impacts the reaction rate and crystallinity of the film, with lower temperatures favouring amorphous films and high temperatures favouring crystalline films.[71, 73]

The main advantages of CVD include:[57, 71, 72]

- the production of large area films with uniform thickness
- the production of low porosity films
- high deposition rates
- good coverage of three-dimensional structures
- the flexibility of both the deposition process and the apparatus
- typically ultra-high vacuums are not required

The main limitations of CVD include:[57, 71, 72]

- relatively high deposition temperatures are sometimes required
- the use of hazardous precursors
- by-products are typically hazardous
- the precise control of film thickness

1.3.2 Variations of CVD

There are now a plethora of different CVD techniques available to suit a wide range of precursors and conditions. These CVD variants are focussed on the two main areas of the CVD method: the transport of the precursor to the substrate (Table 1.2) and the activation of film formation (Table 1.3). The specific CVD technique utilised is normally dictated by the requirements of the precursor being used. With such a wide range of techniques available only the major techniques will be covered here. The work in this thesis is based on thermal aerosol-assisted CVD (AACVD) and low pressure CVD (LPCVD) which are presented in greater detail in Sections 1.3.3 and 1.3.4 respectively.

Table 1.2 CVD variants based on differing precursor transport methods.[71]

Type	Acronym	Summary
Atmospheric pressure CVD	APCVD	Processes at atmospheric pressure. Precursors are volatile at ambient temperature or higher when under atmospheric pressure. Simpler, cheaper and faster to operate
Low pressure CVD	LPCVD	Processes at sub-atmospheric pressure. Precursors are volatile at ambient temperature or higher when under low pressure. More expensive apparatus.
Ultrahigh vacuum CVD	UHVCVD	Processes at pressures of less than 10^{-8} Torr. Precursors are volatile at ambient temperature or higher when under very low pressure. Reduction in impurities. Very expensive apparatus.
Direct liquid injection CVD	DLICVD	Car injectors are used to vaporise the liquid precursor or precursor solution. Vapours are then transported to the substrate surface. Cheap and relatively simple apparatus.
Aerosol-assisted CVD	AACVD	Uses a liquid/gas aerosol to transport the precursor (typically dissolved in a solvent) to the substrate. Cheap and relatively simple apparatus.
Metal-organic CVD	MOCVD	Metal-organic compounds are used as the precursors. These compounds are typically quite volatile. Many precursors are toxic and highly reactive.
Hybrid physical-CVD	HPCVD	Both a precursor gas and a vaporised solid source are chemically decomposed.
Atomic layer deposition	ALD	Precursors are alternately pulsed over the substrate to deposit a film layer by layer. Films are typically very crystalline. Allows very high control over film thickness.

Table 1.3 CVD variants based on the activation of film formation.[71]

Type	Acronym	Summary
Thermal CVD	TCVD	The most common form of CVD. Decomposition is initiated thermally.
Plasma enhanced CVD	PECVD	Plasma is used to enhance the chemical reaction rates and lower the deposition temperature. Allows deposition onto heat sensitive substrates.
Microwave plasma CVD	MPCVD	Plasma is produced using microwaves.
Remote plasma enhanced CVD	RPECVD	Plasma causes precursor decomposition although the substrate is not in direct contact with the plasma.
Hot wire CVD	HWCVD	Uses a heated filament to decompose the gaseous precursors.
Rapid thermal CVD	RTCVD	Rapid heating techniques such as heat lamps are used to quickly heat substrates.
Photo initiated CVD	PICVD	UV light induces precursor decomposition.

Within thermal CVD there are two different reactor designs used for heating the substrate. In a hot wall reactor both the reactor walls and substrate are heated to the same temperature, typically this is achieved by placing the reactor in a furnace. These reactors are typically simpler and cheaper to produce but require more maintenance and precursor as films are deposited on the walls of the reactor as well as the substrate. Contamination of the film from the material on the reactor walls is possible and unwanted gas phase reactions are more likely. In a cold wall reactor only the substrate is heated to the desired temperature. The substrate sits on a heating block which is either heated internally or by a halogen lamp. This design provides greater control of substrate temperature, films with less contamination and uses smaller quantities of precursor. However, film throughputs are typically less and reactors tend to be more expensive.[71, 72, 75]

1.3.3 AACVD

The aerosol-assisted variant of CVD uses an aerosol of a precursor solution to transport the precursor to the substrate. The aerosol is generated by an ultrasonic generator, collision-type atomiser or electrostatic atomisation. Once formed, the aerosol is then transported by a carrier gas to the heated substrate where the solvent evaporates and the precursor decomposes. The major advantage of this technique is that it relies on the precursor being soluble rather than volatile which greatly expands the scope of potential precursors. The impact of using a solution based precursor and aerosol in CVD means precursor concentration, type of solvent and aerosol droplet size can all influence the final morphology of the film.[76-78]

Ultrasonic generators form aerosols by subjecting the precursor solution to ultrasonic vibrations, this causes cavitation within the solution which generates an aerosol mist. In a collision-type atomiser (Figure 1.17), a precursor solution stream is introduced into a high-velocity gas stream, the shear forces experienced by the liquid causes an aerosol to be generated. Electrostatic atomisation generates aerosols by applying an electric potential to a spray nozzle, this forms an aerosol when the precursor solution passes through the nozzle. All of these techniques require a carrier gas, either reactive or inert, to transport the aerosol to the heated substrate.[78]

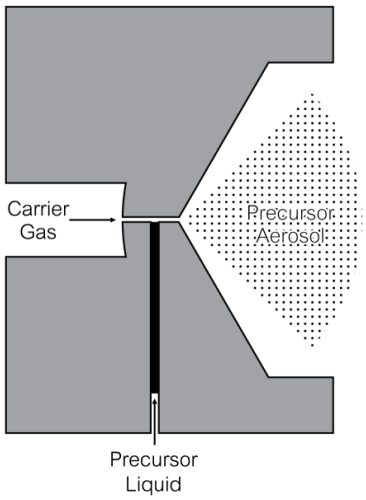

Figure 1.17 Diagram of aerosol generation in a collision-type atomiser.

The most important aspect of AACVD is its reliance on soluble precursors rather than volatile precursors. This greatly expands the scope of potential precursors as numerous solvent systems can be used to solvate the precursor and it allows greater freedom in precursor design. This also makes precursor handling more straightforward as less volatile compounds tend to be more stable and simpler to synthesise. AACVD can also provide excellent stoichiometric control as regulating the ratios of different precursors is much simpler in solution as opposed to the vapour phase. The use of an aerosol to deliver the precursor also provides higher deposition rates as mass transport rates are higher.[76]

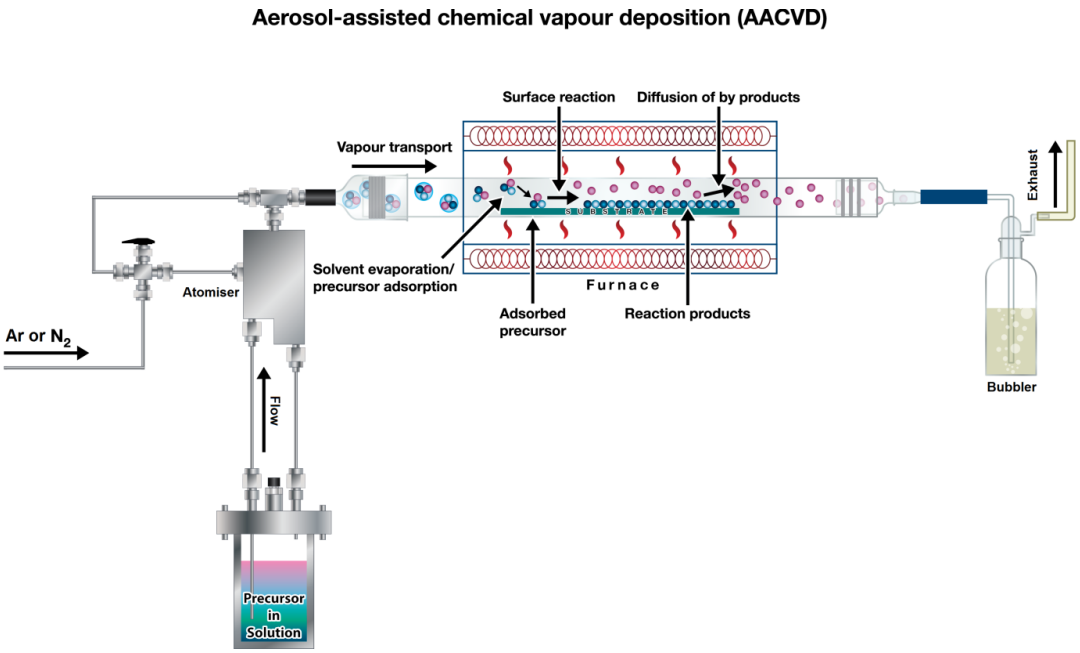

Figure 1.18 Diagram of the AACVD experimental set-up used in this thesis.

The experimental set-up of the AACVD apparatus used in this thesis is shown in Figure 1.18. The precursor solution flows up the lines to the atomiser (TSI 3076 constant output atomiser) where a flow of argon or nitrogen gas is used to generate the aerosol. The aerosol is then transported by the carrier gas to the quartz reactor tube contained within a furnace. Here, the precursor aerosol comes into contact with the heated substrate and the solvent evaporates. The precursor adsorbs onto the substrate surface and decomposes to form a film with any by-products passing through the bubbler to the exhaust.

1.3.4 LPCVD

Low pressure variants of CVD proceed at sub-atmospheric pressures and are typically used when precursors have insufficient volatility at atmospheric pressure. The main benefits of LPCVD are that the films produced usually have greater uniformity, better coverage and improved quality when compared to films produced at atmospheric pressure. The main drawbacks to this technique are the slower throughputs, higher costs and greater complexities of the equipment.[72]

In most LPCVD techniques, precursors are contained within bubblers surrounded by temperature controlled jackets which maintain a constant temperature to regulate the flow of precursor. Carrier gases are typically used to aid transport of the precursor to the substrate and precursor lines are temperature controlled to prevent precursor condensation.[72] For precursors that are less volatile e.g. metal oxides, the precursor can be placed in the reaction chamber closer to the substrate. Temperature control can either be independent of, or the same as, the substrate.[2]

The experimental set-up of the LPCVD apparatus used in this thesis is shown in Figure 1.19. The quartz reactor tube which is enclosed at one end is contained within a furnace. A quartz boat containing the precursor is placed at the closed end of the reactor and the substrates are then placed upstream of the precursor boat. Within the furnace the substrates are positioned in the middle (hotter) with the precursor boat towards the edge (cooler) to provide a temperature gradient. The system is evacuated and purged with inert gas three times prior to starting a deposition run. When the system is under a stable dynamic vacuum (1 mbar), the experiment is started by turning the furnace on, to ramp to the desired temperature.

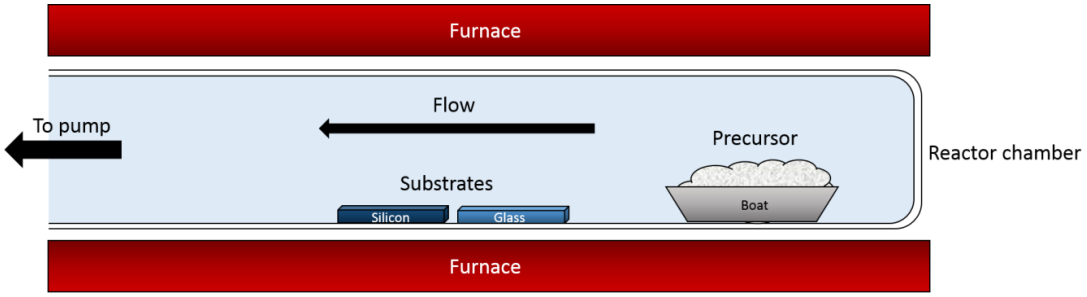

Figure 1.19 Diagram of the LPCVD experimental set-up used in this thesis.

1.4 CVD precursors

Precursors are typically volatile compounds that contain the constituent elements of the desired film and decompose at a defined temperature to deposit the required material. With the advent of solution based CVD methods such as AACVD, there is now less reliance on volatility and more onus on solubility. The use of the most appropriate precursors is essential in determining the identity, morphology and microstructure of CVD based thin films. Therefore it is vital that the precursors being used are designed to provide the optimum thin film quality. Two precursor methodologies are used in CVD: multi-source and single-source precursors. [71, 72]

1.4.1 Multi-source precursors

Multi-source precursors utilise separate molecules as sources for each distinct element within the film, for example SiH_4 and O_2 are used to deposit SiO_2. This class of precursor is by far the most commonly utilised within industry, typically due to their higher volatility and lower cost. These precursors are usually relatively simple molecules which makes their synthesis easier and cheaper. The major disadvantage to using these precursors is the difficulty in handling them, many compounds are sensitive to air or moisture and are highly toxic e.g. H_2S.[66, 79]

1.4.2 Single-source precursors

Single molecules that contain all of the elements for the film to be deposited are called single-source precursors. These molecules typically contain direct bonds between the elements of the desired film. Various ligands are used to stabilise the compounds and impart the desired properties onto the molecule. With decomposition, the ligands within the complex break down to form volatile by-products and the desired film is deposited.[66, 77, 79]

The main advantages of single-source precursors are:[66, 77]

- Lower deposition temperatures
- Simpler reactor set-up
- Reduced chance of unwanted gas phase decomposition
- Reduced toxicity
- Greater stability towards moisture and air

The main disadvantages are:

- Difficulty in controlling stoichiometry
- Low volatility
- More complex synthesis

The control of final film stoichiometry when using single-source precursors is not straightforward. Intuitively, the elemental ratio within the precursor would be retained in the final film. While there are examples of this occurring, typically a different stoichiometry is adopted. The decomposition pathways are generally complex within single-source precursors and the final product will depend on a delicate balance between bonds breaking and those that are preserved. There are also examples of the core structure within the precursor templating the final film although again this is not representative of most results.[66, 79]

1.4.3 Precursor design

Designing precursors to possess the desired properties for depositing high quality thin films is vitally important and requires an understanding of the deposition process. Modification of the precursor is achieved by either changing to a completely different ligand set or by altering the ligands e.g. changing R groups. There are a number of requirements that are desirable for a precursor to have:[79-83]

- Good volatility or solubility
- Good thermal stability until desired decomposition temperature is reached
- Ability to cleanly decompose at the intended temperature to form the desired film
- High purity
- Long term stability

- Low toxicity
- Simple and cheap synthetic route

Enhancing volatility requires the reduction of the polarizability, dipoles, H-bonding and other intermolecular interactions between precursor molecules. This can be achieved by using heteroleptic ligands to hinder crystal packing, polydentate ligands to discourage oligomerisation or large alkyl or fluorinated ligands to increase vapour pressure.[79, 80] Increasing the solubility of a precursor depends on the choice of solvent although preventing oligomerisation by using polydentate ligands aids solubility in most cases. The introduction of greater ionic character into a precursor can help solubility in polar solvents while the use of long alkyl chains can improve the solubility in non-polar solvents.[76]

To prevent early decomposition, precursor molecules must be thermally stable until the desired decomposition temperature is reached. The use of polydentate ligands to block empty coordination sites, sterically bulky ligands to prevent oligomerisation and homoleptic ligands to stop ligand scrambling all can increase thermal stability.[80] Using ligands with well understood and clean decomposition pathways can reduce thin film contamination. Ligands able to undergo β-hydride elimination (Scheme 1.1) typically decompose cleanly with the loss of a volatile alkene.[84, 85] Labile ligands, which are themselves stable molecules (e.g. CO), also provide clean decomposition routes.[79]

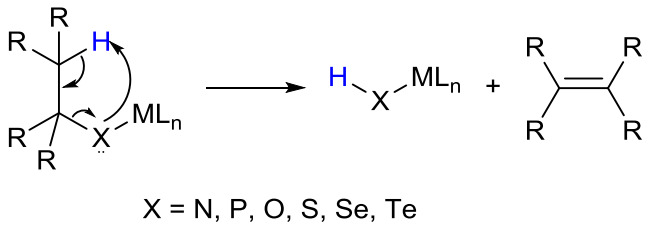

Scheme 1.1 General mechanism of β-hydride elimination.[85]

High purity of the precursor and simple/cheap synthetic routes both require optimisation of the precursor synthesis. By reducing unwanted side products, high purity compounds can be manufactured while the use of cheap and easily available starting materials reduces costs.

1.5 Metal chalcogenide single-source precursors

There is a huge range of chalcogen containing ligands exploited for metal chalcogenide single-source precursors. Ligands containing sulfur are the most prevalent while there are fewer examples of selenium and tellurium containing ligands due to their reduced stability. This section contains a brief overview of the main chalcogen containing ligand sets used for metal chalcogenide deposition. Readers are directed towards the reviews by A. N. Gleizes,[66] Afzaal *et al.*[86] and Knapp *et al.*[77] for a thorough evaluation of metal chalcogenide single-source precursors.

1.5.1 Chalcogenolates

Metal chalcogenolates, $[M(ER)_n]$ (e.g. Figure 1.20), are amongst the earliest and simplest examples of single-source metal chalcogen precursors and one of the few chalcogen based ligands that can easily incorporate tellurium into the molecule.[66, 87] Chalcogenolates are monodentate ligands which can act as both terminal and bridging ligands, incorporation of a further chalcogenol onto the R group forms a dichalcegonolate which binds to a metal centre in a bidentate manner.[66, 88] Examples of metal thiolates used to produce metal sulfides include the metals: Ti, Cu, Zn, Zr, Nb, Mo, Cd, In, Sn, Sb and Ta. While, Ti, V, Zn, Zr, Cd, In, Sn, Hf and Hg selenolates have all been used to produce the corresponding metal selenides. Only a handful of metal tellurolates (Zn, Cd and Hg) have been utilised to deposit the equivalent metal tellurides.[70, 79, 88, 90-93]

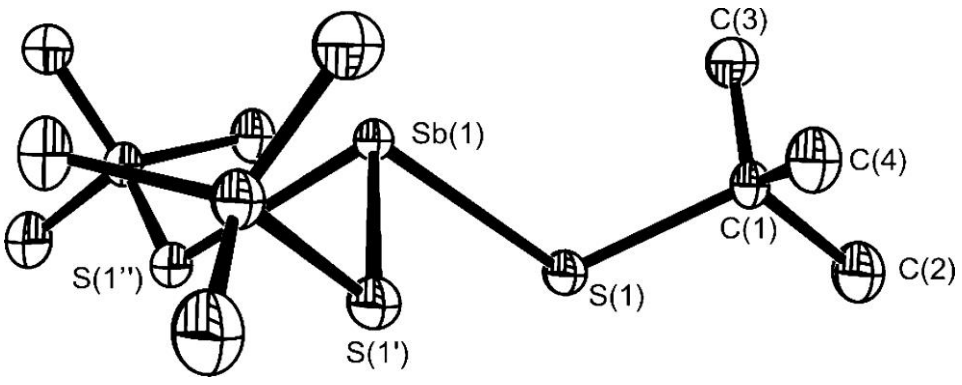

Figure 1.20 Molecular structure of the metal chalcogenolate complex, $Sb(S^tBu)_3$.[89]

The four most common routes to the synthesis of metal chalcogenolates (Scheme 1.2) are: the protonolysis of a metal amide with a chalcogenol, the metathesis

reaction between a metal halide and alkali metal chalcogenolate salt, the reaction between a metal halide and chalcogenol in the presence of a base (typically NH_3 or NEt_3), and the oxidation of a metal with diphenyl dichalcogenide.[89-92]

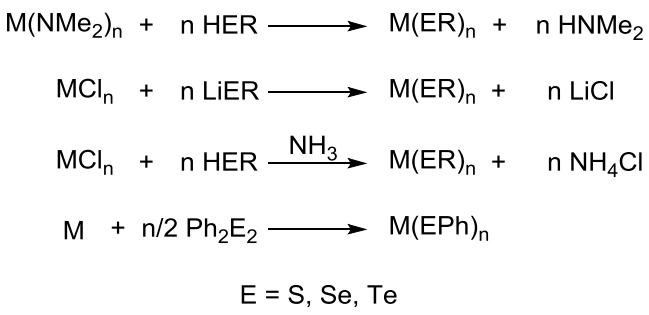

Scheme 1.2 Typical synthetic routes to metal chalcogenolates.

Common R groups used in metal chalcogenolate precursors are -^{i}Pr, -^{t}Bu, -Ph, -$C(SiMe_3)_3$, -$Si(SiMe_3)_3$, -$C_6H_2(^{t}Bu)_3$ and -$C_6H_2(CF_3)_3$. These large, bulky substituents are used to increase the volatility of the compound and prevent oligomerisation. This is especially important for group 12 metal chalcogenolates which are prone to forming less volatile, polymeric compounds when smaller R groups are used.[93-96]

The choice of R group can also influence the film deposited during CVD by altering the decomposition pathway. Molloy *et al.* have reported that the precursor $[Sn(SPh)_4]$, deposits films of Sn_3O_4 rather than films of tin sulfide.[97] Further analysis of the precursor decomposition pathway using thermogravimetric analysis and mass spectrometry showed the elimination of the disulfide, PhS-SPh. This suggested that tin metal was deposited which subsequently reacted with traces of oxygen to form the oxide. Altering the ligand to the bidentate dithiolate, $[Sn(SCH_2CH_2S)_2]$, hindered the formation of the disulfide species and formed SnS in the temperature range 400 - 550 °C.[88]

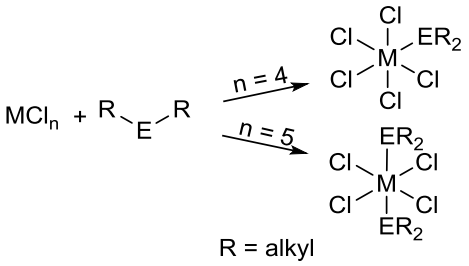

Scheme 1.3 Synthesis of metal chalcogenoether complexes.

Chalcogenoethers are a subset of chalcogenolates where the chalcogen atom is bound to two alkyl chains and the ligand is formally a neutral donor rather than monoanionic. Synthesis of these complexes (Scheme 1.3) occurs by the addition of the chalcogenoether to a metal chloride resulting in the formation of a metal chloride chalcogenoether adduct (Figure 1.21). Examples of metal chalcogenides produced include: TiS_2, $TiSe_2$, VSe_2, NbS_2, $NbSe_2$, SnS_2 and $SnSe_2$.[98-102]

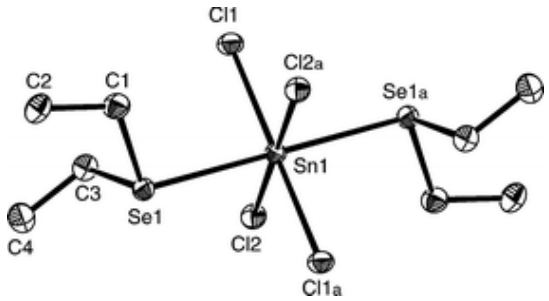

Figure 1.21 Molecular structure of the metal chalcogenether complex, *trans*-$[SnCl_4(Et_2Se)_2]$.[98]

1.5.2 Dichalcogenocarbamates

Dichalcogenocarbamates are one of the most common classes of metal chalcogenide precursors with a wide range of deposited metal sulfides and selenides reported in the literature.[66, 77, 86] Figure 1.22 shows the typical binding modes of metal dichalcogenocarbamates, the bidentate mode (κ^2-*E*,*E*) is by far the most commonly observed although the anisobidentate, monodentate and bridging modes are known.[103] Electron density is delocalised across the planar $\{E_2CN\}$ core of the ligand with the lone pair on the nitrogen donating towards the $\{E_2C\}$ moiety.[104, 105] Examples of metal sulfides produced by metal dithiocarbamates include the metals: Cr, Mn, Fe, Co, Ni, Cu, Zn, Ga, Mo, Pd, Cd, In, Sn, Sb, Pb and Bi.[65, 86, 106-109] Examples of metal selenides produced by metal diselenocarbamates include the metals: Co, Cu, Zn, Ga, Cd, In and Bi.[77, 86, 110-112]

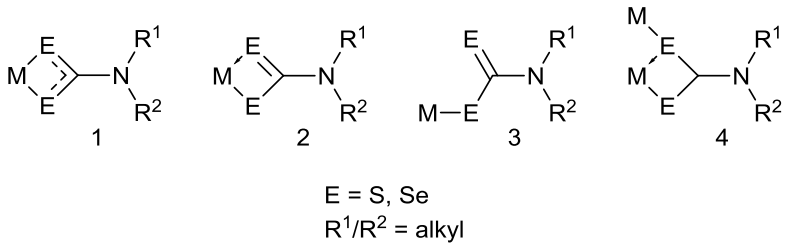

Figure 1.22 Binding modes of metal dichalcogenocarbamates: 1 – bidentate, 2 – anisobidentate, 3 – monodentate, 4 – bridging.

Synthesis of metal dichalcogenocarbamates is typically performed via three different routes (Scheme 1.4). The first route involves the metathesis reaction between a metal halide, typically the chloride, and an alkali metal or ethylammonium dichalcogenocarbamate salt. Once synthesised the metal dichalcogenocarbamate must be separated from the resulting alkali metal or ethylammonium halide salt.[110, 112] The second route involves the direct insertion of carbon dichalcogenide into a metal amide containing the desired R groups. This method produces high yields of product with little to no side products.[113] The final route involves the oxidation of a metal carbonyl by a thiuram disulfide to form the metal dichalcogenocarbamate with the loss of carbon monoxide.[65] Production of the metal diselenocarbamates uses very toxic carbon diselenide, which is typically produced *in situ* and reacted immediately to prevent exposure.[112]

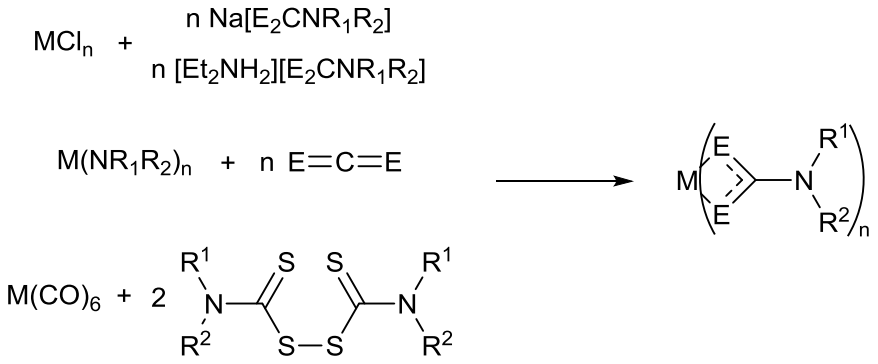

Scheme 1.4 Typical synthetic routes to metal dichalcogenocarbamates.

The most common metal dichalcogenocarbamate precursors used are the metal diethyldichalcogenocarbamate complexes, likely due to the commercial availability of the ethyl based starting materials. Introduction of unsymmetrical R groups (e.g. Figure 1.23) into the ligand can increase the volatility of the complex compared to similar symmetrically substituted compounds.[114] Thermal decomposition of the metal dichalcogenocarbamate complexes is reported to occur via the elimination of the R group as an alkene, followed by the loss of HCN. Any remaining chalcogen is eliminated in its elemental form to the gas phase and the metal chalcogenide is produced.[115]

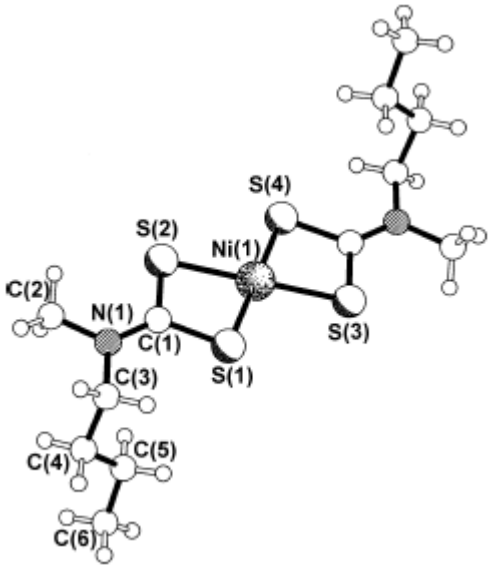

Figure 1.23 Molecular structure of the unsymmetrically substituted dithiocarbamate complex, $[Ni(S_2CNMe^nBu)_2]$.[106]

Monothiocarbamates are a sub class of the dichalcogenocarbamates where the two chalcogen atoms are oxygen and sulfur. Synthetic routes are similar to the rest of the dichalcogenocarbamates (Scheme 1.4) with carbonyl sulfide used in place of the carbon dichalcogenide. O'Brien *et al.* have reported the deposition of Ga, Cd and In sulfides with the Et and ^{i}Pr monothiocarbamates.[116-119]

1.5.3 Monothiocarboxylates

Monothiocarboxylates closely resemble monothiocarbamates except the amine group is replaced by either an alkyl or aryl group. Unlike monothiocarbamates, monothiocarboxylates frequently bind to the metal centre in a monodentate mode (Figure 1.24) although the bidentate and bridging modes are also observed. Mark J. Hampden-Smith's group has pioneered the use of these ligands in metal sulfide single-source precursors for the metals: Ca, Zn, Ga, Sr, Cd, In and Ba.[120-124] O'Brien *et al.* have also reported their use in the deposition of In_2S_3 and mixed indium/silver sulfide phases.[125, 126]

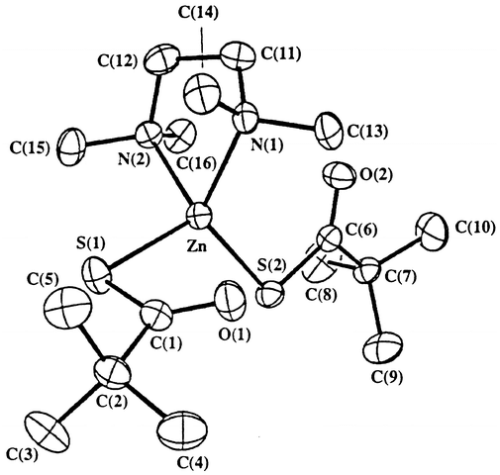

Figure 1.24 Molecular structure of the metal monothiocarboxylate complex, $Zn(SOCC(CH_3)_3)_2TMEDA$.[122]

The metal monothiocarboxylates are synthesised by two different methods shown in Scheme 1.5. In the first route a metal alkyl, hydride or carbonate is reacted with an appropriate amount of the desired thiocarboxylic acid. In the second route, a metathesis reaction is performed between a metal nitrate or chloride salt and the appropriate amount of the sodium thiocarboxylate salt. Both methods typically require the addition of a chelating ligand such as TMEDA or a crown ether to stabilise the final product.[120, 125] Upon heating, the metal monothiocarboxylates decompose to form the metal sulfide with the loss of a thioanhydride and any chelating ligands.[120]

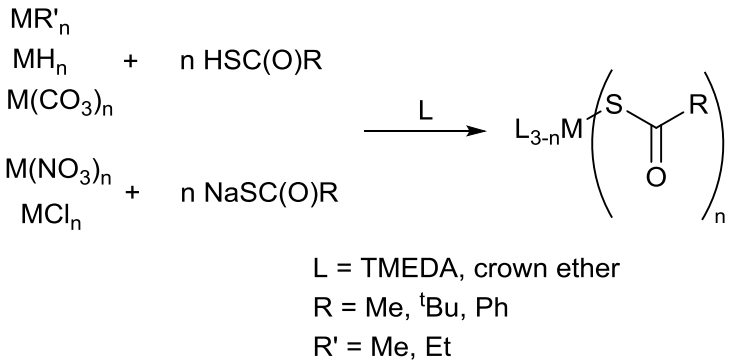

Scheme 1.5 Synthesis of metal monothiocarboxylates.

1.5.4 Xanthates

Metal xanthates or dithiocarbonates, $[M(S_2COR)_n]$, are another common class of metal sulfide precursors. Metal xanthates are synthesised (Scheme 1.6) via similar

routes to that of metal dithiocarbamates with the most common method being the metathesis reaction between a metal salt (normally chloride or nitrate) and the alkali metal xanthate salt. The alkali metal xanthate salt is easily synthesised by the equimolar reaction of an alkali metal hydroxide, an alcohol with an appropriate R group and carbon disulfide.[127] Metal xanthates can also be formed by the insertion of CS_2 into a metal alkoxide or the oxidation of a metal carbonyl using a dixanthogen.[128]

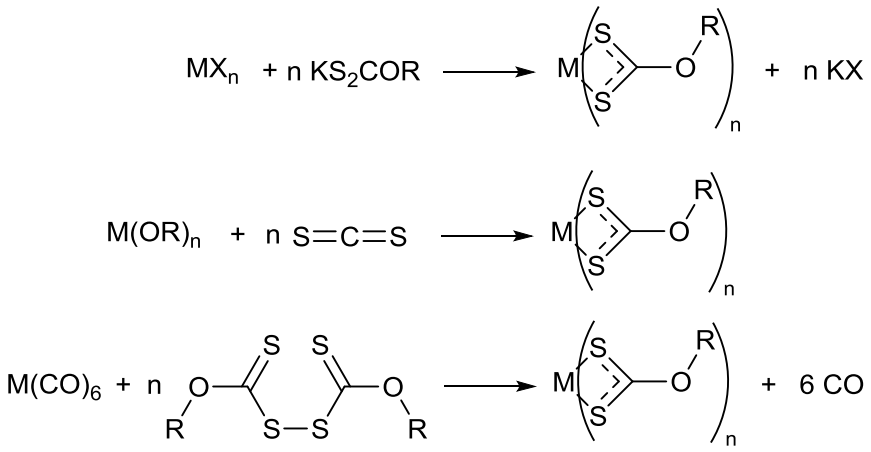

Scheme 1.6 Typical synthetic routes to metal xanthates.

The most common metal-xanthate binding mode is the *S*,*S*-bidentate mode although examples of *S*-monodentate, *O*,*S*-chelating and *S*,*S*-bridging modes are known (Figure 1.25). In *S*,*S*-bidentate mode, the electron density is delocalised across the planar {S_2CO} moiety with C-S and C-O bonds adopting shorter bond lengths than typically found for the corresponding single bonds.[129]

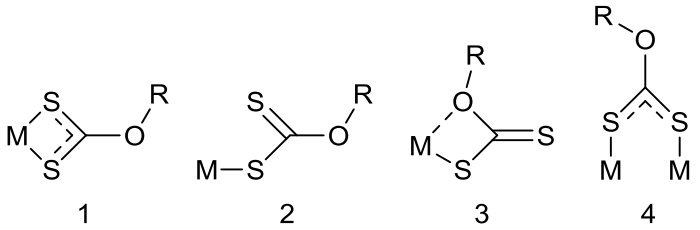

Figure 1.25 Xanthate binding modes: 1 – *S*,*S*-bidentate, 2 – *S*-monodentate, 3 – *O*,*S*-chelating, 4 – *S*,*S*-bridging.

Thermal decomposition of a metal xanthate normally occurs via the Chugaev elimination shown in Scheme 1.7. First, in a concerted *syn*-elimination via a six-membered cyclic transition state, the R group is lost as an alkene. Further

decomposition occurs with the loss of carbonyl sulfide to form a metal thiol which further breaks down to form the metal sulfide with the loss of hydrogen sulfide.[85] Examples of metal sulfides produced from metal xanthate complexes include the metals: Ni, Zn, Cd, In, Pd, Sb, Pb, Mn, Cu, Ag and Hg.[66, 77, 86, 130, 131]

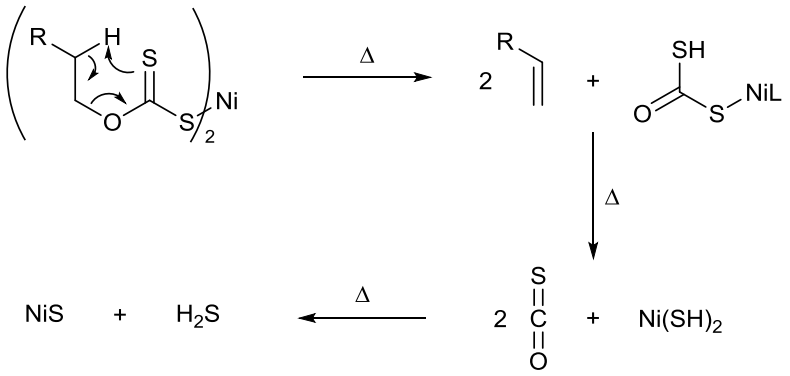

Scheme 1.7 Example of the Chugaev elimination mechanism for a nickel xanthate.[85]

1.5.5 Dichalcogenphosphinates

Metal dichalcogenphosphinates are a less commonly used class of metal chalcogen precursors which are typically used to deposit metal selenides due to the relative ease of incorporating Se into the ligand. The dichalcogenphosphinates act as chelating ligands, generally binding in a bidentate manner as shown in Figure 1.26, although monodentate and bridging modes are known.[132] The coordination geometry adopted around the phosphorus is distorted tetrahedral with the P-E bond lengths somewhere between single and double bonds suggesting delocalisation across the {E-P-E} moiety.[133] Examples of metal sulfides produced by metal dithiophosphinates include the metals: Cu, Zn, Cd and In.[134] Examples of metal selenides produced by metal diselenophosphinates include the metals: Mo, Cu, Zn, Cd and Sn.[135, 136]

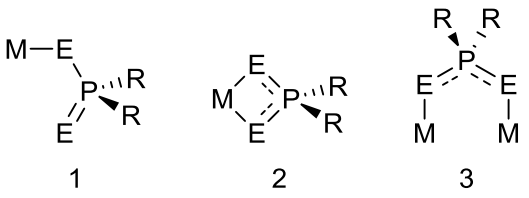

Figure 1.26 Dichalcogenphosphinate binding modes: 1 – monodentate, 2 – bidentate, 3 – bridging.

Synthesis of metal dichalcogenphosphinates (Scheme 1.8) occurs via the metathesis reaction between a metal chloride and either a potassium dichalcogenphosphinate

salt, an alkyl ammonium dichalcogenphosphinate salt or a bis(dialkylchalcogenophosphenyl)chalcogenide in the appropriate molar ratio.[133, 135-137] These phosphinate ligands are not commercially available and typically require a number of steps to synthesise; therefore there are only a few examples of metal dichalcogenphosphinates in the literature.[132]

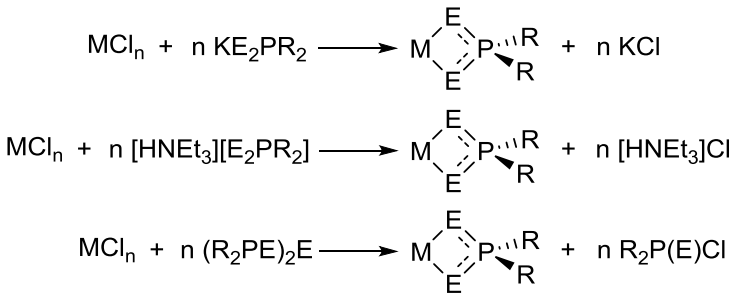

Scheme 1.8 Typical synthetic routes to metal dichalcogenphosphinates.

1.5.6 Phosphinochalcogenoic amidates

Another class of phosphorus-based chalcogen ligands is the phosphinochalcogenoic amidates utilised by Manfred Bochmann. These are bidentate ligands which bind to the metal centre via the chalcogen and nitrogen atoms. Bochmann *et al.* have primarily focussed on the selenium and tellurium derivatives although the sulfur analogues are known. Synthesis of the ligand (Scheme 1.9) occurs via the addition of $^{t}Bu_2PCl$ to LiNHR (R = ^{i}Pr or cyclohexyl) which forms the aminophosphine, $^{t}Bu_2PNHR$. Refluxing the aminophosphine with elemental selenium or tellurium forms the corresponding phosphinochalcogenoic amide, $^{t}Bu_2P(E)NHR$. Further reaction with Li^{n}Bu in THF forms the lithium phosphinochalcogenoic amidate salt.[138-140]

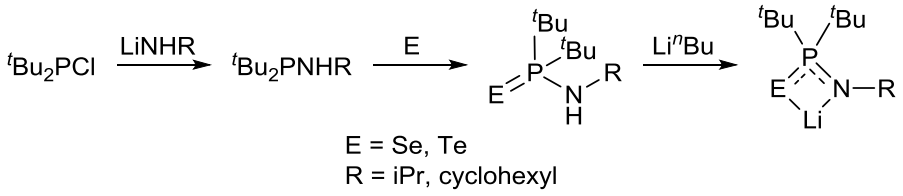

Scheme 1.9 Synthesis of phosphinochalcogenoic amidate ligand.

Synthesis of the metal phosphinochalcogenoic amidate complexes can occur by the two pathways shown in Scheme 1.10. The first method utilises the protonolysis of the metal amide with the phosphinochalcogenoic amide to form the desired metal

complex, while the second method involves the metathesis reaction between the metal chloride and the lithium phosphinochalcogenoic amidate salt. Examples of metal selenides produced by this precursor class include the metals: Cr, Mn, Fe, Co, Ni, Zn and Cd. While examples of metal tellurides produced by this precursor class include the metals: Mn, Fe, Co, Zn and Cd.[139, 140]

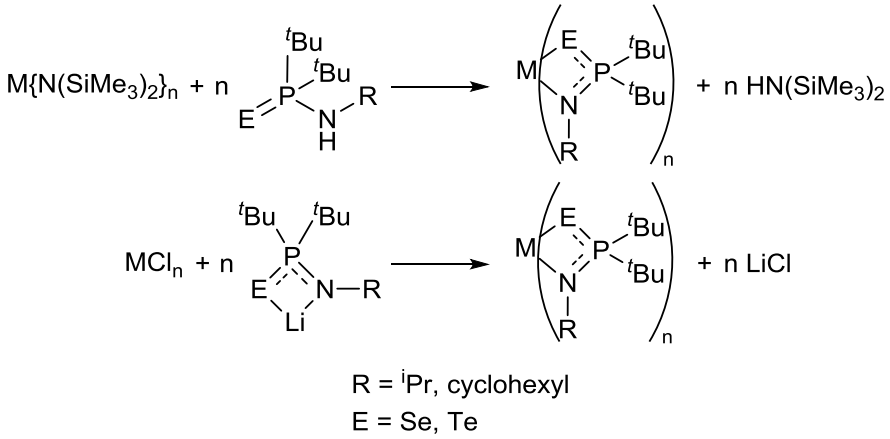

Scheme 1.10 Synthesis of metal phosphinochalcogenoic amidate complexes.

While zinc and cadmium phosphinochalcogenoic amidates produce only the monochalcogenides, the transition metal based complexes actually produce various stoichiometries with a range of metal oxidation states. Generally, the metal selenides produced have a lower chalcogen to metal ratio when compared to the metal tellurides which typically have a higher ratio. This difference in metal chalcogen stoichiometry is caused by differing decomposition pathways which are shown in Scheme 1.11. The metal selenide precursors decompose to the metal selenide with the loss of selenium containing by-products while the corresponding tellurium based by-products are tellurium free.[139, 140]

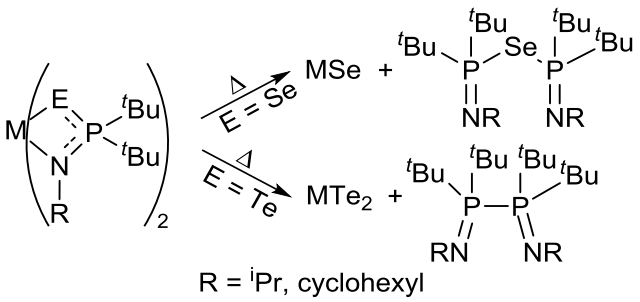

Scheme 1.11 Decomposition pathways of metal phosphinochalcogenoic amidate complexes.

1.5.7 Dichalcogenoimidodiphosphinates

Metal dichalcogenoimidodiphosphinates are a class of metal chalcogen precursors championed by Paul O'Brien due to the relative ease at synthesising the sulfur, selenium and tellurium analogues. The monoanionic ligand is composed of a P-N-P backbone with two aryl or alkyl substituents and one chalcogen atom bound to each phosphorus atom. Three binding modes exist for the ligand with all binding to the metal centre through the two chalcogen atoms. The bidentate binding mode is by far the most common with only a handful of the bridging and chelating-bridging modes observed (Figure 1.27).[86, 132, 141]

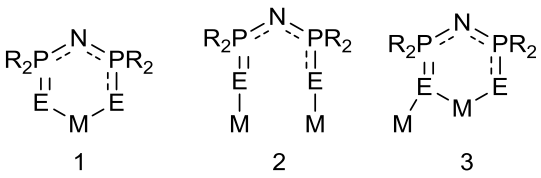

Figure 1.27 Dichalcogenoimidodiphosphinate binding modes: 1 – bidentate, 2 – bridging, 3 – chelating-bridging.

Synthesis of the dichalcogenoimidodiphosphinate ligand (Scheme 1.12) first involves the reaction between two equivalents of R_2PCl (where R = ^{i}Pr or Ph) and one equivalent of $HN(SiMe_3)_2$ to form R_2PNHPR_2. The subsequent reaction with elemental sulfur or selenium in refluxing toluene forms the neutral compound $R_2P(E)NHP(E)R_2$ where E is sulfur or selenium.[142] As tellurium is less oxidising than sulfur and selenium an alternative preparation is needed for the tellurium analogue. First, R_2PNHPR_2 is reacted with NaH to form the sodium metal salt, $Na[N(PR_2)_2]$, the addition of two equivalents of tellurium in hot toluene (with TMEDA) then forms the sodium salt of the tellurium analogue, $Na[N(TePR_2)_2]$.[143]

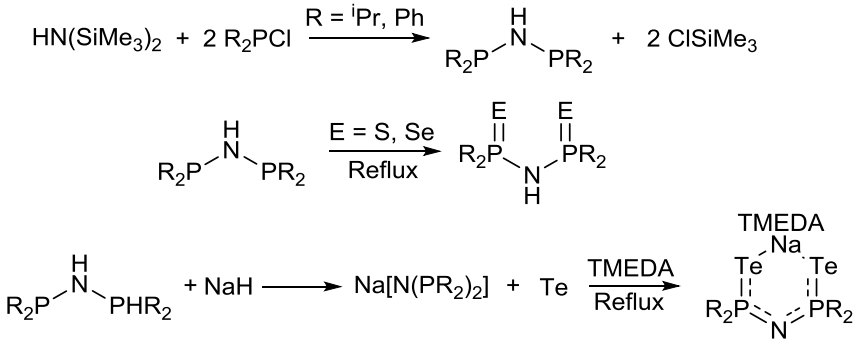

Scheme 1.12 Synthetic routes to dichalcogenoimidodiphosphinate ligands.

Synthesis of the metal dichalcogenoimidophosphinate can be performed by three different metathesis or protonolysis reactions (Scheme 1.13). The first involves the addition of $R_2P(E)NHP(E)PR_2$ to a metal carbonate to form the metal dichalcogenoimidophosphinate. The second method involves the reaction between the metal halide and the sodium dichalcogenoimidophosphinate salt. While the final method involves the deprotonation of $R_2P(E)NHP(E)PR_2$ with NaOMe followed by the direct reaction between the anionic ligand and a metal halide.[142, 144]

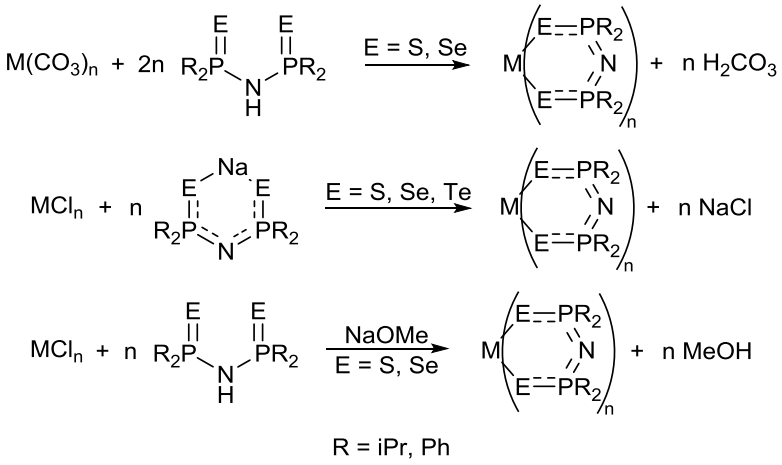

Scheme 1.13 Synthetic routes to metal dichalcogenoimidodiphosphinate complexes.

Examples of metal sulfides produced by this precursor class include the metals: Cu, Zn, Cd, In and Bi. While examples of metal selenides produced by this precursor class include the metals: Co, Ni, Cu, Zn, Ga, Cd, In and Bi. Examples of metal tellurides produced by this precursor class include the greatest range of metals: Cu, Ga, Ag, Cd, In, Sb and Au.[77, 86, 141, 144-149]

The greatest drawback to these precursors is the potential contamination of films with phosphorus or elemental chalcogen. The precursor $[Co\{(SeP^iPr_2)_2N\}_2]$, for example, produces various phases of cobalt selenides with cobalt phosphide produced at higher temperatures.[149] In contrast, the precursor $[Cd\{(TeP^iPr_2)_2N\}_2]$ produces a mixture of cubic CdTe and hexagonal tellurium when deposited at 375 °C.[147]

1.5.8 Thio-/dithio-biurets

Metal thio- and dithio-biurets produce metal sulfides as both thin films (from AACVD) and nanoparticles. The typical synthetic route to the precursors is shown in

Scheme 1.14 where either a *N,N'*-dialkylcarbamyl chloride or *N,N'*-dialkylthiocarbamyl chloride is reacted with sodium thiocyanate and the relevant dialkylamine. The synthesised ligand is then reacted in the appropriate molar ratio with the corresponding metal acetate to form the final complex. The ligands bind in a bidentate manner with a distorted tetrahedral geometry adopted at the metal centre when n = 2 and an octahedral geometry adopted when n = 3. Examples of metal sulfides produced by this precursor class include the metals: Fe, Co, Ni, Cu, Zn, Cd, In and Pb.[150-155]

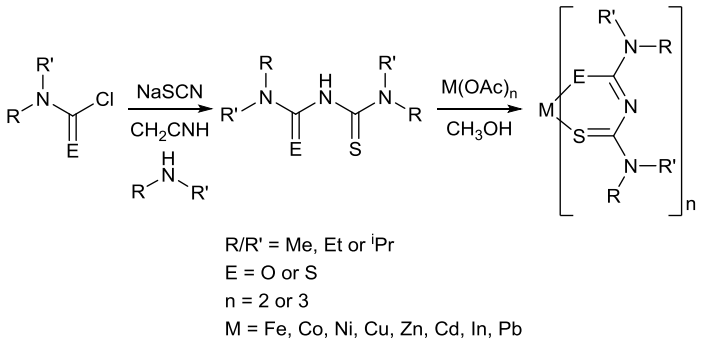

Scheme 1.14 Synthesis of thio- and dithio-biuret metal precursors.[150]

1.5.9 Thiourea adducts and thioureides

There are only a handful of examples of thiourea/thioureide-based precursors in the literature. In terms of metal sulfide CVD there are only examples of Co, Ni and Sn sulfide deposition, while examples of metal sulfide nanoparticle formation include the metals Cu, Cd and Pb. Metal thiourea/thioureide complexes are synthesised by two different methods shown in Scheme 1.15. In the first method, two equivalents of the desired thiourea is reacted with a metal chloride to form the metal-thiourea adduct. In the second method, an insertion reaction is used to insert an isothiocyanate into a metal amide bond to form the bidentate thioureide *in situ*. [156-160]

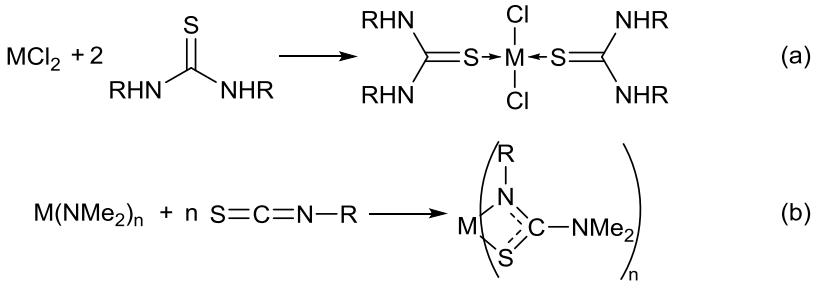

Scheme 1.15 Synthesis of (a) metal-thiourea adducts; (b) metal thioureide complexes.

There are three possible binding modes for the resulting thioureide ligand with the adopted mode dependant on both electronic and steric effects. Figure 1.28 shows the three thioureide binding modes with the inserted isothiocyanate highlighted in blue and the original metal amide nitrogen labelled as N'. The most common binding mode is the κ^2-*S,N* mode where the sulfur and nitrogen atoms of the isothiocyanate bind to the metal centre and electron density is delocalised across the {NCS} moiety. In the κ^2-*S,N'* mode the ligand binds to the metal centre via the sulfur atom from the isothiocyanate and the nitrogen atom from the original amide group. The nitrogen atom binds datively to the metal centre with the carbon and nitrogen atoms of the original isothiocyanate bound by a double bond. In the final κ^2-*N,N'* mode, the ligand binds via the two nitrogen atoms with the nitrogen from the amide forming a dative bond with the metal centre, the bond between the carbon and sulfur atoms is formally a double bond.[161]

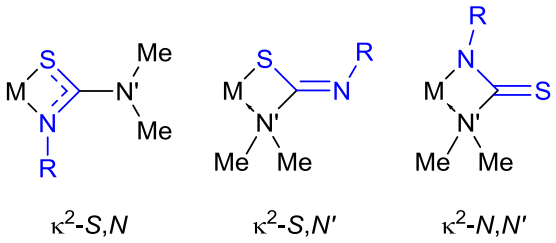

Figure 1.28 The three binding modes of thioureide ligands, inserted isothiocyanate in blue.

Previous work in the group on the efficient formation of metal ureides/thioureides and their ability to control the polymorph of the metal sulfide produced, has led to a large proportion of the work in this thesis to be based upon metal thioureides.[157, 162]

1.6 Insertion reactions

One of the most common synthetic routes to producing the metal chalcogenide precursors previously described is the insertion reaction. In this reaction a heteroallene inserts itself in between a metal-heteroatom bond to form a new ligand (Scheme 1.16), typically with the former heteroallene forming a four-membered metallacycle. These reactions are essentially stoichiometric and 100 % atom efficient as long as there are no competing side reactions.[163]

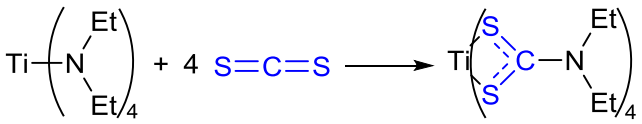

Scheme 1.16 Example of CS_2 insertion into $[Ti(NEt_2)_4]$.[113]

This reaction is important for metal chalcogenide precursor synthesis as it allows the facile incorporation of chalcogens into commonly used metal starting materials. It is an extremely versatile method as a variety of isoelectronic heteroallenes (Figure 1.29) can be reacted interchangeably with a range of metal complexes including metal amides, imides, alkoxides and alkyls to form a huge number of metal complexes such as: dichalcogenocarbamates, xanthates, thioureides, iso-ureates, amidinates and guanidinates.[163, 164] The formation of typically bidentate chelating ligands aids in the stabilisation of the metal complex although, as described previously (Figure 1.22 and Figure 1.25), these ligands also have alternative bidentate, monodentate and bridging binding modes.[103, 129]

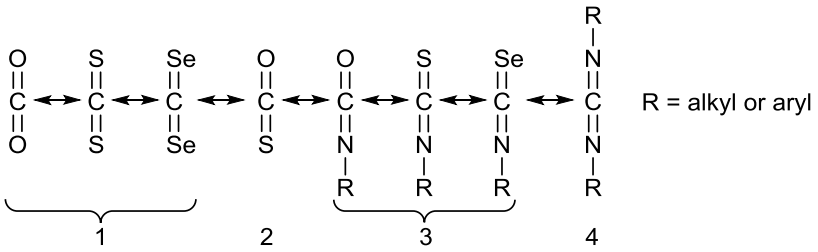

Figure 1.29 Isoelectronic heteroallenes: 1 – carbon dichalcogenides, 2 – carbonyl sulfide, 3 – isochalcogenocyanates, 4 – carbodiimides.

While some insertion reactions are very stable e.g. synthesis of sodium xanthate salts,[165] they can also be relatively labile with examples of CO_2 de-inserting from metal alkoxides reported. Varying the R group on the alkoxide alters the lability of this reaction, allowing a degree of control.[166] Reactions can also occur multiple times into the same metal heteroatom bond forming so called ‘double insertion’ products (Figure 1.30), the ligand typically remains bidentate with the metallacycle increasing in size e.g. from 4 to 6 atoms.[167] Changing the R group on certain heteroallenes from alkyl to aryl (stronger electron-withdrawing group) increases the electrophilicity of the central carbon atom allowing the insertion to proceed faster when more nucleophilic heteroatoms are bound to the metal centre.[163]

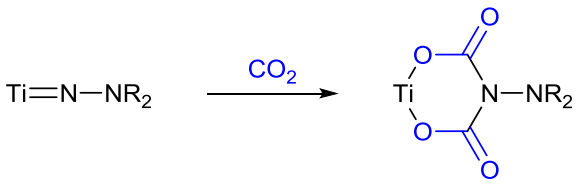

Figure 1.30 Example of a double CO_2 insertion into a metal imide, inserted CO_2 in blue.[167]

1.7 Aims and objectives

The aim of the work in this thesis is the development of single-source precursors for the CVD of TMDs. The materials of interest are the transition metal disulfides of group IV, V and VI: TiS_2, ZrS_2, HfS_2, TaS_2, MoS_2 and WS_2. The synthesis, chemistry and decomposition profile of each precursor will be investigated and the most promising complexes will be used as CVD precursors. The identity, crystallinity and quality of any deposited films will be analysed.

1.8 References

1. A. Gupta, T. Sakthivel and S. Seal, *Prog. Mater Sci.*, 2015, **73**, 44-126.
2. M. Chhowalla, H. S. Shin, G. Eda, L. J. Li, K. P. Loh and H. Zhang, *Nat. Chem.*, 2013, **5**, 263-275.
3. A. F. Morpurgo, *Nat. Phys.*, 2015, **11**, 625-626.
4. K. S. Novoselov, A. K. Geim, S. V. Morozov, D. Jiang, Y. Zhang, S. V. Dubonos, I. V. Grigorieva and A. A. Firsov, *Science*, 2004, **306**, 666-669.
5. P. Miro, M. Audiffred and T. Heine, *Chem. Soc. Rev.*, 2014, **43**, 6537-6554.
6. A. C. Ferrari, F. Bonaccorso, V. Fal'ko, K. S. Novoselov, S. Roche, P. Boggild, S. Borini, F. H. L. Koppens, V. Palermo, N. Pugno, J. A. Garrido, R. Sordan, A. Bianco, L. Ballerini, M. Prato, E. Lidorikis, J. Kivioja, C. Marinelli, T. Ryhanen, A. Morpurgo, J. N. Coleman, V. Nicolosi, L. Colombo, A. Fert, M. Garcia-Hernandez, A. Bachtold, G. F. Schneider, F. Guinea, C. Dekker, M. Barbone, Z. Sun, C. Galiotis, A. N. Grigorenko, G. Konstantatos, A. Kis, M. Katsnelson, L. Vandersypen, A. Loiseau, V. Morandi, D. Neumaier, E. Treossi, V. Pellegrini, M. Polini, A. Tredicucci, G. M. Williams, B. Hee Hong, J.-H. Ahn, J. Min Kim, H. Zirath, B. J. van Wees, H. van der Zant, L. Occhipinti, A. Di Matteo, I. A. Kinloch, T. Seyller, E. Quesnel, X. Feng, K. Teo, N. Rupesinghe, P. Hakonen, S. R. T. Neil, Q. Tannock, T. Lofwander and J. Kinaret, *Nanoscale*, 2015, **7**, 4598-4810.
7. A. K. Geim and I. V. Grigorieva, *Nature*, 2013, **499**, 419-425.
8. S. Lee and Z. Zhong, *Nanoscale*, 2014, **6**, 13283-13300.
9. J. A. Wilson and A. D. Yoffe, *Adv. Phys.*, 1969, **18**, 193-335.
10. R. A. Bromley, R. B. Murray and A. D. Yoffe, *J. Phys. C: Solid State Phys.*, 1972, **5**, 759.
11. B. Radisavljevic, A. Radenovic, J. Brivio, V. Giacometti and A. Kis, *Nat. Nanotechnol.*, 2011, **6**, 147-150.
12. B. K. Vainshtein, V. M. Friedkin and V. L. Indenbom, *Structure of Crystals*, 2nd Ed., Springer-Verlag, Berlin, Heidelberg, 1995.

13. O. Hassel, *Z. Kristallogr.*, 1924, **61**, 92.
14. W. J. Schutte, J. L. De Boer and F. Jellinek, *J. Solid State Chem.*, 1987, **70**, 207-209.
15. A. Kuc, N. Zibouche and T. Heine, *Phys. Rev. B*, 2011, **83**, 245213.
16. L. Britnell, R. M. Ribeiro, A. Eckmann, R. Jalil, B. D. Belle, A. Mishchenko, Y.-J. Kim, R. V. Gorbachev, T. Georgiou, S. V. Morozov, A. N. Grigorenko, A. K. Geim, C. Casiraghi, A. H. C. Neto and K. S. Novoselov, *Science*, 2013, **340**, 1311-1314.
17. A. Kuc, in *Chemical Modelling: Volume 11*, The Royal Society of Chemistry, 1st Ed., 2015, vol. 11, pp. 1-29.
18. J. Echeverria, E. Cremades, A. J. Amoroso and S. Alvarez, *Chem. Commun.*, 2009, 4242-4244.
19. R. Kappera, D. Voiry, S. E. Yalcin, B. Branch, G. Gupta, A. D. Mohite and M. Chhowalla, *Nat. Mater.*, 2014, **13**, 1128-1134.
20. K. F. Mak, C. Lee, J. Hone, J. Shan and T. F. Heinz, *Phys. Rev. Lett.*, 2010, **105**, 136805.
21. I. Song, C. Park and H. C. Choi, *RSC Adv.*, 2015, **5**, 7495-7514.
22. A. Splendiani, L. Sun, Y. Zhang, T. Li, J. Kim, C.-Y. Chim, G. Galli and F. Wang, *Nano Lett.*, 2010, **10**, 1271-1275.
23. E. W. Roberts, *Tribol. Int.*, 1990, **23**, 95-104.
24. *Molylube Multipurpose Extreme Pressure Grease with Moly*, Bel-Ray Company, 2014, http://www.belray.com/molylube-multipurpose-extreme-pressure-grease-moly, Accessed 14/06/2016.
25. S. Bertolazzi, J. Brivio and A. Kis, *ACS Nano*, 2011, **5**, 9703-9709.
26. J. V. Lauritsen, J. Kibsgaard, G. H. Olesen, P. G. Moses, B. Hinnemann, S. Helveg, J. K. Nørskov, B. S. Clausen, H. Topsøe, E. Lægsgaard and F. Besenbacher, *J. Catal.*, 2007, **249**, 220-233.
27. M. S. Whittingham, *Chem. Rev.*, 2004, **104**, 4271-4302.
28. J. E. Trevey, C. R. Stoldt and S.-H. Lee, *J. Electrochem. Soc.*, 2011, **158**, A1282-A1289.
29. *U.S. Pat.*, US4224390 A, 1980.
30. Y. Jung, Y. Zhou and J. J. Cha, *Inorg. Chem. Front.*, 2016, **3**, 452-463.
31. M. A. Lukowski, A. S. Daniel, C. R. English, F. Meng, A. Forticaux, R. J. Hamers and S. Jin, *Energy Environ. Sci.*, 2014, **7**, 2608-2613.
32. M. A. Lukowski, A. S. Daniel, F. Meng, A. Forticaux, L. Li and S. Jin, *J. Am. Chem. Soc.*, 2013, **135**, 10274-10277.
33. S. Li, C. Wang and H. Qiu, *Int. J. Hydrogen Energy*, 2015, **40**, 15503-15509.
34. T. F. Jaramillo, K. P. Jørgensen, J. Bonde, J. H. Nielsen, S. Horch and I. Chorkendorff, *Science*, 2007, **317**, 100-102.
35. J. Pu, L.-J. Li and T. Takenobu, *Phys. Chem. Chem. Phys.*, 2014, **16**, 14996-15006.
36. J. Kumar, M. A. Kuroda, M. Z. Bellus, S.-J. Han and H.-Y. Chiu, *Appl. Phys. Lett.*, 2015, **106**, 123508.
37. K. Xu, Z. Wang, F. Wang, Y. Huang, F. Wang, L. Yin, C. Jiang and J. He, *Adv. Mater.*, 2015, **27**, 7881-7887.
38. C. Lee, J. Hong, M.-H. Whangbo and J. H. Shim, *Chem. Mater.*, 2013, **25**, 3745-3752.
39. A. Carladous, R. Coratger, F. Ajustron, G. Seine, R. Péchou and J. Beauvillain, *Phys. Rev. B*, 2002, **66**, 045401.

40. Q. H. Wang, K. Kalantar-Zadeh, A. Kis, J. N. Coleman and M. S. Strano, *Nat. Nanotechnol.*, 2012, **7**, 699-712.
41. H. Li, Z. Yin, Q. He, H. Li, X. Huang, G. Lu, D. W. H. Fam, A. I. Y. Tok, Q. Zhang and H. Zhang, *Small*, 2012, **8**, 63-67.
42. N. Al-Dulaimi, E. A. Lewis, D. J. Lewis, S. K. Howell, S. J. Haigh and P. O'Brien, *Chem. Commun.*, 2016, **52**, 7878-7881.
43. R. Lv, J. A. Robinson, R. E. Schaak, D. Sun, Y. Sun, T. E. Mallouk and M. Terrones, *Acc. Chem. Res.*, 2015, **48**, 56-64.
44. M. Bosi, *RSC Adv.*, 2015, **5**, 75500-75518.
45. H. Schäfer, *Chemical Transport Reactions*, 1st Ed., Academic Press, New York, 1964.
46. K. S. Novoselov, D. Jiang, F. Schedin, T. J. Booth, V. V. Khotkevich, S. V. Morozov and A. K. Geim, *Proc. Natl. Acad. Sci. U.S.A.*, 2005, **102**, 10451-10453.
47. Z. Zhiyuan, Y. Zongyou, H. Xiao, L. Hai, H. Qiyuan, L. Gang, B. Freddy and Z. Hua, *Angew. Chem. Int. Ed.*, 2011, **50**, 11093-11097.
48. M. B. Dines, *Mater. Res. Bull.*, 1975, **10**, 287-291.
49. P. Joensen, R. F. Frindt and S. R. Morrison, *Mater. Res. Bull.*, 1986, **21**, 457-461.
50. G. Eda, H. Yamaguchi, D. Voiry, T. Fujita, M. Chen and M. Chhowalla, *Nano Lett.*, 2011, **11**, 5111-5116.
51. J. N. Coleman, M. Lotya, A. O'Neill, S. D. Bergin, P. J. King, U. Khan, K. Young, A. Gaucher, S. De, R. J. Smith, I. V. Shvets, S. K. Arora, G. Stanton, H.-Y. Kim, K. Lee, G. T. Kim, G. S. Duesberg, T. Hallam, J. J. Boland, J. J. Wang, J. F. Donegan, J. C. Grunlan, G. Moriarty, A. Shmeliov, R. J. Nicholls, J. M. Perkins, E. M. Grieveson, K. Theuwissen, D. W. McComb, P. D. Nellist and V. Nicolosi, *Science*, 2011, **331**, 568-571.
52. R. J. Smith, P. J. King, M. Lotya, C. Wirtz, U. Khan, S. De, A. O'Neill, G. S. Duesberg, J. C. Grunlan, G. Moriarty, J. Chen, J. Wang, A. I. Minett, V. Nicolosi and J. N. Coleman, *Adv. Mater.*, 2011, **23**, 3944-3948.
53. G. R. Bhimanapati, Z. Lin, V. Meunier, Y. Jung, J. Cha, S. Das, D. Xiao, Y. Son, M. S. Strano, V. R. Cooper, L. Liang, S. G. Louie, E. Ringe, W. Zhou, S. S. Kim, R. R. Naik, B. G. Sumpter, H. Terrones, F. Xia, Y. Wang, J. Zhu, D. Akinwande, N. Alem, J. A. Schuller, R. E. Schaak, M. Terrones and J. A. Robinson, *ACS Nano*, 2015, **9**, 11509-11539.
54. A. Y. Cho and J. R. Arthur, *Prog. Solid State Chem.*, 1975, **10**, 157-191.
55. A. Koma, K. Sunouchi and T. Miyajima, *Microelectron. Eng.*, 1984, **2**, 129-136.
56. A. T. Barton, R. Yue, S. Anwar, H. Zhu, X. Peng, S. McDonnell, N. Lu, R. Addou, L. Colombo, M. J. Kim, R. M. Wallace and C. L. Hinkle, *Microelectron. Eng.*, 2015, **147**, 306-309.
57. T. Kodas and M. Hampden-Smith, eds., *The Chemistry of Metal CVD*, 1st Ed., VCH, Weinheim, 1994.
58. Y.-H. Lee, L. Yu, H. Wang, W. Fang, X. Ling, Y. Shi, C.-T. Lin, J.-K. Huang, M.-T. Chang, C.-S. Chang, M. Dresselhaus, T. Palacios, L.-J. Li and J. Kong, *Nano Lett.*, 2013, **13**, 1852-1857.
59. Y.-H. Lee, X.-Q. Zhang, W. Zhang, M.-T. Chang, C.-T. Lin, K.-D. Chang, Y.-C. Yu, J. T.-W. Wang, C.-S. Chang, L.-J. Li and T.-W. Lin, *Adv. Mater.*, 2012, **24**, 2320-2325.

60. S. Balendhran, J. Z. Ou, M. Bhaskaran, S. Sriram, S. Ippolito, Z. Vasic, E. Kats, S. Bhargava, S. Zhuiykov and K. Kalantar-zadeh, *Nanoscale*, 2012, **4**, 461-466.
61. Y. Zhan, Z. Liu, S. Najmaei, P. M. Ajayan and J. Lou, *Small*, 2012, **8**, 966-971.
62. X.-L. Li, J.-P. Ge and Y.-D. Li, *Chem. Eur. J.*, 2004, **10**, 6163-6171.
63. N. Imanishi, K. Kanamura and Z. Takehara, *J. Electrochem. Soc.*, 1992, **139**, 2082-2087.
64. J. Cheon, J. E. Gozum and G. S. Girolami, *Chem. Mater.*, 1997, **9**, 1847-1853.
65. A. Adeogun, M. Afzaal and P. O'Brien, *Chem. Vap. Deposition*, 2006, **12**, 597-599.
66. A. N. Gleizes, *Chem. Vap. Deposition*, 2000, **6**, 155-173.
67. R. L. Puurunen, *J. Appl. Phys.*, 2005, **97**.
68. Z. Jin, S. Shin, D. H. Kwon, S.-J. Han and Y.-S. Min, *Nanoscale*, 2014, **6**, 14453-14458.
69. J.-G. Song, J. Park, W. Lee, T. Choi, H. Jung, C. W. Lee, S.-H. Hwang, J. M. Myoung, J.-H. Jung, S.-H. Kim, C. Lansalot-Matras and H. Kim, *ACS Nano*, 2013, **7**, 11333-11340.
70. Y. Kim, J.-G. Song, Y. J. Park, G. H. Ryu, S. J. Lee, J. S. Kim, P. J. Jeon, C. W. Lee, W. J. Woo, T. Choi, H. Jung, H.-B.-R. Lee, J.-M. Myoung, S. Im, Z. Lee, J.-H. Ahn, J. Park and H. Kim, *Sci. Rep.*, 2016, **6**, 18754.
71. J.-O. Carlsson and P. M. Martin, in *Handbook of Deposition Technologies for Films and Coatings*, ed. P. M. Martin, William Andrew Publishing, Boston, 3rd Ed., 2010, pp. 314-363.
72. H. O. Pierson, *Handbook of Chemical Vapor Deposition (CVD)*, 2nd Ed., Noyes Publications/William Andrew Publishing, 1999.
73. K. F. Jensen and W. Kern, in *Thin Film Processes*, Academic Press, San DiegoEd., 1991, pp. 283-368.
74. K. Oura, V. G. Lifshits, A. Saranin, A. V. Zotov and M. Katayama, *Surface Science: An Introduction*, 1st Ed., Springer-Verlag, Berlin, Heidelberg, 2003.
75. P. M. Martin, *Handbook of Deposition Technologies for Films and Coatings*, 3rd Ed., William Andrew; Elsevier Science [distributor], Norwich, N.Y.; Oxford, 2009.
76. P. Marchand, I. A. Hassan, I. P. Parkin and C. J. Carmalt, *Dalton Trans.*, 2013, **42**, 9406-9422.
77. C. E. Knapp and C. J. Carmalt, *Chem. Soc. Rev.*, 2016, **45**, 1036-1064.
78. X. Hou and K. L. Choy, *Chem. Vap. Deposition*, 2006, **12**, 583-596.
79. F. Maury, *Chem. Vap. Deposition*, 1996, **2**, 113-116.
80. L. McElwee-White, *Dalton Trans.*, 2006, **0**, 5327-5333.
81. A. C. Jones and M. L. Hitchman, *Chemical Vapour Deposition: Precursors, Processes and Applications*, 1st Ed., RSC, 2009.
82. M. Ritala and J. Niinisto, in *Chemical Vapour Deposition : Precursors, Processes and Applications*, Royal Society of Chemistry, 1st Ed., 2009, pp. 158-206.
83. F. Maury, *J. Phys. IV France*, 1995, **05**, C5-449-C445-463.
84. J. R. Castro, K. C. Molloy, Y. Liu, C. S. Lai, Z. L. Dong, T. J. White and E. R. T. Tiekink, *J. Mater. Chem.*, 2008, **18**, 5399-5405.
85. N. Alam, M. S. Hill, G. Kociok-Köhn, M. Zeller, M. Mazhar and K. C. Molloy, *Chem. Mater.*, 2008, **20**, 6157-6162.

86. M. Afzaal, M. A. Malik and P. O'Brien, *J. Mater. Chem.*, 2010, **20**, 4031-4040.
87. M. Bochmann, I. Hawkins and L. M. Wilson, *J. Chem. Soc., Chem. Commun.*, 1988, 344-345.
88. I. P. Parkin, L. S. Price, T. G. Hibbert and K. C. Molloy, *J. Mater. Chem.*, 2001, **11**, 1486-1490.
89. J. Rodriguez-Castro, P. Dale, M. F. Mahon, K. C. Molloy and L. M. Peter, *Chem. Mater.*, 2007, **19**, 3219-3226.
90. S. Otsuka, M. Kamata, K. Hirotsu and T. Higuchi, *J. Am. Chem. Soc.*, 1981, **103**, 3011-3014.
91. C. J. Carmalt, E. S. Peters, I. P. Parkin and D. A. Tocher, *New J. Chem.*, 2005, **29**, 620-624.
92. R. Kumar, H. E. Mabrouk and D. G. Tuck, *J. Chem. Soc., Dalton Trans.*, 1988, 1045-1047.
93. *U.S. Pat.*, US5157136 A, 1992.
94. M. Bochmann, K. J. Webb, M. B. Hursthouse and M. Mazid, *J. Chem. Soc., Dalton Trans.*, 1991, 2317-2323.
95. H. S. Park, M. Mokhtari and H. W. Roesky, *Chem. Vap. Deposition*, 1996, **2**, 135-139.
96. A. L. Seligson and J. Arnold, *J. Am. Chem. Soc.*, 1993, **115**, 8214-8220.
97. G. Barone, T. G. Hibbert, M. F. Mahon, K. C. Molloy, L. S. Price, I. P. Parkin, A. M. E. Hardy and M. N. Field, *J. Mater. Chem.*, 2001, **11**, 464-468.
98. S. D. Reid, A. L. Hector, W. Levason, G. Reid, B. J. Waller and M. Webster, *Dalton Trans.*, 2007, 4769-4777.
99. S. L. Benjamin, Y.-P. Chang, C. Gurnani, A. L. Hector, M. Huggon, W. Levason and G. Reid, *Dalton Trans.*, 2014, **43**, 16640-16648.
100. S. L. Benjamin, C. H. de Groot, C. Gurnani, A. L. Hector, R. Huang, K. Ignatyev, W. Levason, S. J. Pearce, F. Thomas and G. Reid, *Chem. Mater.*, 2013, **25**, 4719-4724.
101. A. L. Hector, M. Jura, W. Levason, S. D. Reid and G. Reid, *New J. Chem.*, 2009, **33**, 641-645.
102. P. J. McKarns, T. S. Lewkebandara, G. P. A. Yap, L. M. Liable-Sands, A. L. Rheingold and C. H. Winter, *Inorg. Chem.*, 1998, **37**, 418-424.
103. I. I. Ozturk, C. N. Banti, N. Kourkoumelis, M. J. Manos, A. J. Tasiopoulos, A. M. Owczarzak, M. Kubicki and S. K. Hadjikakou, *Polyhedron*, 2014, **67**, 89-103.
104. M. Colapietro, A. Vaciago, D. C. Bradley, M. B. Hursthouse and I. F. Rendall, *J. Chem. Soc. D*, 1970, 743-744.
105. M. Colapietro, A. Vaciago, D. C. Bradley, M. B. Hursthouse and I. F. Rendall, *J. Chem. Soc., Dalton Trans.*, 1972, 1052-1057.
106. P. O'Brien and J. Waters, *Chem. Vap. Deposition*, 2006, **12**, 620-626.
107. M. A. Ehsan, H. N. Ming, V. McKee, T. A. N. Peiris, U. Wijayantha-Kahagala-Gamage, Z. Arifin and M. Mazhar, *New J. Chem.*, 2014, **38**, 4083-4091.
108. S. Saeed, R. Hussain and R. J. Butcher, *J. Coord. Chem.*, 2014, **67**, 1693-1701.
109. S. Khalid, M. A. Malik, D. J. Lewis, P. Kevin, E. Ahmed, Y. Khan and P. O'Brien, *J. Mater. Chem. C*, 2015, **3**, 12068-12076.
110. M. B. Hursthouse, M. A. Malik, M. Motevalli and P. O'Brien, *Polyhedron*, 1992, **11**, 45-48.

111. J. McAleese, P. O′Brien and D. J. Otway, *Chem. Vap. Deposition*, 1998, **4**, 94-96.
112. P. O'Brien, D. J. Otway and J. R. Walsh, *Chem. Vap. Deposition*, 1997, **3**, 227-229.
113. D. C. Bradley and M. H. Gitlitz, *J. Chem. Soc. A*, 1969, 1152-1156.
114. P. O'Brien, J. R. Walsh, I. M. Watson, L. Hart and S. R. P. Silva, *J. Cryst. Growth*, 1996, **167**, 133-142.
115. T. Ouyang, K. P. Loh, H. Zhang, J. J. Vittal, M. Vetrichelvan, W. Chen, X. Gao and A. T. S. Wee, *J. Phys. Chem. B*, 2004, **108**, 17537-17545.
116. G. A. Horley, P. O'Brien, J.-H. Park, A. J. P. White and D. J. Williams, *J. Mater. Chem.*, 1999, **9**, 1289-1292.
117. M. Chunggaze, M. Azad Malik, P. O'Brien, A. J. P. White and D. J. Williams, *J. Chem. Soc., Dalton Trans.*, 1998, 3839-3844.
118. G. A. Horley, M. Chunggaze, P. O'Brien, A. J. P. White and D. J. Williams, *J. Chem. Soc., Dalton Trans.*, 1998, 4205-4210.
119. M. Chunggaze, M. A. Malik and P. O'Brien, *Adv. Mater. Opt. Electron.*, 1997, **7**, 311-316.
120. K. Kunze, L. Bihry, P. Atanasova, M. J. Hampden-Smith and E. N. Duesler, *Chem. Vap. Deposition*, 1996, **2**, 105-108.
121. M. Nyman, M. J. Hampden-Smith and E. N. Duesler, *Chem. Vap. Deposition*, 1996, **2**, 171-174.
122. M. Nyman, K. Jenkins, M. J. Hampden-Smith, T. T. Kodas, E. N. Duesler, A. L. Rheingold and M. L. Liable-Sands, *Chem. Mater.*, 1998, **10**, 914-921.
123. G. Shang, M. J. Hampden-Smith and E. N. Duesler, *Chem. Commun.*, 1996, 1733-1734.
124. G. Shang, K. Kunze, M. J. Hampden-Smith and E. N. Duesler, *Chem. Vap. Deposition*, 1996, **2**, 242-244.
125. T. C. Deivaraj, J.-H. Park, M. Afzaal, P. O'Brien and J. J. Vittal, *Chem. Commun.*, 2001, 2304-2305.
126. T. C. Deivaraj, J.-H. Park, M. Afzaal, P. O'Brien and J. J. Vittal, *Chem. Mater.*, 2003, **15**, 2383-2391.
127. M. Akhtar, N. Revaprasadu, M. A. Malik and J. Raftery, *Mater. Sci. Semicond. Process.*, 2015, **30**, 368-375.
128. T. Ito, *Acta Crystallogr., Sect. E*, 2002, **58**, m517-m518.
129. E. R. T. Tiekink and I. Haiduc, in *Progress in Inorganic Chemistry, Vol 54*, ed. K. D. Karlin, John Wiley & Sons Inc, New York, 1st Ed., 2005, vol. 54, pp. 127-319.
130. N. Pradhan, B. Katz and S. Efrima, *J. Phys. Chem. B*, 2003, **107**, 13843-13854.
131. C. Zhang, S. Zhang, L. Yu, Z. Zhang, P. Zhang and Z. Wu, *Mater. Lett.*, 2012, **85**, 77-80.
132. I. Haiduc, *J. Organomet. Chem.*, 2001, **623**, 29-42.
133. C. Q. Nguyen, M. Afzaal, M. A. Malik, M. Helliwell, J. Raftery and P. O'Brien, *J. Organomet. Chem.*, 2007, **692**, 2669-2677.
134. S. N. Malik, A. Q. Malik, R. F. Mehmood, G. Murtaza, Y. G. Alghamdi and M. A. Malik, *New J. Chem.*, 2015, **39**, 4047-4054.
135. C. Q. Nguyen, A. Adeogun, M. Afzaal, M. A. Malik and P. O'Brien, *Chem. Commun.*, 2006, 2182-2184.
136. P. Kevin, S. N. Malik, M. A. Malik and P. O'Brien, *Chem. Commun.*, 2014, **50**, 14328-14330.

137. C. Q. Nguyen, A. Adeogun, M. Afzaal, M. A. Malik and P. O'Brien, *Chem. Commun.*, 2006, 2179-2181.
138. M. Bochmann, *Chem. Vap. Deposition*, 1996, **2**, 85-96.
139. G. C. Bwembya, X. Song and M. Bochmann, *Chem. Vap. Deposition*, 1995, **1**, 78-80.
140. X. Song and M. Bochmann, *J. Chem. Soc., Dalton Trans.*, 1997, 2689-2692.
141. M. Afzaal, D. Crouch, M. A. Malik, M. Motevalli, P. O'Brien and J.-H. Park, *J. Mater. Chem.*, 2003, **13**, 639-640.
142. D. Cupertino, D. J. Birdsall, A. M. Z. Slawin and J. D. Woollins, *Inorg. Chim. Acta*, 1999, **290**, 1-7.
143. G. G. Briand, T. Chivers and M. Parvez, *Angew. Chem. Int. Ed.*, 2002, **41**, 3468-3470.
144. M. Afzaal, D. Crouch, Mohmmad A. Malik, M. Motevalli, P. O'Brien, J.-H. Park and J. D. Woollins, *Eur. J. Inorg. Chem.*, 2004, **2004**, 171-177.
145. M. C. Copsey, A. Panneerselvam, M. Afzaal, T. Chivers and P. O'Brien, *Dalton Trans.*, 2007, 1528-1538.
146. S. S. Garje, M. C. Copsey, M. Afzaal, P. O'Brien and T. Chivers, *J. Mater. Chem.*, 2006, **16**, 4542-4547.
147. S. S. Garje, J. S. Ritch, D. J. Eisler, M. Afzaal, P. O'Brien and T. Chivers, *J. Mater. Chem.*, 2006, **16**, 966-969.
148. S. S. Garje, D. J. Eisler, J. S. Ritch, M. Afzaal, P. O'Brien and T. Chivers, *J Am Chem Soc*, 2006, **128**, 3120-3121.
149. A. Panneerselvam, C. Q. Nguyen, J. Waters, M. A. Malik, P. O'Brien, J. Raftery and M. Helliwell, *Dalton Trans.*, 2008, 4499-4506.
150. K. Ramasamy, M. A. Malik, P. O'Brien and J. Raftery, *Dalton Trans.*, 2010, **39**, 1460-1463.
151. K. Ramasamy, M. A. Malik, M. Helliwell, J. Raftery and P. O'Brien, *Chem. Mater.*, 2011, **23**, 1471-1481.
152. A. L. Abdelhady, K. Ramasamy, M. A. Malik, P. O'Brien, S. J. Haigh and J. Raftery, *J. Mater. Chem.*, 2011, **21**, 17888-17895.
153. A. L. Abdelhady, M. A. Malik and P. O'Brien, *J. Mater. Chem.*, 2012, **22**, 3781-3785.
154. K. Ramasamy, M. A. Malik, J. Raftery, F. Tuna and P. O'Brien, *Chem. Mater.*, 2010, **22**, 4919-4930.
155. P. J. Thomas, G. L. Stansfield, N. Komba, D. J. H. Cant, K. Ramasamy, E. Albrasi, H. Al-Chaghouri, K. L. Syres, P. O'Brien, W. R. Flavell, E. Mubofu, F. Bondino and E. Magnano, *RSC Adv.*, 2015, **5**, 62291-62299.
156. L. P. Mgabi, B. S. Dladla, M. A. Malik, S. S. Garje, J. Akhtar and N. Revaprasadu, *Thin Solid Films*, 2014, **564**, 51-57.
157. I. Y. Ahmet, M. S. Hill, A. L. Johnson and L. M. Peter, *Chem. Mater.*, 2015, **27**, 7680-7688.
158. M. J. Moloto, N. Revaprasadu, G. A. Kolawole, P. O'Brien and M. A. Malik, *S. Afr. J. Sci.*, 2005, **101**, 463-465.
159. M. J. Moloto, N. Revaprasadu, P. O'Brien and M. A. Malik, *J. Mater. Sci. - Mater. Electron.*, 2004, **15**, 313-316.
160. T. Mandal, V. Stavila, I. Rusakova, S. Ghosh and K. H. Whitmire, *Chem. Mater.*, 2009, **21**, 5617-5626.
161. M. B. Harkness, E. Alvarado, A. C. Badaj, B. C. Skrela, L. Fan and G. G. Lavoie, *Organometallics*, 2013, **32**, 3309-3321.

162. T. Wildsmith, M. S. Hill, A. L. Johnson, A. J. Kingsley and K. C. Molloy, *Chem. Commun.*, 2013, **49**, 8773-8775.
163. A. E. Sinyakov and N. A. Ovchinnikova, *Russ. J. Inorg. Chem.*, 2013, **58**, 1694-1707.
164. A. M. Willcocks, T. Pugh, J. A. Hamilton, A. L. Johnson, S. P. Richards and A. J. Kingsley, *Dalton Trans.*, 2013, **42**, 5554-5565.
165. A. A. Mohamed, I. Kani, A. O. Ramirez and J. P. Fackler, *Inorg. Chem.*, 2004, **43**, 3833-3839.
166. L. Ferro, P. B. Hitchcock, M. P. Coles, H. Cox and J. R. Fulton, *Inorg. Chem.*, 2011, **50**, 1879-1888.
167. P. J. Tiong, A. Nova, L. R. Groom, A. D. Schwarz, J. D. Selby, A. D. Schofield, E. Clot and P. Mountford, *Organometallics*, 2011, **30**, 1182-1201.

Chapter 2

Ti, Zr and Hf sulfide precursors

2.1 Introduction

The focus of this chapter is the development of single-source precursors for the deposition of titanium, zirconium and hafnium disulfides. The precursors being investigated will be based on group IV metal thioureide and dithiocarbamate complexes.

2.1.1 Group IV disulfides

Of all the group IV dichalcogenide systems, the material that has garnered the most attention is TiS_2. The major interest in TiS_2 is centred on its use as a cathode material in Li ion batteries. TiS_2 is the lightest TMD, is semimetallic and forms a single phase lithium intercalate, which are all extremely beneficial properties for device construction. Cathodes made from TiS_2 show good cyclability and can complete over 1000 charging/discharging cycles before battery life is affected.[1]

While TiS_2 is of interest for its intercalation properties, ZrS_2 and HfS_2 are of interest for their semiconducting properties. Both materials have band gaps and electron mobilities suitable for their incorporation into FETs. These materials are also relevant for use in optoelectronic devices due to their high photoresponse and photogain values.[2, 3]

Bulk titanium, zirconium and hafnium disulfide all adopt the 1T polymorph with the metal centre in an octahedral environment. The space group adopted in all three structures is $P\bar{3}m1$ with cell parameters of a = 3.40 and c = 5.69 Å for TiS_2, a = 3.66 and c = 5.83 Å for ZrS_2, and a = 3.63 and c = 5.85 Å for HfS_2.[4, 5] Monolayers are ~0.7 nm thick and can adopt either the 1H or 1T phase although the 1T phase is more favoured.[6, 7] Both ZrS_2 and HfS_2 are diamagnetic, n-type semiconductors with indirect band gaps of 1.7 eV and 2.1 eV respectively, while TiS_2 has a band gap of 0.3 eV and is classed as a semimetal.[4, 5, 8]

2.1.2 TiS_2 precursors

The majority of precursors for the deposition of group IV sulfides focus on titanium. Multi-source CVD methods for depositing TiS_2 involve the precursors $TiCl_4$ and H_2S[9, 10], $TiCl_4$ and thiols (^{t}BuSH, 1-methyl-1-propanthiol, $HS(CH_2)_2SH$, $HSCMe_3$, $S(SiMe_3)_2$)[11-14], and $Ti(NMe_2)_4$ and thiols (^{t}BuSH and $^tBu_2S_2$)[15, 16] at temperatures of

175-600 °C under a variety of conditions which include low pressure, atmospheric pressure and plasma CVD.

Single-source TiS_2 precursors are mainly based on titanium thiolate or sulfide compounds. The most commonly used precursor is the red titanium thiolate compound, $[Ti(S^tBu)_4]$, first reported by Bochmann *et al.* in 1988. Deposition under low pressure conditions at 130 to 200 °C produces amorphous purple films on glass which have a titanium to sulfur ratio of 1:1.[17] Further investigation by Cheon *et al.* reported amorphous grey-blue TiS_2 films (ratio 1:2) under low pressure (10^{-4} torr) in the temperature range of 150-300 °C on quartz, silicon and stainless steel substrates (Figure 2.1). Analysis of the volatile by-products shows $[Ti(S^tBu)_4]$ decomposes to form TiS_2, isobutylene, ^{t}BuSH and H_2S. Cheon *et al*. suggested that the removal of water and oxygen from the reactor meant TiS_2 was formed rather than TiS.[18] Experiments by Carmalt *et al.* show the precursor can be made *in situ* by reacting $Ti(NMe_2)_4$ or $Ti(NEt_2)_4$ with ^{t}BuSH in a variety of solvents (hexanes, toluene and dichloromethane). The direct AACVD of these precursor solutions show faster growth rates and more uniform films for the *in situ* preparation compared to experiments with the isolated precursor. Amorphous gold TiS_2 films were produced on glass substrates for all experiments across the temperature range 150-300 °C.[16]

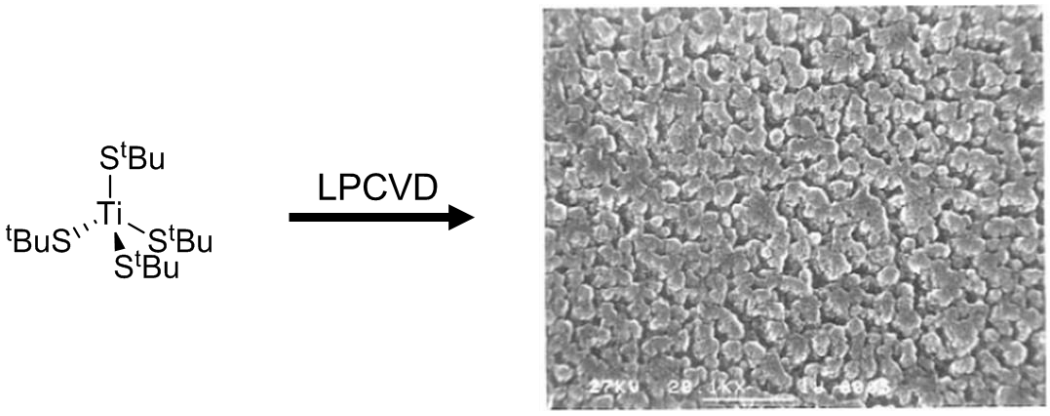

Figure 2.1 SEM image of TiS_2 film on quartz deposited from $[Ti(S^tBu)_4]$ at 150 °C by Cheon *et al.*[18]

Reaction of $Ti(NMe_2)_4$ with the thiol CF_3CH_2SH produces the ionic complex $[Me_2NH_2]_2[Ti(SCH_2CF_3)_6]$ shown in Figure 2.2, rather than the neutral thiolate complex as seen for ^{t}BuSH. Low pressure deposition (0.03 mmHg) at 550 °C produces amorphous purple TiS_2 films on glass substrates.[19] Low pressure

experiments with the complexes $[Cp_2Ti(S^tBu)_2]$ and $[Cp_2Ti(SEt)_2]$ produce sulfur-deficient films of TiS_2 in the temperature range 400-650 °C.[20]

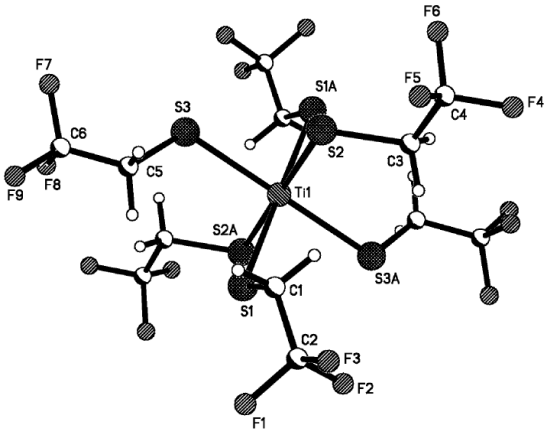

Figure 2.2 Molecular structure of Ti containing anion in $[Me_2NH_2]_2[Ti(SCH_2CF_3)_6]$.[19]

Winter *et al.* have explored a range of $TiCl_4$ based precursors with two organothiol-based adducts (general formula $[TiCl_4(HSR)_2]$) or two organic sulfide-based adducts (general formula $[TiCl_4(SR_2)_2]$). Deposition at low pressure (0.1 – 0.2 mmHg) with $[TiCl_4(HSC_6H_{11})_2]$ and $[TiCl_4(HSC_5H_9)_2]$ produces crystalline bronze-coloured TiS_2 films on glass and silicon in a hot walled reactor at 200 – 600 °C. Films show a (001) crystallographic orientation suggesting the TiS_2 layers lie parallel to the substrate surface. Low pressure deposition with $[(TiCl_4)_2(MeSSMe)]$ (Figure 2.3) produces TiS_2 at 400 – 600 °C.[21-23]

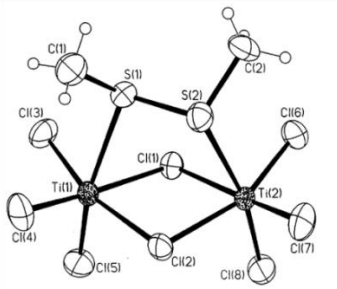

Figure 2.3 Molecular structures of $[(TiCl_4)_2(MeSSMe)]$.[21]

Carmalt *et al.* have also reported that the reaction between $TiCl_4$ and three equivalents of either pyridinethiol or pyrimidinethiol forms the pseudo-pentagonal bipyramidal complexes $[TiCl(SC_5H_4N)_3]$ and $[TiCl(SC_4H_3N_2)_3]$ (Figure 2.4), respectively. Low pressure deposition with the pyridine complex, $[TiCl(SC_5H_4N)_3]$, produces crystalline brown/gold films of sulfur-deficient TiS_2 at 600 °C and

TiS_2/TiO_2 at 500 °C. While deposition with the pyrimidine complex, $[TiCl(SC_4H_3N_2)_3]$, produces amorphous films of sulfur-deficient TiS_2 with chlorine, carbon and nitrogen contamination.[24]

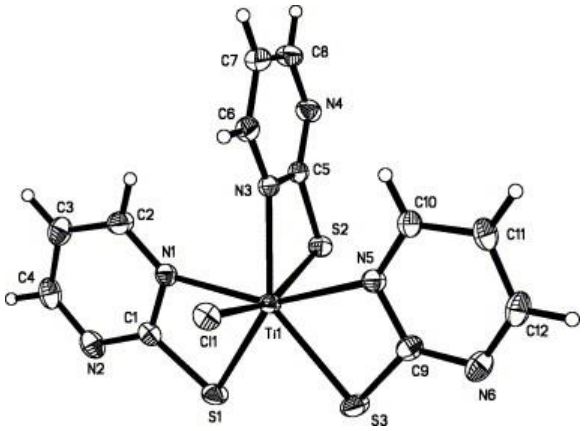

Figure 2.4 Molecular structure of $[TiCl(SC_4H_3N_2)_3]$.[24]

2.1.3 ZrS_2 precursors

There are very few examples of either multi-source or single-source ZrS_2 precursors reported in the literature. König *et al.* have patented the multi-source route of $ZrCl_4$ with either H_2S, SF_6, SF_4, SO_2 or COS for depositing ZrS_2 at temperatures of 500 – 700 °C and pressures of 50 – 1000 Pa.[25] While Zhang *et al.* have recently reported the deposition of monolayer ZrS_2 onto a h-BN coated SiO_2/Si substrate using $ZrCl_4$ and S at 950 °C.[3] In contrast, Thiyagarajan *et al.* have reported that an aqueous solution of $ZrO_2Cl_2 \cdot 8H_2O$ and thiourea deposits polycrystalline micron thick films of ZrS_2 on glass (Figure 2.5) using a spray pyrolysis method at 430 °C.[26]

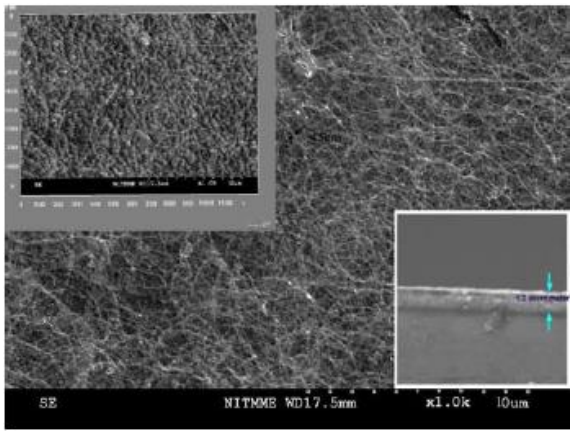

Figure 2.5 SEM image of ZrS_2 film on glass substrate deposited from a 0.01 M solution of $ZrO_2Cl_2 \cdot 8H_2O$ and thiourea by Thiyagarajan *et al.*[26]

To our knowledge there is only one example of a single-source precursor that has been used to deposit ZrS_2 although the quality of material deposited is very poor. Senocq *et al.* have reported that the zirconium complex, $Cp_2Zr(S^tBu)_2$, has been used to deposit sulfur-deficient films of ZrS_x (x = <2) under low pressure conditions at 400 to 650 °C.[20] Carmalt *et al.* produced the potential precursor $[Me_2NH_2][Zr_2(\mu\text{-}S^tBu)_3(S^tBu)_6]$, although thermal analysis showed decomposition prior to volatilisation, meaning the compound could not be used as a LPCVD precursor.[19] The dearth of potential precursors means there is huge scope for the development of a viable ZrS_2 single-source precursor.

2.1.4 HfS_2 precursors

To the best of our knowledge there are only two examples of HfS_2 deposition reported in the literature, both are patents covering the use of $HfCl_4$ with either S, H_2S, SF_6, SF_4, SO_2 or COS.[25, 27] The similar paucity of potential precursors for HfS_2 deposition indicates there is a huge opportunity to develop single-source precursors.

2.1.5 Group IV selenide and telluride precursors

While the focus of this chapter is single-source group IV metal sulfide precursors, it is important to review single-source group IV metal selenide and telluride precursors as some ligand sets can be used to provide a range of chalcogenides within complexes.

Reports of single-source group IV selenide precursors focus on two main ligand sets: selenolates and seleno-ethers. McKarns *et al.* were the first to report the deposition of $TiSe_2$ using the single-source precursor $[TiCl_4(Se(CH_2CH_3)_2)_2]$. Rose-bronze coloured films of crystalline $TiSe_2$ were deposited on glass at 500 – 600 °C under low pressure conditions, the films were unstable in air and decomposed to form TiO_2.[28] Reid *et al.* have reported the majority of examples of single-source group IV selenide precursors with the similar seleno-ethers, $[TiCl_4\{o\text{-}C_6H_4(CH_2SeMe)_2\}]$ and $[TiCl_4(Se^nBu_2)_2]$, depositing crystalline films of $TiSe_2$ at 500 °C using LPCVD.[29, 30] Deposition at low pressures (10^{-1} mmHg) with the precursors, $[Cp_2M(Se^tBu)_2]$ (where M = Ti, Zr and Hf), produced metal selenide films on silica substrates at 450 – 600 °C, the majority of films were crystalline.[31]

There are no reports of the successful deposition of group IV tellurides, LPCVD studies with the group IV metal tellurolate complexes, $[Cp_2M(Te^tBu)_2]$ (where M = Zr and Hf), only produced elemental tellurium.[31] These examples show that there are very few examples of any zirconium and hafnium chalcogenide single-source precursors.

2.2 Group IV thioureides

As described in Chapter 1, previous work in the group has focussed on isocyanate and isothiocyanate insertions into metal amide bonds to form the corresponding ureides and thioureides. These precursors allow the control of stoichiometry in tin chalcogenide systems where multiple stoichiometries are possible.[32, 33] Due to the promising nature of these precursors, similar insertion reactions were investigated for group IV amide systems.

2.2.1 Existing group IV thioureide systems

Group IV thioureide systems have been known for some time although they have never been applied to thin film production. The majority of complexes having been designed and synthesised as catalysts, or catalyst precursors, for the polymerisation of α-olefins.[34] The bulk of group IV metal thioureide complexes are synthesised via the insertion of an isothiocyanate into a metal amide[34-36] or imide bond[37]. There are also examples of group IV metal thioureide synthesis by the metathesis reaction between sodium thioureide salts and titanium chlorides.[38] Instances of all three thioureide binding modes: κ^2-*S*,*N*, κ^2-*S*,*N'* and κ^2-*N*,*N'* (Figure 2.6) are exhibited in various group IV metal thioureides.

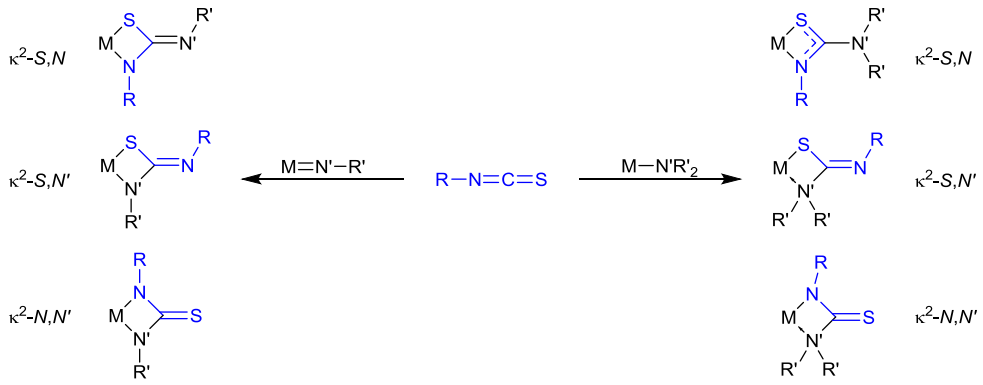

Figure 2.6 Possible coordination modes of thioureide ligands after the insertion of an isothiocyanate into a metal imide or amide bond, inserted isothiocyanate in blue.

Xie *et al.* have described the insertion of *n*-butyl isothiocyanate into the metal amide bonds of the complexes $[\sigma:\eta^1:\eta^5\text{-}(OCH_2)(R_2NCH_2)C_2B_9H_9]Ti(NR_2)$ (where R = Me, Et) and $[\eta^5:\sigma\text{-}Me_2A(C_9H_6)(C_2B_{10}H_{10})]Zr(NMe_2)_2$ (where A = C, Si).[34, 35] On addition of one equivalent of the isothiocyanate, the corresponding metal thioureide complexes $[\sigma:\eta^1:\eta^5\text{-}(OCH_2)(R_2NCH_2)C_2B_9H_9]Ti\text{-}[\eta^3\text{-}SC(NR_2)N^nBu]$ (Figure 2.7a) and $[\eta^5:\sigma\text{-}Me_2A(C_9H_6)(C_2B_{10}H_{10})]Zr(NMe_2)[\eta^2\text{-}SC(NMe_2)N^nBu]$ are formed. Insertion of an additional isothiocyanate unit into the zirconium complex results in the formation of the product, $[\eta^5:\sigma\text{-}Me_2C(C_9H_6)(C_2B_{10}H_{10})]Zr[\eta^2\text{-}SC(NMe_2)N^nBu]_2$ (Figure 2.7b). In all of the above examples the thioureide ligand binds to the metal centre via the κ^2-*S,N* mode with the original amide nitrogen no longer bound to the metal centre.

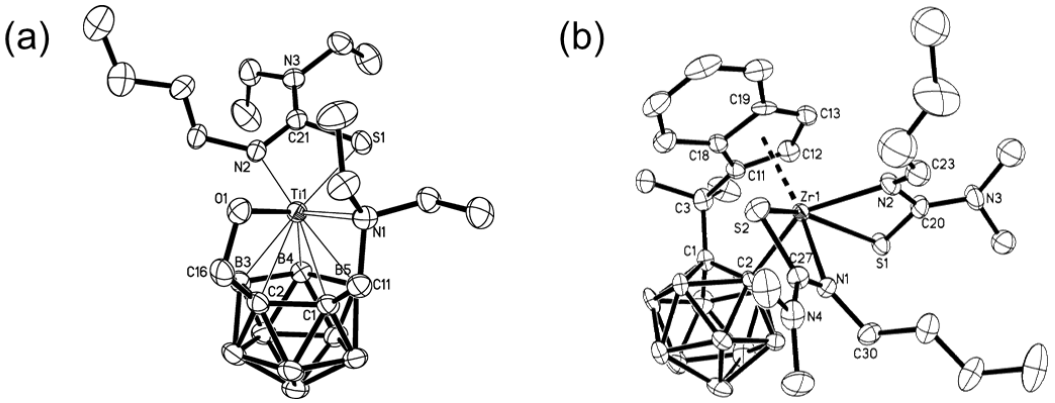

Figure 2.7 Molecular structures of: (a) $[\sigma:\eta^1:\eta^5\text{-}(OCH_2)(Et_2NCH_2)\text{-}C_2B_9H_9]Ti[\eta^3\text{-}SC(NEt_2)N^nBu]$; (b) $[\eta^5:\sigma\text{-}Me_2C(C_9H_6)(C_2B_{10}H_{10})]Zr[\eta^2\text{-}SC(NMe_2)N^nBu]_2$, showing the κ^2-*S,N* thioureide binding mode.[34, 35]

Weitershaus *et al.* have reported that the reaction between the metal imide, $[Cp^*Ti(N^{Xyl}N)\{N\text{-}NPh_2\}(^tBuNH_2)]$ (where Xyl = xylyl) and phenyl isothiocyanate forms two products. The major product, $[Cp^*Ti(N^{Xyl}N)\{\kappa^2\text{-}N(NPh_2)C(NPh)S\}]$ (Figure 2.8a), contains the thioureide in the κ^2-*S,N'* mode where the nitrogen from the original imide is still bound to the metal centre. In the minor product, $[Cp^*Ti(N^{Xyl}N)\{\kappa^2\text{-}N(NPh_2)C(S)NPh\}]$ (Figure 2.8b), the thioureide is bound to the metal centre in the κ^2-*N,N'* mode with the sulfur atom not bound to the metal centre.[39]

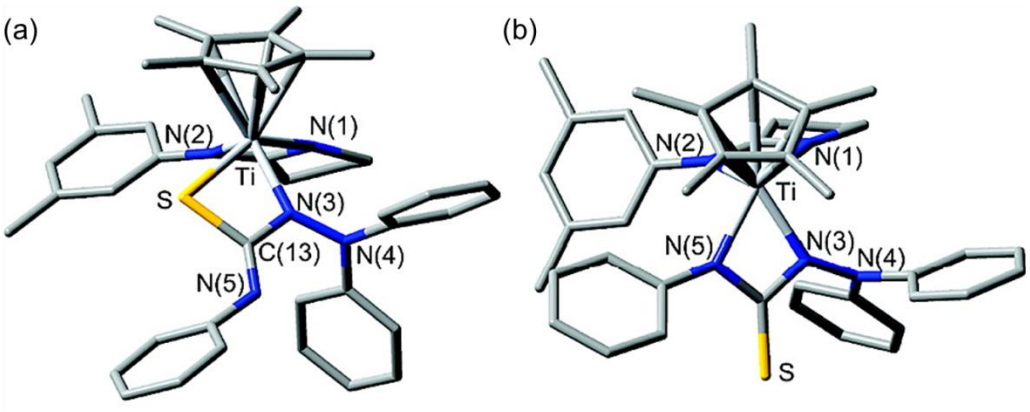

Figure 2.8 Computed molecular structures of: (a) [Cp*Ti(N^{Xyl}N){κ^2-N(NPh_2)C(NPh)S}] - showing the κ^2-*S,N'* binding mode; (b) [Cp*Ti(N^{Xyl}N){κ^2-N(NPh_2)C(S)NPh}] - showing the κ^2-*N,N'* binding mode.[39]

Harkness *et al.* have also shown that group IV metal thioureide complexes can be formed via the reaction between a sodium thioureide salt synthesised *in situ* with various titanium chloride compounds (Scheme 2.1). Mono-thioureide and bis-thioureide titanium complexes have been reported in which the thioureide ligand binds to the metal centre in a κ^2-*S,N* mode.[38]

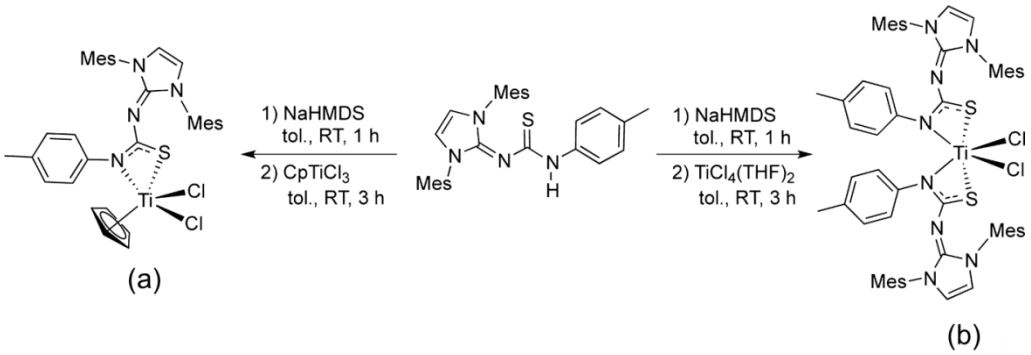

Scheme 2.1 Synthesis of: (a) $CpTiCl_2$[IMesN(CS)N-*p*-tolyl]; (b) $TiCl_2$[IMesN(CS)N-*p*-tolyl]$_2$.[38]

2.2.2 Synthesis and characterisation of titanium thioureide systems

As noted previously, group IV thioureide systems can be synthesised by the facile reaction between metal amide bonds (M-NR_2) and isothiocyanates (R-NCS, where R = aryl or alkyl).[32] The reactions of tetrakis(dimethylamido) titanium, [Ti(NMe_2)$_4$], in hexane with iso-propyl, *tert*-butyl and phenyl isothiocyanates were investigated. In all cases reactions occurred instantaneously on the addition of the isothiocyanate resulting in the formation of red solutions, stirring overnight ensured complete reaction. Products could be crystallised and isolated from the reaction mixture at

reduced temperatures or by recrystallisation from toluene solution. All reactions were performed under inert conditions using Schlenk line techniques.

Analysis of the products from the 2:1 reaction of the iso-propyl, *tert*-butyl and phenyl isothiocyanates with [Ti(NMe$_2$)$_4$] by ^{1}H and ^{13}C{^{1}H} NMR spectroscopy, allowed the number of isothiocyanate insertions to be determined from the ratio of un-inserted amide groups to inserted amide groups (or number of R groups). NMR spectroscopy showed separate un-inserted and inserted NMe$_2$ resonances, integration of the peaks gave a ratio of 1:1 suggesting the bis-insertion products had been formed (Scheme 2.2).

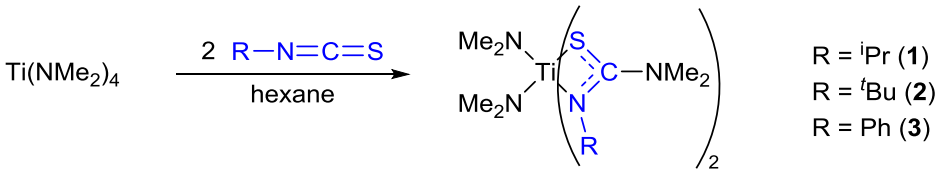

Scheme 2.2 Reaction of [Ti(NMe$_2$)$_4$] with two equivalents of the iso-propyl, *tert*-butyl and phenyl isothiocyanates forms the bis-insertion products **1**, **2** and **3** respectively.

Closer inspection of the ^{1}H NMR spectrum of the iso-propyl complex, **1**, showed the CH and CH$_3$ resonances of the iso-propyl group to be broad signals suggesting the complex is fluxional in solution. The ^{13}C{^{1}H} NMR spectrum displayed multiple iso-propyl group environments supporting this theory. No resonance was observed for the {N$_2$CS} carbon resonance although work by Glaser *et al.* shows similar carbon resonances in isothiocyanates can be difficult to observe in fluxional environments especially when the expected carbon peak is of low intensity.[40]

The ^{1}H NMR spectrum of the *tert*-butyl complex, **2**, showed two *tert*-butyl environments indicating two separate thioureide binding modes are present. The ^{13}C{^{1}H} NMR spectrum displayed a single {N$_2$CS} carbon resonance at 160.4 ppm but exhibited multiple R group environments supporting the presence of two different ligand binding modes. The ^{1}H NMR spectrum of the phenyl complex, **3**, showed a single thioureide ligand environment with sharp NMe$_2$ singlets suggesting the complex is not fluxional. The ^{13}C{^{1}H} NMR spectrum displayed all carbon environments as single resonances with the {N$_2$CS} carbon resonance observed at 179.7 ppm.

For the 4:1 reaction, ^{1}H and $^{13}C\{^{1}H\}$ NMR spectroscopy showed independent Ti-NMe_2 and inserted NMe_2 resonances for the iso-propyl and *tert*-butyl isothiocyanate reactions indicating the bis-insertion products, **1** and **2**, had again been formed. Identical products were also recovered for the 3:1 and 1:1 reactions. In contrast, the 4:1 (and 3:1) phenyl isothiocyanate insertion only displayed a single NMe_2 resonance potentially consistent with the tetrakis-insertion product, $[Ti\{SC(NMe_2)NPh\}_4]$. However, elemental analysis suggested the product was not the tetrakis-inserted complex but rather a monosulfide titanium complex coordinated by two thioureide ligands, $[TiS\{SC(NMe_2)NPh\}_2]$ (**4**).

Previous work within the group has shown metal thioureide complexes containing un-inserted amide groups to decompose via the loss of a guanidine derivative.[32] Therefore it is proposed that complex **4** is formed by the mechanism presented in Scheme 2.3 with the initial insertion of three phenyl isothiocyanates followed by the loss of phenyl guanidine, complex **4** could exist as either a monomer or dimer. The broad resonances in the ^{1}H NMR spectrum, multiple NMe_2/phenyl carbon environments in the $^{13}C\{^{1}H\}$ NMR spectrum and no $\{N_2CS\}$ carbon resonances suggest the complex has a degree of fluxionality in solution.

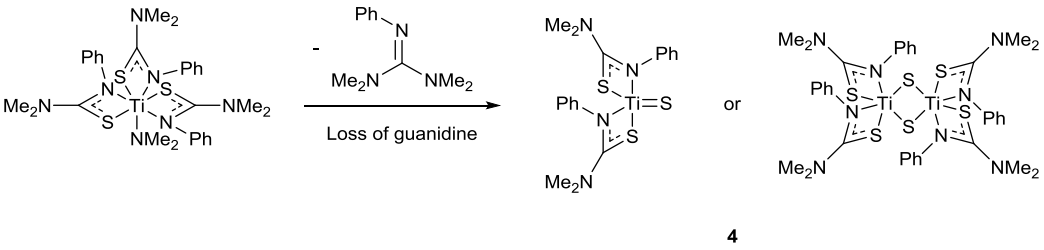

Scheme 2.3 Proposed mechanism for the formation of **4**, the product could be a monomer or dimer.

Dark red crystals of the iso-propyl complex, **1**, were analysed using single crystal X-ray diffraction. The molecular structure obtained (Figure 2.9) was consistent with the bis-inserted product predicted from the ^{1}H and $^{13}C\{^{1}H\}$ NMR spectra, selected bond lengths and angles are shown in Table 2.1. The complex crystallised in a monoclinic $P2_1/c$ space group with the asymmetric unit containing a single molecule. Two dimethylamide and two bidentate κ^2-*S*,*N* thioureide ligands are bound to the titanium metal centre which adopts a distorted octahedral geometry.

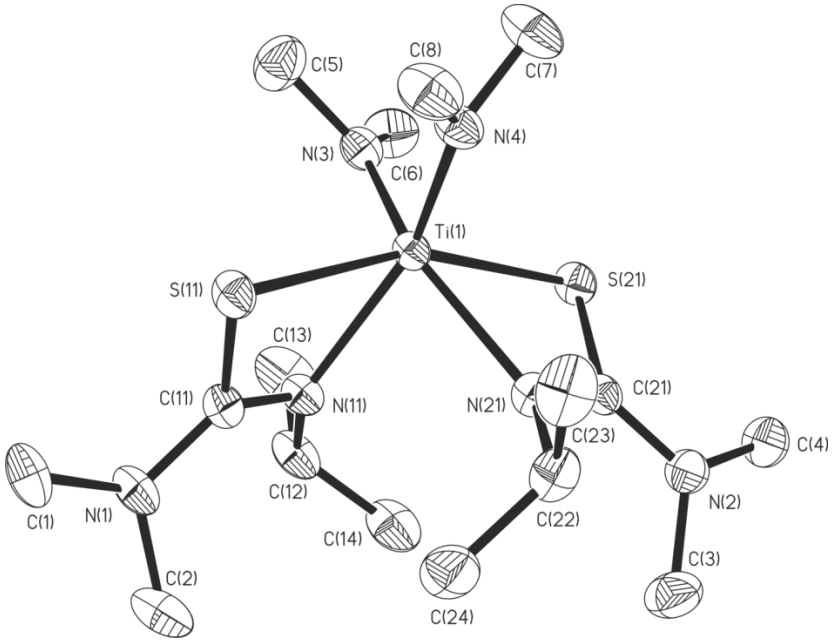

Figure 2.9 Molecular structure of complex **1**. Thermal ellipsoids are shown at 50 % probability, with hydrogen atoms omitted for clarity.

Table 2.1 Selected bond lengths and angles for **1** with e.s.d.s. in parentheses.

Bond	Bond length / Å	Angle	Bond angle / °
$Ti\text{-}N_{amide}$	1.9318(12), 1.9371(13)	$Ti\text{-}N\text{-}C_{Me}$	115.34(10), 116.11(10), 135.01(11), 135.38(11)
		κ^2-*S*,*N* mode	
Ti-S	2.4871(4), 2.4874(4)	$S\text{-}Ti\text{-}N_{iPr}$	65.25(3), 65.32(3)
$Ti\text{-}N_{iPr}$	2.2258(12), 2.2290(12)	Ti-S-C	80.37(5), 80.46(5)
S-C	1.7515(15), 1.7538(15)	$Ti\text{-}N_{iPr}\text{-}C$	101.42(9), 101.44(9)
$C\text{-}N_{iPr}$	1.3010(18), 1.3032(17)	$S\text{-}C\text{-}N_{iPr}$	112.41(11), 112.61(10)
$N\text{-}C_{iPr}$	1.4821(18), 1.4832(18)	S-C-N’	119.65(10), 119.90(10)
C-N’	1.3704(18), 1.3731(19)	$N_{iPr}\text{-}C\text{-}N’$	127.69(13), 127.75(13)

The two $Ti\text{-}N_{amide}$ bond lengths (1.9318(12) and 1.9371(13) Å) and the tilted nature of the $\{TiNC_2\}$ moiety with one carbon atom closer to the metal centre (Ti(1)-N(3)-C(5) = 115.34(10)°, Ti(1)-N(3)-C(6) = 135.01(11)°), are consistent with the values reported for the amide group in the starting material, $[Ti(NMe_2)_4]$.[41] Both thioureide ligands bind to the metal centre via the κ^2-*S*,*N* mode with the Ti-S (2.4871(4), 2.4874(4) Å) bond lengths statistically identical and the $Ti\text{-}N_{iPr}$ (2.2258(12),

2.2290(12) Å) bond lengths longer than those found for the thioureide ligand in the complex, $[\sigma:\eta^1:\eta^5\text{-}(OCH_2)(Et_2NCH_2)\text{-}C_2B_9H_9]Ti[\eta^3\text{-}SC(NEt_2)N^nBu]$ (Ti-S = 2.492(1) Å, Ti-N = 2.062(3) Å).[34] Within the thioureide ligand, the relatively short $C\text{-}N_{iPr}$ (1.3010(18), 1.3032(17) Å) and C-N' (1.3704(18), 1.3731(19) Å) bond lengths, and the planarity of the C atom (sum of angles = 360°) suggests electron density is delocalised across the $\{SC(N')N_{iPr}\}$ moiety. However, the longer C-N' bond lengths, the slight pyramidalisation of the N' atom (sum of angles: N(1) = 353.8°, N(2) = 355.2°) and the rotation of the $N'Me_2$ group around the C-N' axis indicates the majority of the delocalised electron density is centred on the $\{SCN_{iPr}\}$ moiety.

The *tert*-butyl complex, **2**, formed dark red crystals which were analysed using single crystal X-ray diffraction. The molecular structure obtained (Figure 2.10) was consistent with the bis-inserted product however, in this case the molecular structure contains one thioureide ligand in the κ^2-*S,N* binding mode and the other in the κ^2-*S,N'* mode. The presence of two different binding modes was predicted from the ^1H and $^{13}C\{^1H\}$ NMR spectra. A selection of bond lengths and angles are presented in Table 2.2. The complex crystallised in a triclinic *P*-1 space group with the asymmetric unit containing two almost identical molecules, the following discussion will focus on the molecule containing Ti(1). The titanium metal centre in complex **2** adopts a very similar geometry to that observed in the iso-propyl complex **1**.

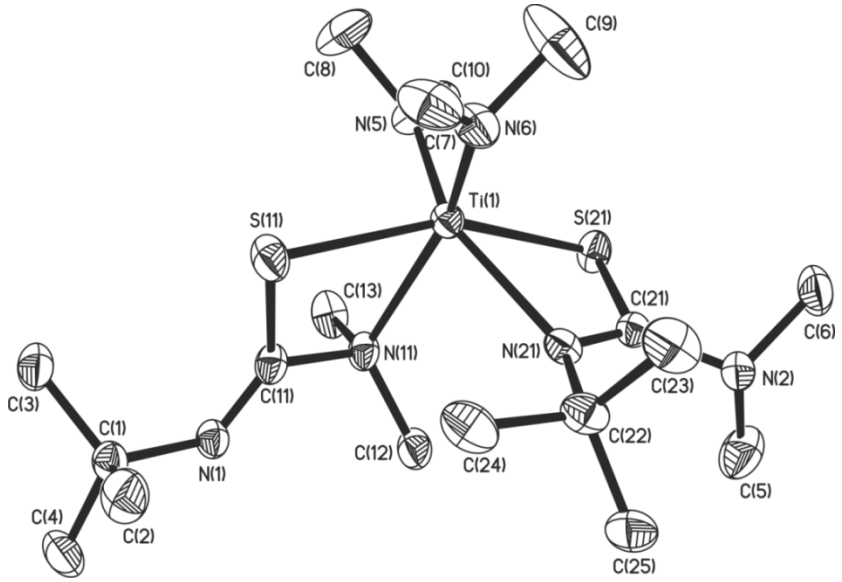

Figure 2.10 Molecular structure of complex **2**. Thermal ellipsoids are shown at 50 % probability, with hydrogen atoms omitted for clarity.

Table 2.2 Selected bond lengths and angles for **2** with e.s.d.s. in parentheses.

Bond	Bond length / Å	Angle	Bond angle / °
$Ti\text{-}N_{amide}$	1.911(3), 1.929(3)	$Ti\text{-}N\text{-}C_{Me}$	114.4(2), 118.4(2), 133.0(2), 136.1(2)
		κ^2-*S,N* mode	
Ti-S	2.4980(8)	$S\text{-}Ti\text{-}N_{tBu}$	65.32(6)
$Ti\text{-}N_{tBu}$	2.274(2)	Ti-S-C	79.331(9)
S-C	1.754(3)	$Ti\text{-}N_{tBu}\text{-}C$	98.53(1)
$C\text{-}N_{tBu}$	1.287(3)	$S\text{-}C\text{-}N_{tBu}$	115.3(2)
$N\text{-}C_{tBu}$	1.508(4)	S-C-N’	119.6(2)
C-N’	1.438(4)	$N_{tBu}\text{-}C\text{-}N’$	125.0(2)
		κ^2-*S,N’* mode	
Ti-S	2.4379(9)	S-Ti-N’	66.28(6)
Ti-N’	2.328(3)	Ti-S-C	87.49(10)
C-S	1.750(3)	Ti-N’-C	98.22(17)
$C\text{-}N’_{Me2}$	1.490(3)	S-C-N’	106.9(2)
$C\text{-}N_{tBu}$	1.264(4)	$S\text{-}C\text{-}N_{tBu}$	135.1(2)
$N\text{-}C_{tBu}$	1.484(3)	$N_{tBu}\text{-}C\text{-}N’$	118.0(3)

When compared to the κ^2-*S,N* iso-propyl thioureide ligand in **1**, the κ^2-*S,N tert*-butyl thioureide ligand in **2** shows a considerable pyramidalisation of the N’ atom (sum of angles = 333.5°) with the methyl carbon atoms rotated to sit above and below the $\{SCN_2\}$ plane. This change in geometry along with a shorter $C\text{-}N_{tBu}$ bond (1.287(3) Å) and longer C-N’ bond (1.438(4) Å) suggests electron density is delocalised exclusively across the $\{SCN_{tBu}\}$ moiety. The κ^2-*S,N tert*-butyl thioureide ligand in **2** also shows an elongation of the Ti-S (2.4980(8) Å) and Ti-N (2.274(2) Å) bonds indicating that steric bulk of the *tert*-butyl group prevents the thioureide ligand from binding as closely.

The presence of the κ^2-*S,N’* binding mode suggests the *tert*-butyl group is too large for two thioureide ligands to bind via the κ^2-*S,N* mode and hence one of the ligands has to assume the κ^2-*S,N’* binding mode to reduce the steric demands of the ligand. Compared to the κ^2-*S,N* mode, the κ^2-*S,N’* mode has a shorter Ti-S bond (2.4379(9)

Å) but longer Ti-N' bond (2.328(3) Å) which is indicative of the N' atom binding to the metal centre via its lone pair. There is also an elongation of the C-N' bond (1.490(3) Å) and a very slight shortening of the C-N_{tBu} bond (1.264(4) Å) suggesting an increase in electron density across the {SCN_{tBu}} moiety. A slight change in geometry between the titanium atom and κ^2-*S,N'* thioureide ligand is also observed with the Ti-S-C angle increasing and the S-C-N angle decreasing in size.

Analysis of the phenyl complex, **3**, using single crystal X-ray diffraction showed the molecular structure (Figure 2.11) was consistent with the bis-inserted product predicted from the ^{1}H and ^{13}C{^{1}H} NMR spectra. Table 2.3 presents selected bond lengths and angles of complex **3** which crystallised in a triclinic *P*-1 space group with the asymmetric unit containing a single molecule. The structure of the phenyl complex, **3**, is effectively a structural isomer of the iso-propyl complex, **1**, with two dimethylamide and two bidentate κ^2-*S,N* thioureide ligands binding to the titanium metal centre which adopts a distorted octahedral geometry. In the phenyl complex, **3**, the sulfur atoms are positioned in a *cis* arrangement while in the iso-propyl complex, **1**, they adopt a *trans* orientation.

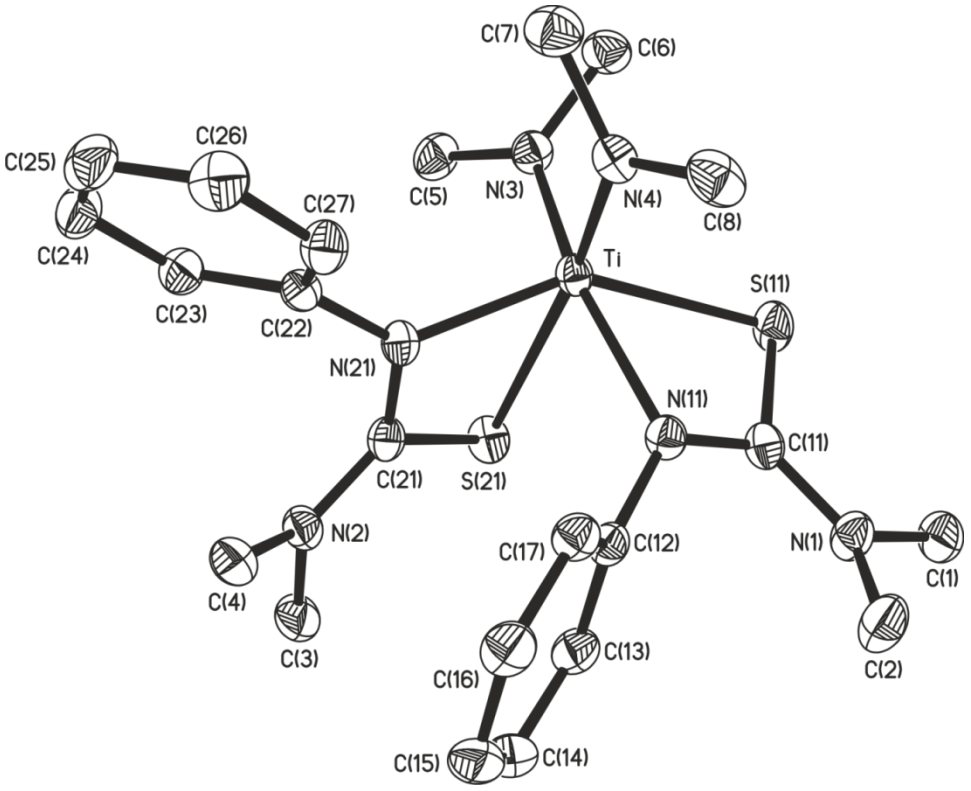

Figure 2.11 Molecular structure of complex **3**. Thermal ellipsoids are shown at 50 % probability, with hydrogen atoms omitted for clarity.

Table 2.3 Selected bond lengths and angles for **3** with e.s.d.s. in parentheses.

Bond	Bond length / Å	Angle	Bond angle / °
$Ti\text{-}N_{amide}$	1.9251(14), 1.9255(14)	$Ti\text{-}N\text{-}C_{Me}$	122.87(11)-126.25(11)
		κ^2-*S*,*N* mode	
Ti-S	2.5012(5), 2.6464(5)	$S\text{-}Ti\text{-}N_{Ph}$	64.69(4), 65.56(4)
$Ti\text{-}N_{Ph}$	2.0838(13), 2.1963(13)	Ti-S-C	75.11(5), 79.86(6)
S-C	1.7276(16), 1.7436(17)	$Ti\text{-}N_{Ph}\text{-}C$	101.90(10), 105.26(10)
$C\text{-}N_{Ph}$	1.319(2), 1.348(2)	$S\text{-}C\text{-}N_{Ph}$	112.39(12), 113.12(12)
$N\text{-}C_{Ph}$	1.427(2), 1.422(2)	S-C-N’	120.51(12), 122.05(12)
C-N’	1.355(2), 1.344(2)	$N_{Ph}\text{-}C\text{-}N’$	124.72(14), 127.08(15)

Unlike the $Ti\text{-}NMe_2$ group in the iso-propyl complex, **1**, the $Ti\text{-}NMe_2$ groups in **3** show only a small degree of tilt across the $\{TiNC_2\}$ moiety ($Ti\text{-}N\text{-}C_{Me}$ = 122.87(11) - 126.25(11)°). The κ^2-*S*,*N* phenyl thioureide ligand in **3**, adopts a very similar geometry to that of the κ^2-*S*,*N* iso-propyl thioureide ligand in **1**, with **3** exhibiting slightly longer Ti-S bonds (2.5012(5), 2.6464(5) Å) and slightly shorter Ti-N bonds (2.0838(13), 2.1963(13) Å). The phenyl ring planes within the ligand are orientated at angles of 94 and 125° to the {NCS} plane suggesting there is no conjugation between the {NCS} moiety and phenyl ring.

Analysis of the phenyl sulfide complex, **4**, using single crystal X-ray diffraction showed the complex adopted a dimeric structure (Figure 2.12) in the solid state; selected bond lengths and angles are shown in Table 2.4. The dimer consists of a central $\{Ti(\mu\text{-}S)_2Ti\}$ four-membered ring with two κ^2-*S*,*N* phenyl thioureide ligands binding to each titanium atom. The complex crystallised in a triclinic *P*-1 space group with the asymmetric unit containing half a molecule and two molecules of toluene, equivalent atoms were generated using the symmetry operator (-x, -y+1, -z+1). The single binding mode of the thioureide ligand is consistent with the ^1H and $^{13}C\{^1H\}$ NMR spectra.

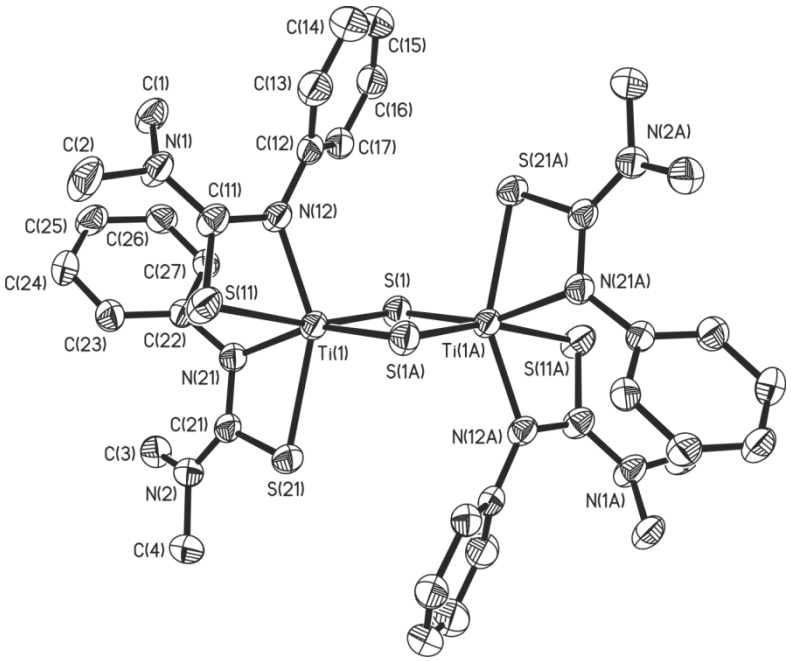

Figure 2.12 Molecular structure of complex **4**. Thermal ellipsoids are shown at 50 % probability, with hydrogen atoms omitted for clarity.

Table 2.4 Selected bond lengths and angles for **4** with e.s.d.s. in parentheses.

Bond	Bond length / Å	Bond angle	Angle / °
Ti-S_μ	2.2865(8), 2.3122(8)	Ti-S_μ-Ti	86.87(3)
		S_μ-Ti-S_μ	93.13(3)
		κ^2-*S,N* mode	
Ti-S	2.4692(8), 2.5397(8)	S-Ti-N_{Ph}	66.72(6), 66.88(6)
Ti-N_{Ph}	2.083(2), 2.121(2)	Ti-S-C	76.18(9), 79.46(8)
S-C	1.730(3), 1.747(3)	Ti-N_{Ph}-C	102.23(15), 103.09(16)
C-N_{Ph}	1.337(3), 1.348(3)	S-C-N_{Ph}	110.57(18), 112.63(18)
N-C_{Ph}	1.417(3), 1.427(3)	S-C-N’	121.6(2), 121.69(18)
C-N’	1.334(3), 1.336(3)	N_{Ph}-C-N’	125.7(2), 127.6(2)

The central {Ti(μ-S)$_2$Ti} ring is planar (internal angles = 360°) with the Ti···Ti distance (3.1619(7) Å) and Ti-S_μ bond lengths (2.2865(8), 2.3122(8) Å) consistent with values reported by Gyepes *et al.* for the {Ti(μ-S)$_2$Ti} moiety in a range of sulfide bridged titanium cage clusters.[42] The Ti-S_μ bonds are shorter than the Ti-S bonds (2.4692(8), 2.5397(8) Å) between the metal centre and thioureide ligands, which suggests that the lack of bulky ligand on the S_μ atom allows it to bind more

closely to the titanium atom. The phenyl thioureide ligand geometries adopted in complex **4** are equivalent to the phenyl thioureide ligand geometries observed in complex **3**.

2.2.3 Synthesis and characterisation of zirconium and hafnium thioureide systems

The reactions of tetrakis(dimethylamido) zirconium, [$Zr(NMe_2)_4$], and tetrakis(dimethylamido) hafnium, [$Hf(NMe_2)_4$], in hexane with the iso-propyl, *tert*-butyl and phenyl isothiocyanates were also investigated. In all cases reactions occurred instantaneously resulting in the formation of a pale yellow precipitate (iso-propyl), yellow solution (*tert*-butyl) or white precipitate (phenyl), stirring overnight ensured complete reaction. Products could be crystallised and isolated from the reaction mixture at reduced temperatures or by recrystallisation from toluene solution.

^{1}H and $^{13}C\{^{1}H\}$ NMR spectroscopy of the products from the reaction of the iso-propyl and *tert*-butyl isothiocyanates with [$Zr(NMe_2)_4$] (Scheme 2.4) showed separate inserted and un-inserted NMe_2 resonances, integration of the peaks gave a ratio of 3:1 suggesting the tris-insertion products had been formed. In contrast, the product from the reaction of the phenyl isothiocyanate with [$Zr(NMe_2)_4$] only displayed a single NMe_2 resonance consistent with an inserted NMe_2 group. Elemental analysis results supported the formation of the tetrakis-insertion product. These products were recovered irrespective of the isothiocyanate to metal amide ratio used at the start of the reaction.

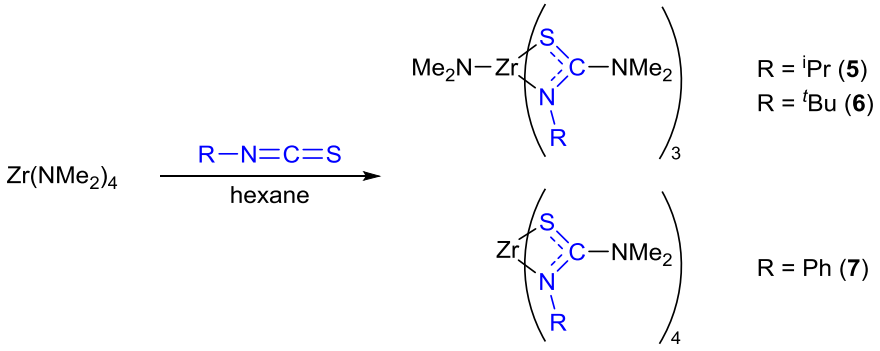

Scheme 2.4 Reaction of [$Zr(NMe_2)_4$] with the iso-propyl, *tert*-butyl and phenyl isothiocyanates forms the products **5**, **6** and **7** respectively.

The analogous reaction of the iso-propyl, *tert*-butyl and phenyl isothiocyanates with [$Hf(NMe_2)_4$] (Scheme 2.5) exclusively produced the tris-inserted products. ^1H and $^{13}C\{^1H\}$ NMR spectroscopy of the products showed separate inserted and un-inserted NMe_2 resonances, integration of the peaks gave a ratio of 3:1. These products were recovered irrespective of the isothiocyanate to metal amide ratio used at the start of the reaction.

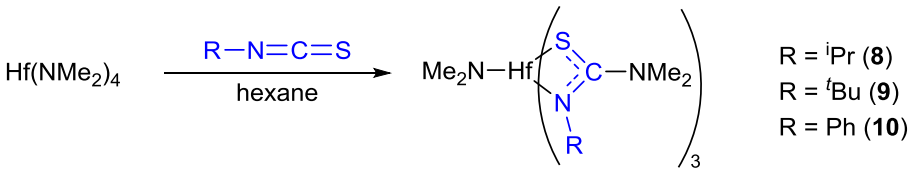

Scheme 2.5 Reaction of [$Hf(NMe_2)_4$] with the iso-propyl, *tert*-butyl and phenyl isothiocyanates forms the products **8**, **9** and **10** respectively.

The identities of iso-propyl zirconium (**5**) and hafnium (**8**) complexes could only be ascertained at high temperatures (373 K) using variable temperature NMR, as the spectra at room temperature were complex and exhibited multiple CH and CH_3 iso-propyl environments. At higher temperatures the resonances coalesced to form a single set of broad singlets indicating rapid exchange between the different iso-propyl environments. The $^{13}C\{^1H\}$ NMR spectra for both complexes showed multiple iso-propyl environments but did not display the inserted {N_2CS} carbon resonance suggesting the ligand is undergoing rapid exchange. The fluxional nature of the iso-propyl thioureide ligand in complexes **5** and **8** is mirrored in the iso-propyl titanium complex, **1**.

For the *tert*-butyl zirconium (**6**) and hafnium (**9**) complexes the ^1H NMR spectra showed two separate thioureide ligand environments indicating two different binding modes were present. The un-inserted NMe_2 resonance was displayed as two separate peaks suggesting each methyl is found in a different environment; this suggests the dimethylamide group cannot freely rotate around the M-N axis. Two resonances were observed for the {N_2CS} peak in the $^{13}C\{^1H\}$ NMR spectra of **6** (191.1 and 164.2 ppm) and **9** (190.6 and 164.3 ppm) which again suggests two different thioureide ligand binding modes are present. The existence of two different thioureide binding modes is also observed in the *tert*-butyl titanium complex, **2**.

Even though the phenyl zirconium (**7**) and hafnium (**10**) complexes contain four and three thioureide ligands respectively, both presented sharp singlets in the ^{1}H NMR spectra and showed a single thioureide environment. Similarly, the $^{13}C\{^{1}H\}$ NMR spectra also showed a single phenyl thioureide environment with $\{N_2CS\}$ resonances of 181.2 ppm (**7**) and 180.2 ppm (**10**). The $\{N_2CS\}$ resonances sit in between the values recorded for the *tert*-butyl complexes **6** and **9**. The resonances observed for the phenyl thioureide ligand in **7** are also consistent with those reported for the phenyl thioureide ligand in the complex $[Zr\{C_4H_2N(2\text{-}CH_2N^tBu)(5\text{-}CH_2NMe_2)\}\{PhNC(NMe_2)S\}(NMe_2)]$ which had a $\{N_2CS\}$ resonance of 179.6 ppm.[36]

Single crystal X-ray diffraction analysis of the iso-propyl zirconium (**5**) and hafnium (**8**) complexes provided isostructural molecular structures (Figure 2.13), which were consistent with the tris-inserted product. Both structures crystallised in a triclinic *P*-1 space group with a single molecule contained within the asymmetric unit; selected bond lengths and angles are presented in Table 2.5. The structures exhibit two separate thioureide binding modes with two ligands binding κ^2-*S,N* and one binding κ^2-*N,N'*. The presence of different binding modes is consistent with the multiple iso-propyl environments observed in the ^{1}H and $^{13}C\{^{1}H\}$ NMR spectra at room temperature. The metal centres adopt a distorted pentagonal bipyramidal geometry with the equatorial plane consisting of a κ^2-*S,N* ligand, a κ^2-*N,N'* ligand and a sulfur atom from the remaining κ^2-*S,N* ligand.

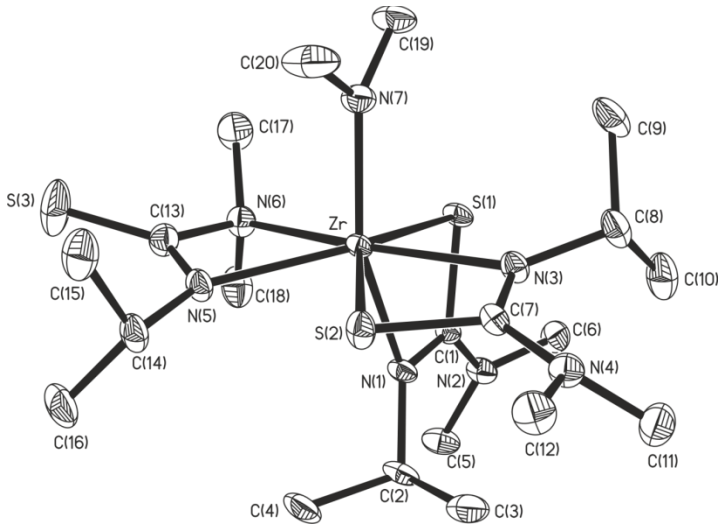

Figure 2.13 Molecular structure of complex **5**, complex **8** is isostructural. Thermal ellipsoids are shown at 50 % probability, with hydrogen atoms omitted for clarity.

Table 2.5 Selected bond lengths and angles for **5** and **8** with e.s.d.s. in parentheses.

Bond length / Å			Bond angle / °		
Bond	**5 (M = Zr)**	**8 (M = Hf)**	**Angle**	**5 (M = Zr)**	**8 (M = Hf)**
$M\text{-}N_{amide}$	2.040(3)	2.047(2)	$M\text{-}N\text{-}C_{Me}$	113.4(2), 137.0(3)	117.0(2), 134.3(2)
			κ^2-*S,N* mode		
M-S	2.6068(9), 2.6469(9)	2.5826(8), 2.6329(7)	$S\text{-}M\text{-}N_{iPr}$	62.19(7), 62.45(7)	62.61(6), 63.02(6)
$M\text{-}N_{iPr}$	2.300(3), 2.358(3)	2.285(2), 2.337(2)	M-S-C	79.95(11), 81.76(11)	81.81(10), 79.59(10)
S-C	1.746(4), 1.756(3)	1.750(3), 1.754(3)	$M\text{-}N_{iPr}\text{-}C$	101.6(2), 103.9(2)	101.81(18), 103.30(18)
$C\text{-}N_{iPr}$	1.314(4), 1.314(4)	1.313(4), 1.317(3)	$S\text{-}C\text{-}N_{iPr}$	113.7(2), 113.7(3)	113.0(2), 114.1(2)
$N\text{-}C_{iPr}$	1.479(5), 1.487(4)	1.485(4), 1.489(3)	S-C-N'	118.8(2), 119.2(3)	118.8(2), 119.2(2)
C-N'	1.370(4), 1.351(4)	1.360(4), 1.365(4)	$N_{iPr}\text{-}C\text{-}N'$	127.1(3), 127.4(3)	127.0(3), 127.9(3)
			κ^2-*N,N'* mode		
M-N'	2.453(3)	2.442(3)	$N_{iPr}\text{-}M\text{-}N'$	56.22(10)	56.47(9)
$M\text{-}N_{iPr}$	2.290(3)	2.268(2)	$M\text{-}N_{iPr}\text{-}C$	102.3(2)	102.75(19)
C-N'	1.473(5)	1.476(4)	M-N'-C	90.5(2)	90.34(17)
$C\text{-}N_{iPr}$	1.314(5)	1.313(4)	$N_{iPr}\text{-}C\text{-}N'$	106.8(3)	106.3(2)
C-S	1.672(4)	1.670(3)	$S\text{-}C\text{-}N_{iPr}$	132.3(3)	133.1(2)
$N\text{-}C_{iPr}$	1.484(5)	1.485(4)	S-C-N'	120.9(3)	120.6(2)

Both complexes exhibited almost identical bond lengths and angles across the molecule, the only exceptions are the metal-ligand bond lengths in the hafnium complex, **8**, which are slightly shorter than those in the zirconium complex, **5**. Predictably, the equivalent metal-ligand bond lengths in the iso-propyl titanium complex, **1**, are considerably shorter, however the geometry of the κ^2-*S,N* thioureide ligand is equivalent across all three iso-propyl complexes **1**, **5** and **8**.

As expected, the M-N_{iPr} bond lengths (e.g. 2.290(3) Å in **5**) are shorter than the M-N' bond lengths (e.g. 2.453(3) Å in **5**) for the κ^2-*N,N'* mode due to the N' atom binding to the metal centre via its lone pair. The κ^2-*N,N'* thioureide ligand shows a shortening of the C-S bond and elongation of the C-N' bond when compared to the κ^2-*S,N* thioureide ligand, which indicates there is increased electron density delocalised across the {SCN_{iPr}} moiety. While the shortening of the C-S distance suggests the bond has more double bond character, the bond is still considerably longer than the C=S bond (1.529(4) Å) found in CS_2.[43]

The *tert*-butyl zirconium complex, **6**, formed yellow crystals which were analysed using single crystal X-ray diffraction, the molecular structure of the *tert*-butyl hafnium complex, **9**, was not recorded. The molecular structure obtained (Figure 2.14) was consistent with the tris-inserted product containing two distinct thioureide binding modes (κ^2-*S,N* and κ^2-*S,N'*), as predicted from the ^{1}H and ^{13}C{^{1}H} NMR spectra. A selection of bond lengths and angles are presented in Table 2.6. The complex crystallised in a monoclinic $P2_1/c$ space group with the asymmetric unit containing two almost identical molecules, the following discussion will focus on the molecule containing Zr(1). The metal centre adopts a distorted pentagonal bipyramidal geometry with the equatorial plane consisting of two κ^2-*S,N'* ligands and a sulfur atom from the remaining κ^2-*S,N* ligand. The strong correlation between the results from the NMR spectroscopy suggests that the *tert*-butyl hafnium complex, **9**, would adopt a similar structure to that of the *tert*-butyl zirconium complex, **6**.

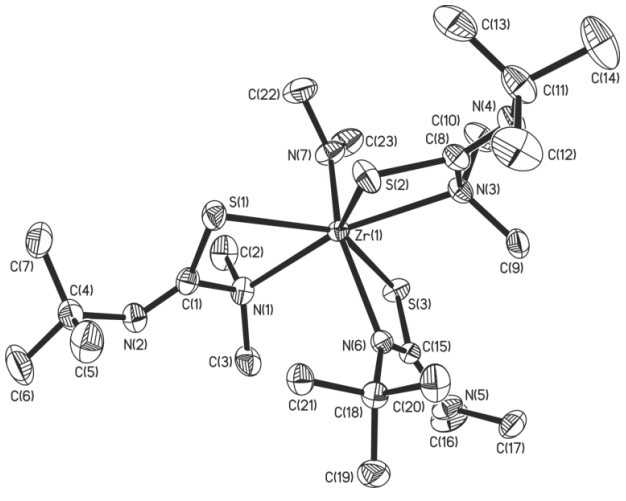

Figure 2.14 Molecular structure of complex **6**. Thermal ellipsoids are shown at 50 % probability, with hydrogen atoms omitted for clarity.

Table 2.6 Selected bond lengths and angles for **6** with e.s.d.s. in parentheses.

Bond	Bond length / Å	Angle	Bond angle / °
Zr-N_{amide}	2.036(3)	Zr-N-C_{Me}	114.1(2), 137.1(2)
	κ^2-*S,N* mode		
Zr-S	2.6175(9)	S-Zr-N_{tBu}	62.71(7)
Zr-N_{tBu}	2.321(3)	Zr-S-C	80.54(12)
S-C	1.751(3)	Zr-N_{tBu}-C	102.4(2)
C-N_{tBu}	1.312(4)	S-C-N_{tBu}	114.1(3)
N-C_{tBu}	1.509(4)	S-C-N’	117.9(3)
C-N’	1.376(4)	N_{tBu}-C-N’	128.0(3)
	κ^2-*S,N’* mode		
Zr-S	2.5716(10), 2.5960(10)	S-Zr-N’	61.85(7), 62.41(7)
Zr-N’	2.483(3), 2.493(3)	Zr-S-C	88.32(12), 89.66(12)
C-S	1.750(4), 1.760(4)	Zr-N’-C	99.5(2), 99.7(2)
C-N’	1.472(5), 1.482(4)	S-C-N’	107.8(2), 108.0(3)
C-N_{tBu}	1.240(5), 1.257(5)	S-C-N_{tBu}	133.3(3), 133.9(3)
N-C_{tBu}	1.481(5), 1.488(5)	N_{tBu}-C-N’	118.0(3), 118.9(3)

The *tert*-butyl zirconium complex, **6**, exhibits very similar bond lengths and geometries to those observed in the *tert*-butyl titanium complex, **2**, except for the metal ligand bonds which are longer and the κ^2-*S,N* C-N’ bond which is shorter. Once again, the pyramidalisation of the N’ atom (sum of angles = 348.6°) in the κ^2-*S,N* mode suggests electron density is delocalised exclusively across the {SCN_{tBu}} moiety. The adoption of two κ^2-*S,N’* thioureide modes within the complex indicate the steric bulk of the *tert*-butyl group is too great for more than one *tert*-butyl κ^2-*S,N* mode to exist within the group IV thioureide complexes.

Single crystal X-ray diffraction of the colourless phenyl zirconium complex, **7**, provided the molecular structure in Figure 2.15 which was consistent with the tetra-inserted product. The complex crystallised in a triclinic *P*-1 space group with the asymmetric unit containing a single molecule of **7** and three molecules of toluene, selected bond lengths and angles are presented in Table 2.7. The structure exhibited a single κ^2-*S,N* thioureide binding mode with the zirconium metal centre adopting a

distorted square antiprismatic geometry. The geometry of the phenyl κ^2-*S*,*N* thioureide ligand in **7**, compares very closely to the analogous ligand in the phenyl titanium complex, **3**, and the sulfur bridged phenyl titanium complex, **4**, predictably the metal ligand bond length is increased in the zirconium complex.

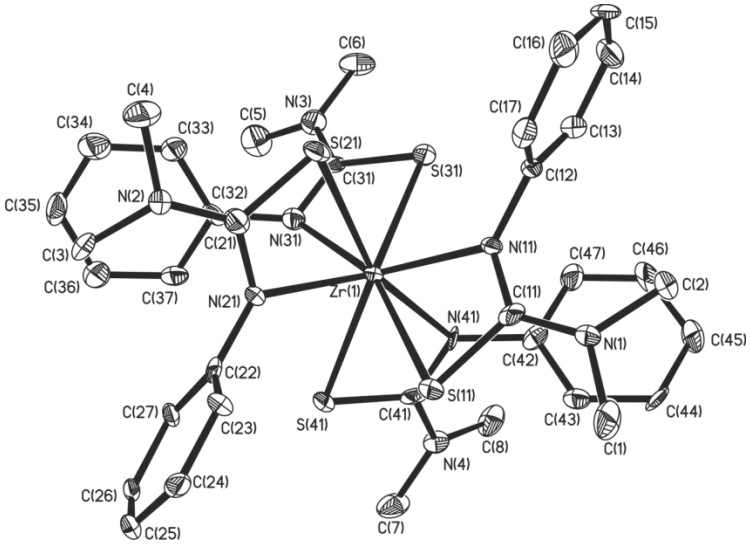

Figure 2.15 Molecular structure of complex **7**. Thermal ellipsoids are shown at 50 % probability, with hydrogen atoms omitted for clarity.

Table 2.7 Selected bond lengths and angles for **7** with e.s.d.s. in parentheses.

Bond	Bond length / Å	Angle	Bond angle / °
Zr-S	2.660(2) - 2.694(2)	S-Zr-N_{Ph}	60.81(16) - 61.94(18)
Zr-N_{Ph}	2.279(6) - 2.310(6)	Zr-S-C	79.7(3) - 80.8(3)
S-C	1.710(8) - 1.764(8)	Zr-N_{Ph}-C	103.7(5) - 106.0(5)
C-N_{Ph}	1.304(10) - 1.362(10)	S-C-N_{Ph}	112.4(6) - 114.6(6)
N-C_{Ph}	1.413(9) - 1.456(10)	S-C-N’	119.1(7) - 123.6(7)
C-N’	1.339(9) - 1.354(9)	N_{Ph}-C-N’	123.4(7) - 128.0(8)

The phenyl hafnium complex, **10**, formed colourless crystals which were analysed using single crystal X-ray diffraction. The molecular structure obtained (Figure 2.16) was consistent with the tris-inserted product as predicted from the ^{1}H and ^{13}C{^{1}H} NMR spectra, a selection of bond lengths and angles are presented in Table 2.8. The complex crystallised in a monoclinic $P2_1/c$ space group with the asymmetric unit containing a single molecule. Similar to the other tris-inserted complexes (**5**, **6** and **8**), the hafnium atom in **10** adopts a distorted pentagonal bipyramidal geometry, the

equatorial plane of the complex is composed of two κ^2-*S,N* thioureide ligands and the nitrogen atom from the final κ^2-*S,N* ligand.

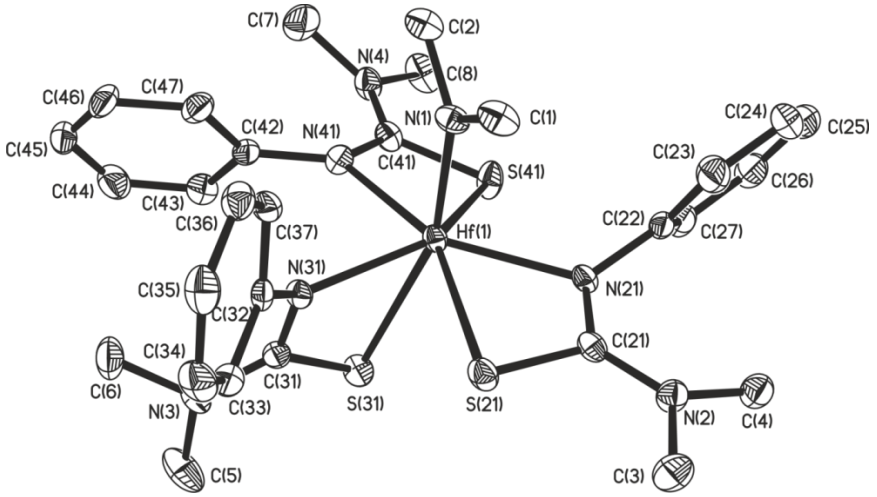

Figure 2.16 Molecular structure of complex **10**. Thermal ellipsoids are shown at 50 % probability, with hydrogen atoms omitted for clarity.

Table 2.8 Selected bond lengths and angles for **10** with e.s.d.s. in parentheses.

Bond	**Bond length / Å**	**Angle**	**Bond angle / °**
Hf-N_{amide}	2.051(3)	Hf-N-C_{Me}	121.1(2), 130.5(2)
		κ^2-*S,N* mode	
Hf-S	2.6114(9) - 2.7042(8)	S-Hf-N_{Ph}	61.75(7) - 62.42(7)
Hf-N_{Ph}	2.251(2) - 2.284(3)	Hf-S-C	78.19(11) - 80.76(11)
S-C	1.733(3) - 1.739(3)	Hf-N_{Ph}-C	103.6(2) - 105.46(19)
C-N_{Ph}	1.318(4) - 1.336(4)	S-C-N_{Ph}	112.2(2) - 114.2(2)
N-C_{Ph}	1.418(4) - 1.437(4)	S-C-N’	120.2(2) - 121.3(2)
C-N’	1.343(4) - 1.351(4)	N_{Ph}-C-N’	124.4(3) - 127.1(3)

The phenyl thioureide ligand geometry adopted in **10** is comparable to that of the phenyl thioureide ligand geometries in the titanium (**3** and **4**) and zirconium phenyl (**7**) complexes. As expected, the metal ligand bonds are longer in the hafnium complex **10** than those observed in the phenyl titanium complexes (**3** and **4**); however the metal ligand bonds are slightly shorter than those displayed in the phenyl zirconium complex, **7**. While reported values for the atomic radii of zirconium and hafnium (1.45 and 1.44 Å respectively) and the ionic radii of Zr^{4+} and

Hf^{4+} (0.74 and 0.75 Å respectively)[44] are almost identical due to the lanthanide contraction, there is likely a small difference between the two elements that causes complex **7** to be 8-coordinate and **10** to be 7-coordinate. Metal ligand bonds within the isostructural iso-propyl complexes **5** and **8** show the hafnium ligand bonds to be shorter suggesting in these cases the effective hafnium radii is slightly smaller and can therefore not accommodate an 8-coordinate coordination sphere.

2.2.4 Thermogravimetric analysis

Thermogravimetric analysis for the group IV thioureide complexes was performed using closed pans to limit the exposure of the complexes to air and moisture. Analysis was repeated a number of times to ensure the traces were accurate.

The TGA traces for the titanium thioureide complexes **1**, **2**, **3** and **4** are shown in Figure 2.17 with a summary of results presented in Table 2.9. Complex **1** decomposed via an initial mass loss of ~56 % between 120 and 210 °C and then a further mass loss of ~13 % up to the decomposition end point at 350 °C. The final weight percentage of 30.8 % is higher than the expected TiS_2 weight of 26.3 %. Complex **2** decomposed via a similar two step decomposition process with an initial mass loss of ~68 % between 65 and 190 °C, a further mass loss of ~10 % was observed between 190 and 325 °C. The final mass of 21.9 % is slightly lower than the expected value for TiS_2 of 24.6 %.

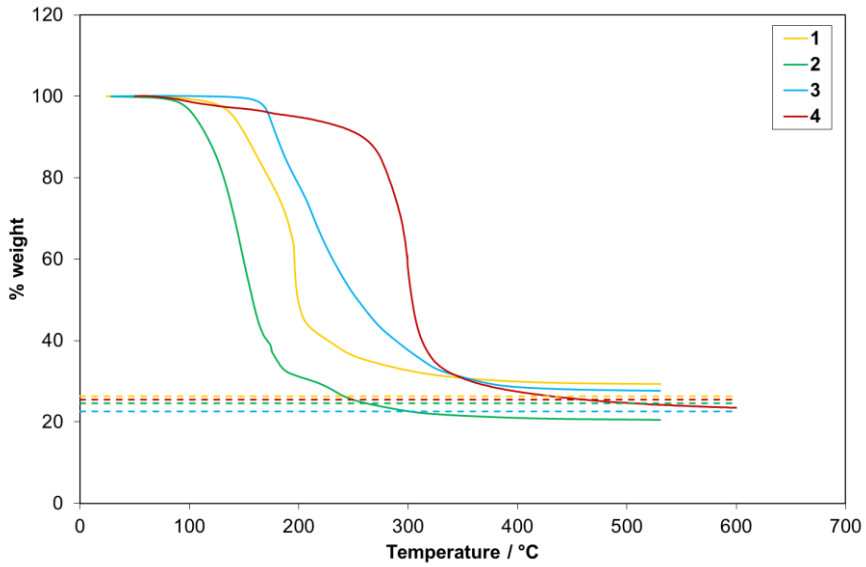

Figure 2.17 TGA traces for the titanium complexes **1**, **2**, **3** and **4** in closed pans. Dashed lines represent the expected % weight for TiS_2.

The decomposition of complex **3** showed a one-step pathway with the onset occurring quite rapidly and then a gradual slowdown in decomposition was observed until the end point was reached at 450 °C. A final weight of 28.0 % is higher than that expected for TiS_2 (22.6 %). Complex **4** exhibited an initial reduction in weight percentage of 8 % between 100 and 245 °C whereupon the main decomposition event occurred with a further mass loss of ~63 % up to 375 °C. The final weight percentage of 29.1 % is higher than the value of 25.5 % expected for TiS_2. All the titanium thioureide complexes show relatively promising clean decomposition steps although final weight percentages do differ to those expected for TiS_2 indicating the desired product may not have been formed.

Table 2.9 Summary of TGA data for the titanium complexes **1**, **2**, **3** and **4**.

Compound	Onset / °C	End point / °C	% weight expected for TiS_2	End point % weight
1	120	350	26.3	30.8
2	65	325	24.6	21.9
3	140	450	22.6	28.0
4	100	375	25.5	29.1

The TGA traces for the zirconium thioureide complexes **5**, **6** and **7** are shown in Figure 2.18 with a summary of the results presented in Table 2.10. The decomposition of **5** initiated at 175 °C with a mass loss of ~29 % by 240 °C, a further rapid mass loss of ~45 % was then observed between 240 and 270 °C with a final ~9 % loss up to the end point at 350 °C. The final percentage weight of 17.2 % is considerably lower than the expected value of 27.2 % for ZrS_2 indicating the complex is potentially volatile or the final product is ZrN (18.4 %) or zirconium metal (16.0 %).

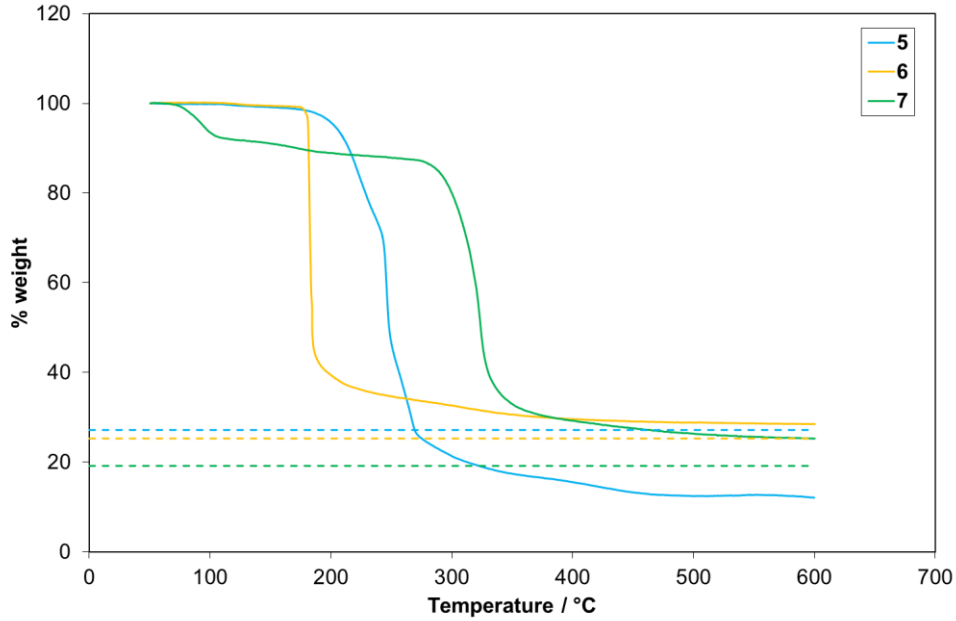

Figure 2.18 TGA traces for the zirconium complexes **5**, **6** and **7** in closed pans. Dashed lines represent the expected % weight for ZrS_2.

Complex **6** has a very sharp initial decomposition step which occurred over the narrow range of 175 to 215 °C with a mass loss of ~63 %, a slow reduction in mass of ~7 % then followed until 375 °C. The final percentage weight of 30.0 % is higher than that expected for ZrS_2 (25.3 %). The decomposition of **7** took place via a distinct multi step pathway with an initial loss of ~8 % between 75 and 110 °C which could be due to residual solvent within the sample. A further loss of ~5 % was then observed between 110 and 270 °C followed by the major mass loss of ~56 % between 270 and 370 °C. The final weight percentage of 30.8 % is considerably higher than the value expected for ZrS_2 (19.2 %) suggesting complex **7** is not a viable ZrS_2 precursor.

Table 2.10 Summary of TGA data for the zirconium complexes **5**, **6** and **7**.

Compound	Onset / °C	End point / °C	% weight expected for ZrS_2	End point % weight
5	175	355	27.2	17.2
6	175	375	25.3	30.0
7	75	370	19.2	30.8

The TGA traces for the hafnium thioureide complexes **8**, **9** and **10** are shown in Figure 2.19 with a summary of the results presented in Table 2.11. Complexes **8** and **10** showed very similar three step decomposition pathways to those seen for the zirconium complex **5**. The decomposition of **8** initially proceeded via a ~34 % loss between 160 and 265 °C, a further rapid loss of ~33 % was then observed in the narrow temperature range of 265 to 285 °C with a final ~9 % loss up to the end point at 365 °C. The decomposition of **10** occurred in much the same manner with a loss of 38 % between 195 and 310 °C, followed by a further loss of ~39 % by 340 °C and a final loss of ~4 % by the end point at 390 °C. Final percentage weights of 24.4 % and 17.9 % for **8** and **10** respectively are considerably lower than the expected HfS_2 values of 36.9 % and 31.9 %. These low values again suggest the compounds could be volatile or alternative products have been produced.

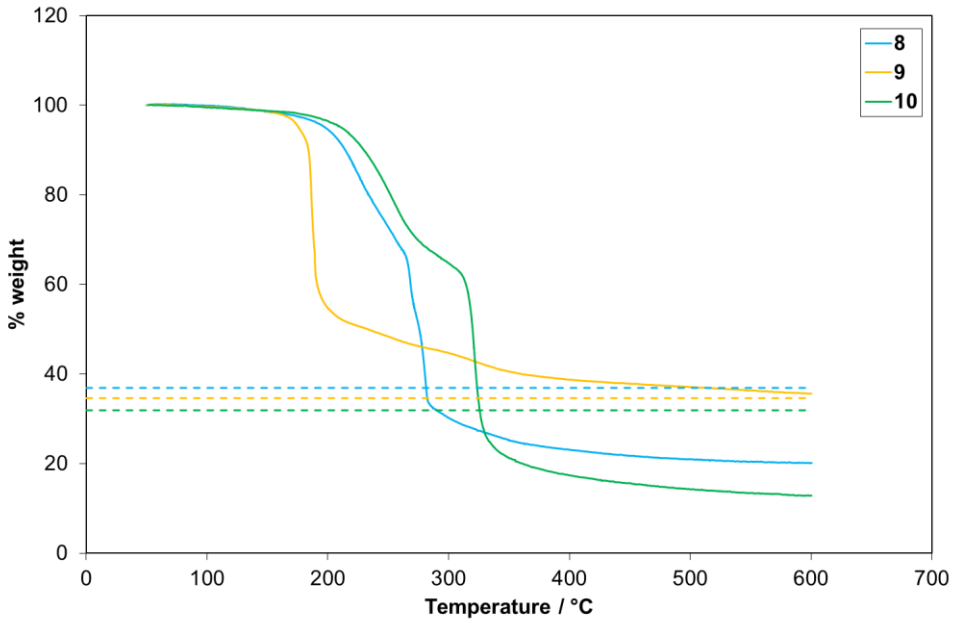

Figure 2.19 TGA traces for the hafnium complexes **8**, **9** and **10** in closed pans. Dashed lines represent the expected % weight for HfS_2.

Complex **9** showed a similar two step decomposition pathway to complex **6** with a major mass loss between 160 and 200 °C of ~46 % followed by a much slower loss of ~14 % by the end point at 370 °C. Again the final weight percentage is considerably higher at 39.6 % than the expected percentage weight for HfS_2 of 34.6 %.

Table 2.11 Summary of TGA data for the hafnium complexes **8**, **9** and **10**.

Compound	Onset / °C	End point / °C	% weight expected for HfS_2	End point % weight
8	160	365	36.9	24.4
9	160	370	34.6	39.6
10	195	390	31.9	17.9

While most group IV thioureide complexes showed reasonable decomposition profiles, the majority of complexes showed final percentage weights quite different to those expected for MS_2 suggesting these complexes are not viable precursors. The zirconium iso-propyl (**5**) and *tert*-butyl (**6**) thioureide complexes were taken forward to deposition studies to verify the results of the thermogravimetric analysis. These complexes were chosen as they were representative of the complexes providing final percentage weights lower (**5**) and higher (**6**) than those expected for MS_2.

2.2.5 AACVD of group IV thioureides

AACVD was carried out with separate 0.04 M toluene solutions of the zirconium iso-propyl (**5**) and *tert*-butyl (**6**) thioureide complexes using argon as a carrier gas at a pressure of 18 psi. Deposition times of 45 minutes provided films on both glass and Si substrates at 275, 300 and 325 °C for precursor **5** and at 200, 250 and 300 °C for precursor **6**. Films were slightly yellow and transparent on glass and gold to purple on Si with refringence patterns visible (Figure 2.20).

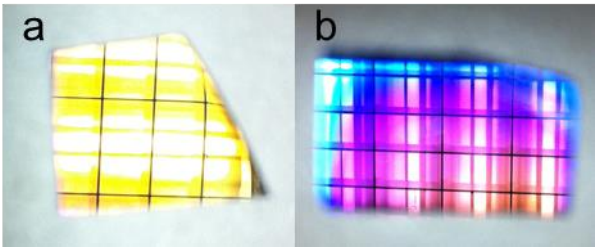

Figure 2.20 Images of the films deposited on Si: a – from **5** at 300 °C, b – from **6** at 200 °C.

Analysis of these films with PXRD showed all films to be amorphous, regardless of the specific precursor, substrate or temperature used in the deposition process. Raman spectroscopy did not provide any further indication of the identity of the

films with only substrate peaks observed. SEM images of the films presented in Figure 2.21 showed all films to have a similar morphology. All films were flat with few surface features; the pieces of material observed on the surface of the films were identified to be small fragments of Si substrate. EDX analysis showed the films to be composed of zirconium and oxygen with only traces of sulfur present in some samples. The zirconium and oxygen stoichiometry could not be accurately determined due to the presence of oxygen within the glass and Si substrates.

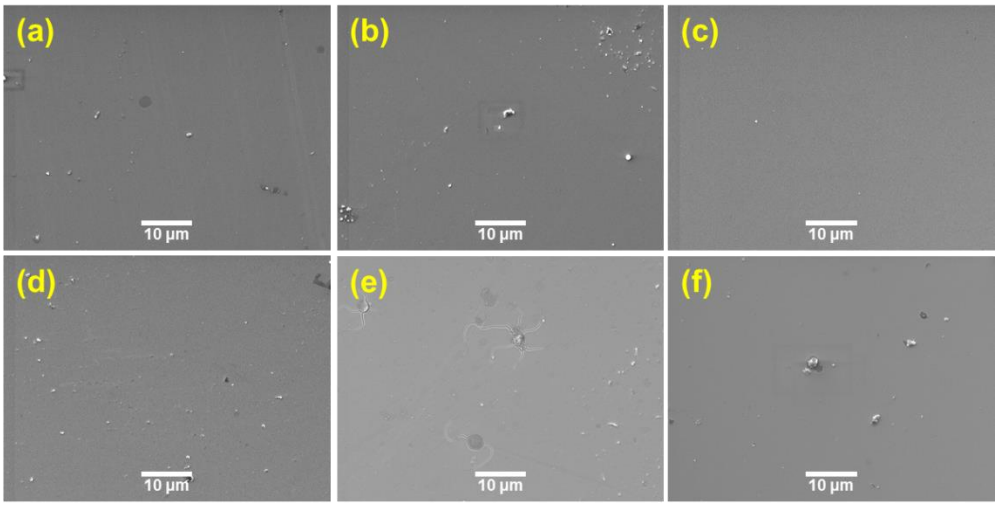

Figure 2.21 SEM images (magnification of x2k) of the films deposited on Si from **5** at 275 °C (a), 300 °C (b) and 325 °C (c), and from **6** at 200 °C (d), 250 °C (e) and 300 °C (f).

The most likely source of oxygen is from remaining air or moisture within the AACVD apparatus, however rapid oxidation of the film post production cannot be ruled out. Precursor solutions were prepared in a glovebox using degassed solvents to limit oxygen exposure. Prior to deposition the AACVD apparatus was purged with argon gas for 15 minutes at room temperature followed by a further 10 minutes while the furnace was heated to the desired deposition temperature. Even after taking these precautions to limit oxygen/water exposure, the results suggest a superior oxygen/water removal technique is required.

In an attempt to reduce the exposure of the precursors to oxygen/water, further experiments were carried out under vacuum. Both precursors **5** and **6** were heated under vacuum (1 mbar) with glass and silicon substrates to assess their viability as LPCVD precursors. Neither complex showed any form of volatility or deposition therefore no further deposition experiments were carried out with the group IV

thioureides. Due to time constraints no other group IV thioureide complex was used as a precursor in deposition experiments.

2.3 Group IV Dithiocarbamates

The inability of the group IV thioureides to form the corresponding metal disulfide meant a shift in focus for the project. The extensive use of other metal dithiocarbamates to deposit metal sulfides suggested group IV dithiocarbamates could be a viable group of precursors.[45-47]

2.3.1 Existing group IV dithiocarbamate systems

The homoleptic group IV dithiocarbamates were first reported in the 1960s by Bradley *et al.* and were synthesised by the insertion of CS_2 into a metal amide (Scheme 2.6). These complexes containing four bidentate dithiocarbamate ligands were some of the earliest examples of 8-coordinate titanium compounds. The dimethyl derivatives were reported to be insoluble in most common organic solvents however increasing the length of the alkyl chain increased their solubility. To the best of our knowledge these complexes have never been investigated as CVD precursors.[48-52]

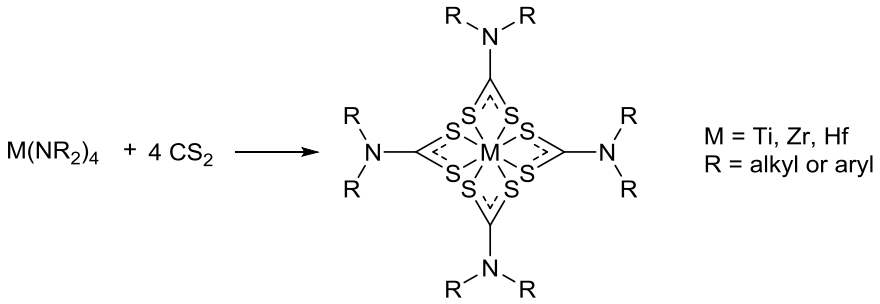

Scheme 2.6 General reaction scheme for the synthesis of homoleptic group IV dithiocarbamates.

The majority of heteroleptic group IV dithiocarbamates are 7-coordinate compounds which contain three bidentate dithiocarbamate ligands and a single monodentate hetero-ligand. Fay *et al.* have pioneered the synthesis of these pentagonal bipyramidal 7-coordinate heteroleptic compounds with most examples based on Cp-substituted complexes, although -Cl, -O^{i}Pr (Figure 2.22) and -O^{t}Bu derivatives are known. The Cp-substituted compounds are typically synthesised by the metathesis reaction between a Cp-substituted metal chloride and sodium dithiocarbamate salts.

The dithiocarbamate ligands within these complexes are inequivalent as two of the ligands inhabit the equatorial plane while the third ligand binds in both the equatorial and axial positions.[53-57] The group IV heteroleptic mono- and bis-dithiocarbamate compounds such as $[K(15\text{-crown-}5)_2][Ti(CO)_4(S_2CNR_2)]$ (where R = Me, Et, C_5H_{10} or pentamethylene)[58] and $[Ti(S_2CNEt_2)_2(O^iPr)_2]$[57] respectively are also known, however compounds of this type are much less common.

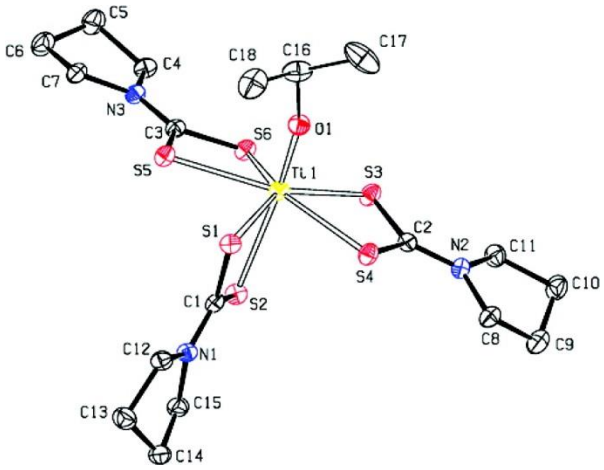

Figure 2.22 Molecular structure of the heteroleptic 7-coordinate group IV dithiocarbamate complex, $[Ti(S_2CNC_4H_8)_3(O^iPr)]$.[57]

2.3.2 Synthesis and characterisation

The synthesis of group IV dithiocarbamates was performed using two methods i.e. either by the metathesis reaction between the metal chloride and sodium dithiocarbamate salt or the insertion of CS_2 into a metal amide. The main focus of the synthesis was to produce the diethyldithiocarbamate derivatives as these are considerably more soluble than the dimethyl complexes and hence are more suitable for AACVD.[48] The diethyl starting materials are also cheaper and more readily available compared to other longer R groups.

$[Ti(S_2CNEt_2)_4]$ (**11**) was synthesised by the metathesis reaction (Scheme 2.7) reported by Bhat *et al.* between $TiCl_4$ and four equivalents of NaS_2CNEt_2 in DCM.[53] After refluxing for 5 hours the reaction mixture was filtered to remove NaCl. Concentration of the liquor and subsequent layering with hexane produced large dark red crystals of **11**.

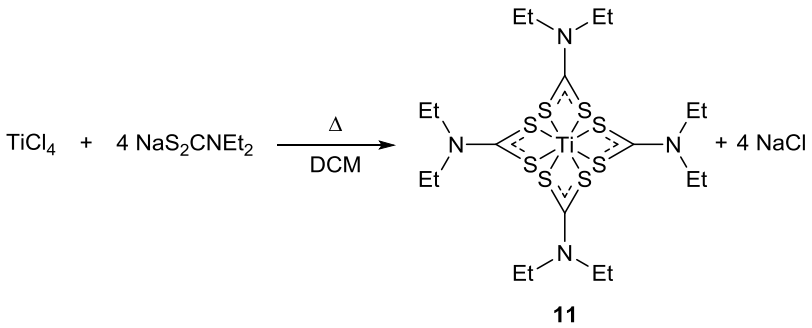

Scheme 2.7 Synthesis of $[Ti(S_2CNEt_2)_4]$, **11**.

For the zirconium and hafnium dithiocarbamates, the complexes were synthesised by the insertion of CS_2 into the metal amide first reported by Bradley *et al*. (Scheme 2.8). [48] After the addition of CS_2 to the metal tetrakis(diethylamide) in toluene, the reaction mixture was heated at 75 °C for 90 mins. Crystals were obtained from the reaction mixture after layering with hexane. For the CS_2 reaction with the metal tetrakis(ethylmethylamide), the reaction was performed in hexane with the mixture refluxed for 1 hour. Removal of the solvent *in vacuo* provided the solid products. The following complexes were synthesised via this route: $[Zr(S_2CNEt_2)_4]$ (**12**), $[Hf(S_2CNEt_2)_4]$ (**13**), $[Zr(S_2CNEtMe)_4]$ (**14**) and $[Hf(S_2CNEtMe)_4]$ (**15**).

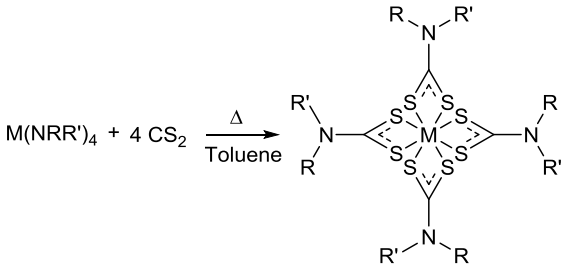

M	R	R'	Complex
Zr	Et	Et	**12**
Hf	Et	Et	**13**
Zr	Et	Me	**14**
Hf	Et	Me	**15**

Scheme 2.8 Reaction scheme for the synthesis of $[Zr(S_2CNEt_2)_4]$ (**12**), $[Hf(S_2CNEt_2)_4]$ (**13**), $[Zr(S_2CNEtMe)_4]$ (**14**) and $[Hf(S_2CNEtMe)_4]$ (**15**).

Cyclopentadienyl-based metal dithiocarbamate complexes were also synthesised for titanium and zirconium (Scheme 2.9) using the methods reported by Fay *et al*.[55] The reaction of Cp_2TiCl_2 with two equivalents of NaS_2CNEt_2 and half an equivalent of tetraethylthiuram disulfide in THF formed a green solution after stirring for 18 hours. THF was removed *in vacuo* to provide an orange/green solid which was dissolved in DCM. This solution was filtered and then volatiles were removed *in vacuo* to provide the orange solid, $[CpTi(S_2CNEt_2)_3]$ (**16**). The zirconium analogue was synthesised by refluxing Cp_2ZrCl_2 and three equivalents of NaS_2CNEt_2 in DCM

for 24 hours. The orange solution produced, was filtered and a small portion of hexane was added. Concentration *in vacuo* and storage at -28 °C provided yellow crystals of $[CpZr(S_2CNEt_2)_3]$ (**17**). The analogous hafnium complex was not synthesised due to the high cost of the Cp_2HfCl_2 starting material which would preclude its use in industry.

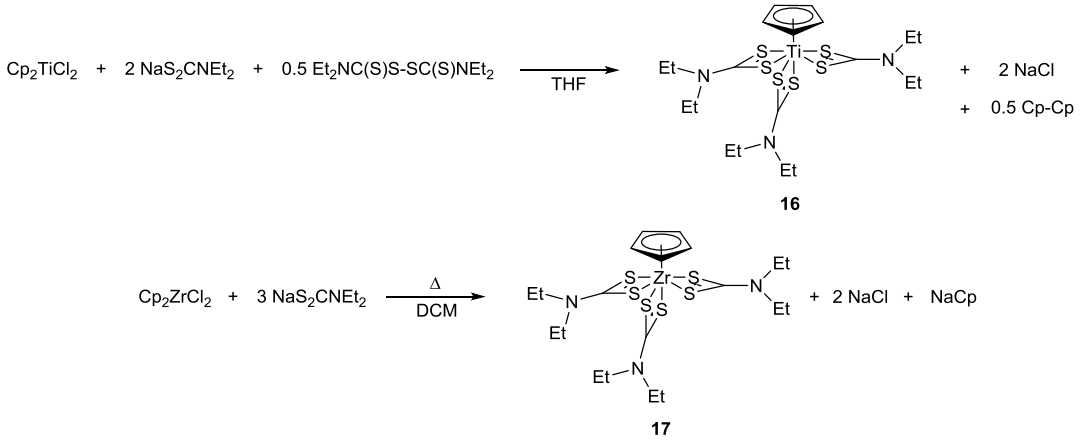

Scheme 2.9 Synthesis of $[CpTi(S_2CNEt_2)_3]$ (**16**) and $[CpZr(S_2CNEt_2)_3]$ (**17**).

The ^1H and $^{13}C\{^1H\}$ NMR spectra for the homoleptic dithiocarbamate complexes, **11-15**, all displayed the expected resonances for the inserted CS_2 carbon atom and the ethyl or methyl R groups. All spectra showed a single environment for both the ethyl and methyl groups suggesting the four dithiocarbamate ligands are equivalent. In the $^{13}C\{^1H\}$ NMR spectra the $\{S_2CN\}$ carbon atom resonances were found in the range 205 – 208 ppm indicating the formation of the dithiocarbamate.

^1H and $^{13}C\{^1H\}$ NMR spectra for the Cp-based dithiocarbamates, **16** and **17**, displayed the expected resonances for the Cp and ethyl groups, although the ethyl group's resonances were displayed as multiplets suggesting the dithiocarbamate ligands are not equivalent. In the $^{13}C\{^1H\}$ NMR spectra the $\{S_2CN\}$ carbon atom resonances were found in the range 208-205 ppm indicating the formation of the dithiocarbamate with **17** showing two resonances (205.8, 208.0 ppm) which also suggests multiple dithiocarbamate environments.

The structure of $[Ti(S_2CNEt_2)_4]$ (**11**) has previously been reported by Colapietro *et al.* but has been recollected to compare with the unreported structures of the analogous zirconium (**12**) and hafnium (**13**) complexes.[51, 52] The complexes **11**, **12** and **13** are isostructural and crystallised in the triclinic space group *P*-1 with two

molecules occupying the asymmetric unit. Each metal centre adopted an 8-coordinate distorted square antiprismatic geometry with each dithiocarbamate ligand binding in a bidentate manner (Figure 2.23). Both molecules within the asymmetric unit assume almost identical structures, therefore only the molecule containing M(1) will be discussed in detail. For all three complexes, one of the dithiocarbamate ligands exhibits a small amount of disorder within the two ethyl groups.

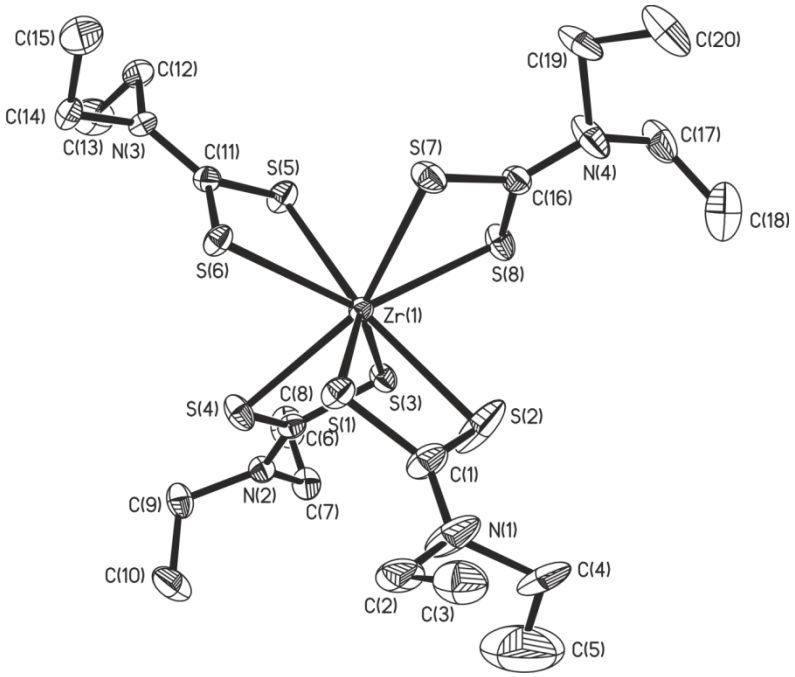

Figure 2.23 Molecular structure of complex **12**, complexes **11** and **13** are isostructural. Thermal ellipsoids are shown at 50 % probability, with hydrogen atoms omitted for clarity.

Table 2.12 compares selected bond lengths for **11**, **12** and **13**. M-S bond lengths are shortest for the titanium complex, **11**, (average bond length of 2.557 Å), while the zirconium complex, **12**, has the longest with an average of 2.6614 Å. The hafnium complex, **13**, has slightly shorter M-S bond lengths (average - 2.6473 Å) than **12** which supports the results observed for the group IV thioureides. The binding between the dithiocarbamate and metal centre is asymmetric with one M-S bond longer than the other within each ligand e.g. Ti(1)-S(1) is 2.6102(9) Å whilst Ti(1)-S(2) is 2.4971(11) Å. Although the M-S bonds differ in length, the C-S bonds within the ligand are essentially equivalent across all three complexes with only a very slight increase in **12** and **13**. The N(1)-C(1) bond lengths within the $\{S_2CN\}$ moiety are considerably shorter than the N-C bond lengths within the $\{NEt_2\}$ moiety, this indicates electron density is delocalised across the $\{S_2CN\}$ bonds.

Table 2.12 Selected bond lengths for **11**, **12** and **13** with e.s.d.s. in parentheses.

	Bond length / Å		
Bond	**11 (M = Ti)**	**12 (M = Zr)**	**13 (M = Hf)**
M-S range	2.4971(11) – 2.6165(8)	2.6239(9) – 2.6909(7)	2.6092(9) – 2.6819(9)
M(1)-S(1)	2.6102(9)	2.6864(7)	2.6786(8)
M(1)-S(2)	2.4971(11)	2.6239(9)	2.6115(10)
S(1)-C(1)	1.692(3)	1.702(3)	1.703(4)
S(2)-C(1)	1.715(3)	1.719(3)	1.715(4)
S(3)-C(6)	1.704(3)	1.718(3)	1.721(3)
S(4)-C(6)	1.710(3)	1.713(3)	1.710(4)
N(1)-C(1)	1.321(4)	1.323(4)	1.336(4)
N(1)-C(2)	1.473(4)	1.466(4)	1.469(5)
N(1)-C(4)	1.456(9)	1.510(10)	1.502(15)

Selected bond angles for one dithiocarbamate ligand in each of **11**, **12** and **13** are shown in Table 2.13, each dithiocarbamate ligand adopts a very similar geometry. The sum of internal angles within each $\{MS_2C\}$ four membered ring equals ~359° for **11**, **12** and **13** indicating the ring is essentially planar. The S(1)-M(1)-S(2) angles are relatively acute (65.42(2) – 66.97(3)°) while the S(1)-C(1)-S(2) angles are relatively obtuse (111.68(18) – 114.02(11)°) with the C-S-M angles close to 90° (88.69(11) – 91.98(12)°). The S(1)-M(1)-S(2) angles are slightly larger in the titanium complex, **11**, compared to the zirconium (**12**) and hafnium (**13**) complexes (66.97° vs. 65.42(2)/65.62(3)°), while the S(1)-C(1)-S(2) angles are slightly smaller (111.68(18)° vs. 114.02(17)/114.0(2)°). The sum of the angles around the $\{NCS_2\}$ carbon and $\{CNC_2\}$ nitrogen atoms are close to 360° (357.7 – 360.08°) showing the $\{S_2CNC_2\}$ moiety is planar which suggests both the carbon and nitrogen atoms are sp^2 hybridised with electron density delocalised across the $\{S_2CN\}$ bonds.

Table 2.13 Selected bond angles for **11**, **12** and **13** with e.s.d.s. in parentheses.

	Angle / °		
Angle	**11 (M = Ti)**	**12 (M = Zr)**	**13 (M = Hf)**
S(1)-M(1)-S(2)	66.97(3)	65.42(2)	65.62(3)
C(1)-S(1)-M(1)	88.69(11)	89.02(10)	88.82(12)
C(1)-S(2)-M(1)	91.98(12)	90.74(11)	90.80(13)
S(1)-C(1)-S(2)	111.68(18)	114.02(17)	114.0(2)
N(1)-C(1)-S(1)	125.1(2)	123.6(2)	123.8(3)
N(1)-C(1)-S(2)	123.3(3)	122.4(2)	122.2(3)
C(1)-N(1)-C(2)	122.2(3)	122.6(3)	122.0(3)
C(1)-N(1)-C(4)	121.6(5)	118.2(5)	121.9(11)
C(2)-N(1)-C(4)	115.6(5)	118.8(5)	113.8(11)

Exposure of a DCM/hexane solution of complex **11** to the atmosphere forms an oxygen bridged dititanium complex, [{μ-O}{Ti(S_2CNEt_2)$_3$}$_2$] (**11a**), with three dithiocarbamate ligands bound to each metal centre (Scheme 2.10). This side product was recovered in very small amounts, therefore only single crystal X-ray diffraction was used to characterise the complex.

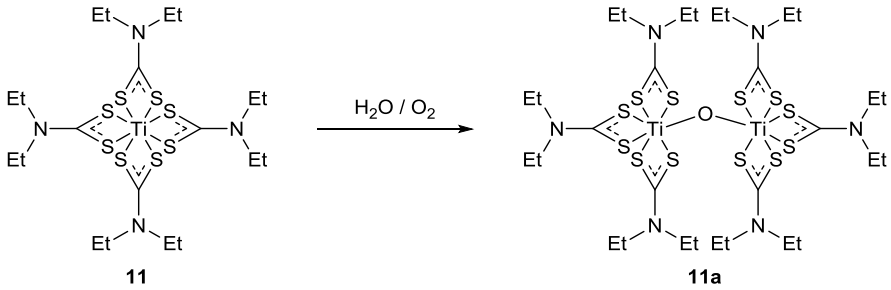

Scheme 2.10 Reaction of **11** with air to form the oxygen bridged complex, [{μ-O}{Ti(S_2CNEt_2)$_3$}$_2$] (**11a**).

11a (Figure 2.24) crystallised in a monoclinic *C*2/*c* space group with the asymmetric unit containing half a molecule, equivalent atoms were generated using the symmetry operator (-x+1, y, -z+3/2). Both metal centres are 7-coordinate with each dithiocarbamate ligand binding in a bidentate manner. A distorted pentagonal bipyramidal geometry is adopted around the metal centres with the oxygen bridging

atom and a sulfur atom adopting the axial positions; the equatorial plane is composed of five sulfur atoms.

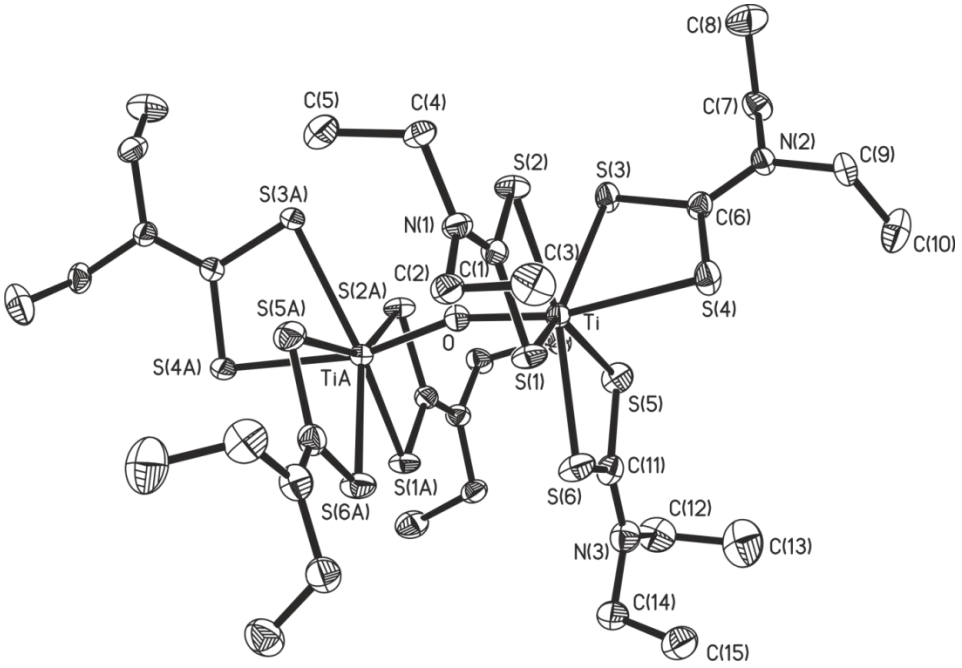

Figure 2.24 Molecular structure of complex **11a**. Thermal ellipsoids are shown at 50 % probability, with hydrogen atoms omitted for clarity.

Selected bond lengths and angles for **11a** are shown in Table 2.14. The bond lengths and angles within the dithiocarbamate ligand are extremely similar to those found in complex **11** and show the $\{S_2CNC_2\}$ moiety is planar. As expected, the Ti-O bond (1.8064(5) Å) is considerably shorter than the Ti-S bonds (2.4915(6) – 2.5821(6) Å). The TiA-O-Ti bond angle of 160.07(12)° is considerably larger than the angle of 109.5° expected with VSEPR theory. This larger angle is presumably due to the steric bulk of the dithiocarbamate ligands which moves the metal centres further apart increasing the TiA-O-Ti angle. The axial O-Ti-S(4) angle of 165.18(6)° and axial-equatorial O-Ti-(S equatorial) angles of 87.77(4) – 101.03(4)° show the distorted nature of the pentagonal bipyramidal geometry when angles of 180° and 90° respectively are expected.

Table 2.14 Selected bond lengths and angles for **11a** with e.s.d.s. in parentheses.

	Bond length / Å		**Angle / °**
Ti-O	1.8064(5)	TiA-O-Ti	160.07(12)
Ti-S range	2.4915(6) – 2.5821(6)	O-Ti-S(1)	101.03(4)
Ti-S(1)	2.5058(6)	O-Ti-S(2)	87.77(4)
Ti-S(2)	2.5565(6)	O-Ti-S(4)	165.18(6)
S(1)-C(1)	1.717(2)	S(1)-Ti-S(2)	68.220(19)
S(2)-C(1)	1.709(2)	C(1)-S(1)-Ti	90.42(7)
N(1)-C(1)	1.318(3)	C(1)-S(2)-Ti	88.92(7)
N(1)-C(2)	1.470(3)	S(2)-C(1)-S(1)	111.93(12)
N(1)-C(4)	1.470(2)	N(1)-C(1)-S(1)	122.84(15)
		N(1)-C(1)-S(2)	125.23(15)
		C(1)-N(1)-C(2)	121.87(17)
		C(1)-N(1)-C(4)	121.58(17)
		C(2)-N(1)-C(4)	116.53(17)

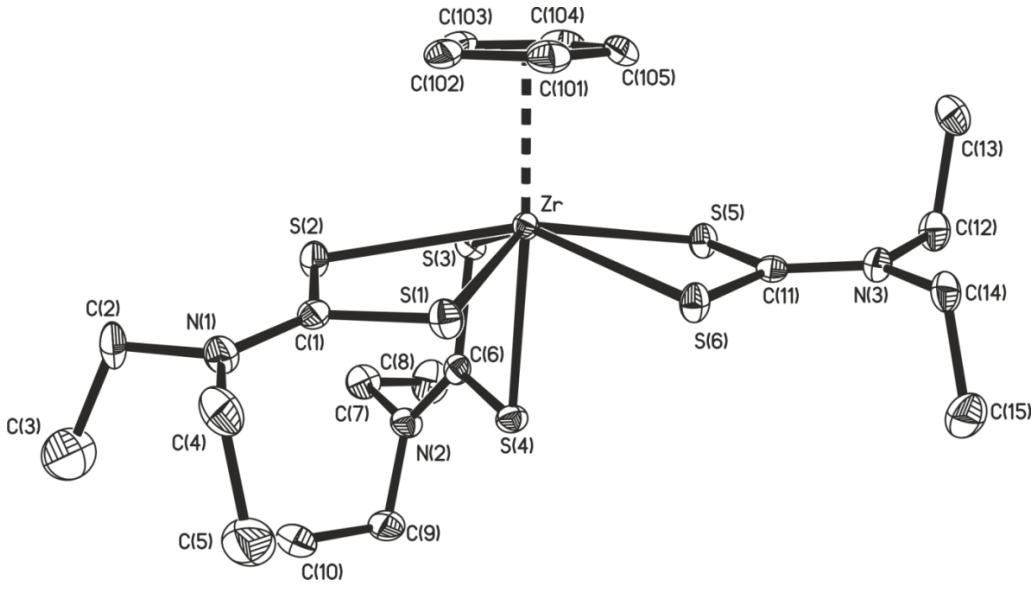

Figure 2.25 Molecular structure of complex **17**. Thermal ellipsoids are shown at 50 % probability, with hydrogen atoms omitted for clarity.

For the Cp-substituted complexes, only the zirconium analogue, **17**, was analysed using single crystal X-ray diffraction (Figure 2.25). This complex crystallised in the monoclinic *Pc* space group with the asymmetric unit containing a single molecule.

Complex **17** adopted a similar distorted pentagonal bipyramidal geometry as the metal centres in complex **11a** with the Cp and a sulfur atom adopting the axial positions. The axial (Cp centroid)-Zr-S(4) angle of 171.34° and the axial-equatorial (Cp centroid)-Zr-(S equatorial) angles of 98.39 – 105.70° show the distorted nature of the geometry.

Table 2.15 Selected bond lengths and angles for **17** with e.s.d.s. in parentheses.

	Bond length / Å		**Angle / °**
Zr-C range	2.522(4) - 2.560(4)	S(1)-Zr-S(2)	64.52(3)
Zr-S range	2.6464(10) - 2.7268(10)	C(1)-S(1)-Zr	91.02(13)
Zr-S(1)	2.6876(10)	C(1)-S(2)-Zr	90.26(13)
Zr-S(2)	2.7268(10)	S(2)-C(1)-S(1)	114.2(2)
S(1)-C(1)	1.734(4)	N(1)-C(1)-S(1)	122.4(3)
S(2)-C(1)	1.708(4)	N(1)-C(1)-S(2)	123.4(3)
N(1)-C(1)	1.328(5)	C(1)-N(1)-C(2)	121.4(3)
N(1)-C(2)	1.467(5)	C(1)-N(1)-C(4)	121.4(3)
N(1)-C(4)	1.471(5)	C(2)-N(1)-C(4)	117.2(3)

In terms of the dithiocarbamate ligand geometry, the bond lengths and angles within complex **17** (Table 2.15) are very similar to those found in $[Zr(S_2CNEt_2)_4]$ (**12**). The only difference is a slight elongation of the Zr-S bonds, 2.6464(10) - 2.7268(10) Å compared to 2.6239(9) – 2.6909(7) Å in **12**. The Zr-C bond lengths show a small range (2.522(4) - 2.560(4) Å) suggesting the Zr atom does not sit directly below the Cp centroid. The average internal angle (C-C-C) of the Cp ligand is equal to 108° suggesting no distortion of the Cp ring.

2.3.3 Thermogravimetric analysis

Due to the more stable nature of the solid group IV dithiocarbamate species **11** to **17**, TGA experiments were performed in open pans. The TGA traces for the homoleptic species, **11** to **15**, are shown in Figure 2.26 with both ethylmethyl complexes, **14** and **15**, showing similar one step decomposition pathways. The diethyl complexes, **11** to **13**, displayed similar traces except for small kinks in the region of 240 – 260 °C. These kinks correspond to mass losses of 17.0 % (**11**), 20.2 % (**12**) and 28.5 % (**13**)

and indicate the potential loss of 4, 5 and 8 ethyl groups respectively in the form of ethene. For the diethyl complexes the titanium complex (**11**) had the lowest decomposition end point of 340 °C (Table 2.16) followed by the hafnium (**13**) at 390 °C and the zirconium (**12**) at 400 °C. Interestingly, the ethylmethyl complexes **15** and **16** had lower (400 vs. 370 °C) and higher (410 vs. 390 °C) decomposition end point temperatures respectively when compared to the corresponding diethyl complexes, **12** and **13**. All complexes showed relatively similar decomposition ranges of ~250 °C and final percentage weights close to the values expected for MS_2 suggesting these compounds are viable MS_2 precursors.

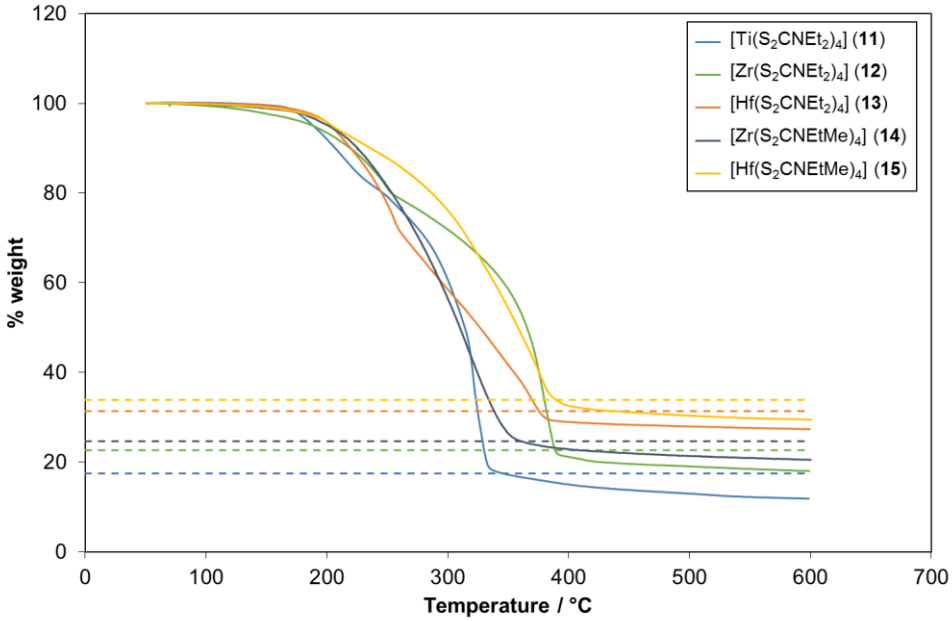

Figure 2.26 TGA traces for **11**, **12**, **13**, **14** and **15** in open pans. Dashed lines represent the expected % weight for MS_2.

Table 2.16 Summary of TGA data for **11**, **12**, **13**, **14** and **15**.

Compound	Onset / °C	End point / °C	% weight expected for MS_2	End point % weight
11	150	340	17.5	17.9
12	160	400	22.7	21.2
13	175	390	31.4	29.2
14	175	370	24.7	24.0
15	170	410	33.9	32.1

Thermogravimetric analysis – mass spectrometry (TGA-MS) was performed on $[Zr(S_2CNEt_2)_4]$ (**12**) (Figure 2.27) to elucidate the decomposition pathway and products. An increase in ion fragments was observed at 160 °C when the decomposition initiates with the majority of ion fragments detected in the range 305 to 380 °C. Possible ion fragment assignments for the major mass peaks observed in the decomposition are shown in Table 2.17. The most common mass peaks were observed at 76 and 30 m/z which could be the loss of CS_2 and ethane respectively. Other prevalent mass peaks include 58, 29 and 27 m/z, which indicate CSN, deprotonated ethane and HCN, respectively, were also lost. A further peak at 64 m/z occurs after the decomposition end point and suggests either the loss of elemental sulfur in the form S_2 or the formation of SO_2.

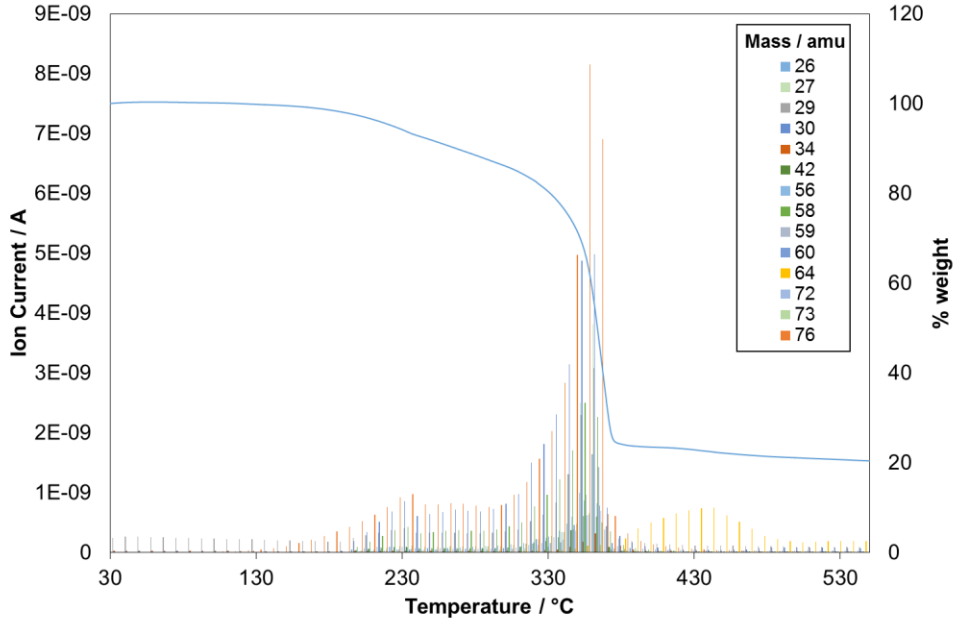

Figure 2.27 TGA-MS results for **12**: graph shows the major ion fragments present as temperature is increased, TGA trace is overlaid.

Decomposition studies by Ouyang *et al.* on the analogous Mo compound, $Mo(S_2CNEt_2)_4$, report dithiocarbamate ligands decomposing via the loss of ethene, HCN and S.[59] The presence of ethene could not be determined due to the large amount of N_2 from the air passing through the mass spectrometer (both have a mass of 28 m/z). While both HCN and S were observed, the large amounts of CS_2, ethane and CSN suggest alternative decomposition pathways occurring. All peaks were observed throughout the decomposition range indicating a variety of decomposition pathways were taking place simultaneously.

Table 2.17 Possible ion fragment assignment for the decomposition of **12**.

Mass / m/z	Fragment
26	CN^+, $C_2H_2^+$
27	HCN^+
29	$Butane^{2+}$, CSN^{2+}, $C_2H_5^+$
30	$C_2H_6^+$
58	CSN^+
64	S_2^+, SO_2^+
76	CS_2^+

Unlike the homoleptic dithiocarbamate species, the Cp substituted complexes (**16** and **17**) showed quite different TGA traces when the central metal atom is changed, the TGA traces and a summary of the TGA data are shown in Figure 2.28 and Table 2.18 respectively. Both **16** and **17** decomposed via one step processes although the profiles vary quite dramatically. Complex **16** rapidly lost mass after the onset of decomposition at 110 °C with the major decomposition step ending at 300 °C. This value is lower than that of **11** (340 °C) although there is a continued gradual mass loss up to 600 °C. The end point percentage weight of 37.3 % is much higher than that expected for TiS_2 (20.1 %). The high final percentage weight and continued loss of mass up to 600 °C indicate this compound will be a poor precursor.

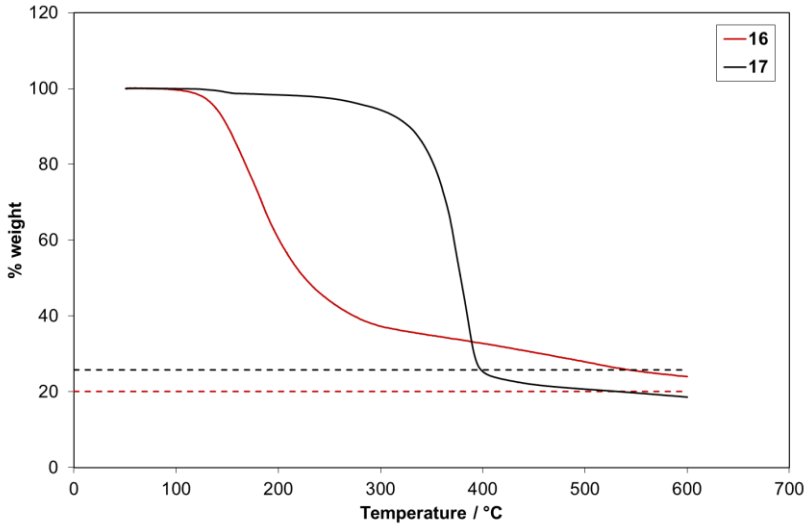

Figure 2.28 TGA traces for **16** and **17** in open pans. Dashed lines represent the expected % weight for MS_2.

Complex **17** showed a slight mass loss at 130 °C of only ~1.2 % which is most likely the loss of a small amount of residual solvent. The onset of the one step decomposition pathway was observed at 240 °C and ended at 405 °C with a percentage weight of 24.5 %, very close to the expected ZrS_2 percentage weight of 25.8 %. Unlike **16**, complex **17** shows a much similar profile to those of the homoleptic dithiocarbamate Zr complexes, **12** and **14**. The one step decomposition pathway and a similar final percentage weight to ZrS_2 suggest complex **17** is a promising ZrS_2 precursor.

Table 2.18 Summary of TGA data for **16** and **17**.

Compound	Onset / °C	End point / °C	% weight expected for MS_2	End point % weight
16	110	300	20.1	37.3
17	240	405	25.8	24.5

Thermogravimetric analysis shows the homoleptic dithiocarbamate species to be a more promising precursor class than the Cp-substituted dithiocarbamate species due to consistent final percentage weights close to those expected for MS_2. Therefore further work will only involve the homoleptic dithiocarbamate complexes and more specifically only the diethyl derivatives due to the availability of the starting materials.

2.3.4 AACVD of $[Zr(S_2CNEt_2)_4]$ (12)

Initially AACVD was attempted with a 0.03 M solution of $[Zr(S_2CNEt_2)_4]$ (**12**) in dry toluene. Deposition onto glass and Si substrates was observed in the temperature range 300 to 500 °C with a deposition time of 60 minutes. Films were transparent with refringence patterns particularly visible for the films on Si (Figure 2.29).

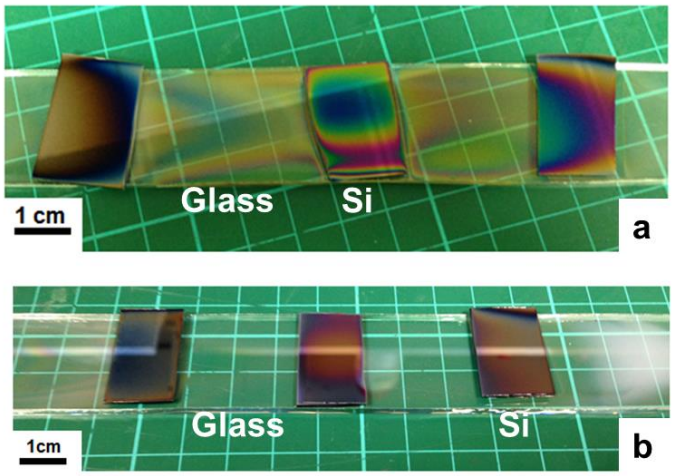

Figure 2.29 Images of the films deposited from the AACVD of **12** on glass and Si substrates at: a – 400 °C and b – 500 °C.

PXRD analysis of these films showed lower temperatures (300 – 350 °C) produced amorphous films whilst higher temperatures (400 – 500 °C) produced crystalline films (Figure 2.30) of monoclinic ZrO_2 (JCPDS card #83-0944).[60] The PXRD results and the transparency of the films indicated precursor **12** produced ZrO_2 under AACVD conditions much like precursors **5** and **6**, therefore no further work was carried out on the group IV dithiocarbamates using AACVD. Again, oxygen or moisture from the air is the most likely source of the oxygen in the films. To reduce the exposure of the group IV dithiocarbamate precursors to oxygen and water, further CVD experiments were carried out under low pressure conditions.

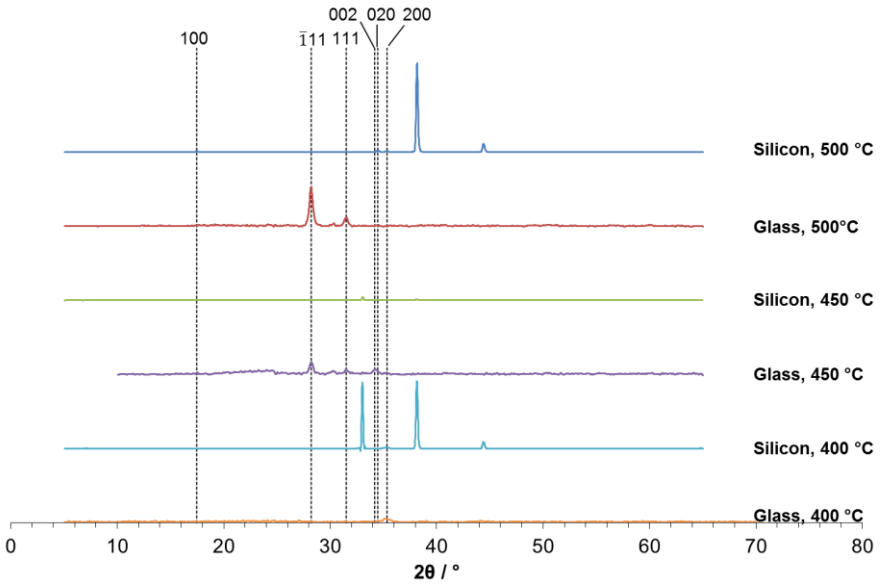

Figure 2.30 PXRD patterns for the films deposited from the AACVD of **12** at 400 to 500 °C.

2.3.5 LPCVD of $[Ti(S_2CNEt_2)_4]$ (11)

Preliminary LPCVD experiments with precursors **11**, **12** and **13** showed deposition of TiS_2, ZrS_2 and HfS_2 films respectively on both glass and Si substrates. Further experiments were then carried out to determine the full identity of these films and the temperatures over which deposition occurred. A schematic of the experimental set-up used for the LPCVD experiments is shown in Figure 2.31.

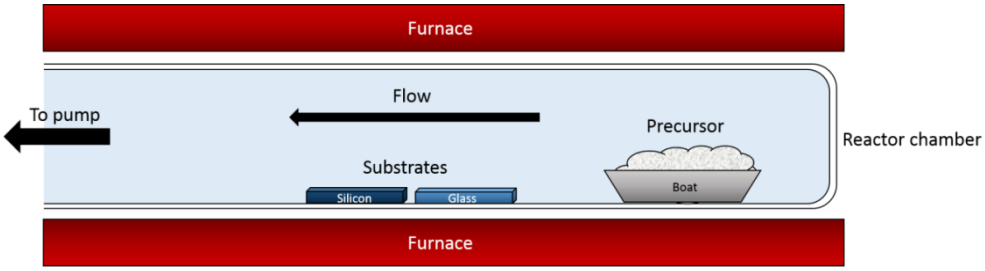

Figure 2.31 Schematic of the LPCVD apparatus used within this section.

In a standard experiment 0.1 g of precursor was placed in a quartz boat at the capped end of the quartz reactor tube towards the edge of the furnace. Glass and Si substrates were then positioned upstream of the precursor in the centre of the furnace. The reactor tube was then evacuated and refilled with nitrogen gas three times prior to the start of the experiment. Once under a stable vacuum (1 mbar), the furnace was turned on and allowed to heat to the desired deposition temperature for 30 minutes. After the deposition run was complete the reactor tube was removed from the furnace and allowed to cool to room temperature.

For precursor **11** good quality films were only deposited at 350 °C on both glass and Si substrates. Higher (375 °C) and lower (325 °C) deposition temperatures produced particles of TiS_2, as determined by Raman spectroscopy, although no continuous films were present. Further analysis was only performed on the films produced at 350 °C due to the poor quality of the higher and lower temperature material. Images of the films produced at 350 °C are presented in Figure 2.32 and show brown/gold films on glass (a) and gold films on Si(b).

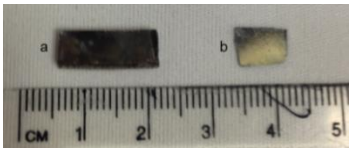

Figure 2.32 Image of the films deposited from **11** at 350 °C on a – glass and b - Si.

PXRD analysis showed these films to be crystalline 1T-TiS_2 (Figure 2.33) with the predominant reflection in the (001) orientation suggesting the layers are sitting parallel to the substrate surface.[61] Other than the (001) reflection, the film on the glass substrate exhibited no other reflections whilst the film on Si also displayed reflections corresponding to the (100) and (003) orientations (JCPDS card #88-2479)[62] with the peak at ~33° originating from the Si substrate. These orientations are consistent with some of the TiS_2 films deposited from $TiCl_4$ and ^{t}BuSH at 500 – 600 °C by Winter *et al.*[11] but differ to those reported by Carmalt *et al.* using the same precursors at similar temperatures where the dominant orientation was (011).[14]

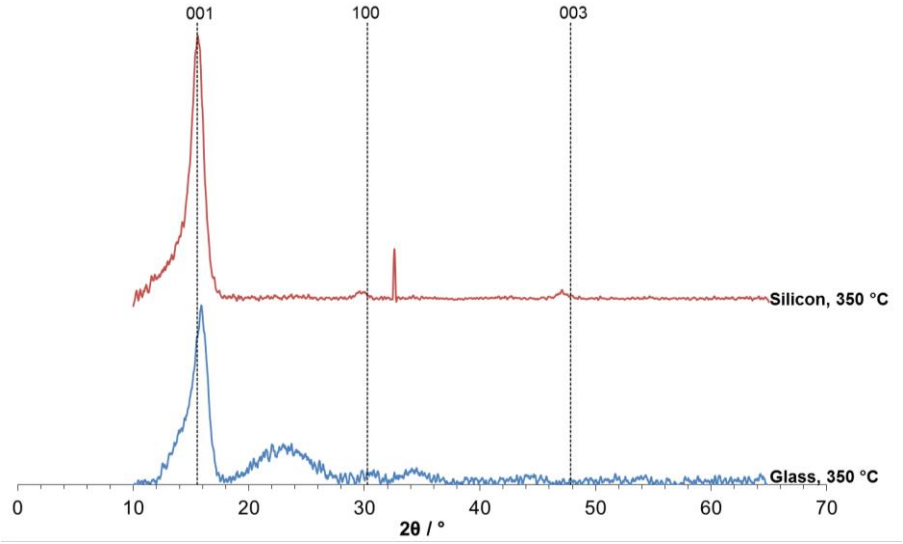

Figure 2.33 PXRD patterns for the films deposited from **11** at 350 °C.

Raman analysis of the films on both glass and Si showed spectra (Figure 2.34) consistent with TiS_2. Peaks at 223 cm^{-1} and 227 cm^{-1} for the films on glass and Si respectively match those reported for the E_g mode by Unger *et al.* (232 cm^{-1})[63] and Jiménez Sandoval *et al.* (244 cm^{-1}).[64] The peaks at 332 cm^{-1} (glass) and 328 cm^{-1} (Si) also match those reported by Unger *et al.* (336 cm^{-1}) and Jiménez Sandoval *et al.* (339 cm^{-1}) for the A_{1g} mode. The shoulder observed at around 380 cm^{-1} is also identified by Jiménez Sandoval *et al.* and Carmalt *et al.*[14] as part of the TiS_2 spectrum. The spectra showed no evidence of either TiS_3 or TiO_2 in either of the films.

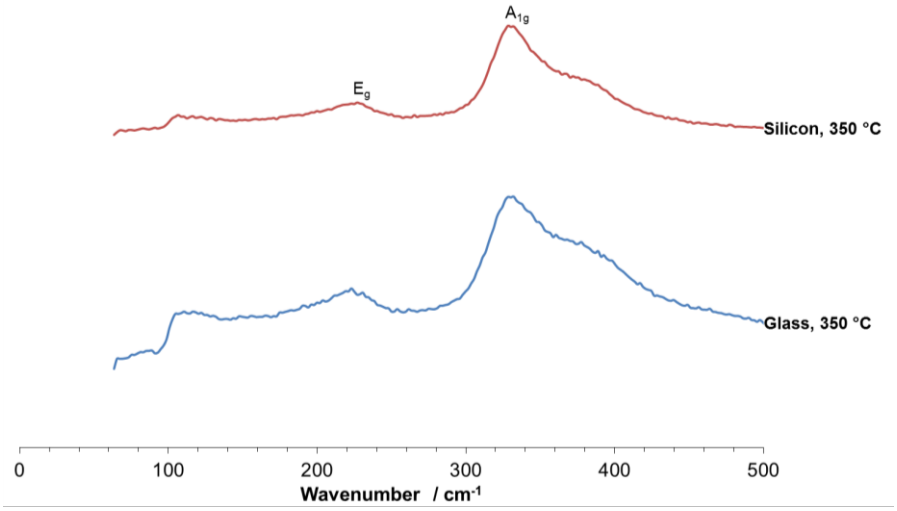

Figure 2.34 Raman spectra of the films deposited from **11** at 350 °C.

SEM images of the TiS_2 films on both glass and Si are shown in Figure 2.35 at a range of magnifications. The film on glass is composed of clumps of relatively large rough particles 1 – 3 μm in size. The film on Si is also composed of particles but these have a much smoother appearance, are more consistently sized at ~1 μm and are pressed together to form an angular surface structure. The large particle morphology of the film suggests growth occurs via a Volmer-Weber mechanism (island growth). The particulate appearance of the films is similar to those reported by Peters *et al.* using the precursors $Ti(NMe_2)_4$ and ^{t}BuSH at 250 and 300 °C.[15]

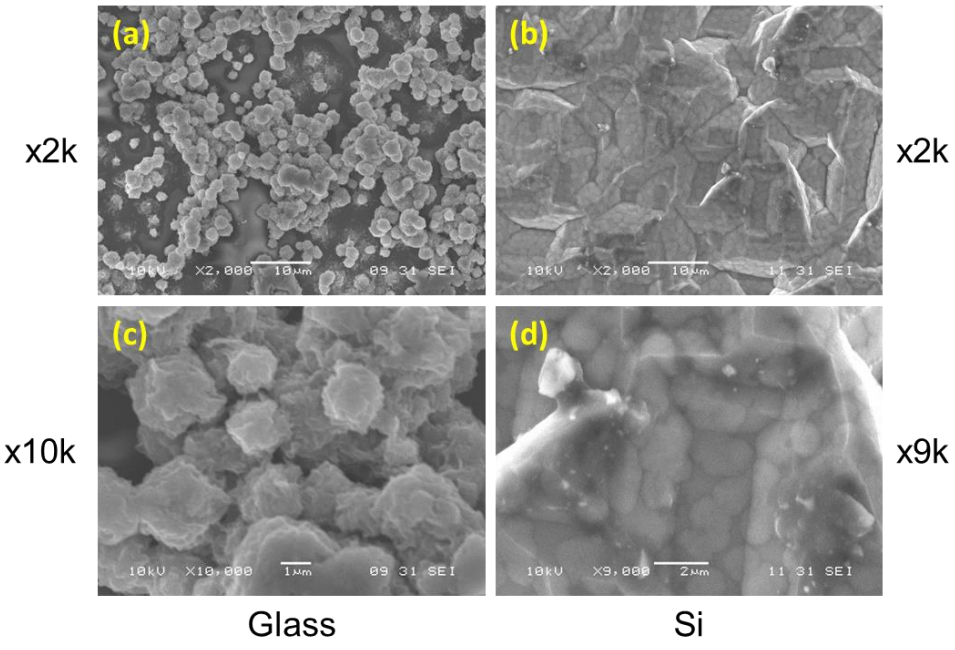

Figure 2.35 SEM images of the films deposited from **11** at 350°C.

AFM surface plots of the TiS_2 films on both glass and Si (Figure 2.36) support the particulate nature of the films observed in the SEM images. The AFM plot of the film on glass shows the discontinuous nature of the film with islands of aggregated particles. Interestingly, whilst the particulate nature of the film on Si is retained, the particles appear to be larger at 3 to 4 μm compared to the smaller particles observed in the SEM. This difference is likely due to a different part of the film with a slightly different morphology being analysed. Both SEM and AFM images show the more continuous nature of the film on Si compared to the more irregular film on glass. RMS values of 0.201 μm and 62.4 nm for the films on glass and Si respectively show the TiS_2 film on Si is an order of magnitude smoother than the film on glass.

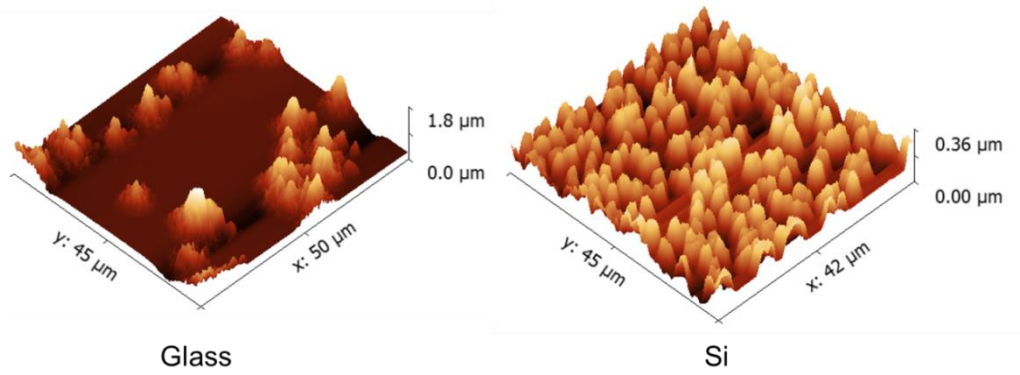

Figure 2.36 AFM surface plots of the films deposited from **11** at 350 °C.

EDX analysis of the films provided stoichiometries of TiS_2 and $TiS_{1.7}$ for the films on glass and Si respectively (Table 2.19), showing TiS_2 had been deposited. Traces of carbon and oxygen were recorded but the degree of oxidation could not be determined due to oxygen being present in both substrates.

Table 2.19 Ti:S stoichiometries calculated from the EDX data.

Temperature / °C	Substrate	Ti:S stoichiometry
350	Glass	TiS_2
350	Si	$TiS_{1.7}$

XPS analysis was performed on the TiS_2 film deposited on Si at 350 °C with Ar sputter etching used to determine the elemental composition of the bulk material. Analysis showed the main component of the film to be TiO_2 (average stoichiometry $TiO_{1.4}$) although TiS_2 was present with a maximum Ti:S ratio of $TiS_{1.2}$ (etch time of

120 s). Contamination was also observed from carbon, nitrogen and silicon (likely from substrate) giving an average film stoichiometry of $TiC_{0.4}N_{0.2}O_{1.4}S_{1.1}Si_{0.2}$. The Ti $2p_{3/2}$ binding energy showed two peaks at 458.6 – 458.9 eV and 456.3 – 456.8 eV, these were attributed to TiO_2 (458.4 eV)[65] and TiS_2 (456.5 eV)[18] respectively. The O 1s peak at 530.1 – 530.6 eV and the S 2p3/2 peak at 160.9 – 161.7 eV also matched those reported for TiO_2 (529.9 eV)[65] and TiS_2 (161.3 eV)[18]. Both of these samples were analysed 3 months after deposition and after storage under ambient conditions, this suggests the films are unstable in air with the TiS_2 decomposing to form TiO_2.

2.3.6 LPCVD of $[Zr(S_2CNEt_2)_4]$ (12)

Precursor **12** deposited films on both glass and Si at 400, 425 and 450 °C (Figure 2.37), deposition at 375 °C did not yield any films. The films on glass were orange/yellow and transparent (a, c, e) whilst films on Si were purple to blue with refringence patterns (b, d, f). Visibly the film on glass at 425 °C (c) was the least transparent indicating this was the thickest film. Films were visible across all of the substrates suggesting relatively continuous films were produced.

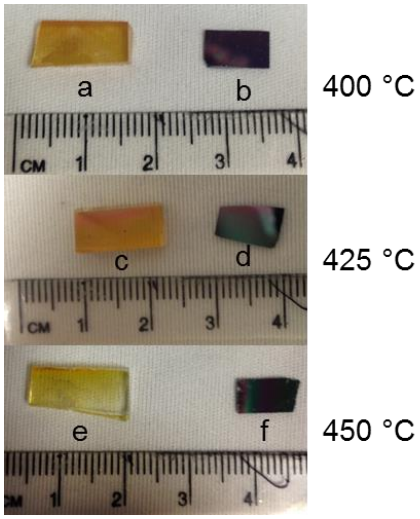

Figure 2.37 Images of the films deposited from **12** on glass: a, c, e and Si: b, d, f at 400, 425 and 450 °C.

PXRD analysis (Figure 2.38) showed all six films to be crystalline 1T-ZrS_2 with the major reflection corresponding to the (001) orientation (JCPDS card #88-4786)[66], this indicates the S-Zr-S layers are lying parallel to the substrate surface.[61] This differs to the ZrS_2 films deposited from zirconium oxychloride and thiourea by Thiyagarajan *et al.* where the major reflection was from the (110) plane.[26] The

PXRD patterns for the films on glass at 400 and 450 °C only showed the (001) reflection while the film on glass at 425 °C also displayed low intensity reflections at (002), (003) and (004) which represent planes parallel to the (001) plane. All films on Si showed the same reflections as the film on glass at 425 °C although additional low intensity reflections of (011) (400 and 450 °C) and (012) (400 °C) were also observed. The extremely high intensity of the (001) peak indicates that all of these films are highly orientated although the higher intensities of the ZrS_2 peaks on Si substrates imply these films are more crystalline than those found on glass.

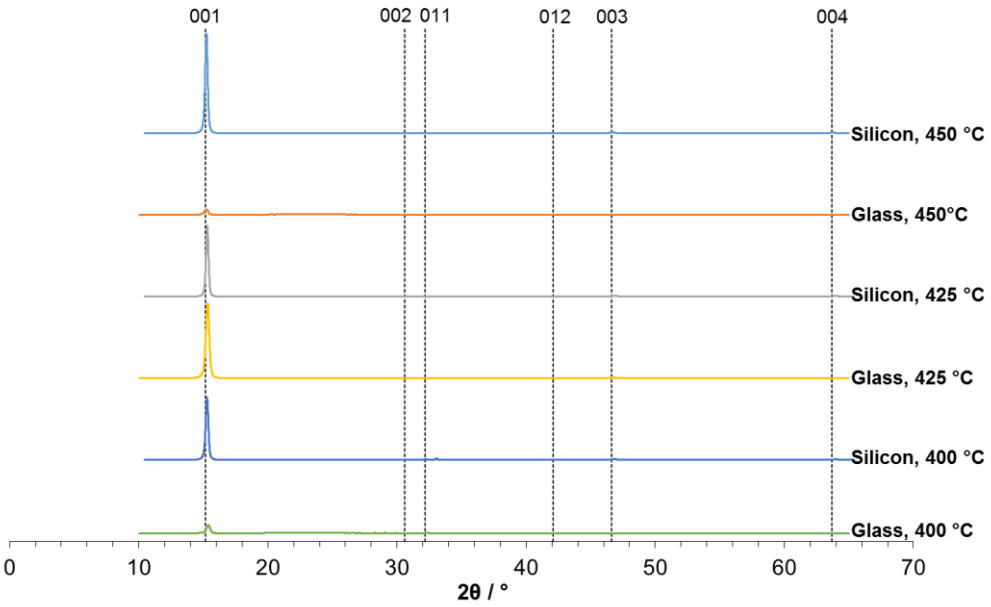

Figure 2.38 PXRD patterns for the films deposited from **12**.

The Raman spectra for the ZrS_2 films produced from **12** are presented in Figure 2.39. The peaks at ~247 and ~333 cm^{-1} are in good agreement with those for the ZrS_2 E_g and A_{1g} modes respectively reported by Iwasaki *et al.* (E_g – 248 cm^{-1}, A_{1g} – 333 cm^{-1}),[67] Roubi *et al.* (E_g – 251 cm^{-1}, A_{1g} – 333 cm^{-1})[68] and Stacy *et al.* (E_g – 249 cm^{-1}, A_{1g} – 331 cm^{-1}).[69] The shoulder at ~318 cm^{-1} is also comparable to the ZrS_2 A_{2u} mode reported by Iwasaki *et al.* (318 cm^{-1}) and Roubi *et al.* (316 cm^{-1}). The good agreement between the experimental and reported Raman data supports the presence of ZrS_2 in the films.

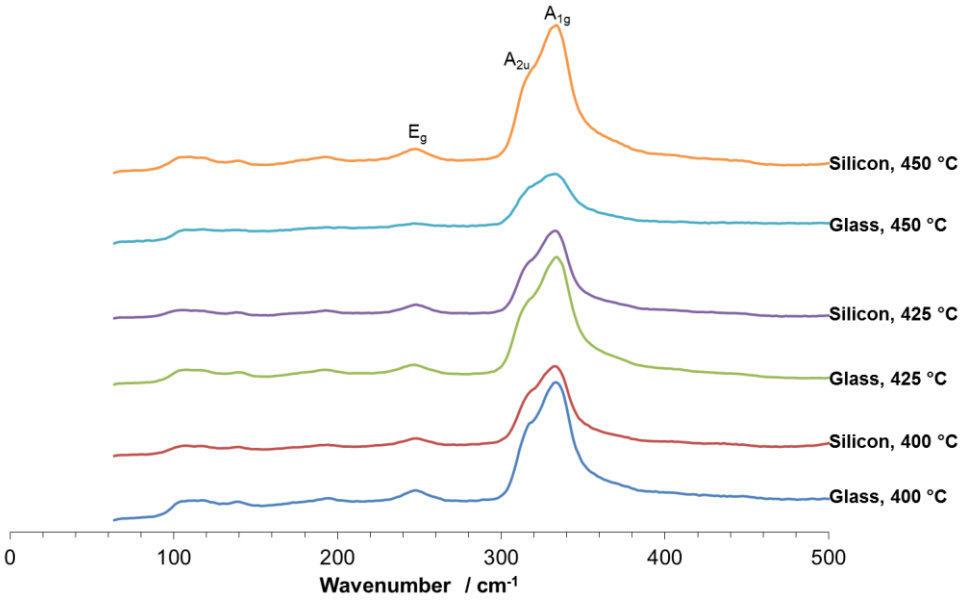

Figure 2.39 Raman spectra of the films deposited from **12**.

SEM images of the ZrS_2 films at a magnification of x25k are presented in Figure 2.40. Similar to the TiS_2 films, all of the ZrS_2 films are composed of particles although the degree of agglomeration is dependent on temperature. At 400 °C both the films on glass (a) and Si (b) are composed of relatively distinct particles 100 – 300 nm and 300 – 400 nm in size respectively. With an increase in temperature to 425 °C the particles in the film on glass (c) are of similar size at 150 – 300 nm although they have aggregated to a greater extent to form a more continuous film. The particles in the film on Si (d) have increased in size to 350 – 500 nm and formed a very continuous film with the individual particles quite difficult to observe. On increasing the deposition temperature to 450 °C the film on glass (e) has a patchy structure with areas of smaller separate particles 150 – 250 nm in size and areas of more continuous film. For the film on Si at 450 °C (f) the film is still very continuous although it is now composed of much smaller particles 50 – 120 nm in size. These images show the best coverage of the substrates to be at 425 °C. The morphology of the ZrS_2 films differs quite dramatically to those reported by Thiyagarajan *et al.* where ZrS_2 nanowires were deposited, this difference is likely due to the use of LPCVD rather than spray pyrolysis.[26] The particulate morphology of the film suggests growth occurs via a Volmer-Weber mechanism (island growth).

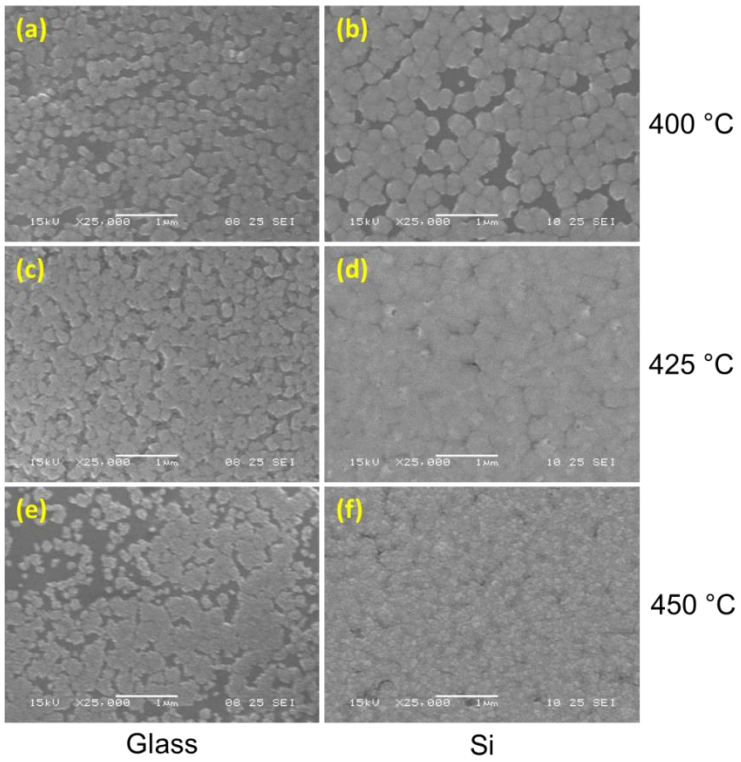

Figure 2.40 SEM images (x25k magnification) of the films deposited from **12**.

AFM surface plots of the ZrS_2 films deposited on both glass and Si at 425 °C are shown in Figure 2.41. The plot of the film on glass shows a similar morphology to the SEM image with particles of 150 – 300 nm in size combining to form a relatively continuous film. Again the AFM surface plot of the film on Si is very similar to the SEM image with a very continuous film, only some distinct particles are observed and these are 300 – 550 nm in size. The lower RMS value of 14.5 nm for the film on glass indicates it is slightly smoother than the film on Si which has an RMS value of 15.2 nm. These films are considerably smoother than the TiS_2 films.

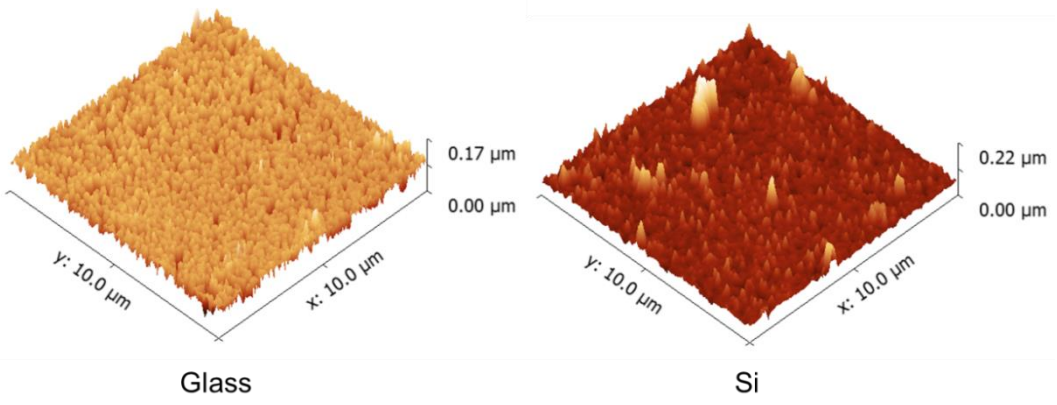

Figure 2.41 AFM surface plots of the films deposited from **12** at 425 °C.

Table 2.20 shows the Zr:S stoichiometries, calculated from the EDX data, for the films produced from **12**. All films displayed a degree of sulfur deficiency with the highest sulfur stoichiometry of $ZrS_{1.8}$ found for the film deposited on glass at 425 °C and the lowest stoichiometry of $ZrS_{1.2}$ for the film deposited on glass at 400 °C. The ratio of zirconium to sulfur has no correlation to the substrate used although higher temperatures provide films with higher sulfur contents. Again, traces of carbon and oxygen were recorded but the degree of oxidation could not be determined due to oxygen being present in both substrates.

Table 2.20 Zr:S stoichiometries calculated from the EDX data.

Temperature / °C	Substrate	Zr:S stoichiometry
400	Glass	$ZrS_{1.2}$
400	Si	$ZrS_{1.3}$
425	Glass	$ZrS_{1.8}$
425	Si	$ZrS_{1.6}$
450	Glass	$ZrS_{1.5}$
450	Si	$ZrS_{1.5}$

XPS analysis was performed on the ZrS_2 film deposited at 425 °C on silicon. Much like the XPS for the TiS_2 film, the ZrS_2 film was also exposed to ambient conditions for 3 months prior to analysis. The major component of the film was ZrO_x with an average stoichiometry of $ZrO_{2.8}$ although ZrS_x was also present with a maximum stoichiometry of $ZrS_{1.1}$. This suggests that ZrS_2 is unstable in air and decomposes to form ZrO_2. Other than oxygen, the films were also contaminated with chlorine, carbon, nitrogen and silicon (from the substrate) giving an average stoichiometry of $ZrC_{0.4}Cl_{1.1}N_{0.1}O_{2.7}S_{0.5}Si_{0.8}$. The Zr $3d_{5/2}$ peaks at 182.4 – 182.9 eV and 180.5 – 181.1 eV were attributed to ZrO_2 (182.7 eV)[70] and ZrS_2 (181.8 eV)[71] respectively. The O 1s peaks at 530.7 – 531.1 eV and the S $2p_{3/2}$ peaks at 161.8 – 162.2 eV also matched those for ZrO_2 (530.4 eV)[70] and ZrS_2 (161.6 eV)[71]. These results suggest that ZrS_2 is unstable in air and decomposes to form ZrO_2 over time.

2.3.7 LPCVD of $[Hf(S_2CNEt_2)_4]$ (13)

LPCVD experiments with precursor **13** deposited films on glass and Si substrates at 400, 425 and 450 °C, images of the films are presented in Figure 2.42. The films on glass were transparent with a yellow/brown colour at 400 (a) and 425 °C (c), and a very pale yellow colour at 450 °C (e). The films on Si (b, d, f) had a similar appearance to the ZrS_2 Si films with a purple to blue colour and refringence patterns visible especially on the film at 450 °C (f). Films appeared to be continuous on Si but patchy on glass with the film at 450 °C (e) only just visible.

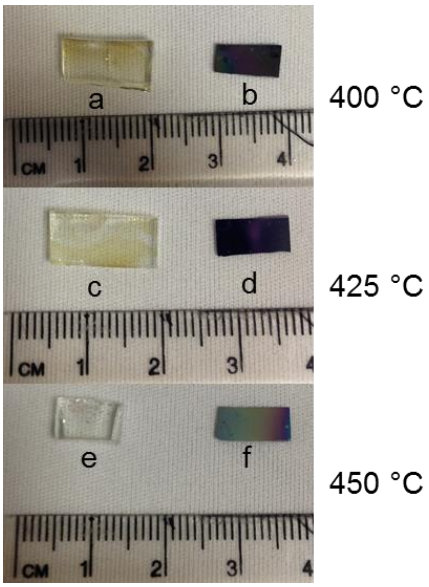

Figure 2.42 Images of the films deposited from **13** on glass: a, c, e and Si: b, d, f at 400, 425 and 450 °C.

All films deposited from precursor **13** were crystalline except for the film on glass at 450 °C which was amorphous (Figure 2.43). Much like the TiS_2 and ZrS_2 films, the crystalline films exhibited the major (001) reflection of 1T-HfS_2 (JCPDS card #28-0444) indicating HfS_2 had successfully been deposited with the S-Hf-S layers parallel to the substrate surface.[61] For the films on glass at 400 and 425 °C only the (001) reflections were present and were of relatively low intensity. The (001) reflection for the films on Si were of much greater intensity with the parallel (002) and (003) also present in all three films. The film on Si at 425 °C also showed the parallel (004) reflection and the reflection for the (100) plane. There was no evidence of any oxide or other hafnium sulfide stoichiometries within the PXRD patterns.

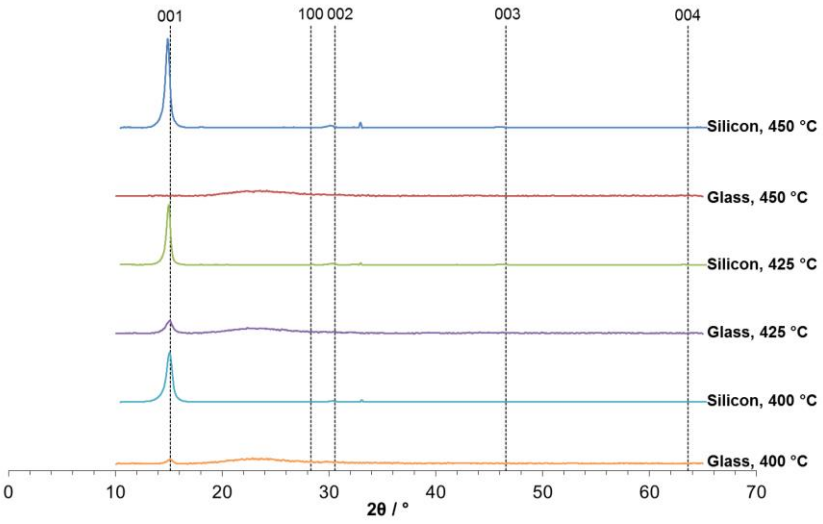

Figure 2.43 PXRD patterns for the films deposited from **13**.

Raman spectroscopy (Figure 2.44) showed the presence of HfS_2 for all of the films including the amorphous film on glass at 450 °C. The A_{1g} mode was observed in the range 338-340 cm^{-1} for all films and matches the values reported by Iwasaki *et al.* (337 cm^{-1}),[67] Roubi *et al.* (337 cm^{-1})[68] and Stacy *et al.* (336 cm^{-1}).[69] The films on Si across all temperatures and on glass at 400 °C also exhibited the E_g mode at 258-260 cm^{-1} which are close to the values reported by Iwasaki *et al.* (260 cm^{-1}), Roubi *et al.* (262 cm^{-1}) and Stacy *et al.* (258 cm^{-1}). The intensity of the more intense A_{1g} mode is relatively low for the films on glass at 425 and 450 °C which indicates the magnitude of the missing E_g mode is likely too low to distinguish the peak from the baseline. The peak observed at ~304 cm^{-1} in the spectra for the films on Si is attributed to a phonon mode of Si.[72] The spectra showed no evidence of any oxide formation.

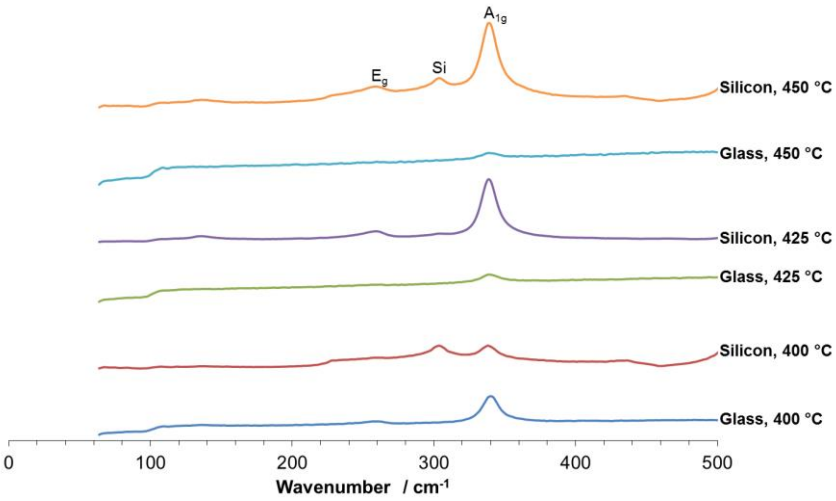

Figure 2.44 Raman spectra of the films deposited from **13**.

SEM images of the HfS_2 films at x25k magnification are shown in Figure 2.45. Similar to the TiS_2 and ZrS_2 films, the HfS_2 films are mainly composed of particles agglomerated to form a relatively continuous film. The main exception is the film on glass at 450 °C (e) which has a discontinuous appearance with many holes between the disordered agglomerates. Films on both glass (a) and Si (b) at 400 °C show a relatively densely packed layer of particles 100 – 200 nm and 250 – 300 nm in size respectively. Increasing the temperature to 425 °C creates a more densely packed film on glass (c) with particles reducing in size to 50 – 100 nm although a number of holes in the films are present. In contrast the increase in temperature for the Si film (d) creates a densely packed film of larger particles (400 – 600 nm) surrounded by much smaller particles (100 – 200 nm). Another increase in temperature to 450 °C for the film on Si (f) reduces the packing density of the film although the size of particle increases to 600 – 700 nm. The films on glass show a decrease in particle size as the temperature increases while the films on Si exhibit an increase in particle size. The particulate morphology of the film suggests growth occurs via a Volmer-Weber mechanism (island growth).

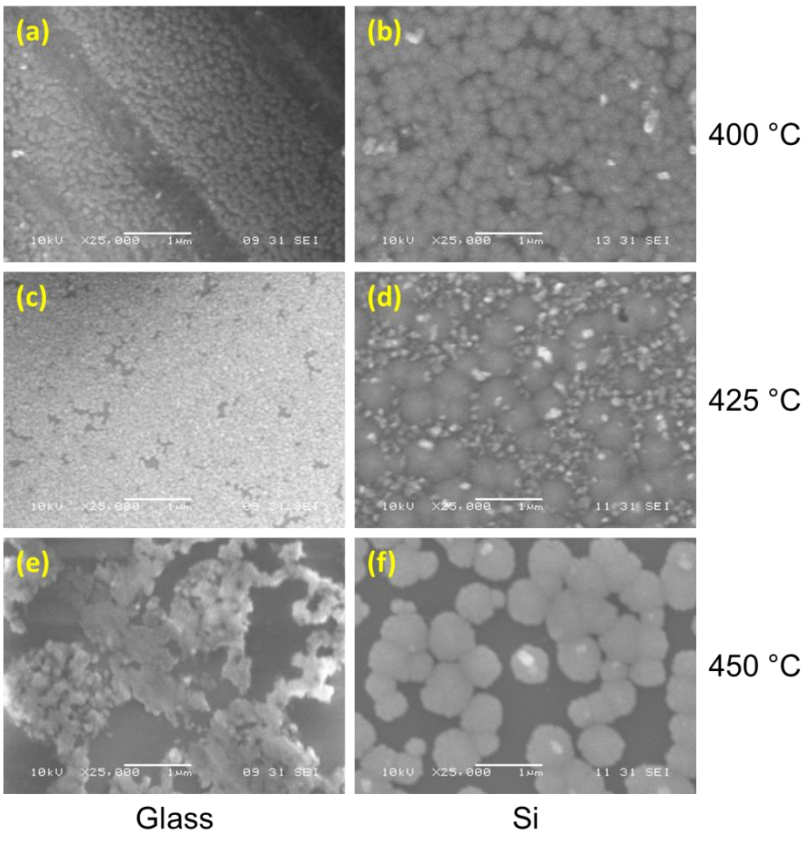

Figure 2.45 SEM images (x25k magnification) of the films deposited from **13**.

For the HfS_2 depositions only the films produced at 425 °C were analysed using AFM; the AFM surface plots are shown in Figure 2.46. The AFM surface plot of the film on glass at 425 °C shows a very similar surface morphology to the SEM image. The closely packed film, composed of slightly larger (100 – 200 nm) regularly sized particles, is occasionally separated by small gaps around 40 nm deep. The SEM image and AFM surface plot are almost identical for the film on Si at 425 °C with a densely packed film of larger particles (400 – 600 nm) surrounded by much smaller particles (100 – 200 nm). The regular particle size observed in the film on glass provides a lower RMS value of 12.6 nm while the more irregular film on Si has a larger surface roughness of 15.6 nm. These films are a similar roughness to the ZrS_2 films but considerably smoother than the TiS_2 films.

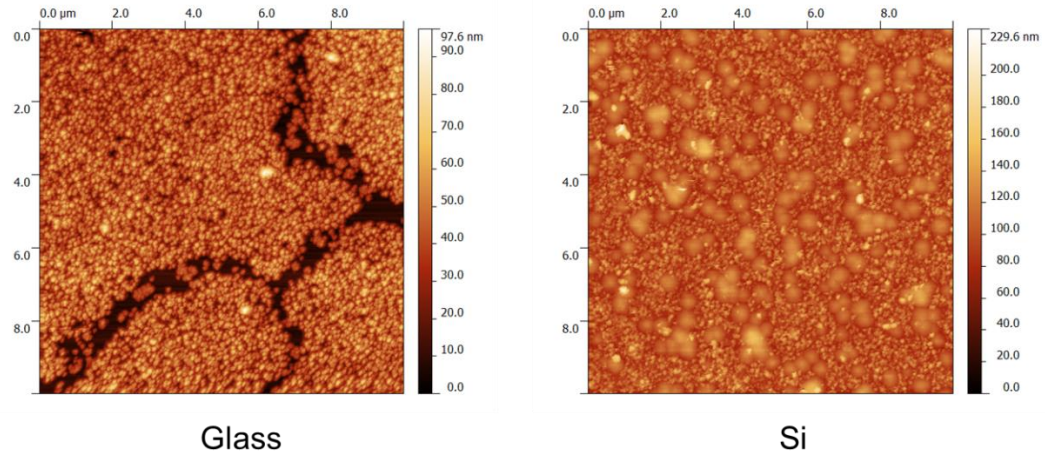

Figure 2.46 AFM surface plots of the films deposited from **13** at 425 °C.

EDX analysis of the films produced from **13** showed the presence of both hafnium and sulfur although stoichiometries could not be calculated due to the emissions for hafnium and silicon overlapping. Traces of carbon and oxygen were again present although the degree of oxidation could not be determined. While the stoichiometries were not obtained, the PXRD and Raman results, along with the EDX spectra, suggest HfS_2 was deposited.

XPS analysis was performed on the HfS_2 film deposited at 425 °C on silicon. Similarly to the TiS_2 and ZrS_2 XPS samples, the HfS_2 film was also exposed to ambient conditions for 3 months prior to analysis. The major component of the film was HfO_x with an average stoichiometry of $HfO_{1.9}$, HfS_x was also present with a maximum stoichiometry of $HfS_{0.4}$. This suggests that HfS_2 is unstable in air and

decomposes to form HfO_2, it also suggests HfS_2 is the least stable of the group IV disulfides as the ratio of metal to sulfur is the lowest. These films were the least contaminated with only small amounts of nitrogen and silicon (from the substrate) present, the average stoichiometry of the film was calculated to be $HfN_{0.2}O_{1.9}S_{0.3}Si_{0.2}$. For HfO_2, a Hf $4f_{7/2}$ binding energy of 17.3 – 18.0 eV and O 1s binding energy of 530.6 – 531.2 eV were consistent with those reported previously (Hf $4f_{7/2}$ - ~18 eV, O 1s - ~531.5 eV)[73]. The second Hf $4f_{7/2}$ peak of 14.7 – 15.2 eV was attributed to HfS_2 as the previous group IV metal sulfides had seen a reduction in metal binding energy for the metal sulfide when compared to the oxide. The S $2p_{3/2}$ peaks at 161.6 – 162.2 eV were consistent with those observed for TiS_2 and ZrS_2. These results suggest HfS_2 is unstable in air and decomposes to form HfO_2.

2.4 Conclusion

A range of group IV metal thioureide complexes have been synthesised via the insertion reaction between the metal tetrakis(dimethylamide) and the iso-propyl, *tert*-butyl and phenyl isothiocyanates. For the titanium complexes the bis-insertion products (**1**, **2**, and **3**) were recovered for all three R groups. A sulfur-bridged dititanium thioureide complex (**4**) was attained when three or four equivalents of the phenyl isothiocyanate were used. For the zirconium and hafnium complexes the tris-insertion products (**5**, **6**, **8**, **9** and **10**) were formed for all reactions except that between $[Zr(NMe_2)_4]$ and the phenyl isothiocyanate where the tetrakis-insertion product was formed (**7**). These complexes showed the most common thioureide ligand binding mode to be the κ^2-*S*,*N* mode although the κ^2-*N*,*N'* and the κ^2-*S*,*N'* modes were observed in the iso-propyl (**5** and **8**) and *tert*-butyl (**2**, **6** and **9**) complexes respectively. The iso-propyl thioureide ligands were observed to be fluxional in solution.

Thermogravimetric analysis of these complexes showed most to provide final percentage weights quite different to those expected for MS_2 suggesting they would be poor precursors. AACVD experiments with the iso-propyl (**5**) and *tert*-butyl (**6**) zirconium complexes provided films of ZrO_2 suggesting the precursors require a completely inert environment for viable use as MS_2 precursors.

The group IV homoleptic diethyl- and ethylmethyl-dithiocarbamates **11**, **12**, **13**, **14** and **15** have also been synthesised by either the metathesis reaction between the metal chloride and the sodium dithiocarbamate salt or the insertion reaction between the metal amide and carbon disulfide. The metal centres within these complexes are 8-coordinate with the equivalent dithiocarbamate ligands providing a square antiprismatic geometry. Thermogravimetric analysis showed clean decomposition pathways with final percentage weights close to those expected for MS_2.

The heteroleptic Cp-substituted titanium (**16**) and zirconium (**17**) diethyldithiocarbamates were also synthesised via the metathesis reaction between Cp_2MCl_2 and the sodium diethyldithiocarbamate salt. The complexes produced adopted a distorted pentagonal bipyramidal structure with two dithiocarbamate ligand environments. Thermogravimetric analysis showed the zirconium complex (**17**) to be the most promising precursor with a final percentage weight close to that expected for ZrS_2.

LPCVD experiments with the group IV diethyldithiocarbamates **11**, **12** and **13** produced crystalline films of TiS_2, ZrS_2 and HfS_2 respectively. PXRD, Raman and EDX all showed the presence of the respective metal disulfide. Within the PXRD patterns, the major reflection observed was the (001) orientation which suggested the S-M-S layers lie parallel to the substrate surface. The particulate morphology of the film suggests the material grows via an island growth mechanism (Volmer-Weber). Storage of the films for long periods of time (3 months) sees the metal sulfide decompose to the metal oxide.

The reactions and complexes presented in Chapter 2 are summarised below in Figure 2.47.

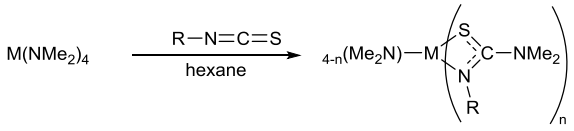

M	R	n	Complex
Ti	^{i}Pr	2	**1**
Ti	^{t}Bu	2	**2**
Ti	Ph	2	**3**
Zr	^{i}Pr	3	**5**
Zr	^{t}Bu	3	**6**
Zr	Ph	4	**7**
Hf	^{i}Pr	3	**8**
Hf	^{t}Bu	3	**9**
Hf	Ph	3	**10**

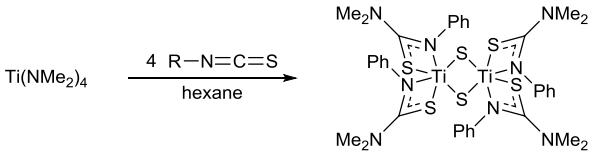

4

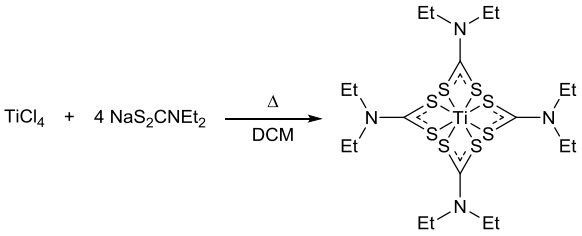

11

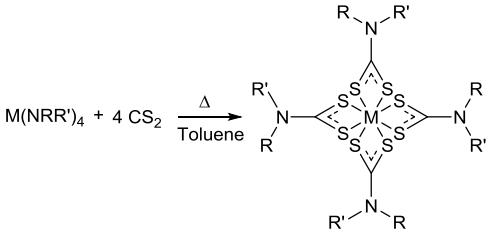

M	R	R'	Complex
Zr	Et	Et	**12**
Hf	Et	Et	**13**
Zr	Et	Me	**14**
Hf	Et	Me	**15**

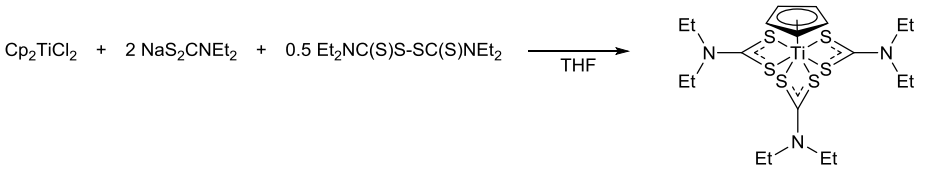

16

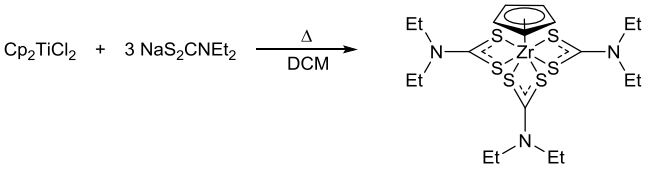

17

Figure 2.47 Summary of reactions and complexes presented within Chapter 2.

2.5 References

1. M. S. Whittingham, *Chem. Rev.*, 2004, **104**, 4271-4302.
2. S. H. Chae, Y. Jin, T. S. Kim, D. S. Chung, H. Na, H. Nam, H. Kim, D. J. Perello, H. Y. Jeong, T. H. Ly and Y. H. Lee, *ACS Nano*, 2016.
3. M. Zhang, Y. Zhu, X. Wang, Q. Feng, S. Qiao, W. Wen, Y. Chen, M. Cui, J. Zhang, C. Cai and L. Xie, *J. Am. Chem. Soc.*, 2015, **137**, 7051-7054.
4. L. E. Conroy and K. C. Park, *Inorg. Chem.*, 1968, **7**, 459-463.
5. J. A. Wilson and A. D. Yoffe, *Adv. Phys.*, 1969, **18**, 193-335.
6. J.-t. Jang, S. Jeong, J.-w. Seo, M.-C. Kim, E. Sim, Y. Oh, S. Nam, B. Park and J. Cheon, *J. Am. Chem. Soc.*, 2011, **133**, 7636-7639.
7. M. Chhowalla, H. S. Shin, G. Eda, L. J. Li, K. P. Loh and H. Zhang, *Nat. Chem.*, 2013, **5**, 263-275.
8. H. Tian, M. L. Chin, S. Najmaei, Q. Guo, F. Xia, H. Wang and M. Dubey, *Nano Res.*, 2016, **9**, 1543-1560.
9. K. Kanehori, F. Kirino, Y. Ito, K. Miyauchi and T. Kudo, *J. Electrochem. Soc.*, 1989, **136**, 1265-1270.
10. S. Kikkawa, M. Miyazaki, Y. Liu and F. Kanamaru, *Solid State Ionics*, 1990, **40–41**, 553-556.
11. C. H. Winter, T. S. Lewkebandara and J. W. Proscia, *Chem. Mater.*, 1992, **4**, 1144-1146.
12. J. R. Bottin, P. R. McCurdy and E. R. Fisher, *Rev. Sci. Instrum.*, 1997, **68**, 2149-2155.
13. G. Che, K. B. Jirage, E. R. Fisher, C. R. Martin and H. Yoneyama, *J. Electrochem. Soc.*, 1997, **144**, 4296-4302.
14. C. J. Carmalt, I. P. Parkin and E. S. Peters, *Polyhedron*, 2003, **22**, 1263-1269.
15. E. S. Peters, C. J. Carmalt and I. P. Parkin, *J. Mater. Chem.*, 2004, **14**, 3474-3477.
16. C. J. Carmalt, S. A. O'Neill, I. P. Parkin and E. S. Peters, *J. Mater. Chem.*, 2004, **14**, 830-834.
17. M. Bochmann, I. Hawkins and L. M. Wilson, *J. Chem. Soc., Chem. Commun.*, 1988, 344-345.
18. J. Cheon, J. E. Gozum and G. S. Girolami, *Chem. Mater.*, 1997, **9**, 1847-1853.
19. C. J. Carmalt, E. S. Peters, I. P. Parkin and D. A. Tocher, *New J. Chem.*, 2005, **29**, 620-624.
20. F. Senocq, N. Viguier and A. Gleizes, *Eur. J. Solid State Inorg. Chem.*, 1996, **33**, 1185-1197.
21. T. Suren Lewkebandara, P. J. McKarns, B. S. Haggerty, G. P. A. Yap, A. L. Rheingold and C. H. Winter, *Polyhedron*, 1998, **17**, 1-9.
22. C. H. Winter, T. S. Lewkebandara, J. W. Proscia and A. L. Rheingold, *Inorg. Chem.*, 1993, **32**, 3807-3808.
23. *U.S. Pat.*, US5298295 A, 1994.
24. C. J. Carmalt, E. S. Peters, I. P. Parkin and D. A. Tocher, *Polyhedron*, 2007, **26**, 43-48.
25. *E.P. Pat.*, EP1170398A1, 2002.
26. R. Thiyagarajan, M. Mahaboob Beevi and M. Anusuya, *J. Am. Sci.*, 2009, **5**, 6-12.
27. *Chinese Pat.*, CN105236762A, 2016.

28. P. J. McKarns, T. S. Lewkebandara, G. P. A. Yap, L. M. Liable-Sands, A. L. Rheingold and C. H. Winter, *Inorg. Chem.*, 1998, **37**, 418-424.
29. S. L. Benjamin, C. H. de Groot, C. Gurnani, A. L. Hector, R. Huang, K. Ignatyev, W. Levason, S. J. Pearce, F. Thomas and G. Reid, *Chem. Mater.*, 2013, **25**, 4719-4724.
30. S. D. Reid, A. L. Hector, W. Levason, G. Reid, B. J. Waller and M. Webster, *Dalton Trans.*, 2007, 4769-4777.
31. A. L. Hector, W. Levason, G. Reid, S. D. Reid and M. Webster, *Chem. Mater.*, 2008, **20**, 5100-5106.
32. I. Y. Ahmet, M. S. Hill, A. L. Johnson and L. M. Peter, *Chem. Mater.*, 2015, **27**, 7680-7688.
33. T. Wildsmith, M. S. Hill, A. L. Johnson, A. J. Kingsley and K. C. Molloy, *Chem. Commun.*, 2013, **49**, 8773-8775.
34. H. Shen, H.-S. Chan and Z. Xie, *Organometallics*, 2007, **26**, 2694-2704.
35. H. Wang, H.-W. Li and Z. Xie, *Organometallics*, 2003, **22**, 4522-4531.
36. J.-W. Hsu, Y.-C. Lin, C.-S. Hsiao, A. Datta, C.-H. Lin, J.-H. Huang, J.-C. Tsai and W.-C. Hsu, *Dalton Trans.*, 2012, **41**, 7700-7707.
37. A. D. Schofield, A. Nova, J. D. Selby, A. D. Schwarz, E. Clot and P. Mountford, *Chemistry*, 2011, **17**, 265-285.
38. M. B. Harkness, E. Alvarado, A. C. Badaj, B. C. Skrela, L. Fan and G. G. Lavoie, *Organometallics*, 2013, **32**, 3309-3321.
39. K. Weitershaus, J. Lloret Fillol, H. Wadepohl and L. H. Gade, *Organometallics*, 2009, **28**, 4747-4757.
40. R. Glaser, R. Hillebrand, W. Wycoff, C. Camasta and K. S. Gates, *J. Org. Chem.*, 2015, **80**, 4360-4369.
41. M. E. Davie, T. Foerster, S. Parsons, C. Pulham, D. W. H. Rankin and B. A. Smart, *Polyhedron*, 2006, **25**, 923-929.
42. R. Gyepes, I. Císařová, J. Pinkas, J. Kubišta, M. Horáček and K. Mach, *Eur. J. Inorg. Chem.*, 2013, **2013**, 3316-3322.
43. B. M. Powell, G. Dolling and B. H. Torrie, *Acta Crystallogr., Sect. B*, 1982, **38**, 28-32.
44. F. A. Cotton and G. Wilkinson, *Advanced Inorganic Chemistry*, 3rd Ed., Interscience Publishers, 1972.
45. A. N. Gleizes, *Chem. Vap. Deposition*, 2000, **6**, 155-173.
46. M. Afzaal, M. A. Malik and P. O'Brien, *J. Mater. Chem.*, 2010, **20**, 4031-4040.
47. C. E. Knapp and C. J. Carmalt, *Chem. Soc. Rev.*, 2016, **45**, 1036-1064.
48. D. C. Bradley and M. H. Gitlitz, *J. Chem. Soc. A*, 1969, 1152-1156.
49. D. C. Bradley and M. H. Gitlitz, *Chem. Commun.*, 1965, 289a-289a.
50. D. C. Bradley, I. F. Rendall and K. D. Sales, *J. Chem. Soc., Dalton Trans.*, 1973, 2228-2233.
51. M. Colapietro, A. Vaciago, D. C. Bradley, M. B. Hursthouse and I. F. Rendall, *J. Chem. Soc. D*, 1970, 743-744.
52. M. Colapietro, A. Vaciago, D. C. Bradley, M. B. Hursthouse and I. F. Rendall, *J. Chem. Soc., Dalton Trans.*, 1972, 1052-1057.
53. A. N. Bhat, R. C. Fay, D. F. Lewis, A. F. Lindmark and S. H. Strauss, *Inorg. Chem.*, 1974, **13**, 886-892.
54. A. H. Bruder, R. C. Fay, D. F. Lewis and A. A. Sayler, *J. Am. Chem. Soc.*, 1976, **98**, 6932-6938.
55. R. C. Fay, J. R. Weir and A. H. Bruder, *Inorg. Chem.*, 1984, **23**, 1079-1089.

56. W. L. Steffen, H. K. Chun and R. C. Fay, *Inorg. Chem.*, 1978, **17**, 3498-3503.
57. A. Donzelli and P. G. Potvin, *Inorg. Chem.*, 2009, **48**, 4171-4178.
58. R. E. Jilek, G. Tripepi, E. Urnezius, W. W. Brennessel, V. G. Young, Jr. and J. E. Ellis, *Chem Commun (Camb)*, 2007, 2639-2641.
59. T. Ouyang, K. P. Loh, H. Zhang, J. J. Vittal, M. Vetrichelvan, W. Chen, X. Gao and A. T. S. Wee, *J. Phys. Chem. B*, 2004, **108**, 17537-17545.
60. B. Bondars, G. Heidemane, J. Grabis, K. Laschke, H. Boysen, J. Schneider and F. Frey, *J. Mater. Sci.*, 1995, **30**, 1621-1625.
61. H. S. W. Chang and D. M. Schleich, *J. Solid State Chem.*, 1992, **100**, 62-70.
62. J. R. Dahn, W. R. McKinnon, R. R. Haering, W. J. L. Buyers and B. M. Powell, *Can. J. Phys.*, 1980, **58**, 207-213.
63. W. K. Unger, J. M. Reyes, O. Singh, A. E. Curzon, J. C. Irwin and R. F. Frindt, *Solid State Commun.*, 1978, **28**, 109-112.
64. S. J. Sandoval, X. K. Chen and J. C. Irwin, *Phys. Rev. B*, 1992, **45**, 14347-14353.
65. S. H. Nam, J.-S. Hyun and J.-H. Boo, *Mater. Res. Bull.*, 2012, **47**, 2717-2721.
66. G. Haegg and N. Schoenberg, *Ark. Kemi.*, 1954.
67. T. Iwasaki, N. Kuroda and Y. Nishina, *J. Phys. Soc. Jpn*, 1982, **51**, 2233-2240.
68. L. Roubi and C. Carlone, *Phys. Rev. B*, 1988, **37**, 6808-6812.
69. A. M. Stacy and D. T. Hodul, *J. Phys. Chem. Solids*, 1985, **46**, 405-409.
70. J. Liu, M. Liao, M. Imura, A. Tanaka, H. Iwai and Y. Koide, *Sci. Rep.*, 2014, **4**, 6395.
71. X. Wang, L. Huang, X.-W. Jiang, Y. Li, Z. Wei and J. Li, *J. Mater. Chem. C*, 2016, **4**, 3143-3148.
72. M. Khorasaninejad, J. Walia and S. S. Saini, *Nanotechnology*, 2012, **23**, 275706.
73. E. O. Filatova, A. A. Sokolov, A. A. Ovchinnikov, S. Y. Tveryanovich, E. P. Savinov, D. E. Marchenko, V. V. Afanas'ev and A. S. Shulakov, *J. Electron. Spectrosc. Relat. Phenom.*, 2010, **181**, 206-210.

Chapter 3

Ta sulfide precursors

3.1 Introduction

The focus of this chapter is the development of single-source precursors for the deposition of tantalum disulfide. The precursors being investigated will be based on tantalum thioureide and dithiocarbamate complexes.

3.1.1 Tantalum disulfide

Traditionally the major interest in TaS_2 has been as a cathode material in Li ion batteries. TaS_2 was the first TMD to be investigated for a range of ion intercalation reactions; this was intended to increase the superconducting transition temperature of the material. While it did increase the transition temperature it also showed that the intercalation reaction could be performed in a reversible manner, paving the way for Li ion batteries.[1, 2] Now the major interest in TaS_2 is focussed on its superconducting and CDW properties.[3]

TaS_2 has a range of potential polymorphs (Figure 3.1) that include: the 1T phase (space group: $P\bar{3}m$, a = 3.36, c = 5.90 Å), 2H phase (space group: $P6_a/mmc$, a = 3.315, c = 12.10 Å), 3R (space group: $R3m$, a = 3.32, c = 17.9 Å), the 4H(a) phase (space group: $P\bar{6}2c$), the 4H(b) phase (space group: $P6_3/mmc$, a = 3.328, c = 23.716 Å) and the 6R phase (space group: $R3m$, a = 3.335, c = 35.85 Å). The metal centre environment in the 1T polymorph is octahedral, whilst in the 2H, 3R and 4H(a) polymorphs it is trigonal prismatic. The 4H(b) and 6R polymorphs contain layers of alternating octahedral and trigonal prismatic metal centre environments. At room temperature the 1T and 2H phases are most common.[4-6] TaS_2 is a semimetal with both superconducting and CDW characteristics.[7]

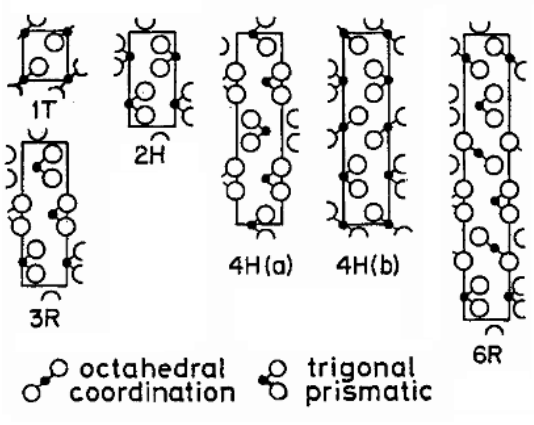

Figure 3.1 Polymorphs of TaS_2.[5]

3.1.2 TaS_2 precursors

To our knowledge, there is only one example of TaS_2 grown by CVD reported in the literature. Peters *et al*. used a precursor solution of $Ta(NMe_2)_5$ and excess ^tBuSH in hexanes or dichloromethane to deposit amorphous TaS_2 using AACVD over the temperature range 225 to 450 °C. The films produced were composed of clusters, 0.4 μm (dichloromethane) to 0.8 μm (hexanes) in size with only slight surface contamination from carbon and oxygen. The most likely identity of the precursor molecule was determined to be the mixed tantalum amide thiolate compound, $[Ta(S^tBu)_2(NMe_2)_3]$.[8]

Benjamin *et al.* did report the synthesis of the compounds $[TaCl_5(S^nBu_2)]$ and $[(TaCl_5)_2\{o\text{-}C_6H_4(CH_2SEt)_2\}]$ but LPCVD experiments did not yield any films.[9] Molecular beam epitaxy and chemical vapour transport have both been used to deposit TaS_2 films from tantalum and sulfur elemental sources.[10-12]

3.2 Tantalum thioureides

There is only one report of a tantalum complex containing thiourea in the literature. Baghlaf *et al.* described the synthesis of the yellow tantalum(V) chloride tetramethlthiourea adduct, $TaCl_5{\cdot}SC(N\{CH_3\}_2)_2$, which was formed by the reaction between $TaCl_5$ and tetramethylthiourea in DCM. No investigation into the suitability of this compound as a TaS_2 precursor was carried out.[13]

This section will investigate isothiocyanate insertions into tantalum amides to form the corresponding tantalum thioureide complexes as there are no reports of these reactions within the literature. Reactions with the homoleptic complex, $[Ta(NMe_2)_5]$ (PDMAT), will be explored in section 3.2.1 while reactions with the heteroleptic species, $[(^tBuN)Ta(NMe_2)_3]$, will be examined in section 3.2.2.

3.2.1 Synthesis and characterisation of PDMAT based complexes

The reaction between PDMAT and the iso-propyl, *tert*-butyl and phenyl isothiocyanates was investigated. In the first instance, a PDMAT to isothiocyanate ratio of 1:3 was used. All reactions were carried out in toluene and resulted in an immediate formation of a yellow solution. Concentration of the mother liquor *in vacuo* and storage of the solution at -28 °C yielded yellow crystals for the *tert*-butyl

reaction and yellow solid for the iso-propyl and phenyl reactions. Subsequent analysis of these products using ^{1}H and $^{13}C\{^{1}H\}$ NMR spectroscopy indicated that numerous complexes were present, although the identities of these complexes could not be determined. Single crystal X-ray diffraction of the yellow *tert*-butyl reaction product provided a molecular structure for the single *tert*-butyl isothiocyanate insertion into PDMAT, indicating only a single insertion would occur.

The reactions between PDMAT and the iso-propyl, *tert*-butyl and phenyl isothiocyanates were then repeated using a reaction ratio of 1:1 (Scheme 3.1). Addition of the isothiocyanates to the toluene solutions of PDMAT resulted in the immediate formation of a yellow solution; experiments were stirred overnight to ensure a complete reaction. Filtration of the reaction mixture and concentration of the filtrate *in vacuo* followed by storage at -28 °C yielded yellow crystals. The identity of the phenyl insertion product could not be determined using ^{1}H and $^{13}C\{^{1}H\}$ NMR spectroscopy or single crystal X-ray diffraction.

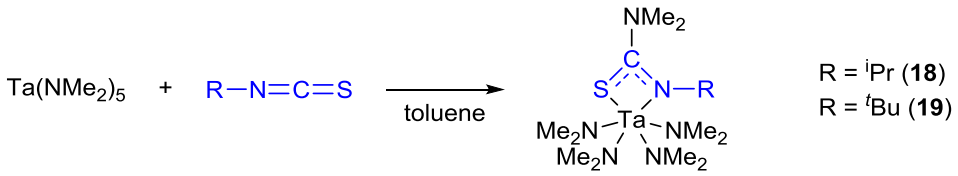

Scheme 3.1 Reaction of PDMAT with the iso-propyl and *tert*-butyl isothiocyanates forms the products **18** and **19** respectively.

The ^{1}H NMR spectra of the yellow crystals from both the iso-propyl and *tert*-butyl reactions displayed two separate products. All of the products in the spectra had an un-inserted to inserted NMe_2 integration ratio of 4:1 suggesting the mono-insertion products had been formed. This also indicated that the two separate products were structural isomers of the mono-insertion product. These products were also in equilibrium as a temperature change from 25 to 70 °C changed the major to minor ratio from 2.35:1 to 3.14:1 for the iso-propyl complex and from 1.25:1 to 1:1.47 for the *tert*-butyl complex. Elemental analysis was in good agreement with the expected values for the mono-insertion product.

For the iso-propyl complex, **18**, the major product displayed three un-inserted NMe_2 environments in the ^{1}H NMR spectra at 3.58, 3.48 and 3.47 ppm with a ratio of 6:12:6, while in the minor product these resonances had shifted to 3.37, 3.09 and

3.04 ppm with a ratio of 6:6:12. The presence of three un-inserted NMe_2 environments supports the formation of an octahedral mono-insertion product. An octahedral complex would provide two equivalent NMe_2 ligands in the axial positions and two inequivalent NMe_2 ligands in the equatorial plane. The iso-propyl resonances shifted downfield from 4.06 (CH) and 1.15 (CH_3) ppm in the major product to 4.77 and 1.42 ppm in the minor product. Interestingly, the inserted NMe_2 resonances were observed at 2.55 ppm for both products, suggesting similar inserted NMe_2 environments are adopted. The $^{13}C\{^1H\}$ NMR spectrum exhibited multiple NMe_2 and iso-propyl carbon atom environments with the $\{SCN_2\}$ carbon atom resonance only displayed for the major product at 187.4 ppm.

In contrast, only the major product identified by NMR spectroscopy for the *tert*-butyl complex, **19**, displayed three un-inserted NMe_2 environments in the ^1H NMR spectra. The peaks at 3.37, 3.11 and 3.09 ppm had a ratio of 6:6:12, while the minor product exhibited a single broad resonance at 3.53 ppm equivalent to all of the un-inserted NMe_2 environments suggesting rapid exchange was occurring. Both the *tert*-butyl CH_3 (major – 1.79 ppm, minor – 1.41 ppm) and inserted NMe_2 (major – 2.60 ppm, minor – 2.36 ppm) resonances shifted upfield in the minor product. The $^{13}C\{^1H\}$ NMR spectrum exhibited multiple NMe_2 and *tert*-butyl carbon atom environments with the $\{SCN_2\}$ carbon atom resonance displayed at 197.2 ppm for the major product and at 198.3 ppm for the minor product.

Attempts to collect the molecular structure of the iso-propyl product, **18**, using single crystal X-ray diffraction were unsuccessful due to severe twinning within the crystals. The molecular structure of the *tert*-butyl product, **19**, was obtained and is displayed in Figure 3.2 with selected bond lengths and angles presented in Table 3.1. The complex crystallised in an orthorhombic *Pbca* space group with two similar molecules contained within the asymmetric unit, the following discussion will focus on the molecule containing Ta(1). The molecular structure shows that the complex is the mono-insertion product and in the solid state the thioureide ligand adopts the κ^2-*N,N'* binding mode. The ligands adopt a distorted octahedral geometry around the 6-coordinate metal centre with the thioureide ligand situated in the equatorial plane. The NMe_2 ligands situated in the axial positions possess slightly longer bond lengths than those in the equatorial plane. As expected, the metal-nitrogen bonds are slightly shorter than those observed in the zirconium (**5**) and hafnium (**8**) iso-propyl

complexes containing the κ^2-*N*,*N'* mode in Chapter 2, although the internal ligand geometries are essentially equivalent.

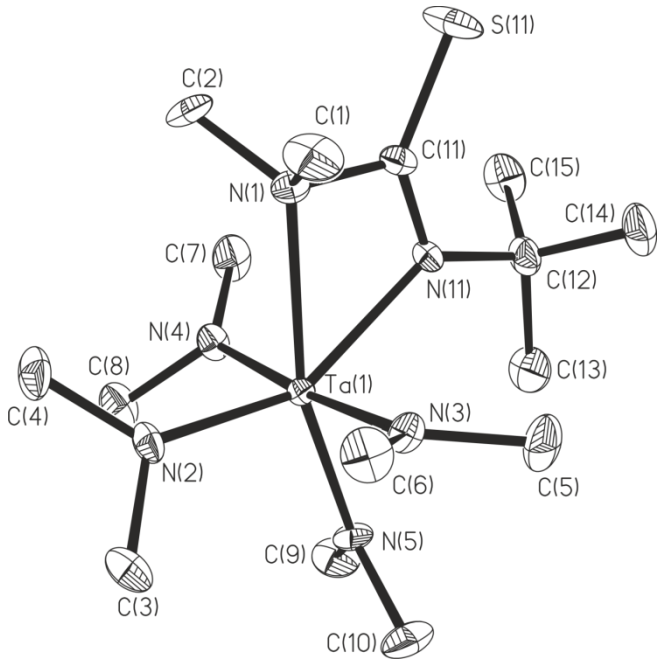

Figure 3.2 Molecular structure of complex **19**. Thermal ellipsoids are shown at 50 % probability, with hydrogen atoms omitted for clarity.

Table 3.1 Selected bond lengths and angles for **19** with e.s.d.s. in parentheses.

Bond	**Bond length / Å**	**Angle**	**Bond angle / °**
Ta(1)-N_{amide}	1.984(3) - 2.057(3)	N(11)-Ta(1)-N(1)	57.91(11)
Ta(1)-N(11)	2.245(3)	C(11)-N(11)-Ta(1)	103.4(2)
Ta(1)-N(1)	2.409(3)	C(11)-N(1)-Ta(1)	91.1(2)
N(11)-C(11)	1.315(5)	N(11)-C(11)-N(1)	107.5(3)
N(1)-C(11)	1.482(5)	N(11)-C(11)-S(1)	133.4(3)
S(1)-C(11)	1.676(4)	N(1)-C(11)-S(1)	119.1(3)
N(11)-C(12)	1.511(5)		
N(1)-C(2)	1.486(5)		
N(1)-C(1)	1.492(5)		

The similarities in the NMR spectra of the minor iso-propyl product and the major *tert*-butyl product suggest these complexes are the same structural isomers. Assuming the major NMR product for the *tert*-butyl complex is the same as the

structure observed in the solid state then this would suggest the minor NMR product for the iso-propyl complex contains the thioureide ligand in the κ^2-*N,N'* mode. As both iso-propyl NMR products exhibit identical inserted NMe_2 environments (2.55 ppm) in the ^{1}H NMR spectra but differing iso-propyl environments (major – 1.15 ppm, minor – 1.42 ppm), this would indicate the thioureide ligand in the major iso-propyl product would adopt the κ^2-*S,N'* mode with the dimethylamide also bound to the metal centre. Consequently, the differing NMR environments to all other products for the minor *tert*-butyl product suggests the thioureide ligand adopts the κ^2-*S,N* mode. The proposed identities of the iso-propyl and *tert*-butyl NMR products are displayed in Figure 3.3.

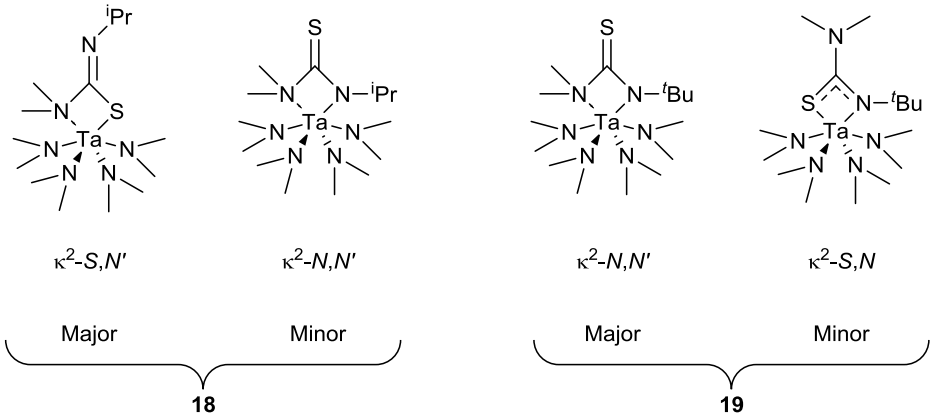

Figure 3.3 Proposed structures of the major and minor NMR products of complexes **18** and **19**.

3.2.2 Synthesis and characterisation of [(^{t}BuN)Ta(NMe_2)$_3$] (20) based complexes

Due to the limited number of complexes produced from the reactions with PDMAT and isothiocyanates, the reactions between isothiocyanates and the *tert*-butylimidotris(dimethylamido) tantalum(V) complex, [(^{t}BuN)Ta(NMe_2)$_3$] (**20**), were also investigated. Complex **20** was synthesised by reacting PDMAT with one equivalent of *tert*-butylamine in hexane (Scheme 3.2). After stirring for 18 hours, the yellow solution was filtered, concentrated *in vacuo* and stored at -28 °C to provide pale orange crystals of complex **20**.[14]

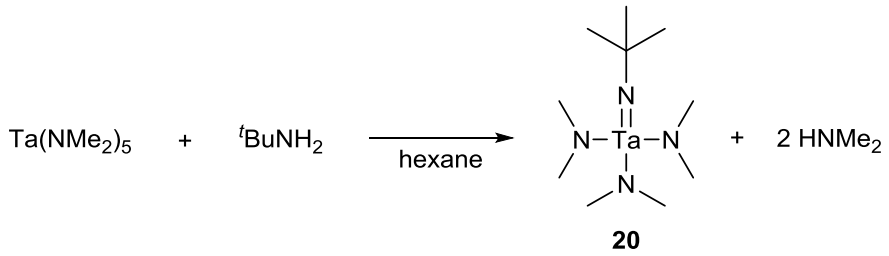

Scheme 3.2 Synthesis of [(^{t}BuN)Ta(NMe$_2$)$_3$] (**20**).

The reaction between complex **20** and three equivalents of *tert*-butyl isothiocyanate resulted in an immediate reaction; however the identity of the product could not be determined using NMR spectroscopy or single crystal X-ray diffraction. The reaction between complex **20** and three equivalents of iso-propyl isothiocyanate in toluene (Scheme 3.3) also resulted in the immediate formation of a yellow solution. After stirring overnight the solvent was removed *in vacuo* to provide a yellow solid which was dissolved in hexane. This solution was filtered and stored at -28 °C to provide yellow crystals of complex **21**.

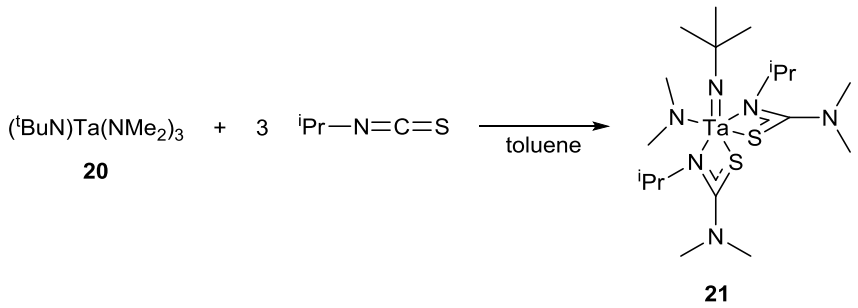

Scheme 3.3 Synthesis of [(^{t}BuN)Ta(NMe$_2$)(SC{NMe$_2$}N^{i}Pr)$_2$] (**21**).

^{1}H NMR spectroscopy indicated the complex was the bis-insertion product (Scheme 3.3) as the ratio of integrals for the un-inserted and inserted NMe$_2$ environments was 1:2. Two separate inserted NMe$_2$ (2.55 and 2.58 ppm) and iso-propyl CH (4.15-4.06 and 4.28-4.39 ppm) resonances were observed suggesting the thioureide ligands were not equivalent. Discrete iso-propyl CH$_3$ (1.22, 1.30, 1.35 and 1.49) and un-inserted NMe$_2$ (3.93 and 4.32 ppm) environments, equal to a single methyl group each, implied that rotation was hindered around the N-^{i}Pr and Ta-NMe$_2$ axes respectively. A single resonance for the *tert*-butyl imide group was recorded at 1.57 ppm. These observations were supported by the ^{13}C{^{1}H} NMR spectrum which displayed two {SNCN} carbon atom resonances (186.7 and 188.7 ppm), two iso-

propyl CH environments (42.1 and 42.2 ppm) and four iso-propyl CH_3 environments (24.5, 24.6, 24.9 and 26.0 ppm). Elemental analysis was in good agreement with the expected values for the bis-insertion product.

As the bis-insertion product (**21**) was formed for the iso-propyl reaction, only two equivalents of phenyl isothiocyanate were reacted with complex **20** in toluene (Scheme 3.4). An immediate reaction occurred with the formation of a yellow solution, the reaction mixture was stirred overnight to ensure a complete reaction. Concentration of the solution *in vacuo* provided a yellow precipitate which was heated back into solution, storage at room temperature yielded yellow crystals of complex **22**.

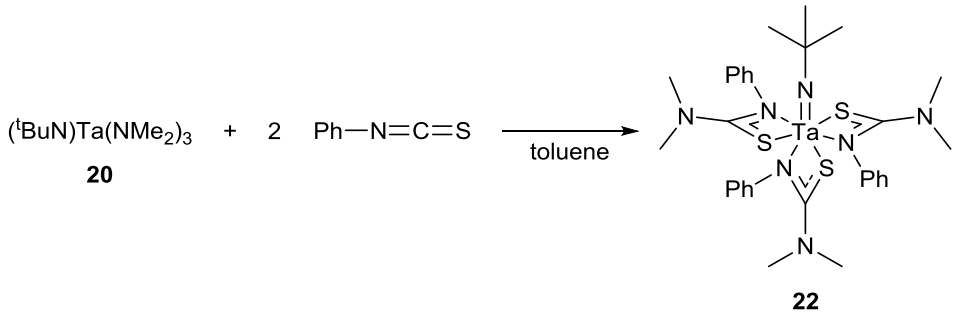

Scheme 3.4 Synthesis of [(^{t}BuN)Ta(SC{NMe_2}NPh)$_3$] (**22**).

Analysis of the product using ^{1}H and ^{13}C{^{1}H} NMR spectroscopy indicated the tris-insertion product, **22** (Scheme 3.4), had actually been formed as there were no un-inserted NMe_2 environments within the spectra. Single resonances were observed in both spectra for the ^{t}Bu and NMe_2 groups, the broad singlet in the ^{1}H NMR spectrum for the NMe_2 resonance suggested there was a degree of fluxionality. Elemental analysis was in good agreement with the expected values for the tris-insertion product.

The molecular structure (Figure 3.4) of the iso-propyl complex, **21**, was obtained using single crystal X-ray diffraction. The structure showed the bis-insertion product had been formed in agreement with the NMR spectra. The complex crystallised in a monoclinic $P2_1/c$ space group with a single molecule contained within the asymmetric unit. The metal centre adopts a distorted octahedral geometry with the *tert*-butyl imide and dimethylamide groups situated *cis*. Both thioureide ligands bind to the metal centre via the κ^2-*S,N* mode, with the two sulfur atoms located *cis*. All

iso-propyl and both un-inserted NMe_2 methyls are situated in different chemical environments supporting what was observed in the NMR spectra.

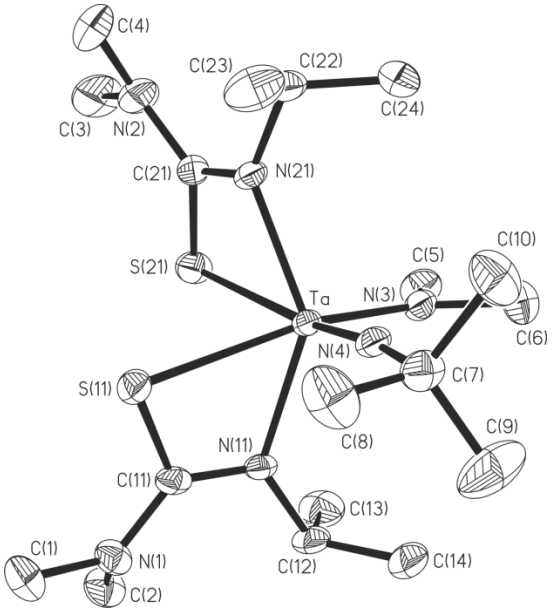

Figure 3.4 Molecular structure of complex **21**. Thermal ellipsoids are shown at 50 % probability, with hydrogen atoms omitted for clarity.

Table 3.2 Selected bond lengths and angles for **21** with e.s.d.s. in parentheses.

Bond	Bond length / Å	Angle	Bond angle / °
Ta-N(4)	1.781(4)	C(7)-N(4)-Ta	172.1(3)
Ta-N(3)	2.009(4)	N(11)-Ta-S(11)	63.11(10)
Ta-S(11)	2.6518(12)	N(21)-Ta-S(21)	62.78(10)
Ta-S(21)	2.7066(12)	C(11)-S(11)-Ta	77.67(16)
Ta-N(11)	2.191(3)	C(21)-S(21)-Ta	76.35(16)
Ta-N(21)	2.169(4)	C(11)-N(11)-Ta	105.2(3)
S(11)-C(11)	1.731(5)	C(21)-N(21)-Ta	106.4(3)
S(21)-C(21)	1.731(5)	N(11)-C(11)-S(11)	113.7(3)
N(11)-C(11)	1.320(6)	N(21)-C(21)-S(21)	114.2(3)
N(21)-C(21)	1.332(6)	N(1)-C(11)-S(11)	120.3(4)
N(1)-C(11)	1.377(6)	N(2)-C(21)-S(21)	120.3(4)
N(2)-C(21)	1.354(6)	N(1)-C(11)-N(11)	126.0(4)
N(11)-C(12)	1.483(6)	N(2)-C(21)-N(21)	125.5(5)
N(21)-C(22)	1.483(6)		

Selected bond lengths and angles for complex **21** are presented in Table 3.2. The bond lengths between the metal centre and the *tert*-butyl imide (1.781(4) Å) or dimethylamide (2.009(4) Å) ligands are comparable to those found by Nugent *et al.* for the starting material, **20** (Ta-N^{t}Bu = 1.77(2) Å, Ta-NMe_2 = 1.99(1) Å). While the bond lengths are similar, there is a slight reduction in the Ta-N-C angle for the *tert*-butylimide ligand (172.1(3)° vs linear in **20**).[15] The only differences with regards to the thioureide ligands are the metal-ligand bond lengths; the ligand with the longer Ta-S bond has a shorter Ta-N bond. The geometries of the κ^2-*S*,*N* thioureide ligands also match those observed for the analogous ligands in the zirconium (**5)** and hafnium (**8**) iso-propyl thioureide complexes described in Chapter 2.

The phenyl complex, **22**, also crystallised in a monoclinic $P2_1/c$ space group with a single molecule occupying the asymmetric unit. The molecular structure is presented in Figure 3.5 with selected bond lengths and angles displayed in Table 3.3. The structure shows that the complex is the tris-insertion product with all three thioureide ligands binding via the κ^2-*S*,*N* mode. The 7-coordinate metal centre adopts a distorted pentagonal bipyramidal geometry with the *tert*-butylimide ligand and a sulfur atom from a thioureide ligand positioned axially.

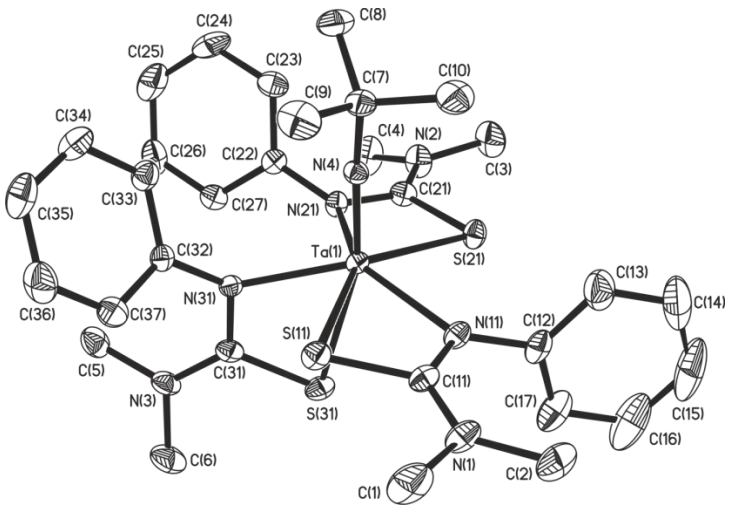

Figure 3.5 Molecular structure of complex **22**. Thermal ellipsoids are shown at 50 % probability, with hydrogen atoms omitted for clarity.

Within the complex the thioureide ligand geometries are essentially equivalent with only slight differences in the orientation of the phenyl ring. In all cases, the phenyl ring is not in plane with the {SNCN} plane suggesting there is no conjugation across these two moieties. Both the *tert*-butylimide and thioureide ligands have similar

geometries to the analogous ligands in the iso-propyl complex, **21**. Interestingly, the Ta-S bonds are slightly shorter in the phenyl complex, **22**, while the thioureide Ta-N bonds are slightly shorter in the iso-propyl complex, **21**. The geometries of the phenyl thioureide ligands also match those observed for the analogous ligands in the titanium (**3**), zirconium (**7)** and hafnium (**10**) phenyl thioureide complexes described in Chapter 2.

Table 3.3 Selected bond lengths and angles for **22** with e.s.d.s. in parentheses.

Bond	Bond length / Å	Angle	Bond angle / °
Ta(1)-N(4)	1.775(2)	C(7)-N(4)-Ta(1)	169.81(18)
Ta(1)-S(11)	2.5992(6)	N(11)-Ta(1)-S(11)	62.43(6)
Ta(1)-S(21)	2.5810(6)	N(21)-Ta(1)-S(21)	62.63(5)
Ta(1)-S(31)	2.6842(7)	N(31)-Ta(1)-S(31)	63.04(6)
Ta(1)-N(11)	2.228(2)	C(11)-S(11)-Ta(1)	81.09(9)
Ta(1)-N(21)	2.2595(19)	C(21)-S(21)-Ta(1)	81.39(9)
Ta(1)-N(31)	2.194(2)	C(31)-S(31)-Ta(1)	77.29(9)
S(11)-C(11)	1.731(3)	C(11)-N(11)-Ta(1)	106.05(16)
S(21)-C(21)	1.740(3)	C(21)-N(21)-Ta(1)	104.65(16)
S(31)-C(31)	1.736(3)	C(31)-N(31)-Ta(1)	105.63(16)
C(11)-N(11)	1.327(3)	N(11)-C(11)-S(11)	110.42(18)
C(21)-N(21)	1.317(3)	N(21)-C(21)-S(21)	111.05(18)
C(31)-N(31)	1.333(3)	N(31)-C(31)-S(31)	114.03(19)
C(11)-N(1)	1.347(3)	N(1)-C(11)-S(11)	120.7(2)
C(21)-N(2)	1.349(3)	N(2)-C(21)-S(21)	121.6(2)
C(31)-N(3)	1.354(3)	N(3)-C(31)-S(31)	120.7(2)
N(11)-C(12)	1.426(3)	N(11)-C(11)-N(1)	128.9(2)
N(21)-C(22)	1.426(3)	N(21)-C(21)-N(2)	127.3(2)
N(31)-C(32)	1.430(3)	N(31)-C(31)-N(3)	125.2(2)

3.2.3 Thermogravimetric analysis

Thermogravimetric analysis for the tantalum thioureide complexes was performed using closed pans to limit the exposure of the complexes to air and moisture. Analysis was repeated a number of times to ensure the traces were accurate.

The PDMAT-based iso-propyl and *tert*-butyl complexes, **18** and **19**, showed almost identical TGA decomposition traces (Figure 3.6); a summary of results is presented in Table 3.4. Both decompositions initiated at 130 °C with the major decomposition step in the range 155 to 220 °C where a mass loss of ~38 % occurred, further decomposition ending at 380 °C proceeded with a mass loss of ~13 %. While the final percentage weights are very close to the values expected for TaS_2, the Ta:S ratios in the complexes prior to decomposition are 1:1 which indicates TaS_2 may not have been formed.

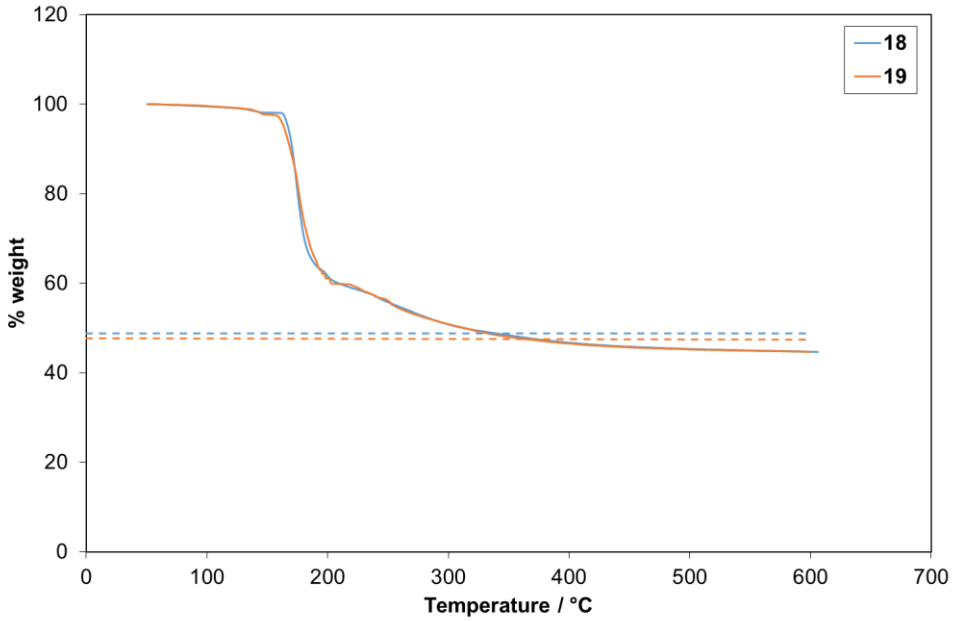

Figure 3.6 TGA traces for **18** and **19** in closed pans. Dashed lines represent the expected % weight for TaS_2.

Table 3.4 Summary of TGA data for **18** and **19**.

Compound	Onset / °C	End point / °C	% weight expected for TaS_2	End point % weight
18	130	380	48.8	47.4
19	130	380	47.4	47.0

Unsurprisingly, the *tert*-butylimide based iso-propyl and phenyl complexes, **21** and **22**, show differing decomposition pathways. TGA traces for the complexes are displayed in Figure 3.7, while a summary of the results is presented in Table 3.5. The iso-propyl complex, **21**, displayed an initial gradual mass loss from 170 °C before a

major decomposition event at 235 to 250 °C occurred with the loss of ~39 %. Additional decomposition followed ending at 370 °C with the further loss of ~15 % to provide a final mass of 40.4 %, which is close to the expected mass of TaS_2 (41.8 %). In contrast, the phenyl complex, **22**, decomposed via a one-step decomposition pathway with a mass loss of 52 % in the range 230 to 350 °C. The final percentage weight of 48.0 % was considerably higher than the value for TaS_2 (31.0 %) suggesting this complex would not be a viable precursor.

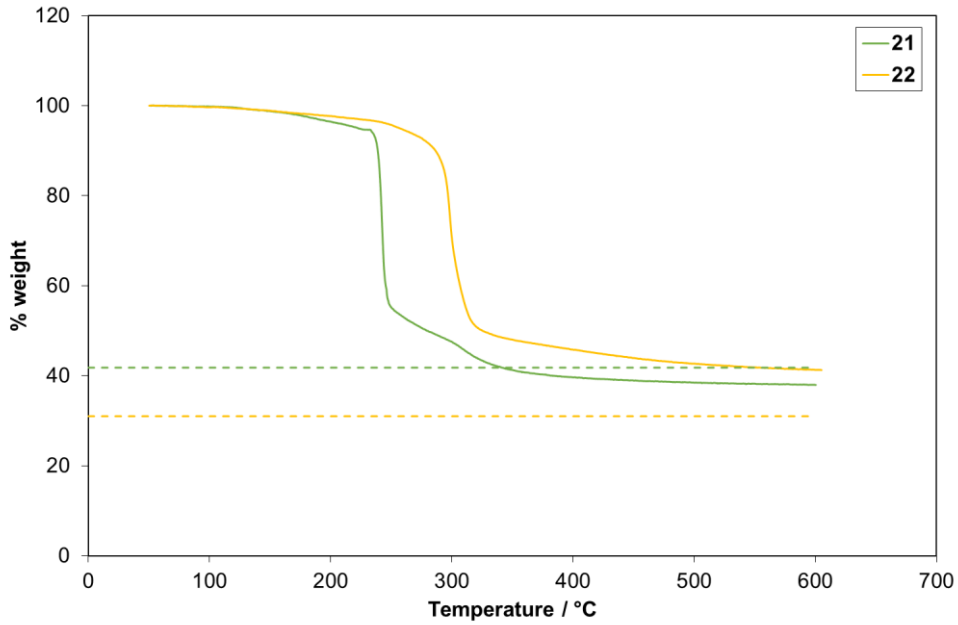

Figure 3.7 TGA traces for **21** and **22** in closed pans. Dashed lines represent the expected % weight for TaS_2.

Table 3.5 Summary of TGA data for **21** and **22**.

Compound	Onset / °C	End point / °C	% weight expected for TaS_2	End point % weight
21	170	370	41.8	40.4
22	230	350	31.0	48.0

Of all the tantalum thioureide complexes, the *tert*-butylimide based iso-propyl complex, **21**, was the most promising with a final percentage weight close to the value expected for TaS_2. While the PDMAT based complexes, **18** and **19**, both attained final percentage weights close to the values of TaS_2, the low Ta:S ratio in the starting complex suggests TaS_2 may not have been formed.

3.3 Tantalum dithiocarbamates

There are only a handful of tantalum dithiocarbamates reported in the literature and there are no examples of these complexes being utilised as CVD precursors. The homoleptic pentakisdimethyldithiocarbamate tantalum(V) complex, $[Ta(S_2CNMe_2)_5]$, has been reported by Bradley *et al*. and is formed via the insertion of CS_2 into PDMAT.[16] This compound is insoluble in most common organic solvents suggesting it would not be a suitable AACVD precursor. Smith *et al*. then reported the synthesis of the ethyl derivative, $[Ta(S_2CNEt_2)_5]$, by reacting $TaCl_5$ with five equivalents of NaS_2CNEt_2.[17] Later attempts to synthesise $[Ta(S_2CNEt_2)_5]$ resulted in the formation of the sulfide and disulfide trisdiethyldithiocarbamate tantalum(V) complexes, $[Ta(S)(S_2CNEt_2)_3]$ and $[Ta(S_2)(S_2CNEt_2)_3]$ (Figure 3.8a), respectively when $TaCl_5$ reacts with NaS_2CNEt_2.[18-21] These complexes are also relatively insoluble in common organic solvents; again this suggests they would not be suitable AACVD precursors.

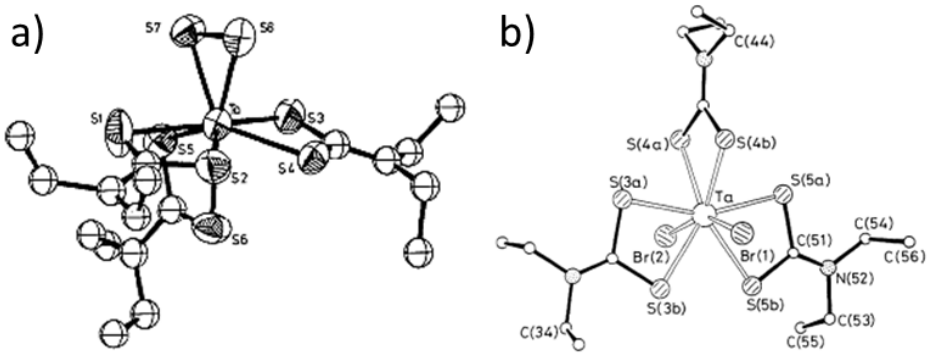

Figure 3.8 Molecular structures of a) $[Ta(S_2)(S_2CNEt_2)_3]$[21] and b) $[Ta(S_2CNEt_2)_3Br_2]$.[22]

Most heteroleptic tantalum dithiocarbamate species are based on halide or *tert*-butylimide species. Heckley *et al*. synthesised the diethyldithiocarbamate tantalum(V) halide species, $[Ta(S_2CNEt_2)_2X_3]$ (X = Cl and Br) and $[Ta(S_2CNEt_2)_4X]$ (X = Cl, Br and I), by reacting the metal halides with the appropriate ratio of NaS_2CNEt_2.[18] In contrast, Dilworth *et al*. synthesised the complexes $[Ta(S_2CNEt_2)_3X_2]$ (X = Cl, Br and I) displayed in Figure 3.8b, by reacting the dinitrogen complex $[\{Ta(S_2CNEt_2)_3\}_2(\mu\text{-}N_2)]$ with the appropriate anhydrous hydrogen halide.[22] For the *tert*-butylimide species Tan *et al*. reacted $TaCl_5$ with three equivalents of both *tert*-butylamine and $Me_3SiS_2CNR_2$ (R = Me and Et) to form the complexes, $[(^tBuN)Ta(S_2CNMe_2)_3]$ and $[(^tBuN)Ta(S_2CNEt_2)_3]$.[23] Of all the tantalum

dithiocarbamate species, the *tert*-butylimide complexes are the most promising for the AACVD of TaS_2 as they are soluble in most common organic solvents and they do not contain halides which could potentially contaminate the resulting films.

This section will focus on the synthesis of *tert*-butylimide based tantalum dithiocarbamate complexes. The complexes, [(^{t}BuN)Ta(NR_2)$_3$] (where R = Me and Et), will be reacted with CS_2 to form standard dithiocarbamates and the cyclic 2-thiazoline-2-thiol compound which contains the dithiocarbamate {S_2CN} moiety. While standard dithiocarbamates tend to bind via the κ^2-*S,S* mode the use of cyclic molecules containing the dithiocarbamate {S_2CN} moiety could provide the alternative κ^2-*S,N* binding mode (Figure 3.9).

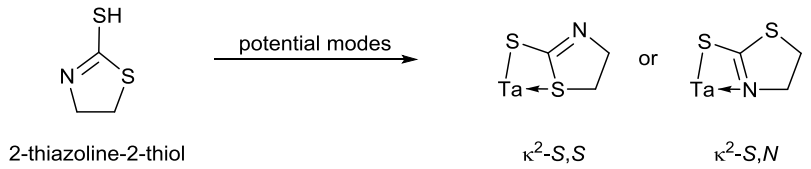

Figure 3.9 Potential binding modes of cyclic molecules containing the dithiocarbamate {S_2CN} moiety.

3.3.1 Synthesis and characterisation

The *tert*-butylimide-based tantalum dithiocarbamate complexes, [(^{t}BuN)Ta(S_2CNMe_2)$_3$] (**23**) and [(^{t}BuN)Ta(S_2CNEt_2)$_3$] (**24**), were synthesised by an alternative method to the one reported by Tan *et al*.[23] It is well known that CS_2 insertions into metal amide bonds form metal dithiocarbamates, therefore [(^{t}BuN)Ta(NMe_2)$_3$] and [(^{t}BuN)Ta(NEt_2)$_3$] were reacted with four equivalents of CS_2 in THF to form the complexes, **23** and **24** (Scheme 3.5).[16] For the methyl complex, **23**, addition of CS_2 immediately resulted in the formation of a yellow/brown precipitate. After stirring for 18 hours, the heated solution was filtered, concentrated *in vacuo* and then stored at -28 °C to afford yellow crystals in very high yields. For the ethyl complex, **24**, addition of CS_2 resulted in the immediate formation of a yellow solution. After stirring for 18 hours the solvent was removed *in vacuo*, recrystallisation from toluene at 4 °C provided orange crystals in very high yields.

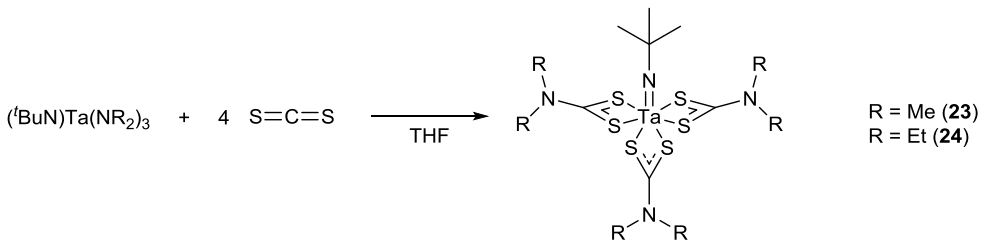

Scheme 3.5 Synthesis of [(^{t}BuN)Ta(S_2CNMe_2)$_3$] (**23**) and [(^{t}BuN)Ta(S_2CNEt_2)$_3$] (**24**).

$^{13}C\{^1H\}$ NMR spectra of complexes **23** and **24** exhibited {S_2CN} carbon atom resonances at 204.8/208.6 and 203.7 ppm respectively indicating the dithiocarbamate ligands had been successfully formed. The ^1H NMR spectrum of the methyl complex, **23**, displayed three separate methyl resonances of equal integration at 2.40, 2.46 and 2.59 ppm while in the spectrum of complex **24**, the ethyl CH_2 and CH_3 resonances were exhibited as multiplets at 3.10 – 3.33 and 0.69 – 0.97 ppm respectively. Multiple R group environments were also displayed in the $^{13}C\{^1H\}$ NMR spectra of both complexes. The presence of multiple R group resonances indicates the dithiocarbamate ligands are not equivalent; this is unsurprising as the species are heteroleptic. *Tert*-butylimide resonances were also observed as singlets at 1.67 (**23**) and 1.64 (**24**) ppm. Elemental analysis values were in good agreement with the expected values for both complexes. Attempts were made to attain the single crystal X-ray diffraction structure of complex **24** but severe twinning meant the data could not be solved.

The *tert*-butylimidotris(dimethylamido) tantalum(V) complex (**20**) was also reacted with three equivalents of 2-thiazoline-2-thiol which contains the dithiocarbamate {S_2CN} moiety (Scheme 3.6). The intention of this reaction was to substitute the dimethylamide groups with the 2-thiazoline-2-thiol. Stirring for 2 hours provided a pale green solution which was filtered and then concentrated *in vacuo*. Storage at room temperature provided colourless crystals of complex **25.**

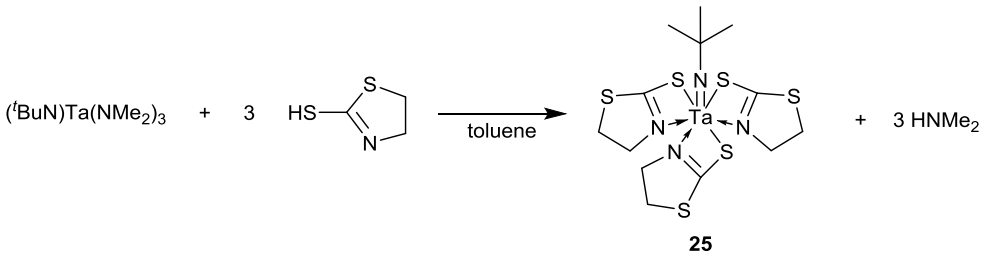

Scheme 3.6 Synthesis of [(^{t}BuN)Ta($SC_3H_4NS)_3$] (**25**).

^{1}H and ^{13}C{^{1}H} NMR spectroscopy of complex **25** showed the loss of the dimethylamide groups and the presence of resonances attributed to the 2-thiazoline-2-thiol at 4.56 – 4.35, 4.23 – 3.83 and 3.55 – 3.34 ppm. These resonances were displayed as multiplets indicating multiple 2-thiazoline-2-thiol environments were present. The ratio of 2-thiazoline-2-thiol to *tert*-butylimide indicated three 2-thiazoline-2-thiol ligands were present within the molecule. The *tert*-butylimide peak was displayed as a singlet at 1.17 ppm which was shifted upfield compared to the same resonance in the starting material (**20**) at 1.45 ppm. The {S_2CN} carbon atom resonance was observed at 189.7 ppm which was shifted upfield compared to the same resonances in the dithiocarbamate complexes **23** and **24**. Elemental analysis results were in good agreement with the expected values.

Single crystal X-ray diffraction performed on the colourless crystals of complex **25** provided the molecular structure displayed in Figure 3.10. The complex crystallised in a monoclinic $P2_1/c$ space group with a single molecule of **25** and a molecule of toluene occupying the asymmetric unit. The metal centre adopted a 7-coordinate distorted pentagonal bipyramidal geometry similar to the structure of the phenyl thioureide tantalum complex, **22**, with the *tert*-butylimide and a sulfur atom occupying the axial positions. Rather than binding by the κ^2-*S*,*S* mode, the 2-thiazoline-2-thiol binds to the tantalum metal centre by the κ^2-*S*,*N* mode.

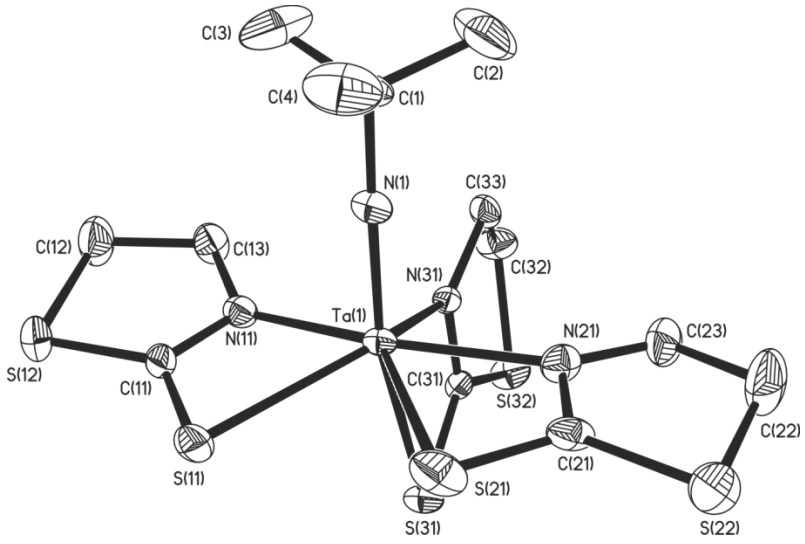

Figure 3.10 Molecular structure of complex **25**. Thermal ellipsoids are shown at 50 % probability, with hydrogen atoms omitted for clarity.

Table 3.6 Selected bond lengths and angles for **25** with e.s.d.s. in parentheses.

Bond	Bond length / Å	Angle	Bond angle / °
Ta-N(1)	1.759(2)	C(1)-N(1)-Ta	177.86(19)
N(1)-C(1)	1.446(3)	N(11)-Ta-S(11)	63.34(5)
Ta-S(11)	2.5921(7)	N(21)-Ta-S(21)	63.29(6)
Ta-S(21)	2.6065(7)	N(31)-Ta-S(31)	61.77(5)
Ta-S(31)	2.7859(6)	C(11)-S(11)-Ta	78.29(9)
Ta-N(11)	2.207(2)	C(21)-S(21)-Ta	77.97(9)
Ta-N(21)	2.211(2)	C(31)-S(31)-Ta	73.43(8)
Ta-N(31)	2.1731(19)	C(11)-N(11)-Ta	103.20(17)
S(11)-C(11)	1.712(3)	C(21)-N(21)-Ta	103.34(18)
S(21)-C(21)	1.715(3)	C(31)-N(31)-Ta	106.00(14)
S(31)-C(31)	1.710(2)	N(11)-C(11)-S(11)	114.7(2)
N(11)-C(11)	1.293(3)	N(21)-C(21)-S(21)	115.3(2)
N(21)-C(21)	1.292(3)	N(31)-C(31)-S(31)	118.78(17)
N(31)-C(31)	1.300(3)	N(11)-C(11)-S(12)	116.9(2)
S(12)-C(11)	1.743(3)	N(21)-C(21)-S(22)	116.7(2)
S(22)-C(21)	1.743(3)	N(31)-C(31)-S(32)	115.59(17)
S(32)-C(31)	1.749(2)	S(11)-C(11)-S(12)	128.32(15)
N(11)-C(13)	1.454(3)	S(21)-C(21)-S(22)	127.95(16)
N(21)-C(23)	1.459(4)	S(31)-C(31)-S(32)	125.62(14)
N(31)-C(33)	1.464(3)		

Selected bond lengths and angles for complex **25** are displayed in Table 3.6. The *tert*-butylimide ligand adopted a very similar geometry to that observed in the starting material, **20**, reported by Nugent *et al.*[15] Compared to the complex, $[(^{t}BuC_5H_4)_2Ta(H)\{SC(S)NPh\}]$ (Ta-S = 2.567(3) Å, Ta-N = 2.203(8) Å), reported by Brunner *et al*. which contains the $\{S_2CN\}$ moiety binding to the metal centre via the κ^2-*S,N* mode, complex **25** has slightly longer Ta-S bonds but Ta-N bonds of a similar length.[24] The geometries within the 2-thiazoline-2-thiol ligands are all equivalent, although the metal ligand bond geometries vary depending on the position of the ligand. The axial position of the S(31) atom provided a longer Ta-S bond length of 2.7859(6) Å compared to the equatorially positioned sulfur atoms (Ta-S(11) =

2.5921(7) Å, Ta-S(21) = 2.6065(7) Å). Within the axial 2-thiazoline-2-thiol ligand, the Ta-N bond (Ta-N(31) = 2.1731(19) Å) was shorter than the Ta-N bonds (Ta-N(11) = 2.207(2) Å, Ta-N(21) = 2.211(2) Å) in the equatorial ligands. The {S_2CN} carbon atoms are sp^2 hybridised (sum of angles = ~360°) with the C-N bond lengths of ~1.3 Å in the carbon-nitrogen double bond range of 1.279-1.316 Å as reported by Allen *et al.*[25]

3.3.2 Thermogravimetric analysis

Thermogravimetric analysis for the tantalum dithiocarbamate complexes was performed using open pans. Analysis was repeated a number of times to ensure the traces were accurate. The TGA traces for both complexes, **23** and **24**, are presented in Figure 3.11 with a summary of the results displayed in Table 3.7. Both complexes showed similar one step decomposition pathways, with the ethyl complex, **24**, exhibiting a slight kink in the trace at ~193 °C. Decomposition was initiated in both complexes at 140 °C, although the methyl complex, **23**, decomposed over a narrower range (140 – 325 °C) when compared to the ethyl complex, **24** (140 – 365 °C). Final percentage weights were lower than the expected TaS_2 values for both complexes indicating they may be volatile.

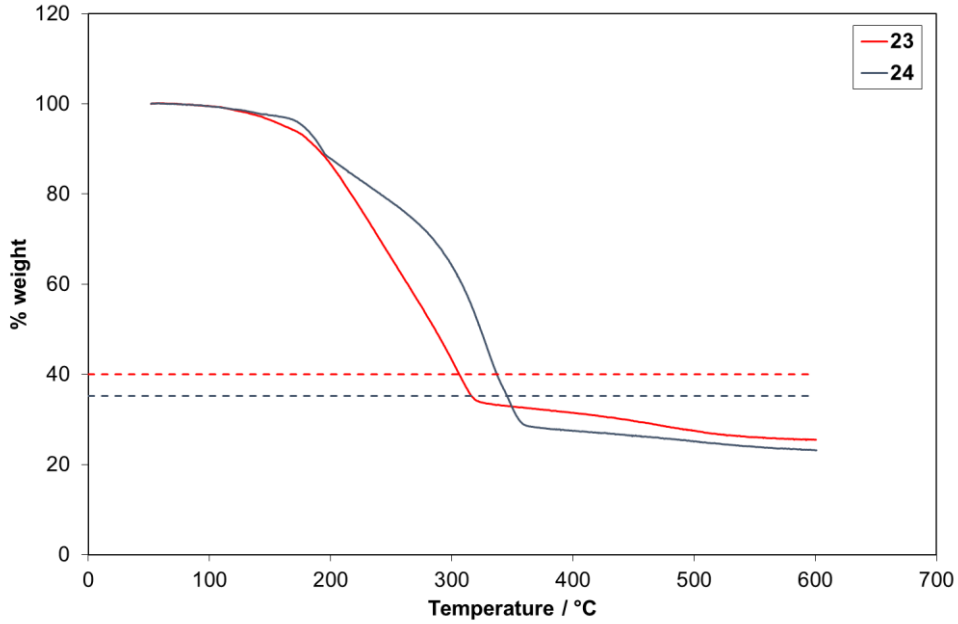

Figure 3.11 TGA traces for **23** and **24** in open pans. Dashed lines represent the expected % weight for TaS_2.

Table 3.7 Summary of TGA data for **23** and **24**.

Compound	Onset / °C	End point / °C	% weight expected for TaS_2	End point % weight
23	140	325	40.0	33.8
24	140	365	35.2	28.4

TGA-MS was performed on the ethyl complex, **24**, to further elucidate the decomposition pathway, the TGA trace and major mass peaks recorded on decomposition are displayed in Figure 3.12. The majority of decomposition occurred in the range 280 to 340 °C with major mass peaks observed at 15, 26, 27, 29, 41, 55, 56, 76 and 78 m/z, possible identities of the these fragments are presented in Table 3.8. The most intense mass peaks were situated at 76 and 41 m/z which most likely correspond to the loss of CS_2 and H_3CCN respectively. A less intense peak at 56 m/z suggests some of the *tert*-butylimide groups decompose via the loss of $H_2C{=}C(CH_3)_2$, while a peak at 27 m/z also indicates that HCN is a decomposition product. After the decomposition had finished a small peak at 64 m/z is observed which suggests the TaS_2 final product is decomposing further with the loss of S_2 or SO_2.

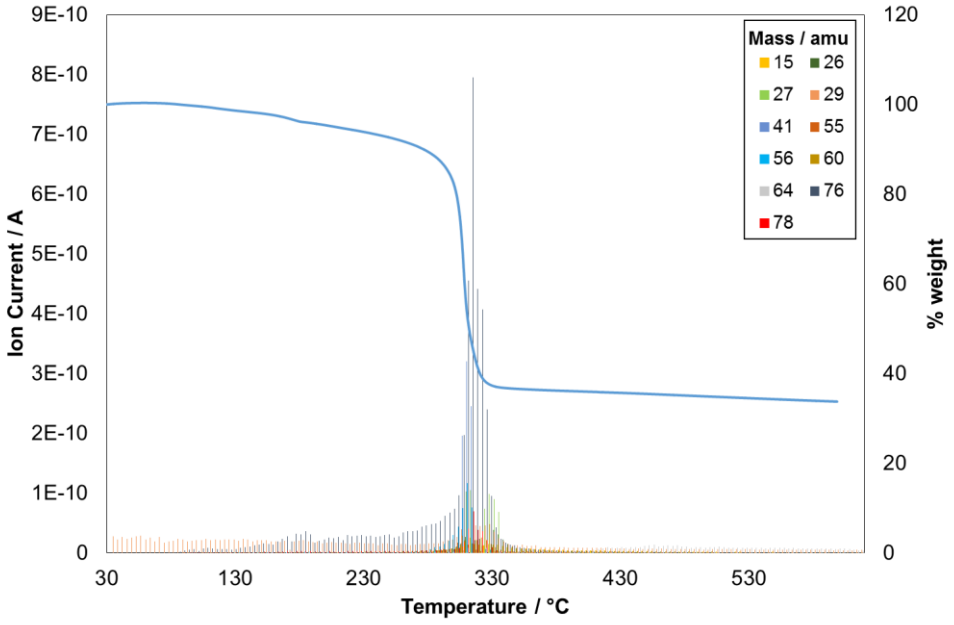

Figure 3.12 TGA-MS results for **24**: graph shows the major ion fragments present as temperature is increased, TGA trace is overlaid.

Table 3.8 Possible ion fragment assignment for the decomposition of **24**.

Mass / m/z	Fragment
15	CH_3^+
26	CN^+, $C_2H_2^+$
27	HCN^+
29	$C_2H_5^+$
41	H_3CCN^+
56	$H_2C{=}C(CH_3)_2^+$
64	S_2^+, SO_2^+
76	CS_2^+

The 2-thiazoline-2-thiol based complex, **25**, decomposed over a relatively large temperature range of 70 – 530 °C (Figure 3.13), the TGA data is summarised in Table 3.9. In the initial decomposition step between 70 and 100 °C a mass loss of ~12 % was observed followed by the major mass loss event of ~35 % between 100 and 320 °C. The mass slowly decreased until the end point was reached at 530 °C where a final mass comparable to TaS_2 was recorded.

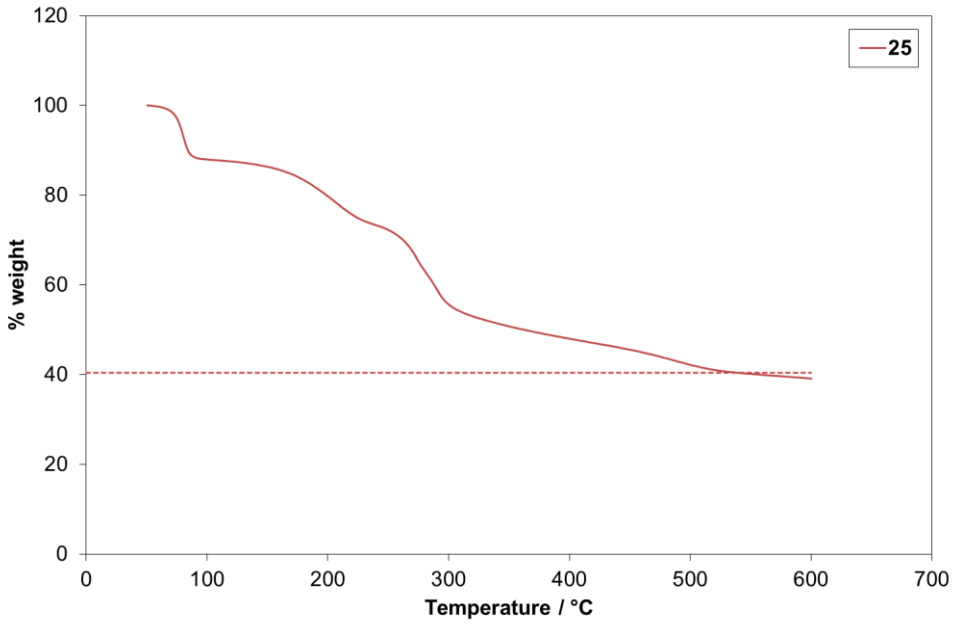

Figure 3.13 TGA trace for **25** in an open pan. The dashed line represents the expected % weight for TaS_2.

While complex **25** provided a final percentage weight close to the value expected for TaS_2, the end point temperature of 530 °C is considerably higher than the values recorded for the dithiocarbamate complexes **23** (325 °C) and **24** (365 °C). The lower end point temperatures of the dithiocarbamate complexes are more favourable for deposition studies as the experiments will require less energy, this is especially important for larger scale studies. Therefore, deposition experiments will focus on the dithiocarbamate complexes and more specifically the ethyl derivative, **24**, as it is considerably more soluble in toluene.

Table 3.9 Summary of TGA data for **25**.

Compound	Onset / °C	End point / °C	% weight expected for TaS_2	End point % weight
25	70	530	40.4	40.7

3.3.3 AACVD of [(^{t}BuN)Ta(S_2CNEt_2)$_3$] (24)

AACVD experiments were carried out using a 0.05 M solution of complex **24** in toluene. The glass and silicon substrates were cleaned using IPA and O_2 plasma (20 mins) before being placed in the quartz reactor tube. Depositions were run for 60 minutes at temperatures of 350, 375 and 400 °C. Images of the films produced are displayed in Figure 3.14 and show the films on glass were transparent while the films on Si were purple to yellow in colour, all films showed refringence patterns.

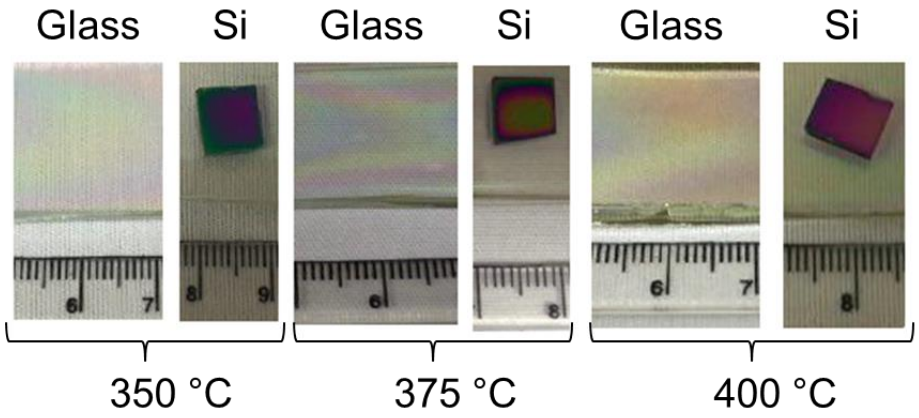

Figure 3.14 Images of films produced from the AACVD of **24** on glass and Si substrates at 350, 375 and 400 °C.

Analysis of the films using PXRD showed the films to be amorphous while no active modes were detected using Raman spectroscopy. EDX analysis of the films showed the presence of tantalum but not sulfur. Large amounts of oxygen were present suggesting tantalum oxide was formed rather than TaS_2, however Ta:O ratios could not be determined due to the overlap of the tantalum M and silicon K lines. Smaller quantities of carbon were also present within the films. Oxygen or moisture from the air is the most likely source of the oxygen in the films. To reduce the exposure of the complex **24** to atmospheric oxygen and water, further CVD experiments were carried out under low pressure conditions.

3.3.4 LPCVD of [(^{t}BuN)Ta(S_2CNEt_2)$_3$] (24)

LPCVD experiments were performed with 0.5 g of complex **24** contained within a quartz boat. The glass and Si substrates were first rinsed with IPA then O_2 plasma cleaned for 20 minutes. Depositions were performed for 60 minutes at temperatures of 350, 375 and 400 °C under a pressure of 1 mbar; images of the films produced are displayed in Figure 3.15. Films were opaque and black in colour with considerable deposition observed at 375 °C. The films deposited on Si were more uniform than those on glass. The appearance of the films did alter over time when stored in air suggesting a degree of oxidation was occurring.

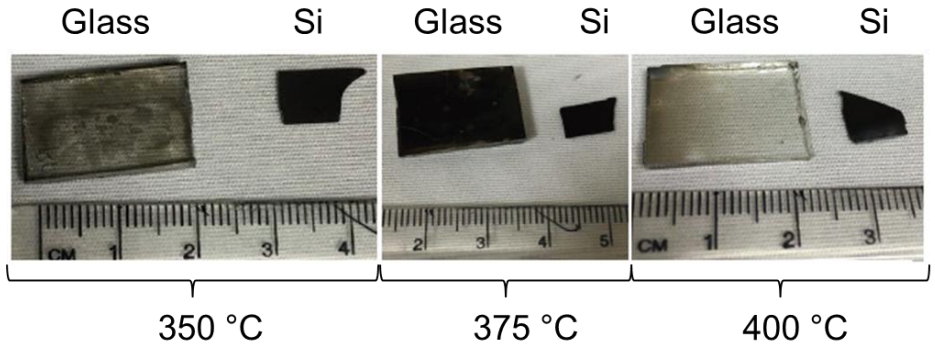

Figure 3.15 Images of films produced from the LPCVD of **24** on glass and Si substrates at 350, 375 and 400 °C.

The majority of the films were shown to be amorphous using PXRD, however the film on glass at 375 °C and on Si at 400 °C did display crystalline reflections (Figure 3.16). Both films exhibited broad reflections at ~15° and ~30.5° which indicated either 2H- (JCPDS card #88-1008)[26] or 3R-TaS_2 (JCPDS card #89-2756)[4] had been

formed. The peaks at ~15° likely corresponded to the (001) reflection in 2H-TaS_2 (15.011°) or the (003) reflection in 3R-TaS_2 (14.835°), while the peaks at ~30.5° were indicative of the (002)/(100) reflections in 2H-TaS_2 (30.287/30.654°) or the (006) reflection in 3R-TaS_2 (29.926°). As only a couple of peaks were observed it was not possible to distinguish between the two TaS_2 phases. The film on Si also presented a number of low intensity sharp peaks at 17.0, 28.8, 32.4, 38.8, 42.6 and 46.9° indicative of the (140), (200), (270), (0140), (0180) and (002) reflections in *L*-Ta_2O_5.[27] This suggested some oxidation of the film had occurred even though the films were analysed only four days after deposition. The broad peak at ~24° on the glass pattern and the sharp peak at 33° on the Si pattern correspond to the underlying substrates.

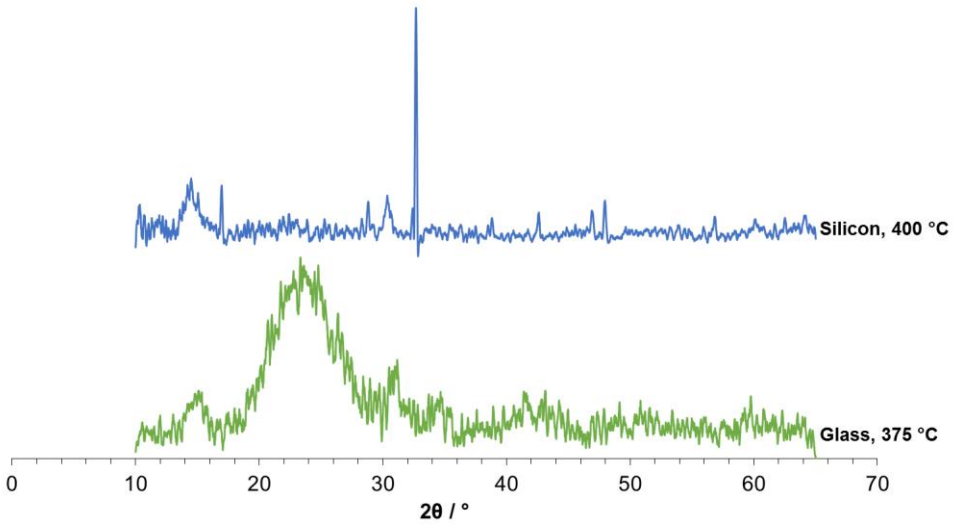

Figure 3.16 PXRD patterns for the films produced from the LPCVD of **24**.

Raman spectra of all the films (Figure 3.17) displayed very low intensity peaks similar to those observed for TaS_2 by Hirata *et al*. at 100, 243, 306 and 381 cm^{-1} at 297 K.[28] The spectra of the films on both glass and Si at 375 and 400 °C all displayed the modes reported for TaS_2. For the films at 350 °C, the film on glass only displayed the peak at ~100 cm^{-1} while the film on Si exhibited the modes at ~100 cm^{-1} and ~306 cm^{-1}. There was no evidence of any oxide within the spectra.

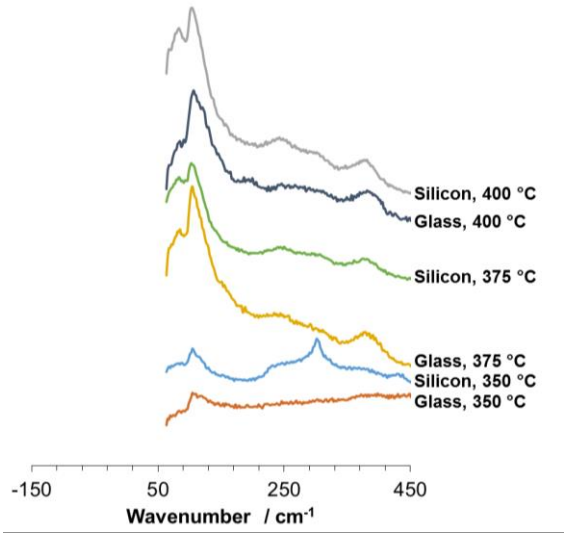

Figure 3.17 Raman spectra of the films produced from the LPCVD of **24**.

SEM images of the films deposited at 375 and 400 °C are displayed in Figure 3.18. The films deposited at 375 °C were composed of a patchwork of randomly orientated small needles. The film on glass had an increasingly uniform appearance while the film on Si was patchier with slightly longer needles. The needle-like appearance of these films is similar to the morphology of some other TMD based films such as MoS_2.[29] In contrast, the films deposited at 400 °C were composed of small, distinct particles. The particles in both films were similar in size, although for the film on Si, the particles were packed closer together. The particulate nature of the films at 400 °C resembles the TaS_2 films deposited by Peters *et al*. and suggests an island growth mechanism (Volmer-Weber).[8]

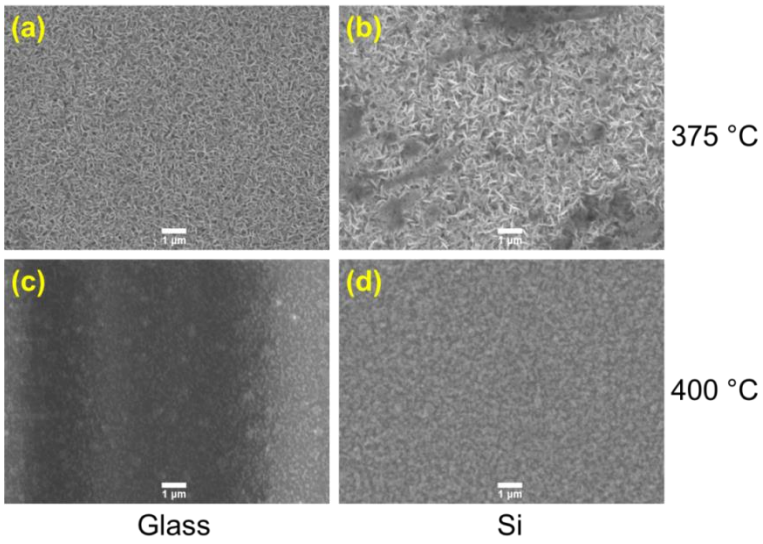

Figure 3.18 SEM images (x10k magnification) of the films produced from the LPCVD of **24**.

SEM imaging was not performed on the films deposited at 350 °C; however AFM surface plots were recorded and are displayed in Figure 3.19. Both plots showed a similar morphology to the films deposited at 400 °C with the films composed of individual particles. The film on Si was composed of much larger particles than those observed for the film on glass. The differences in particle size lead the film on Si to be much rougher with an RMS value of 39.5 nm while the film on glass had a value of 9.22 nm. It is interesting to note that the films deposited at 375 °C have a drastically different morphology to those deposited at 350 and 400 °C.

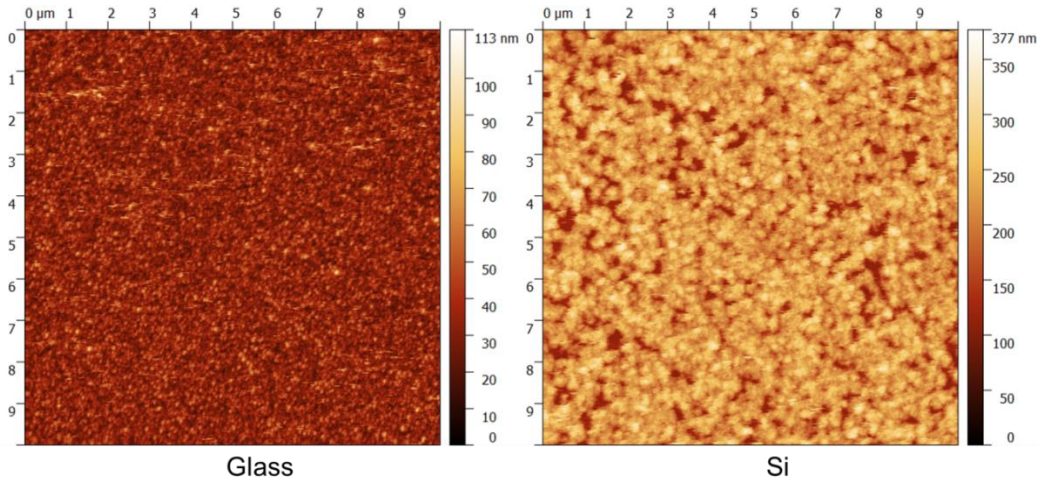

Figure 3.19 AFM surface plots of the films produced from **24** at 350 °C.

EDX analysis was only performed on the samples deposited at 375 and 400 °C. All samples showed the presence of tantalum and sulfur within the spectra, although Ta:S ratios could not be determined due to the overlap of the tantalum M and silicon K lines. The samples deposited at 375 °C showed higher levels of sulfur while those deposited at 400 °C showed higher levels of oxygen. All samples showed the peaks corresponding to the underlying substrates which meant the level of oxidation could not be determined. Small amounts of carbon contamination were also detected. These results suggest that 375 °C was the optimum deposition temperature for TaS_2.

3.4 Conclusion

A range of tantalum thioureide complexes have been synthesised by the insertion of isothiocyanates into PDMAT or [(^{t}BuN)Ta(NMe_2)$_3$] (**20**). Reactions with PDMAT and the iso-propyl or *tert*-butyl isothiocyanates formed the mono-insertion products, **18** and **19** respectively. In solution, both these complexes exhibited two structural

isomers while in the solid state the thioureide ligand in complex **19** bound to the metal centre via the κ^2-*N,N'* mode. For the reactions with [(^{t}BuN)Ta(NMe$_2$)$_3$] (**20**) and the iso-propyl or phenyl isothiocyanates the bis- (**22**) and tris-insertion (**23**) products were respectively formed. The thioureide binding mode exclusively adopted in these complexes was the κ^2-*S,N* mode. Thermogravimetric analysis of these complexes showed all to provide final percentage weights close to the expected values for TaS_2 except for the phenyl complex, **23**. The *tert*-butylimide based iso-propyl complex, **22**, was determined to be a more promising precursor than the mono-insertion products as it had an appropriate Ta:S ratio of 1:2.

The tantalum dithiocarbamate complexes, [(^{t}BuN)Ta(S$_2$CNMe$_2$)$_3$] (**23**) and [(^{t}BuN)Ta(S$_2$CNEt$_2$)$_3$] (**24**), were synthesised by the insertion of CS_2 into the metal amide bonds of, [(^{t}BuN)Ta(NR$_2$)$_3$], where R is Me or Et. Thermogravimetric analysis showed both complexes to provide final percentage weights slightly lower than the expected values for TaS_2. AACVD experiments with the ethyl complex, **24**, produced tantalum oxide with no evidence of TaS_2. In contrast, LPCVD experiments provided films containing TaS_2 at 375 and 400 °C as determined by Raman spectroscopy. Films deposited on glass at 375 °C and on Si at 400 °C contained some crystalline TaS_2 while the film on Si also showed the presence of crystalline Ta_2O_5. EDX analysis showed all of the films deposited at 375 and 400 °C contained tantalum and sulfur, although relatively high levels of oxygen were also observed for the films deposited at 400 °C. From these results it was determined that 375 °C was the optimum deposition temperature for TaS_2.

The 2-thiazoline-2-thiol based complex, **25**, containing the dithiocarbamate moiety {S$_2$CN}, was synthesised by reacting complex **20** and three equivalents of 2-thiazoline-2-thiol. The complex adopted a 7-coordinate distorted pentagonal bipyramidal geometry with the 2-thiazoline-2-thiol ligands binding via the κ^2-*S,N* mode. Thermogravimetric analysis of the complex provided a final percentage weight close to the value expected for TaS_2 although the decomposition end point temperature was considerably higher than the dithiocarbamate complexes.

The reactions and complexes presented in Chapter 3 are summarised below in Figure 3.20.

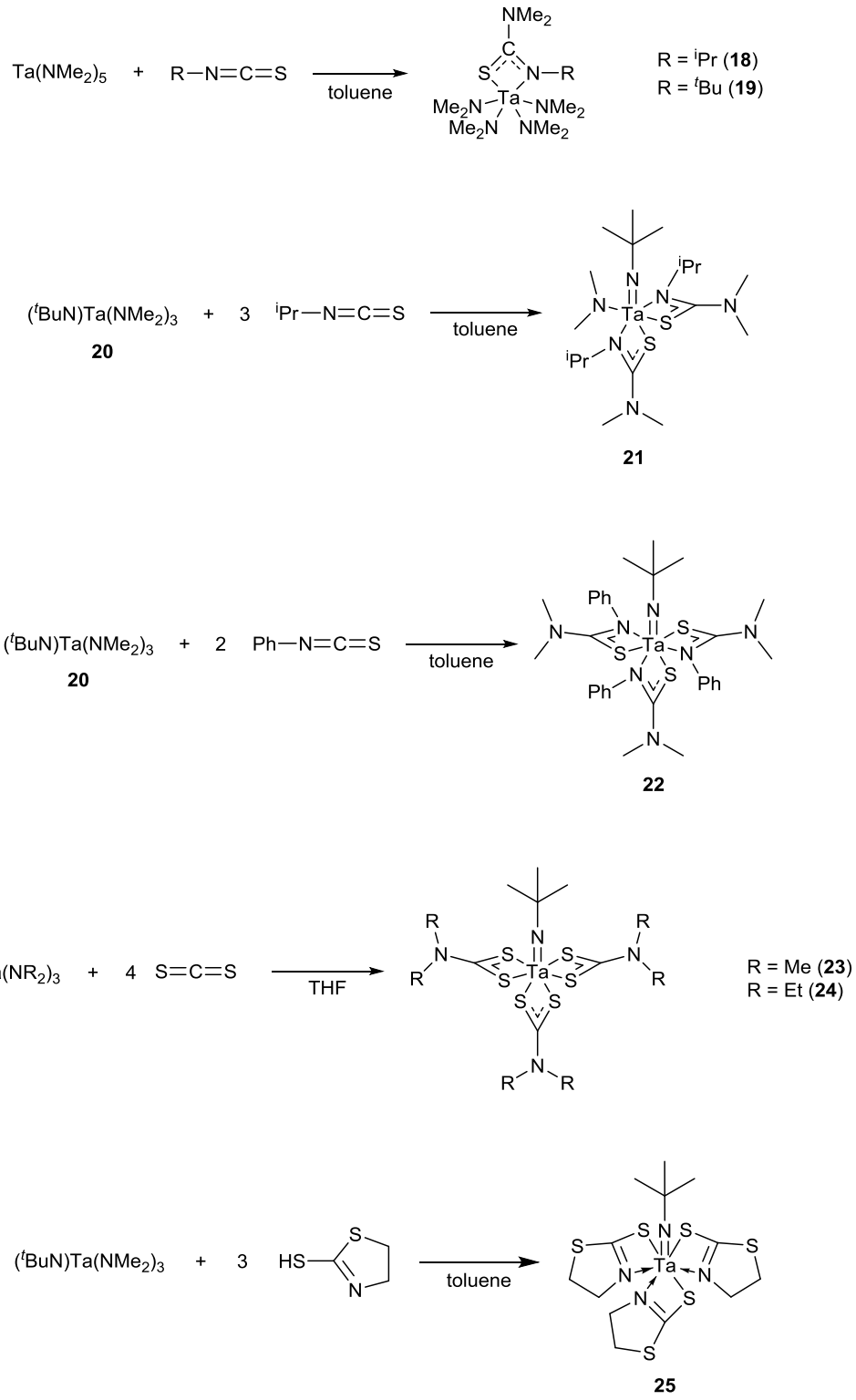

Figure 3.20 Summary of reactions and complexes presented within Chapter 3.

3.5 References

1. M. S. Whittingham, *Chem. Rev.*, 2004, **104**, 4271-4302.
2. F. R. Gamble, J. H. Osiecki, M. Cais, R. Pisharody, F. J. DiSalvo and T. H. Geballe, *Science*, 1971, **174**, 493-497.

3. M. Chhowalla, H. S. Shin, G. Eda, L. J. Li, K. P. Loh and H. Zhang, *Nat. Chem.*, 2013, **5**, 263-275.
4. F. Jellinek, *J. Less-Common Met.*, 1962, **4**, 9-15.
5. J. A. Wilson, F. J. Di Salvo and S. Mahajan, *Adv. Phys.*, 2001, **50**, 1171-1248.
6. S. F. Meyer, R. E. Howard, G. R. Stewart, J. V. Acrivos and T. H. Geballe, *J. Chem. Phys.*, 1975, **62**, 4411-4419.
7. J. A. Wilson and A. D. Yoffe, *Adv. Phys.*, 1969, **18**, 193-335.
8. E. S. Peters, C. J. Carmalt, I. P. Parkin and D. A. Tocher, *Eur. J. Inorg. Chem.*, 2005, **2005**, 4179-4185.
9. S. L. Benjamin, Y.-P. Chang, C. Gurnani, A. L. Hector, M. Huggon, W. Levason and G. Reid, *Dalton Trans.*, 2014, **43**, 16640-16648.
10. T. Shimada, F. S. Ohuchi and A. Koma, *Surf. Sci.*, 1993, **291**, 57-66.
11. E. Hiroyuki, K. Takanori, K. Masayuki, T. Yoshiki and S. Kazuko, *Jpn. J. Appl. Phys.*, 2004, **43**, L123.
12. J. E. Dutrizac, *J. Less-Common Met.*, 1982, **85**, 55-69.
13. A. O. Baghlaf, K. Behzadi and A. Thompson, *J. Less-Common Met.*, 1978, **61**, 31-37.
14. W. A. Nugent, *Inorg. Chem.*, 1983, **22**, 965-969.
15. W. A. Nugent and R. L. Harlow, *J. Chem. Soc., Chem. Commun.*, 1978, 579-580.
16. D. C. Bradley and M. H. Gitlitz, *J. Chem. Soc. A*, 1969, 1152-1156.
17. J. N. Smith and T. M. Brown, *Inorg. Nucl. Chem. Lett.*, 1970, **6**, 441-443.
18. P. R. Heckley and D. G. Holah, *Inorg. Nucl. Chem. Lett.*, 1970, **6**, 865-869.
19. E. J. Peterson, R. B. Von Dreele and T. M. Brown, *Inorg. Chem.*, 1978, **17**, 1410-1415.
20. M. G. B. Drew, D. A. Rice and D. M. Williams, *J. Chem. Soc., Dalton Trans.*, 1985, 1821-1828.
21. M. G. B. Drew, D. M. Williams and D. A. Rice, *Inorg. Chim. Acta*, 1984, **89**, L19-L20.
22. J. R. Dilworth, R. A. Henderson, A. Hills, D. L. Hughes, C. Macdonald, A. N. Stephens and D. R. M. Walton, *J. Chem. Soc., Dalton Trans.*, 1990, 1077-1085.
23. L. S. Tan, G. V. Goeden and B. L. Haymore, *Inorg. Chem.*, 1983, **22**, 1744-1750.
24. H. Brunner, M. M. Kubicki, J.-C. Leblanc, C. Moise, F. Volpato and J. Wachter, *J. Chem. Soc., Chem. Commun.*, 1993, 851-852.
25. F. H. Allen, O. Kennard, D. G. Watson, L. Brammer, A. G. Orpen and R. Taylor, *J. Chem. Soc., Perkin Trans. 2*, 1987, S1-S19.
26. A. Spijkerman, J. L. de Boer, A. Meetsma, G. A. Wiegers and S. van Smaalen, *Phys. Rev. B*, 1997, **56**, 13757-13767.
27. N. C. Stephenson and R. S. Roth, *Acta Crystallogr., Sect. B*, 1971, **27**, 1037-1044.
28. T. Hirata and F. S. Ohuchi, *Solid State Commun.*, 2001, **117**, 361-364.
29. A. Adeogun, M. Afzaal and P. O'Brien, *Chem. Vap. Deposition*, 2006, **12**, 597-599.

Chapter 4

Mo and W sulfide precursors

4.1 Introduction

The focus of this chapter is the development of single-source precursors for the deposition of molybdenum and tungsten disulfides. The precursors being investigated will be based on group VI metal thioureide, dithiocarbamate and xanthate complexes.

4.1.1 Group VI disulfides

Interest in group VI disulfides is mainly focussed on their use in either FETs or as hydrogen evolution catalysts.[1-5] The band gaps of monolayer MoS_2 and WS_2 are ideally placed for incorporation into FETs with devices exhibiting impressive ON/OFF current ratios. The flexibility of monolayers and the low power requirements of group VI disulfide devices make these materials ideally suited for use in portable, flexible and transparent displays.[6]

Monolayers of both MoS_2 and WS_2 show promising results as hydrogen evolution catalysts.[2, 3] Reports indicate that the monolayer edges are the active site which suggests why the bulk material performs poorly. Synthesis of the metallic 1T phase enhances the catalytic properties as electron transfer from the electrode to the active sites is improved. Both MoS_2 and WS_2 are also considerably cheaper than the standard hydrogen evolution catalyst, platinum.[6, 7]

Bulk MoS_2 and WS_2 naturally exhibit the 2H polymorph with synthetic routes also providing the 3R (from CVD) or 1T (from lithium intercalation) phases. The 2H polymorphs possess the $P6_3/mmc$ space group with cell parameters of a = 3.16 Å, c = 12.29 Å and a = 3.153 Å and c = 12.323 Å for MoS_2 and WS_2 respectively. In contrast, the 3R polymorphs adopt the $R3m$ space group with cell parameters of a = 3.17 Å, c = 18.38 Å and a = 3.162 Å, c = 18.50 Å for MoS_2 and WS_2 respectively.[8-10] Monolayers (~0.7 nm thick) exhibit both the 1T and 1H polymorphs although the 1H is most commonly found.[11]

MoS_2 and WS_2 are both diamagnetic indirect semiconductors in the bulk with band gaps of 1.2 eV and 1.4 eV respectively.[12, 13] Due to quantum confinement effects, monolayer MoS_2 and WS_2 are direct semiconductors with band gaps of 1.8 eV and 1.9 eV respectively.[13] MoS_2 monolayers exhibit high strengths with in plane stiffnesses of 180 ± 60 Nm^{-1} and a Young's modulus of 270 ± 100 GPa.[14]

4.1.2 MoS_2 precursors

The deposition of MoS_2 has mainly focussed on the use of multi-source precursors with only a handful of single-source precursors reported. Multi-source precursors used to deposit MoS_2 include: MoO_3 and S,[15-25] Mo and S,[26] $Mo(CO)_6$ and H_2S/S,[27] and $MoCl_5$ and H_2S/S.[28-30] To date only multi-source precursors have been reported to deposit monolayer MoS_2, with most literature sources using MoO_3 and S.[6]

The first MoS_2 single-source precursor was the molybdenum thiolate compound, $[Mo(S^tBu)_4]$, reported by Cheon *et al.*[31] LPCVD (10^{-4} Torr) experiments deposit MoS_2 on quartz, silicon and stainless steel substrates at temperatures of 110 to 350 °C. The MoS_2 films were polycrystalline and composed of closely packed granules 30 to 90 nm in size (Figure 4.1). Film thicknesses of ~1 μm were attained at 200 °C after several hours of deposition using 0.3 g of precursor. Films had significant quantities of carbon and oxygen on the surface of the films with a reduced amount found further into the films, the carbon content was determined to be graphitic in nature.[31, 32]

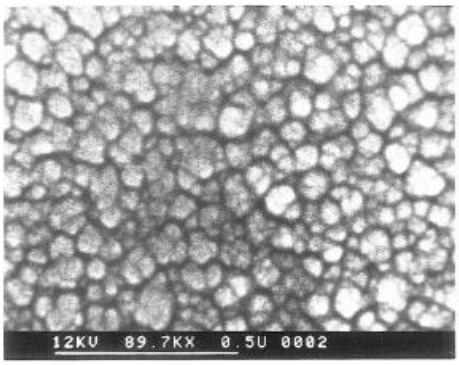

Figure 4.1 SEM image of a MoS_2 film grown from $[Mo(S^tBu)_4]$ at 200 °C on a quartz substrate.[31]

The majority of MoS_2 single-source precursors reported are based on the molybdenum (IV) dithiocarbamates, $[Mo(S_2CNEt_2)_4]$,[33-40] and $[Mo(S_2CN^nBu_2)_4]$.[37] Loh *et al.* first reported the deposition of MoS_2 on nickel, mica, silicon, germanium, gold, gold coated silicon and gold coated germanium substrates using $[Mo(S_2CNEt_2)_4]$. The depositions were performed using a Knudsen cell for the evaporation of $[Mo(S_2CNEt_2)_4]$ at 300 °C under pressures of 1×10^{-5} Torr. Crystalline MoS_2 was deposited on all substrates at temperatures above 400 °C with low carbon contamination levels, $MoSi_2$ and $MoGe_2$ were also deposited on the gold

coated silicon and germanium films respectively due to gold favouring the formation of eutectic alloys.[33] Loh *et al.* then demonstrated that varying the deposition temperature alters the morphology of the MoS_2 on a nickel substrate. When increasing the deposition temperature from room temperature to 600 °C, the nanosheets within the film curl up to form inverted nanocones as shown in Figure 4.2.[34, 35]

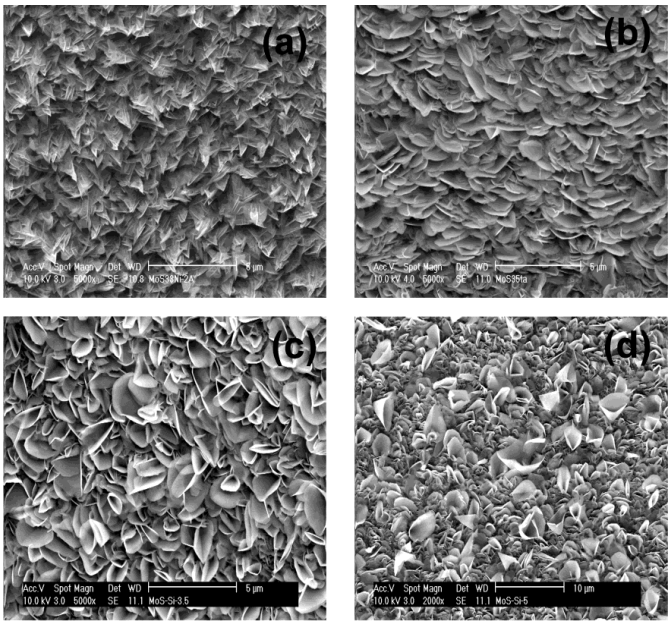

Figure 4.2 SEM images of MoS_2 films deposited with $[Mo(S_2CNEt_2)_4]$ on nickel at (a) room temperature, (b) 400 °C, (c) 500 °C and (d) 600 °C.[35]

Loh *et al.* also deposited MoS_2 nanotubes (Figure 4.3) utilising the previously mentioned method although an alumina membrane was used as a template instead of a substrate. The MoS_2 nanotubes formed in the template with lower temperatures providing porous nanotubes and higher temperatures resulting in solid nanotubes.[36]

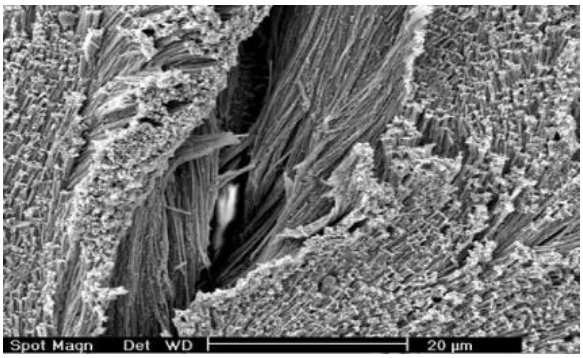

Figure 4.3 SEM image of MoS_2 nanotubes grown from $[Mo(S_2CNEt_2)_4]$ with an alumina membrane template.[36]

O'Brien and co-workers reported the first use of both $[Mo(S_2CNEt_2)_4]$ and $[Mo(S_2CN^nBu_2)_4]$ in AACVD to deposit MoS_2 at temperatures of 400 – 475 °C on glass. The precursors (200 mg) were dissolved in THF (30 ml) and these precursor solutions were run for 90 minutes to provide film thicknesses of *ca.* 400 – 500 nm. Figure 4.4 shows how morphology changes with precursor and temperature. $[Mo(S_2CNEt_2)_4]$ provides films with layers lying parallel to the substrate surface with nanotubes at 400 – 425 °C and platelets at 450 – 475 °C, while $[Mo(S_2CN^nBu_2)_4]$ provides films with a variety of layer orientations with lamellar plate-like structures at 425 – 450 °C and randomly orientated grains at 475 °C.[32, 36] More recently, MoS_2 films doped with both chromium and rhenium have been produced by the combined AACVD of $[Mo(S_2CNEt_2)_4]$ with $[Cr(S_2CNEt_2)_3]$ and $[Re(\mu\text{-}S^iPr)_3(S^iPr)_6]$ respectively.[39, 40]

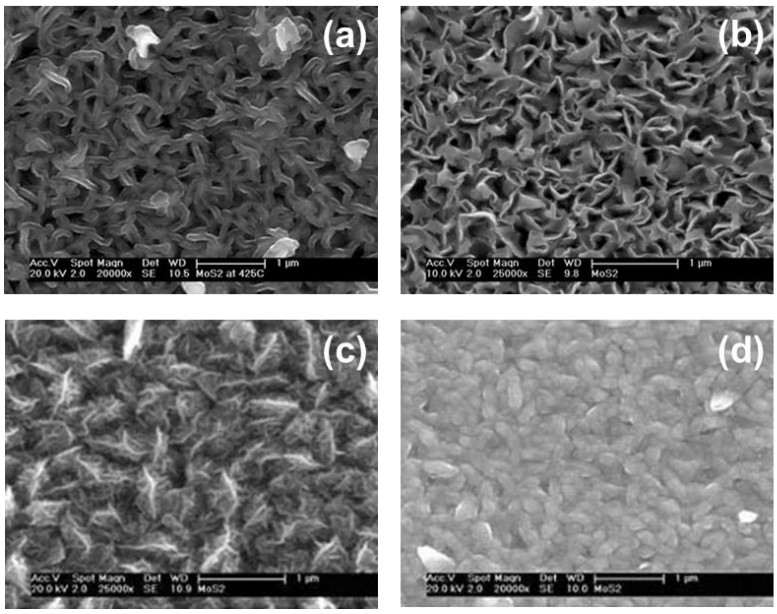

Figure 4.4 SEM images of MoS_2 films deposited from $[Mo(S_2CNEt_2)_4]$ at (a) 425 °C, (b) 475 °C and from $[Mo(S_2CN^nBu_2)_4]$ at (c) 425 °C, (d) 475 °C.[37]

McCain *et al.* have also utilised the AACVD of $[Mo(S_2CNEt_2)_4]$ to deposit 1.5 – 1.8 μm thick films of weakly crystalline MoS_2 on both glass and steel substrates at 400 °C. Film deposition on steel occurs via the initial formation of a crystalline FeS layer then the deposition of MoS_2. Film morphology is dependent on the substrate with MoS_2 films on steel composed of platelets perpendicular to the surface.[38]

The Mo(V) single-source precursors, $[Mo_2O_3(S_2CNEt_2)_4]$ and $[Mo_2O_3(S_2COEt)_4]$, have also been investigated by O'Brien and co-workers. AACVD onto glass using

the dithiocarbamate precursor exclusively produces MoS_2 at 425 to 475 °C, while the xanthate precursor produces a mixture of MoO_3, MoO_2 and MoS_2 at 300 to 450 °C. The production of MoO_3 and MoO_2 was attributed to the formation of O_2 gas which subsequently poisoned the reaction.[41]

Olofinjana *et al.* have used the bis(*S*,*S*-morpholinodithioato)molybdenum precursor to deposit MoS_2 on glass at 420 °C.[42] The Mo(0) thioureide precursors, $[Mo(CO)_5(SC\{NMe_2\}_2)]$ and $[Mo(CO)_4(SC\{NMe_2\}_2)_2]$, synthesised by Shupp *et al.*, decompose to form amorphous MoS_2 at 300 °C under an argon atmosphere, no deposition studies have been performed with this precursor.[43]

4.1.3 WS_2 precursors

To the best of our knowledge there is only one example of WS_2 being deposited by a single-source precursor in the literature. The thesis of Pearce reports the deposition of crystalline WS_2 by the complex, $[W(S_2CNEt_2)_4]$, using AACVD in the temperature range 425 to 475 °C on SiO_2 and Cu substrates.[44] Analysis of the films by PXRD shows both the 2H- and 3R-WS_2 phases are present within the films as well as contamination from tungsten oxide. No elemental analysis was carried out to determine the stoichiometry of the films. Guo *et al.* have also reported that the thermal decomposition of $[W(S_2CNEt_2)_4]$ forms WS_2 flakes at 320, 400, 600 and 800 °C although no CVD was performed.[45]

Table 4.1 W and S precursor combinations.[25, 27, 29, 30, 46-49]

W precursor	**S precursor**
WO_3	S
W	S
$W(CO)_6$	H_2S, S, $HS(CH_2)_2SH$, $HSC(CH_3)_3$
WCl_6	H_2S, S, $HS(CH_2)_2SH$, $HSC(CH_3)_3$
$WOCl_4$	$HS(CH_2)_2SH$, $HSC(CH_3)_3$

The only other complexes reported that could act as single-source precursors are the W(0) thiourea precursors, $[W(CO)_5(SC\{NMe_2\}_2)]$ and $[W(CO)_4(SC\{NMe_2\}_2)_2]$, synthesised by Shupp *et al*. These complexes decompose to form amorphous WS_2 at 300 °C under an argon atmosphere, no deposition studies were carried out.[43] Table

4.1 shows the multi-source precursor combinations used for the deposition of WS_2. Much like molybdenum, monolayer deposition of WS_2 is typically accomplished using WO_3 and S.[25]

4.2 Group VI thioureides

While the group IV and V thioureide precursors described in Chapters 2 and 3, respectively, have shown varying degrees of success, the group VI thioureides have also been investigated as potential CVD precursors. Two synthetic routes were chosen for the synthesis of these complexes. The first, described in section 4.2.2, involves the substitution reaction between a bis(*tert*-butylimido)-bis(amido) group VI metal complex and two equivalents of a *N,N'*-disubstituted thiourea. The second route, described in section 4.2.3, involves the insertion reaction between isothiocyanates and the bis(*tert*-butylimido)-bis(dimethylamido) group VI metal complexes. Rather than the homoleptic metal amide species as starting materials the bis(imido)-bis(amido) group VI metal complexes were used due to their greater stability.

4.2.1 Existing group VI thioureide systems

Only a handful of group VI thioureide systems have previously been reported. The most simple systems are synthesised by the thermal or photochemical reactions between group VI metal hexacarbonyls and substituted thioureas to form the adducts, $[M(CO)_{6-n}(SC\{NR^1R^2\}_2)_n]$.[50] Shupp *et al.* have shown that the complexes, *cis*-$[M(CO)_5(SC\{NMe_2\}_2)]$ and *cis*-$[M(CO)_4(SC\{NMe_2\}_2)_2]$ (Figure 4.5) (where M = Mo and W), decompose to form the corresponding metal disulfides at 300 °C.[43]

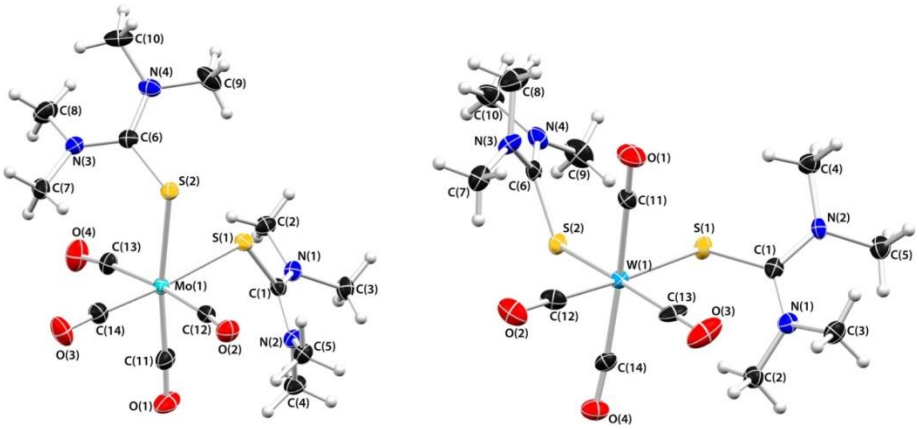

Figure 4.5 Molecular structures of *cis*-$[Mo(CO)_4(SC\{NMe_2\}_2)_2]$ and *cis*-$[W(CO)_4(SC\{NMe_2\}_2)_2]$.[43]

Group VI thioureides have also been synthesised by the insertion of phenyl isothiocyanate into the metal imide bond in the compound, $[Mo(NAr)_2(O^tBu)_2]$ (where Ar = 2,6-$^i Pr_2C_6H_3$), to form the molybdenum thioureide complex, $[Mo(NAr)\{NPhC(S)NAr\}(O^tBu)_2]$ (Figure 4.6a). Within the resulting complex, the thioureide ligand binds to the metal centre via the κ^2-*N,N'* mode rather than the expected κ^2-*S,N* mode.[51] While there are no examples of isothiocyanate insertions into group VI metal amide bonds, there are examples of isocyanates performing this reaction to form the ureate ligand. Lam *et al.* reported that the addition of *tert*-butyl isocyanate to $[(^tBuN)_2W(NH^tBu)_2]$ forms the complex $[(^tBuN)_2W(OC(NH^tBu)N^tBu)_2]$ where the ureate ligand binds via the κ^2-*O,N* mode.[52] This suggests similar reactions with isothiocyanates could be possible.

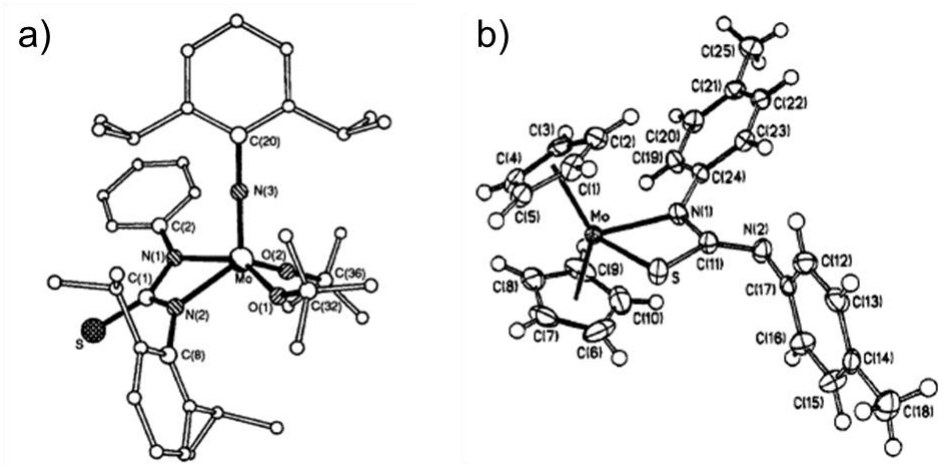

Figure 4.6 Molecular structures of: a) $[Mo(NAr)\{NPhC(S)NAr\}(O^tBu)_2]$[51] and b) $[Cp_2Mo(SC(N\text{-}tolyl)N\text{-}toly)]$.[53]

Addition of di-*p*-tolylcarbodiimide and PMe_3 to $[Cp_2MoS_2]$ has also been reported to form molybdenum thioureide complexes with the formation of $[Cp_2Mo(SC(N\text{-}tolyl)N\text{-}tolyl)]$ (Figure 4.6b). Within the complex, the thioureide ligand binds via the κ^2-*S,N* mode with the non-metal centre bound nitrogen atom binding to the central carbon atom by a C=N double bond.[53]

4.2.2 Synthesis and characterisation of substitution reaction products

For the thiourea substitution reactions different bis(*tert*-butylimido)-bis(amido) group VI metal complexes were used as starting materials for the molybdenum and tungsten-based reactions. For the molybdenum-based reactions the complex $[(^tBuN)_2Mo(NMe_2)_2]$ (**26**) was used, while for the tungsten reactions the complex

[(^{t}BuN)$_2$W(NH^{t}Bu)$_2$] (**27**) was used. The use of different starting materials was due to the lower cost and simpler synthesis of the tungsten complex **27** compared to the tungsten analogue of **26**.

The synthesis of the molybdenum complex, **26**, involved a three step reaction displayed in Scheme 4.1 to provide the final product. In the first step, dme solutions of trimethylsilyl chloride, *tert*-butylamine and trimethylamine were added to a stirred suspension of sodium molybdate in dme and heated at 70 °C for 12 hours.[54] The resulting orange solid of [(^{t}BuN)$_2$MoCl$_2$(dme)] (**26a**) was then reacted with excess pyridine to form the pyridine adduct, [(^{t}BuN)$_2$MoCl$_2$py$_2$] (**26b**), the subsequent reaction with two equivalents of lithium dimethylamide formed complex **26** which was purified by distillation at 80 °C (1x10^{-1} mbar).[55]

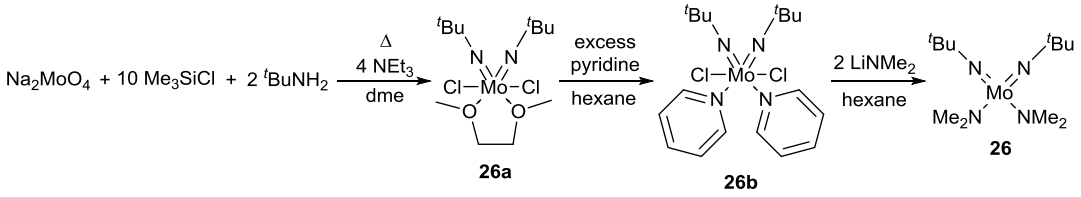

Scheme 4.1 Synthesis of [(^{t}BuN)$_2$Mo(NMe$_2$)$_2$] (**26**).

The synthesis of the tungsten complex, **27**, (Scheme 4.2) involved the facile reaction of WCl_6 and ten equivalents of *tert*-butylamine in hexane. After stirring for 72 hours, the brown mixture was filtered to provide a brown liquor, solvent removal *in vacuo* provided the light brown solid of **27**.[56]

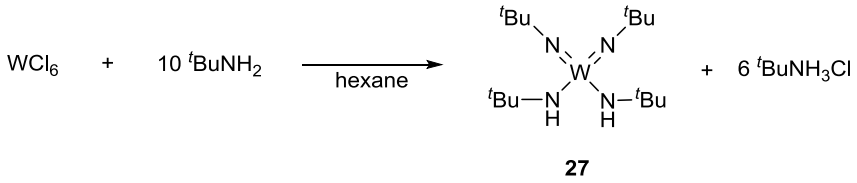

Scheme 4.2 Synthesis of [(^{t}BuN)$_2$W(NH^{t}Bu)$_2$] (**27**).

The bis(*tert*-butylimido)-bis(amido) group VI metal complexes (**26** and **27**) were then reacted with two equivalents of *N*,*N'*-dimethyl, *N*,*N'*-diethyl or *N*,*N'*-dibutyl thioureas in hexane to provide the group VI metal thioureides (Scheme 4.3). Reaction mixtures were stirred overnight forming yellow/orange precipitates or solutions. Products could be crystallised and isolated from the reaction mixture at

reduced temperatures or by recrystallisation from toluene solution. All reactions were performed under inert conditions using Schlenk line techniques.

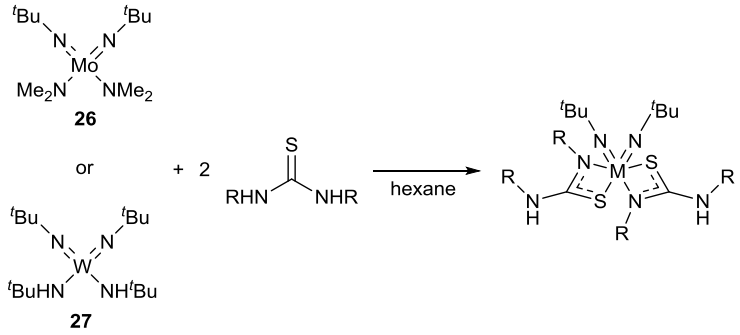

M	R	Complex
Mo	Me	**28**
Mo	Et	**29**
Mo	^{n}Bu	**30**
W	Me	**31**
W	Et	**32**
W	^{n}Bu	**33**

Scheme 4.3 General reaction scheme for the substitution reaction between **26**/**27** and two equivalents of *N*,*N'*-disubstituted thioureas.

Analysis of the products from the reactions with the molybdenum complex **26** and the *N*,*N'*-dimethyl, *N*,*N'*-diethyl and *N*,*N'*-dibutyl thioureas using ^{1}H and ^{13}C{^{1}H} NMR spectroscopy, showed the loss of both NMe_2 groups and the presence of the appropriate R group. Further analysis of the ^{1}H NMR spectra showed single *tert*-butyl proton resonances in the range 1.52 – 1.60 ppm indicating both *tert*-butyl imido groups are equivalent. Single NH proton resonances equivalent to two protons suggest a single κ^2-*S*,*N* thioureide binding mode is present, interestingly the peak shifts downfield from 3.97 ppm (**28**) to 4.49 ppm (**30**) with increasing chain length.

The R group resonances showed two different environments within each complex again supporting the presence of a single κ^2-*S*,*N* thioureide binding mode however, these resonances were present as either broad singlets or multiplets suggesting a degree of fluxionality. Elevated temperatures (349 K) were required to record the spectra for the ethyl (**29**) and *n*-butyl (**30**) complexes due to the fluxional nature of the thioureide ligands.

The ^{13}C{^{1}H} NMR spectra exhibited the resonances expected for the R group carbon atoms although the resonances for the {$C(CH_3)_3$} and {SCN_2} carbon atoms were not observed even in long NMR experiments. These resonances are typically of low intensity and can be difficult to observe in fluxional environments.[57] The NMR spectra and elemental analysis data suggested the substitution reactions had been successful and the molybdenum thioureide complexes **28**, **29** and **30** had been formed.

^{1}H and ^{13}C{^{1}H} NMR spectra of the products from the analogous reactions with the tungsten complex **27** showed a more complicated picture. The ^{1}H NMR spectra of all three reaction products presented resonances for both the *tert*-butyl imido group and the expected R group in the appropriate ratio for the products **31**, **32** and **33** (Scheme 4.3), however the spectra observed differ to those recorded for the equivalent molybdenum complexes. For the ethyl (**32**) and *n*-butyl (**33**) complexes, two NH proton resonances were observed (each equal to one proton) at 6.12/6.36 and 6.11/6.31 ppm respectively indicating two environments were present within the molecules. The methyl complex (**31**) on the other hand, only exhibited a single NH peak at 6.32 ppm with an integral of one which suggested either the second expected NH resonance was not present or it was of too low an intensity/too broad to observe.

For the *tert*-butyl proton resonances, both the methyl (**31**) and ethyl (**32**) complexes displayed a single resonance (integral equal to two *tert*-butyl groups) at 1.32 and 1.31 ppm respectively while the *n*-butyl complex, **33**, displayed two peaks at 1.30 and 1.32 ppm (integral equal to one *tert*-butyl group each) indicating there were two different environments present in the latter complex. For all three tungsten complexes single environments were observed for each R group, however these signals were broad and typically exhibited as multiplets indicating the ligands were fluxional and the environments were averaging out on the NMR timescale.

The ^{13}C{^{1}H} NMR spectra of the methyl complex, **31**, only exhibited R group carbon resonances regardless of the length of the NMR experiment. Both the ethyl (**32**) and *n*-butyl (**33**) complexes displayed two {S*C*N$_2$} resonances at 162.0/171.3 and 171.9/182.8 ppm respectively, indicating two thioureide ligand environments were present. Both complexes also presented two separate {*C*(CH$_3$)$_3$} environments at 49.4/60.1 ppm (**32**) and 54.9/65.6 ppm (**33**) also suggesting two *tert*-butyl environments were present. Multiple R group resonances were observed for all three complexes.

Similar reactions with **26**/**27** and the 1,3-di-isopropyl-2-thiourea or *N*,*N'*-diphenyl thiourea did result in some form of reaction although the identity of the products could not be determined. Addition of two equivalents of 1,3-di-*tert*-butyl-2-thiourea to the molybdenum complex, **26**, resulted in the same outcome. The equivalent reaction between the tungsten complex, **27**, and 1,3-di-*tert*-butyl-2-thiourea did

result in a red crystalline product being formed (**34**) which was isolated and analysed using ^{1}H and $^{13}C\{^{1}H\}$ NMR spectroscopy.

Complex **34** displayed three separate *tert*-butyl proton environments of equal integration at 1.11, 1.48 and 1.81 ppm in the ^{1}H NMR spectrum indicative of a *tert*-butyl imido group and a di-*tert*-butyl thioureide ligand. A resonance at 5.37 ppm equivalent to one NH proton (*tert*-butyl:NH ratio – 9:1) suggested the presence of the protonated thioureide ligand. For the $^{13}C\{^{1}H\}$ NMR spectrum, a single {S*C*N_2} carbon atom environment (173.2 ppm) was present along with three separate {*C*$(CH_3)_3$} (54.1, 57.4 and 69.4 ppm) and {C(*C*$H_3)_3$} (30.8, 30.9 and 32.3 ppm) carbon atom environments.

These results are potentially consistent with the bis(*tert*-butylimido)-bis(thioureide) tungsten complex [(^{t}BuN)$_2$W{SC(NH^{t}Bu)N^{t}Bu}$_2$]. However, elemental analysis suggested the complex was actually a tungsten sulfide complex (Figure 4.7) which could be present as either a monomer, [(^{t}BuN)W{SC(NH^{t}Bu)N^{t}Bu}(S)], or dimer, [{(^{t}BuN)W(SC{NH^{t}Bu}N^{t}Bu)(μ-S)}$_2$]. These results are similar to those observed for the sulfur bridged titanium complex, **4**, in Chapter 2 and suggest this compound may have formed via the loss of a guanidine system.

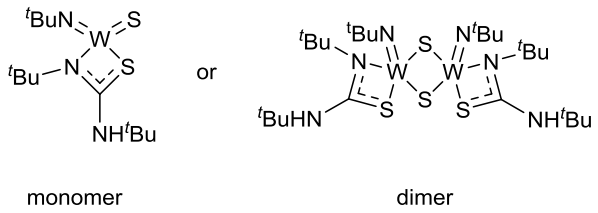

Figure 4.7 Possible identities of complex **34**.

For the molybdenum complexes **28**, **29** and **30**, only the molecular structure of the methyl complex, **28**, was obtained (Figure 4.8). The complex crystallised in a monoclinic $P2_1/c$ space group with the asymmetric unit containing two almost identical molecules and a single molecule of toluene. The following discussion will focus on the molecule containing Mo(1). The molecular structure shows that two *tert*-butylimide and two κ^2-*S*,*N* mode thioureide ligands are bound to the 6-coordinate molybdenum metal centre which adopts a distorted octahedral geometry. Selected bond lengths and angles are shown in Table 4.2.

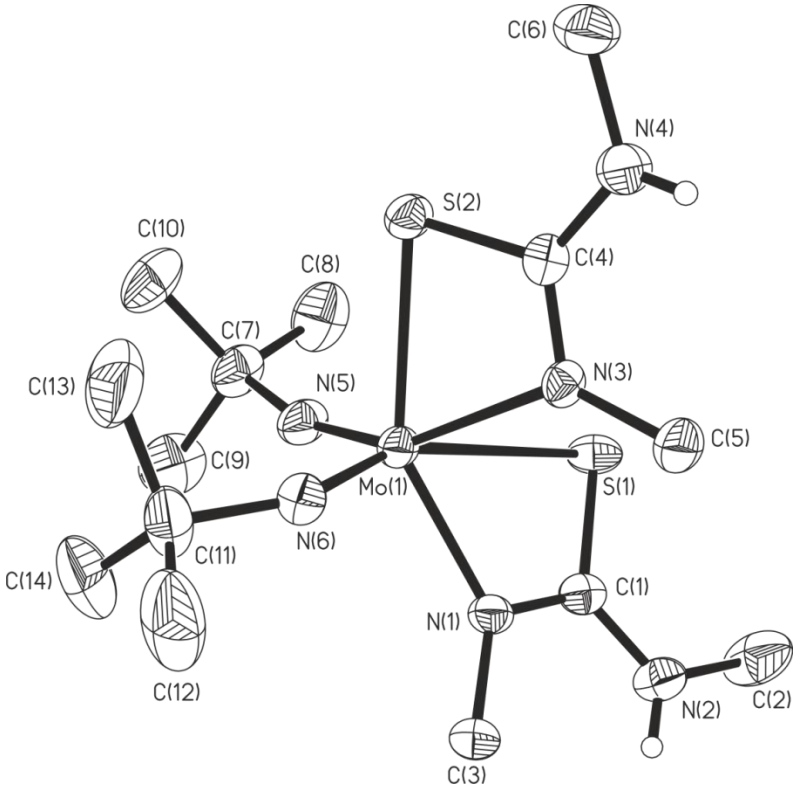

Figure 4.8 Molecular structure of complex **28**. Thermal ellipsoids are shown at 50 % probability, with all hydrogen atoms except the NH atoms within the thioureide ligand omitted for clarity.

The main bond length differences within the molecule are between the central molybdenum atom and the ligands. For both the thioureide and *tert*-butylimide ligands, one ligand is bound more closely with shorter Mo-S/Mo-N and Mo-N_{imido} bond lengths respectively. Interestingly, the *tert*-butylimide ligand that exhibits a slightly longer Mo-N_{imido} bond length also displays a smaller Mo-N_{imido}-C bond angle (149.45(17)° vs. 164.51(17)°).

The Mo-S/Mo-N bond lengths are comparable to the equivalent bond lengths in the complex, [Cp_2Mo(SC(N-tolyl)N-tolyl)], where Mo-S = 2.462(1) Å and Mo-N = 2.128(4) Å. However, the thioureide ligand geometry differs as the tolyl thioureide ligand does not contain a proton and therefore the C-N' bond is a double bond.[53]

Bond lengths within the ligands are essentially equivalent with only slight differences in geometry exhibited. Similar C-N bond lengths across the central {SNCN} moiety and angles equalling ~360 ° around the {SNCN} carbon atom and {CNCH} nitrogen atom suggests electron density is delocalised across the {SNCN}

moiety. The similarities between the NMR spectra of **28**, **29** and **30** suggest all three complexes adopt an analogous structure to that shown in Figure 4.8.

Table 4.2 Selected bond lengths and bond angles for **28** with e.s.d.s. in parenthesis.

Bond	Bond length / Å	Angle	Bond angle / °
Mo(1)-S(1)	2.8632(6)	N(1)-Mo(1)-S(1)	60.45(5)
Mo(1)-S(2)	2.4968(5)	N(3)-Mo(1)-S(2)	64.84(5)
Mo(1)-N(1)	2.1126(17)	N(5)-Mo(1)-N(6)	106.73(9)
Mo(1)-N(3)	2.2190(16)	C(1)-S(1)-Mo(1)	72.27(7)
Mo(1)-N(5)	1.7479(18)	C(4)-S(2)-Mo(1)	80.65(7)
Mo(1)-N(6)	1.760(2)	C(1)-N(1)-Mo(1)	110.61(13)
S(1)-C(1)	1.719(2)	C(4)-N(3)-Mo(1)	102.96(13)
S(2)-C(4)	1.758(2)	C(3)-N(1)-Mo(1)	129.12(14)
N(1)-C(1)	1.317(3)	C(5)-N(3)-Mo(1)	136.37(14)
N(3)-C(4)	1.297(3)	C(7)-N(5)-Mo(1)	164.51(17)
N(1)-C(3)	1.462(3)	C(11)-N(6)-Mo(1)	149.45(17)
N(3)-C(5)	1.451(3)	N(1)-C(1)-S(1)	116.29(16)
N(2)-C(1)	1.341(3)	N(3)-C(4)-S(2)	111.51(15)
N(4)-C(4)	1.336(3)	N(2)-C(1)-S(1)	121.69(17)
N(2)-C(2)	1.447(3)	N(4)-C(4)-S(2)	121.59(17)
N(4)-C(6)	1.450(3)	N(1)-C(1)-N(2)	122.01(19)
N(5)-C(7)	1.456(3)	N(3)-C(4)-N(4)	126.9(2)
N(6)-C(11)	1.452(3)		

The tungsten complexes **31**, **32** (Figure 4.9) and **33** are isostructural and crystallised in a monoclinic unit cell with **31** and **33** adopting a $P2_1/n$ space group and **32** a $P2_1/c$ space group. All asymmetric units contain a single molecule. Selected bond lengths are shown in Table 4.3 while selected bond angles are shown in Table 4.4. The 6-coordinate tungsten metal centres adopted a distorted octahedral geometry with one thioureide ligand binding via the κ^2-*S*,*N* mode and the other via the κ^2-*N*,*N* mode.

Formally, this would give the complexes an overall charge of -1 due to the κ^2-*N*,*N* thioureide ligand becoming -2 charged rather than -1 charged when in the κ^2-*S*,*N*

mode. However, a difference is observed in the *tert*-butylimide ligands with one W-N bond lengthening (1.981(13) vs. 1.731(13) Å in **31**) and the longer bond displaying a smaller W-N-C angle (142.6(13) ° vs. 164.6(15)° in **31**). The tungsten(VI) metallacarborane imido complex $[W(N^tBu)(NH^tBu)_2(C_2B_9H_{11})]$ synthesised by Batsanov *et al.*, contains both a *tert*-butylimide (W-N = 1.721(3) Å, W-N-C = 165.3(3)°) and *tert*-butylamide (W-N = 1.955(3) Å, W-N-C = 141.6(3)°) ligand.[58] The similarities in bond lengths and angles suggest complexes **31**, **32** and **33** contain both *tert*-butylimide and *tert*-butylamide ligands. The lack of *tert*-butylamide protons in the electron difference map suggest the proximity of the protons to the considerable electron density situated on the tungsten atom masks the presence of this proton. The existence of two separate NH environments within the ^{1}H NMR spectra for **32** and **33** supports this hypothesis.

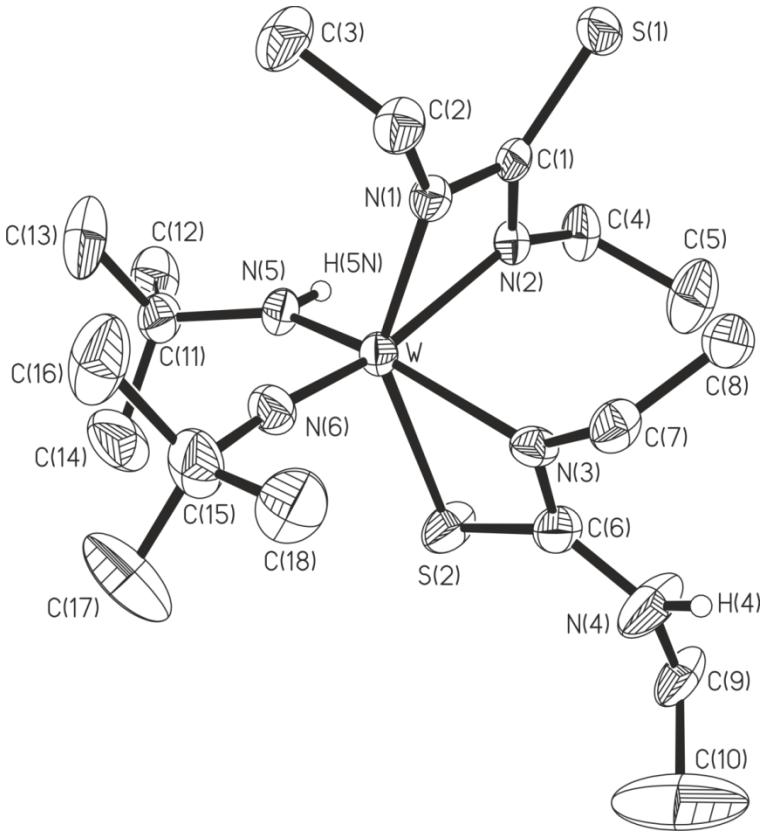

Figure 4.9 Molecular structure of complex **32**, complexes **31** and **33** are isostructural. Thermal ellipsoids are shown at 50 % probability, with all hydrogen atoms except the NH atoms within the thioureide ligand and amide ligand omitted for clarity.

Across **31**, **32** and **33** the bond lengths and angles are reasonably consistent with only very small variations in size. The bond lengths and angles found for the κ^2-*S*,*N*

thioureide ligands are also consistent with those found in the molybdenum complex **28**. Within both binding modes the sum of angles around the {N_2CS} carbon atom equal ~360° indicating electron density is delocalised across the moiety. The nitrogen atoms within the κ^2-*N,N* thioureide ligand bind unsymmetrically to the metal centre and central carbon atom with one nitrogen atom having a longer W-N bond length and shorter N-C bond length. The C-S bond length observed in the κ^2-*N,N* mode is slightly shorter than the equivalent length observed in the κ^2-*S,N* mode.

Table 4.3 Selected bond lengths for **31**, **32** and **33** with e.s.d.s. in parentheses.

	Bond length / Å		
Bond	**31 (R = Me)**	**32 (R = Et)**	**33 (R = ^{n}Bu)**
$W\text{-}N_{imido}$	1.731(13)	1.735(4)	1.718(6)
$W\text{-}N_{amido}$	1.981(13)	1.942(4)	1.932(6)
$N_{imido}\text{-}C$	1.50(2)	1.461(6)	1.472(9)
$N_{amido}\text{-}C$	1.45(2),	1.495(6)	1.501(9)
	κ^2-*S,N*		
W-S	2.494(4)	2.5021(13)	2.4885(19)
$W\text{-}N_R$	2.154(10)	2.145(4)	2.168(6)
S-C	1.768(16)	1.762(5)	1.747(7)
$N_R\text{-}C$	1.31(2)	1.296(6)	1.312(9)
$C\text{-}N'_R$	1.36(2)	1.328(6)	1.345(9)
$N_R\text{-}C_R$	1.48(2)	1.465(5)	1.458(9)
$N'_R\text{-}C`_R$	1.47(3)	1.525(12)	1.459(9)
	κ^2-*N,N*		
W-N	2.018(11), 2.237(11)	1.999(4), 2.217(3)	1.981(6), 2.231(5)
N-C	1.31(2), 1.358(17)	1.319(5), 1.395(5)	1.332(10), 1.414(9)
$N\text{-}C_R$	1.41(2), 1.426(19)	1.446(5), 1.451(5)	1.444(9), 1.440(10)
C-S	1.740(15)	1.699(5)	1.687(8)

Table 4.4 Selected bond angles for **31**, **32** and **33** with e.s.d.s. in parentheses.

	Bond angle / °		
Angle	**31 (R = Me)**	**32 (R = Et)**	**33 (R = ^{n}Bu)**
W-N_{imido}-C	164.6(15)	169.3(4)	169.9(5)
W-N_{amido}-C	142.6(13)	137.6(3)	137.0(5)
	κ^2-*S*,*N*		
S-W-N_R	66.5(4)	64.99(10)	65.23(15)
W-S-C	78.5(6)	79.58(17)	80.4(2)
W-N_R-C	102.7(10)	105.5(3)	103.9(4)
N_R-C-S	112.1(11)	109.7(4)	110.5(5)
S-C-N'$_R$	119.8(13)	122.2(4)	123.2(6)
N_R-C-N'$_R$	128.0(15)	128.1(5)	126.4(7)
	κ^2-*N*,*N*		
N-W-N	62.1(5)	61.88(14)	62.0(2)
W-N-C	88.9(9), 97.3(10)	92.0(3), 99.5(3)	92.1(4), 100.7(5)
N-C-N	111.4(13)	106.5(4)	105.2(6)
N-C-S	124.1(13), 124.3(11)	124.2(3), 129.2(3)	125.6(6), 129.3(6)

The tungsten sulfide complex, **34**, crystallised in a triclinic *P*-1 space group with one molecule of both **34** and toluene occupying the asymmetric unit, selected bond lengths and angles are displayed in Table 4.5. The molecular structure (Figure 4.10) shows complex **34** is the sulfur bridged dimer complex [{(^{t}BuN)W(SC{NH^{t}Bu}N^{t}Bu)(μ-S)}$_2$] in the solid state. The two tungsten atoms are bridged by two sulfur atoms to form a {W_2S_2} four-membered saddle ring in which the sulfur atoms are 0.325 Å above the plane of the tungsten atoms. This results in a saddle angle of 154.44° at the S-S hinge. Both metal centres are pseudo 5-coordinate and adopt a distorted square pyramidal geometry with the imido groups positioned axially.

Within the electron difference map there is no evidence of the thioureide proton; however, the presence of the NH protons in the ^{1}H NMR spectrum and the similarity

between the geometry of the thioureide ligand within complex **34** and the thioureide ligands in **31**, **32** and **33** suggest the thioureide ligand is in fact protonated. The *tert*-butyl imido geometry is comparable to those found in the tungsten complexes, **31**, **32** and **33**.

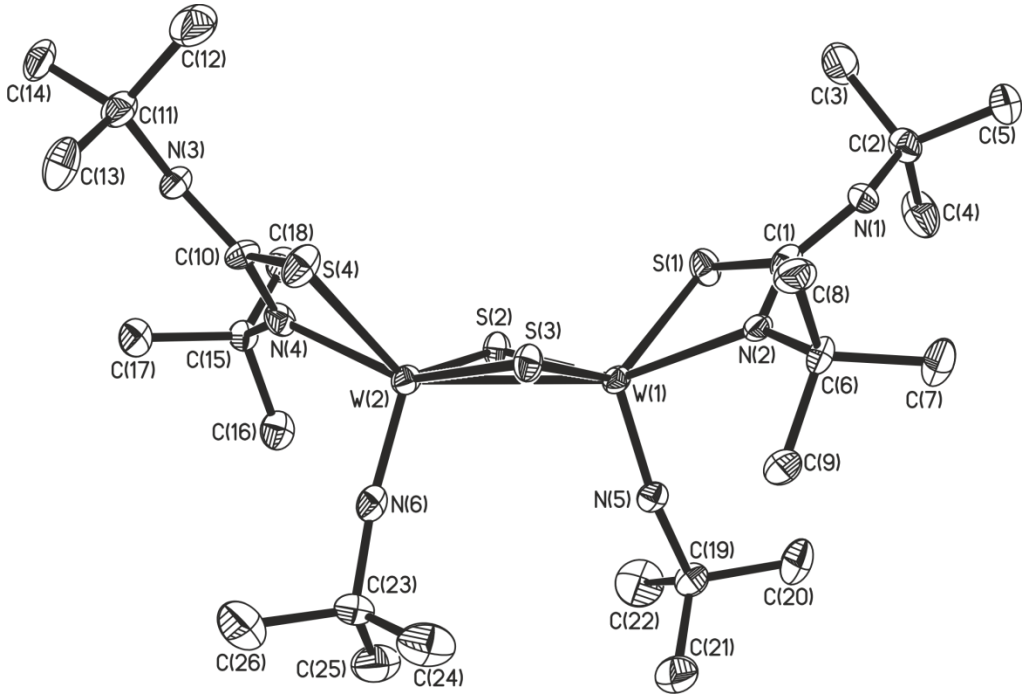

Figure 4.10 Molecular structure of complex **34**. Thermal ellipsoids are shown at 50 % probability, with all hydrogen atoms omitted for clarity.

Formally the tungsten metal centres would be in the +5 oxidation state and the complex would be paramagnetic however, NMR spectroscopy suggests the complex is diamagnetic. The W···W distance of 2.8659(4) Å is comparable to W-W single bond lengths reported in the sulfur bridged complexes $[Cp_2W_2(\mu\text{-}S)_2(NSiMe_3)_2]$ (W-W = 2.903(3) Å),[59] $[W(\eta^5\text{-}(C_5Me_5)(S)(S_2PC^tBu)]_2$ (W-W = 3.068(2) Å)[60] and $KCs_5[W_4(\mu^3\text{-}S)_4(CN)_{12}]\cdot CH_3OH\cdot 2H_2O$ (W-W = 2.8212(8) – 2.8914(8) Å)[61] indicating a W-W single bond is present. The W-W single bond would cause the complex to be diamagnetic rather than paramagnetic as the unpaired electrons would be paired in the W-W bond. The overall structure of the molecule is very similar to the tungsten(V) complexes $[W_2S_4\{S_2P(OEt)_2\}_2]$, $[W_2S_4(S_2O(OEt)_2\}_2]$ and $[W_2S_4(S_2CNEt_2)_2]$ reported by Drew *et al*. which also contain the $\{W_2S_2\}$ moiety.[62]

Table 4.5 Selected bond lengths and bond angles for **34** with e.s.d.s. in parenthesis.

Bond	Bond length / Å	Angle	Bond angle / °
W-W	2.8659(4)	W-S_μ-W	75.32(6), 75.64(6)
W-S_μ	2.319(2), 2.333(2), 2.3547(17), 2.3572(17)	S_μ-W-S_μ	102.08(6), 102.42(7)
W-N_{imido}	1.722(6), 1.727(5)	W-N-C$^t_{Bu}$	164.0(5), 168.9(5)
N_{imido}-C	1.444(10), 1.467(8)	S-W-N_R	66.01(16), 66.23(18)
W-S	2.423(2), 2.4388(19)	W-S-C	81.2(2), 82.2(3)
W-N_R	2.187(5), 2.202(6)	W-N_R-C	102.1(5), 102.5(4)
S-C	1.766(7)	S-C-N_R	109.2(6), 109.4(5)
N_R-C	1.315(9), 1.325(10)	S-C-N'$_R$	123.2(6), 123.4(5)
C-N'$_R$	1.339(9), 1.356(8)	N_R-C-N'$_R$	127.0(7), 127.5(7)
N_R-C_R	1.502(8), 1.503(8)		
N'$_R$-C`$_R$	1.498(10), 1.520(9)		

4.2.3 Synthesis and characterisation of insertion reaction products

For the insertion of isothiocyanates into group VI metal amides, the bis(*tert*-butylimido)-bis(dimethylamido) group VI metal complexes were used as the starting material as they did not contain any protonated amides. The tungsten analogue required an alternative synthetic route (Scheme 4.4) to the one described for the molybdenum complex, **26**, in section 4.2.2. First, the *tert*-butyl trimethylsilylamide, ^{t}Bu(Me$_3$Si)NH (**35**), was synthesised via the reaction between *tert*-butyl amine and trimethylsilyl chloride.[63] Four equivalents of **35** were then reacted with tungsten(VI) chloride in toluene to form the bridged complex [(^{t}BuN)$_2$WCl$_2$(NH$_2$^{t}Bu)]$_2$ (**36a**). Addition of excess pyridine formed the green pyridine adduct [(^{t}BuN)$_2$WCl$_2$py$_2$] (**36b**), reaction with two equivalents of lithium dimethylamide afforded the product, [(^{t}BuN)$_2$W(NMe$_2$)$_2$] (**36**), which was purified by distillation at 80 °C (1x10^{-1} mbar).[64]

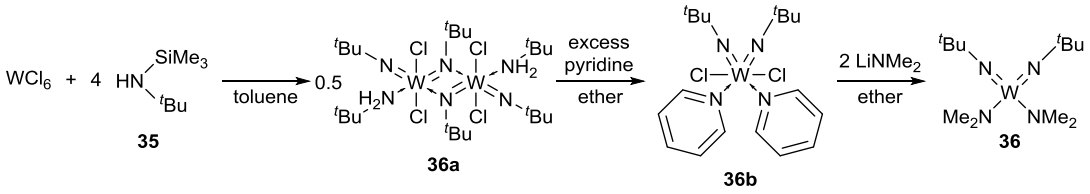

Scheme 4.4 Synthesis of [(^{t}BuN)$_2$W(NMe$_2$)$_2$] (**36**).

The bis(*tert*-butylimido)-bis(dimethylamido) group VI metal complexes (**26** and **36**) were then reacted with two equivalents of the iso-propyl or phenyl isothiocyanates in hexane to provide the group VI metal thioureides (Scheme 4.5). The reactions occurred almost immediately with the solutions turning orange; reaction mixtures were allowed to stir overnight to ensure a complete reaction. Orange or yellow crystals of the iso-propyl molybdenum (**37**) and tungsten (**39**) thioureide complexes, respectively, were recovered after storage of the mother liquor at -28 °C, while orange or yellow crystals of the phenyl molybdenum (**38**) and tungsten (**40**) thioureide complexes, respectively, were attained after storage of the mother liquor at room temperature. Reaction with the *tert*-butyl isothiocyanate only yielded the starting materials **26** and **36** suggesting the steric bulk of the *tert*-butyl group was too large for insertion to occur.

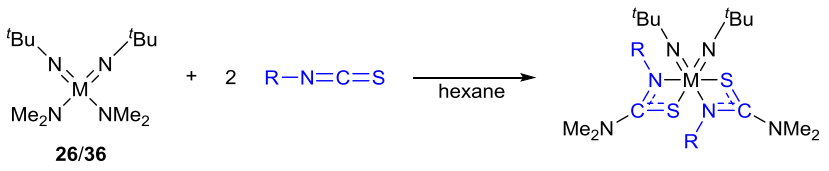

M	R	Complex
Mo	^{i}Pr	**37**
Mo	Ph	**38**
W	^{i}Pr	**39**
W	Ph	**40**

Scheme 4.5 General reaction scheme for isothiocyanate insertions into **26** and **36**.

^{1}H NMR spectra of the iso-propyl complexes, **37** and **39**, showed a variety of iso-propyl environments at room temperature indicating the insertion had occurred although a number of thioureide binding modes were present. Increasing the temperature to 349 K caused these environments to coalesce to form broad multiplets which suggested the complex was fluxional. Integration of the iso-propyl, *tert*-butyl and methyl resonances suggested the intended 2:1 insertion product had been formed. An upfield shift in the NMe$_2$ resonances suggested the insertions had occurred into the M-NMe$_2$ bonds.

$^{13}C\{^{1}H\}$ NMR spectra of both complexes at 337 K exhibited multiple resonances attributed to the *tert*-butyl, methyl and iso-propyl carbon environments however no peaks were observed for the inserted {NSCN} carbon atom. Again this is likely due to the fluxional nature of the complex.[57] Elemental analysis results were in good agreement with the expected values.

The phenyl complexes, **38** and **40**, exhibited the expected phenyl, methyl and *tert*-butyl resonances in the ^{1}H NMR spectra although the *tert*-butyl resonance in the tungsten complex, **40**, was displayed as a multiplet suggesting more than one environment was present. Integration of the phenyl, *tert*-butyl and methyl resonances suggested the intended 2:1 insertion product had been formed. An upfield shift in the NMe_2 resonances indicated the insertions had occurred into the M-NMe_2 bonds.

The $^{13}C\{^{1}H\}$ NMR spectra of the molybdenum complex, **38**, showed all the expected carbon atom resonances for the phenyl, methyl and *tert*-butyl groups. In contrast, the tungsten complex, **40**, displayed a number of carbon atom environments for the phenyl and *tert*-butyl resonances suggesting a degree of fluxionality. Neither complex displayed the {NSCN} carbon atom resonance. Elemental analysis results for the phenyl complexes were in good agreement with the calculated values.

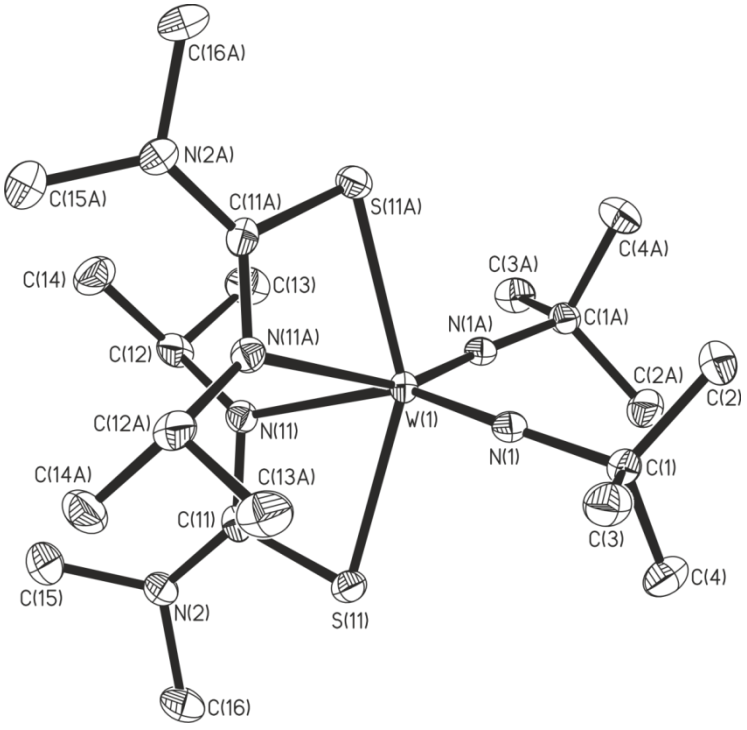

Figure 4.11 Molecular structure of complex **39**, complex **37** is isostructural. Thermal ellipsoids are shown at 50 % probability, with all hydrogen atoms omitted for clarity.

The iso-propyl complexes, **37** and **39**, are isostructural and crystallised in an orthorhombic *Pbcn* space group. The asymmetric unit contains half a molecule with the equivalent atoms generated by the symmetry operator (x+1, y, -z+1/2). The molecular structure displayed in Figure 4.11 shows iso-propyl isothiocyanate insertions into the dimethylamido groups to form two κ^2-*S,N* thioureide ligands. The 6-coordinate metal centre adopts a distorted octahedral geometry with the *tert*-butyl imido ligands adopting a *cis* orientation. The molecular structures support the results from NMR spectra and elemental analysis.

The bond lengths and bond angles for both complexes are displayed in Table 4.6 and Table 4.7 respectively. Both complexes exhibit almost identical geometries with only very slight differences observed. The iso-propyl thioureide ligand geometries are also equivalent to those observed in the group IV iso-propyl species (**1**, **5** and **8**) described in Chapter 2. The *tert*-butyl imido groups adopt a similar geometry to the imido groups in the complex $[W(N^tBu)(NH^tBu)_2(C_2B_9H_{11})]$ (W-N(1) = 1.721(3) Å, W–N(1)–C(11) = 165.3(3)°),[58] while the M-S and M-N bond lengths are comparable to those observed in the molybdenum thioureide complex $[Cp_2Mo\{SC(=N\text{-tolyl})N\text{-tolyl}\}]$ where Mo-S = 2.462(1) Å and Mo-N(1) = 2.128(4)°.[53]

Table 4.6 Selected bond lengths for **37** and **39** with e.s.d.s. in parentheses.

	Bond length / Å	
Bond	**37 (M = Mo)**	**39 (M = W)**
M(1)-N(1)	1.7501(15)	1.763(2)
N(1)-C(1)	1.453(2)	1.453(4)
M(1)-S(11)	2.4732(5)	2.4646(7)
M(1)-N(11)	2.3760(15)	2.362(2)
S(11)-C(11)	1.7622(19)	1.762(3)
N(11)-C(11)	1.296(2)	1.302(3)
N(2)-C(11)	1.377(2)	1.373(4)
N(11)-C(12)	1.478(2)	1.477(4)
N(2)-C(15)	1.459(3)	1.459(4)
N(2)-C(16)	1.458(3)	1.462(4)

Table 4.7 Selected bond angles for **37** and **39** with e.s.d.s. in parentheses.

	Bond angle / °	
Angle	**37 (M = Mo)**	**39 (M = W)**
C(1)-N(1)-M(1)	162.83(13)	162.9(2)
N(11)-M(1)-S(11)	63.63(4)	63.77(6)
C(11)-S(11)-M(1)	84.18(6)	84.40(10)
C(11)-N(11)-M(1)	99.48(11)	99.91(18)
N(11)-C(11)-S(11)	112.64(13)	111.8(2)
N(2)-C(11)-S(11)	119.02(14)	119.4(2)
N(11)-C(11)-N(2)	128.33(17)	128.8(3)

For the phenyl complexes only the molecular structure of the molybdenum complex, **38**, was recorded (Figure 4.12). The complex crystallised in a monoclinic $P2_1/n$ space group with the asymmetric unit containing two molecules, the following discussion will focus on the molecule containing Mo(1). The molecular structure confirms two phenyl isothiocyanates inserted into the dimethylamide groups to form the 2:1 insertion product with two κ^2-*S*,*N* thioureide ligands. The 6-coordinate metal centre adopts a distorted octahedral geometry with the *tert*-butylimide ligands adopting a *cis* orientation. Selected bond lengths and angles are presented in Table 4.8.

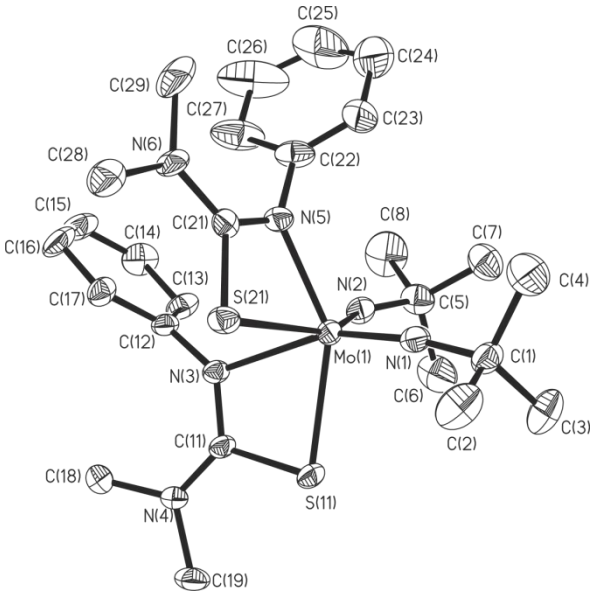

Figure 4.12 Molecular structure of complex **38**. Thermal ellipsoids are shown at 50 % probability, with all hydrogen atoms omitted for clarity.

As observed in the molybdenum methyl thioureide complex, **28**, one of the *tert*-butyl imido ligands is bent in complex **38** with a C(5)-N(2)-Mo(1) angle of 151.7(4)°. While this suggests the ligand may have more amido character, the Mo-N bond length is equivalent to reported W-N imido bond lengths (W-N(1) = 1.721(3) Å)[58] indicating this is not the case. Both thioureide ligands differ in their Mo-S/Mo-N bond lengths, the ligand with the shorter Mo-S bond length also possesses a longer Mo-N bond length. The Mo-N bond lengths are shorter than those observed in the iso-propyl complexes, **37** and **39**. The overall phenyl thioureide ligand geometry is similar to the geometry observed in the group IV phenyl thioureide complexes, **3**, **4**, **7** and **10**, described in Chapter 2.

Table 4.8 Selected bond lengths and bond angles for **38** with e.s.d.s. in parenthesis.

Bond	**Bond length / Å**	**Angle**	**Bond angle / °**
Mo(1)-N(1)	1.743(5)	C(1)-N(1)-Mo(1)	171.5(4)
Mo(1)-N(2)	1.754(5)	C(5)-N(2)-Mo(1)	151.7(4)
N(1)-C(1)	1.447(7)	N(3)-Mo(1)-S(11)	64.38(11)
N(2)-C(5)	1.454(7)	N(5)-Mo(1)-S(21)	61.50(13)
Mo(1)-S(11)	2.4781(14)	C(11)-S(11)-Mo(1)	82.95(17)
Mo(1)-N(3)	2.260(4)	C(21)-S(21)-Mo(1)	75.9(2)
Mo(1)-S(21)	2.7572(16)	C(11)-N(3)-Mo(1)	103.3(3)
Mo(1)-N(5)	2.145(4)	C(21)-N(5)-Mo(1)	109.5(3)
S(11)-C(11)	1.772(5)	N(3)-C(11)-S(11)	109.3(4)
S(21)-C(21)	1.731(5)	N(5)-C(21)-S(21)	112.8(4)
N(3)-C(11)	1.315(6)	N(4)-C(11)-S(11)	121.2(4)
N(5)-C(21)	1.332(7)	N(6)-C(21)-S(21)	120.1(4)
N(4)-C(11)	1.339(7)	N(3)-C(11)-N(4)	129.5(5)
N(6)-C(21)	1.357(7)	N(5)-C(21)-N(6)	127.1(5)
N(3)-C(12)	1.429(6)		
N(5)-C(22)	1.434(7)		
N(4)-C(18)	1.448(7)		
N(4)-C(19)	1.466(6)		
N(6)-C(28)	1.447(8)		
N(6)-C(29)	1.491(9)		

4.2.4 Thermogravimetric analysis

Thermogravimetric analysis for the group VI thioureide complexes was performed using closed pans to limit the exposure of the complexes to air and moisture. Analysis was repeated a number of times to ensure the traces were accurate.

The TGA traces for the molybdenum methyl (**28**), ethyl (**29**) and *n*-butyl (**30**) thioureide complexes are shown in Figure 4.13 with a summary of results presented in Table 4.9. All three complexes displayed relatively wide decomposition windows with continued mass loss even after the major decomposition events had occurred. The methyl (**28**) and *n*-butyl (**30**) complexes both provide final weight percentages lower than the values expected for MoS_2 while the ethyl complex, **29**, provides a value slightly higher than the expected weight. The complexes show varying decomposition pathways although the major decomposition events all occur in the range 200 to 300 °C.

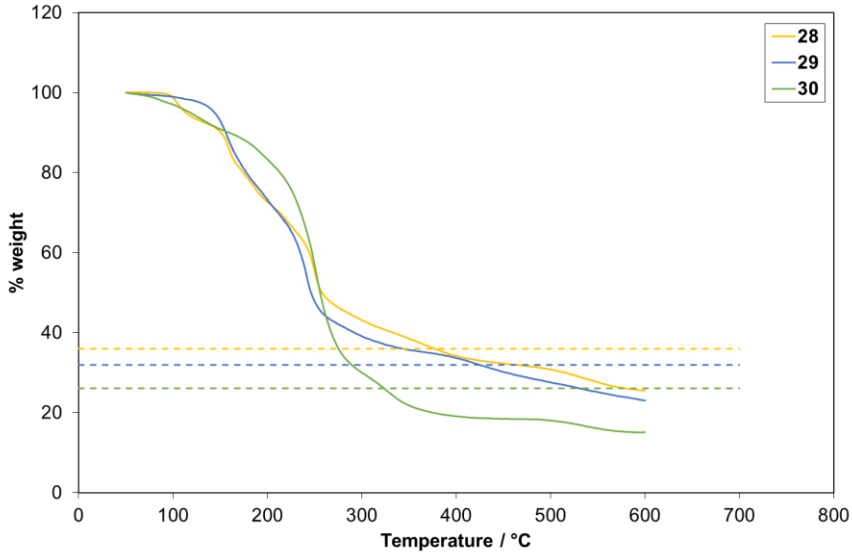

Figure 4.13 TGA traces for **28**, **29** and **30** in closed pans. Dashed lines represent the expected % weight for MoS_2.

The methyl complex, **28**, decomposed via a three step process with an initial mass loss of ~9 % observed between 90 and 145 °C followed by a further mass loss of ~29 % up to 245 °C, a final mass loss of ~29 % was recorded between 245 and 425 °C. Complex **29** on the other hand decomposed via a two-step process; initially a ~35 % mass loss occurred between 125 and 225 °C this was then followed by a mass loss of ~30% up to 370 °C. For the *n*-butyl complex, **30**, there was a relatively fast rate of

mass loss from almost the start of the experiment (70 °C) with the major decomposition event (45 % loss) occurring between 215 and 280 °C.

Table 4.9 Summary of TGA data for **28**, **29** and **30**.

Compound	Onset / °C	End point / °C	% weight expected for MoS_2	End point % weight
28	90	425	36.0	33.0
29	125	370	32.0	35.0
30	70	400	26.1	19.1

The TGA traces for the tungsten methyl (**31**), ethyl (**32**), *n*-butyl (**33**) and sulfur bridged *tert*-butyl (**34**) thioureide complexes are shown in Figure 4.14 with a summary of results presented in Table 4.10. The methyl complex, **31**, decomposed relatively gradually over the range 130 to 370 °C with a continued mass loss even after the main decomposition event had occurred. The final weight percentage is lower than the value expected for WS_2 and the continued mass loss indicates the compound may be volatile. The ethyl (**32**) and *n*-butyl (**33**) complexes possess almost identical decomposition profiles with the only difference being the final percentage weight. While the ethyl complex, **32**, provides a final percentage weight higher than expected for WS_2 the *n*-butyl complex, **33**, affords a value slightly lower.

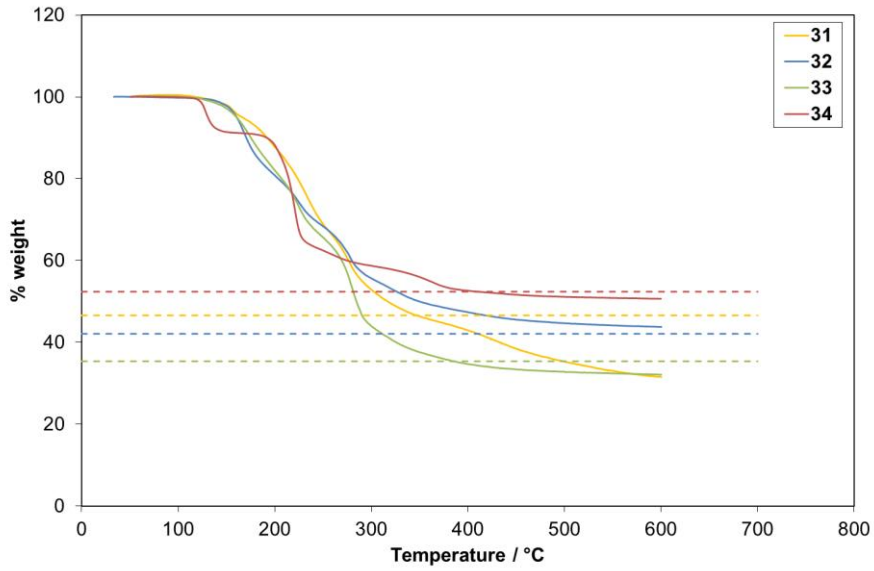

Figure 4.14 TGA traces for **31**, **32**, **33** and **34** in closed pans. Dashed lines represent the expected % weight for WS_2.

The sulfur bridged *tert*-butyl complex, **34**, displayed a distinct three step decomposition pathway. In the first step a ~9% mass loss occured, following this a mass loss of ~26 % took place and finally a loss of ~12 % took the final mass to 52.6 % which is almost identical to the expected weight for WS_2 (52.4 %).

Table 4.10 Summary of TGA data for **31**, **32**, **33** and **34**.

Compound	Onset / °C	End point / °C	% weight expected for WS_2	End point % weight
31	130	370	46.6	45.0
32	125	375	42.1	48.5
33	120	400	35.4	34.7
34	110	400	52.4	52.6

The TGA traces for the molybdenum iso-propyl (**37**) and phenyl (**38**) thioureide complexes are displayed in Figure 4.15 with a summary of results presented in Table 4.11. Both complexes provide final percentage weights slightly lower than the values expected for MoS_2 suggesting these complexes would be viable precursors. The phenyl complex, **38**, essentially decomposed via a single step process while the iso-propyl complex, **37**, underwent a three step decomposition pathway. In the initial step a ~28 % mass loss was observed between 160 and 240 °C, the next step between 240 and 290 °C involved the loss of ~21 % while the final mass loss up to the end point at 360 °C involved the loss of a further ~10 %.

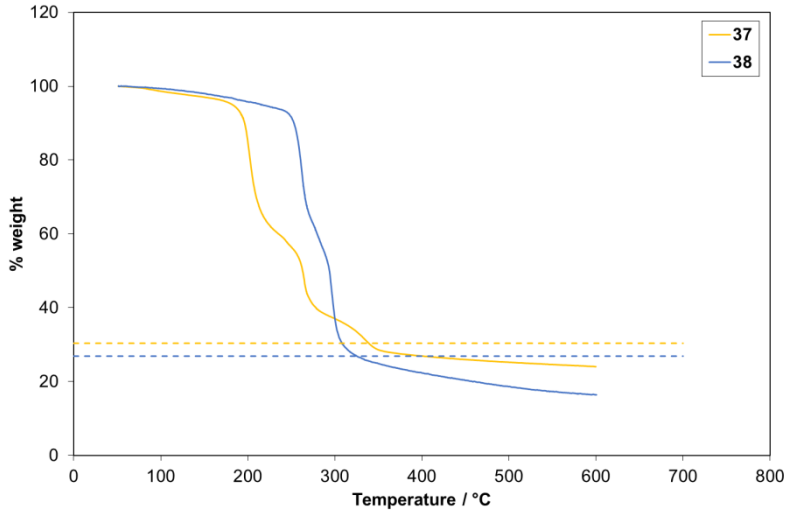

Figure 4.15 TGA traces for **37** and **38** in closed pans. Dashed lines represent the expected % weight for MoS_2.

The molybdenum iso-propyl (**37**) and phenyl (**38**) complexes showed cleaner decomposition profiles over a narrower range than the methyl (**28**), ethyl (**29**) and *n*-butyl (**30**) complexes. The residual masses are also more stable and the decomposition end points were attained at lower temperatures. This suggests the inserted molybdenum thioureide complexes are more promising precursors.

Table 4.11 Summary of TGA data for **36** and **37**.

Compound	Onset / °C	End point / °C	% weight expected for MoS_2	End point % weight
37	160	360	30.4	28.0
38	235	350	26.9	24.9

The TGA traces of the iso-propyl (**39**) and phenyl (**40**) tungsten thioureide complexes (Figure 4.16, Table 4.12) show similar profiles to those observed for the equivalent molybdenum complexes **37** and **38** respectively although the decomposition temperature range is increased. The residual mass of the iso-propyl complex, **39**, is found to be lower than the expected mass for WS_2 while the opposite is observed for the phenyl complex, **40**. The decomposition end point temperatures are higher than those recorded for the tungsten methyl (**31**), ethyl (**32**), *n*-butyl (**33**) and sulfur bridged *tert*-butyl (**34**) thioureide complexes.

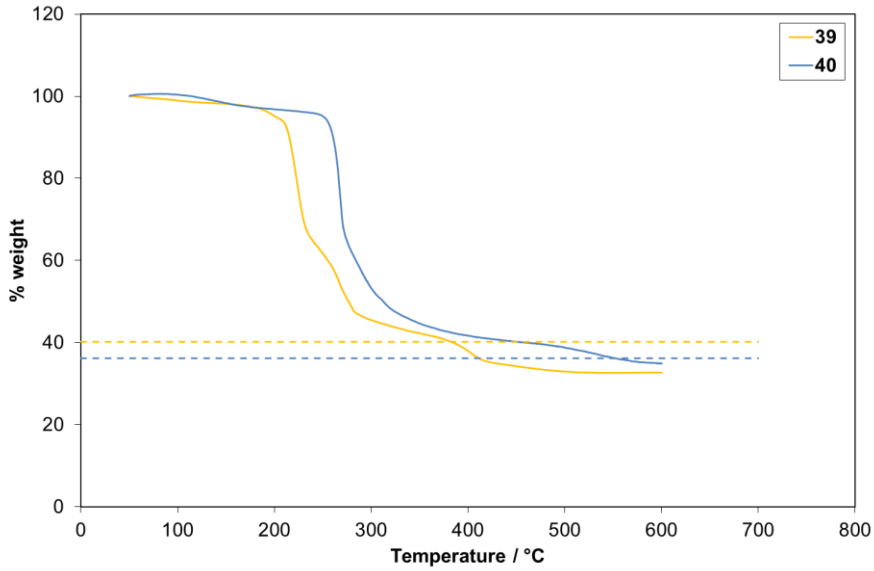

Figure 4.16 TGA traces for **39** and **40** in closed pans. Dashed lines represent the expected % weight for WS_2.

Of all the group VI thioureide complexes, the iso-propyl molybdenum (**37**) and tungsten (**39**) thioureide complexes were determined to be the most promising for further investigation. Both displayed relatively clean decomposition profiles with stable residual masses below the values expected for the metal sulfide. Both complexes could also be consistently recovered in relatively high yields which was beneficial for deposition experiments.

Table 4.12 Summary of TGA data for **39** and **40**.

Compound	Onset / °C	End point / °C	% weight expected for WS_2	End point % weight
39	175	425	40.2	35.1
40	240	430	36.2	40.7

TGA-MS was performed on the iso-propyl tungsten thioureide complex, **39**, to elucidate the decomposition pathway. The TGA trace and major mass peaks recorded on decomposition are displayed in Figure 4.17. The majority of the decomposition occured in the range 120 to 260 °C with major mass peaks observed at 15, 27, 41, 42, 43, 45 and 101 m/z, possible identities of the these fragments are presented in Table 4.13. The most intense mass peaks are those at 27 and 41 m/z which suggest the loss of hydrogen cyanide and acetonitrile. Interestingly the presence of a peak at 101 m/z is highly suggestive of the iso-propyl isothiocyanate which indicates some form of de-insertion is taking place. The majority of mass peaks correspond to iso-propyl or *tert*-butyl imide decomposition fragments. Further decomposition in the range 260 to 400 °C sees major mass peaks observed at 27, 41 and 56 m/z. Again this suggests the loss of hydrogen cyanide and acetonitrile along with the *tert*-butyl imido decomposition products $(H_3C)_2CCH_2^+$, $(H_3C)_2CN^+$. Ahmet *et al.* previously reported that the tin thioureide complex, $[Sn(\{C_6H_5\}NCSN\{Me_2\})(NMe_2)]$, decomposes via the loss of a phenyl guanidine derivative which was isolated and identified by ^1H and $^{13}C\{^1H\}$ NMR spectroscopy.[65] In our experiments no mass peaks were observed for an equivalent guanidine breakdown product.

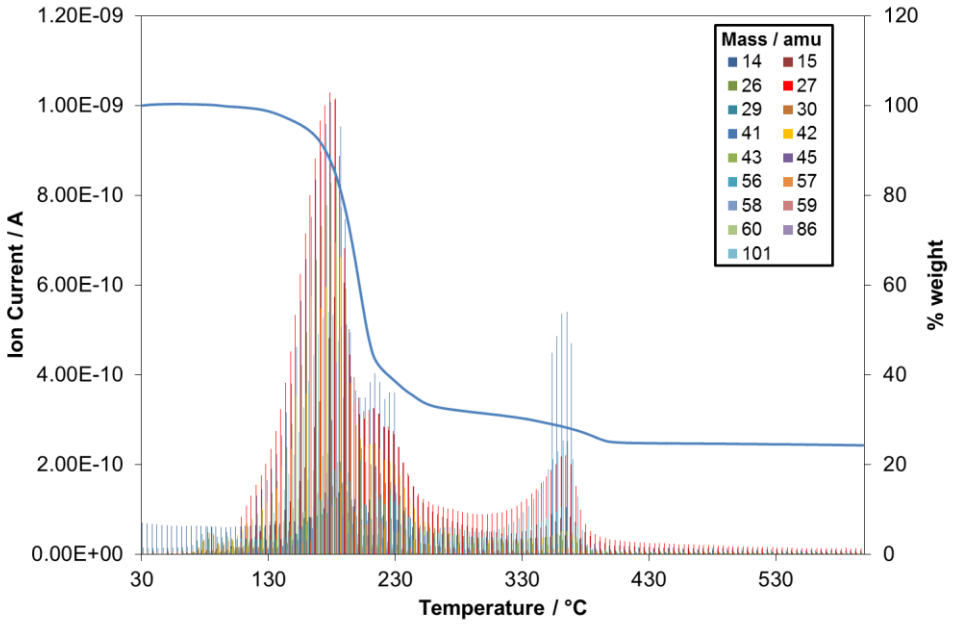

Figure 4.17 TGA-MS results for **39**: graph shows the major ion fragments present as temperature is increased, TGA trace is overlaid.

Table 4.13 Possible ion fragment assignment for the decomposition of **39**.

Mass / m/z	Fragment
15	CH_3^+
27	HCN^+
41	H_3CCN^+
42	N3+, H_3CCHN^+, $H_3CCHCH_2^+$
43	H_3CCHNH^+, $(H_3C)_2CH^+$
45	$H_3CCH_2NH_2^+$
56	$(H_3C)_2CCH_2^+$, $(H_3C)_2CN^+$
101	$^iPrN{=}C{=}S^+$

As previously described, the iso-propyl molybdenum (**37**) and tungsten (**39**) thioureide complexes were determined to be the most promising for further investigation. Therefore, these complexes were chosen for deposition studies using AACVD.

4.2.5 AACVD of [(^{t}BuN)$_2$Mo(SC{NMe$_2$}N^{i}Pr)$_2$] (37)

For the AACVD experiments, a 0.05 M solution of complex **37** in toluene was prepared in the glovebox. Glass and Si substrates were rinsed with IPA and then O_2 plasma cleaned for 20 minutes. Experiments were performed at 350, 400, 450 and 500 °C with a deposition time of 60 minutes. Depositions at 350, 400 and 450 °C provided grey to silvery grey films which were amorphous. Raman spectroscopy could not identify the composition of the films therefore no further characterisation was performed. Deposition at 500 °C yielded reflective silvery films on both substrates as displayed in Figure 4.18.

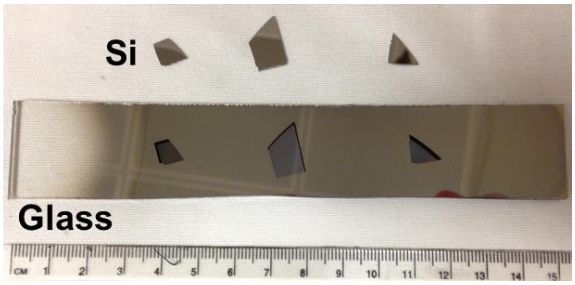

Figure 4.18 Image of films on glass and Si deposited from the AACVD of **37** at 500 °C.

PXRD analysis (Figure 4.19) showed the film on glass to contain crystalline MoS_2 with a predominant peak at ~13.9° corresponding to either the 2H (14.402° = (002) - JCPDS card #87-2416)[66] or 3R (14.453° = (003) - JCPDS card #89-5112)[67] phases, no other reflections were observed. In contrast, the film on Si displayed low intensity peaks attributed to orthorhombic MoO_3 (JCPDS card #89-5108)[68] with no evidence of any MoS_2.

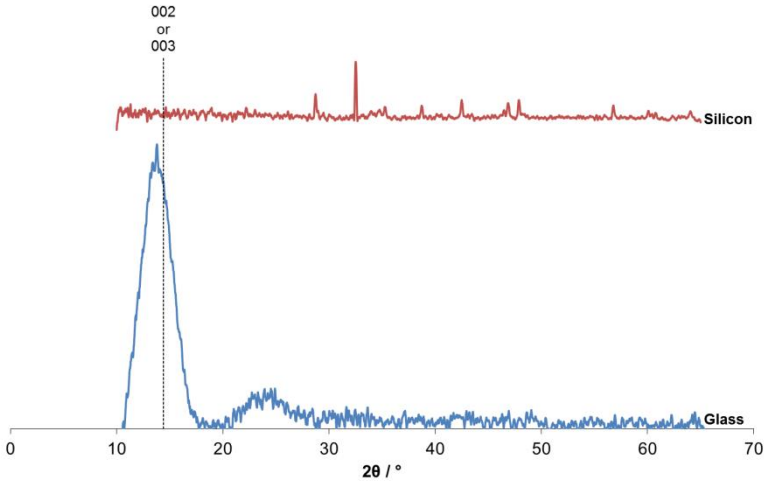

Figure 4.19 PXRD patterns for the films deposited from **37**.

Further analysis of the films using Raman spectroscopy (Figure 4.20) again showed the presence of MoS_2 in the film on glass. Peaks at 380 and 406 cm^{-1} were attributed to the E^1_{2g} (383 cm^{-1}) and A_{1g} (408 cm^{-1}) modes reported by Stacy *et al.* for bulk MoS_2.[69] The Raman spectrum of the film on Si did not display resonances associated with either MoS_2 or MoO_3.

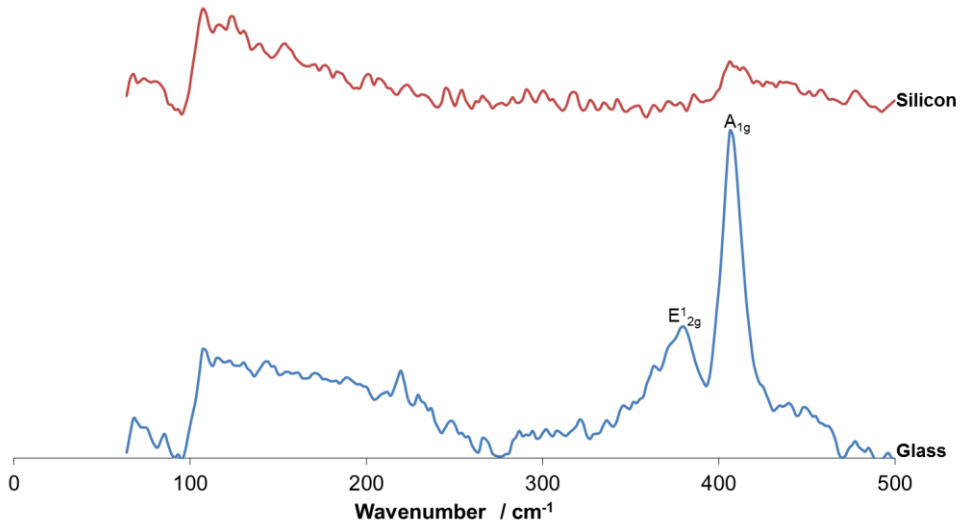

Figure 4.20 Raman spectra of films deposited from **37**.

SEM, XPS and EDX analysis were performed on the film on glass by the Properties and Surface Analysis department at NSG Group, UK while the film on Si was analysed at the University of Bath. EDX analysis of the samples showed the presence of Mo, S, C, N and O in both the films on glass and Si. Only small amounts of sulfur were detected which meant Mo:S stoichiometries could not be determined due to the overlap of the sulfur K and molybdenum L lines. XPS analysis of the glass based sample provided an average film elemental ratio of $MoS_{0.7}C_{0.2}N_{3.2}$. Depth profiling of the film using XPS (Figure 4.21) shows the elemental ratio to be consistent throughout the film thickness. The presence of sulfur in the elemental analysis and MoS_2 in the PXRD patterns and Raman spectra suggest the film on glass contains some MoS_2. The high levels of nitrogen detected in the XPS analysis suggest the film is mostly composed of some form of molybdenum nitride. The exact identity of the film on Si has still not been determined but it is likely to be a composite of Mo, S, C, N and O.

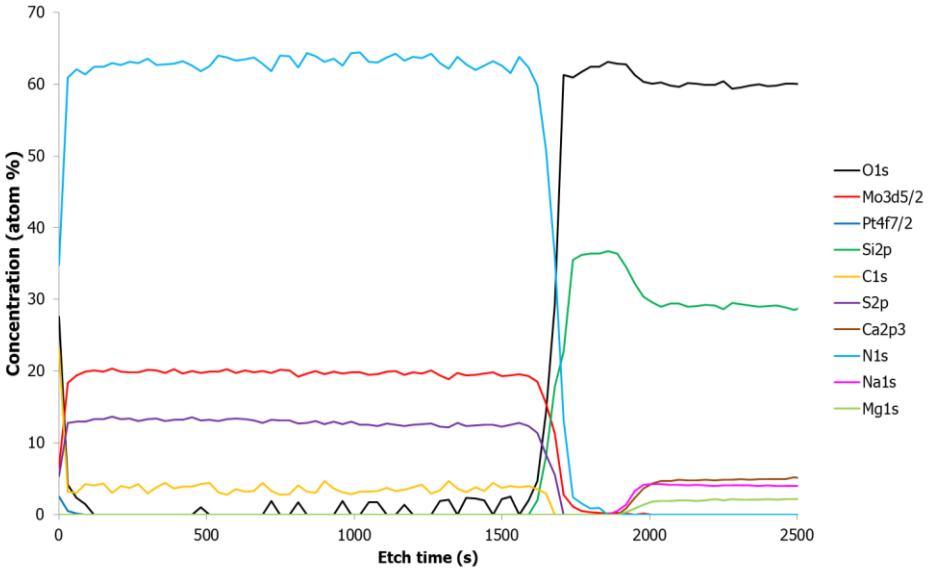

Figure 4.21 XPS depth profile of film deposited from **37** on glass.

Both films were then annealed under a nitrogen atmosphere at 500 °C for 1 hour to see what effect this would have upon the composition of the film. Visually the film on glass went from silvery and reflective to white and opaque, while the film on Si went from silvery and reflective to blue/purple and opaque. PXRD patterns (Figure 4.22) of both the film on glass and on Si showed the presence of crystalline orthorhombic MoO_3 (JCPDS card #89-5108)[68]; the major expected reflections are highlighted on the spectra. Differences in peak intensities indicate that the MoO_3 film on glass was thicker than the film on Si. Remaining H_2O or O_2 within the annealing apparatus is probably the source of the oxygen within the films.

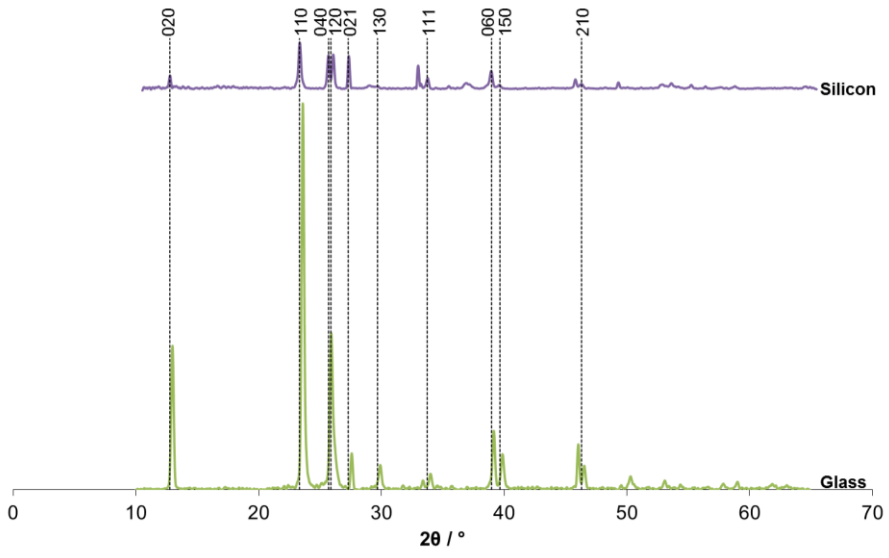

Figure 4.22 PXRD patterns for the annealed films deposited from **37**.

Raman spectroscopy of both samples supported the presence of MoO_3 within the films. The spectra displayed in Figure 4.23 show major peaks at 995, 818, 669 and 292 cm^{-1} which correspond to the resonances at 996 (A_g/B_{1g}), 820 (A_g/B_{1g}), 666 (B_{2g}/B_{3g}) and 291 (B_{3g}) cm^{-1} reported by Seguin *et al.* for orthorhombic MoO_3.[70] The minor peaks observed in the range 100 to 400 cm^{-1} also correspond to MoO_3. There was no evidence of MoS_2 in either sample. EDX analysis of both samples showed considerable amounts of Mo, O and C within the films. Mo:O stoichiometries of MoO_4 and $MoO_{2.7}$ for the films on glass and Si respectively suggest the films contain a considerable amount of MoO_3.

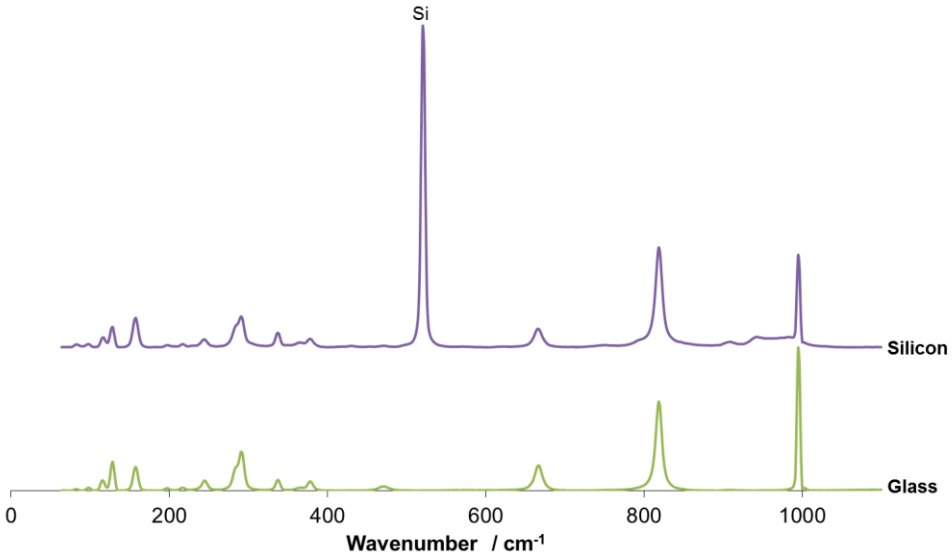

Figure 4.23 Raman spectra of annealed films deposited from **37**.

SEM images of both the 'as deposited' and annealed films are presented in Figure 4.24 and show a change in morphology on annealing. Both the 'as deposited' films are composed of small particles; the film on glass has a more uniform appearance with only the occasional large particle embedded in the film while the film on Si has larger spherical particles interspersed across the film of much smaller particles. On annealing, the film on glass develops a patchy appearance with raised areas of material; small particles are no longer visible. For the films on Si annealing causes the films to crack and for pinholes to form. Some larger spherical particles remain but the majority have disappeared.

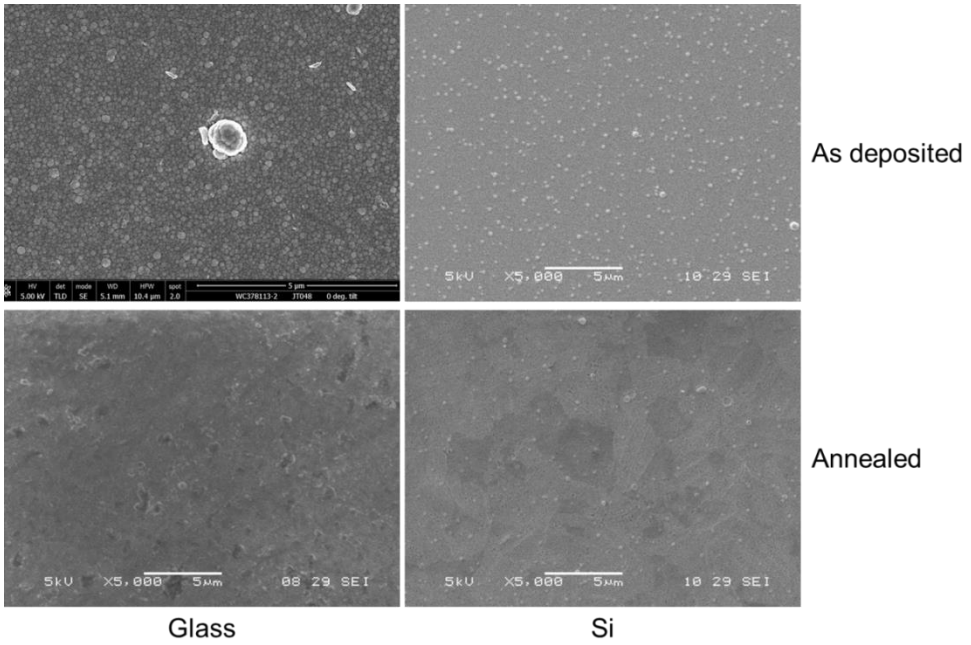

Figure 4.24 SEM images of 'as deposited' and annealed films produced from **37**.

4.2.6 AACVD of [(^{t}BuN)$_2$W(SC{NMe$_2$}N^{i}Pr)$_2$] (39)

The AACVD experiments with the tungsten complex, **39**, used the same set of conditions as those used for the depositions with the molybdenum complex, **37**, although no experiment at 350 °C was performed. Depositions at 400 and 450 °C provided brown/black films which were amorphous and exhibited no Raman active modes. As the identity of the films could not be determined from PXRD or Raman spectroscopy, no further characterisation was performed. In contrast, deposition at 500 °C yielded reflective silvery films on both glass and Si substrates (Figure 4.25) similar to those observed for the depositions with complex **37**. PXRD analysis of these films showed both to be amorphous with no reflections observed.

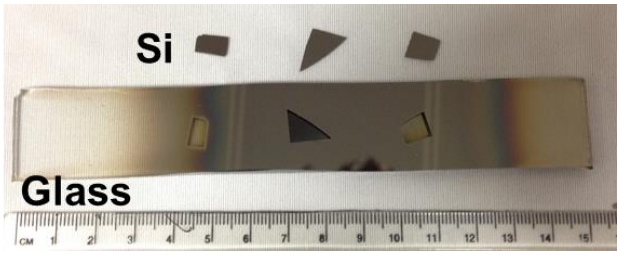

Figure 4.25 Image of films on glass and Si deposited from the AACVD of **39** at 500 °C.

The Raman spectra for both films are displayed in Figure 4.26 and indicate both WS_2 and WO_3 are present within the films. Modes at 353 and 420 cm^{-1} closely match

those reported for the E^1_{2g} (352 cm^{-1}) and A_{1g} (421 cm^{-1}) modes of WS_2 reported by Stacy *et al.*[69], while peaks at 808, 702, 260, 124 and 81 cm^{-1} are highly suggestive of orthorhombic WO_3 reported by Gabrusenoks *et al.*[71] These spectra suggest the films have a mixed composition with both WS_2 and WO_3 present.

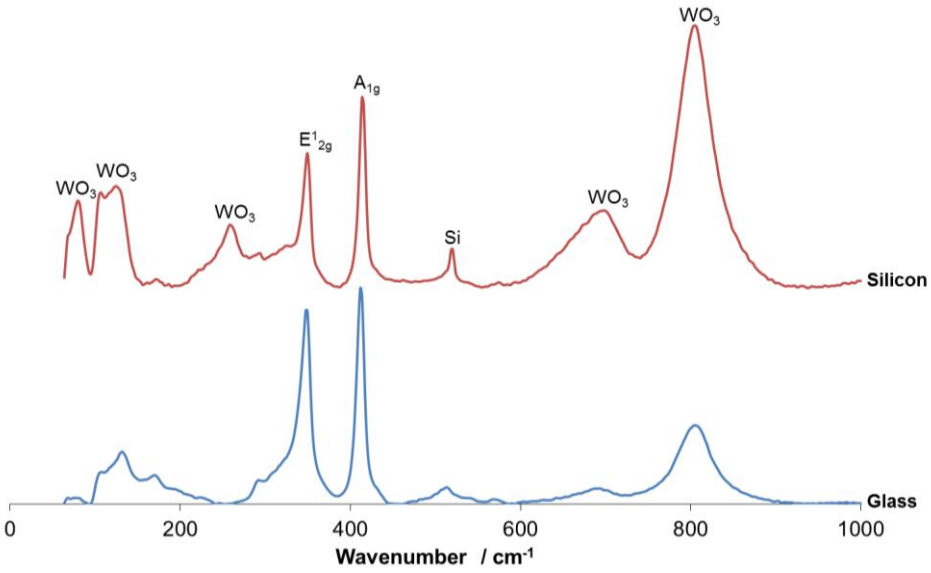

Figure 4.26 Raman spectra of films deposited from **39**.

SEM, XPS and EDX analysis were performed on the film on glass by the Properties & Surface Analysis department at NSG Group, UK while the film on Si was analysed at the University of Bath. EDX analysis of the samples showed the presence of W, S, C, N and O in both the films on glass and Si. W:S stoichiometries could not be determined due to the low levels of sulfur and the overlap of the tungsten M and silicon K lines. XPS analysis of the glass based sample provided an average film elemental ratio of $WS_{0.3}O_{0.2}N_{0.6}$. Depth profiling of the film using XPS (Figure 4.27) shows the elemental ratio to be consistent throughout the film thickness. The presence of sulfur in the elemental analysis and WS_2 in the Raman spectra suggest the film on glass contains some WS_2 but also contains a considerable amount of tungsten nitride and WO_3.

These results suggest complex **39** does not decompose cleanly under AACVD conditions to form WS_2 but rather forms a variety of materials. One potential reason for the lack of sulfur in the films could be that the iso-propyl isothiocyanate de-inserts from the complex. The existence of iso-propyl isothiocyanate in the TGA-MS of complex **39** (Figure 4.17) supports this hypothesis. The large disparity in

elemental composition for the molybdenum ($MoS_{0.7}C_{0.2}N_{3.2}$) and tungsten ($WS_{0.3}O_{0.2}N_{0.6}$) based films on glass is unexpected when both precursors **37** and **39** display very similar TGA traces, the reason for this difference in composition is unclear.

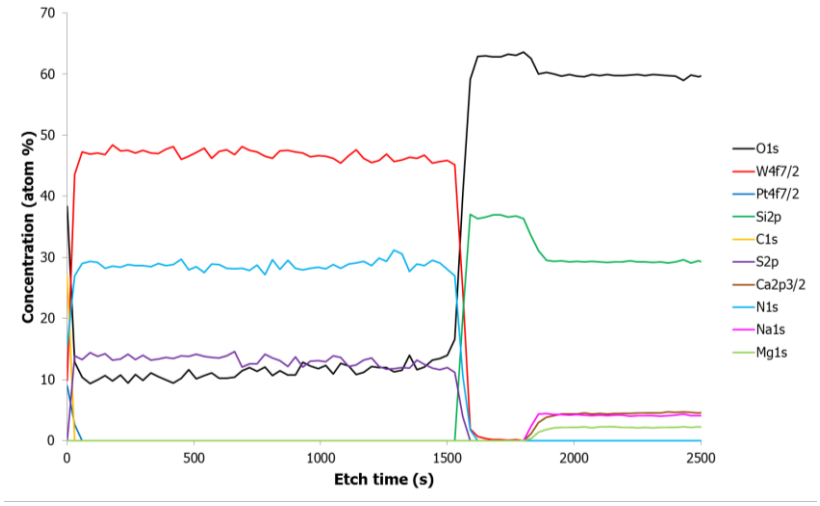

Figure 4.27 XPS depth profile of film deposited from **39** on glass.

Both films were then annealed under a nitrogen atmosphere at 500 °C for 1 hour. The film on glass went from silvery and reflective to brown and reflective with refringence patterns visible, while the film on Si went from silvery and reflective to green/purple and opaque. PXRD patterns (Figure 4.28) of both the film on glass and on Si showed the presence of crystalline orthorhombic WO_3 with the major reflections matching those of JCPDS card #89-4479.[72] No reflections attributed to WS_2 or tungsten nitride were observed.

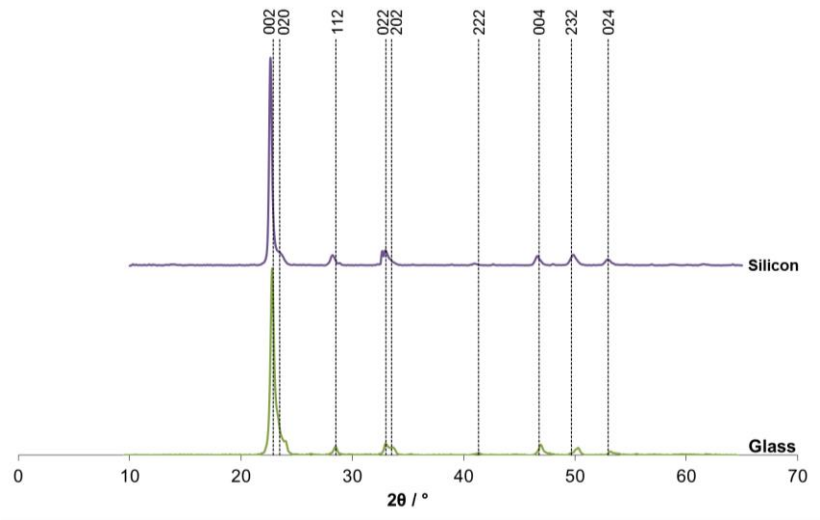

Figure 4.28 PXRD patterns for the annealed films deposited from **39**.

Raman spectra (Figure 4.29) of both samples again showed the presence of WS_2 and WO_3. Modes at 353 and 421 cm^{-1} closely match those reported for the E^1_{2g} (352 cm^{-1}) and A_{1g} (421 cm^{-1}) modes of WS_2 reported by Stacy *et al.*[69], while peaks at 808, 705, 326 and 271 cm^{-1} are highly suggestive of orthorhombic WO_3 reported by Gabrusenoks *et al.*[71] These spectra again indicate the films have a mixed composition with both WS_2 and WO_3 present, however some changes in composition have occurred as a number of peak intensities have varied and some peaks are no longer present. EDX analysis showed a considerable increase in the amount of oxygen within the samples and a decrease in the amount of sulfur. W:S:O stoichiometries could not be determined due to the overlap of the tungsten M and silicon K lines.

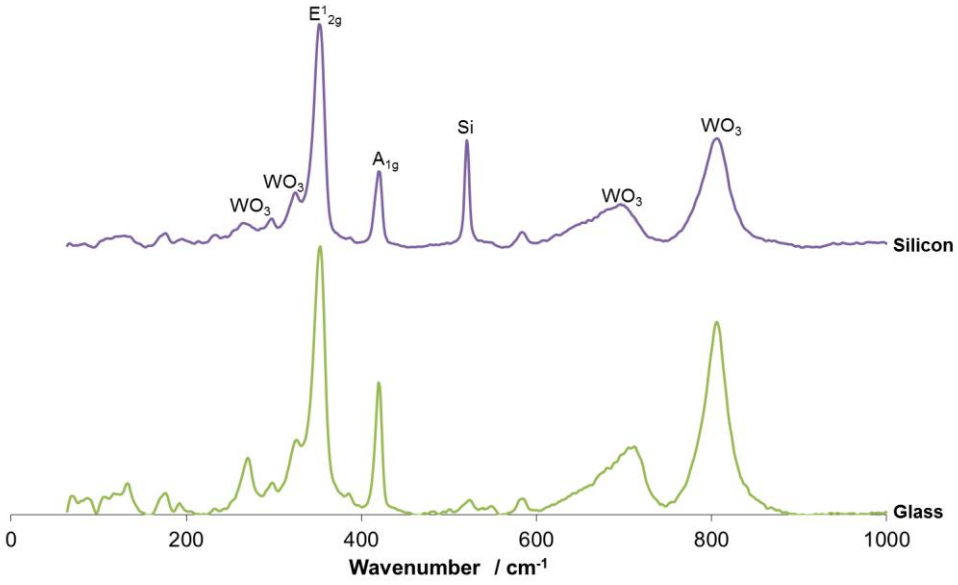

Figure 4.29 Raman spectra of annealed films deposited from **39**.

SEM images of both the 'as deposited' and annealed films are presented in Figure 4.30 and show a change in morphology on annealing. Both the 'as deposited' films are flat and featureless with the occasional small particle present on the surface. On annealing, both films exhibit pock-marked surfaces with a number of pin-holes present. The film on glass still has a relatively smooth appearance with a number of pinholes visible. In contrast the film on Si has broken down to a greater extent with more particles on the surface and a number of craters present across the film.

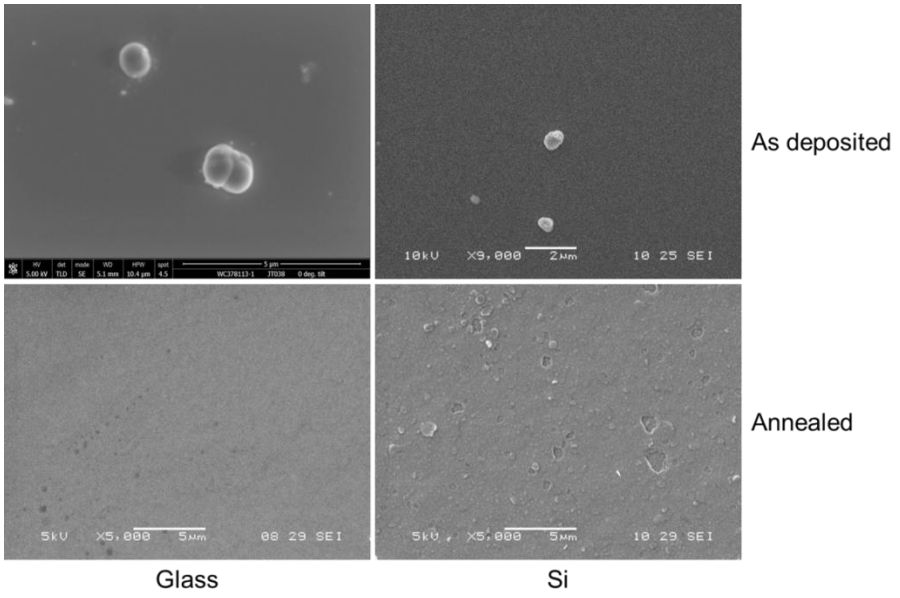

Figure 4.30 SEM images of 'as deposited' and annealed films produced from **39**.

4.3 Group VI dithiocarbamates

Previous work in the literature has shown molybdenum(IV) and tungsten(IV) diethyldithiocarbamates as viable MoS_2 and WS_2 CVD precursors. The majority of this work has focused on the deposition of MoS_2 primarily using LPCVD although deposition with AACVD has also been reported.[33-38] Deposition of WS_2 using AACVD has also been demonstrated although only limited deposition studies have been performed.[44] While both molybdenum(IV) and tungsten(IV) diethyldithiocarbamates have been used as MoS_2 and WS_2 CVD precursors, there is still an opportunity to expand the range of deposition substrates and evaluate alternative deposition conditions.

4.3.1 Synthesis and characterisation

Both $[Mo(S_2CNEt_2)_4]$ (**41**) and $[W(S_2CNEt_2)_4]$ (**42**) were synthesised by the reaction between the corresponding metal hexacarbonyl and two equivalents of tetraethylthiuram disulfide in refluxing THF (Scheme 4.6).[73] The product was washed with hexane to extract any remaining metal hexacarbonyl then recrystallised in THF to provide dark purple crystals. IR spectra displayed stretching modes indicative of C-S stretching vibrations at 1000 cm^{-1} for the molybdenum complex, **41**, and at 989 cm^{-1} for the tungsten complex, **42**, suggesting the reactions had been successful.[74] Elemental analysis results were consistent with the calculated values.

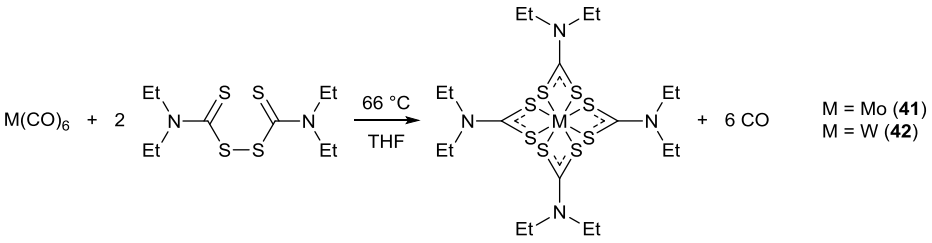

Scheme 4.6 Reaction scheme for the synthesis of **41** and **42**.

Complexes **41** and **42** are isostructural and crystallised in a monoclinic *C*2/*c* space group with the asymmetric unit containing half a molecule, equivalent atoms were generated using the symmetry operator (-x, y, -z+3/2). The molecular structure of the tungsten complex, **42**, is displayed in Figure 4.31 while selected bond lengths and angles for both complexes are displayed in Table 4.14. The group VI complexes are also isostructural with the analogous group IV complexes, **11**, **12** and **13**, which were described in Chapter 2.

As expected for elements with very similar atomic radii, the Mo-S and W-S bond lengths are comparable in distance.[75] M-S bond lengths typically vary within each dithiocarbamate ligand, with one longer and one shorter, e.g. Mo-S(3) = 2.5485(7) Å and Mo-S(4) = 2.5227(6) Å. In contrast all of the S-C bond lengths are effectively equivalent. The geometry of the dithiocarbamate ligands indicate electron density is delocalised across the {S_2CN} moiety as the moiety is planar and the N-C bond lengths are shorter than those with the ethyl carbon atoms.

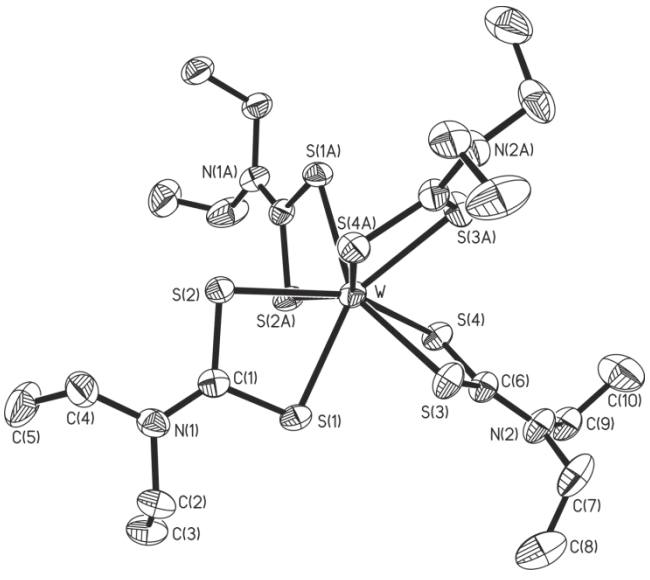

Figure 4.31 Molecular structure of complex **42**, complex **41** is isostructural. Thermal ellipsoids are shown at 50 % probability, with all hydrogen atoms omitted for clarity.

Table 4.14 Selected bond lengths and angles for **41** and **42** with e.s.d.s. in parenthesis.

	Bond length / Å			Bond angle / °	
Bond	**41 (M = Mo)**	**42 (M = W)**	**Angle**	**41 (M = Mo)**	**42 (M = W)**
M-S(1)	2.5307(7)	2.5228(7)	S(1)-M-S(2)	67.20(2)	67.20(2)
M-S(2)	2.5375(7)	2.5357(7)	S(3)-M-S(4)	67.72(2)	67.64(2)
M-S(3)	2.5485(7)	2.5430(7)	C(1)-S(1)-M	91.27(9)	91.75(10)
M-S(4)	2.5227(6)	2.5178(7)	C(1)-S(2)-M	90.92(9)	91.09(10)
S(1)-C(1)	1.704(3)	1.704(3)	C(6)-S(3)-M	90.22(9)	90.54(10)
S(2)-C(1)	1.709(3)	1.714(3)	C(6)-S(4)-M	91.14(9)	91.34(10)
S(3)-C(6)	1.716(3)	1.713(3)	S(1)-C(1)-S(2)	110.58(14)	109.97(16)
S(4)-C(6)	1.714(3)	1.716(3)	S(3)-C(6)-S(4)	110.91(15)	110.47(16)
N(1)-C(1)	1.335(3)	1.331(4)	N(1)-C(1)-S(1)	124.1(2)	124.6(2)
N(1)-C(2)	1.467(3)	1.472(4)	N(1)-C(1)-S(2)	125.3(2)	125.4(2)
N(1)-C(4)	1.467(4)	1.456(4)	N(2)-C(6)-S(3)	124.2(2)	124.6(2)
N(2)-C(6)	1.325(3)	1.332(4)	N(2)-C(6)-S(4)	124.86(19)	124.9(2)
N(2)-C(7)	1.464(4)	1.464(4)			
N(2)-C(9)	1.483(3)	1.473(4)			

4.3.2 Thermogravimetric analysis

The TGA traces for **41** and **42** are shown in Figure 4.32 with a summary of the results presented in Table 4.15. The molybdenum complex, **41**, has previously been reported by Ouyang *et al*. to decompose via the loss of ethene, HCN and excess sulfur to form MoS_2.[33] The initial decomposition step for **41** occurred between 140 and 250 °C with a mass loss of ~57 %, this was followed by a slight pause in decomposition between 250 and 315 °C whereupon the final decomposition step took place with a loss of ~23 % up to 385 °C. The final percentage weight of 20.0 % is close to the value expected for MoS_2 indicating MoS_2 has been formed. None of the decomposition steps have mass losses equivalent to the reported decomposition by-products.

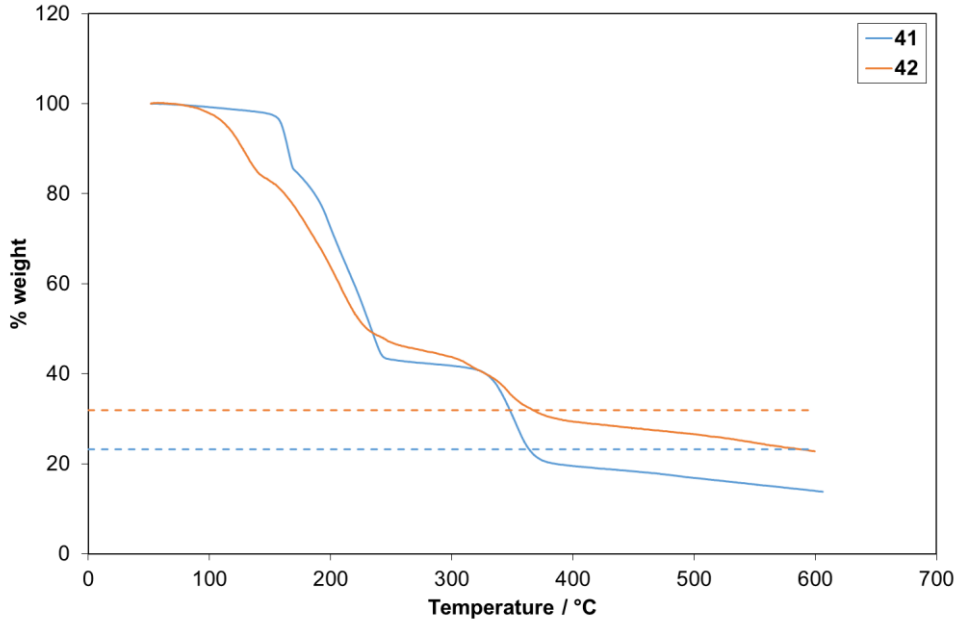

Figure 4.32 TGA traces for **41** and **42** in open pans. Dashed lines represent the expected % weight for MS_2.

For the tungsten complex, **42**, a similar decomposition pathway appears to occur. Initially between 85 and 255 °C there was a mass loss of ~54 %, this was followed by a reduction in the rate of decomposition. Between 255 and 380 °C a further mass loss of ~24 % took place to provide a final mass of 30.4 % which is close to the expected value for WS_2 again indicating WS_2 has been formed.

Table 4.15 Summary of TGA data for **40** and **41**.

Compound	Onset / °C	End point / °C	% weight expected for MS_2	Final % weight
41	140	385	23.2	20.0
42	85	380	31.9	30.4

TGA-MS (Figure 4.33) was performed on the tungsten complex, **42**, to elucidate the decomposition pathway. An increase in ion fragments was observed at 80 °C when the decomposition initiates with the majority of ion fragments detected in the range 185 to 255 °C. Possible ion fragment assignments for the major mass peaks observed in the decomposition are shown in Table 4.16. The most common mass peaks were observed at 76 and 29 m/z which suggest the loss of CS_2 and deprotonated ethane respectively. Further peaks at 48 and 64 m/z occur after the decomposition end point

and indicate the tungsten disulfide is decomposing via the loss of SO and S_2/SO_2 respectively. These results are similar to those observed for the analogous zirconium complex, **12**, described in Chapter 2 and suggest a different decomposition mechanism is occurring to the one proposed by Ouyang *et al.*[33]

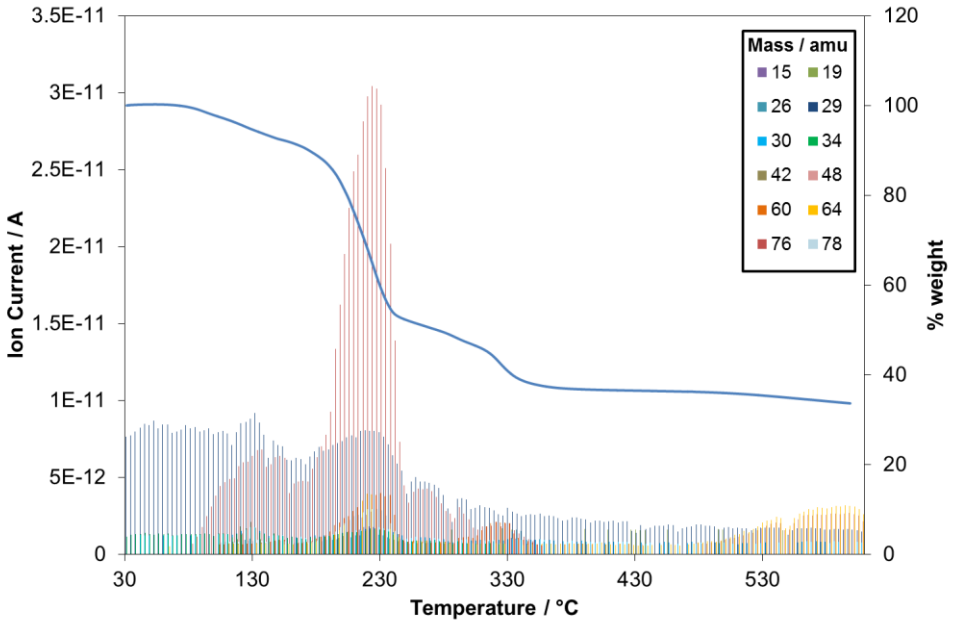

Figure 4.33 TGA-MS results for **42**: graph shows the major ion fragments present as temperature is increased, TGA trace is overlaid.

Table 4.16 Possible ion fragment assignment for the decomposition of **42**.

Mass / m/z	Fragment
26	CN^+, $C_2H_2^+$
29	Butane^{2+}, CSN^{2+}, $C_2H_5^+$
30	$C_2H_6^+$
48	SO^+
64	S_2^+, SO_2^+
76	CS_2^+

4.3.3 AACVD of $[Mo(S_2CNEt_2)_4]$ (41)

Depositions with complex **41** were carried out using AACVD, although the conditions differed to those reported by Adeogun *et al.*[37] In a typical experiment a 0.01 M solution of complex **41** in toluene was used. Glass and Si substrates were

rinsed with IPA prior to the start of the experiment. Depositions at 250, 300 and 350 °C were unsuccessful while experiments at 400, 450 and 500 °C provided golden brown to purple films (Figure 4.34).

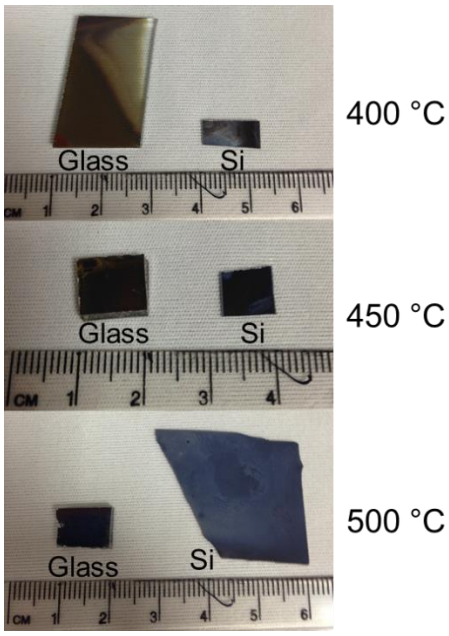

Figure 4.34 Images of films deposited on glass and Si from the AACVD of **41**.

PXRD patterns of the films at 400, 450 and 500 °C are displayed in Figure 4.35 with the major reflection labelled at ~14.4° corresponding to the (002) or (003) Miller plane in bulk MoS_2. The single reflection in the spectra does not give enough information to distinguish between the 2H (14.402° = (002) - JCPDS card #87-2416)[66] or 3R (14.453° = (003) - JCPDS card #89-5112)[67] phases. Higher deposition temperatures provides more intense (002)/(003) peaks indicating an increase in film crystallinity. The films on glass and Si at 400 °C show only a minor reflection at ~14.4° indicating they are mainly amorphous while the films at higher temperatures are relatively crystalline. A strong reflection from the (002)/(003) plane indicates the films have a preferred orientation with the S-Mo-S layers lying parallel to the substrate surface.[27, 76] Reflections at ~33° for the films on Si at 450 and 500 °C correspond to the Si substrate.[67]

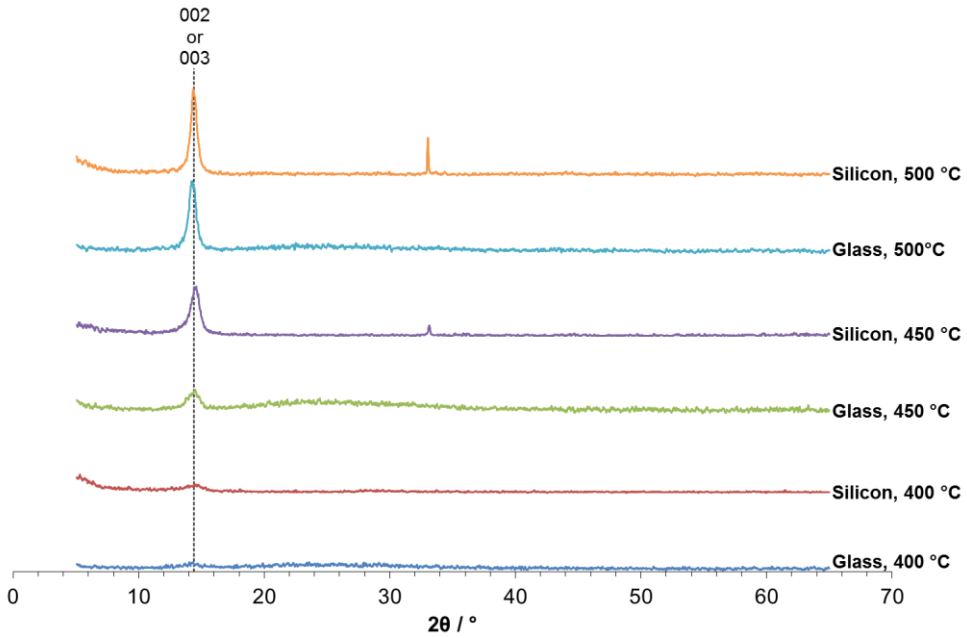

Figure 4.35 PXRD patterns for the films deposited from **41**.

Raman spectra of the films are presented in Figure 4.36 with the major E^1_{2g} (383 cm^{-1}) and A_{1g} (408 cm^{-1}) modes in bulk MoS_2 labelled.[77-79] All films showed the presence of these peaks indicating the films contain MoS_2. Peaks at ~520 cm^{-1} correspond to the silicon substrate. There is no evidence of any oxide phases within the films.

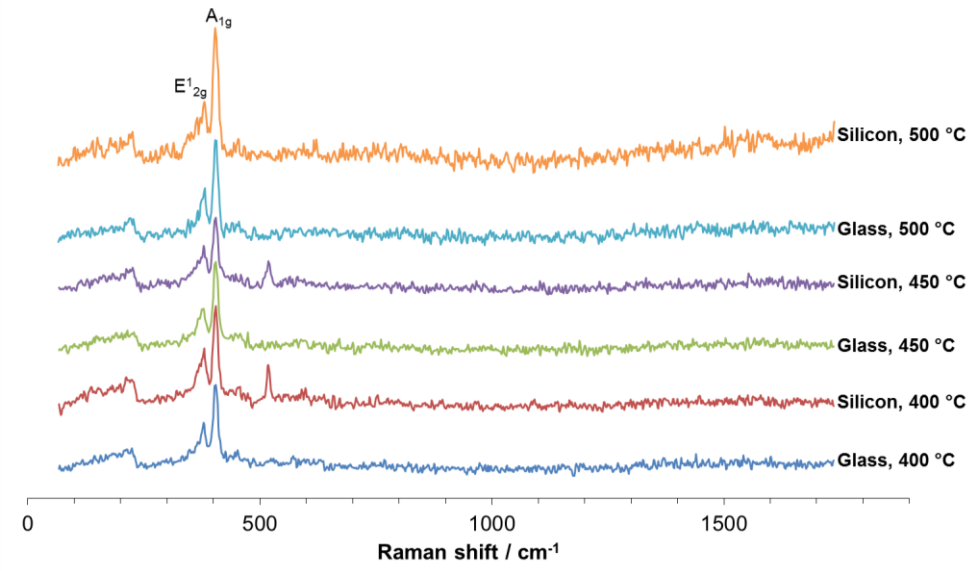

Figure 4.36 Raman spectra of the films deposited from **41**.

SEM imaging of the samples showed the morphology of the MoS_2 films was dependent on both the substrate and deposition temperature (Figure 4.37).

Deposition on glass at 400 and 450 °C yields a dense mixture of nanotubules and platelets while an increase in temperature to 500 °C provides predominantly folded platelets. This is similar to the films deposited on glass by Adeogun *et al.* that showed a change from nanotubules to platelets with increasing deposition temperature.[37] The deposition of MoS_2 on silicon provides particulate films with a granular appearance at 400 °C and a rippled platelet-like appearance at 450 °C, increasing the temperature to 500 °C gives the film a folded leaf like morphology. The films on glass had a more uniform coverage than the films on silicon at all three deposition temperatures, coverage uniformity increased with temperature for the films on silicon. Film thicknesses on glass ranged from ~100 nm at 400 °C to ~1.5 μm at 500 °C and on silicon ranged from ~30 nm at 400 °C to ~160 nm at 500 °C.

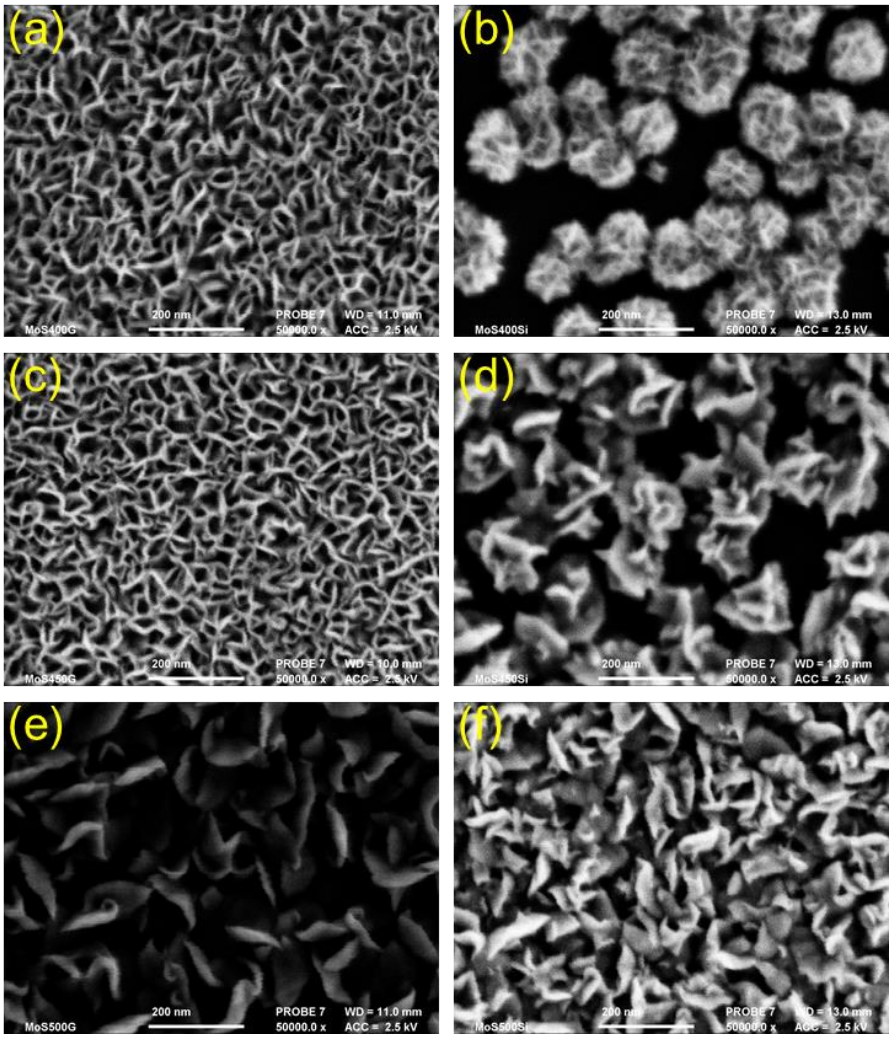

Figure 4.37 SEM images of the films deposited from **41** on glass at (a) 400 °C, (c) 450 °C and (e) 500 °C, and on silicon at (b) 400 °C, (d) 450 °C and (f) 500 °C.

EDX analysis showed the presence of both molybdenum and sulfur in all of the films. As relatively high amounts of sulfur were present within the films it was possible to estimate the Mo:S stoichiometries which are listed in Table 4.17. All films provided Mo:S stoichiometries close to 1:2 indicating MoS_2 had been deposited, slightly sulfur rich films were attained at all temperatures on glass and at 450 °C on Si, while slightly sulfur deficient films were deposited at 400 and 500 °C on Si. There was a small amount of carbon contamination within each film although this is common for films deposited using AACVD.[80] The oxygen content of the films could not be determined as both the glass and Si substrates contain oxygen.

Table 4.17 Mo:S stoichiometries calculated from the EDX data.

Temperature / °C	Substrate	Mo:S stoichiometry
400	Glass	$MoS_{2.3}$
400	Si	$MoS_{1.8}$
450	Glass	$MoS_{2.2}$
450	Si	$MoS_{2.3}$
500	Glass	$MoS_{2.2}$
500	Si	$MoS_{1.9}$

4.3.4 AACVD of $[W(S_2CNEt_2)_4]$ (42)

For the AACVD experiments with complex **42**, the same set of conditions were utilised although a 0.003 M precursor solution was used due to the lower solubility of **42** in toluene. Depositions were run for 90 minutes and successfully deposited golden brown to purple films at 400, 450 and 500 °C on both glass and Si substrates (Figure 4.38); a deposition run at 350 °C was unsuccessful.

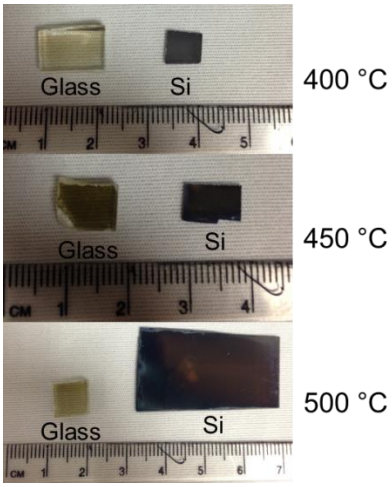

Figure 4.38 Images of films deposited on glass and Si from the AACVD of **42**.

PXRD patterns of the films are displayed in Figure 4.39 with the major peak labelled at ~14.3° corresponding to either the (002) or (003) reflection in bulk WS_2. The prevalence of this peak suggests the structure is orientated with the S-W-S planes lying parallel to the substrate surface. The single reflection in the spectra does not give enough information to distinguish between the 2H (14.320° = (002) - JCPDS card #87-2417)[66] and 3R (14.359° = (003) - JCPDS card #84-1399)[9] phases in the majority of cases. The small peak at 32.6° for the film on silicon at 450 °C however suggests this film adopts the 2H phase with the reflection corresponding to the (100) plane (32.760°).

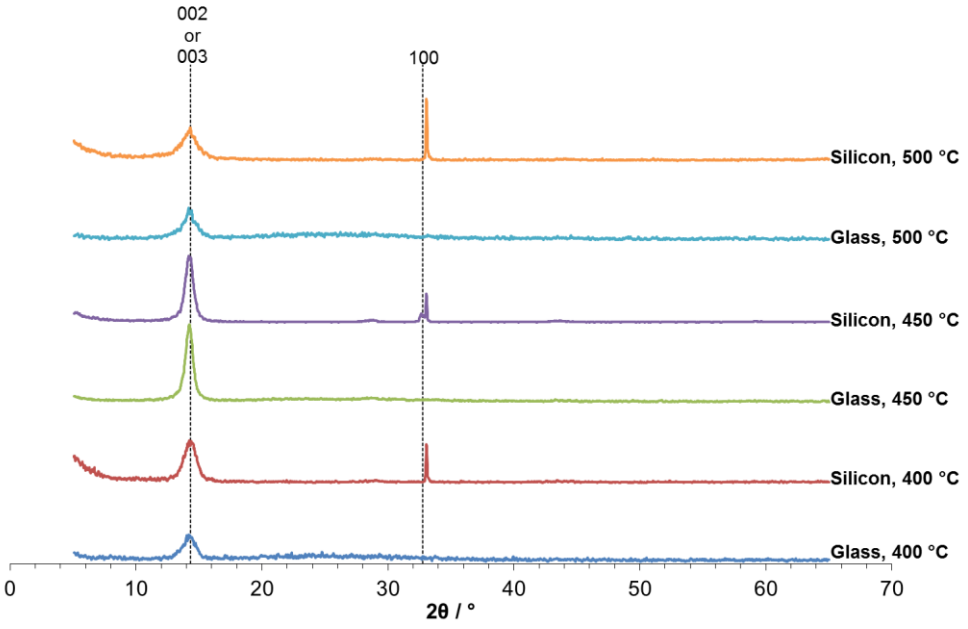

Figure 4.39 PXRD patterns for the films deposited from **42**.

Raman spectroscopy (Figure 4.40) showed the presence of the major E^1_{2g} (355 cm^{-1}) and A_{1g} (420 cm^{-1}) modes as well as a resonance at 178 cm^{-1} corresponding to bulk WS_2 for all of the films. The films deposited at 500 °C on both substrates and 450 °C on glass also showed resonances at 232, 298, 326, 582 and 702 cm^{-1} consistent with bulk WS_2. Films on the glass substrate also exhibited peaks at 523 cm^{-1} corresponding to bulk WS_2; these peaks were not observed for the films on Si as a Si substrate resonance is situated at 520 cm^{-1}.[81, 82]

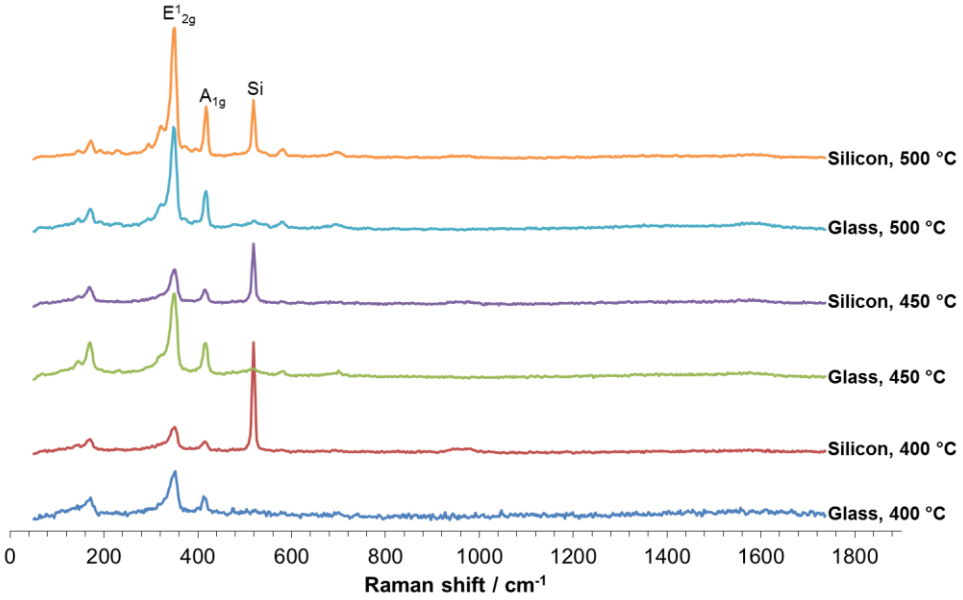

Figure 4.40 Raman spectra of the films deposited from **42**.

Film morphology varied with both temperature and substrate for the WS_2 films (Figure 4.41). As with the MoS_2 films, the WS_2 films on glass were more platelet-like and the low temperature films on Si were particulate-like. The films on glass changed from thicker platelets at 400 and 450 °C to thinner folded platelets at 500 °C. In contrast, the films on Si were composed of small particulates at 400 °C, closely packed platelets at 450 °C and folded platelets at 500 °C. Good coverage and uniformity were achieved for all the films except that at 400 °C on silicon which was composed of small particulates. Average film thicknesses varied on glass from ~100 nm at 400 °C to ~1.1 μm at 500 °C, while on Si they ranged from ~50 nm at 400 °C to ~300 nm at 500 °C.

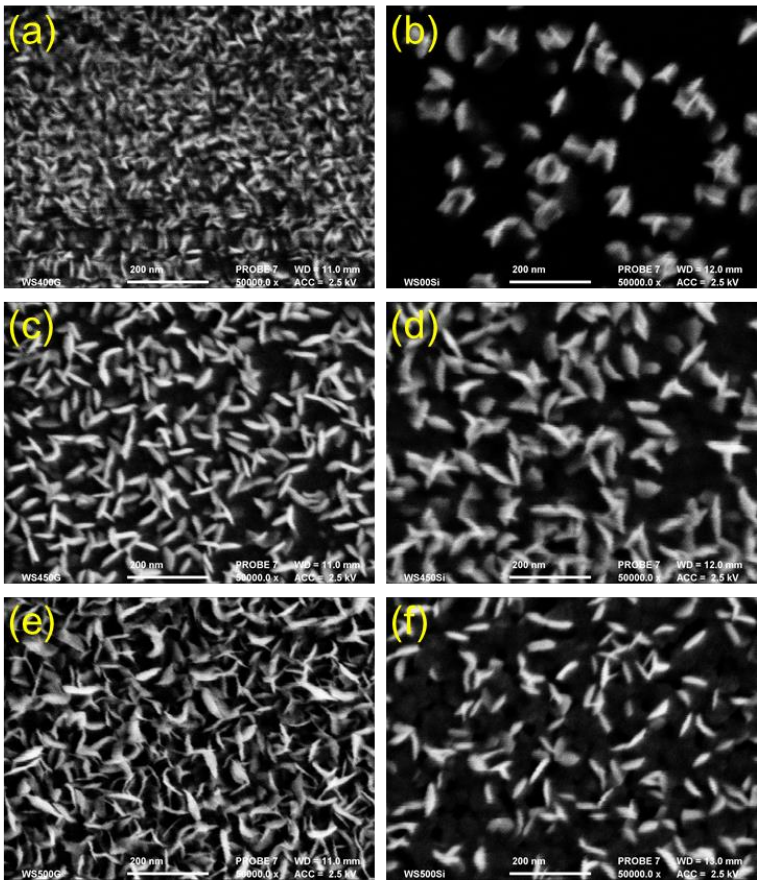

Figure 4.41 SEM images of films deposited from **42** on glass at (a) 400 °C, (c) 450 °C and (e) 500 °C, and on silicon at (b) 400 °C, (d) 450 °C and (f) 500 °C.

AFM surface plots of the films deposited at 400 °C on both glass and Si are displayed in Figure 4.42. The film on glass is composed of relatively small plate-like particles while the film on Si contains much larger rounder particles, this supports what was observed in the SEM images (Figure 4.41). The plots show the film on Si is much rougher than the film on glass with RMS values of 27.7 and 8.90 nm respectively. Much greater height variations are observed for the film on Si.

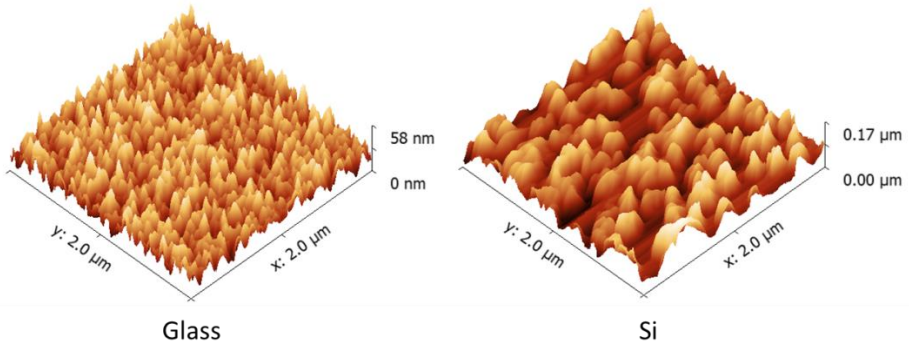

Figure 4.42 AFM surface plots of the films deposited from **42** at 400 °C.

EDX analysis showed the presence of both tungsten and sulfur in all of the films, W:S stoichiometries are listed in Table 4.18. All films provided W:S stoichiometries close to 1:2 indicating WS_2 had been deposited, slightly sulfur rich films were attained at all temperatures on glass and at 450 °C on Si, while slightly sulfur deficient films were deposited at 400 and 500 °C on Si. Again, there was a small amount of carbon contamination within each film although this is common for films deposited using AACVD.[80] The oxygen content of the films could not be determined as both the glass and Si substrates contain oxygen.

Table 4.18 W:S stoichiometries calculated from the EDX data.

Temperature / °C	Substrate	W:S stoichiometry
400	Glass	$WS_{2.1}$
400	Si	$WS_{1.9}$
450	Glass	$WS_{2.4}$
450	Si	$WS_{2.3}$
500	Glass	$WS_{2.5}$
500	Si	$WS_{1.9}$

4.3.5 AACVD of $[W(S_2CNEt_2)_4]$ (42) onto graphene

As complex **42** was successful at depositing WS_2 on glass and Si, further experiments were performed to evaluate the deposition of WS_2 on graphene. The direct deposition of WS_2 onto graphene is vitally important for the future manufacture of Van der Waals based heterostructures. Currently, most devices produced rely on the physical transfer of different layers on top of each other however; direct growth of layers on the underlying layer is much preferred as this technique is more efficient for large scale production. Graphene is an integral component in most Van der Waals heterostructures and therefore growth on this substrate would be highly beneficial. An added benefit of using graphene as a substrate is that both WS_2 and graphene have a hexagonal structure which could enhance the deposition of WS_2.[83]

Graphene substrates were produced by Andrew Rushworth and consisted of a piece of graphene approximately 1 cm^2 on a SiO_2/Si wafer (SiO_2 layer 300 nm thick) 2-3

cm^2 in size. The graphene was produced using the LPCVD of methane and hydrogen. In a standard experiment copper foil was treated with nitric acid, water and IPA. The cleaned foil was then loaded into a quartz reactor and annealed for 2 hours at 1100 °C under a flow of H_2 gas (15 sccm) at ~500 mbar. The temperature was then reduced to 1090 °C and a flow of methane (5 sccm) was introduced for 15 minutes. After the graphene growth period both gas flows were stopped and the copper foil was moved out of the furnace for rapid cooling.

The graphene was then transferred onto a SiO_2/Si wafer using the following method. In the first step, the graphene bearing copper foils were spin coated with PMMA. The uncoated side of the copper was then etched with nitric acid to remove unwanted graphene and then etched with an aqueous 0.25 M sodium persulfate solution to remove the copper. The PMMA-graphene stack was rinsed with de-ionised water, hydrochloric acid and then de-ionised water once again before the stack was floated onto the SiO_2/Si wafer. After drying in air for 30 minutes, the substrate was annealed at 150 °C for 15 minutes prior to the removal of PMMA using refluxing acetone (2 hours).

For the AACVD of WS_2 onto graphene, similar conditions as the depositions onto glass and Si were used. The aim of this work was to produce WS_2 films as thin as possible and hence the lowest deposition temperature of 400 °C was used to limit growth. Deposition times were also varied in an attempt to limit thin film growth.

Films were successfully deposited on the graphene substrates at deposition times of 60, 30, 15 and 10 minutes. Deposition times of less than 10 minutes did not yield any reasonable thin films. PXRD patterns of the films are displayed in Figure 4.43 with the (002)/(003), (004)/(006), (006)/(009) and (008)/(0012) Miller planes of 2H/3R-WS_2 labelled (2H - JCPDS card #87-2417,[66] 3R - JCPDS card #84-1399)[9]. Once again the phase of the material could not be determined due to both the 2H and 3R phases having very similar spectra. The major reflection corresponds to the (002)/(003) Miller plane for all films suggesting the S-W-S layers lie parallel to the substrate surface. In contrast to the films on glass and Si, the films on graphene display reflections with much greater intensity indicating an increase in crystallinity. This is supported by the appearance of the parallel reflections at (004)/(006), (006)/(009) and (008)/(0012). As deposition time reduces the intensity of the WS_2

peaks decreases and the intensity of the Si substrate peak at ~33° increases. This change in intensity suggests the WS_2 film gets thinner as deposition time is reduced.

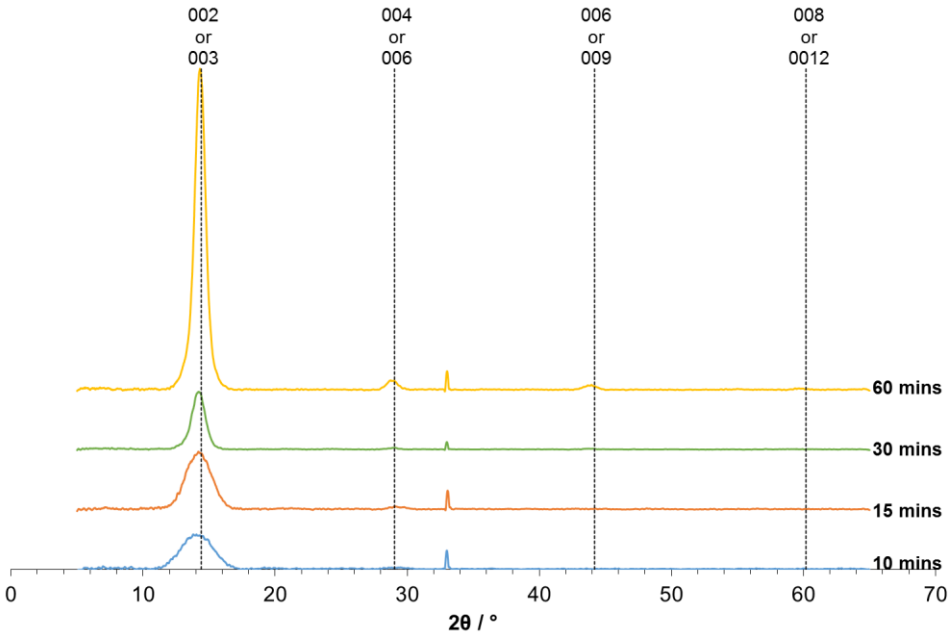

Figure 4.43 PXRD patterns for the films deposited on graphene using precursor **42**.

Raman spectra for the films deposited on graphene are presented in Figure 4.44 for the WS_2 region while Figure 4.45 displays the graphene region. All spectra exhibit the major E^1_{2g} (~355 cm^{-1}) and A_{1g} (~420 cm^{-1}) modes as well as a resonances at ~178, ~232, ~298, ~326, ~582 and ~702 cm^{-1} consistent with bulk WS_2.[81, 82] There is no evidence of any monolayer WS_2 or tungsten oxides. Similar to the PXRD patterns, the intensity of the Si substrate peak increases with decreasing deposition time which indicates the WS_2 films get thinner as the time reduces.

The spectra of the graphene region show the G and 2D peaks of the graphene are maintained suggesting the graphene is still intact even after deposition, there is no evidence of any increase in disorder.[84] The broad peak at 1200 – 1400 cm^{-1} indicates there is amorphous carbon present within the film, the peak intensity rises with increasing deposition time suggesting this is a by-product of WS_2 deposition.

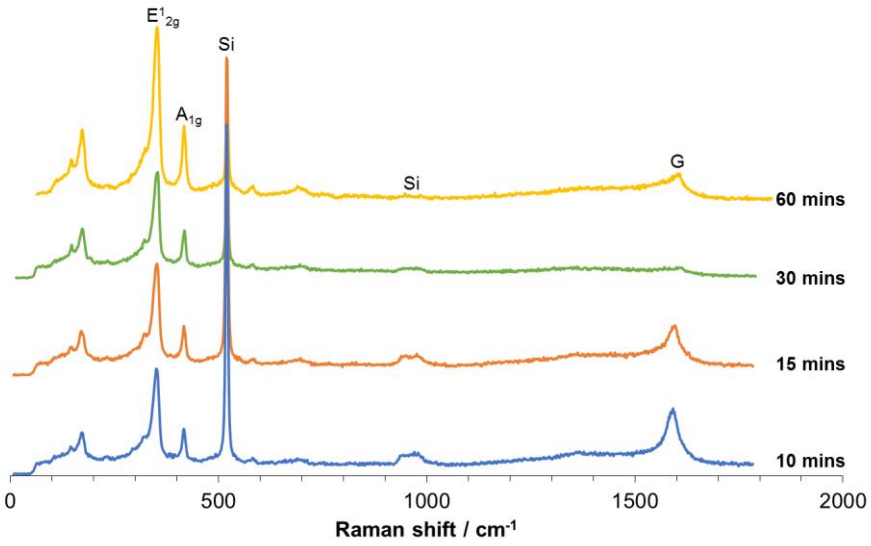

Figure 4.44 Raman spectra of the WS_2 region for the films deposited on graphene using precursor **42**.

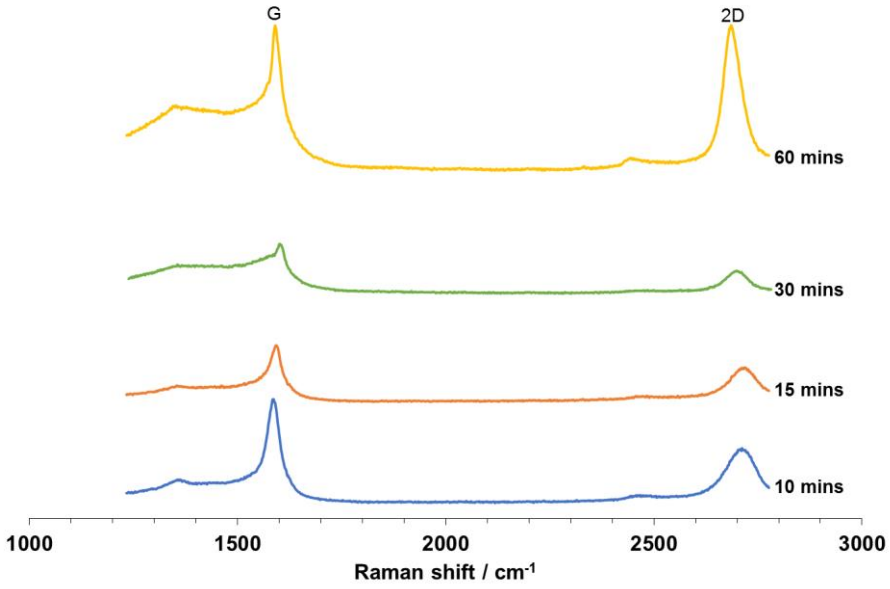

Figure 4.45 Raman spectra of the graphene region for the films deposited on graphene using precursor **42**.

SEM images of the films are displayed in Figure 4.46, the morphology of the films on graphene are considerably different to the films deposited on glass and Si. These films are more uniform and appear to be much flatter. There is also no evidence of any flakes or larger particles which were observed in the films on glass and Si. The film deposited at 60 minutes appears to show a number of crystallites embedded in

the film with raised ridges crossing most areas. These ridges are believed to be 'wrinkles' in the underlying graphene. The film deposited at 30 minutes has a similar appearance although the crystallites are smaller and there are much fewer ridges. A change in morphology is observed for the final two films at 15 and 10 minutes with the crystallites no longer visible. A number of 'wrinkles' are still present along with a number of very small particles sitting on top of the films. EDX analysis was carried out on the films but the films were too thin for reliable data to be recorded. The film deposited after 60 minutes did show the presence of both tungsten and sulfur.

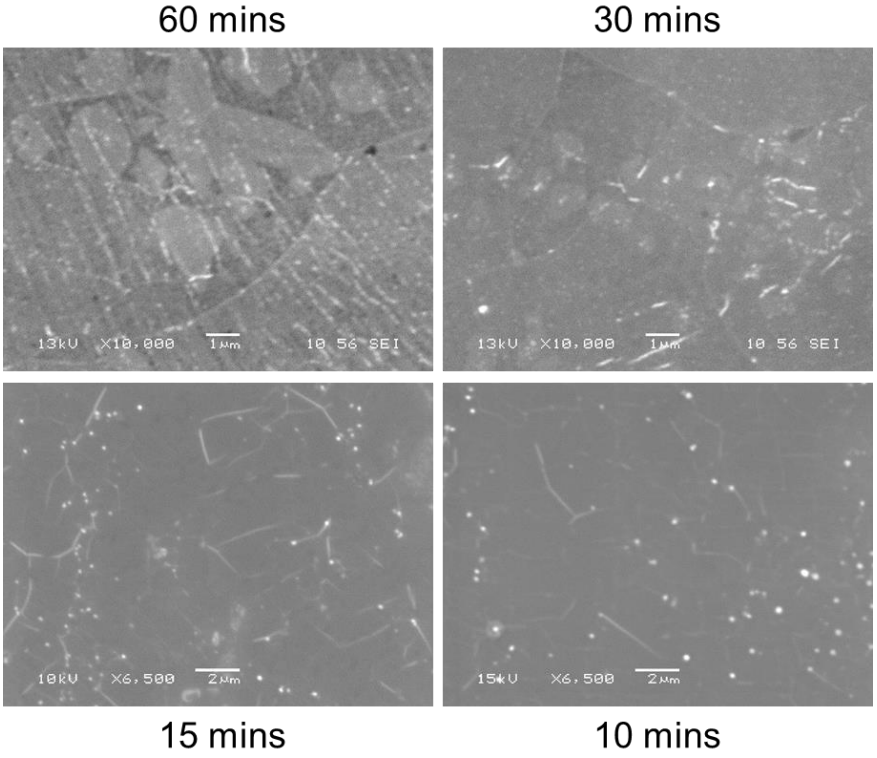

Figure 4.46 SEM images of the films deposited on graphene using precursor **42**.

AFM surface plots of the films are presented in Figure 4.47; the edges of the films were chosen so film thicknesses could be determined. The AFM surface plots support the observations from the SEM imaging with the films exhibiting extremely flat morphologies. The crystallites are again observed in the film deposited at 60 minutes and are slightly raised (~5 nm) above the rest of the film. The ridges are also raised above the film and form the highest points. The film deposited at 30 minutes shows a slightly different morphology to that observed in the SEM, with no crystallites visible and very few 'wrinkles'. There is quite a considerable build-up of particles on the surface of the film. Once again, the films at 15 and 10 minutes have

a similar morphology with no visible crystallites but a number of ‘wrinkles’ present. These ‘wrinkles’ along with some of the damaged parts of the films are the highest points.

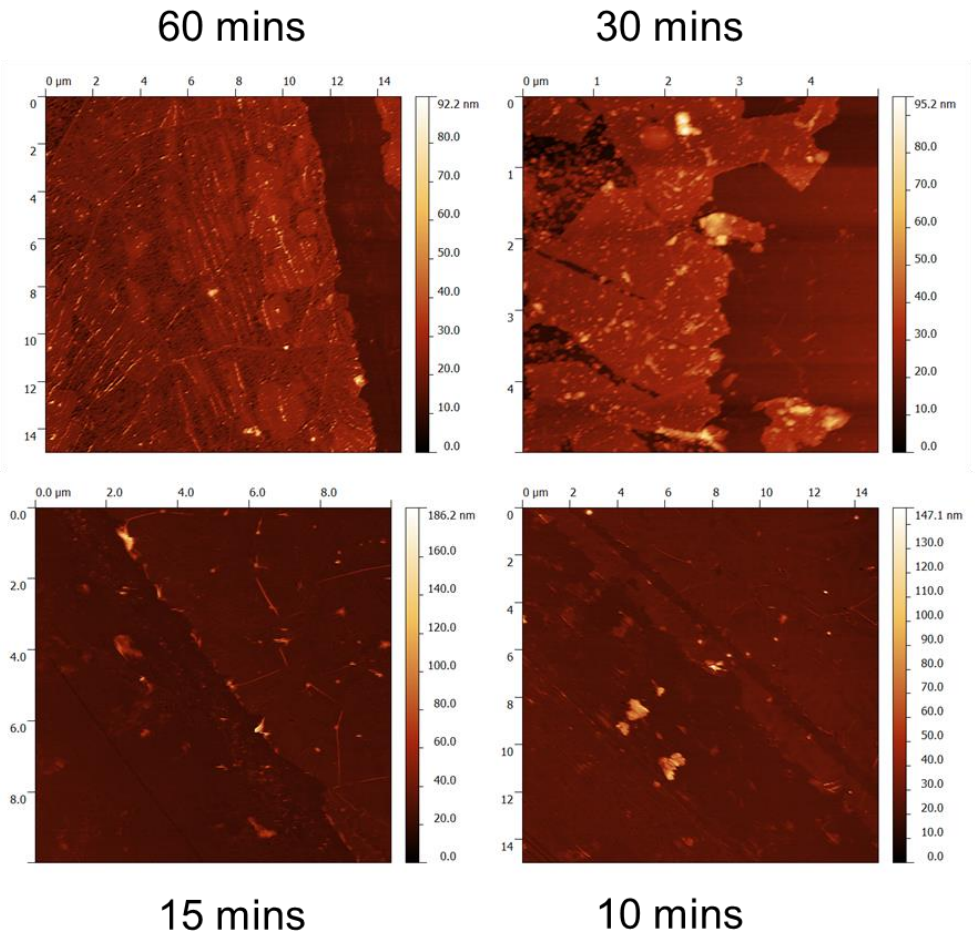

Figure 4.47 AFM surface plots of the films deposited on graphene using precursor **42**.

Films thicknesses (Figure 4.48) were determined by measuring the step height difference between the WS_2/graphene film and the SiO_2/Si substrate. A minimum film thickness of ~5 nm was attained for the film deposited after 10 minutes. Increasing the deposition time, increased the film thickness up to ~12 nm after 60 minutes of deposition.

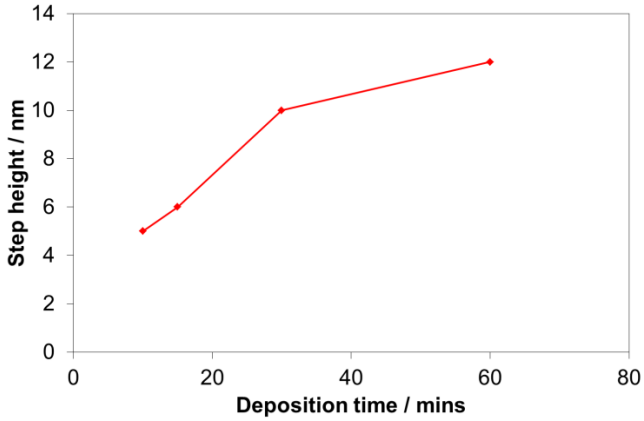

Figure 4.48 Step height plotted against deposition time for the films deposited on graphene using precursor **42**.

Closer visual inspection of the films using a microscope indicated that the WS_2 deposited preferentially on the graphene rather than the SiO_2/Si wafer at 400 °C. Figure 4.49 displays optical microscopy images of the substrates after deposition at 400 and 450 °C (deposition time - 60 minutes). The WS_2 has a distinct green colour which completely covers the graphene but not the SiO_2 at 400 °C, while at 450 °C both the graphene and SiO_2 are covered by WS_2. Raman spectroscopy of the film at 400 °C showed both WS_2 and graphene were present on the green areas while only trace amounts of WS_2 could be detected on the orange areas. For the film at 450 °C, WS_2 was found across both areas. This suggests that at 400 °C the WS_2 has a higher growth rate on graphene than it does on SiO_2.

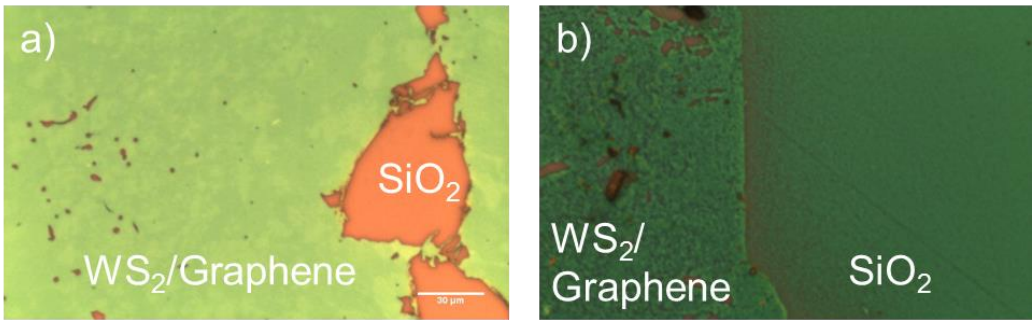

Figure 4.49 Optical microscopy images of the interface between the WS_2/graphene and SiO_2 at: a) 400 °C and b) 450 °C (Deposition time of 30 minutes).

A Raman map (Figure 4.50) of an interface region on the film deposited at 400 °C was performed to provide further evidence of preferential growth. Figure 4.50a shows an optical image of the area that was mapped with the greener WS_2/graphene

region taking up the majority of the image on the left hand side. The maps clearly show that the WS_2 is mainly confined to the area of graphene observed in the optical image. These results suggest that WS_2 preferentially grows on graphene rather than SiO_2 at 400 °C; this is likely due to both materials adopting a hexagonal structure.

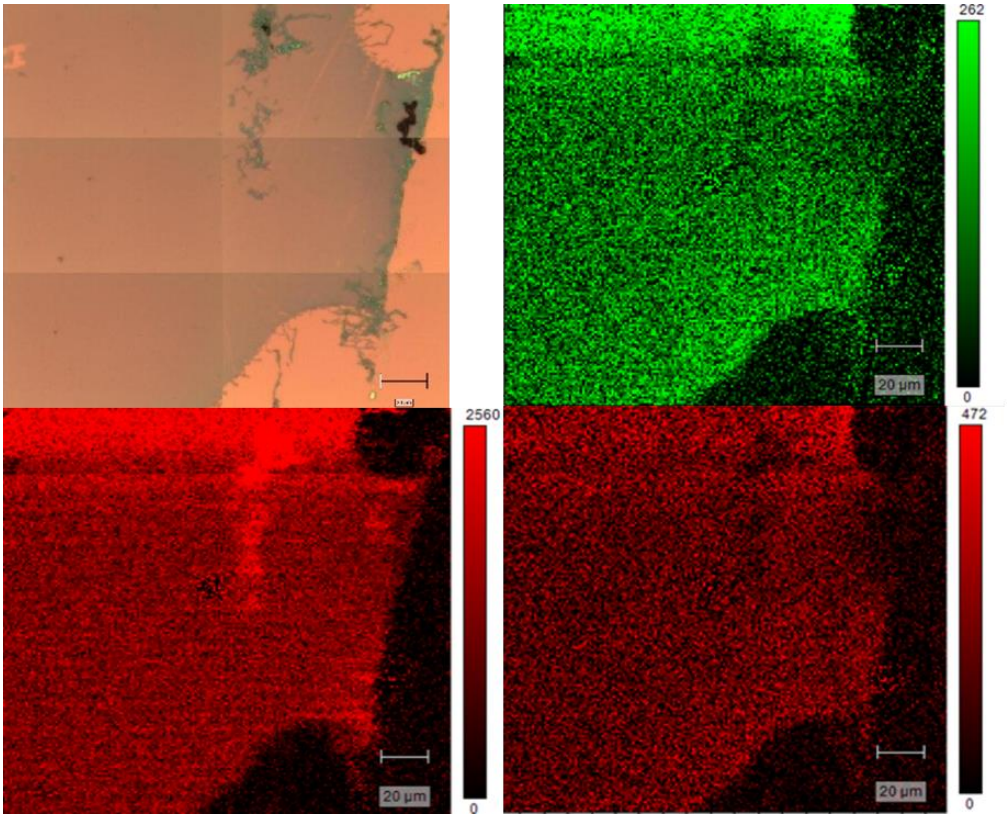

Figure 4.50 a) Optical image of mapped area – sample deposited at 400 °C; b) map of WS_2 E^1_{2g} mode intensity; c) map of graphene G mode intensity; d) map of graphene 2D mode intensity.

4.4 Group VI xanthates

The only evidence of homoleptic molybdenum or tungsten xanthate complexes containing a single metal centre in the literature is the patent by Nagatomi *et al.* which describes the synthesis of molybdenum(IV) xanthate species, $[Mo(S_2COR)_4]$, by the reaction of $MoCl_5$ and KS_2COR in DCM.[85] Beyond this patent, homoleptic species such as $[Mo_2(S_2COEt)_4]$ contain two molybdenum atoms with the xanthates acting as bridging ligands.[86] The vast majority of group VI xanthate species are heteroleptic with most being the oxo derivatives e.g. $[MoO_2(S_2CNEt_2)]$.[87, 88] The work in this section will focus on the synthesis of homoleptic group VI xanthate complexes containing a single metal centre.

4.4.1 Synthesis and characterisation

The molybdenum ethyl xanthate complex, $[Mo(S_2COEt)_4]$ (**43**), was synthesised by the reaction between molybdenum(V) chloride and five equivalents of potassium ethyl xanthate in DCM (Scheme 4.7).[85] After stirring the reaction for 18 hours the resulting purple mixture was filtered and the remaining liquor was layered with hexane to form purple crystals. The IR spectrum displayed a C-S stretching mode at 997 cm^{-1} indicating the xanthate had been formed.[74] Elemental analysis results were consistent with the calculated values.

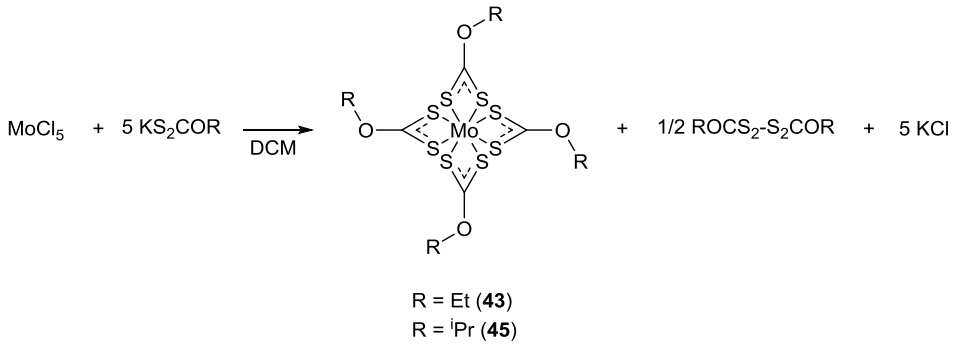

Scheme 4.7 Reaction scheme for the synthesis of **43** and **45**.

Addition of carbon disulfide to a stirring solution of potassium hydroxide in IPA provided the yellow potassium iso-propyl xanthate salt, KS_2CO^iPr (**44**). Reaction of five equivalents of compound **44** and molybdenum(V) chloride in DCM (Scheme 4.7) resulted in a purple mixture. Filtration of the reaction mixture and storage of the liquor at -28 °C provided a small number of dark purple crystals of $[Mo(S_2CO^iPr)_4]$ (**45**). Due to the very low yield of crystals, complex **45** was only analysed using single crystal X-ray crystallography.

Reactions to form the molybdenum *n*-butyl xanthate formed a purple mixture but the identity of the product could not be determined. The analogous reaction between tungsten(VI) chloride and six equivalents of the ethyl, iso-propyl or *n*-butyl potassium xanthate salts resulted in the formation of a green suspension, the identity of this product could not be determined.

Single crystal X-ray diffraction provided the molecular structures of complexes **43** and **45** (Figure 4.51) which are essentially isostructural with only slight differences in the orientation of some of the R groups. Both complexes crystallised in the

monoclinic $P2_1/n$ space group with two molecules inhabiting the asymmetric unit, the following discussion focusses on the molecule containing Mo(1). Each metal centre adopted an 8-coordinate distorted square antiprismatic geometry with all ligands binding via the bidentate κ^2-*S*,*S* mode.

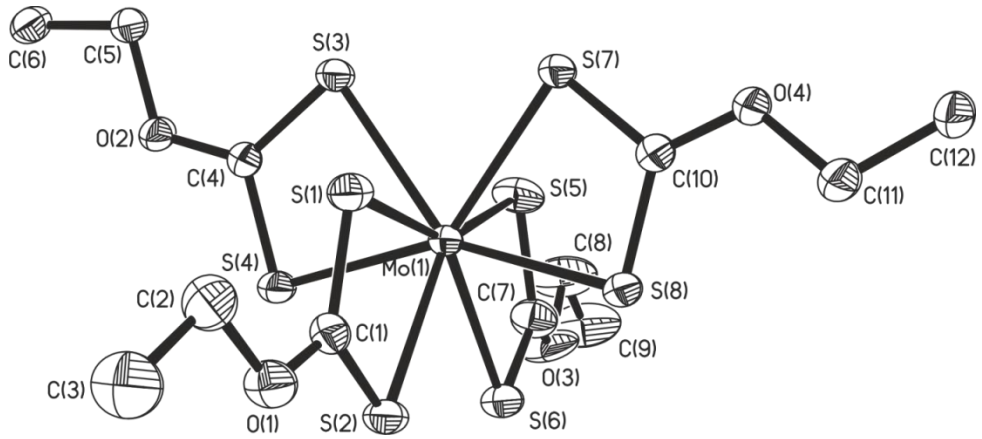

Figure 4.51 Molecular structure of complex **43**, complex **45** is isostructural. Thermal ellipsoids are shown at 50 % probability, with all hydrogen atoms omitted for clarity.

The bond lengths (Table 4.19) and angles (Table 4.20) displayed within both complexes are essentially equivalent except for some of the C-O bonds in complex **43** which are slightly shorter. The Mo-S and C-S bonds are shorter in the xanthate complexes than those observed in the dithiocarbamate complex, **41**. Much like the dithiocarbamate complex, the Mo-S bond lengths vary within each ligand with one being shorter and the other being longer. The sum of the angles around the $\{S_2CO\}$ carbon atom in all of the ligands equals ~360° indicating the carbon atom is sp^2 hybridised. The S_2C-O bonds are considerably shorter than the O-C_R bonds which indicates the oxygen lone pairs are partially delocalised across the S_2C-O bond.

Table 4.19 Selected bond lengths for **43** and **45** with e.s.d.s. in parenthesis.

Bond	**Bond length / Å**	
	43 (R = Et)	**45 (R = ^{i}Pr)**
Mo-S	2.4987(7) - 2.5643(7)	2.4971(10) - 2.5609(10)
S-C	1.671(3) - 1.691(3)	1.667(4) - 1.697(4)
C-O	1.210(18) - 1.328(3)	1.320(5) - 1.334(4)
O-C_R	1.455(3) - 1.48(2)	1.468(5) - 1.492(4)

Table 4.20 Selected bond angles for **43** and **45** with e.s.d.s. in parenthesis.

Angle	Bond angle / °	
	43 (R = Et)	**45 (R = ^{i}Pr)**
S-Mo-S	67.50(2) - 67.79(2)	67.20(3) - 67.74(3)
Mo-S-C	87.81(9) - 90.30(11)	88.09(13) - 90.87(13)
S-C-S	113.50(18) - 114.15(17)	112.6(2) - 113.5(2)
S-C-O	119.0(2) - 127.2(2)	118.6(3) - 127.9(3)
C-O-C_R	117.3(2) - 121.3(13)	117.7(3) - 119.4(3)

4.4.2 Thermogravimetric analysis

The TGA trace for the decomposition of complex **43** is displayed in Figure 4.52 with a summary of the data presented in Table 4.21. Complex **43** underwent decomposition at a considerably lower temperature than the corresponding dithiocarbamate (**41**), similar trends are seen in nickel xanthates/dithiocarbamates.[89] An initial mass loss of ~7 % occurred between 100 and 110 °C before the major mass loss event of ~43 % between 110 and 190 °C. Further decomposition up to 360 °C saw the loss of a further ~16 % to provide a final percentage weight of 33.8 % which is higher than the expected value of 27.6 %.

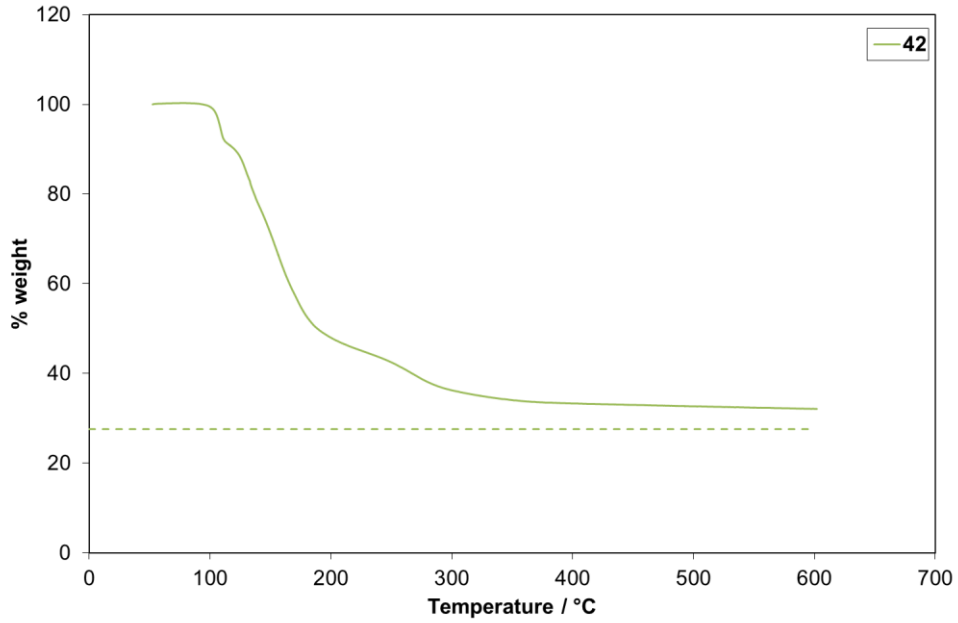

Figure 4.52 TGA trace for **43** in a closed pan. Dashed line represents the expected % weight for MoS_2.

Table 4.21 Summary of TGA data for **43**.

Compound	Onset / °C	End point / °C	% weight expected for MoS_2	Final % weight
43	100	360	27.6	33.8

TGA-MS of complex **43** provided the major mass fragments exhibited in Figure 4.53, possible ion fragment assignments are displayed in Table 4.22. The major mass peak observed between 90 and 190 °C is the peak at 60 m/z which likely corresponds to the loss of OCS. Other major mass peaks observed in the range 110 to 320 °C are those at 26, 27 and 29 m/z which could be the loss of the ethyl group as the fragments $C_2H_2^+$, $C_2H_3^+$ and $C_2H_5^+$ respectively. It was not possible to detect whether there was ethene present as the peak at 28 m/z also corresponds to atmospheric nitrogen which exists in much higher concentrations. A further peak at 76 m/z suggests that CS_2 is also lost in the decomposition. Metal xanthates are reported to decompose by the Chugaev elimination reaction with the loss of the R group as an alkene, OCS and H_2S.[89] Within the TGA-MS spectra there is evidence for the loss of the ethyl group and OCS but no H_2S was observed. These results suggest that complex **43** was probably decomposing by a range of different pathways.

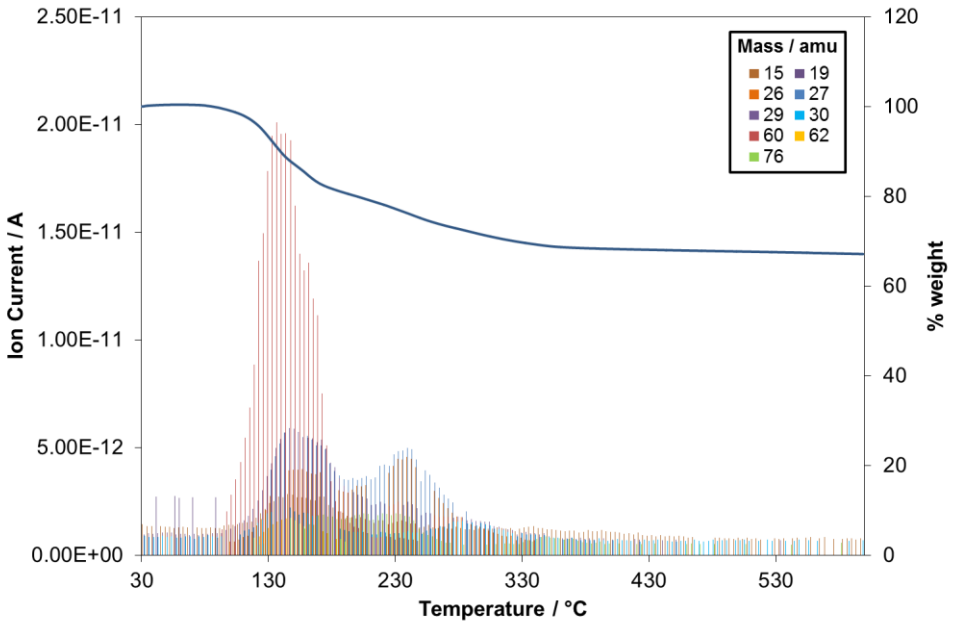

Figure 4.53 TGA-MS results for **43**: graph shows the major ion fragments present as temperature is increased, TGA trace is overlaid.

Table 4.22 Possible ion fragment assignment for the decomposition of **43**.

Mass / m/z	Fragment
15	CH_3^+
26	$C_2H_2^+$
27	$C_2H_3^+$
29	$C_2H_5^+$
30	$C_2H_6^+$
60	OCS^+
76	CS_2^+

4.4.3 AACVD of $[Mo(S_2COEt)_4]$ (43)

Due to a lower decomposition temperature than the dithiocarbamate complex, **41**, the xanthate complex **43** was investigated as a precursor for AACVD. Depositions onto glass and Si substrates were performed for 90 minutes with a 0.01 M solution of **43** in toluene. Golden brown films were successfully deposited at 300, 350, 400 and 450 °C on glass and at 350, 400 and 450 °C on Si (Figure 4.53), depositions at 300 °C on Si and at 250 °C on both glass and Si were unsuccessful.

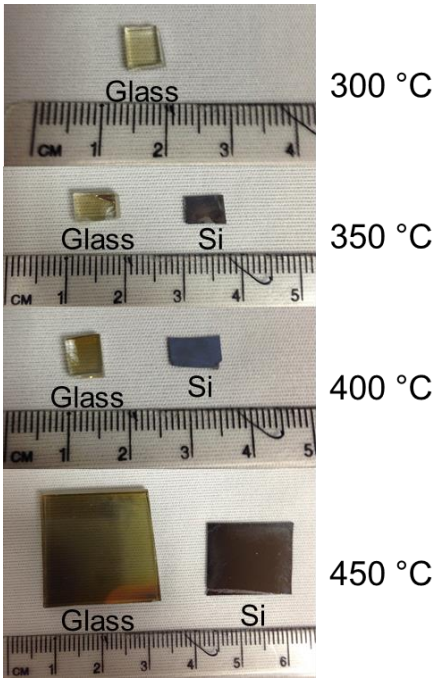

Figure 4.54 Images of films deposited on glass and Si from the AACVD of **43**.

PXRD patterns of the successfully deposited films are displayed in Figure 4.55 with the labelled reflection at ~14.4° corresponding to the (002) or (003) Miller plane in 2H- or 3R-MoS_2 respectively (2H - 14.402° = (002) - JCPDS card #87-2416,[66] 3R - 14.453° = (003) - JCPDS card #89-5112)[67]. The peaks at 33, 38.1 and 44.3° are attributed to the silicon substrate. Films deposited on glass at 300, 350 and 400 °C showed no reflections indicating they are amorphous. The films on glass at 450 °C and on Si at 350 and 400 °C presented major reflections at ~14.4° for the (002)/(003) plane indicating the presence of crystalline MoS_2 with the S-Mo-S layers lying parallel to the substrate surface. The single reflection in the spectra does not give enough information to distinguish between the 2H or 3R phases of MoS_2. The film on Si at 450 °C displayed the reflection at ~14.4° but the most intense peak was found at ~32.8° which is indicative of the (100) plane of 2H-MoS_2. The greater intensity of the (100) reflection compared to the (002) reflection indicates the film is orientated with the S-Mo-S layers orientated perpendicular to the substrate surface.[27, 76]

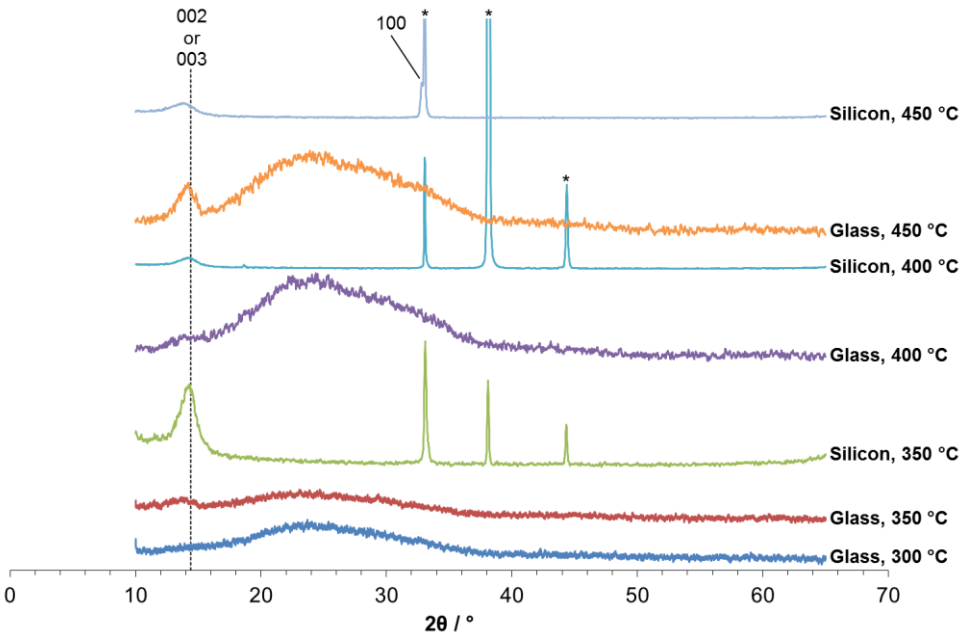

Figure 4.55 PXRD patterns for the films deposited from **43**; *Si substrate peaks.

Raman spectra of all the successfully deposited films are shown in Figure 4.56 with the major E^1_{2g} and A_{1g} resonances of bulk MoS_2 labelled. All films display these bulk MoS_2 resonances suggesting MoS_2 has been deposited even for the more amorphous films. There were no peaks corresponding to oxide formation recorded.[77]

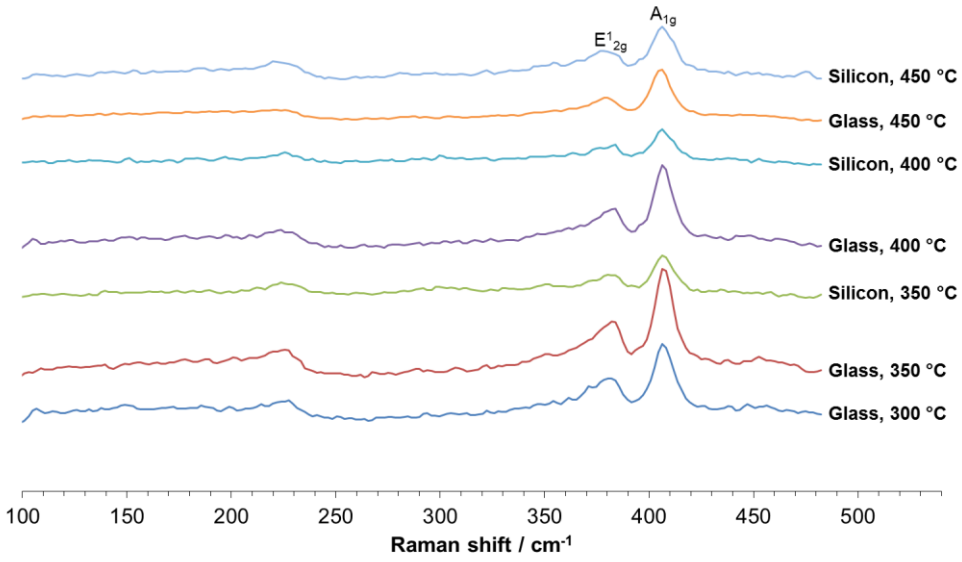

Figure 4.56 Raman spectra of the films deposited from **43**.

The morphology of the films deposited from **43** (Figure 4. 57) varies little with temperature and substrate unlike those deposited from **41**. Films on both glass and silicon are composed of small particles which create relatively uniform layers. Increasing temperature for the films on glass reduces the size of these particles while on Si they remain relatively the same size over the temperature range. Film thicknesses varied from ~50 to ~1000 nm on glass while on Si they varied from about ~80 to ~150 nm.

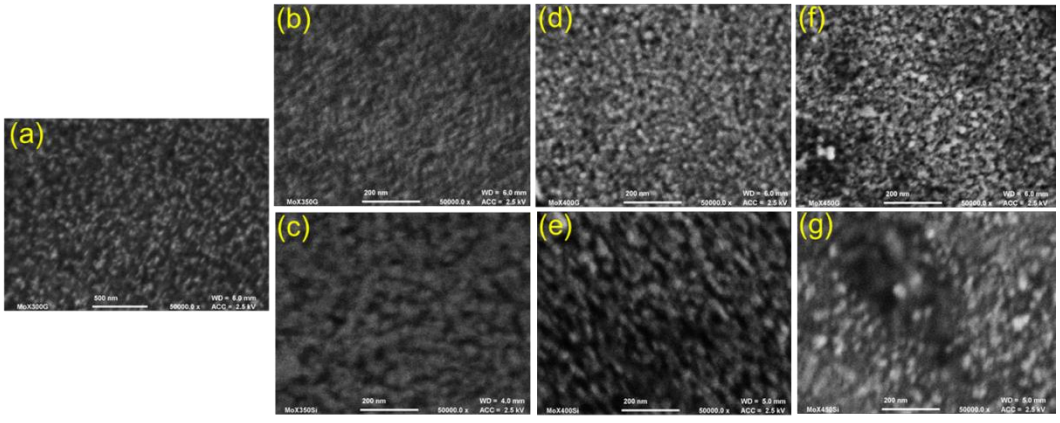

Figure 4. 57 SEM images of films deposited from **43** on glass at (a) 300 °C, (b) 350 °C, (d) 400 °C and (f) 450 °C, and on silicon at (c) 350 °C, (e) 400 °C and (g) 450 °C.

EDX analysis showed both molybdenum and sulfur were present in all of the films, Mo:S stoichiometries are listed in Table 4.23. The films deposited at 350, 400 and

450 °C all provided Mo:S stoichiometries close to 1:2 indicating MoS_2 had been deposited. In contrast, the film deposited on glass at 300 °C exhibited a lower Mo:S ratio of 1:1.2 suggesting the films were sulfur deficient. The highest Mo:S ratios were achieved at 400 °C for the films deposited on both substrates suggesting this was the optimum deposition temperature. There was a small amount of carbon contamination within each film although this is common for films deposited using AACVD.[80] The oxygen content of the films could not be determined as both the glass and Si substrates contain oxygen.

Table 4.23 Mo:S stoichiometries calculated from the EDX data.

Temperature / °C	Substrate	Mo:S stoichiometry
300	Glass	$MoS_{1.2}$
350	Glass	$MoS_{1.7}$
350	Si	$MoS_{1.6}$
400	Glass	$MoS_{1.9}$
400	Si	$MoS_{2.0}$
450	Glass	$MoS_{1.8}$
450	Si	$MoS_{1.8}$

4.5 Conclusion

A range of group VI metal thioureide complexes have been synthesised by either the substitution reaction between a bis(*tert*-butylimido)-bis(amido) group VI metal complex and a *N,N'*-disubstituted thiourea or the insertion reaction between isothiocyanates and the bis(*tert*-butylimido)-bis(dimethylamido) group VI metal complexes.

The reaction between $[(^tBuN)_2Mo(NMe_2)_2]$ (**26**) and two equivalents of the methyl, ethyl and *n*-butyl disubstituted thioureas forms the bis(*tert*-butylimido)-bis(thioureide)molybdenum complexes **28**, **29** and **30** where the thioureide ligands bind via the κ^2-*S,N* mode. In contrast, the analogous reaction between $[(^tBuN)_2W(NH^tBu)_2]$ (**27**) and two equivalents of the methyl, ethyl and *n*-butyl disubstituted thioureas forms the (*tert*-butylimido)(*tert*-butylamido)bis(thioureide)tungsten complexes **31**, **32** and **33** where one of the imido

groups is replaced with an amido group and the thioureide ligands bind via the κ^2-*S,N* and κ^2-*N,N* modes. The reaction of $[(^tBuN)_2W(NH^tBu)_2]$ (**27**) and two equivalents of the 1,3-di-*tert*-butyl-2-thiourea forms the sulfur bridged tungsten(V) complex $[\{(^tBuN)W(SC\{NH^tBu\}N^tBu)(\mu\text{-}S)\}_2]$ (**34**), which contains a W-W single bond and both thioureide ligands in the κ^2-*S,N* mode.

The insertion reaction between $[(^tBuN)_2M(NMe_2)_2]$ (Mo (**26**), W (**36**)) and two equivalents of iso-propyl or phenyl isothiocyanates forms the 1:2 insertion products **37**, **38**, **39** and **40**. Both isothiocyanates insert into the M-NMe_2 bond to form the thioureide ligand that binds via the κ^2-*S,N* mode. Reactions with the *tert*-butyl isothiocyanate were unsuccessful.

The majority of group VI metal thioureide complexes provided final percentage weights quite close to the values expected for MS_2 in the TGA suggesting they could be viable precursors. AACVD experiments with the iso-propyl molybdenum (**37**) and tungsten (**38**) complexes provided films with elemental ratios of $MoS_{0.7}C_{0.2}N_{3.2}$ and $WS_{0.3}O_{0.2}N_{0.6}$ respectively. Some MS_2 was detected but the films were determined to be a mixture of various species. Annealing of these films under a nitrogen atmosphere formed the corresponding metal oxide.

The molybdenum(IV) and tungsten(IV) diethyldithiocarbamate complexes **41** and **42** were synthesised by the reaction between the metal hexacarbonyl and two equivalents of the tetraethylthiuram disulfide. Thermogravimetric analysis indicated both complexes decompose to form the corresponding MS_2. Using AACVD, crystalline MS_2 with the S-M-S layers lying parallel to the substrate surface were deposited on glass and Si substrates over the temperature range 400 – 500 °C. Further deposition studies with the tungsten complex, **42**, deposited crystalline WS_2 films ~5 to 12 nm thick onto graphene substrates. At 400 °C complex **42** preferentially deposited WS_2 on graphene rather than SiO_2.

The homoleptic molybdenum(IV) ethyl (**43**) and iso-propyl (**45**) xanthate complexes have been synthesised from the reaction between molybdenum(V) chloride and the corresponding potassium xanthate salts. Structural characterisation showed both complexes to adopt an 8-coordinate distorted square antiprismatic geometry with all xanthate ligands binding by the κ^2-*S,S* mode. AACVD experiments with the ethyl complex, **43**, successfully deposited crystalline MoS_2 on Si at 350, 400 and 450 °C

and on glass at 450 °C. Amorphous films of MoS_2 were deposited on glass at 300, 350 and 400 °C.

The reactions and complexes presented in Chapter 4 are summarised below in Figure 4.58.

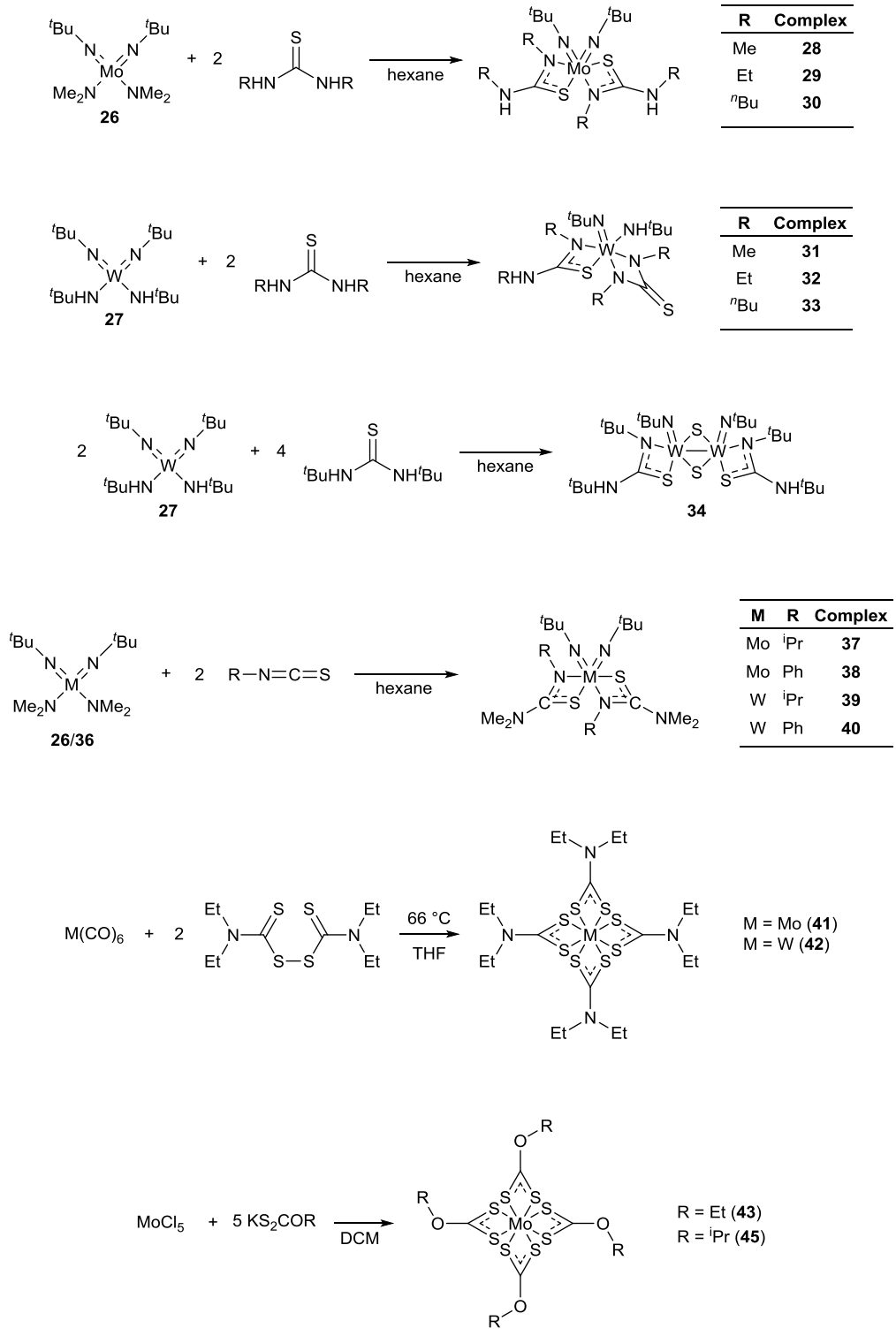

Figure 4.58 Summary of reactions and complexes presented within Chapter 4.

4.6 References

1. A. B. Laursen, S. Kegnaes, S. Dahl and I. Chorkendorff, *Energy Environ. Sci.*, 2012, **5**, 5577-5591.
2. M. A. Lukowski, A. S. Daniel, C. R. English, F. Meng, A. Forticaux, R. J. Hamers and S. Jin, *Energy Environ. Sci.*, 2014, **7**, 2608-2613.
3. M. A. Lukowski, A. S. Daniel, F. Meng, A. Forticaux, L. Li and S. Jin, *J. Am. Chem. Soc.*, 2013, **135**, 10274-10277.
4. B. Radisavljevic, A. Radenovic, J. Brivio, V. Giacometti and A. Kis, *Nat. Nanotechnol.*, 2011, **6**, 147-150.
5. S. Das, J. A. Robinson, M. Dubey, H. Terrones and M. Terrones, *Annu. Rev. Mater. Res.*, 2015, **45**, 1-27.
6. M. Chhowalla, H. S. Shin, G. Eda, L. J. Li, K. P. Loh and H. Zhang, *Nat. Chem.*, 2013, **5**, 263-275.
7. A. Ambrosi, Z. Sofer and M. Pumera, *Chem. Commun.*, 2015, **51**, 8450-8453.
8. F. Jellinek, G. Brauer and H. Muller, *Nature*, 1960, **185**, 376-377.
9. W. J. Schutte, J. L. De Boer and F. Jellinek, *J. Solid State Chem.*, 1987, **70**, 207-209.
10. J. C. Wildervanck and F. Jellinek, *Z. Anorg. Allg. Chem.*, 1964, **328**, 309-318.
11. R. Kappera, D. Voiry, S. E. Yalcin, B. Branch, G. Gupta, A. D. Mohite and M. Chhowalla, *Nat. Mater.*, 2014, **13**, 1128-1134.
12. K. F. Mak, C. Lee, J. Hone, J. Shan and T. F. Heinz, *Phys. Rev. Lett.*, 2010, **105**, 136805.
13. Q. H. Wang, K. Kalantar-Zadeh, A. Kis, J. N. Coleman and M. S. Strano, *Nat. Nanotechnol.*, 2012, **7**, 699-712.
14. S. Bertolazzi, J. Brivio and A. Kis, *ACS Nano*, 2011, **5**, 9703-9709.
15. W. Park, J. Baik, T.-Y. Kim, K. Cho, W.-K. Hong, H.-J. Shin and T. Lee, *ACS Nano*, 2014, **8**, 4961-4968.
16. J. Zhang, H. Yu, W. Chen, X. Tian, D. Liu, M. Cheng, G. Xie, W. Yang, R. Yang, X. Bai, D. Shi and G. Zhang, *ACS Nano*, 2014, **8**, 6024-6030.
17. M. R. Laskar, L. Ma, S. Kannappan, P. Sung Park, S. Krishnamoorthy, D. N. Nath, W. Lu, Y. Wu and S. Rajan, *Appl. Phys. Lett.*, 2013, **102**, -.
18. S. Najmaei, Z. Liu, W. Zhou, X. Zou, G. Shi, S. Lei, B. I. Yakobson, J.-C. Idrobo, P. M. Ajayan and J. Lou, *Nat. Mater.*, 2013, **12**, 754-759.
19. A. M. van der Zande, P. Y. Huang, D. A. Chenet, T. C. Berkelbach, Y. You, G.-H. Lee, T. F. Heinz, D. R. Reichman, D. A. Muller and J. C. Hone, *Nat. Mater.*, 2013, **12**, 554-561.
20. S. Balendhran, J. Z. Ou, M. Bhaskaran, S. Sriram, S. Ippolito, Z. Vasic, E. Kats, S. Bhargava, S. Zhuiykov and K. Kalantar-zadeh, *Nanoscale*, 2012, **4**, 461-466.
21. Y.-H. Lee, L. Yu, H. Wang, W. Fang, X. Ling, Y. Shi, C.-T. Lin, J.-K. Huang, M.-T. Chang, C.-S. Chang, M. Dresselhaus, T. Palacios, L.-J. Li and J. Kong, *Nano Lett.*, 2013, **13**, 1852-1857.
22. Y.-H. Lee, X.-Q. Zhang, W. Zhang, M.-T. Chang, C.-T. Lin, K.-D. Chang, Y.-C. Yu, J. T.-W. Wang, C.-S. Chang, L.-J. Li and T.-W. Lin, *Adv. Mater.*, 2012, **24**, 2320-2325.
23. W. Zhang, J.-K. Huang, C.-H. Chen, Y.-H. Chang, Y.-J. Cheng and L.-J. Li, *Adv. Mater.*, 2013, **25**, 3456-3461.

24. X. Ling, Y.-H. Lee, Y. Lin, W. Fang, L. Yu, M. S. Dresselhaus and J. Kong, *Nano Lett.*, 2014, **14**, 464-472.
25. S. Tongay, W. Fan, J. Kang, J. Park, U. Koldemir, J. Suh, D. S. Narang, K. Liu, J. Ji, J. Li, R. Sinclair and J. Wu, *Nano Lett.*, 2014, **14**, 3185-3190.
26. Y. Zhan, Z. Liu, S. Najmaei, P. M. Ajayan and J. Lou, *Small*, 2012, **8**, 966-971.
27. W. Hofmann, *J. Mater. Sci.*, 1988, **23**, 3981-3986.
28. N. Imanishi, K. Kanamura and Z. Takehara, *J. Electrochem. Soc.*, 1992, **139**, 2082-2087.
29. X.-L. Li, J.-P. Ge and Y.-D. Li, *Chem. Eur. J.*, 2004, **10**, 6163-6171.
30. X. Zhang, F. Meng, J. R. Christianson, C. Arroyo-Torres, M. A. Lukowski, D. Liang, J. R. Schmidt and S. Jin, *Nano Lett.*, 2014, **14**, 3047-3054.
31. J. Cheon, J. E. Gozum and G. S. Girolami, *Chem. Mater.*, 1997, **9**, 1847-1853.
32. S. Otsuka, M. Kamata, K. Hirotsu and T. Higuchi, *J. Am. Chem. Soc.*, 1981, **103**, 3011-3014.
33. T. Ouyang, K. P. Loh, H. Zhang, J. J. Vittal, M. Vetrichelvan, W. Chen, X. Gao and A. T. S. Wee, *J. Phys. Chem. B*, 2004, **108**, 17537-17545.
34. J. Zhang, J. M. Soon, K. P. Loh, J. Yin, J. Ding, M. B. Sullivian and P. Wu, *Nano Lett.*, 2007, **7**, 2370-2376.
35. H. Zhang, K. P. Loh, C. H. Sow, H. Gu, X. Su, C. Huang and Z. K. Chen, *Langmuir*, 2004, **20**, 6914-6920.
36. K. P. Loh, H. Zhang, W. Z. Chen and W. Ji, *J. Phys. Chem. B*, 2005, **110**, 1235-1239.
37. A. Adeogun, M. Afzaal and P. O'Brien, *Chem. Vap. Deposition*, 2006, **12**, 597-599.
38. M. N. McCain, B. He, J. Sanati, Q. J. Wang and T. J. Marks, *Chem. Mater.*, 2008, **20**, 5438-5443.
39. N. Al-Dulaimi, D. J. Lewis, X. L. Zhong, M. Azad Malik and P. O'Brien, *J. Mater. Chem. C*, 2016, **4**, 2312-2318.
40. D. J. Lewis, A. A. Tedstone, X. L. Zhong, E. A. Lewis, A. Rooney, N. Savjani, J. R. Brent, S. J. Haigh, M. G. Burke, C. A. Muryn, J. M. Raftery, C. Warrens, K. West, S. Gaemers and P. O'Brien, *Chem. Mater.*, 2015, **27**, 1367-1374.
41. N. Savjani, J. R. Brent and P. O'Brien, *Chem. Vap. Deposition*, 2015, **21**, 71-77.
42. B. Olofinjana, *J. Mod. Phys.*, 2011, **02**, 341-349.
43. J. P. Shupp, A. S. Kinne, H. D. Arman and Z. J. Tonzetich, *Organometallics*, 2014.
44. A. Pearce, PhD Thesis, University of Manchester, 2014.
45. J. Guo, X. Chen, Y. Yi, W. Li and C. Liang, *RSC Adv.*, 2014, **4**, 16716-16720.
46. M. Shanmugam, T. Bansal, C. A. Durcan and B. Yu, *Appl. Phys. Lett.*, 2012, **101**.
47. C. J. Carmalt, I. P. Parkin and E. S. Peters, *Polyhedron*, 2003, **22**, 1499-1505.
48. J. W. Chung, Z. R. Dai and F. S. Ohuchi, *J. Cryst. Growth*, 1998, **186**, 137-150.
49. N. Peimyoo, J. Shang, C. Cong, X. Shen, X. Wu, E. K. L. Yeow and T. Yu, *ACS Nano*, 2013, **7**, 10985-10994.

50. U. Bodensieck, Y. Carraux, H. Stoeckli-Evans and G. Süss-Fink, *Inorg. Chim. Acta*, 1992, **195**, 135-137.
51. V. C. Gibson, C. Redshaw, W. Clegg and M. R. J. Elsegood, *J. Chem. Soc., Chem. Commun.*, 1994, 2635-2636.
52. H.-W. Lam, G. Wilkinson, B. Hussain-Bates and M. B. Hursthouse, *J. Chem. Soc., Dalton Trans.*, 1993, 781-788.
53. R. S. Pilato, K. A. Eriksen, E. I. Stiefel and A. L. Rheingold, *Inorg. Chem.*, 1993, **32**, 3799-3800.
54. P. W. Dyer, V. C. Gibson, J. A. K. Howard, B. Whittle and C. Wilson, *Polyhedron*, 1995, **14**, 103-111.
55. V. Miikkulainen, M. Suvanto and T. A. Pakkanen, *Chem. Mater.*, 2006, **19**, 263-269.
56. W. A. Nugent, *Inorg. Chem.*, 1983, **22**, 965-969.
57. R. Glaser, R. Hillebrand, W. Wycoff, C. Camasta and K. S. Gates, *J. Org. Chem.*, 2015, **80**, 4360-4369.
58. A. S. Batsanov, A. E. Goeta, J. A. K. Howard, A. K. Hughes, A. L. Johnson and K. Wade, *J. Chem. Soc., Dalton Trans.*, 2001, 1210-1217.
59. M. Herberhold, W. Jellen and M. L. Ziegler, *Inorg. Chim. Acta*, 1986, **118**, 15-20.
60. S. E. d'Arbeloff, P. B. Hitchcock, J. F. Nixon, T. Nagasawa, H. Kawaguchi and K. Tatsumi, *J. Organomet. Chem.*, 1998, **564**, 189-191.
61. V. P. Fedin, I. V. Kalinina, D. G. Samsonenko, Y. V. Mironov, M. N. Sokolov, S. V. Tkachev, A. V. Virovets, N. V. Podberezskaya, M. R. J. Elsegood, W. Clegg and A. G. Sykes, *Inorg. Chem.*, 1999, **38**, 1956-1965.
62. M. G. B. Drew, R. J. Hobson, P. P. E. M. Mumba, D. A. Rice and N. Turp, *J. Chem. Soc., Dalton Trans.*, 1987, 1163-1167.
63. R. M. Pike, *J. Org. Chem.*, 1961, **26**, 232-236.
64. J. S. Becker, S. Suh, S. Wang and R. G. Gordon, *Chem. Mater.*, 2003, **15**, 2969-2976.
65. I. Y. Ahmet, M. S. Hill, A. L. Johnson and L. M. Peter, *Chem. Mater.*, 2015, **27**, 7680-7688.
66. V. L. Kalikhman, *Izv. Akad. Nauk SSSR, Neorg. Mater.*, 1983.
67. B. Schönfeld, J. J. Huang and S. C. Moss, *Acta Crystallogr., Sect. B*, 1983, **39**, 404-407.
68. G. Andersson, A. Magnéli, L. G. Sillén and M. Rottenberg, *Acta Chem. Scand.*, 1950, **4**, 793-797.
69. A. M. Stacy and D. T. Hodul, *J. Phys. Chem. Solids*, 1985, **46**, 405-409.
70. L. Seguin, M. Figlarz, R. Cavagnat and J. C. Lassègues, *Spectrochim. Acta, Part A*, 1995, **51**, 1323-1344.
71. J. Gabrusenoks, A. Veispals, A. von Czarnowski and K. H. Meiwes-Broer, *Electrochim. Acta*, 2001, **46**, 2229-2231.
72. T. Vogt, P. M. Woodward and B. A. Hunter, *J. Solid State Chem.*, 1999, **144**, 209-215.
73. M. Decoster, F. Conan, J. E. Guerchais, Y. Le Mest, J. Sala Pala, J. C. Jeffery, E. Faulques, A. Leblanc and P. Molinie, *Polyhedron*, 1995, **14**, 1741-1750.
74. T. M. Brown and J. N. Smith, *J. Chem. Soc., Dalton Trans.*, 1972, 1614-1616.

75. D. F. Shriver, P. W. Atkins, T. L. Overton, J. P. Rourke, M. T. Weller and F. A. Armstrong, *Inorganic Chemistry*, 4th Ed., Oxford University Press, Oxford, 2006.
76. W. Y. Lee, T. M. Besmann and M. W. Stott, *J. Mater. Res.*, 1994, **9**, 1474-1483.
77. C. W. Bret, W. G. Sawyer and W. H. David, *Tribol. Lett.*, 2011.
78. S.-L. Li, H. Miyazaki, H. Song, H. Kuramochi, S. Nakaharai and K. Tsukagoshi, *ACS Nano*, 2012, **6**, 7381-7388.
79. H. Li, Q. Zhang, C. C. R. Yap, B. K. Tay, T. H. T. Edwin, A. Olivier and D. Baillargeat, *Adv. Funct. Mater.*, 2012, **22**, 1385-1390.
80. P. Marchand, I. A. Hassan, I. P. Parkin and C. J. Carmalt, *Dalton Trans.*, 2013, **42**, 9406-9422.
81. T. Sekine, T. Nakashizu, K. Toyoda, K. Uchinokura and E. Matsuura, *Solid State Commun.*, 1980, **35**, 371-373.
82. A. Berkdemir, H. R. Gutiérrez, A. R. Botello-Méndez, N. Perea-López, A. L. Elías, C.-I. Chia, B. Wang, V. H. Crespi, F. López-Urías, J.-C. Charlier, H. Terrones and M. Terrones, *Sci. Rep.*, 2013, **3**.
83. L. Britnell, R. M. Ribeiro, A. Eckmann, R. Jalil, B. D. Belle, A. Mishchenko, Y.-J. Kim, R. V. Gorbachev, T. Georgiou, S. V. Morozov, A. N. Grigorenko, A. K. Geim, C. Casiraghi, A. H. C. Neto and K. S. Novoselov, *Science*, 2013, **340**, 1311-1314.
84. L. M. Malard, M. A. Pimenta, G. Dresselhaus and M. S. Dresselhaus, *Phys. Rep.*, 2009, **473**, 51-87.
85. *W.O. Pat.*, WO2008113814 A1, 2008.
86. F. A. Cotton, M. W. Extine and R. H. Niswander, *Inorg. Chem.*, 1978, **17**, 692-696.
87. E. R. T. Tiekink and I. Haiduc, in *Progress in Inorganic Chemistry, Vol 54*, ed. K. D. Karlin, John Wiley & Sons Inc, New York, 1st Ed., 2005, vol. 54, pp. 127-319.
88. R. N. Jowitt and P. C. H. Mitchell, *J. Chem. Soc. A*, 1970, 1702-1708.
89. N. Alam, M. S. Hill, G. Kociok-Köhn, M. Zeller, M. Mazhar and K. C. Molloy, *Chem. Mater.*, 2008, **20**, 6157-6162.

Chapter 5

Final conclusion

5.1 Final conclusion

Unlike main group metal thioureides which have been shown as promising metal sulfide precursors,[1] transition metal thioureides have proved to be unsuccessful at depositing transition metal disulfides. While ineffective as precursors, these complexes have shown an interesting array of thioureide ligand binding modes and reactivities.

For the group IV thioureide systems, synthesised by the insertion of iso-propyl, *tert*-butyl or phenyl isothiocyanates into the tetrakis(dimethylamido) group IV metal complexes, a wide variety of binding modes were observed. The phenyl thioureide ligand exclusively adopted the κ^2-*S,N* mode while the iso-propyl (κ^2-*S,N* and κ^2-*N,N'*) and *tert*-butyl (κ^2-*S,N* and κ^2-*S,N'*) thioureide ligands both adopted two different modes. Bis- (Ti), tris- (Zr and Hf) and tetra-substituted (Zr) thioureide complexes were formed with one example of a sulfur bridged dititanium complex (**4**).

For the tantalum thioureide systems synthesised by the insertion of iso-propyl or *tert*-butyl isothiocyanates into PDMAT, only the mono-substituted tantalum thioureide complexes, **18** and **19** respectively, were recovered. The *tert*-butyl complex, **19**, crystallised with the thioureide ligand binding via the κ^2-*N,N'* mode although both complexes displayed two structural isomers in solution. Insertion of the iso-propyl or phenyl isothiocyanate into the complex, [(^{t}BuN)Ta(NMe$_2$)$_3$] (**20**), provided the bis- and tris-substituted thioureide complexes, **22** and **23** respectively with all ligands binding via the κ^2-*S,N* mode.

Group VI thioureide systems synthesised by the reaction between a bis(*tert*-butylimido)bis(amido) group VI metal (Mo and W) complex and a methyl, ethyl or *n*-butyl disubstituted thiourea formed the corresponding bis-substituted thioureide complexes. For the molybdenum complexes, both thioureide ligands bind via the κ^2-*S,N* mode with both *tert*-butyl imido ligands retained. In contrast, the tungsten complexes incorporated two different thioureide binding modes (κ^2-*S,N* and κ^2-*N,N*), with the κ^2-*N,N* thioureide ligand formally a di-anion. Only one *tert*-butyl imido ligand was retained with the other replaced by a *tert*-butyl amido ligand. The reaction of [(^{t}BuN)$_2$W(NH^{t}Bu)$_2$] (**27**) with 1,3-di-*tert*-butyl-2-thiourea formed the

sulfur bridged tungsten(V) complex, **34**, which contained a W-W single bond and both thioureide ligands in the κ^2-*S,N* mode.

The insertion of iso-propyl or phenyl isothiocyanates into the bis(*tert*-butylimido)bis(dimethylamido) group VI metal (Mo and W) complexes produced the bis(tert-butylimido)bis(thioureide) complexes, **37**, **38**, **39** and **40**, with the thioureide ligands exclusively binding via the κ^2-*S,N* mode. Deposition studies with the iso-propyl complexes, **37** and **38**, provided films with mixed stoichiometries although the predominant phase appeared to be that of the corresponding metal nitride.

The homoleptic molybdenum xanthate complex, **43**, deposited MoS_2 at temperatures lower than those observed for the molybdenum dithiocarbamate complex, **41**. While the deposition temperatures were lower (favoured in industry), the quality of the films produced was poorer and the synthesis of the precursor was more problematic.

Of the different metal disulfide precursors synthesised in this thesis, the metal dithiocarbamates are by far the most promising precursor class. The dithiocarbamates of group IV, V and VI metals consistently produced thin films of metal disulfide under a variety of conditions onto a range of substrates. All complexes were synthesised under inert conditions with the solid product stable under ambient conditions for some time.

The early transition metal dithiocarbamates (group IV and V) were sensitive to oxide formation during the deposition process. Experiments using AACVD, where the exclusion of air and moisture is more difficult, provided the corresponding metal oxide. The use of LPCVD limited the exposure of the precursor to air and moisture encouraging the growth of the metal disulfide. The sensitivity of these deposition processes to air and moisture were mirrored in the stability of the resulting metal disulfides, which were unstable to oxide formation when stored under ambient conditions. The later transition metal dithiocarbamates (group VI) were considerably more stable which meant AACVD could be used to deposit the metal disulfide with the films stable under ambient conditions.

5.2 References

1. I. Y. Ahmet, M. S. Hill, A. L. Johnson and L. M. Peter, *Chem. Mater.*, 2015, **27**, 7680-7688.

Chapter 6

Experimental

6.1 General experimental

All reactions were performed under inert conditions, unless otherwise stated, using standard Schlenk line and glove box techniques under either argon or nitrogen atmospheres. All starting chemicals were provided by Sigma-Aldrich, Fisher Scientific, Alfa Aesar or Acros. The compounds: $[Ti(NMe_2)_4]$, $[Zr(NMe_2)_4]$, $[Zr(NEtMe)_4]$, $[Zr(NEt_2)_4]$, $[Hf(NMe_2)_4]$, $[Hf(NEtMe)_4]$, $[Hf(NEt_2)_4]$ and $[Ta(NMe_2)_5]$ had previously been prepared within the group by a modified literature procedure.[1] *tert*-butylamine [$^tBuNH_2$] and pyridine [C_5H_5N, py] were dried by refluxing over calcium hydride. All solvents were dried under argon using an Innovative Technologies solvent purification system, then degassed once (twice for THF and diethyl ether) using cold vacuum degassing (77 K) and argon. Solvents were stored in J Youngs ampules over molecular sieves. Deuterated benzene (C_6D_6) NMR solvent was purchased from Sigma-Aldrich and dried by refluxing over potassium before isolating by vacuum distillation.

NMR experiments were carried out using J Youngs valve NMR tubes prepared in a glove box. NMR data was collected at 25 °C unless otherwise stated using either a Bruker Avance AV-300, Avance AV-400 or Avance II+ AV-500 spectrometer.

IR spectra were recorded on a PerkinElmer Spectrum 100 UATR FTIR and analysed in Excel.

Elemental analysis was performed under inert conditions by the elemental analysis service at the Science Centre, London Metropolitan University, UK.

Single crystal X-ray diffraction data were collected at 150 K using either a Nonius Kappa CCD, an Agilent Xcalibur or an Agilent SuperNova Dual diffractometer with either Mo-Kα (λ = 0.71073 Å) or Cu-Kα (λ = 1.5418 Å) radiation. The data collected by the diffractometers were processed using the proprietary Nonius or Agilent software. Structures were solved by full-matrix least squares refinement using either the WinGX-170 suite of programs or the programme suite X-SEED. All structural data were obtained by Dr Andrew Johnson with structure refinement performed by Dr Andrew Johnson or Dr Gabriele Kociok-Köhn.

TGA was performed under nitrogen (20 ml/min) at a ramp rate of 5 °C/min between 50 and 600 °C on a PerkinElmer TGA4000 with autosampler; samples were

contained in either crimped aluminium pans (closed pans) or in alumina crucibles (open pans).

TGA-MS was performed under argon (20 ml/min) at a ramp rate of 5 °C/min between 30 and 600 °C on a Setaram Setsys Evolution TGA 16/18 with the evolved gases passing through a Pfeiffer Vacuum Omnistar GSD 320 quadrapole mass spectrometer. Samples were contained in alumina crucibles. Experiments were performed by CCAF, University of Bath, UK, and results were analysed using Excel.

Substrates used were SiCO coated float glass supplied by NSG Group, UK, silicon (100) wafers supplied by MEMC Electronic Materials S.p.a., Italy, and 300 nm of SiO_2 on silicon wafers supplied by IDB Technologies, UK.

The AACVD system comprised of a TSI 3076 Constant Output Atomiser using argon at a pressure of 18 psi to generate the aerosol and act as a carrier gas. The aerosol passed through a quartz tube containing the substrate, enclosed within an Elite Thermal Systems Ltd tube furnace.

The LPCVD system comprised of a quartz reactor tube with one end capped contained within an Elite Thermal Systems Ltd tube furnace. The open end of the reactor was connected to a Schlenk line to provide both inert gas and a vacuum to the reactor. Precursors were contained within a quartz boat. The standard deposition pressure was 1 mbar.

PXRD patterns were collected on either a Siemens Kristalloflex D5000 (Cu-Kα radiation, λ = 1.54056 Å) or Bruker AXS D8 Advance (Cu-Kα radiation, λ = 1.5418 Å) diffractometer in flat plate mode at 298 K. Results were analysed in EVA and Excel.

SEM images were collected on either a JEOL FESEM6301F or a JEOL SEM6480LV. EDX analysis was performed on the JEOL SEM6480LV using an Oxford INCA X-Act SDD X-ray detector. Samples were mounted on stainless steel stubs or clamps using carbon tape and stored under vacuum. SEM images were analysed using ImageJ software.

Raman spectra were recorded on a Renishaw inVia system using a 532 nm laser and analysed using the programs Wire and Excel.

AFM was performed in contact mode on either a Veeco Multimode Nanoscope III using Bruker SNL-10 tips or a Nanosurf Flex-Axiom using Budget Sensors Contact-G tips. Images were processed in Gwyddion.

XPS was carried out using a Thermo Scientific K-Alpha system by NEXUS at Newcastle University, UK. Data was analysed using CasaXPS.

A number of films were analysed using SEM, EDX and XPS by the Material Properties & Surface Analysis department at NSG Group, UK.

6.2 Experimental for Chapter 2

6.2.1 $[(Me_2N)_2Ti(SC\{NMe_2\}N^iPr)_2]$ (1)

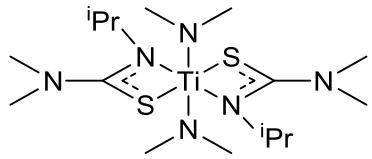

A stirred hexane (10 ml) solution of $Ti(NMe_2)_4$ (0.24 ml, 1 mmol) was treated with *iso*-propyl isothiocyanate (0.43 ml, 4 mmol) and stirred for 24 hours to form a dark red solution. The volume of solution was reduced *in vacuo* with dark red crystals attained after storage at 4 °C.

Yield: 0.38 g, 88 %

^{1}H NMR (300 MHz, C_6D_6) δ 4.05 (br s, 2H, C*H*CH_3), 3.52 (br s, 12H, NC*H*$_3$), 2.61 (br s, 12H, CNC*H*$_3$), 1.30 (br s, 12H, CHC*H*$_3$)

^{13}C{^{1}H} NMR (75MHz, C_6D_6) δ 51.4, 49.8, 47.61, 46.9, 42.0, 39.7, 23.9, 23.2

Elemental analysis found (calculated for $C_{16}H_{38}N_6S_2Ti$): C – 44.90 (45.06), H – 9.08 (8.98), N – 19.62 (19.70) %

6.2.2 [$(Me_2N)_2Ti(SC\{NMe_2\}N^tBu)$ $(SC\{N^tBu\}NMe_2)$] (2)

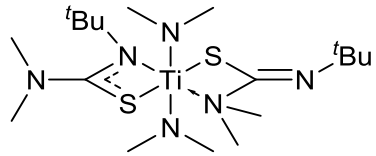

A stirred hexane (10 ml) solution of $Ti(NMe_2)_4$ (0.24 ml, 1 mmol) was treated with *tert*-butyl isothiocyanate (0.51 ml, 4 mmol) and stirred for 24 hours to form an orange/red solution. The volume of solvent was reduced *in vacuo* with dark red crystals attained after storage at -28 °C.

Yield: 0.28 g, 62 %

^{1}H NMR (300 MHz, C_6D_6) δ 3.34-3.01 (m, 12H, NCH_3), 2.75-2.68 (m, 6H, CNCH_3), 2.30 (m, 6H, CNCH_3), 1.61-1.38 (m, 18H, CCH_3)

^{13}C{^{1}H} NMR (75MHz, C_6D_6) δ 160.4, 58.6, 54.6, 50.7, 48.3, 47.2, 46.0, 44.5, 43.9, 39.9, 31.4, 30.5, 30.2, 29.9, 29.6, 28.6

Elemental analysis found (calculated for $C_{18}H_{42}N_6S_2Ti$): C – 47.36 (47.56), H – 9.46 (9.31), N – 18.35 (18.49) %

6.2.3 [$(Me_2N)_2Ti(SC\{NMe_2\}NPh)_2$] (3)

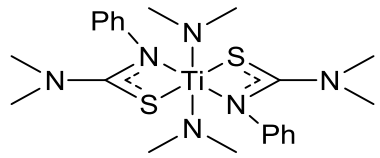

A stirred hexane (10 ml) solution of $Ti(NMe_2)_4$ (0.48 ml, 2 mmol) was treated with phenyl isothiocyanate (0.24 ml, 2 mmol) and stirred for 24 h to form a dark red precipitate. The precipitate was heated back into solution with dark red crystals attained after storage at room temperature.

Yield: 0.24 g, 24%

^{1}H NMR (300 MHz, THF-d_8) δ 7.16-7.08 (m, 4H, *meta*-C_6H_5), 6.97-6.91 (m, 4H, *ortho*-C_6H_5), 6.88-6.81 (m, 2H, *para*-C_6H_5), 3.28 (s, 12H, NCH_3), 2.61 (s, 12H, CNCH_3)

$^{13}C\{^{1}H\}$ NMR (75MHz, THF-d_8) δ 179.7, 150.4, 128.5, 124.0, 122.7, 48.8, 40.9

Elemental analysis found (calculated for $C_{22}H_{34}N_6S_2Ti$): C – 53.32 (53.43), H – 6.29 (6.93), N – 16.90 (16.99) %

6.2.4 [{Ti(SC{NMe$_2$}NPh)$_2$(μ-S)}$_2$] (4)

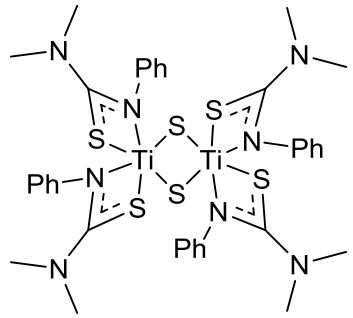

A stirred hexane (10 ml) solution of Ti(NMe$_2$)$_4$ (0.23 ml, 1 mmol) was treated with phenyl isothiocyanate (0.36 ml, 3 mmol) resulting in the immediate formation of a red precipitate. After stirring for 48 hours, volatiles were removed *in vacuo* to provide a red solid. Dissolution in toluene (10 ml) and layering with hexane (25 ml) provided red crystals after storage at room temperature.

Yield: 0.24 g, 55 %

^{1}H NMR (300 MHz, C_6D_6) δ 7.39 (br s, 8H, *meta*-C_6H_5), 7.22 (m, 8H, *ortho*-C_6H_5), 6.96 (m, 4H, *para*-C_6H_5), 2.30 (br s, 24H, NCH_3)

$^{13}C\{^{1}H\}$ NMR (75MHz, C_6D_6) δ 151.4, 150.9, 129.1, 127.7, 127.4, 125.8, 125.1, 124.6, 123.3, 122.9, 41.2, 41.0, 39.7

Elemental analysis found (calculated for $C_{36}H_{44}N_8S_6Ti_2$:1.8C_7H_8): C – 55.60 (55.98), H – 6.03 (5.64), N – 10.56 (10.75) %

6.2.5 [(Me$_2$N)Zr(Me$_2$NC{S}N^{i}Pr)(SC{NMe$_2$}N^{i}Pr)$_2$] (5)

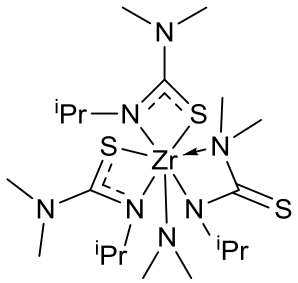

A stirred hexane (20 ml) solution of Zr(NMe$_2$)$_4$ (0.27 g, 1 mmol) was treated with isopropyl isothiocyanate (0.43 ml, 4 mmol), resulting in the formation of a pale yellow precipitate. The reaction solution was stirred at ambient temperature for 24 h, before the precipitate was heated into solution and filtered through Celite®. Crystallisation of the resultant liquor at -28 °C gave the product as yellow crystals.

Yield: 0.39 g, 69 %

^{1}H NMR (500 MHz, 375 K, C_6D_6) δ 4.13 (br s, 3H, C*H*CH$_3$), 3.19 (br s, 6H, NC*H*$_3$), 2.65 (br s, 18H, CNC*H*$_3$), 1.38 (br s, 18H, CHC*H*$_3$)

^{13}C{^{1}H} NMR (125 MHz, 375 K, C_6D_6) δ 51.7, 42.3, 39.8, 23.9, 23.2

Elemental analysis found (calculated for $C_{20}H_{45}N_7S_3Zr$): C – 42.20 (42.07), H – 7.84 (7.94), N – 16.95 (17.17) %

6.2.6 [(Me$_2$N)Zr(SC{NMe$_2$}N^{t}Bu)(SC{N^{t}Bu}NMe$_2$)$_2$] (6)

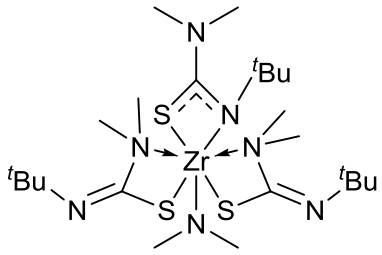

A stirred hexane (20 ml) solution of Zr(NMe$_2$)$_4$ (0.27 g, 1 mmol) was treated with *tert*-butyl isothiocyanate (0.51 ml, 4 mmol), resulting in the formation of a yellow solution. After stirring the reaction mixture for 24 hours at ambient temperature, the mixture was filtered through Celite® and the liquor was concentrated *in vacuo.* Crystallisation of the resultant liquor at -28 °C gave the product as yellow crystals.

Yield: 0.51 g, 63 %

^{1}H NMR (300 MHz, C_6D_6) δ 3.21 (br s, 3H, NC*H*$_3$), 2.80 (br s, 15H, NC*H*$_3$/CNC*H*$_3$), 2.21 (s, 6H, CNC*H*$_3$), 1.58 (s, 18H, CC*H*$_3$), 1.36 (s, 9H, CC*H*$_3$)

^{13}C{^{1}H} NMR (75MHz, C_6D_6) δ 191.1, 164.2, 57.4, 54.1, 48.9, 46.1, 42.6, 31.1, 28.9

Elemental analysis found (calculated $C_{23}H_{51}N_7S_3Zr$): C – 45.22 (45.06), H – 8.27 (8.38), N – 15.89 (15.99) %

6.2.7 [Zr(SC{NMe$_2$}NPh)$_4$] (7)

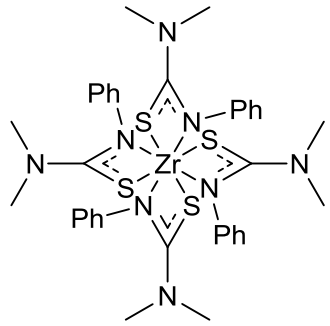

A stirred hexane (20 ml) solution of Zr(NMe$_2$)$_4$ (0.27 g, 1 mmol) was treated with phenyl isothiocyanate (0.48 ml, 4 mmol), resulting in the immediate formation of a white precipitate. The reaction solution was stirred at ambient temperature for 24 h and then the solvent was removed *in vacuo* to provide a white solid. The resulting solid was dissolved in warm toluene (10 ml) and filtered through Celite®. Crystallisation of the resultant liquor at -28 °C gave the product as white crystals.

Yield: 0.40 g, 49 %

^{1}H NMR (300 MHz, C_6D_6) δ 7.40 (m, 8H, *meta*-C_6H_5), 7.20 (m, 8H, *ortho*-C_6H_5), 6.91 (m, 4H, *para*-C_6H_5), 2.29 (s, 24H, CNC*H*$_3$)

^{13}C{^{1}H} NMR (125 MHz, C_6D_6) δ 181.2, 152.1, 129.7, 128.9, 127.3, 126.0, 123.7, 41.0

Elemental analysis found (calculated for $C_{36}H_{44}N_8S_4Zr$): C – 53.70 (53.50), H – 5.66 (5.49), N – 13.76 (13.89) %

6.2.8 [(Me$_2$N)Hf(Me$_2$NC{S}N^{i}Pr)(SC{NMe$_2$}N^{i}Pr)$_2$] (8)

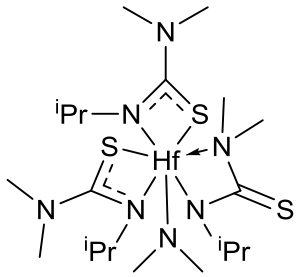

A stirred hexane (20 ml) solution of Hf(NMe$_2$)$_4$ (0.32 ml, 1 mmol) was treated with isopropyl isothiocyanate (0.43 ml, 4 mmol), resulting in the formation of a pale yellow precipitate. The reaction solution was stirred at ambient temperature for 24 h and then the solvent was removed *in vacuo* to provide a white solid. The resulting solid was dissolved in warm toluene (10 ml) and filtered through Celite®. Crystallisation of the resultant liquor at -28 °C gave the product as yellow crystals.

Yield: 0.08 g, 15 %

^{1}H NMR (500 MHz, 373 K, C_6D_6) δ 4.25 (br s, 3H, C*H*CH$_3$), 3.21 (br s, 6H, NC*H*$_3$), 2.64 (br s, 18H, CNC*H*$_3$), 1.36 (br s, 18H, CHC*H*$_3$)

^{13}C{^{1}H} NMR (125 MHz, C_6D_6) δ 53.9, 52.4, 44.9, 42.8, 42.22, 24.3, 23.4, 20.2, 19.9

Elemental analysis found (calculated for $C_{20}H_{45}HfN_7S_3$): C – 36.25 (36.49), H – 6.59 (6.89), N – 14.73 (14.89) %

6.2.9 [(Me$_2$N)Hf(SC{NMe$_2$}N^{t}Bu)(SC{N^{t}Bu}NMe$_2$)$_2$] (9)

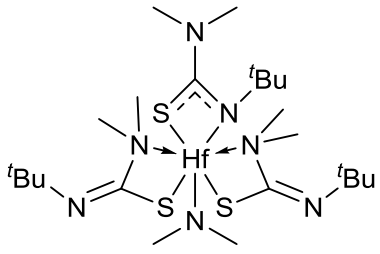

A stirred hexane (20 ml) solution of Hf(NMe$_2$)$_4$ (0.32 ml, 1 mmol) was treated with *tert*-butyl isothiocyanate (0.51 ml, 4 mmol), resulting in the formation of a yellow solution. After stirring the reaction mixture for 24 hours at ambient temperature, the

mixture was filtered through Celite® and the liquor was concentrated *in vacuo.* Crystallisation of the resultant liquor at -28 °C gave the product as yellow crystals.

Yield: 0.42 g, 61 %

^{1}H NMR (500 MHz, C_6D_6) δ 3.32 (br s, 3H, NC*H*$_3$), 2.93 (br s, 3H, NC*H*$_3$), 2.85 (s, 12H, CNC*H*$_3$), 2.22 (s, 6H, CNC*H*$_3$), 1.57 (s, 18H, CC*H*$_3$), 1.37 (s, 9H, CC*H*$_3$)

^{13}C{^{1}H} NMR (125MHz, C_6D_6) δ 190.6, 164.3, 58.0, 54.6, 43.4, 31.9, 29.6

Elemental analysis found (calculated for $C_{23}H_{51}HfN_7S_3$): C – 39.26 (39.44), H – 7.22 (7.34), N – 13.90 (14.00) %

6.2.10 [(Me$_2$N)Hf(SC{NMe$_2$}NPh)$_3$] (10)

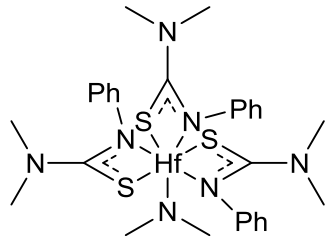

A stirred hexane (20 ml) solution of Hf(NMe$_2$)$_4$ (0.32 ml, 1 mmol) was treated with phenyl isothiocyanate (0.48 ml, 4 mmol), resulting in the formation of a white precipitate. The reaction solution was stirred at ambient temperature for 24 h and then the solvent was removed *in vacuo* to provide a white solid. The resulting solid was dissolved in warm toluene (10 ml) and filtered through Celite®. Crystallisation of the resultant liquor at -28 °C gave the product as white crystals.

Yield: 0.18 g, 23 %

^{1}H NMR (500 MHz, C_6D_6) δ 7.18-7.10 (m, 12H, *meta/ortho*-C$_6$*H*$_5$), 6.85-6.82 (m, 3H, *para*-C$_6$*H*$_5$), 3.62 (s, 6H, NC*H*$_3$), 2.25 (s, 18H, CNC*H*$_3$)

^{13}C{^{1}H} NMR (125MHz, C_6D_6) δ 180.2, 150.2, 128.7, 128.5, 126.0, 123.6, 47.5, 41.2

Elemental analysis found (calculated for $C_{29}H_{39}HfN_7S_3$): C – 45.94 (45.81), H – 5.27 (5.17), N – 12.82 (12.90) %

6.2.11 [Ti(S_2CNEt_2)$_4$] (11)

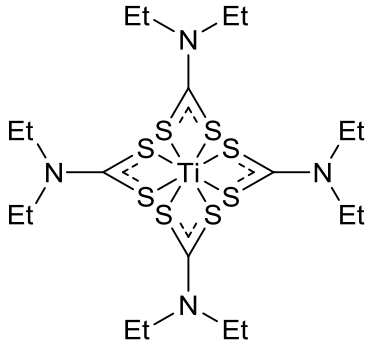

The complex was prepared according to a published procedure.[2]

$TiCl_4$ (0.55 ml, 5 mmol) was added dropwise to a stirring suspension of anhydrous NaS_2CNEt_2 (3.43 g, 20 mmol) in DCM (~50 ml) with an immediate colour change to red observed. After refluxing for 5 hours the resulting red suspension was filtered through Celite® to yield a red liquor. After reducing the volume *in vacuo* to ~15 ml the filtrate was layered with hexane (~50 ml) to attain dark red crystals.

Yield: 2.78 g, 87%

^{1}H NMR (300 MHz, C_6D_6) δ 3.27 (q, *J* = 7.16 Hz, 16H, C*H*$_2$), 0.76 (t, J = 7.16 Hz, 24H, C*H*$_3$)

^{13}C{^{1}H} NMR (75MHz, C_6D_6) δ 207.9, 44.4, 12.9

Elemental analysis found (calculated for $C_{20}H_{40}N_4S_8Ti$): C – 37.35 (37.48), H – 6.42 (6.29), N – 8.60 (8.74) %

6.2.12 [Zr(S_2CNEt_2)$_4$] (12)

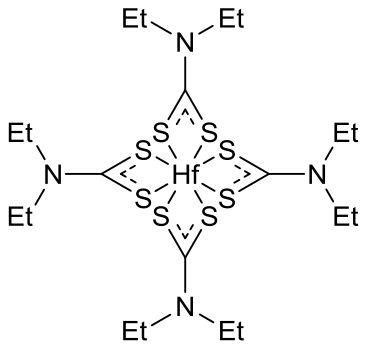

The complex was prepared according to a published procedure.[3]

CS_2 (0.55 ml, 9.1 mmol) was added dropwise to a stirring solution of $Zr(NEt_2)_4$ (0.74 ml, 2 mmol) in toluene (10 ml). The solution was heated at 75 °C for 90 mins and then allowed to cool to room temperature. Layering with hexane provided yellow crystals.

Yield: 1.19 g, 87 %

^{1}H NMR (300 MHz, C_6D_6) δ 3.30 (q, *J* = 7.16 Hz, 16H, C*H*$_2$), 0.76 (t, J = 7.16 Hz, 24H, C*H*$_3$)

^{13}C{^{1}H} NMR (75 MHz, C_6D_6) δ 206.7, 45.0, 12.8

Elemental analysis found (calculated for $C_{20}H_{40}N_4S_8Zr$): C – 35.24 (35.11), H – 6.03 (5.89), N – 8.15 (8.19) %

6.2.13 [Hf(S_2CNEt_2)$_4$] (13)

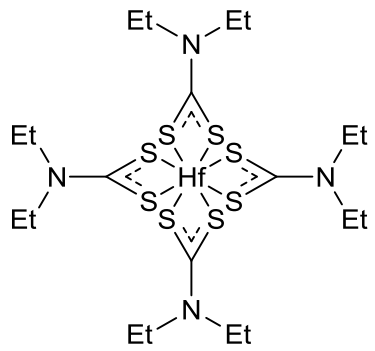

The complex was prepared according to a published procedure.[3]

CS_2 (0.55 ml, 9.1 mmol) was added dropwise to a stirring solution of $Hf(NEt_2)_4$ (0.75 ml, 2 mmol) in toluene (10 ml). The solution was heated at 75 °C for 90 mins and then allowed to cool to room temperature. Layering with hexane provided yellow crystals.

Yield: 1.18 g, 77 %

^{1}H NMR (300 MHz, C_6D_6) δ 3.28 (q, *J* = 7.16 Hz, 16H, C*H*$_2$), 0.78 (t, J = 7.16 Hz, 24H, C*H*$_3$)

^{13}C{^{1}H} NMR (75 MHz, C_6D_6) δ 206.7, 45.4, 12.8

Elemental analysis found (calculated for $C_{20}H_{40}HfN_4S_8$): C – 31.16 (31.14), H – 5.35 (5.23), N – 7.05 (7.26) %

6.2.14 [Zr(S_2CNEtMe)$_4$] (14)

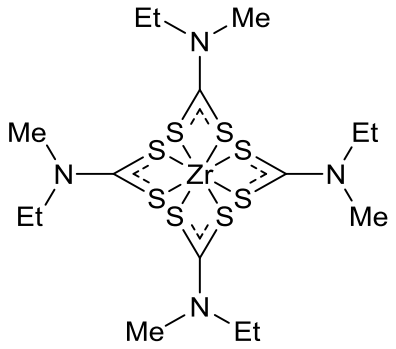

The complex was prepared according to a published procedure.[3]

CS_2 (0.55 ml, 9.1 mmol) was added dropwise to a stirring solution of Zr(NEtMe)$_4$ (0.62 ml, 2 mmol) in hexane (15 ml). The solution was refluxed for 1 hour and then allowed to cool to room temperature. Solvent was removed *in vacuo* to provide a yellow solid.

Yield: 0.51 g, 40 %

^{1}H NMR (300 MHz, CD_2Cl_2) δ 3.85 (q, *J* = 7.16 Hz, 8H, C*H*$_2$), 3.30 (s, 12H, C*H*$_3$), 1.22 (t, *J* = 7.16 Hz, 12H, CH_2CH_3)

^{13}C{^{1}H} NMR (75MHz, CD_2Cl_2) δ 205.2, 48.1, 38.0, 12.4

Elemental analysis found (calculated for $C_{16}H_{32}N_4S_8Zr$): C – 30.28 (30.59), H – 5.53 (5.13), N – 8.65 (8.92) %

6.2.15 [Hf(S_2CNEtMe)$_4$] (15)

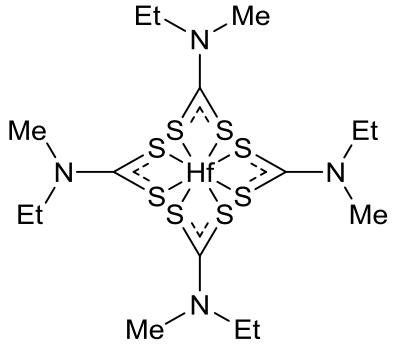

The complex was prepared according to a published procedure.[3]

CS_2 (0.55 ml, 9.1 mmol) was added dropwise to a stirring solution of Hf(NEtMe)$_4$ (0.62 ml, 2 mmol) in hexane (15 ml). The solution was refluxed for 1 hour and then allowed to cool to room temperature. Solvent was removed *in vacuo* to provide a yellow/orange solid.

Yield: 0.76 g, 53 %

^{1}H NMR (300 MHz, C_6D_6) δ 3.24 (q, *J* = 7.16 Hz, 8H, C*H*$_2$), 2.62 (s, 12H, C*H*$_3$), 0.65 (t, *J* = 7.16 Hz, 12H, CH_2CH_3)

^{13}C{^{1}H} NMR (75MHz, C_6D_6) δ 207.1, 47.7, 37.3, 12.1

Elemental analysis found (calculated for $C_{16}H_{32}HfN_4S_8$): C – 26.61 (26.86), H – 4.86 (4.51), N – 7.63 (7.83) %

6.2.16 [CpTi(S_2CNEt$_2$)$_3$] (16)

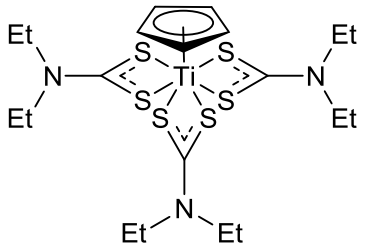

The complex was prepared according to a published procedure.[4]

A mixture of Cp_2TiCl_2 (0.25 g, 1 mmol), NaS_2CNEt_2 (0.34 g, 2 mmol) and tetraethylthiuram disulfide (0.15 g, 0.5 mmol) in THF (25 ml) was stirred for 18 hours to provide a green solution. Removal of the solvent *in vacuo* resulted in a

green/orange solid which was dissolved in DCM (20 ml), filtration through Celite® and the removal of volatiles *in vacuo* provided an orange solid.

Yield: 0.29 g, 52 %

^{1}H NMR (300 MHz, C_6D_6) δ 6.32 (s, 5H, Cp-C*H*), 3.57-3.25 (m, 12H, CH_2), 0.99-0.84 (m, 18H, CH_3)

^{13}C{^{1}H} NMR (75MHz, C_6D_6) δ 206.6, 114.8, 45.0, 44.8, 13.2, 13.0, 12.7

Elemental analysis found (calculated for $C_{20}H_{35}N_3S_6Ti$): C – 43.14 (43.07), H – 6.39 (6.28), N – 7.37 (7.53) %

6.2.17 [CpZr(S_2CNEt_2)$_3$] (17)

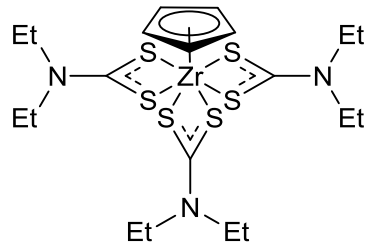

The complex was prepared according to a published procedure.[4]

A stirring mixture of Cp_2ZrCl_2 (1.17 g, 4 mmol) and anhydrous NaS_2CNEt_2 (2.16 g, 12.6 mmol) in DCM (35 ml) was refluxed for 24 hours with the resulting orange solution filtered through Celite®. Hexane (~15 ml) was added to the filtrate which was then reduced in volume; yellow crystals attained after storage at -28 °C.

Yield: 1.03 g, 49 %

^{1}H NMR (300 MHz, C_6D_6) δ 6.41 (s, 5H, Cp-C*H*), 3.52-3.23 (m, 12H, CH_2), 0.98-0.84 (m, 18H, CH_3)

^{13}C{^{1}H} NMR (75MHz, C_6D_6) δ 208.0, 205.8, 112.8, 45.7, 45.5, 45.16, 44.3, 13.0, 13.0, 12.8, 12.7

Elemental analysis found (calculated for $C_{20}H_{35}N_3S_6Zr$): C – 39.79 (39.96), H – 5.68 (5.87), N – 6.89 (6.99) %

6.2.18 AACVD experiments

General procedure – Under an inert atmosphere, a solution of the desired precursor in toluene was placed in the precursor vessel. Glass and Si substrates rinsed with IPA were placed at the centre of quartz reactor tube in a tube furnace. The AACVD apparatus was connected and purged with a flow of argon gas at a pressure of 18 psi for 15 mins. Once the furnace had reached the deposition temperature, the precursor pot was opened to the argon flow to produce the aerosol for the desired deposition time. After deposition, the precursor vessel was stoppered and the substrates were cooled to room temperature. Specific conditions for each experiment are displayed in Table 5.1.

Table 5.1 Summary of conditions for AACVD experiments with precursors **5**, **6** and **12**.

Precursor	Concentration / M	Time / mins	Temperature / °C
5	0.04	45	275
5	0.04	45	300
5	0.04	45	325
6	0.04	45	200
6	0.04	45	250
6	0.04	45	300
12	0.03	60	300
12	0.03	60	350
12	0.03	60	400
12	0.03	60	450
12	0.03	60	500

6.2.19 LPCVD experiments

General procedure – The precursor was placed in a quartz boat at the capped end of the quartz reactor tube towards the edge of the tube furnace. Glass and Si substrates rinsed with IPA and then O_2 plasma cleaned (20 mins) were positioned upstream of the precursor boat at the centre of the furnace. The reactor tube was then evacuated and refilled with nitrogen gas three times prior to the start of the experiment. Once under a stable vacuum (1 mbar), the furnace was turned on and allowed to heat to the

deposition temperature for the desired deposition time. After the experiment was complete, the reactor tube was removed from the furnace and allowed to cool to room temperature. Specific conditions for each experiment are displayed in Table 5.2.

Table 5.2 Summary of conditions for LPCVD experiments with precursors **11**, **12** and **13**.

Precursor	Mass / g	Time / mins	Temperature / °C
11	0.1	30	325
11	0.1	30	350
11	0.1	30	375
12	0.1	30	375
12	0.1	30	400
12	0.1	30	425
12	0.1	30	450
13	0.1	30	400
13	0.1	30	425
13	0.1	30	450

6.3 Experimental for Chapter 3

6.3.1 $[(Me_2N)_4Ta(Me_2NC\{N^iPr\}S)]$ (18)

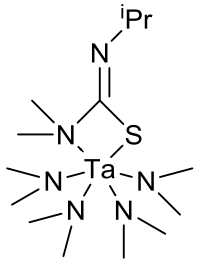

A stirred toluene (10 ml) solution of PDMAT (0.80 g, 2 mmol) was treated with iso-propyl isothiocyanate (0.22 ml, 2 mmol), resulting in the immediate formation of a bright yellow solution. After stirring for 18 hours a small amount of yellow/brown precipitate was formed, the solution was filtered through Celite® and then concentrated *in vacuo* to yield a clear yellow solution. Storage at -28 °C yielded yellow crystals which were washed with hexane.

Yield: 0.26 g, 26 %

Major NMR product:

^{1}H NMR (300 MHz, C_6D_6) δ 4.06 (sept, J = 6.59 Hz, 1H, C*H*), 3.58 (s, 6H, NCH_3), 3.48 (s, 12H, NCH_3), 3.47 (s, 6H, NCH_3), 2.55 (s, 6H, CNCH_3), 1.15 (d, *J* = 6.59 Hz, 6H, CHCH_3)

^{13}C{^{1}H} NMR (75MHz, C_6D_6) δ 187.4, 51.2, 51.0, 48.6, 45.4, 42.9, 23.7

Minor NMR product:

^{1}H NMR (300 MHz, C_6D_6) δ 4.77 (sept, *J* = 6.59 Hz, 1H, C*H*), 3.37 (s, 6H, NCH_3), 3.09 (s, 6H, NCH_3), 3.04 (s, 12H, NCH_3), 2.55 (s, 6H, CNCH_3), 1.42 (d, *J* = 6.59 Hz, 6H, CHCH_3)

^{13}C{^{1}H} NMR (75MHz, C_6D_6) δ 53.0, 51.4, 48.4, 47.5, 45.3, 22.6

Elemental analysis found (calculated for $C_{14}H_{37}N_6STa$): C – 33.30 (33.46), H – 7.42 (7.27), N – 16.72 (16.61) %

6.3.2 [$(Me_2N)_4Ta(Me_2NC\{S\}N^tBu)$] (19)

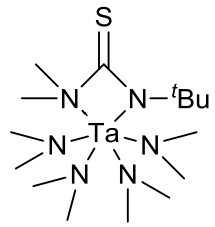

A stirred toluene (10 ml) solution of PDMAT (0.80 g, 2 mmol) was treated with *tert*-butyl isothiocyanate (0.26 ml, 2 mmol), resulting in the immediate formation of a bright yellow solution. After stirring for 18 hours the solution was filtered through Celite® and then concentrated *in vacuo*. Storage at -28 °C yielded yellow crystals which were washed with hexane.

Yield: 0.33 g, 32 %

Major NMR product:

^{1}H NMR (300 MHz, C_6D_6) δ 3.37 (s, 6H, NCH_3), 3.11 (s, 6H, NCH_3), 3.09 (s, 12H, NCH_3), 2.60 (s, 6H, CNCH_3), 1.79 (s, 9H, CCH_3)

$^{13}C\{^{1}H\}$ NMR (75MHz, C_6D_6) δ 197.2, 51.6, 48.9, 48.1, 45.4, 29.8

Minor NMR product:

^{1}H NMR (300 MHz, C_6D_6) δ 3.53 (br s, 24H, NCH_3), 2.36 (s, 6H. CNCH_3), 1.41 (s, 9H, CCH_3)

$^{13}C\{^{1}H\}$ NMR (75MHz, C_6D_6) δ 198.3, 48.7, 48.6, 45.1, 31.4

Elemental analysis found (calculated for $C_{15}H_{39}N_6STa$): C – 34.72 (34.88), H – 7.58 (7.61), N – 16.27 (16.18) %

6.3.3 [(^{t}BuN)Ta(NMe$_2$)$_3$] (20)

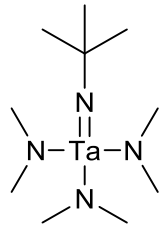

The complex was prepared according to a published procedure.[5]

A solution of Ta(NMe$_2$)$_5$ (4.97 g, 12.4 mmol) in hexane (20 ml) was treated with *tert*-butylamine (1.3 ml, 12.4 mmol) and stirred for 18 hours. The resulting yellow solution was filtered through Celite®, concentrated *in vacuo* and stored at -28 °C to afford pale orange crystals.

Yield: 1.44 g, 31 %

^{1}H NMR (300 MHz, C_6D_6) δ 3.20 (s, 18H, NCH_3), 1.45 (s, 9H, CCH_3)

$^{13}C\{^{1}H\}$ NMR (75MHz, C_6D_6) δ 67.1, 46.6, 34.9

6.3.4 [(^{t}BuN)Ta(NMe$_2$)(SC{NMe$_2$}N^{i}Pr)$_2$] (21)

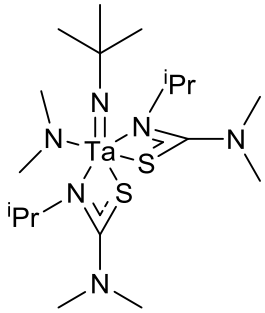

A stirred toluene (10 ml) solution of (^{t}BuN)Ta(NMe$_2$)$_3$ (0.38 g, 1 mmol) was treated with iso-propyl isothiocyanate (0.32 ml, 3 mmol), resulting in the immediate formation of a golden yellow solution. After stirring for 22 hours the solvent was removed *in vacuo* to form a pale yellow solid. The resulting solid was dissolved in a minimal amount of warm hexane, filtered through Celite® and stored at -28 °C to afford yellow crystals.

Yield: 0.27 g, 45 %

^{1}H NMR (300 MHz, C_6D_6) δ 4.39-4.28 (m, 1H, C*H*), 4.32 (s, 3H, NCH_3), 4.15-4.06 (m, 1H, C*H*), 3.93 (s, 3H, NCH_3), 2.58 (s, 6H, CNCH_3), 2.55 (s, 6H, CNCH_3), 1.57 (s, 9H, CCH_3), 1.49 (d, 3H, CHCH_3), 1.35 (d, 3H, CHCH_3), 1.30 (d, 3H, CHCH_3), 1.22 (d, 3H, CHCH_3)

^{13}C{^{1}H} NMR (75MHz, C_6D_6) δ 188.7, 186.7, 65.0, 61.8, 51.4, 51.2, 50.7, 42.2, 42.1, 34.2, 26.0, 24.9, 24.6, 24.5

Elemental analysis found (calculated for $C_{18}H_{41}N_6S_2Ta$): C – 36.68 (36.85), H – 7.11 (7.04), N – 14.21 (14.32) %

6.3.5 [(^{t}BuN)Ta(SC{NMe$_2$}NPh)$_3$] (22)

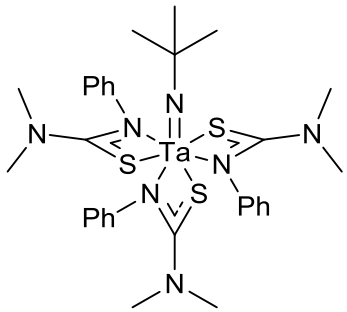

A stirred toluene (10 ml) solution of (^{t}BuN)Ta(NMe$_2$)$_3$ (0.19 g, 0.5 mmol) was treated with phenyl isothiocyanate (0.12 ml, 1 mmol), resulting in the immediate formation of a yellow solution. After stirring the reaction mixture for 18 hours at ambient temperature, the solution was concentrated *in vacuo* until a yellow precipitate formed. The precipitate was heated into solution and stored at room temperature to form yellow crystals.

Yield: 0.18 g, 46 %

^{1}H NMR (300 MHz, C_6D_6) δ 7.39-6.86 (m, 15H, C_6H_5), 2.26 (br s, 18H, CNCH_3), 1.57 (s, 9H, CCH_3)

^{13}C{^{1}H} NMR (75MHz, C_6D_6) δ 150.5, 128.3, 65.0, 40.6, 33.2

Elemental analysis found (calculated for $C_{31}H_{42}N_7S_3Ta$): C – 47.30 (47.14), H – 5.42 (5.36), N – 12.31 (12.41) %

6.3.6 [(^{t}BuN)Ta(S$_2$CNMe$_2$)$_3$] (23)

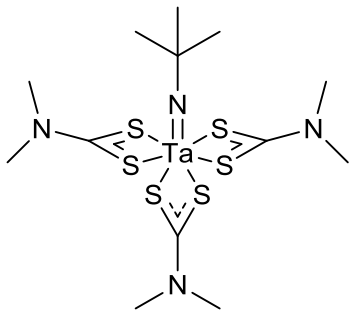

A stirred THF (10 ml) solution of (^{t}BuN)Ta(NMe$_2$)$_3$ (0.38 g, 1 mmol) was treated with CS_2 (0.24 ml, 4 mmol), resulting in the immediate formation of a yellow/brown

precipitate. After stirring for 18 hours the mixture was filtered through Celite® whilst warm, concentrated *in vacuo* and stored at -28 °C to afford yellow crystals.

Yield: 0.56 g, 91 %

^{1}H NMR (300 MHz, C_6D_6) δ 2.59 (s, 6H, NCH_3), 2.46 (s, 6H, NCH_3), 2.40 (s, 6H, NCH_3), 1.67 (s, 9H, CCH_3)

^{13}C{^{1}H} NMR (75MHz, C_6D_6) δ 208.6, 204.8, 68.2, 41.0, 40.5, 39.0, 38.2, 33.0

Elemental analysis found (calculated for $C_{13}H_{27}N_4S_6Ta$): C – 25.61 (25.48), H – 4.34 (4.44), N – 9.06 (9.14) %

6.3.7 [(^{t}BuN)Ta($S_2CNEt_2)_3$] (24)

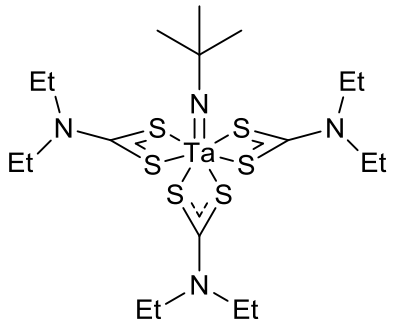

A stirred THF (10 ml) solution of (^{t}BuN)Ta($NEt_2)_3$ (0.37 ml, 1 mmol) was treated with CS_2 (0.24 ml, 4 mmol), resulting in the immediate formation of a dark yellow solution. After stirring for 18 hours the solvent was removed *in vacuo* to form a yellow solid. The resulting solid was dissolved in a minimal amount of warm toluene, filtered through Celite® and stored at 4 °C to afford orange crystals.

Yield: 0.65 g, 93 %

^{1}H NMR (300 MHz, C_6D_6) δ 3.33 - 3.10 (m, 12H, NCH_2), 1.64 (s, 9H, CCH_3), 0.97 – 0.69 (m, 18H, CH_2CH_3)

^{13}C{^{1}H} NMR (75MHz, C_6D_6) δ 203.7, 66.3, 44.9, 44.0, 35.8, 32.8, 12.8, 12.7

Elemental analysis found (calculated for $C_{19}H_{39}N_4S_6Ta$): C – 32.60 (32.75), H – 5.61 (5.64), N – 7.93 (8.04) %

6.3.8 [(^{t}BuN)Ta($SC_3H_4NS)_3$] (25)

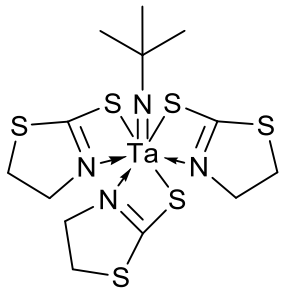

A solution of (^{t}BuN)Ta($NMe_2)_3$ (0.38 g, 1 mmol) in toluene (10 ml) was slowly added to a stirring suspension of 2-thiazoline-2-thiol (0.36 g, 3 mmol) in toluene (10 ml). Stirring for 2 hours provided a pale green solution which was filtered through Celite® and concentrated until a white precipitate was formed. The white precipitate was heated into solution and stored at room temperature to form colourless crystals.

Yield: 0.49 g, 80 %

^{1}H NMR (300 MHz, THF-d_8) δ 4.56-4.35 (m, 2H, CH_2), 4.23-3.83 (m, 5H, CH_2), 3.55-3.34 (m, 5H, CH_2), 1.17 (s, 9H, CCH_3)

^{13}C{^{1}H} NMR (75MHz, THF-d_8) δ 189.7, 63.5, 62.5, 60.6, 35.7, 33.1, 32.9

Elemental analysis found (calculated for $C_{13}H_{21}N_4S_6Ta$): C – 25.96 (25.74), H – 3.63 (3.49), N – 8.89 (9.24) %

6.3.9 AACVD experiments

General procedure – Under an inert atmosphere, a solution of the desired precursor in toluene was placed in the precursor vessel. Glass and Si substrates rinsed with IPA and then O_2 plasma cleaned (20 mins) were placed at the centre of quartz reactor tube in a tube furnace. The AACVD apparatus was connected and purged with a flow of argon gas at a pressure of 18 psi for 15 mins. Once the furnace had reached the deposition temperature, the precursor pot was opened to the argon flow to produce the aerosol for the desired deposition time. After deposition, the precursor vessel was stoppered and the substrates were cooled to room temperature. Specific conditions for each experiment are displayed in Table 5.3.

Table 5.3 Summary of conditions for AACVD experiments with precursor **24**.

Precursor	Concentration / M	Time / mins	Temperature / °C
24	0.05	60	350
24	0.05	60	375
24	0.05	60	400

6.3.10 LPCVD experiments

General procedure – The precursor was placed in a quartz boat at the capped end of the quartz reactor tube towards the edge of the tube furnace. Glass and Si substrates rinsed with IPA and then O_2 plasma cleaned (20 mins) were positioned upstream of the precursor boat at the centre of the furnace. The reactor tube was then evacuated and refilled with nitrogen gas three times prior to the start of the experiment. Once under a stable vacuum (1 mbar), the furnace was turned on and allowed to heat to the deposition temperature for the desired deposition time. After the experiment was complete, the reactor tube was removed from the furnace and allowed to cool to room temperature. Specific conditions for each experiment are displayed in Table 5.4.

Table 5.4 Summary of conditions for LPCVD experiments with precursor **24**.

Precursor	Mass / g	Time / mins	Temperature / °C
24	0.5	60	350
24	0.5	60	375
24	0.5	60	400

6.4 Experimental for Chapter 4

6.4.1 [(^{t}BuN)$_2$Mo(NMe$_2$)$_2$] (26)

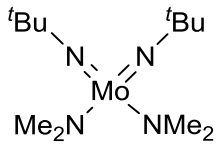

Complex **26a** was prepared by the procedure published by Dyer *et al.*[6] while complexes **26b** and **26** were prepared by the modified procedure published by Miikkulainen *et al.*[7] The full synthesis of complex **26** involved the following three reactions:

Reaction 1 – Na_2MoO_4 + 4 NEt_3 + 11 Me_3SiCl + 2 ^{t}BuNH$_2$ + dme → [(^{t}BuN)$_2$MoCl$_2$(dme)] (**26a**) + 4 $O(SiMe_3)_2$ + 4 Et_3NHCl + 2 NaCl + 3 Me_3SiCl

Reaction 2 – [(^{t}BuN)$_2$MoCl$_2$(dme)] (**26a**) + 2 py → [(^{t}BuN)$_2$MoCl$_2$py$_2$] (**26b**) + dme

Reaction 3 – [(^{t}BuN)$_2$MoCl$_2$py$_2$] (**26b**) + 2 $LiNMe_2$ → [(^{t}BuN)$_2$Mo(NMe$_2$)$_2$] (**26**) + 2 LiCl + 2 pyridine

Synthesis of **26a** – Solutions of trimethylamine (27.1 ml, 194.4 mmol), chlorotrimethylsilane (68 ml, 534.6 mmol) and *tert*-butylamine (10.2 ml, 97.2 mmol) in 1,2-dimethoxyethane (dme) (*ca.* 20 ml each solution) were added sequentially to a stirred suspension of anhydrous Na_2MoO_4 (10g, 48.6 mmol) in dme (~100 ml). After heating at 70 °C for 12 hours a yellow solution with white precipitate was formed. The mixture was filtered through Celite® and the solid was washed with diethyl ether (3 x 40 ml). Solvent was removed *in vacuo* to provide an orange residue, dissolution in diethyl ether (~20 ml) and storage at -28 °C provided orange crystals.

^{1}H NMR (250 MHz, C_6D_6) δ 3.48 (s, 6H, CH_2CH_3), 3.23 (s, 4H, CH_2), 1.41 (s, 18H, $C(CH_3)_3$)

$^{13}C\{^1H\}$ NMR (63 MHz, C_6D_6) δ 72.1, 71.0, 62.9, 30.6

Synthesis of **26b** – To a suspension of [(^{t}BuN)$_2$MoCl$_2$(dme)] (7.00 g, 17.5 mmol) in hexane (~70 ml) an excess of pyridine (8.1 ml, 100 mmol) was added, after stirring for 18 hours solvent was removed *in vacuo* to provide an orange solid.

^{1}H NMR (300 MHz, C_6D_6) δ 9.13 (m, 4H, *ortho*-C*H*), 6.83 (m, 2H, *para*-C*H*), 6.54 (m, 4H, *meta*-C*H*), 1.50 (s, 18H, C(CH_3)$_3$)

^{13}C{^{1}H} NMR (75MHz, C_6D_6) δ 152.1, 137.2, 123.7, 72.1, 30.3

Synthesis of **26** – A suspension of $LiNMe_2$ (2.04 g, 40 mmol) in hexane (~40 ml) was slowly added to a cooled suspension of [(^{t}BuN)$_2$MoCl$_2$py$_2$] (7.84 g, 16.8 mmol) in hexane (~60 ml). After stirring for 18 hours the resulting green/brown suspension was filtered through Celite® to provide a green liquor. Removal of solvent *in vacuo* obtained a brown oil which was vacuum distilled (80 °C, 1x10^{-1} mbar) to collect the product as an orange liquid.

Overall yield: 4.05 g, 41 %

^{1}H NMR (300 MHz, C_6D_6) δ 3.45 (s,12H, N(CH_3)$_2$), 1.37 (s, 18H, C(CH_3)$_3$)

^{13}C{^{1}H} NMR (75MHz, C_6D_6) δ 68.2, 54.7, 33.6

6.4.2 [(^{t}BuN)$_2$W(NH^{t}Bu)$_2$] (27)

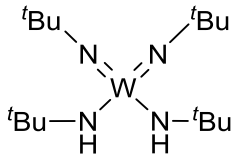

The complex was prepared according to a published procedure.[5]

^{t}BuNH$_2$ (120 ml, 1140 mmol) was slowly added to a stirring suspension of WCl_6 (39.66 g, 100 mmol) in hexane (300 ml). After stirring for 72 hours the resulting brown mixture was filtered through Celite® to afford a brown liquor, volatiles were removed *in vacuo* to provide a light brown solid.

Yield: 15.23 g, 33 %

^{1}H NMR (300 MHz, C_6D_6) δ 5.23 (s, 2H, N*H*), 1.45 (s, 18H, NC(CH_3)$_3$), 1.28 (s, 18H, NHC(CH_3)$_3$)

^{13}C{^{1}H} NMR (75MHz, C_6D_6) δ 66.4, 53.6, 34.2, 34.1

Elemental analysis found (calculated for $C_{16}H_{38}N_4W$): C – 40.71 (40.86), H – 8.06 (8.14), N – 11.82 (11.91) %

6.4.3 [(^{t}BuN)$_2$Mo(SC{NHMe}NMe)$_2$] (28)

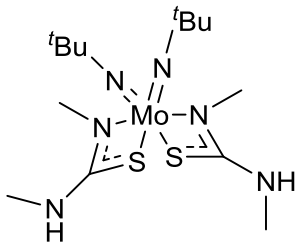

N,*N'*-dimethylthiourea (0.21 g, 2 mmol) was added to a stirring solution of (^{t}BuN)$_2$Mo(NMe$_2$)$_2$ (0.33 g, 1 mmol) in hexane (10 ml). After stirring for 18 hours a yellow precipitate was formed, volatiles were removed *in vacuo* to provide a yellow solid. Dissolution in hot toluene (~10 ml), filtration through Celite® and storage at room temperature yielded orange crystals.

Yield: 0.27 g, 61 %

^{1}H NMR (300 MHz, C_6D_6) δ 3.97 (br s, 2H, N*H*), 2.86 (br s, 6H, CH_3), (2.57 (br s, 6H, CH_3), 1.60 (s, 18H, CCH_3)

^{13}C{^{1}H} NMR (75MHz, C_6D_6) δ 66.3, 32.1, 15.9

Elemental analysis found (calculated for $C_{14}H_{32}MoN_6S_2$): C – 37.72 (37.83), H – 7.15 (7.26), N – 18.81 (18.91) %

6.4.4 [(^{t}BuN)$_2$Mo(SC{NHEt}NEt)$_2$] (29)

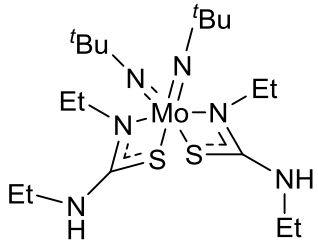

N,*N'*-diethylthiourea (0.26 g, 2 mmol) was added to a stirring solution of (^{t}BuN)$_2$Mo(NMe$_2$)$_2$ (0.33 g, 1 mmol) in hexane (10 ml). After stirring for 18 hours an orange precipitate was formed, volatiles were removed *in vacuo* to provide a orange solid. Dissolution in hot toluene (~10 ml), filtration through Celite® and storage at room temperature yielded a yellow solid.

Yield: 0.18 g, 36 %

^{1}H NMR (400 MHz, 349 K, C_6D_6) δ 4.27 (br s, 2H, N*H*), 3.33-3.19 (m, 8H, CH_2), 1.52 (s, 18H, CCH_3), 1.24-1.17 (m, 6H, CH_2CH_3), 0.89-0.82 (m, 6H, CH_2CH_3)

^{13}C{^{1}H} NMR (75MHz, C_6D_6) δ 38.6, 31.8, 16.2, 15.0

Elemental analysis found (calculated for $C_{18}H_{40}MoN_6S_2$): C – 43.08 (43.18), H – 8.07 (8.05), N – 16.64 (16.79) %

6.4.5 [(^{t}BuN)$_2$Mo(SC{NH^{n}Bu}N^{n}Bu)$_2$] (30)

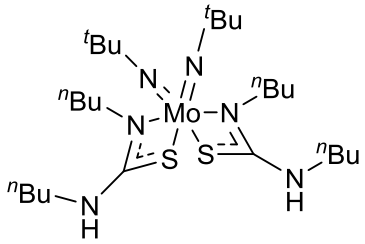

N,*N'*-dibutylthiourea (0.38 g, 2 mmol) was added to a stirring solution of (^{t}BuN)$_2$Mo(NMe$_2$)$_2$ (0.33 g, 1 mmol) in hexane (10 ml). After stirring for 18 hours an orange solution was formed, volatiles were removed *in vacuo* until a precipitate started to form. The precipitate was heated into solution, followed by filtration through Celite®. Storage at -28 °C yielded orange crystals.

Yield: 0.27 g, 44 %

^{1}H NMR (400 MHz, 349 K, C_6D_6) δ 4.49 (br s, 2H, N*H*), 3.38-3.27 (m, 8H, NCH_2), 1.82-1.71 (m, 4H, CH_2), 1.54 (s, 18H, CCH_3), 1.48-1.39 (m, 4H, CH_2), 1.36-1.27 (m, 4H, CH_2), 1.22-1.13 (m, 4H, CH_2), 1.02-0.96 (m, 6H, CH_3), 0.82-0.75 (m, 6H, CH_3)

^{13}C{^{1}H} NMR (75MHz, C_6D_6) δ 44.4, 43.9, 43.7, 33.3, 32.7, 32.0, 21.9, 20.7, 20.5, 14.9, 14.3

Elemental analysis found (calculated for $C_{26}H_{56}MoN_6S_2$): C – 50.80 (50.96), H – 9.35 (9.21), N – 13.60 (13.71) %

6.4.6 [(^{t}BuN)W(MeNC{S}NMe)(NH^{t}Bu)(SC{NHMe}NMe)] (31)

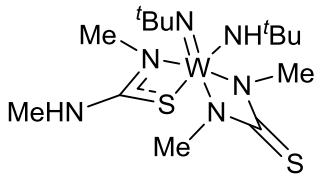

Hexane (20 ml) was added to a Schlenk containing (^{t}BuN)$_2$W(NH^{t}Bu)$_2$ (0.47 g, 1 mmol) and *N*,*N'*-dimethylthiourea (0.21 g, 2 mmol), after stirring for 48 hours a yellow precipitate was formed, volatiles were removed *in vacuo*. The resulting yellow solid was dissolved in hot toluene (~10 ml), filtered through Celite® and stored at room temperature where orange crystals formed.

Yield: 0.10 g, 19 %

^{1}H NMR (300 MHz, THF-*d*$_8$) δ 6.32 (s, 1H, N*H*), 2.91-2.80 (m, 12H, C*H*$_3$), 1.32 (s, 18H, C(C*H*$_3$)$_3$)

^{13}C{^{1}H} NMR (75MHz, THF-*d*$_8$) δ 33.3, 33.0, 32.9, 31.6

Elemental analysis found (calculated for $C_{14}H_{32}N_6S_2W$): C – 31.49 (31.58), H – 6.14 (6.06), N – 15.64 (15.79) %

6.4.7 [(^{t}BuN)W(EtNC{S}NEt)(NH^{t}Bu)(SC{NHEt}NEt)] (32)

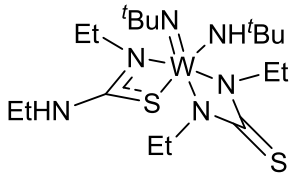

Hexane (20 ml) was added to a Schlenk containing (^{t}BuN)$_2$W(NH^{t}Bu)$_2$ (0.47 g, 1 mmol) and *N*,*N'*-diethylthiourea (0.26 g, 2 mmol), after stirring for 24 hours a yellow precipitate was formed, volatiles were removed *in vacuo*. The resulting yellow solid was dissolved in hot toluene (~10 ml), filtered through Celite® and stored at room temperature where orange crystals formed.

Yield: 0.13 g, 22 %

^{1}H NMR (300 MHz, THF-*d8*) δ 6.36 (s, 1H, N*H*), 6.12 (s, 1H, N*H*), 3.79-3.11 (m, 8H, C*H*$_2$), 1.31 (s, 18H, C(C*H*$_3$)$_3$), 1.24-1.06 (m, 12H, C*H*$_3$)

$^{13}C\{^{1}H\}$ NMR (75MHz, THF-*d8*) δ 171.3, 162.0, 60.1, 49.4, 44.4, 40.6, 38.5, 34.47, 33.3, 32.8, 31.9, 16.6, 16.4, 16.0, 14.9

Elemental analysis found (calculated $C_{18}H_{40}N_6S_2W$): C – 36.54 (36.74), H – 6.73 (6.85), N – 14.55 (14.28) %

6.4.8 [(^{t}BuN)W(^{n}BuNC{S}N^{n}Bu)(NH^{t}Bu)(SC{NH^{n}Bu}N^{n}Bu)] (33)

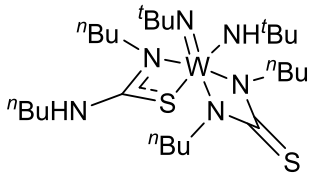

Hexane (20 ml) was added to a Schlenk containing (^{t}BuN)$_2$W(NH^{t}Bu)$_2$ (0.47 g, 1 mmol) and *N*,*N'*-dibutylthiourea (0.38 g, 2 mmol), after stirring for 72 hours an orange precipitate was formed, volatiles were removed *in vacuo*. The resulting orange solid was dissolved hexane (20 ml), filtered through Celite® and stored in a freezer (-28 °C) where orange crystals formed.

Yield: 0.38 g, 54 %

^{1}H NMR (300 MHz, THF-*d8*) δ 6.31 (s, 1H, N*H*), 6.11 (s, 1H, N*H*), 3.75-3.05 (br m, 8H, NCH_2), 1.76-1.34 (m, 16H, CH_2), 1.32 (s, 9H, NC(CH_3)$_3$), 1.30 (s, 9H, NC(CH_3)$_3$), 0.94 (s, 3H, CH_3), 0.92 (s, 6H, CH_3), 0.90 (s, 3H, CH_3)

$^{13}C\{^{1}H\}$ NMR (75MHz, THF-*d8*) δ 182.8, 171.9, 65.6, 54.9, 45.9, 44.7, 43.6, 34.5, 34.1, 33.3, 33.0, 32.9, 32.6, 32.0, 23.7, 22.0, 21.4, 21.2, 21.0, 14.8, 14.6, 14.4

Elemental analysis found (calculated for $C_{26}H_{56}N_6S_2W$): C – 44.42 (44.57), H – 8.21 (8.06), N – 11.83 (11.99) %

6.4.9 [{(^{t}BuN)W(SC{NH^{t}Bu}N^{t}Bu)(μ-S)}$_2$] (34)

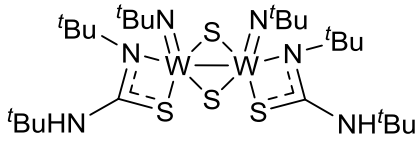

Hexane (20 ml) was added to a Schlenk containing (^{t}BuN)$_2$W(NH^{t}Bu)$_2$ (0.47 g, 1 mmol) and 1,3-di-*tert*-butyl-2-thiourea (0.38 g, 2 mmol), after stirring for 48 hours a

red precipitate was formed, volatiles were removed *in vacuo*. The resulting red solid was dissolved in hot toluene (~10 ml), filtered through Celite® and stored in a freezer (-28 °C) where red crystals formed.

Yield: 0.33 g, 70 %

^{1}H NMR (300 MHz, THF-d_8) δ 5.37 (s, 2H, NH), 1.81 (s, 18H, CNC(CH_3)$_3$), 1.48 (s, 18H, NC(CH_3)$_3$), 1.11 (s, 18H, CNC(CH_3)$_3$)

^{13}C{^{1}H} NMR (75MHz, THF-d_8) δ 173.2, 69.4, 57.4, 54.1, 32.3, 30.9, 30.8

Elemental analysis found (calculated for $C_{26}H_{56}N_6S_4W_2$): C – 33.16 (32.92), H – 5.89 (5.95), N – 8.79 (8.86) %

6.4.10 [^{t}Bu(Me$_3$Si)NH] (35)

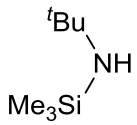

The complex was prepared according to a modified published procedure.[8]

A solution of Me_3SiCl (50 ml, 394 mmol) in hexane (60 ml) was added dropwise to stirring solution of $^{t}BuNH_2$ (88 ml, 837 mmol) in hexane (500 ml) at 0 °C. After the addition of the Me_3SiCl solution the ice bath was removed and the reaction mixture was stirred for 2 hours. After standing overnight, hexane (200 ml) was added prior to filtration through Celite®. The resulting clear solution was distilled at 70 °C to remove the hexane; the remaining liquor was distilled at 110-120 °C to afford the product as a colourless oil.

Yield: 23.1 g, 40 %

^{1}H NMR (300 MHz, C_6D_6) δ 1.11 (s, 9H, C(CH_3)$_3$), 0.12 (s, 9H, Si(CH_3)$_3$)

^{13}C{^{1}H} NMR (75MHz, C_6D_6) δ 49.8, 34.2, 3.1

6.4.11 [(^{t}BuN)$_2$W(NMe$_2$)$_2$] (36)

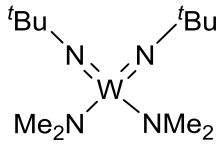

The complex was prepared according to a published procedure by the following three reactions:[9]

Reaction 1 – WCl_6 + 4 ^{t}Bu(Me$_3$Si)NH → ½ [(^{t}BuN)$_2$WCl$_2$(NH$_2$^{t}Bu)]$_2$ (**36a**) + 3 Me$_3$SiCl + (^{t}Bu)(Me$_3$Si)NH$_2$Cl

Reaction 2 – ½ [(^{t}BuN)$_2$WCl$_2$(NH$_2$^{t}Bu)]$_2$ (**36a**) + 2 pyridine → [(^{t}BuN)$_2$WCl$_2$py$_2$] (**36b**) + ^{t}BuNH$_2$

Reaction 3 – [(^{t}BuN)$_2$WCl$_2$py$_2$] (**36b**) + 2 LiNMe$_2$ → [(^{t}BuN)$_2$W(NMe$_2$)$_2$] (**36**) + 2 LiCl + 2 pyridine

Synthesis of **36a** – A solution of ^{t}Bu(Me$_3$Si)NH (23.1 g, 159 mmol) in toluene (30 ml) was added dropwise to a stirring suspension of WCl_6 (13.9 g, 35 mmol) in toluene (200 ml). After stirring for 72 hours the dark red/purple solution was filtered through Celite® to provide a dark brown liquor, volatiles were removed *in vacuo*. The resulting brown solid was mixed with hexane (30 ml) and left in a freezer overnight to remove any impurities. The liquor was filtered off and the remaining yellow/brown solid was dried *in vacuo*.

^{1}H NMR (300 MHz, C_6D_6) δ 2.59 (s, 4H, -N*H*$_2$-), 1.46 (s, 36H, -NC(C*H*$_3$)$_3$), 1.11 (s, 18H, NH$_2$C(C*H*$_3$)$_3$)

^{13}C{^{1}H} NMR (75MHz, C_6D_6) δ 68.7, 52.9, 31.9, 31.1

Synthesis of **36b** – To a stirring suspension of [(^{t}BuN)$_2$WCl$_2$(NH^{t}Bu)]$_2$ in diethyl ether (100 ml), an excess of pyridine (13.9 ml, 171 mmol) was added with an immediate colour change to black. After stirring for a further 24 hours, volatiles were removed *in vacuo* to provide a green solid.

^{1}H NMR (300 MHz, C_6D_6) δ 9.10 (m, 4H, *o*-py), 6.85 (m, 2H, *p*-py), 6.53 (m, 4H, *m*-py), 1.54 (s, 18H, NC(C*H*$_3$)$_3$)

$^{13}C\{^{1}H\}$ NMR (75MHz, C_6D_6) δ 152.5, 137.3, 123.8, 68.3, 31.9

Synthesis of **36** – $LiNMe_2$ (2.9 g, 57 mmol) was added extremely slowly to a stirring suspension of [(^{t}BuN)$_2$WCl$_2$py$_2$] in diethyl ether (150 ml), after stirring overnight a green suspension was formed, volatiles were removed *in vacuo*. The resulting green/brown residue was extracted with hexane (200 ml) and filtered through Celite®. The filtrate was dried *in vacuo* to provide a black/brown residue which was vacuum distilled (80 °C, $1x10^{-1}$ mbar) twice to afford a yellow/orange oil.

Overall yield: 6.03 g, 42 %

^{1}H NMR (300 MHz, C_6D_6) δ 3.49 (s, 12H, N(C*H*$_3$)$_2$), 1.40 (s, 18H, C(C*H*$_3$)$_3$)

$^{13}C\{^{1}H\}$ NMR (75MHz, C_6D_6) δ 66.8, 54.3, 34.5

Elemental analysis found (calculated for $C_{12}H_{30}N_4W$): C – 34.66 (34.79), H – 7.22 (7.30), N – 13.43 (13.53) %

6.4.12 [(^{t}BuN)$_2$Mo(SC{NMe$_2$}N^{i}Pr)$_2$] (37)

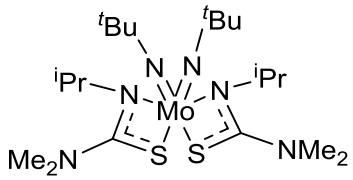

Isopropyl isothiocyanate (0.21 ml, 2 mmol) was added dropwise to a stirring solution of (^{t}BuN)$_2$Mo(NMe$_2$)$_2$ (0.33 g, 1 mmol) in hexane (10 ml). After stirring for 24 hours the resulting orange solution was reduced in volume until cloudy, the precipitate was then heated back into solution. Orange crystals were afforded after storage in a freezer at -28 °C.

Yield: 0.36 g, 68 %

^{1}H NMR (400 MHz, 349 K, C_6D_6) δ 4.21 (br s, 2H, C*H*CH$_3$), 2.64 (br s, 12H, NC*H*$_3$), 1.49 (br s, 40H, CHC*H*$_3$ and CC*H*$_3$)

$^{13}C\{^{1}H\}$ NMR (100 MHz, 337 K, THF-*d*$_8$) δ 51.7, 42.3, 32.6, 31.9, 31.7, 31.6

Elemental analysis found (calculated for $C_{20}H_{44}MoN_6S_2$): C – 47.72 (47.89), H – 8.52 (8.42), N – 13.40 (13.30) %

6.4.13 [(^{t}BuN)$_2$Mo(SC{NMe$_2$}NPh)$_2$] (38)

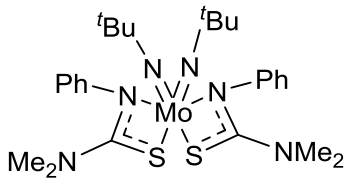

Phenyl isothiocyanate (0.24 ml, 2 mmol) was added dropwise to a stirring solution of (^{t}BuN)$_2$Mo(NMe$_2$)$_2$ (0.33 g, 1 mmol) in hexane (10 ml), an orange solution was immediately formed. After stirring for 18 hours a yellow precipitate was formed, the precipitate was heated back into solution then left to stand at room temperature to attain orange crystals.

Yield: 0.27 g, 45 %

^{1}H NMR (300 MHz, C_6D_6) δ 7.17-6.87 (m, 10H, C*H*), 2.34 (s, 12H, N(C*H*$_3$)$_2$), 1.45 (s, 18H, C(C*H*$_3$)$_3$)

^{13}C{^{1}H} NMR (75MHz, C_6D_6) δ 149.5, 125.0, 122.8, 69.9, 41.1, 31.9

Elemental analysis found (calculated for $C_{26}H_{40}MoN_6S_2$): C – 52.52 (52.33), H – 6.92 (6.76), N – 13.95 (14.08) %

6.4.14 [(^{t}BuN)$_2$W(SC{NMe$_2$}N^{i}Pr)$_2$] (39)

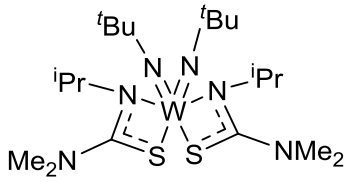

Isopropyl isothiocyanate (0.21 ml, 2 mmol) was added dropwise to a stirring solution of (^{t}BuN)$_2$W(NMe$_2$)$_2$ (0.41 g, 1 mmol) in hexane (10 ml). After stirring for 24 hours the resulting yellow solution was reduced in volume until cloudy, the precipitate was then heated back into solution. Yellow crystals were afforded after storage in a freezer at -28 °C.

Yield: 0.39 g, 63 %

^{1}H NMR (400 MHz, 349 K, C_6D_6) δ 4.34-4.18 (m, 2H, C*H*CH$_3$), 2.71-2.45 (m, 12H, NC*H*$_3$), 1.59-1.47 (m, 18H, CC*H*$_3$), 1.47-1.27 (m, 12H, CHC*H*$_3$)

$^{13}C\{^{1}H\}$ NMR (100 MHz, 337 K, THF-d_8) δ 51.7, 51.6, 51.3, 42.1, 42.0, 41.7, 33.9, 33.1, 32.9

Elemental analysis found (calculated for $C_{21}H_{44}N_5S_2W$): C – 39.06 (38.96), H – 7.08 (7.19), N – 13.61 (13.63) %

6.4.15 [(^{t}BuN)$_2$W(SC{NMe$_2$}NPh)$_2$] (40)

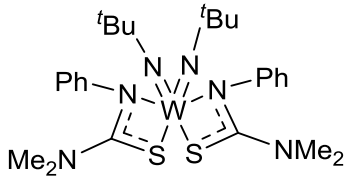

Phenyl isothiocyanate (0.24 ml, 2 mmol) was added dropwise to a stirring solution of (^{t}BuN)$_2$W(NMe$_2$)$_2$ (0.41 g, 1 mmol) in hexane (10 ml), a yellow precipitate was immediately formed. After stirring for a further 2 hours, the precipitate was heated back into solution then left to stand at room temperature to attain yellow crystals.

Yield: 0.32 g, 47 %

^1H NMR (300 MHz, C_6D_6) δ 7.61-6.91 (m, 10H, C*H*), 2.29 (s, 12H, N(C*H*$_3$)$_2$), 1.69-1.28 (m, 18H, C(C*H*$_3$)$_3$)

$^{13}C\{^{1}H\}$ NMR (75MHz, C_6D_6) δ 148.7, 126.6, 126.2, 125.0, 124.5, 124.2, 123.0, 67.5, 41.0, 33.4, 32.7

Elemental analysis found (calculated for $C_{27}H_{40}N_5S_2W$): C – 45.73 (45.62), H – 6.03 (5.89), N – 12.20 (12.28) %

6.4.16 [Mo(S$_2$CNEt$_2$)$_4$] (41)

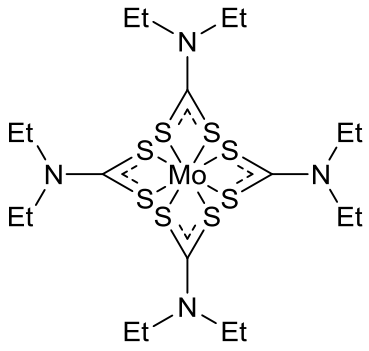

The complex was prepared according to a modified published procedure.[10]

A mixture of $Mo(CO)_6$ (1.32 g, 5 mmol) and tetraethylthiuram disulfide (2.97 g, 10 mmol) in THF (30 ml) was refluxed for *ca.* 66 hours. Solvent was removed *in vacuo* to provide a purple solid which was washed with hexane. The solid was dissolved in warm THF and the solution was slowly cooled to room temperature to yield purple crystals.

Yield: 3.11 g, 90 %

Elemental analysis found (calculated for $C_{20}H_{40}MoN_4S_8$): C – 35.00 (34.86), H – 5.79 (5.85), N – 7.94 (8.13) %

IR: 2930, 1489, 1352, 1271, 1212, 1145, 1075, 1000, 913, 850, 779 cm^{-1}

6.4.17 $[W(S_2CNEt_2)_4]$ (42)

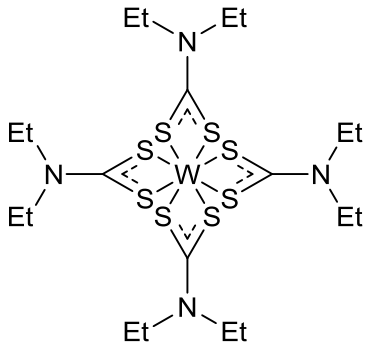

The complex was prepared according to a modified published procedure.[10]

$W(CO)_6$ (1.76 g, 5 mmol) was added to THF (15 ml) and heated until dissolved, this solution was added to a suspension of tetraethylthiuram disulfide (2.97 g, 10 mmol) in THF, the mixture was refluxed for *ca.* 72 hours. Solvent was removed *in vacuo* to provide a purple solid which was washed with hexane. The solid was dissolved in THF and stored at -28 °C to provide purple crystals.

Yield: 3.18 g, 82 %

Elemental analysis found (calculated for $C_{20}H_{40}N_4S_8W$): C – 31.06 (30.92), H – 5.29 (5.19), N – 7.05 (7.21) %

IR: 2929, 1490, 1431, 1353, 1270, 1210, 1146, 1071, 989, 913, 851, 780 cm^{-1}

6.4.18 $[Mo(S_2COEt)_4]$ (43)

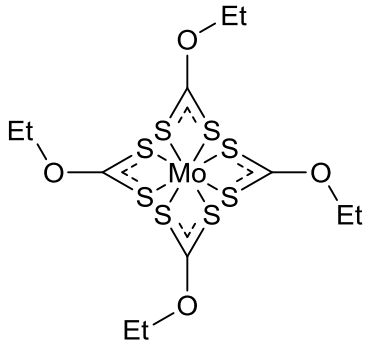

Cold DCM (20 ml) was added to $MoCl_5$ (0.55 g, 2 mmol) and five equivalents of potassium ethyl xanthate (1.60 g, 10 mmol) cooled in liquid N_2. The mixture was allowed to warm to room temperature and stirred for *ca.* 18 hours. The resulting purple mixture was filtered through Celite® to provide a purple solution. The volume of the solution was reduced by half *in vacuo* and layered with hexane (~45 ml) to provide dark purple crystals.

Yield: 0.30 g, 26 %

Elemental analysis found (calculated for $C_{12}H_{20}MoO_4S_8$): C – 24.71 (24.82), H – 3.56 (3.47) %

IR: 2980, 1466, 1367, 1208, 1115, 1031, 997, 861, 808 cm^{-1}

6.4.19 KS_2CO^iPr (44)

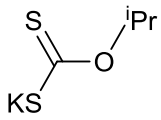

Under ambient conditions, CS_2 (0.99 ml, 20 mmol) was slowly added to a stirring solution of KOH (1.12 g, 20 mmol) in IPA (50 ml) to immediately form a yellow precipitate. After stirring for 2 hours, the precipitate was collected by filtration and then dried *in vacuo* to provide a yellow solid.

Yield: 1.33 g, 45 %

^{1}H NMR (300 MHz, D_2O) δ 5.41 (sept, *J* = 6.22 Hz, 1H, C*H*), 1.22 (d, *J* = 6.22 Hz, 6H, CHCH_3)

$^{13}C\{^{1}H\}$ NMR (75MHz, D_2O) δ 78.2, 21.0

6.4.20 [Mo(S_2CO^iPr)$_4$] (45)

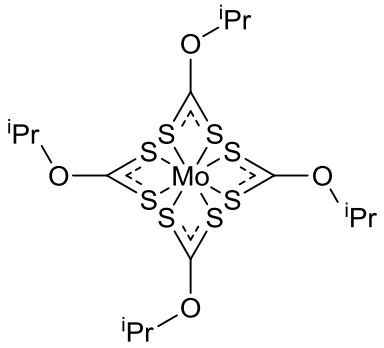

Cold DCM (20 ml) was added to $MoCl_5$ (0.27 g, 1 mmol) and five equivalents of potassium iso-propyl xanthate KS_2OEt (0.87 g, 5 mmol) cooled in liquid N_2. The mixture was allowed to warm to room temperature and stirred for *ca.* 18 hours. The resulting purple mixture was filtered through Celite® to provide a purple solution. Storage at -28 °C provided dark purple crystals.

Product was only analysed using single crystal X-ray diffraction, the yield of the complex was too low for other analytical techniques.

6.4.21 AACVD experiments

General procedure – Under an inert atmosphere, a solution of the desired precursor in toluene was placed in the precursor vessel. Cleaned substrates were then placed at the centre of quartz reactor tube in a tube furnace. The AACVD apparatus was connected and purged with a flow of argon gas at a pressure of 18 psi for 15 mins. Once the furnace had reached the deposition temperature, the precursor pot was opened to the argon flow to produce the aerosol for the desired deposition time. After deposition, the precursor vessel was stoppered and the substrates were cooled to room temperature. Specific conditions for each experiment are displayed in Table 5.5.

Graphene experiments - Graphene substrates were produced by Andrew Rushworth and consisted of a piece of CVD graphene approximately 1 cm^2 on a SiO_2/Si wafer (SiO_2 layer 300 nm thick) 2-3 cm^2 in size. For the deposition experiments, the graphene substrate was placed on top of a microscope slide for stability.

Table 5.5 Summary of conditions for AACVD experiments with precursors **37**, **39**, **41**, **42** and **43**. IPA/O – rinsed with IPA and then O_2 plasma cleaned for 20 mins. IPA – rinsed with IPA.

Precursor	Concentration / M	Substrates	Cleaning	Time / mins	Temperature / °C
37	0.05	Glass, Si	IPA/O	60	350
37	0.05	Glass, Si	IPA/O	60	400
37	0.05	Glass, Si	IPA/O	60	450
37	0.05	Glass, Si	IPA/O	60	500
39	0.05	Glass, Si	IPA/O	60	400
39	0.05	Glass, Si	IPA/O	60	450
39	0.05	Glass, Si	IPA/O	60	500
41	0.01	Glass, Si	IPA	90	250
41	0.01	Glass, Si	IPA	90	300
41	0.01	Glass, Si	IPA	90	350
41	0.01	Glass, Si	IPA	90	400
41	0.01	Glass, Si	IPA	90	450
41	0.01	Glass, Si	IPA	90	500
42	0.003	Glass, Si	IPA	90	350
42	0.003	Glass, Si	IPA	90	400
42	0.003	Glass, Si	IPA	90	450
42	0.003	Glass, Si	IPA	90	500
42	0.003	Graphene	-	60	400
42	0.003	Graphene	-	30	400
42	0.003	Graphene	-	15	400
42	0.003	Graphene	-	10	400
42	0.003	Graphene	-	5	400
42	0.003	Graphene	-	60	450
42	0.003	Graphene	-	30	450
43	0.01	Glass, Si	IPA	90	250
43	0.01	Glass, Si	IPA	90	300
43	0.01	Glass, Si	IPA	90	350
43	0.01	Glass, Si	IPA	90	400
43	0.01	Glass, Si	IPA	90	450

6.5 References

1. D. C. Bradley and I. M. Thomas, *J. Chem. Soc.*, 1960, 3857-3861.
2. A. N. Bhat, R. C. Fay, D. F. Lewis, A. F. Lindmark and S. H. Strauss, *Inorg. Chem.*, 1974, **13**, 886-892.
3. D. C. Bradley and M. H. Gitlitz, *J. Chem. Soc. A*, 1969, 1152-1156.
4. R. C. Fay, J. R. Weir and A. H. Bruder, *Inorg. Chem.*, 1984, **23**, 1079-1089.
5. W. A. Nugent, *Inorg. Chem.*, 1983, **22**, 965-969.
6. P. W. Dyer, V. C. Gibson, J. A. K. Howard, B. Whittle and C. Wilson, *Polyhedron*, 1995, **14**, 103-111.
7. V. Miikkulainen, M. Suvanto and T. A. Pakkanen, *Chem. Vap. Deposition*, 2008, **14**, 71-77.
8. R. M. Pike, *J. Org. Chem.*, 1961, **26**, 232-236.
9. J. S. Becker, S. Suh, S. Wang and R. G. Gordon, *Chem. Mater.*, 2003, **15**, 2969-2976.
10. M. Decoster, F. Conan, J. E. Guerchais, Y. Le Mest, J. Sala Pala, J. C. Jeffery, E. Faulques, A. Leblanc and P. Molinie, *Polyhedron*, 1995, **14**, 1741-1750.

Appendix

Crystal data and structure refinement tables

Table A1. Crystal data and structure refinement for **1**.

Identification code	k13alj10	
Empirical formula	C16 H38 N6 S2 Ti	
Formula weight	426.54	
Temperature	150(2) K	
Wavelength	0.71073 Å	
Crystal system	Monoclinic	
Space group	$P2_1/c$	
Unit cell dimensions	a = 15.1935(2) Å	α= 90°.
	b = 9.7091(2) Å	β= 111.1970(10)°.
	c = 16.3622(2) Å	γ = 90°.
Volume	2250.37(6) $Å^3$	
Z	4	
Density (calculated)	1.259 Mg/m^3	
Absorption coefficient	0.578 mm^{-1}	
F(000)	920	
Crystal size	0.150 x 0.100 x 0.075 mm^3	
Theta range for data collection	2.876 to 27.474°.	
Index ranges	-19<=h<=19, -12<=k<=12, -21<=l<=21	
Reflections collected	40118	
Independent reflections	5142 [R(int) = 0.0457]	
Completeness to theta = 25.242°	99.7 %	
Absorption correction	Semi-empirical from equivalents	
Max. and min. transmission	0.960 and 0.860	
Refinement method	Full-matrix least-squares on F^2	
Data / restraints / parameters	5142 / 0 / 238	
Goodness-of-fit on F^2	1.045	
Final R indices [I>2sigma(I)]	R1 = 0.0294, wR2 = 0.0737	
R indices (all data)	R1 = 0.0410, wR2 = 0.0793	
Extinction coefficient	n/a	
Largest diff. peak and hole	0.299 and -0.532 $e.Å^{-3}$	

Table A2. Crystal data and structure refinement for **2**.

Identification code	k13alj12	
Empirical formula	C18 H42 N6 S2 Ti	
Formula weight	454.59	
Temperature	150(2) K	
Wavelength	0.71073 Å	
Crystal system	Triclinic	
Space group	*P*-1	
Unit cell dimensions	a = 10.1580(2) Å	α= 103.1260(10)°.
	b = 15.6100(2) Å	β= 106.2510(10)°.
	c = 17.0922(3) Å	γ = 90.0810(10)°.
Volume	2527.85(8) $Å^3$	
Z	4	
Density (calculated)	1.194 Mg/m^3	
Absorption coefficient	0.518 mm^{-1}	
F(000)	984	
Crystal size	0.120 x 0.100 x 0.075 mm^3	
Theta range for data collection	3.156 to 30.000°.	
Index ranges	-14<=h<=14, -21<=k<=21, -24<=l<=24	
Reflections collected	29323	
Independent reflections	29323 [R(int) = 0.0472]	
Completeness to theta = 25.242°	93.2 %	
Absorption correction	None	
Refinement method	Full-matrix least-squares on F^2	
Data / restraints / parameters	29323 / 0 / 516	
Goodness-of-fit on F^2	1.117	
Final R indices [I>2sigma(I)]	R1 = 0.0541, wR2 = 0.1550	
R indices (all data)	R1 = 0.0673, wR2 = 0.1661	
Extinction coefficient	n/a	
Largest diff. peak and hole	0.553 and -0.628 $e.Å^{-3}$	

Table A3. Crystal data and structure refinement for **3**.

Identification code	k13alj09	
Empirical formula	C22 H34 N6 S2 Ti	
Formula weight	494.57	
Temperature	150(2) K	
Wavelength	0.71073 Å	
Crystal system	Triclinic	
Space group	*P*-1	
Unit cell dimensions	a = 9.0351(2) Å	α= 72.0407(8)°.
	b = 10.6507(2) Å	β= 72.1707(9)°.
	c = 14.5398(3) Å	γ = 78.5499(11)°.
Volume	1258.67(5) $Å^3$	
Z	2	
Density (calculated)	1.305 Mg/m^3	
Absorption coefficient	0.527 mm^{-1}	
F(000)	524	
Crystal size	0.125 x 0.100 x 0.075 mm^3	
Theta range for data collection	2.840 to 27.377°.	
Index ranges	-11<=h<=11, -13<=k<=13, -18<=l<=18	
Reflections collected	22310	
Independent reflections	5675 [R(int) = 0.0531]	
Completeness to theta = 25.242°	99.6 %	
Absorption correction	Semi-empirical from equivalents	
Max. and min. transmission	0.902 and 0.831	
Refinement method	Full-matrix least-squares on F^2	
Data / restraints / parameters	5675 / 0 / 288	
Goodness-of-fit on F^2	1.027	
Final R indices [I>2sigma(I)]	R1 = 0.0351, wR2 = 0.0845	
R indices (all data)	R1 = 0.0494, wR2 = 0.0919	
Extinction coefficient	n/a	
Largest diff. peak and hole	0.366 and -0.588 $e.Å^{-3}$	

Table A4. Crystal data and structure refinement for **4**.

Identification code	k12alj10	
Empirical formula	C57 H68 N8 S6 Ti2	
Formula weight	1153.35	
Temperature	150(2) K	
Wavelength	0.71073 Å	
Crystal system	Triclinic	
Space group	*P*-1	
Unit cell dimensions	a = 10.0035(4) Å	α= 115.6883(14)°.
	b = 12.7205(5) Å	β= 104.4835(16)°.
	c = 13.6344(7) Å	γ = 95.055(2)°.
Volume	1474.91(11) $Å^3$	
Z	1	
Density (calculated)	1.299 Mg/m^3	
Absorption coefficient	0.527 mm^{-1}	
F(000)	606	
Crystal size	0.100 x 0.100 x 0.080 mm^3	
Theta range for data collection	3.649 to 28.365°.	
Index ranges	-12<=h<=13, -16<=k<=15, -17<=l<=17	
Reflections collected	21500	
Independent reflections	6459 [R(int) = 0.0591]	
Completeness to theta = 25.242°	99.5 %	
Absorption correction	Semi-empirical from equivalents	
Max. and min. transmission	0.970 and 0.903	
Refinement method	Full-matrix least-squares on F^2	
Data / restraints / parameters	6459 / 0 / 355	
Goodness-of-fit on F^2	1.060	
Final R indices [I>2sigma(I)]	R1 = 0.0504, wR2 = 0.1024	
R indices (all data)	R1 = 0.0844, wR2 = 0.1154	
Extinction coefficient	n/a	
Largest diff. peak and hole	0.437 and -0.390 $e.Å^{-3}$	

Table A5. Crystal data and structure refinement for **5**.

Identification code	e14alj15	
Empirical formula	C20 H45 N7 S3 Zr	
Formula weight	571.03	
Temperature	150(2) K	
Wavelength	0.71073 Å	
Crystal system	Triclinic	
Space group	*P*-1	
Unit cell dimensions	a = 8.7660(5) Å	α= 76.626(7)°.
	b = 10.1473(8) Å	β= 75.930(5)°.
	c = 16.7267(12) Å	γ = 75.053(6)°.
Volume	1371.64(18) $Å^3$	
Z	2	
Density (calculated)	1.383 Mg/m^3	
Absorption coefficient	0.651 mm^{-1}	
F(000)	604	
Crystal size	0.300 x 0.180 x 0.100 mm^3	
Theta range for data collection	3.224 to 32.864°.	
Index ranges	-13<=h<=12, -14<=k<=15, -25<=l<=24	
Reflections collected	16045	
Independent reflections	8996 [R(int) = 0.0534]	
Completeness to theta = 25.242°	99.7 %	
Refinement method	Full-matrix least-squares on F^2	
Data / restraints / parameters	8996 / 0 / 294	
Goodness-of-fit on F^2	1.138	
Final R indices [I>2sigma(I)]	R1 = 0.0705, wR2 = 0.1621	
R indices (all data)	R1 = 0.0873, wR2 = 0.1739	
Extinction coefficient	n/a	
Largest diff. peak and hole	2.794 and -1.195 $e.Å^{-3}$	

Table A6. Crystal data and structure refinement for **6**.

Identification code	e14alj14	
Empirical formula	C23 H51 N7 S3 Zr	
Formula weight	613.10	
Temperature	150(2) K	
Wavelength	0.71073 Å	
Crystal system	Monoclinic	
Space group	$P2_1/c$	
Unit cell dimensions	a = 8.44680(10) Å	α= 90°.
	b = 20.0780(3) Å	β= 90.2600(10)°.
	c = 38.0712(6) Å	γ = 90°.
Volume	6456.61(16) $Å^3$	
Z	8	
Density (calculated)	1.261 Mg/m^3	
Absorption coefficient	0.558 mm^{-1}	
F(000)	2608	
Crystal size	0.200 x 0.180 x 0.090 mm^3	
Theta range for data collection	3.533 to 28.449°.	
Index ranges	-10<=h<=10, -26<=k<=21, -39<=l<=51	
Reflections collected	52548	
Independent reflections	13627 [R(int) = 0.0388]	
Completeness to theta = 25.242°	99.2 %	
Absorption correction	Semi-empirical from equivalents	
Max. and min. transmission	1.00000 and 0.95904	
Refinement method	Full-matrix least-squares on F^2	
Data / restraints / parameters	13627 / 0 / 647	
Goodness-of-fit on F^2	1.192	
Final R indices [I>2sigma(I)]	R1 = 0.0512, wR2 = 0.0958	
R indices (all data)	R1 = 0.0680, wR2 = 0.1008	
Extinction coefficient	n/a	
Largest diff. peak and hole	0.627 and -0.518 $e.Å^{-3}$	

Table A7. Crystal data and structure refinement for **7**.

Identification code	e14alj16	
Empirical formula	C57 H68 N8 S4 Zr	
Formula weight	1084.65	
Temperature	150(2) K	
Wavelength	0.71073 Å	
Crystal system	Triclinic	
Space group	*P*-1	
Unit cell dimensions	a = 10.9434(5) Å	α= 85.333(9)°.
	b = 13.179(2) Å	β= 80.990(4)°.
	c = 19.3538(9) Å	γ = 87.271(9)°.
Volume	2746.0(5) $Å^3$	
Z	2	
Density (calculated)	1.312 Mg/m^3	
Absorption coefficient	0.397 mm^{-1}	
F(000)	1140	
Crystal size	0.300 x 0.200 x 0.060 mm^3	
Theta range for data collection	3.389 to 26.456°.	
Index ranges	-13<=h<=13, -11<=k<=16, -24<=l<=24	
Reflections collected	13127	
Independent reflections	13127 [R(int) = ?]	
Completeness to theta = 25.242°	99.7 %	
Absorption correction	Semi-empirical from equivalents	
Max. and min. transmission	1.00000 and 0.96585	
Refinement method	Full-matrix least-squares on F^2	
Data / restraints / parameters	13127 / 36 / 601	
Goodness-of-fit on F^2	0.980	
Final R indices [I>2sigma(I)]	R1 = 0.0531, wR2 = 0.1418	
R indices (all data)	R1 = 0.1033, wR2 = 0.1542	
Extinction coefficient	n/a	
Largest diff. peak and hole	0.623 and -0.597 $e.Å^{-3}$	

Table A8. Crystal data and structure refinement for **8**.

Identification code	s14alj25	
Empirical formula	C20 H45 Hf N7 S3	
Formula weight	658.30	
Temperature	150.01(10) K	
Wavelength	0.71073 Å	
Crystal system	Triclinic	
Space group	*P*-1	
Unit cell dimensions	a = 8.7605(4) Å	α= 76.800(3)°.
	b = 10.1226(4) Å	β= 76.333(3)°.
	c = 16.7378(6) Å	γ = 74.934(4)°.
Volume	1370.47(10) $Å^3$	
Z	2	
Density (calculated)	1.595 Mg/m^3	
Absorption coefficient	4.056 mm^{-1}	
F(000)	668	
Crystal size	0.120 x 0.100 x 0.100 mm^3	
Theta range for data collection	3.463 to 32.780°.	
Index ranges	-13<=h<=12, -14<=k<=15, -24<=l<=24	
Reflections collected	16554	
Independent reflections	8999 [R(int) = 0.0412]	
Completeness to theta = 25.242°	99.7 %	
Absorption correction	Semi-empirical from equivalents	
Max. and min. transmission	1.00000 and 0.91589	
Refinement method	Full-matrix least-squares on F^2	
Data / restraints / parameters	8999 / 0 / 294	
Goodness-of-fit on F^2	1.001	
Final R indices [I>2sigma(I)]	R1 = 0.0335, wR2 = 0.0610	
R indices (all data)	R1 = 0.0384, wR2 = 0.0640	
Extinction coefficient	n/a	
Largest diff. peak and hole	2.051 and -2.185 $e.Å^{-3}$	

Table A9. Crystal data and structure refinement for **10**.

Identification code	s14alj27	
Empirical formula	C29 H39 Hf N7 S3	
Formula weight	760.34	
Temperature	150.00(10) K	
Wavelength	0.71073 Å	
Crystal system	Monoclinic	
Space group	$P2_1/c$	
Unit cell dimensions	a = 19.6584(5) Å	α= 90°.
	b = 10.1965(2) Å	β= 110.212(2)°.
	c = 16.8093(4) Å	γ = 90°.
Volume	3161.89(13) $Å^3$	
Z	4	
Density (calculated)	1.597 Mg/m^3	
Absorption coefficient	3.528 mm^{-1}	
F(000)	1528	
Crystal size	0.130 x 0.100 x 0.080 mm^3	
Theta range for data collection	3.313 to 29.495°.	
Index ranges	-24<=h<=21, -13<=k<=12, -20<=l<=22	
Reflections collected	25053	
Independent reflections	7497 [R(int) = 0.0420]	
Completeness to theta = 25.242°	99.8 %	
Absorption correction	Semi-empirical from equivalents	
Max. and min. transmission	1.00000 and 0.86846	
Refinement method	Full-matrix least-squares on F^2	
Data / restraints / parameters	7497 / 0 / 369	
Goodness-of-fit on F^2	1.024	
Final R indices [I>2sigma(I)]	R1 = 0.0298, wR2 = 0.0548	
R indices (all data)	R1 = 0.0437, wR2 = 0.0606	
Extinction coefficient	n/a	
Largest diff. peak and hole	0.619 and -0.830 $e.Å^{-3}$	

Table A10. Crystal data and structure refinement for **11**.

Identification code	s15alj15	
Empirical formula	C40 H80 N8 S16 Ti2	
Formula weight	1281.88	
Temperature	150(2) K	
Wavelength	0.71073 Å	
Crystal system	Triclinic	
Space group	*P*-1	
Unit cell dimensions	a = 11.3612(4) Å	α= 96.318(3)°.
	b = 15.1888(5) Å	β= 94.856(3)°.
	c = 18.0705(7) Å	γ = 92.372(3)°.
Volume	3084.19(19) $Å^3$	
Z	2	
Density (calculated)	1.380 Mg/m^3	
Absorption coefficient	0.836 mm^{-1}	
F(000)	1352	
Crystal size	0.125 x 0.125 x 0.100 mm^3	
Theta range for data collection	3.358 to 29.419°.	
Index ranges	-15<=h<=14, -20<=k<=18, -22<=l<=24	
Reflections collected	24846	
Independent reflections	14106 [R(int) = 0.0386]	
Completeness to theta = 25.242°	99.7 %	
Absorption correction	Semi-empirical from equivalents	
Max. and min. transmission	1.00000 and 0.99332	
Refinement method	Full-matrix least-squares on F^2	
Data / restraints / parameters	14106 / 32 / 657	
Goodness-of-fit on F^2	1.028	
Final R indices [I>2sigma(I)]	R1 = 0.0495, wR2 = 0.0908	
R indices (all data)	R1 = 0.0722, wR2 = 0.1058	
Extinction coefficient	n/a	
Largest diff. peak and hole	1.879 and -1.235 $e.Å^{-3}$	

Table A11. Crystal data and structure refinement for **11a**.

Identification code	s15alj14	
Empirical formula	C30 H60 N6 O S12 Ti2	
Formula weight	1001.36	
Temperature	150(2) K	
Wavelength	0.71073 Å	
Crystal system	Monoclinic	
Space group	*C*2/*c*	
Unit cell dimensions	a = 16.4332(6) Å	α= 90°.
	b = 12.4780(4) Å	β= 99.201(3)°.
	c = 23.0275(8) Å	γ = 90°.
Volume	4661.1(3) Å^3	
Z	4	
Density (calculated)	1.427 Mg/m^3	
Absorption coefficient	0.913 mm^{-1}	
F(000)	2104	
Crystal size	0.200 x 0.100 x 0.075 mm^3	
Theta range for data collection	3.386 to 29.377°.	
Index ranges	-21<=h<=22, -16<=k<=15, -26<=l<=30	
Reflections collected	18832	
Independent reflections	5609 [R(int) = 0.0407]	
Completeness to theta = 25.242°	99.7 %	
Absorption correction	Semi-empirical from equivalents	
Max. and min. transmission	1.00000 and 0.83065	
Refinement method	Full-matrix least-squares on F^2	
Data / restraints / parameters	5609 / 0 / 237	
Goodness-of-fit on F^2	1.068	
Final R indices [I>2sigma(I)]	R1 = 0.0397, wR2 = 0.0769	
R indices (all data)	R1 = 0.0503, wR2 = 0.0813	
Extinction coefficient	n/a	
Largest diff. peak and hole	0.493 and -0.351 e.Å^{-3}	

Table A12. Crystal data and structure refinement for **12**.

Identification code	s15alj20	
Empirical formula	C20 H40 N4 S8 Zr	
Formula weight	684.26	
Temperature	150.00(10) K	
Wavelength	0.71073 Å	
Crystal system	Triclinic	
Space group	*P*-1	
Unit cell dimensions	a = 11.4109(3) Å	α= 96.601(2)°.
	b = 15.2331(4) Å	β= 95.438(2)°.
	c = 18.3561(6) Å	γ = 91.847(2)°.
Volume	3152.30(16) $Å^3$	
Z	4	
Density (calculated)	1.442 Mg/m^3	
Absorption coefficient	0.896 mm^{-1}	
F(000)	1424	
Crystal size	0.200 x 0.125 x 0.100 mm^3	
Theta range for data collection	3.324 to 29.454°.	
Index ranges	-15<=h<=15, -20<=k<=20, -18<=l<=23	
Reflections collected	26203	
Independent reflections	14423 [R(int) = 0.0302]	
Completeness to theta = 25.242°	99.7 %	
Absorption correction	Semi-empirical from equivalents	
Max. and min. transmission	1.00000 and 0.70947	
Refinement method	Full-matrix least-squares on F^2	
Data / restraints / parameters	14423 / 30 / 670	
Goodness-of-fit on F^2	1.034	
Final R indices [I>2sigma(I)]	R1 = 0.0404, wR2 = 0.0739	
R indices (all data)	R1 = 0.0533, wR2 = 0.0813	
Extinction coefficient	n/a	
Largest diff. peak and hole	2.451 and -1.678 $e.Å^{-3}$	

Table A13. Crystal data and structure refinement for **13**.

Identification code	s15alj16	
Empirical formula	C40 H80 Hf2 N8 S16	
Formula weight	1543.06	
Temperature	150(2) K	
Wavelength	0.71073 Å	
Crystal system	Triclinic	
Space group	*P*-1	
Unit cell dimensions	a = 11.4165(4) Å	α= 96.404(3)°.
	b = 15.2295(5) Å	β= 95.348(3)°.
	c = 18.3284(6) Å	γ = 91.835(3)°.
Volume	3150.14(18) $Å^3$	
Z	2	
Density (calculated)	1.627 Mg/m^3	
Absorption coefficient	3.859 mm^{-1}	
F(000)	1552	
Crystal size	0.100 x 0.100 x 0.100 mm^3	
Theta range for data collection	3.320 to 29.257°.	
Index ranges	-13<=h<=15, -19<=k<=20, -24<=l<=23	
Reflections collected	26937	
Independent reflections	14329 [R(int) = 0.0319]	
Completeness to theta = 25.242°	99.8 %	
Absorption correction	Semi-empirical from equivalents	
Max. and min. transmission	1.00000 and 0.77614	
Refinement method	Full-matrix least-squares on F^2	
Data / restraints / parameters	14329 / 7 / 661	
Goodness-of-fit on F^2	1.030	
Final R indices [I>2sigma(I)]	R1 = 0.0314, wR2 = 0.0611	
R indices (all data)	R1 = 0.0377, wR2 = 0.0639	
Extinction coefficient	n/a	
Largest diff. peak and hole	1.967 and -1.581 $e.Å^{-3}$	

Table A14. Crystal data and structure refinement for **17**.

Identification code	s15alj19	
Empirical formula	C20 H35 N3 S6 Zr	
Formula weight	601.09	
Temperature	150.00(10) K	
Wavelength	0.71073 Å	
Crystal system	Monoclinic	
Space group	*Pc*	
Unit cell dimensions	a = 9.2360(2) Å	α= 90°.
	b = 10.5132(2) Å	β= 97.681(2)°.
	c = 14.0107(3) Å	γ = 90°.
Volume	1348.23(5) $Å^3$	
Z	2	
Density (calculated)	1.481 Mg/m^3	
Absorption coefficient	0.886 mm^{-1}	
F(000)	624	
Crystal size	0.175 x 0.100 x 0.100 mm^3	
Theta range for data collection	3.426 to 29.397°.	
Index ranges	-11<=h<=11, -10<=k<=14, -18<=l<=18	
Reflections collected	10970	
Independent reflections	5656 [R(int) = 0.0300]	
Completeness to theta = 25.242°	99.8 %	
Absorption correction	Semi-empirical from equivalents	
Max. and min. transmission	1.00000 and 0.91127	
Refinement method	Full-matrix least-squares on F^2	
Data / restraints / parameters	5656 / 2 / 277	
Goodness-of-fit on F^2	1.044	
Final R indices [I>2sigma(I)]	R1 = 0.0287, wR2 = 0.0539	
R indices (all data)	R1 = 0.0301, wR2 = 0.0553	
Absolute structure parameter	-0.01(3)	
Extinction coefficient	n/a	
Largest diff. peak and hole	0.321 and -0.351 $e.Å^{-3}$	

Table A15. Crystal data and structure refinement for **19**.

Identification code	s16alj10	
Empirical formula	C15 H39 N6 S Ta	
Formula weight	516.53	
Temperature	150(2) K	
Wavelength	1.54184 Å	
Crystal system	Orthorhombic	
Space group	*Pbca*	
Unit cell dimensions	a = 14.75720(10) Å	α= 90°.
	b = 19.88350(10) Å	β= 90°.
	c = 28.78220(10) Å	γ = 90°.
Volume	8445.41(8) $Å^3$	
Z	16	
Density (calculated)	1.625 Mg/m^3	
Absorption coefficient	10.587 mm^{-1}	
F(000)	4160	
Crystal size	0.075 x 0.050 x 0.050 mm^3	
Theta range for data collection	3.071 to 73.158°.	
Index ranges	-18<=h<=18, -24<=k<=24, -35<=l<=22	
Reflections collected	86365	
Independent reflections	8409 [R(int) = 0.0351]	
Completeness to theta = 67.684°	99.9 %	
Absorption correction	Semi-empirical from equivalents	
Max. and min. transmission	1.00000 and 0.46386	
Refinement method	Full-matrix least-squares on F^2	
Data / restraints / parameters	8409 / 0 / 441	
Goodness-of-fit on F^2	1.110	
Final R indices [I>2sigma(I)]	R1 = 0.0298, wR2 = 0.0761	
R indices (all data)	R1 = 0.0303, wR2 = 0.0765	
Extinction coefficient	n/a	
Largest diff. peak and hole	3.802 and -1.844 $e.Å^{-3}$	

Table A16. Crystal data and structure refinement for **21**.

Identification code	e15alj05	
Empirical formula	C18 H41 N6 S2 Ta	
Formula weight	586.64	
Temperature	150(2) K	
Wavelength	0.71073 Å	
Crystal system	Monoclinic	
Space group	$P2_1/c$	
Unit cell dimensions	a = 17.7256(5) Å	α= 90°.
	b = 16.0383(4) Å	β= 98.621(3)°.
	c = 9.0315(3) Å	γ = 90°.
Volume	2538.54(13) $Å^3$	
Z	4	
Density (calculated)	1.535 Mg/m^3	
Absorption coefficient	4.509 mm^{-1}	
F(000)	1184	
Crystal size	0.180 x 0.180 x 0.120 mm^3	
Theta range for data collection	3.415 to 27.505°.	
Index ranges	-16<=h<=23, -20<=k<=20, -11<=l<=11	
Reflections collected	23020	
Independent reflections	5805 [R(int) = 0.0427]	
Completeness to theta = 25.242°	99.8 %	
Absorption correction	Semi-empirical from equivalents	
Max. and min. transmission	1.00000 and 0.80069	
Refinement method	Full-matrix least-squares on F^2	
Data / restraints / parameters	5805 / 0 / 257	
Goodness-of-fit on F^2	1.067	
Final R indices [I>2sigma(I)]	R1 = 0.0351, wR2 = 0.0682	
R indices (all data)	R1 = 0.0465, wR2 = 0.0717	
Extinction coefficient	n/a	
Largest diff. peak and hole	4.197 and -1.288 $e.Å^{-3}$	

Table A17. Crystal data and structure refinement for **22**.

Identification code	e16alj01	
Empirical formula	C31 H42 N7 S3 Ta	
Formula weight	789.84	
Temperature	150.00(10) K	
Wavelength	0.71073 Å	
Crystal system	Monoclinic	
Space group	$P2_1/c$	
Unit cell dimensions	a = 12.0189(3) Å	α= 90°.
	b = 13.2180(3) Å	β= 94.027(2)°.
	c = 21.5932(4) Å	γ = 90°.
Volume	3421.95(13) Å^3	
Z	4	
Density (calculated)	1.533 Mg/m^3	
Absorption coefficient	3.427 mm^{-1}	
F(000)	1592	
Crystal size	0.320 x 0.220 x 0.110 mm^3	
Theta range for data collection	3.224 to 28.555°.	
Index ranges	-14<=h<=13, -16<=k<=16, -27<=l<=28	
Reflections collected	29453	
Independent reflections	7406 [R(int) = 0.0341]	
Completeness to theta = 25.242°	99.8 %	
Absorption correction	Semi-empirical from equivalents	
Max. and min. transmission	1.00000 and 0.86912	
Refinement method	Full-matrix least-squares on F^2	
Data / restraints / parameters	7406 / 0 / 388	
Goodness-of-fit on F^2	1.040	
Final R indices [I>2sigma(I)]	R1 = 0.0234, wR2 = 0.0434	
R indices (all data)	R1 = 0.0295, wR2 = 0.0457	
Extinction coefficient	n/a	
Largest diff. peak and hole	0.459 and -0.408 e.Å^{-3}	

Table A18. Crystal data and structure refinement for **25**.

Identification code	s16alj01	
Empirical formula	C20 H29 N4 S6 Ta	
Formula weight	698.78	
Temperature	150.00(10) K	
Wavelength	0.71073 Å	
Crystal system	Monoclinic	
Space group	$P2_1/c$	
Unit cell dimensions	a = 10.7039(2) Å	α= 90°.
	b = 15.6423(3) Å	β= 94.454(2)°.
	c = 16.0464(3) Å	γ = 90°.
Volume	2678.59(9) $Å^3$	
Z	4	
Density (calculated)	1.733 Mg/m^3	
Absorption coefficient	4.587 mm^{-1}	
F(000)	1384	
Crystal size	0.250 x 0.170 x 0.100 mm^3	
Theta range for data collection	2.565 to 29.594°.	
Index ranges	-14<=h<=14, -21<=k<=21, -22<=l<=20	
Reflections collected	24256	
Independent reflections	6624 [R(int) = 0.0276]	
Completeness to theta = 25.242°	99.9 %	
Absorption correction	Semi-empirical from equivalents	
Max. and min. transmission	1.00000 and 0.77899	
Refinement method	Full-matrix least-squares on F^2	
Data / restraints / parameters	6624 / 0 / 284	
Goodness-of-fit on F^2	1.074	
Final R indices [I>2sigma(I)]	R1 = 0.0223, wR2 = 0.0411	
R indices (all data)	R1 = 0.0270, wR2 = 0.0425	
Extinction coefficient	n/a	
Largest diff. peak and hole	0.847 and -0.777 $e.Å^{-3}$	

Table A19. Crystal data and structure refinement for **28**.

Identification code	s15alj25	
Empirical formula	C63 H136 Mo4 N24 S8	
Formula weight	1870.19	
Temperature	150.01(10) K	
Wavelength	1.54184 Å	
Crystal system	Monoclinic	
Space group	$P2_1/c$	
Unit cell dimensions	a = 13.78640(10) Å	α= 90°.
	b = 24.0760(2) Å	β= 91.8490(10)°.
	c = 14.10850(10) Å	γ = 90°.
Volume	4680.47(6) $Å^3$	
Z	2	
Density (calculated)	1.327 Mg/m^3	
Absorption coefficient	6.327 mm^{-1}	
F(000)	1956	
Crystal size	0.200 x 0.200 x 0.030 mm^3	
Theta range for data collection	3.633 to 71.890°.	
Index ranges	-15<=h<=16, -29<=k<=25, -16<=l<=17	
Reflections collected	21684	
Independent reflections	9003 [R(int) = 0.0252]	
Completeness to theta = 67.684°	100.0 %	
Absorption correction	Semi-empirical from equivalents	
Max. and min. transmission	1.00000 and 0.62338	
Refinement method	Full-matrix least-squares on F^2	
Data / restraints / parameters	9003 / 0 / 515	
Goodness-of-fit on F^2	1.043	
Final R indices [I>2sigma(I)]	R1 = 0.0253, wR2 = 0.0624	
R indices (all data)	R1 = 0.0290, wR2 = 0.0646	
Extinction coefficient	n/a	
Largest diff. peak and hole	0.543 and -0.364 $e.Å^{-3}$	

Table A20. Crystal data and structure refinement for **31**.

Identification code	e14alj13	
Empirical formula	C14 H30 N6 S2 W	
Formula weight	530.41	
Temperature	150(2) K	
Wavelength	0.71073 Å	
Crystal system	Monoclinic	
Space group	$P2_1/n$	
Unit cell dimensions	a = 14.0529(11) Å	α= 90°.
	b = 10.8642(7) Å	β= 91.163(7)°.
	c = 14.2210(13) Å	γ = 90°.
Volume	2170.7(3) Å^3	
Z	4	
Density (calculated)	1.623 Mg/m^3	
Absorption coefficient	5.521 mm^{-1}	
F(000)	1048	
Crystal size	0.160 x 0.160 x 0.080 mm^3	
Theta range for data collection	3.425 to 27.534°.	
Index ranges	-18<=h<=18, -14<=k<=14, -16<=l<=18	
Reflections collected	5591	
Independent reflections	5591 [R(int) = ?]	
Completeness to theta = 25.242°	99.6 %	
Absorption correction	Semi-empirical from equivalents	
Max. and min. transmission	1.00000 and 0.80133	
Refinement method	Full-matrix least-squares on F^2	
Data / restraints / parameters	5591 / 18 / 219	
Goodness-of-fit on F^2	0.961	
Final R indices [I>2sigma(I)]	R1 = 0.0708, wR2 = 0.1699	
R indices (all data)	R1 = 0.1160, wR2 = 0.1836	
Extinction coefficient	n/a	
Largest diff. peak and hole	4.432 and -1.963 e.Å^{-3}	

Table A21. Crystal data and structure refinement for **32**.

Identification code	s14alj18	
Empirical formula	C18 H39 N6 S2 W	
Formula weight	587.52	
Temperature	150(2) K	
Wavelength	0.71073 Å	
Crystal system	Monoclinic	
Space group	$P2_1/c$	
Unit cell dimensions	a = 8.2279(2) Å	α= 90°.
	b = 13.7426(4) Å	β= 97.688(3)°.
	c = 22.7347(6) Å	γ = 90°.
Volume	2547.57(12) Å^3	
Z	4	
Density (calculated)	1.532 Mg/m^3	
Absorption coefficient	4.712 mm^{-1}	
F(000)	1180	
Crystal size	0.200 x 0.080 x 0.040 mm^3	
Theta range for data collection	3.241 to 29.382°.	
Index ranges	-11<=h<=10, -16<=k<=17, -30<=l<=30	
Reflections collected	21315	
Independent reflections	6160 [R(int) = 0.0534]	
Completeness to theta = 25.242°	99.7 %	
Absorption correction	Semi-empirical from equivalents	
Max. and min. transmission	1.00000 and 0.62703	
Refinement method	Full-matrix least-squares on F^2	
Data / restraints / parameters	6160 / 0 / 278	
Goodness-of-fit on F^2	1.091	
Final R indices [I>2sigma(I)]	R1 = 0.0422, wR2 = 0.0679	
R indices (all data)	R1 = 0.0569, wR2 = 0.0724	
Extinction coefficient	n/a	
Largest diff. peak and hole	1.157 and -0.899 e.Å^{-3}	

Table A22. Crystal data and structure refinement for **33**.

Identification code	s14alj15	
Empirical formula	C26 H54 N6 S2 W	
Formula weight	698.72	
Temperature	150(2) K	
Wavelength	0.71073 Å	
Crystal system	Monoclinic	
Space group	$P2_1/n$	
Unit cell dimensions	a = 11.1570(3) Å	α= 90°.
	b = 20.7975(6) Å	β= 109.131(3)°.
	c = 14.8166(4) Å	γ = 90°.
Volume	3248.13(16) $Å^3$	
Z	4	
Density (calculated)	1.429 Mg/m^3	
Absorption coefficient	3.709 mm^{-1}	
F(000)	1432	
Crystal size	0.370 x 0.160 x 0.120 mm^3	
Theta range for data collection	3.396 to 27.944°.	
Index ranges	-14<=h<=13, -27<=k<=27, -18<=l<=18	
Reflections collected	26284	
Independent reflections	7236 [R(int) = 0.0668]	
Completeness to theta = 25.242°	99.8 %	
Absorption correction	Semi-empirical from equivalents	
Max. and min. transmission	1.00000 and 0.94309	
Refinement method	Full-matrix least-squares on F^2	
Data / restraints / parameters	7236 / 0 / 326	
Goodness-of-fit on F^2	1.178	
Final R indices [I>2sigma(I)]	R1 = 0.0593, wR2 = 0.1171	
R indices (all data)	R1 = 0.0719, wR2 = 0.1226	
Extinction coefficient	n/a	
Largest diff. peak and hole	1.778 and -2.777 $e.Å^{-3}$	

Table A23. Crystal data and structure refinement for **34**.

Identification code	s14alj19	
Empirical formula	C33 H62 N6 S4 W2	
Formula weight	1038.82	
Temperature	150(2) K	
Wavelength	0.71073 Å	
Crystal system	Triclinic	
Space group	*P*-1	
Unit cell dimensions	a = 13.2547(6) Å	α= 115.582(6)°.
	b = 13.4364(9) Å	β= 97.300(4)°.
	c = 13.4407(8) Å	γ = 90.779(4)°.
Volume	2135.3(2) $Å^3$	
Z	2	
Density (calculated)	1.616 Mg/m^3	
Absorption coefficient	5.607 mm^{-1}	
F(000)	1028	
Crystal size	0.260 x 0.200 x 0.100 mm^3	
Theta range for data collection	3.262 to 29.337°.	
Index ranges	-18<=h<=16, -18<=k<=13, -17<=l<=18	
Reflections collected	17684	
Independent reflections	9838 [R(int) = 0.0540]	
Completeness to theta = 25.242°	99.7 %	
Absorption correction	Semi-empirical from equivalents	
Max. and min. transmission	1.00000 and 0.62419	
Refinement method	Full-matrix least-squares on F^2	
Data / restraints / parameters	9838 / 0 / 425	
Goodness-of-fit on F^2	1.077	
Final R indices [I>2sigma(I)]	R1 = 0.0548, wR2 = 0.0859	
R indices (all data)	R1 = 0.0839, wR2 = 0.0992	
Extinction coefficient	n/a	
Largest diff. peak and hole	2.819 and -1.968 $e.Å^{-3}$	

Table A24. Crystal data and structure refinement for **37**.

Identification code	e15alj04	
Empirical formula	C20 H44 Mo N6 S2	
Formula weight	528.67	
Temperature	150(2) K	
Wavelength	0.71073 Å	
Crystal system	Orthorhombic	
Space group	*Pbcn*	
Unit cell dimensions	a = 15.7995(4) Å	α= 90°.
	b = 10.4585(3) Å	β= 90°.
	c = 16.0583(5) Å	γ = 90°.
Volume	2653.46(13) $Å^3$	
Z	4	
Density (calculated)	1.323 Mg/m^3	
Absorption coefficient	0.669 mm^{-1}	
F(000)	1120	
Crystal size	0.320 x 0.200 x 0.150 mm^3	
Theta range for data collection	3.449 to 30.363°.	
Index ranges	-20<=h<=19, -12<=k<=14, -18<=l<=22	
Reflections collected	24643	
Independent reflections	3693 [R(int) = 0.0391]	
Completeness to theta = 25.242°	99.8 %	
Absorption correction	Semi-empirical from equivalents	
Max. and min. transmission	1.00000 and 0.96959	
Refinement method	Full-matrix least-squares on F^2	
Data / restraints / parameters	3693 / 0 / 139	
Goodness-of-fit on F^2	1.077	
Final R indices [I>2sigma(I)]	R1 = 0.0323, wR2 = 0.0632	
R indices (all data)	R1 = 0.0437, wR2 = 0.0672	
Extinction coefficient	n/a	
Largest diff. peak and hole	0.734 and -0.294 $e.Å^{-3}$	

Table A25. Crystal data and structure refinement for **38**.

Identification code	e15alj03	
Empirical formula	C26 H40 Mo N6 S2	
Formula weight	596.70	
Temperature	150(2) K	
Wavelength	0.71073 Å	
Crystal system	Monoclinic	
Space group	$P2_1/n$	
Unit cell dimensions	a = 10.1585(3) Å	α= 90°.
	b = 16.5945(8) Å	β= 91.319(3)°.
	c = 35.1495(11) Å	γ = 90°.
Volume	5923.8(4) Å^3	
Z	8	
Density (calculated)	1.338 Mg/m^3	
Absorption coefficient	0.608 mm^{-1}	
F(000)	2496	
Crystal size	0.600 x 0.150 x 0.100 mm^3	
Theta range for data collection	3.360 to 30.357°.	
Index ranges	-14<=h<=13, -17<=k<=21, -49<=l<=39	
Reflections collected	32987	
Independent reflections	15092 [R(int) = 0.0635]	
Completeness to theta = 25.242°	99.7 %	
Absorption correction	Semi-empirical from equivalents	
Max. and min. transmission	1.00000 and 0.70027	
Refinement method	Full-matrix least-squares on F^2	
Data / restraints / parameters	15092 / 0 / 651	
Goodness-of-fit on F^2	1.111	
Final R indices [I>2sigma(I)]	R1 = 0.0836, wR2 = 0.1801	
R indices (all data)	R1 = 0.1294, wR2 = 0.2062	
Extinction coefficient	n/a	
Largest diff. peak and hole	2.162 and -0.987 e.Å^{-3}	

Table A26. Crystal data and structure refinement for **39**.

Identification code	e14alj21	
Empirical formula	C20 H44 N6 S2 W	
Formula weight	616.58	
Temperature	150(2) K	
Wavelength	0.71073 Å	
Crystal system	Orthorhombic	
Space group	*Pbcn*	
Unit cell dimensions	a = 15.7505(4) Å	α= 90°.
	b = 10.4634(3) Å	β= 90°.
	c = 16.0746(4) Å	γ = 90°.
Volume	2649.15(12) $Å^3$	
Z	4	
Density (calculated)	1.546 Mg/m^3	
Absorption coefficient	4.536 mm^{-1}	
F(000)	1248	
Crystal size	0.100 x 0.075 x 0.075 mm^3	
Theta range for data collection	3.448 to 28.370°.	
Index ranges	-19<=h<=20, -13<=k<=9, -21<=l<=21	
Reflections collected	20859	
Independent reflections	3038 [R(int) = 0.0378]	
Completeness to theta = 25.242°	99.8 %	
Absorption correction	Semi-empirical from equivalents	
Max. and min. transmission	1.00000 and 0.68719	
Refinement method	Full-matrix least-squares on F^2	
Data / restraints / parameters	3038 / 0 / 139	
Goodness-of-fit on F^2	1.096	
Final R indices [I>2sigma(I)]	R1 = 0.0256, wR2 = 0.0361	
R indices (all data)	R1 = 0.0402, wR2 = 0.0392	
Extinction coefficient	n/a	
Largest diff. peak and hole	0.446 and -0.534 $e.Å^{-3}$	

Table A27. Crystal data and structure refinement for **41**.

Identification code	k13alj19	
Empirical formula	C20 H40 Mo N4 S8	
Formula weight	688.98	
Temperature	150(2) K	
Wavelength	0.71073 Å	
Crystal system	Monoclinic	
Space group	*C*2/*c*	
Unit cell dimensions	a = 17.8258(4) Å	α= 90°.
	b = 10.2953(2) Å	β= 91.5262(10)°.
	c = 17.3515(4) Å	γ = 90°.
Volume	3183.25(12) $Å^3$	
Z	4	
Density (calculated)	1.438 Mg/m^3	
Absorption coefficient	0.954 m m^{-1}	
F(000)	1432	
Crystal size	0.200 x 0.075 x 0.050 mm^3	
Theta range for data collection	3.959 to 27.497°.	
Index ranges	-23<=h<=23, -13<=k<=13, -22<=l<=22	
Reflections collected	27512	
Independent reflections	3651 [R(int) = 0.0638]	
Completeness to theta = 25.242°	99.7 %	
Absorption correction	Semi-empirical from equivalents	
Max. and min. transmission	0.932 and 0.840	
Refinement method	Full-matrix least-squares on F^2	
Data / restraints / parameters	3651 / 0 / 163	
Goodness-of-fit on F^2	1.040	
Final R indices [I>2sigma(I)]	R1 = 0.0355, wR2 = 0.0822	
R indices (all data)	R1 = 0.0558, wR2 = 0.0908	
Extinction coefficient	n/a	
Largest diff. peak and hole	0.759 and -0.735 $e.Å^{-3}$	

Table A28. Crystal data and structure refinement for **42**.

Identification code	k14alj07	
Empirical formula	C20 H40 N4 S8 W	
Formula weight	776.89	
Temperature	150(2) K	
Wavelength	0.71073 Å	
Crystal system	Monoclinic	
Space group	*C*2/*c*	
Unit cell dimensions	a = 17.7879(3) Å	α= 90°.
	b = 10.2770(2) Å	β= 91.8212(9)°.
	c = 17.3904(2) Å	γ = 90°.
Volume	3177.47(9) $Å^3$	
Z	4	
Density (calculated)	1.624 Mg/m^3	
Absorption coefficient	4.178 mm^{-1}	
F(000)	1560	
Crystal size	0.200 x 0.125 x 0.075 mm^3	
Theta range for data collection	3.966 to 27.462°.	
Index ranges	-23<=h<=23, -13<=k<=13, -22<=l<=21	
Reflections collected	29787	
Independent reflections	3630 [R(int) = 0.0521]	
Completeness to theta = 25.242°	99.6 %	
Absorption correction	Semi-empirical from equivalents	
Max. and min. transmission	0.447 and 0.329	
Refinement method	Full-matrix least-squares on F^2	
Data / restraints / parameters	3630 / 0 / 171	
Goodness-of-fit on F^2	1.107	
Final R indices [I>2sigma(I)]	R1 = 0.0236, wR2 = 0.0525	
R indices (all data)	R1 = 0.0285, wR2 = 0.0552	
Extinction coefficient	n/a	
Largest diff. peak and hole	1.554 and -1.323 $e.Å^{-3}$	

Table A29. Crystal data and structure refinement for **43**.

Identification code	k14alj11	
Empirical formula	C12 H20 Mo O4 S8	
Formula weight	580.70	
Temperature	150(2) K	
Wavelength	0.71073 Å	
Crystal system	Monoclinic	
Space group	$P2_1/n$	
Unit cell dimensions	a = 16.1891(2) Å	α= 90°.
	b = 15.4267(2) Å	β= 102.5675(5)°.
	c = 18.5712(2) Å	γ = 90°.
Volume	4526.93(9) $Å^3$	
Z	8	
Density (calculated)	1.704 Mg/m^3	
Absorption coefficient	1.332 mm^{-1}	
F(000)	2352	
Crystal size	0.500 x 0.200 x 0.175 mm^3	
Theta range for data collection	3.526 to 27.505°.	
Index ranges	-21<=h<=20, -20<=k<=20, -24<=l<=24	
Reflections collected	63654	
Independent reflections	10307 [R(int) = 0.0484]	
Completeness to theta = 25.242°	99.2 %	
Absorption correction	Semi-empirical from equivalents	
Max. and min. transmission	0.769 and 0.640	
Refinement method	Full-matrix least-squares on F^2	
Data / restraints / parameters	10307 / 0 / 486	
Goodness-of-fit on F^2	1.176	
Final R indices [I>2sigma(I)]	R1 = 0.0309, wR2 = 0.0694	
R indices (all data)	R1 = 0.0364, wR2 = 0.0716	
Extinction coefficient	n/a	
Largest diff. peak and hole	0.840 and -0.541 $e.Å^{-3}$	

Table A30. Crystal data and structure refinement for **45**.

Identification code	k14alj15	
Empirical formula	C16 H28 Mo O4 S8	
Formula weight	636.80	
Temperature	150(2) K	
Wavelength	0.71073 Å	
Crystal system	Monoclinic	
Space group	$P2_1/n$	
Unit cell dimensions	a = 16.7622(2) Å	α= 90°.
	b = 17.9652(2) Å	β= 106.9155(5)°.
	c = 18.4697(2) Å	γ = 90°.
Volume	5321.26(11) $Å^3$	
Z	8	
Density (calculated)	1.590 Mg/m^3	
Absorption coefficient	1.141 mm^{-1}	
F(000)	2608	
Crystal size	0.500 x 0.200 x 0.175 mm^3	
Theta range for data collection	3.106 to 30.515°.	
Index ranges	-23<=h<=22, -24<=k<=24, -25<=l<=25	
Reflections collected	110375	
Independent reflections	14772 [R(int) = 0.0870]	
Completeness to theta = 25.242°	99.6 %	
Absorption correction	Semi-empirical from equivalents	
Max. and min. transmission	0.394 and 0.285	
Refinement method	Full-matrix least-squares on F^2	
Data / restraints / parameters	14772 / 0 / 539	
Goodness-of-fit on F^2	1.095	
Final R indices [I>2sigma(I)]	R1 = 0.0481, wR2 = 0.0966	
R indices (all data)	R1 = 0.0889, wR2 = 0.1087	
Extinction coefficient	n/a	
Largest diff. peak and hole	0.968 and -1.238 $e.Å^{-3}$	

EDX spectra

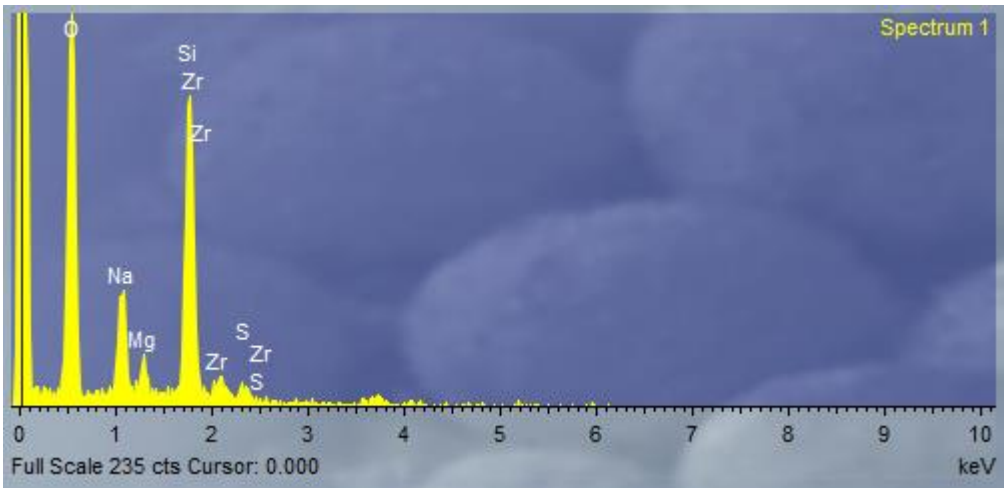

Figure A1. EDX spectrum of the AACVD film deposited on glass at 325 °C using precursor **5**.

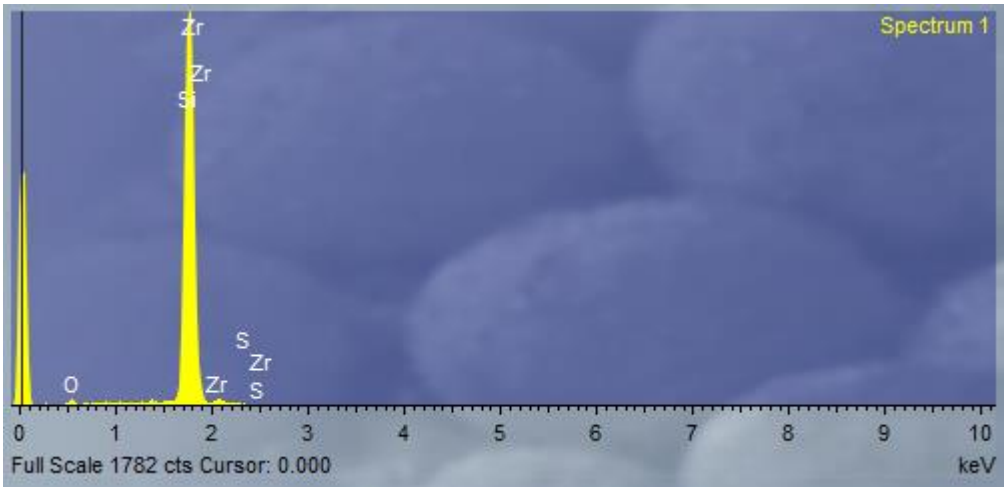

Figure A2. EDX spectrum of the AACVD film deposited on silicon at 325 °C using precursor **5**.

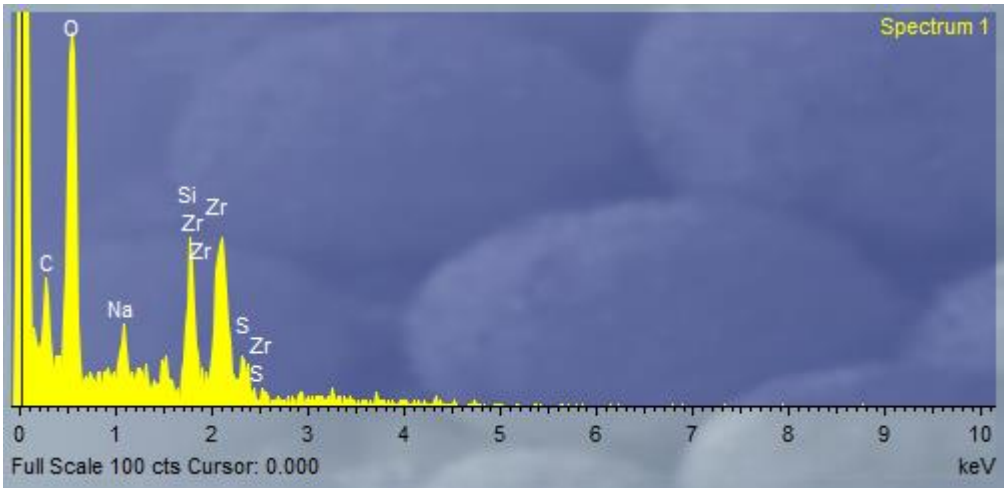

Figure A3. EDX spectrum of the AACVD film deposited on glass at 300 °C using precursor **6**.

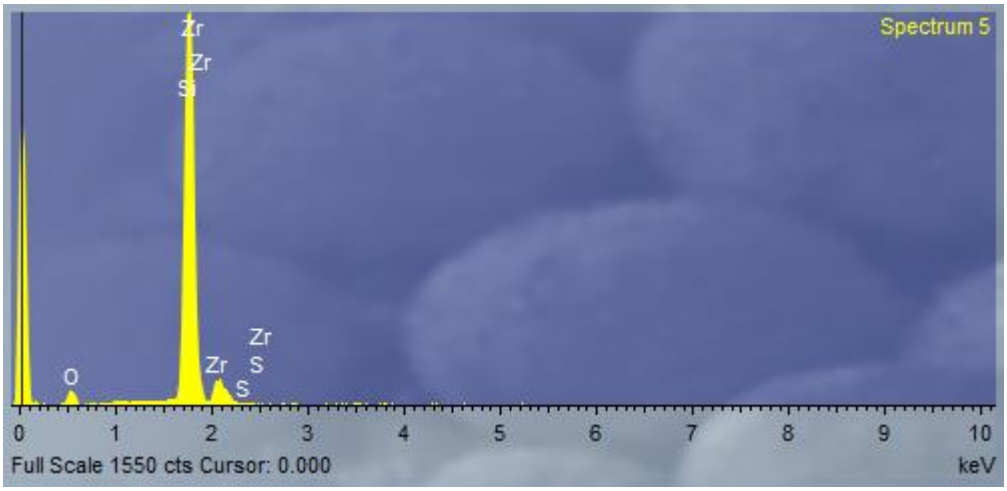

Figure A4. EDX spectrum of the AACVD film deposited on silicon at 300 °C using precursor **6**.

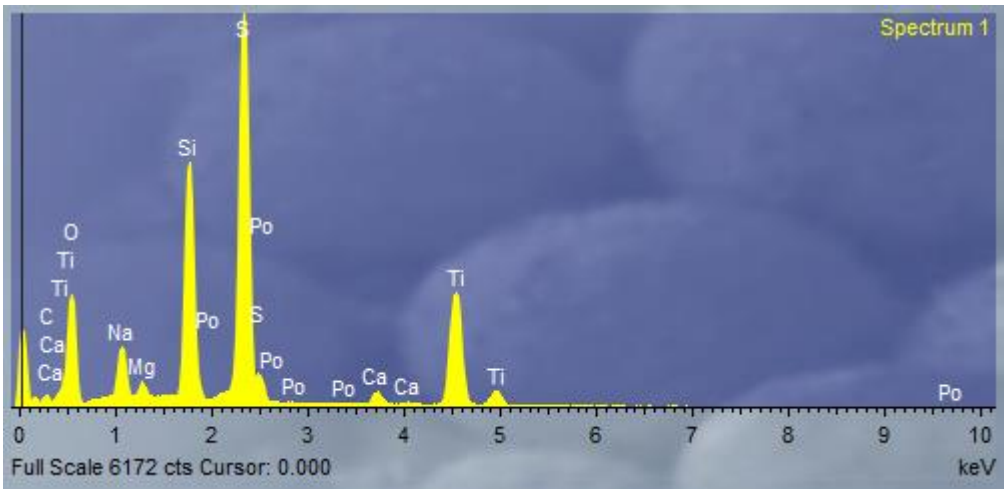

Figure A5. EDX spectrum of the LPCVD film deposited on glass at 350 °C using precursor **11**.

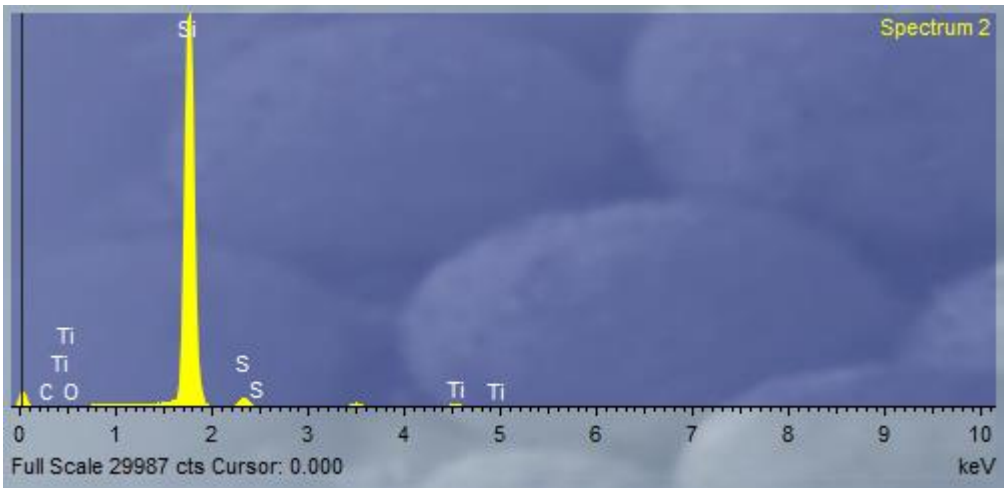

Figure A6. EDX spectrum of the LPCVD film deposited on silicon at 350 °C using precursor **11**.

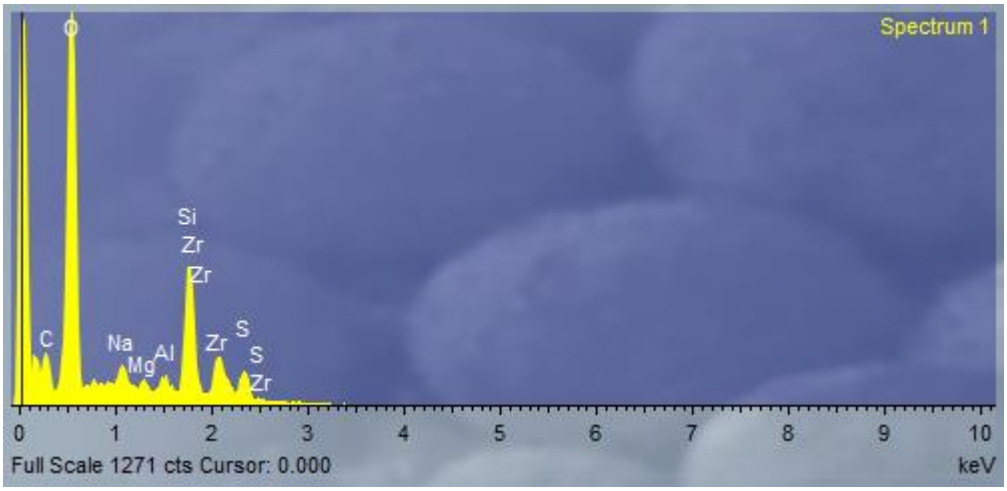

Figure A7. EDX spectrum of the LPCVD film deposited on glass at 400 °C using precursor **12**.

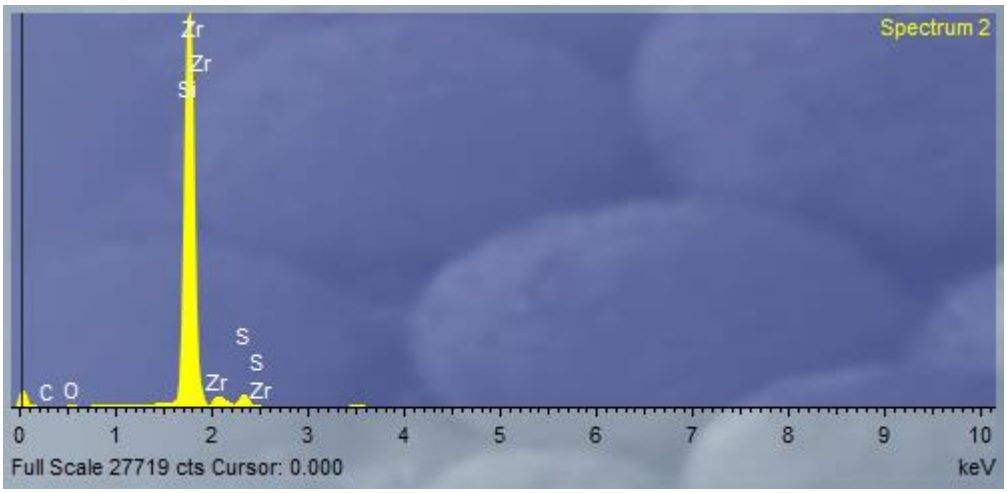

Figure A8. EDX spectrum of the LPCVD film deposited on silicon at 400 °C using precursor **12**.

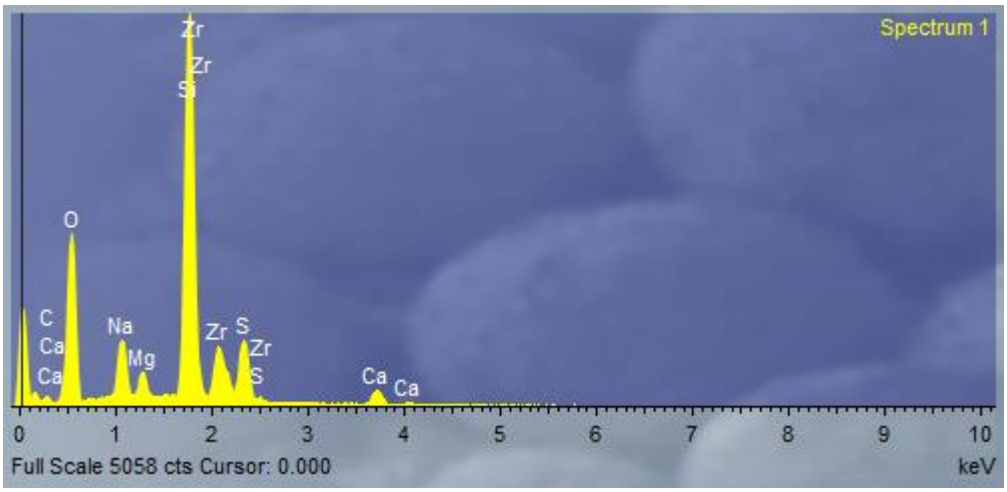

Figure A9. EDX spectrum of the LPCVD film deposited on glass at 425 °C using precursor **12**.

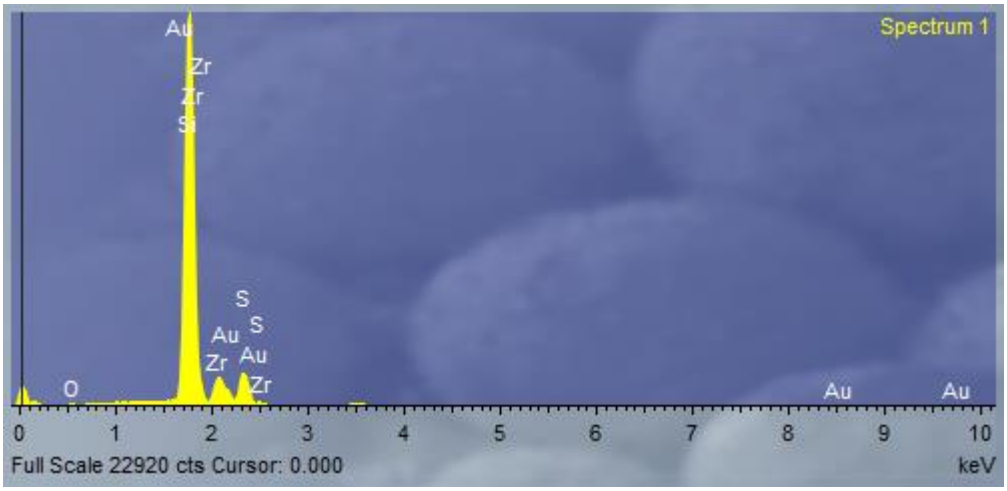

Figure A10. EDX spectrum of the LPCVD film deposited on silicon at 425 °C using precursor **12**.

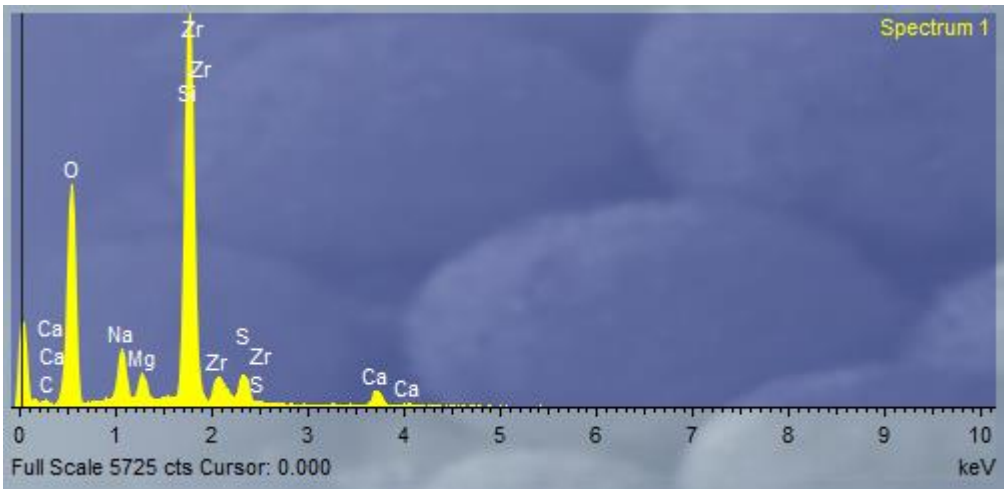

Figure A11. EDX spectrum of the LPCVD film deposited on glass at 450 °C using precursor **12**.

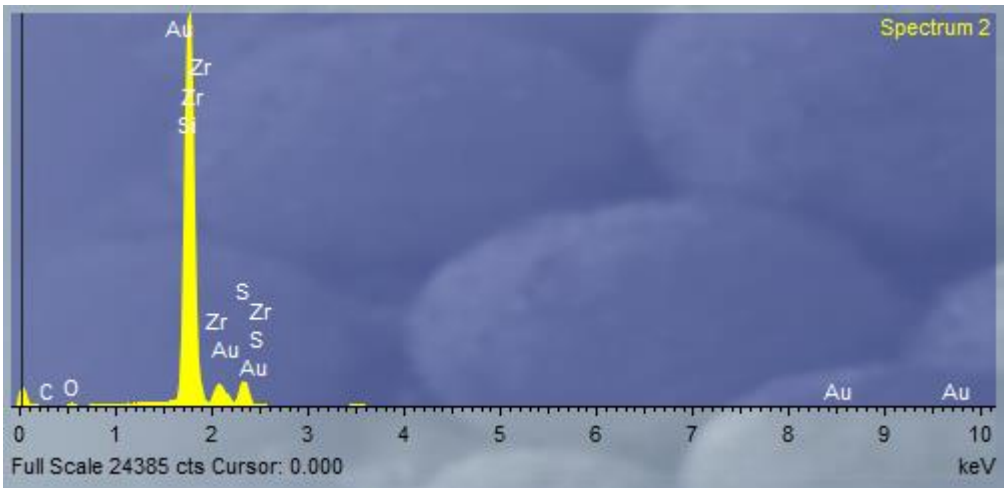

Figure A12. EDX spectrum of the LPCVD film deposited on silicon at 450 °C using precursor **12**.

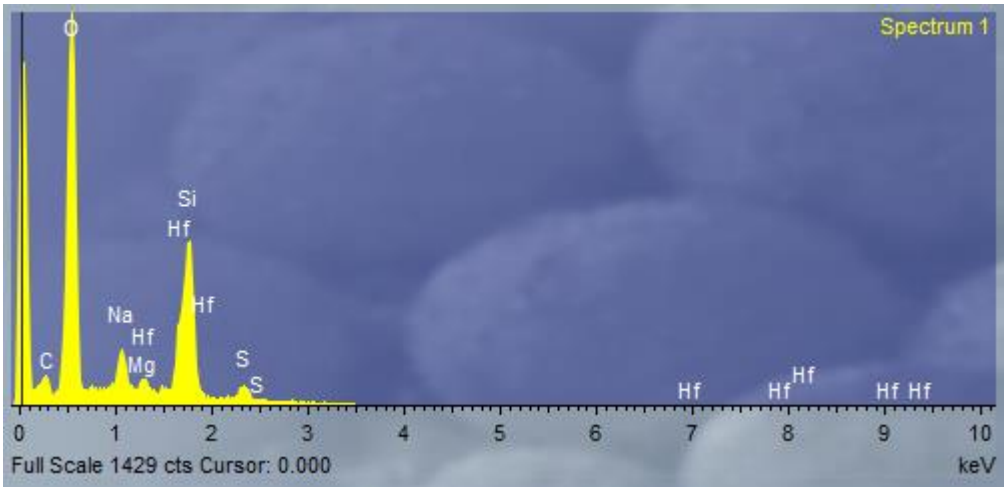

Figure A13. EDX spectrum of the LPCVD film deposited on glass at 400 °C using precursor **13**.

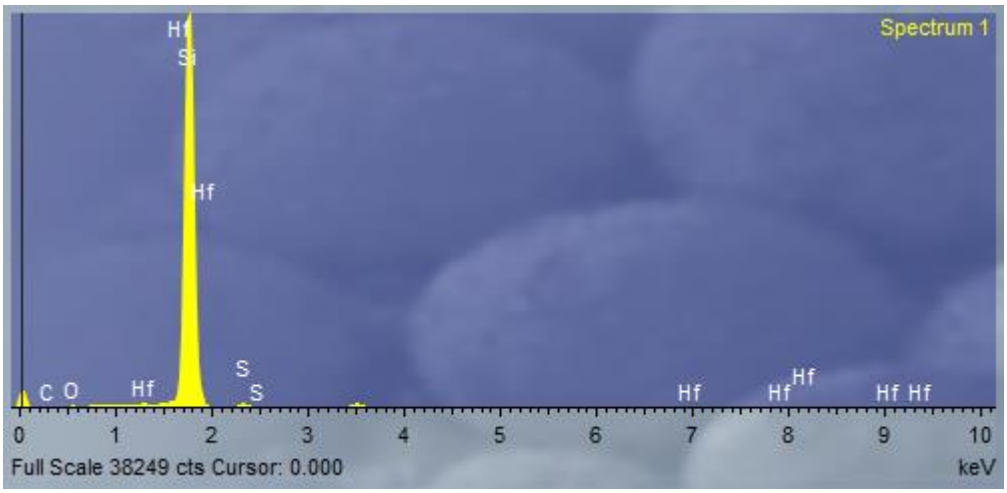

Figure A14. EDX spectrum of the LPCVD film deposited on silicon at 400 °C using precursor **13**.

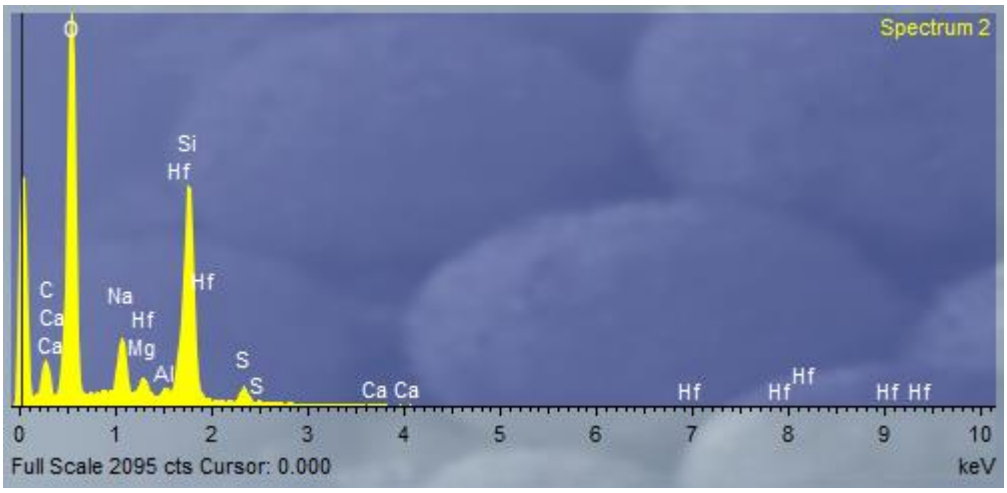

Figure A15. EDX spectrum of the LPCVD film deposited on glass at 425 °C using precursor **13**.

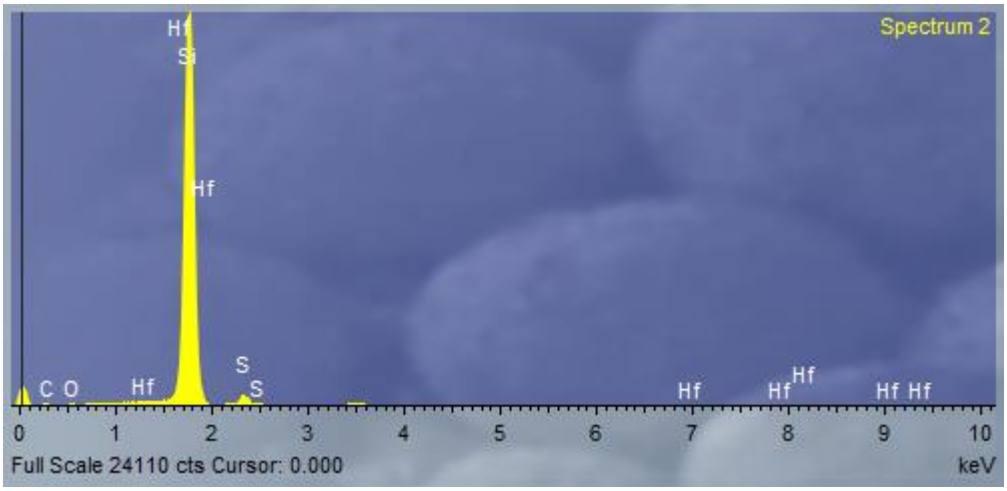

Figure A16. EDX spectrum of the LPCVD film deposited on silicon at 425 °C using precursor **13**.

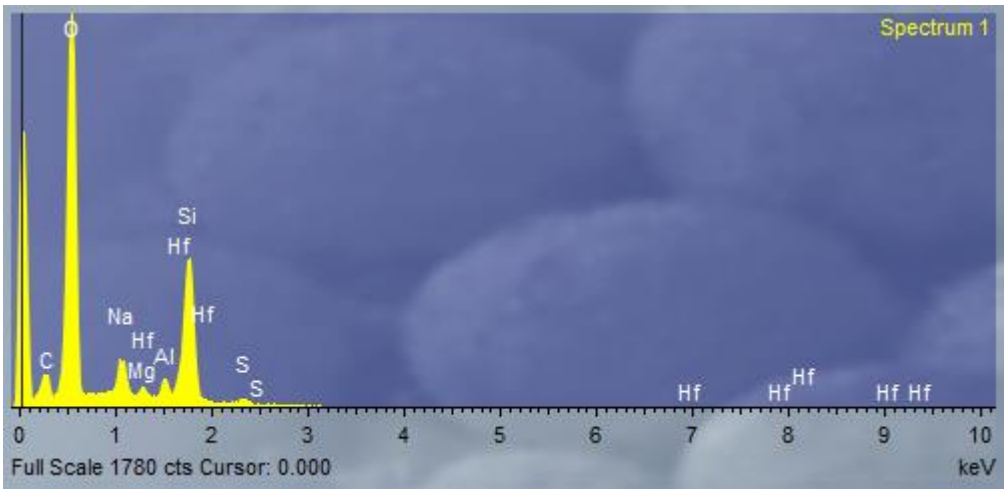

Figure A17. EDX spectrum of the LPCVD film deposited on glass at 450 °C using precursor **13**.

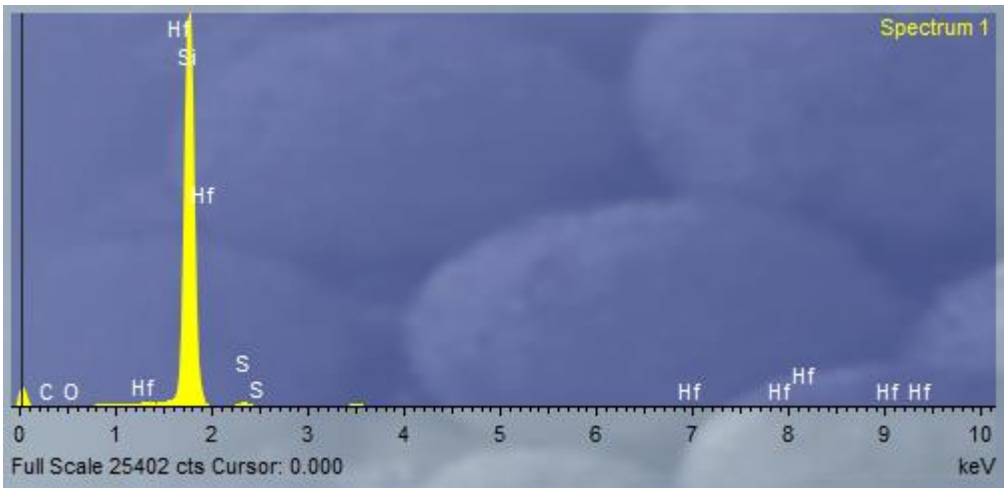

Figure A18. EDX spectrum of the LPCVD film deposited on silicon at 450 °C using precursor **13**.

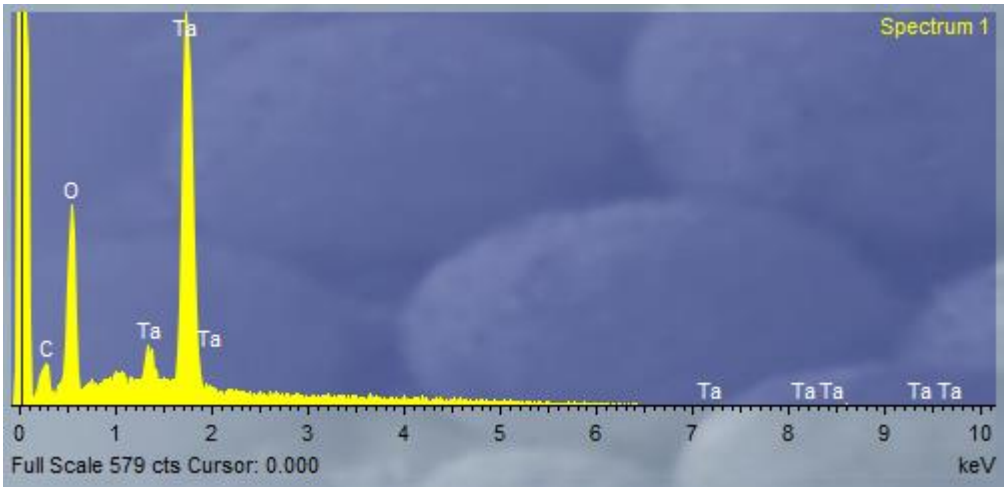

Figure A19. EDX spectrum of the AACVD film deposited on glass at 400 °C using precursor **24**.

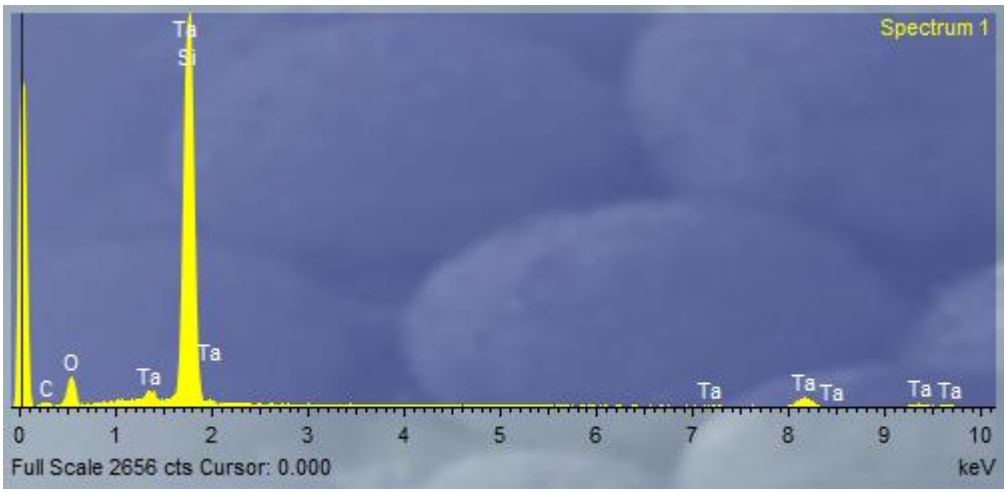

Figure A20. EDX spectrum of the AACVD film deposited on silicon at 400 °C using precursor **24**.

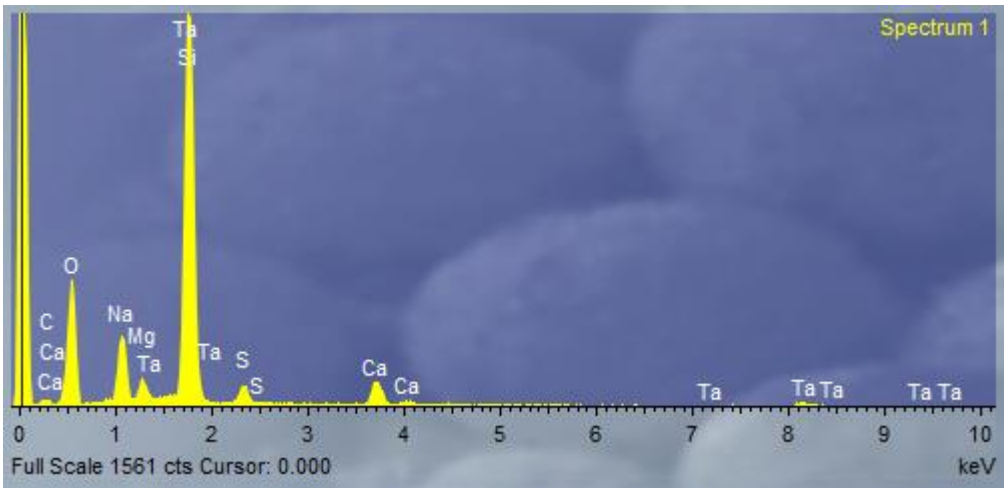

Figure A21. EDX spectrum of the LPCVD film deposited on glass at 375 °C using precursor **24**.

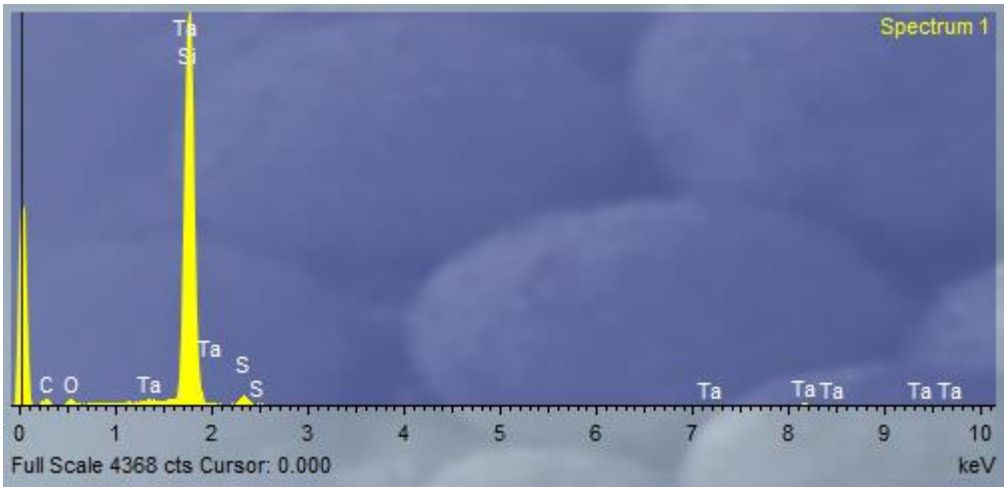

Figure A22. EDX spectrum of the LPCVD film deposited on silicon at 375 °C using precursor **24**.

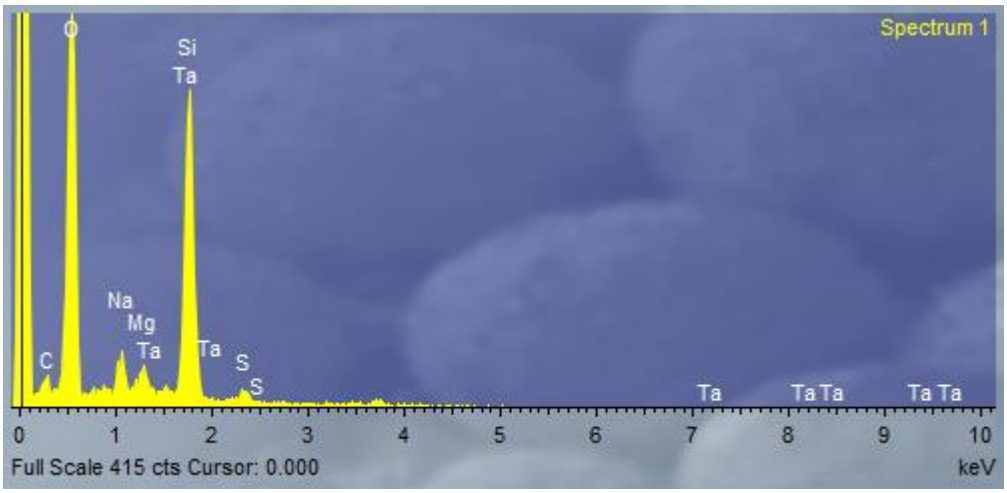

Figure A23. EDX spectrum of the LPCVD film deposited on glass at 400 °C using precursor **24**.

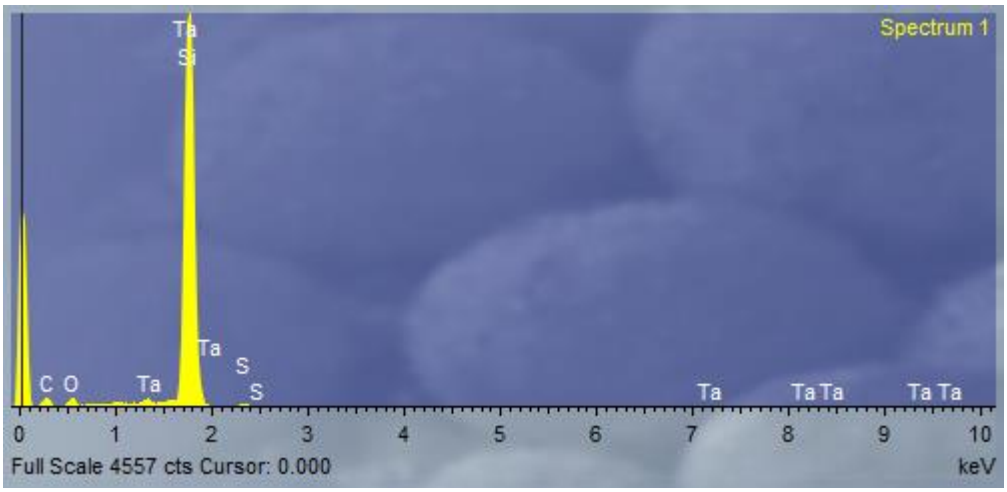

Figure A24. EDX spectrum of the LPCVD film deposited on silicon at 400 °C using precursor **24**.

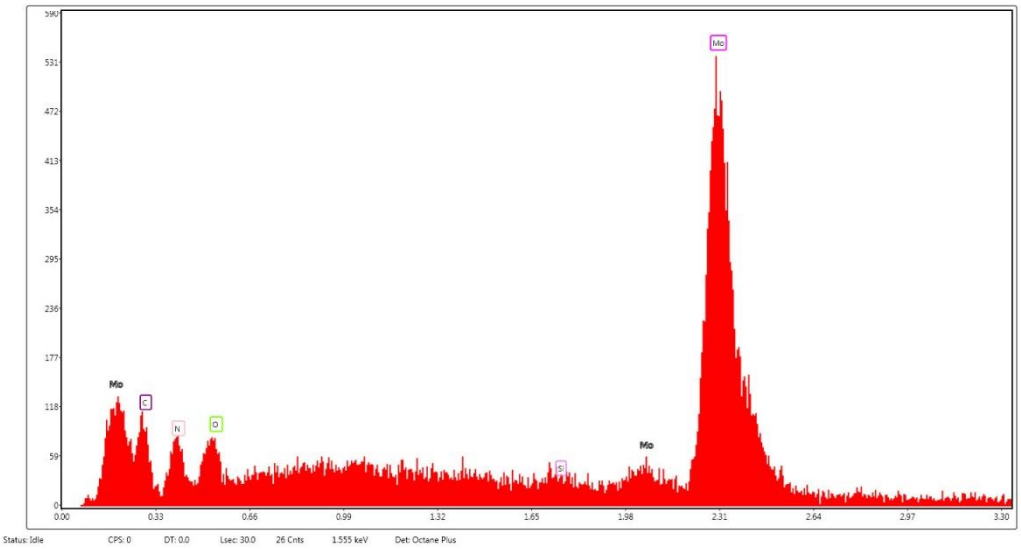

Figure A25. EDX spectrum of the AACVD film deposited on glass at 500 °C using precursor **37**.

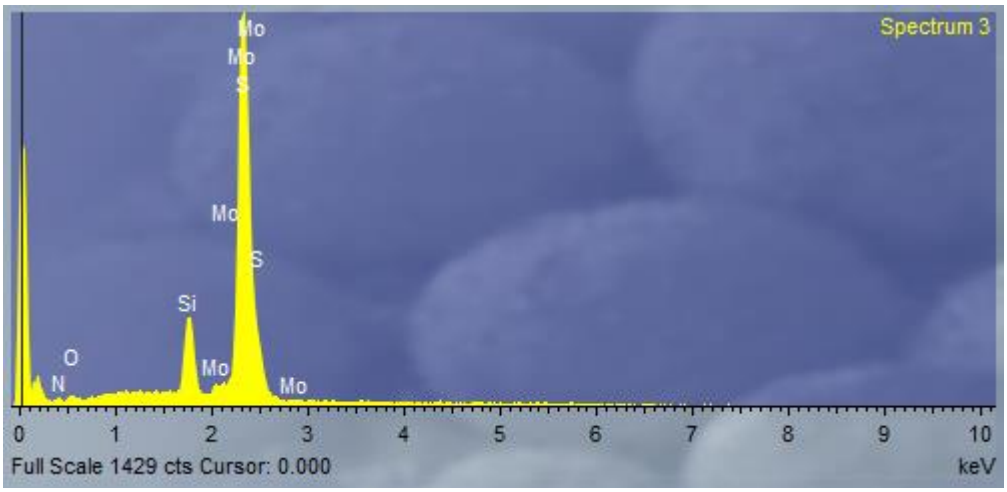

Figure A26. EDX spectrum of the AACVD film deposited on silicon at 500 °C using precursor **37**.

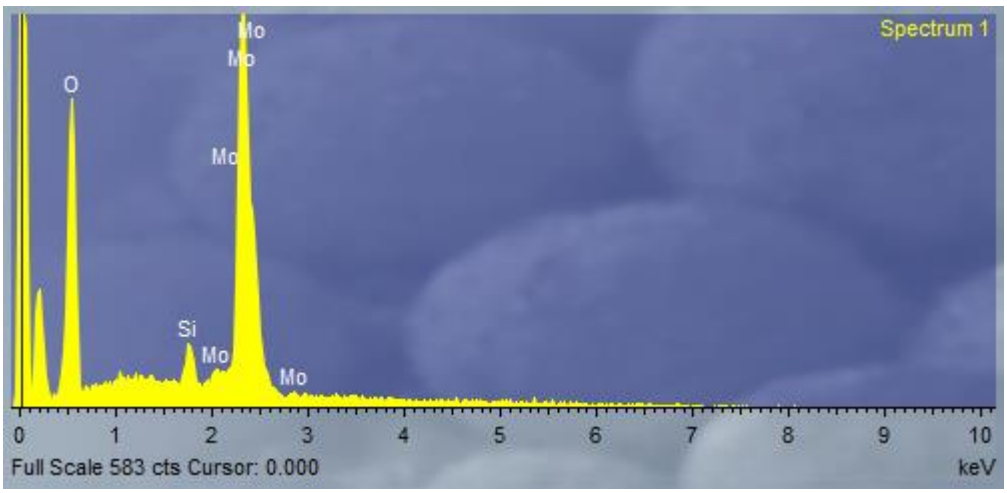

Figure A27. EDX spectrum of the annealed film deposited on glass at 500 °C using precursor **37**.

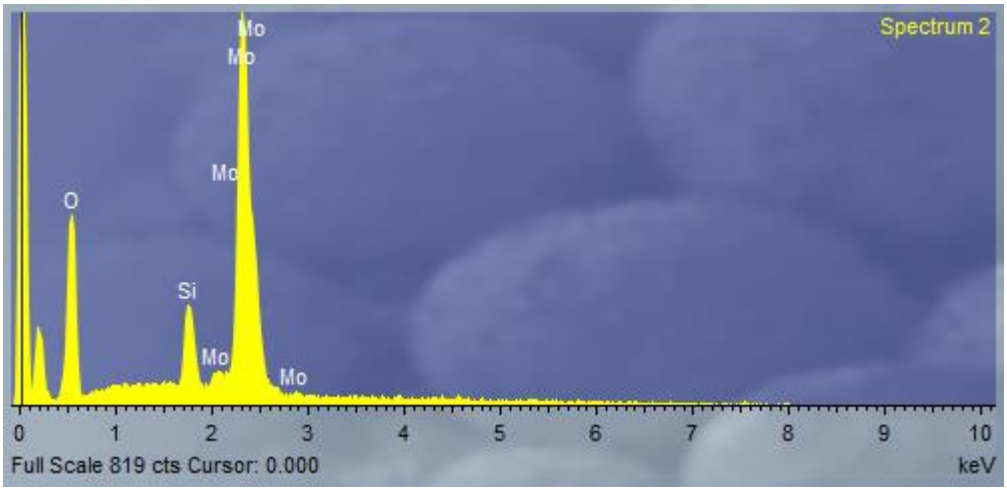

Figure A28. EDX spectrum of the annealed film deposited on silicon at 500 °C using precursor **37**.

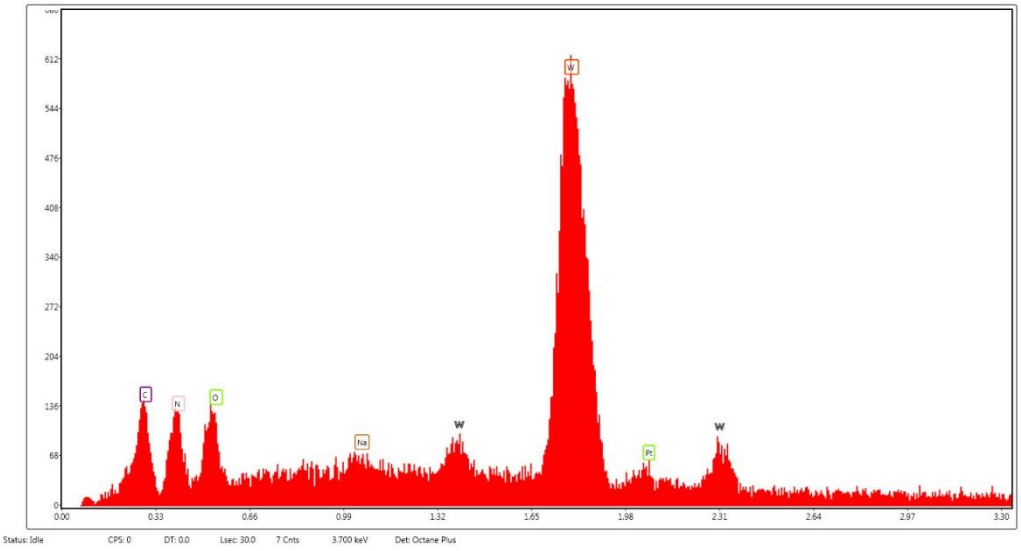

Figure A29. EDX spectrum of the AACVD film deposited on glass at 500 °C using precursor **39**.

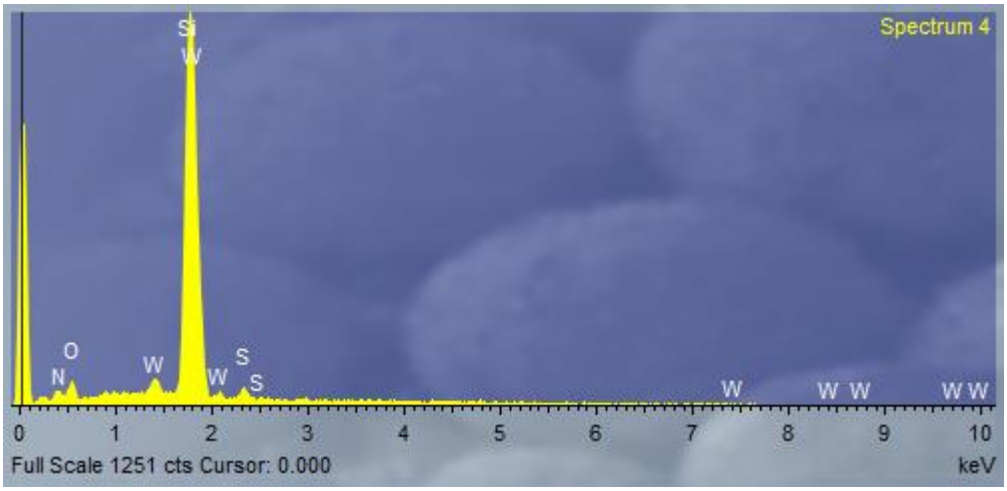

Figure A30. EDX spectrum of the AACVD film deposited on silicon at 500 °C using precursor **39**.

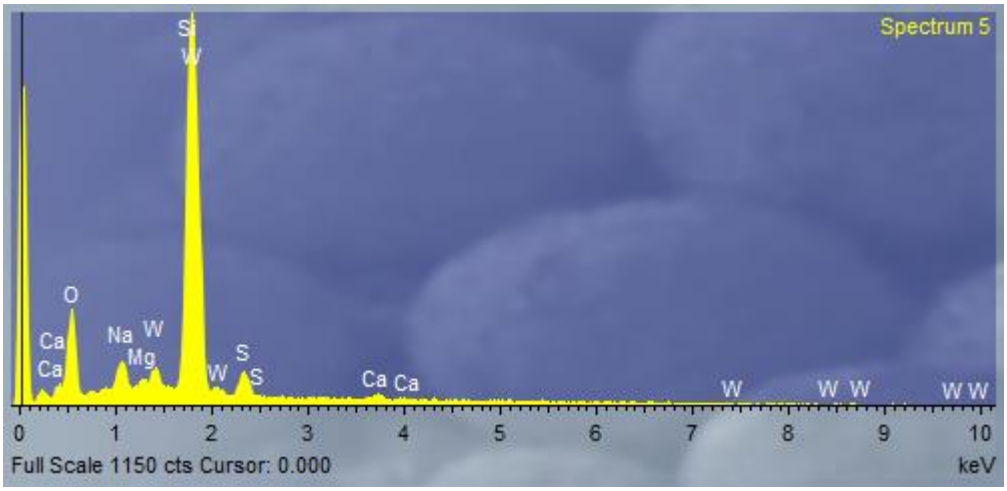

Figure A31. EDX spectrum of the annealed film deposited on glass at 500 °C using precursor **39**.

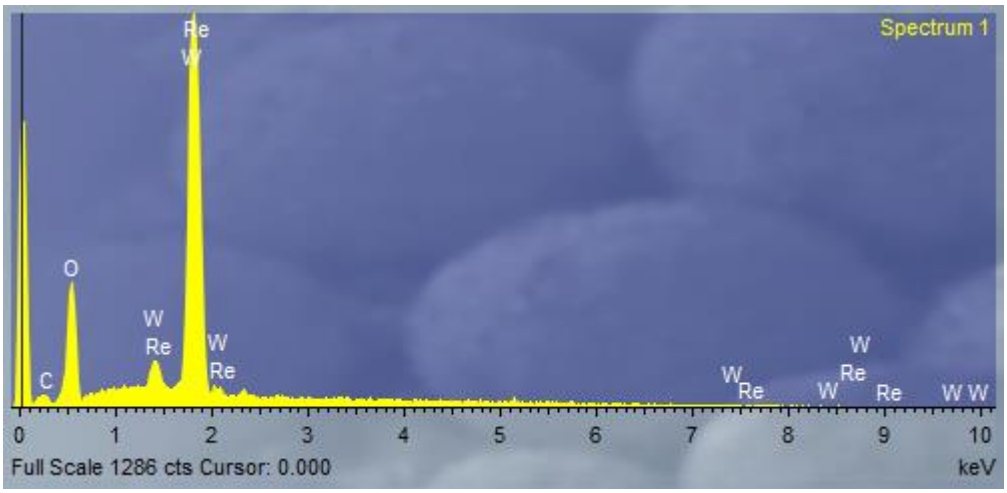

Figure A32. EDX spectrum of the annealed film deposited on silicon at 500 °C using precursor **39**.

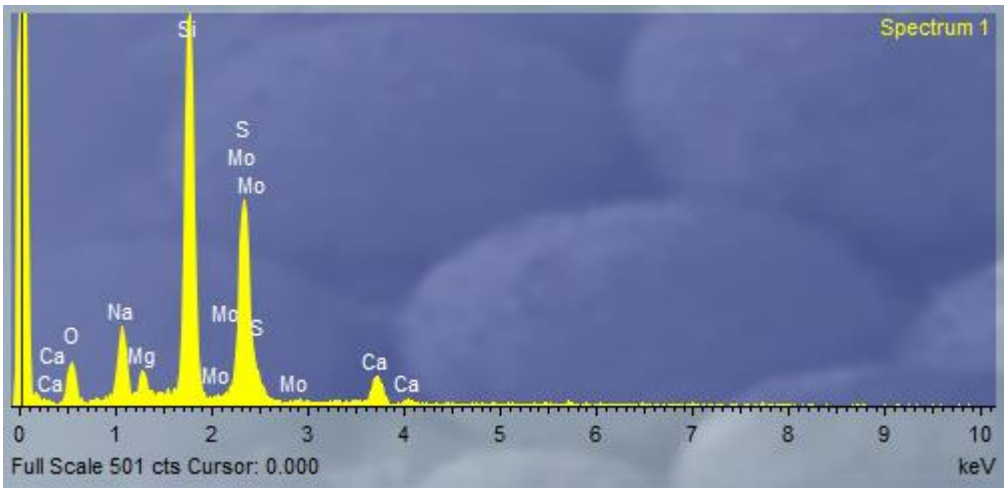

Figure A33. EDX spectrum of the AACVD film deposited on glass at 400 °C using precursor **41**.

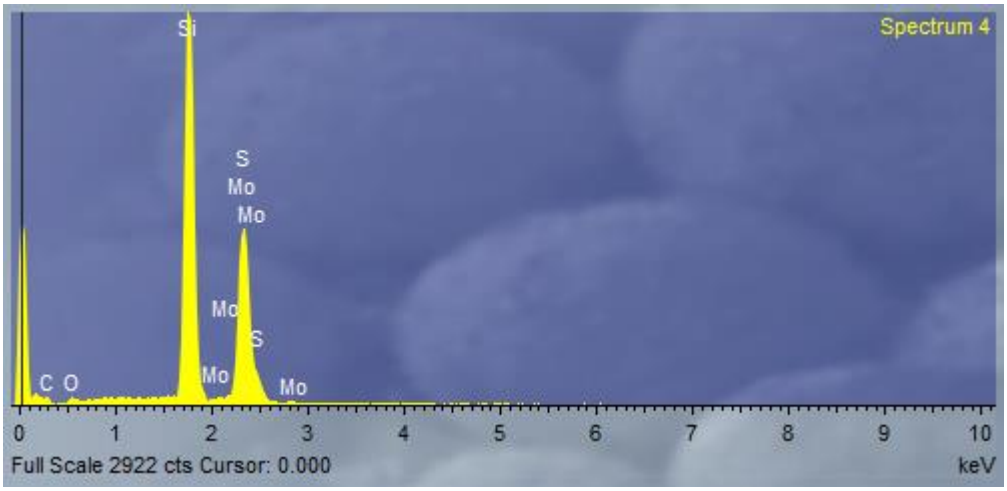

Figure A34. EDX spectrum of the AACVD film deposited on silicon at 400 °C using precursor **41**.

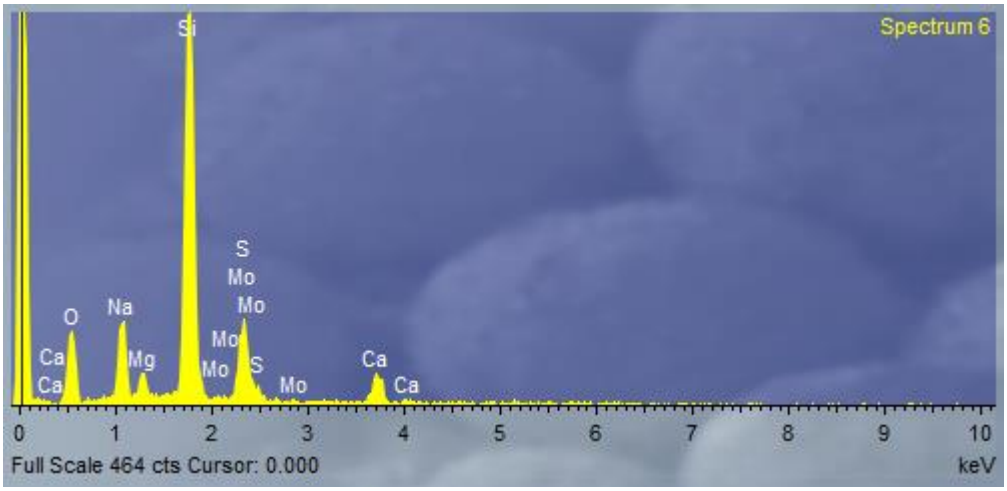

Figure A35. EDX spectrum of the AACVD film deposited on glass at 450 °C using precursor **41**.

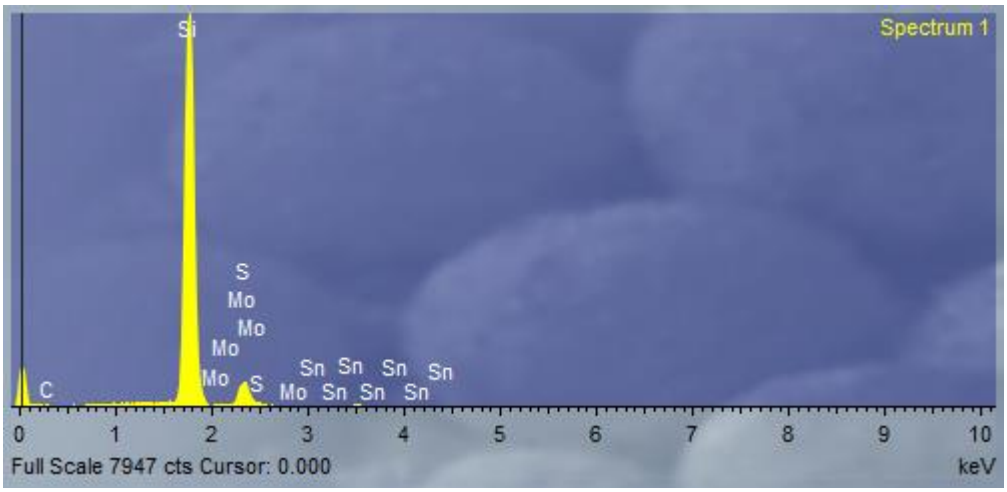

Figure A36. EDX spectrum of the AACVD film deposited on silicon at 450 °C using precursor **41**.

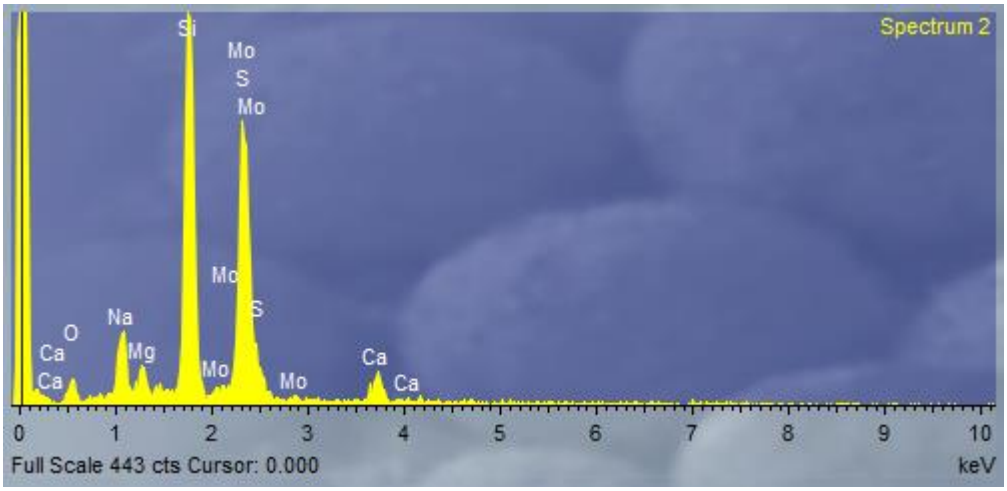

Figure A37. EDX spectrum of the AACVD film deposited on glass at 500 °C using precursor **41**.

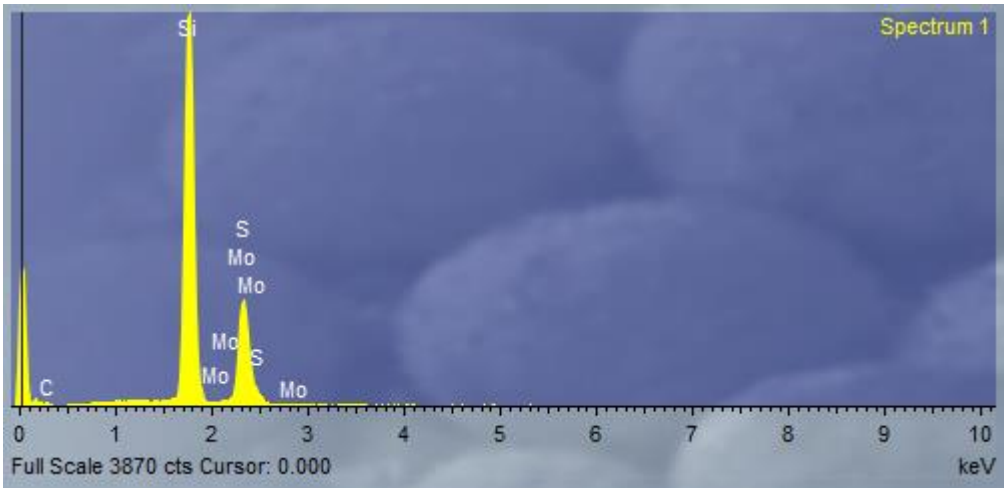

Figure A38. EDX spectrum of the AACVD film deposited on silicon at 500 °C using precursor **41**.

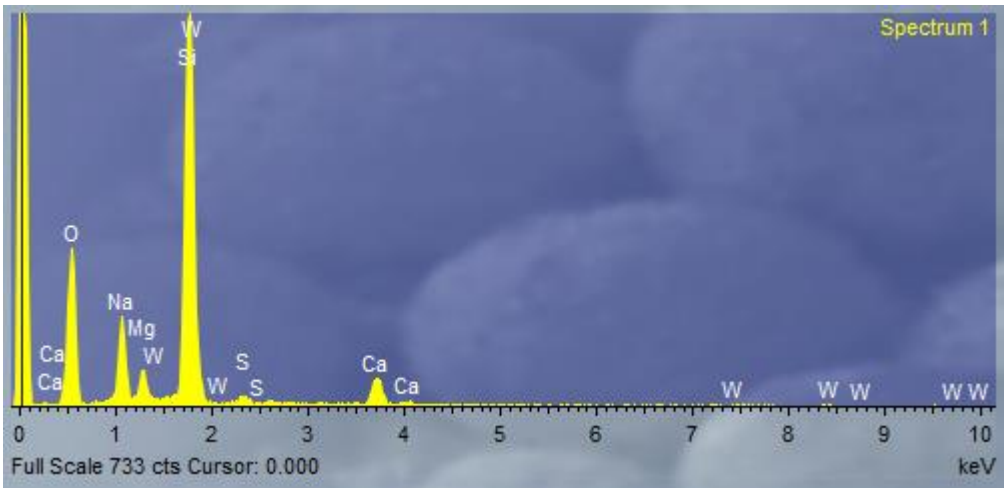

Figure A39. EDX spectrum of the AACVD film deposited on glass at 400 °C using precursor **42**.

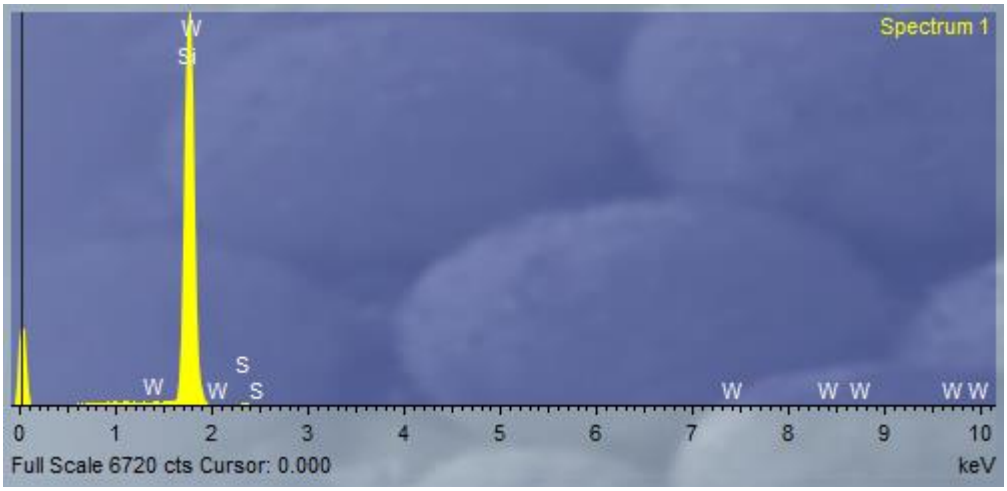

Figure A40. EDX spectrum of the AACVD film deposited on silicon at 400 °C using precursor **42**.

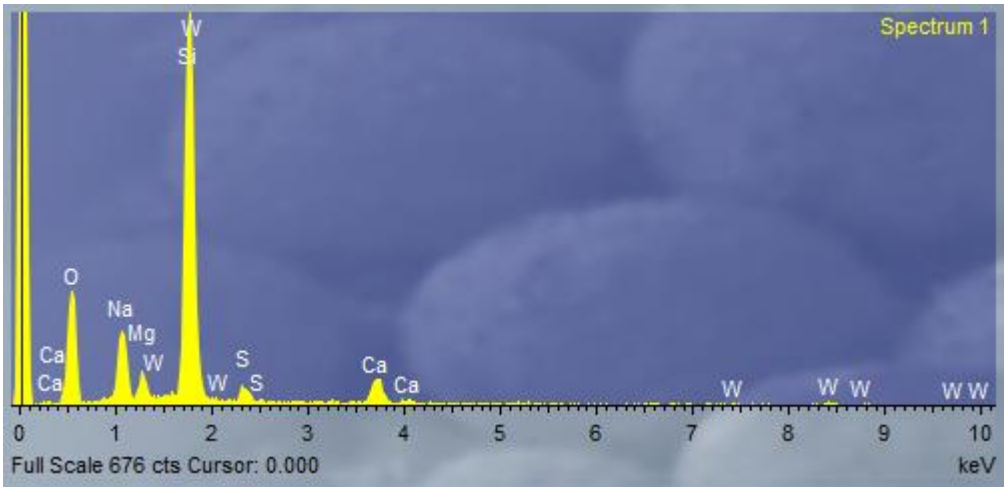

Figure A41. EDX spectrum of the AACVD film deposited on glass at 450 °C using precursor **42**.

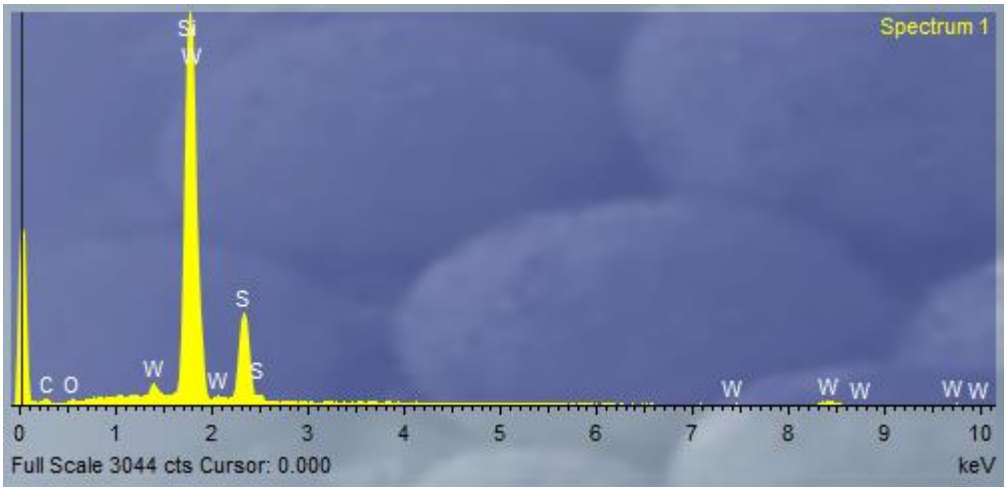

Figure A42. EDX spectrum of the AACVD film deposited on silicon at 450 °C using precursor **42**.

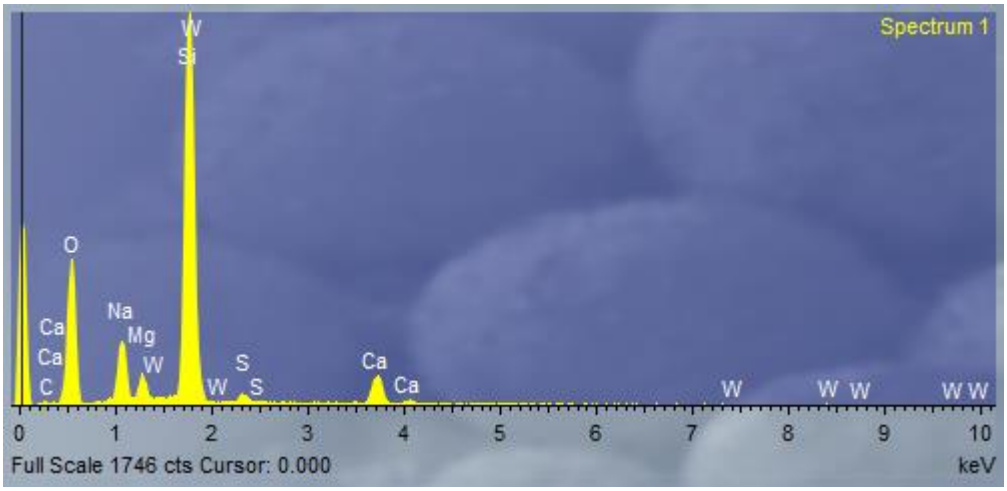

Figure A43. EDX spectrum of the AACVD film deposited on glass at 500 °C using precursor **42**.

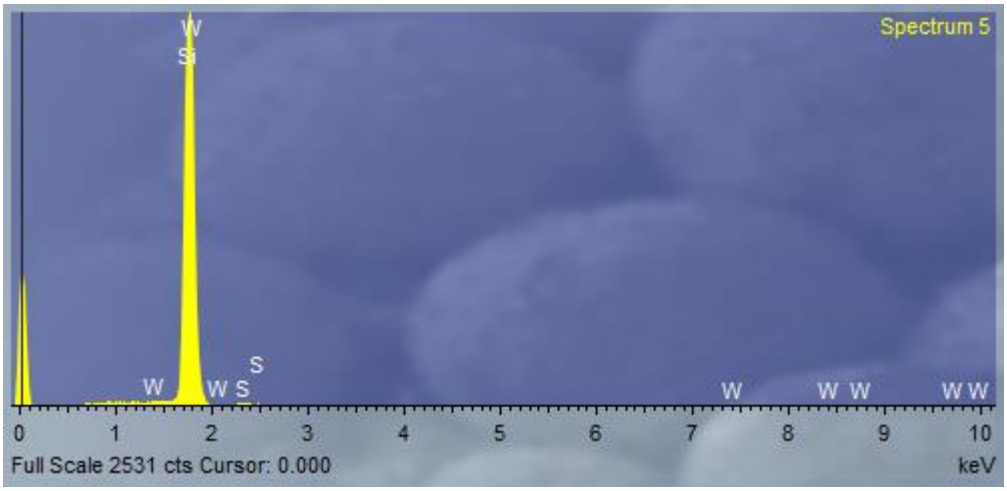

Figure A44. EDX spectrum of the AACVD film deposited on silicon at 500 °C using precursor **42**.

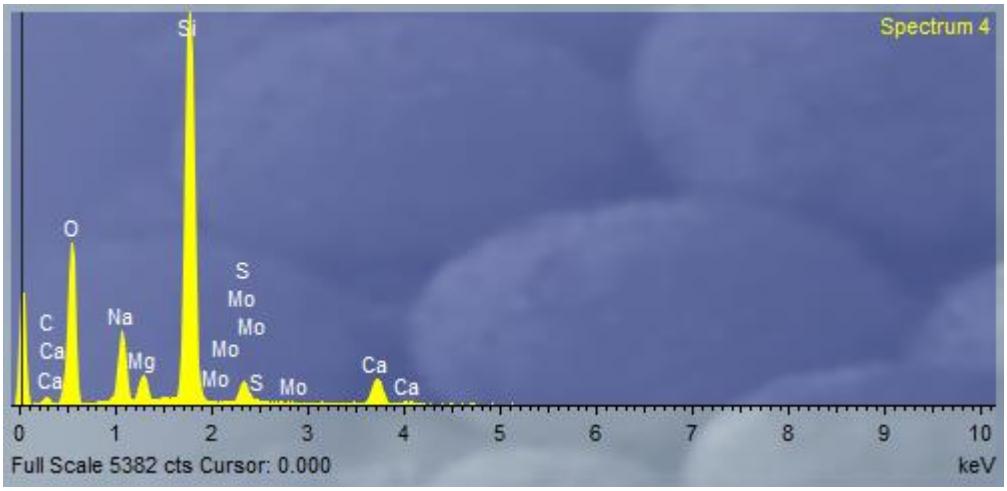

Figure A45. EDX spectrum of AACVD film deposited on glass at 350 °C using precursor **43**.

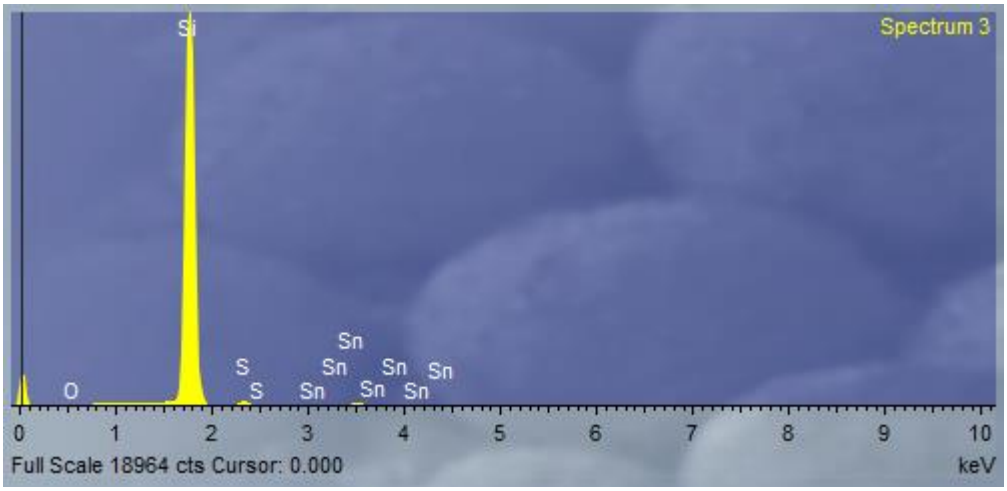

Figure A46. EDX spectrum of AACVD film deposited on silicon at 350 °C using precursor **43**.

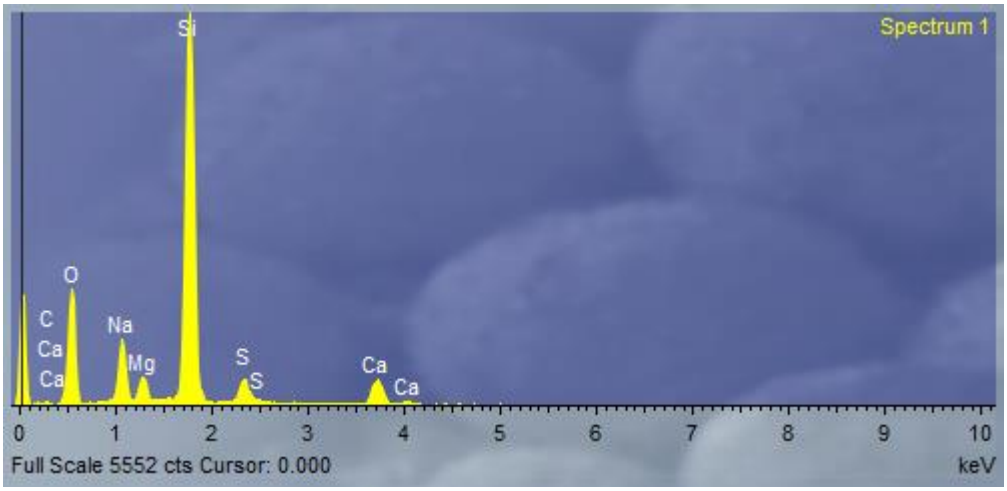

Figure A47. EDX spectrum of AACVD film deposited on glass at 400 °C using precursor **43**.

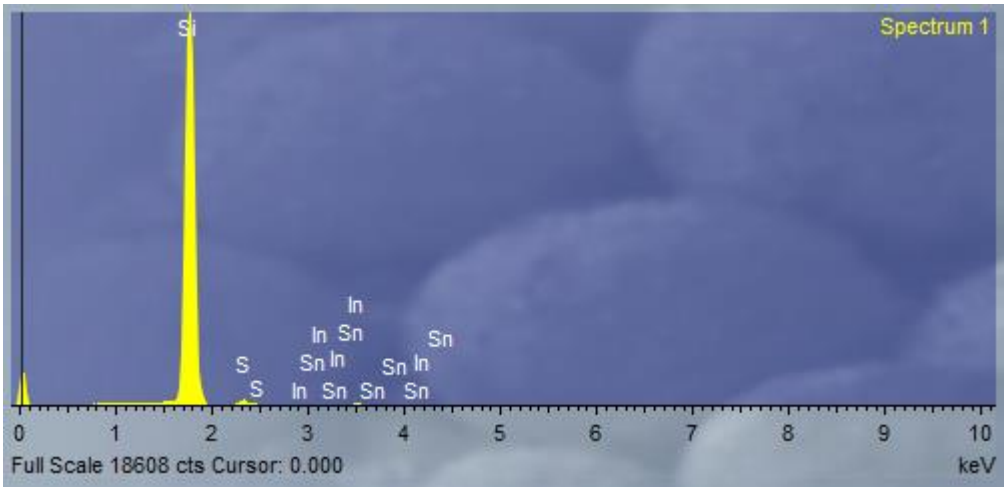

Figure A48. EDX spectrum of AACVD film deposited on silicon at 400 °C using precursor **43**.

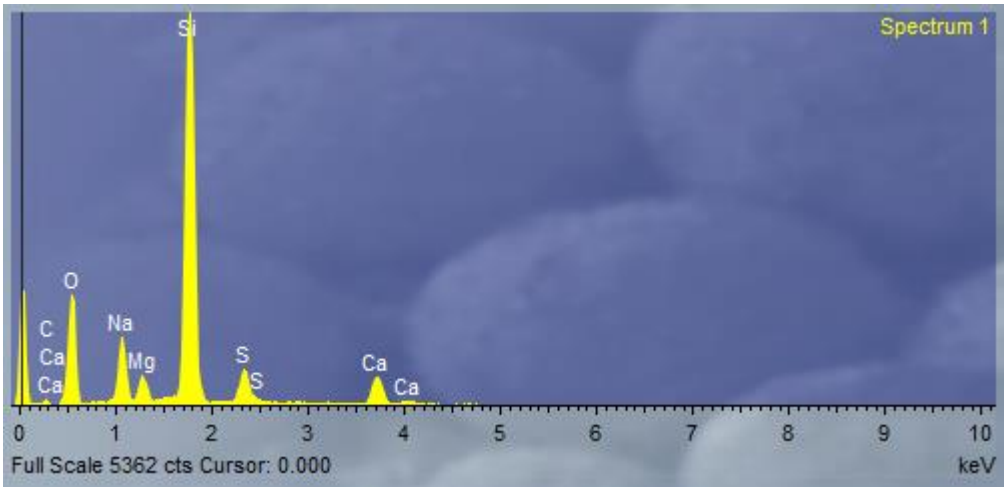

Figure A49. EDX spectrum of AACVD film deposited on glass at 450 °C using precursor **43**.

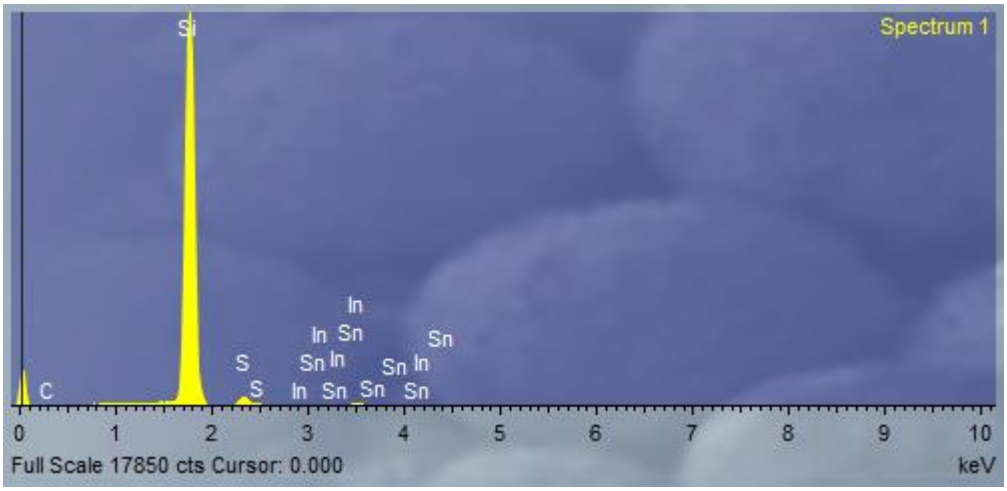

Figure A50. EDX spectrum of AACVD film deposited on silicon at 450 °C using precursor **43**.